Talanta

The International Journal of Pure and Applied Analytical Chemistry

Review

Assessing petroleum oils biodegradation by chemometric analysis of spectroscopic data

O. Abbas [a], C. Rebufa [a,*], N. Dupuy [a], A. Permanyer [b], J. Kister [a]

[a] *Systèmes Chimiques Complexes, UMR 6171, Université Paul Cézanne, case 451, 13397 Marseille Cedex 20, France*
[b] *Dpt de Geoquímica, Petrologia i Prospecció Geològica, Universitat de Barcelona, Martí i Franquès, s/n. 08028 Barcelona, Spain*

Abstract

This study was conducted to classify petroleum oils in terms of their biodegradation stage by using spectroscopic analysis associated to chemometric treatments. Principal Component Analysis (PCA) has been applied on infrared and UV fluorescence spectra of Brazilian and Pyrenean oils. For Brazil samples, the method allowed to distinguish the biodegraded oils from the non-affected ones. Pyrenean sampling including oils at different levels of biodegradation has been chosen to follow their alteration rate.

PCA loadings have shown spectral regions which have differentiated oils after biodegradation whereas Simple-to-use Interactive Self-Modelling Mixture Analysis (SIMPLISMA) has permitted to obtain a repartition in terms of components families (saturated, aromatic and polar ones) characterizing chemical composition of oils at different biodegradation degrees. Results are in good agreement with conclusions of usual hydrocarbon biomarker analysis.
© 2008 Elsevier B.V. All rights reserved.

Keywords: Chemometric; Biodegradation; Petroleum oils; FTIR; Fluorescence; PCA; SIMPLISMA

Contents

* Corresponding author. Tel.: +33 4 91 28 80 91; fax: +33 4 91 28 91 52.
  E-mail address: c.rebufa@univ-cezanne.fr (C. Rebufa).

1. Introduction

The quality of petroleum is mainly influenced by its gravity and viscosity which depend greatly on maturity and biodegradation of oil. Biodegradation modifies oil properties and its chemical composition inducing the diminution of its API (American Petroleum Institute) gravity which is used as oil quality factor in petroleum industry. A strong deterioration of petroleum quality occurs from slight to moderate biodegradation [1]. The biodegradation increases the relative content of resins and asphaltenes, metals (like vanadium and nickel) and sulfur by selectively removing saturate and aromatic hydrocarbons.

Biodegradation may be caused by aerobic bacteria when there is an access to surface recharge waters containing oxygen in a temperature range below 65–75 °C. In deep reservoirs, in which meteoric recharge appeared infeasible, anaerobic bacteria are considered of prime importance [2].

Aerobic and anaerobic microbial degradations follow a general sequence of chemical structures destruction where less resistant compounds classes are attacked prior to the most resistant ones following an order [1] established on the basis of Gas Chromatography (GC) and Gas Chromatography/Mass Spectrometry (GC/SM) analyses: *most susceptible n*-paraffins (*n*-alkanes) > acyclic isoprenoids (norpristane, pristane, phytane, etc. . .) > hopanes (25-norhopanes present) ≥ steranes > hopanes (no 25-norhopanes) ~ diasteranes > aromatic steroids > porphyrins: *least susceptible*). The relative susceptibilities of regular steranes to biodegradation vary depending on circumstances, types of bacteria and chemical characteristic of crude oil [3].

GC and GC/MS are powerful tools for petroleum oils characterization by providing detailed information about their chemical composition. Thus, using the presence or the absence of various biomarkers, petroleum oils can be classified following a scale from 1 to 10 proposed by Peters and Moldowan [2] where "1" indicates a very early degradation (partial loss of *n*-paraffins) and "10" corresponds to a severely oil degradation. These techniques permit a more comprehensive assessment of biodegradation by estimating the loss of *n*-paraffins, acyclic isoprenoids, steranes, terpanes and aromatic steroids [4–7]. Polar compounds [8,9] such as phenols, acids and carbazoles have also been considered as indicators of microbial alteration of oil but their identification required the use of Electrospray Ionization Fourier Transform Ion Cyclotron Resonance Mass Spectrometry [10]. Nevertheless these techniques lead to the destruction of samples and consume much time to separate the different fractions (*n*-alkanes, aromatic and polar ones). Some authors have tried to reduce interpretation time of the large chromatographic data (GC–MS/SIM) by using on chemometric treatments (PCA and Weighted-Least-Square PCA (WLS-PCA) with different preprocessing (alignment and normalization) of chromatograms

sections to decrease variations [11,12]. PCA on oils biomarker data has also permitted to confirm the subdivision in oil families, established on the basis of the molecular and isotopic characteristics [13,14].

Because petroleum development operation is much cost, it could be interesting to look for alternative or complementary methods like spectroscopic techniques, rapid and simple to use in order to evaluate the distribution of chemical compounds families in oil, by a global approach.

Recently, infrared and fluorescence measurements have been used in the field of petroleum development. Investigations were reported to study reservoir continuity [15] and to evaluate thermal maturity [16,17]. Among the several methods of spectroscopic data interpretation, we can talk about the works of Kister and al. [18,19] where indexes have been calculated from area of absorption bands to describe the global structure of oils by Fourier Transformed Infra Red (FTIR) analysis and their aromatic structures by Synchronous excitation–emission Ultra Violet Fluorescence (SUVF). FTIR spectroscopy was used to determine aliphatic, aromatic and functionalized characters for each oil while condensation degree of aromatic rings has been evaluated by Synchronous Ultra Violet Fluorescence analysis [20–23]. Unfortunately calculation of spectroscopic indexes requires much time and is limited when an advanced biodegradation occurs. In this case, some spectral IR bands are overlapped and prevent to integrate area and consequently to calculate the relative indexes (based on the ratio of a specific absorption band area to the sum of all integrated bands area). To avoid these problems, we have proposed chemometric methods which treat the bulk of spectra simultaneously and do not depend on one specific band.

In earlier studies [24,25], we have used mathematical models like PCA (Principal Component Analysis), PLS (Partial Least Squares) and SIMPLISMA (Simple-to-use Interactive Self-Modelling Mixture Analysis) to discriminate, to predict oils geochemical origin and to define compounds families characterizing oils composition, respectively. In the present work, we use the same methodology by applying PCA and SIMPLISMA on spectroscopic data (FTIR-ATR and SUVF spectra) of two oil groups, "Brazilian" and "Pyrenean" samples. The objective is to classify them in function of their biodegradation degree and to identify from PCA loading, the spectral regions which differentiate oils affected or not by the microbial degradation. To know more precisely what chemical structures have been altered by biodegradation process, we have applied SIMPLISMA on FTIR-ATR data to extract mathematically spectra of compounds families describing respectively saturated, aromatic or polar components present in oils. Their associated concentration profiles have permitted to evaluate their relative contribution in oil composition and to visualize their relative abundance according to alteration degree of oils. As

IR absorption bands at $1600\,cm^{-1}$ describing aromatics have been badly resolved (because of the presence of water in some oils) or overlapped (when oil is oxidized), we have resolved SUVF spectra with PCA and SIMPLISMA to estimate the bacterial alteration of their polyaromatic hydrocarbons and to differentiate oils in terms of their rings condensation degree. The aim is to show that the combination of spectroscopic techniques and chemometric tools can be considered as suitable analytical methods for an initial screening of oils state which implies classification of samples and detection of biodegraded oils as proposed by some authors who have used gas chromatography with flame ionization detection and fluorescence spectroscopy [26].

This global approach of oils chemical composition has been validated by a comparison of spectroscopic results with those obtained previously from GC/MS technique [27–30].

2. Materials and methods

2.1. Samples

Samples came from two petroleum basins Brazilian and South East Pyrenees. Oils were previously analyzed by GC and GC/MS and were codified in terms of their geographic origin.

Brazilian oils: they were generated by a Neocomian source rock deposited under fresh to brackish water conditions within the rift lakes formed during the extensional event that culminated with break-up of South America and Africa [27]. They have been sampled from three different fields (noted A, B and C) located on a Brazilian marginal basin. Oil coded 619 was provided from the field A, oil codified 620 was obtained from the field B. The other oils (numbered 621–625) are from the field C. Their GC/MS analyses [28] have revealed the existence of significant differences due to the fact that some oils (620 and 624) are not affected by biodegradation processes.

Pyrenean oils: they came from the Armàncies Formation source rock of Eocene age. They were seeping out directly from the source rock in abandoned bitumen mines [29] in the south eastern Pyrenees and have been sampled at different places in the mines galleries. They ranged from droplets from the gallery ceilings and walls (samples codified M8, M2), to black (M3) and brown (M11) oil floating on water pools and to submerged oil (M4, M5). The GC and GC/MS [30] analyses have shown that the samples are affected by biodegradation at different levels. According to the grading degradation of *n*-alkanes, biodegradation degree is weak for M8 and M2, more marked for M3, M5 and more important for M4 and M11. The iso-cyclo-alkanes rate decreases with the same evolution but sampling (M2, M3, M4, M5) present an equal value.

2.2. Infrared analysis

A Nicolet Avatar spectrometer equipped with a DTGS detector, an Ever-Glo source and a KBr/Germanium beam splitter was employed for spectral measurements. Attenuated total reflectance (ATR) cell was used with a cap in order to avoid volatility of oils. The samples were analyzed by means of a diamond crystal prism manufactured by one bounce on the upper surface. The crystal geometry was a triangle with mirrored 45° angle faces.

Air was taken as reference before collection of each sample spectrum. Data acquisition, made with an absorbance scale, was done from 4000 to $650\,cm^{-1}$ with a $4\,cm^{-1}$ nominal resolution and 100 co-added scans. Five spectra (differentiated by the letter "a", "b", "c", "d" or "e") were recorded for each sample deposited on ATR cell without any preparation or dilution.

2.3. Synchronous Ultra Violet Fluorescence Spectroscopy

To avoid the saturation of signal, oils were dissolved in tetrahydrofuran spectrosol (SDS) (THF is a suitable solvent for avoiding quenching effects) to obtain a concentration of $(10 \pm 1)\,ppm$. Fluorescence measurements in excitation–emission synchronous mode were carried out using a PerkinElmer LS50 luminescence spectrometer. The excitation and emission wavelengths were scanned simultaneously with fixed wavelength interval $(\Delta\lambda)$ of 23 nm. Emission and excitation slits were set at 3 and 4 nm respectively and the scanning speed was kept constant (100 nm/min). Fluorescence spectra of oils were recorded between 200 and 600 nm, in quartz cell of 1 cm length. Optimization of the instrument conditions had been reported in previous studies [31,32].

In order to evaluate the reproducibility of the method, each sample was analyzed three times and differentiated with the letter "a", "b" or "c" on the graphs.

2.4. Mathematical PCA model

Principal Component Analysis (PCA) is an "unsupervised" method describing dataset without *a priori* knowledge of the data structure [33]. The procedure establishes a linear spectral model which allows converting original and correlated variables (absorbance) into uncorrelated variables called principal components or loading. These latent variables contain the main information and have been calculated from differences and similarities of spectra. Also, it reduces data without loss of information: generally, a small number of principal components is sufficient to resume the available spectral information. Then every oil spectrum can be considered as a sum of principal components weighted by score. The representation of these components versus wavelength appears as spectral profile (spectral decomposition model) which has meaning for a spectroscopy user. PCA is oriented towards modelling the variance/covariance structure of the data matrix into a model which is based on the significant spectral differences (significant scores [34]) and considers noise as an error. The number of principal components depends on the model complexity but loadings have to represent the best of variance of spectral data and explain the total variance with a large percentage. Generally the first component extracts the largest source of variance and the last one have above the random noise.

2.5. SIMPLISMA approach

This interactive method [35,36] is used for self-modelling mixture analysis by resolving mixture data in pure component spectra and concentrations profiles without prior information about the mixture. When overlapping spectral features are present in spectroscopic data, this tool is unable to resolve broad spectral components and separates spectral absorption bands characterizing one component. Its concept is based on the determination of pure variables (e.g. a wavelength, a wavenumber in spectroscopic terms) that have contributions from only one component. In mathematical terms, pure variable is a variable with the maximum ratio of the standard deviation to the mean. This ratio, called the purity, is given by the following expression:

$$P_{ij} = W_{ij} * (\sigma_i/(\mu_i + \alpha)) \tag{1}$$

P_{ij} is the purity value of the variable (i is the variable index), from which the jth pure variable will be selected. μ_i and σ_i represent the mean and the standard deviation of variable i. The constant α is added to give pure variables with a low mean value (i.e., in the noise range) a lower purity value P_{ij}. Typical values for α range from 1 to 5% of the maximum of μ_i. The weight factor W_{ij} is a determinant-based function that corrects for previously chosen pure variables. The value of W_{ij} also depend on the value of α. For more details of this function see Ref. [34]. The purity values are represented in the form of spectra. Along with the purity spectrum, the standard deviation spectrum is available, described by:

$$S_{ij} = W_{ij} \times \sigma_i \tag{2}$$

This spectrum has more similarities with the original spectra and is used to facilitate the validation of the pure variables. The interactive process makes it possible to guide the pure variable selection by changing the value of α in combination with the option to exclude certain spectral ranges for the selection of pure variables. This capability is especially useful since pure variables may describe unwanted features in the dataset.

As a result, the intensity of the pure variable can be considered as proportional to a contribution or a relative "concentration" of that component in the mixture. When the pure variables have been determined by iterations procedure with the maximum ratio (called purity) of standard deviation to mean intensity of each spectrum, the original dataset can be resolved into pure components and their contributions in the original mixture spectra. The task of the mixture analysis is to express the dataset as a product of a matrix containing the relative concentrations and a matrix with the spectra of the pure components:

$$D = C^* P^{\mathrm{T}} + E \tag{3}$$

D is the matrix with the original data with the spectra in rows; its size is cv, where c is the number of case (spectra) and v the number of variables (wavenumbers). The matrix C (size cn, where n is the number of pure components) contains the concentrations of the pure components in the mixture. The matrix P (size nv)

contains the resolved spectra. P^{T} represents the transpose of P and E, the residual error. Typically, D exists, but C and P are not known. When the matrices D and C are known through the SIMPLISMA algorithm, the estimate of the pure spectra $\hat{P}$ can be calculated by standard matrix algebra.

$$\hat{P} = D^{\mathrm{T}}C(C^{\mathrm{T}}C)^{-1} \tag{4}$$

In the next step, the contributions are now calculated from $\hat{P}$, which is basically a projection of the original pure variable intensities in the original dataset. This step reduces the noise in the contributions. The equation is:

$$C^* = D\hat{P}(\hat{P}^{\mathrm{T}}\hat{P})^{-1} \tag{5}$$

where C^* stands for the projected C.

Because matrix C does not contain relative concentrations but intensities proportional to concentrations, scaling procedures such as normalization of the resulting spectra in $\hat{P}$ and the associated inverse normalization of C are often used for the quantitative information we refer to as the contributions of the components. The reconstructed dataset can be obtained from:

$$D^{\mathrm{reconstructed}} = C^*\hat{P}^{\mathrm{T}} \tag{6}$$

When the proper number of components has been determined, the difference between D and $D^{\mathrm{reconstructed}}$ is estimated from the relative root of sum of square differences (RRSSQ) as follows:

$$\mathrm{RRSSQ} = \sqrt{\frac{\sum_{t=1}^{n\,\mathrm{spect}}\sum_{j=1}^{n\,\mathrm{var}}(d_{ij} - d_{ij}^{\mathrm{reconstructed}})^2}{\sum_{i=1}^{n\,\mathrm{spect}}\sum_{j=1}^{n\,\mathrm{var}}d_{ij}^2}} \tag{7}$$

where d_{ij} is the ith row and jth column element of D, $d_{ij}^{\mathrm{reconstructed}}$ is the ith row and jth column element of $D^{\mathrm{reconstructed}}$, n_{spect} is the number of mixture spectra and n_{var} is the number of recorded intensities. The value expresses the difference with respect to the original data intensities. For a perfect match, the value is 0.

2.6. Software and data treatments

FTIR-ATR spectra have been recorded by the instrument software OMNIC 4.1b (Thermo Nicolet).

FLWINLAB software has been used for SUVF spectra recording. To avoid possible discrimination due to differences in oils concentration, a preprocessing has been performed on original SUVF spectra by reducing the area under each spectrum to an unit value [37,38] using Microsoft Office Excel software (2007).

Original FTIR-ATR data and SUVF spectra normalized to unit area have been imported in the UNSCRAMBLER software version 9.6 from CAMO (Computer Aided Modelling, Trondheim, Norway) in which infrared spectral data have been before normalized (with the option "mean normalization") while the fluorescence ones were smoothed (using Moving Average Smoothing mode with five points for averaging). For FTIR spectra, the spectral region between 2000 and 2500 cm^{-1} has

been withdrawn. It corresponds to CO_2 response because our apparatus is not purged.

After this data preprocessing, multivariate statistical methods such as PCA was performed by the UNSCRAMBLER program. PCA models were built by *full cross-validation* and done with *centered data* because results can be interpreted in terms of deviations from the average. The optimum num-

ber of factors was taken from the score of each other and from the most significant spectral information given by their loading.

All calculations relating to SIMPLISMA were realized with laboratory written software under Matlab 6.5 computer environment. This software was available from the authors [39]. All data injected in SIMPLISMA came from Unscrambler application.
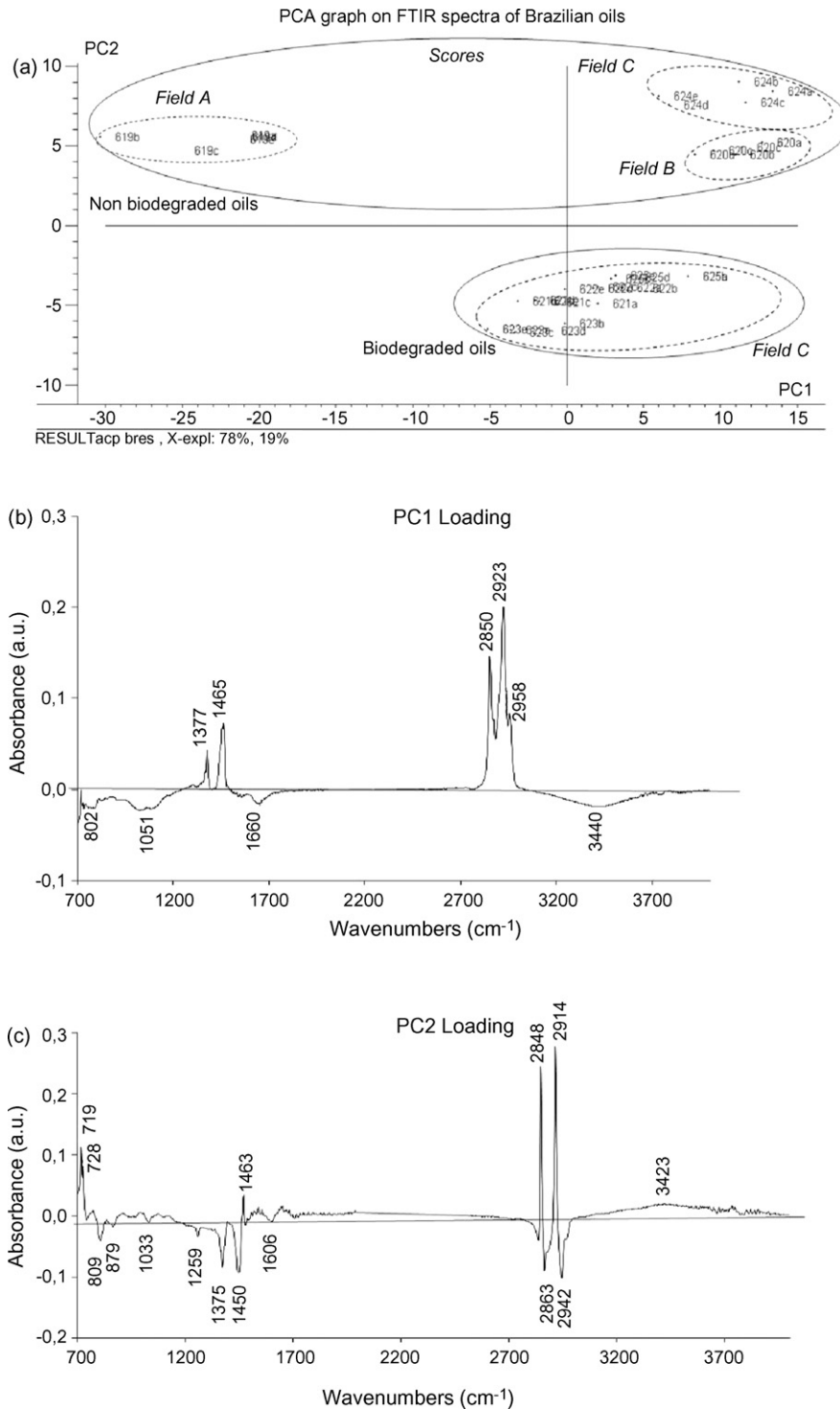

Fig. 1. Brazilian FTIR-ATR PCA scores plot of PC1 vs. PC2 (a) and their associated loadings (b and c).

3. Results and discussions

3.1. Distinction of biodegradation degree of Brazilian oils

3.1.1. PCA on FTIR-ATR spectra

The scores plots of PC1 versus PC2 for PCA model on Brazilian infrared spectra (Fig. 1a) distribute oils according to their field and their biodegradation state. The first principal component represents the maximum of variance (78%) but this axis discriminates only one sample: oil 619 of which the chemical composition is very different. It is an oxidized sample rich in oxygenated structures as the negative part of PC1 loading (Fig. 1b) shows it through the absorption bands pointed at 3440 cm^{-1} (relative to –OH function), 1660 cm^{-1} (characterizing carbonyl group) and large spectral zone around 1051 cm^{-1} describing sulfoxide, ether…. In Fig. 1a, it is the second principal component which discriminates oils according to their biodegradation state with only 19% of variance. The first cluster, in the negative part of PC2, includes biodegraded oils generated from the field C (621, 622, 623 and 625). The second one, in the positive part of PC2, is composed of non-biodegraded oils: 619 from the field A, 620 from the field B and 624 from the field C. Nevertheless, when PCA is done without sample codified 619 (graph not shown here), two groups are separated throughout the first principal component with 86% of variance: non-biodegraded oils 620 and 624 in the positive part of PC1 and the others samples in the negative part. The loading associated to this principal component, separating oils according to their alteration degree without oil 619, is almost the same as the one

presented in Fig. 1c which is obtained when we have taken into account oil 619. On the basis of infrared bands assignments (Table 1), we can see that aliphatic structures characterize mainly non-biodegraded oils. Their specific bands are pointed at 2914, 2848, 1463, 728 and 719 cm^{-1} in the positive part of the graph. Absorption bands in the negative part are attributed to structures, characterizing the degraded oils composition of which relative percentage of branched alkanes, cyclo-alkanes (IR bands pointed at 2942, 2863, 1450, 1375 cm^{-1}), sulfoxide groups (1033 cm^{-1}) and aromatics (1606, 879, 809 cm^{-1}) seems to be more important and conduces to their differentiation.

3.1.2. PCA on SUVF data

To estimate the biodegradation effect on polyaromatic hydro-carbons, a global analysis has been then carried out by the application of PCA on fluorescence data (Fig. 2a). Results expressed from the two first principal components (with an explained variance respectively equal to 84% and 14%) show a repartition of oils in terms of their field location and their biodegradation state. According to the second principal component, not biodegraded oils coded 619 and 620 form their own groups. Oil 624 which is also non-biodegraded moves slightly apart the last ones according to the first principal component. If we examine loadings associated to both components (Fig. 2b and c), we can explain their repartition in function of the condensation degree of their aromatic rings, defined from a specific decoupage of fluorescence spectrum (Table 2). In fact, we can remark that biodegraded oils are described by a relative abun-

Table 1
Infrared assignments

Wavenumber (cm^{-1})	Type of vibration	Intensity	Functional group
3550–3230	O–H str vib	m-s	Hydrogen-bonded O–H (intermolecular)
3080–3010	=C–H str vib	m	=C–H (aromatic)
2975–2950	C–H str vib asym	m-s	–CH$_3$
2940–2915	C–H str vib asym	m-s	–CH$_2$–
2870–2840	C–H str vib sym	m	–CH$_2$–
2885–2865	C–H str vib sym	m	–CH$_3$
1720–1690	C=O str vib	vs	Ketones
1655–1635	C=O str vib	vs	Polycyclic quinones
1625–1590	C=C str vib	v	Ring –C=C–
1525–1470	C=C str vib	v	Ring –C=C–
1465–1440	C–H def vib asym	m	–CH$_3$(alcane)
1390–1370	C–H def vib sym	m-s	C–CH$_3$
1310–1210	C–O str vib	m	–O–Aryl.
1260–1180	O–H def and C–O str vib combination	s	O–H and C–O (phenol)
~1160, ~1075	=C–H in-plane def vib	m	Aromatic =C–H (substituted benzenes)
1070–1030	S=O str vib	vs	>S=O, sulfoxide
1050–1025	C–O str vib	s	Ar–O–CH$_2$–O–Ar
940–920	C–H def	v	Ar–O–CH$_2$–O–Ar
900–830	=C–H oop def vib(1H)	m-s	Aromatic =C–H
850–810	=C–H oop def vib(2H)	w-m	Aromatic =C–H
815–785	=C–H oop def vib(3H)	w	Aromatic =C–H
760–730	=C–H oop def vib(3H)		Aromatic =C–H
770–735	=C–H oop def vib(4H)	s	Aromatic =C–H
725–720	(CH$_2$) rocking	s	Aliphatic (CH$_2$)$_n$
720–680	=C–H oop def vib	s	Aromatic =C–H

Symbols used: vw (very weak), m (medium), s (strong), vs (very strong), v (variable), br (broad), sh (sharp), oop (out-of-plane), asym (asymmetric), sym (symmetric), str (stretching), def (deformation), vib (vibration).
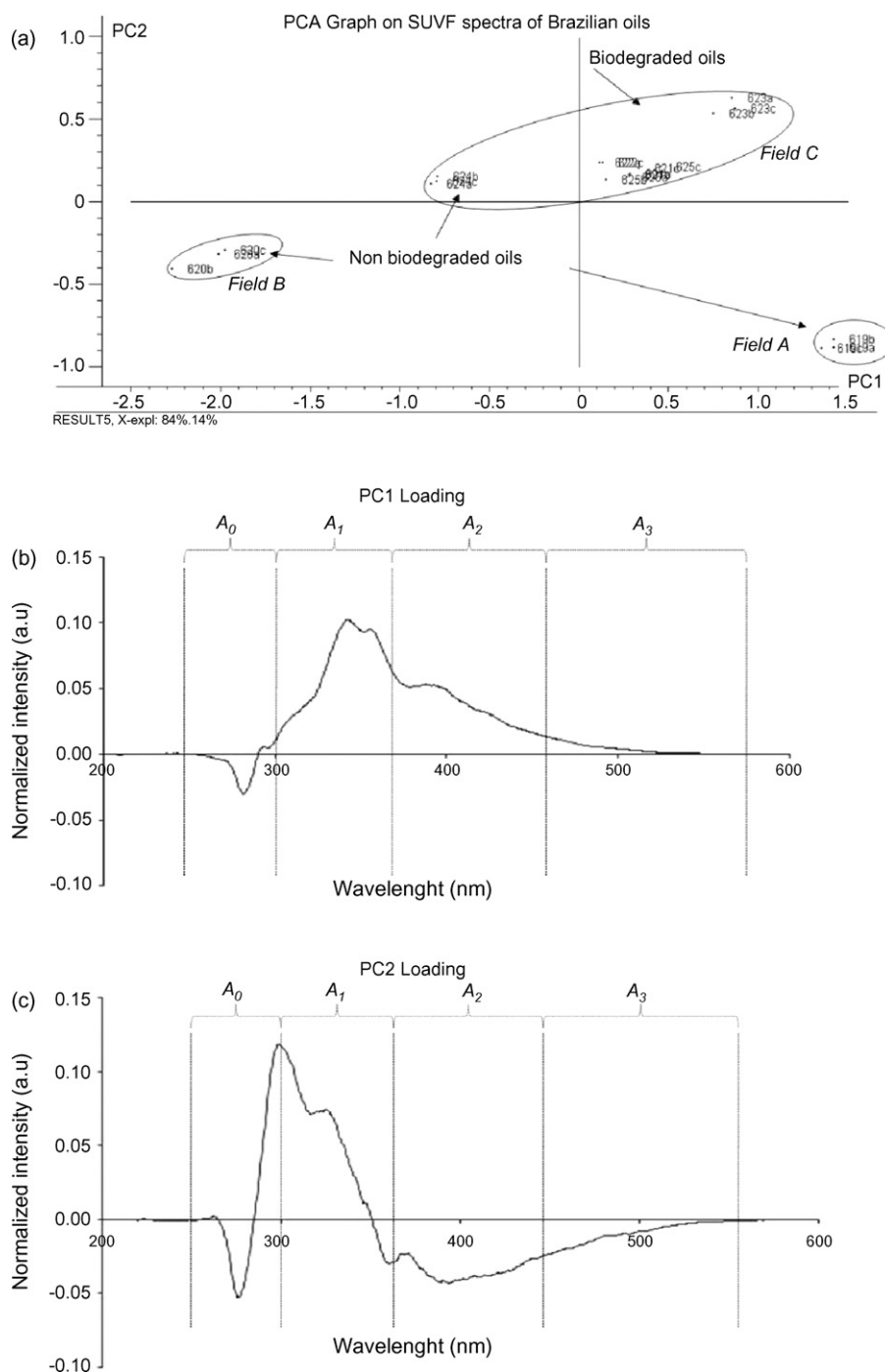
Fig. 2. Brazilian SUVF PCA scores plot of PC1 vs. PC2 (a) and their associated loadings (b and c).

Table 2
Assignment of different SUVF spectral area

Indexes	Spectral regions (nm)	Assignment versus condensation rate
A0	250–300	One aromatic ring
A1	300–370	Two condensed aromatic rings
A2	370–460	Three or four condensed aromatic rings
A3	460–580	Five or more condensed aromatic rings

dance of structures with 2, 3 and/or 4 condensed rings. The last ones give a fluorescence signature in the positive part between 300 and 460 nm for the first loading and in the spectral region from 280 to 350 nm for the second one. Non-biodegraded oils are characterized by the presence of a greater number of compounds weakly condensed (1–2 condensation type) in addition to the highly condensed ones encountered in samples 619 and 620. Oil 619 is a particular case in which aromatic structures are in an environment with a lot of polar compounds resulting of oil oxidation detected on its FTIR-ATR spectrum. This oils repartition

in 2D space of PC1 and PC2 confirms the fact that weakly condensed aromatic compounds can be also consumed when an advanced biodegradation occurs; as has been already cited in literature [40,41].

3.2. Following biodegradation evolution of Pyrenean samples

Permanyer et al. [29,42] have deduced from GC and GC/MS analyses the various degrees of biodegradation for these oils which have induced compositional differences, prior to describe it from spectroscopic indexes [43]. In this study, we have tried to discriminate the different levels of the alteration by PCA treatment of their spectroscopic data.

3.2.1. PCA on FTIR-ATR spectra

PCA performed on infrared spectra results on 93% of variance with only the first principal component. Then the other factors considered as non-significant have been eliminated. Thus, a line plot versus the scores of the first factor has per-

mitted to visualize the different biodegradation stages of oils (Fig. 3a). This axe regroups in the positive part, oils not or weakly biodegraded (as M8, M2 and M3 samples) while the negative zone is essentially characterized by the presence of very biodegraded oils (M4, M5 and M11). PC1 loading (Fig. 3b) shows that aliphatic structures (absorption bands pointed at 2962, 2923, 2912, 1463, 1376, 723 cm^{-1}) regroup not or weakly biodegraded oils because of their abundance. The most biodegraded oils exhibit similarities in spectral zones describing present water which prevents us to identify vibrations bands of their aromatic or oxygenated compounds because of their overlapping with water bands.

3.2.2. PCA on SUVF data

On scores plot of PC1 versus PC2 (Fig. 4a) explaining 93% of the total variation in the sample set, oils repartition corresponds to the three stages of biodegradation as defined above: weak, moderate and heavy biodegradation.

Through the associated loadings (Fig. 4b and c), we are able to see that heavy biodegraded oils (M4, M5 and M11, classified in
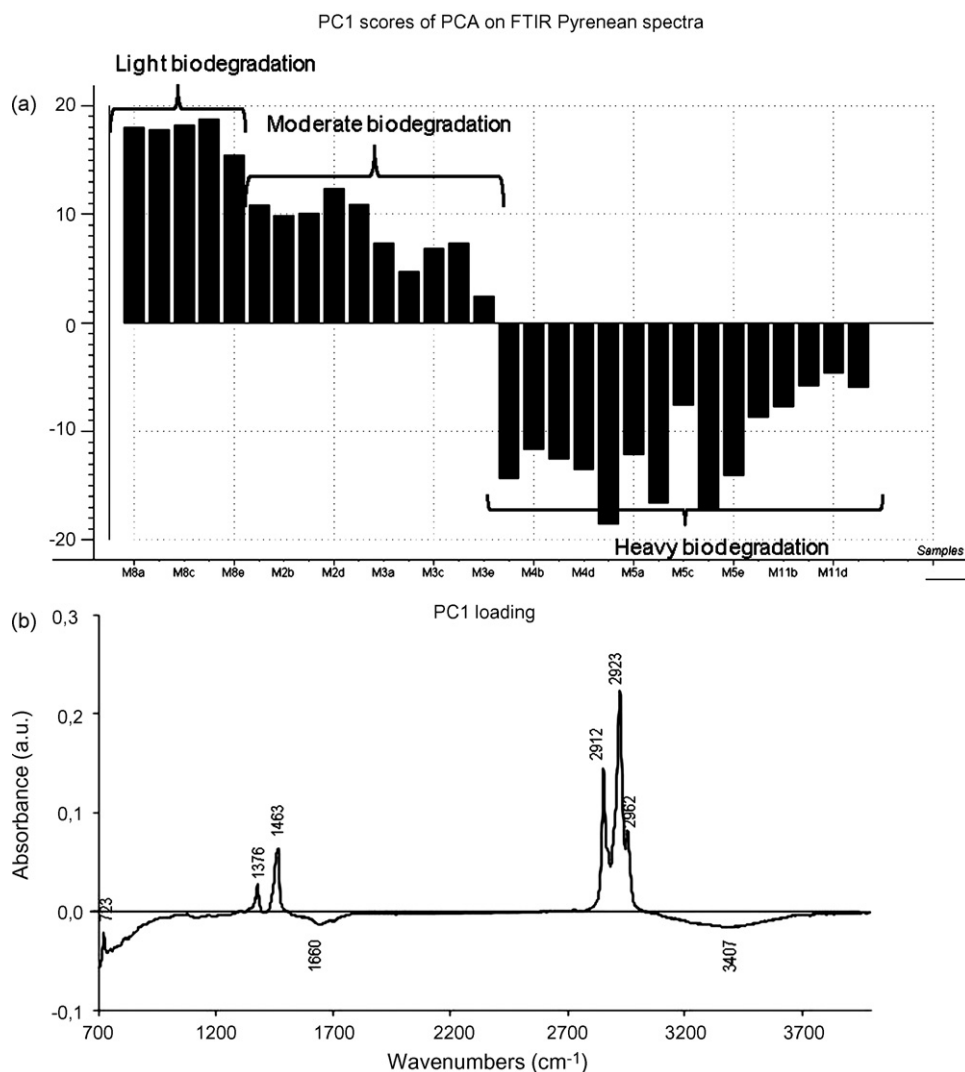
Fig. 3. Pyrenean FTIR-ATR PC1 scores plot (a) and his associated loading (b).
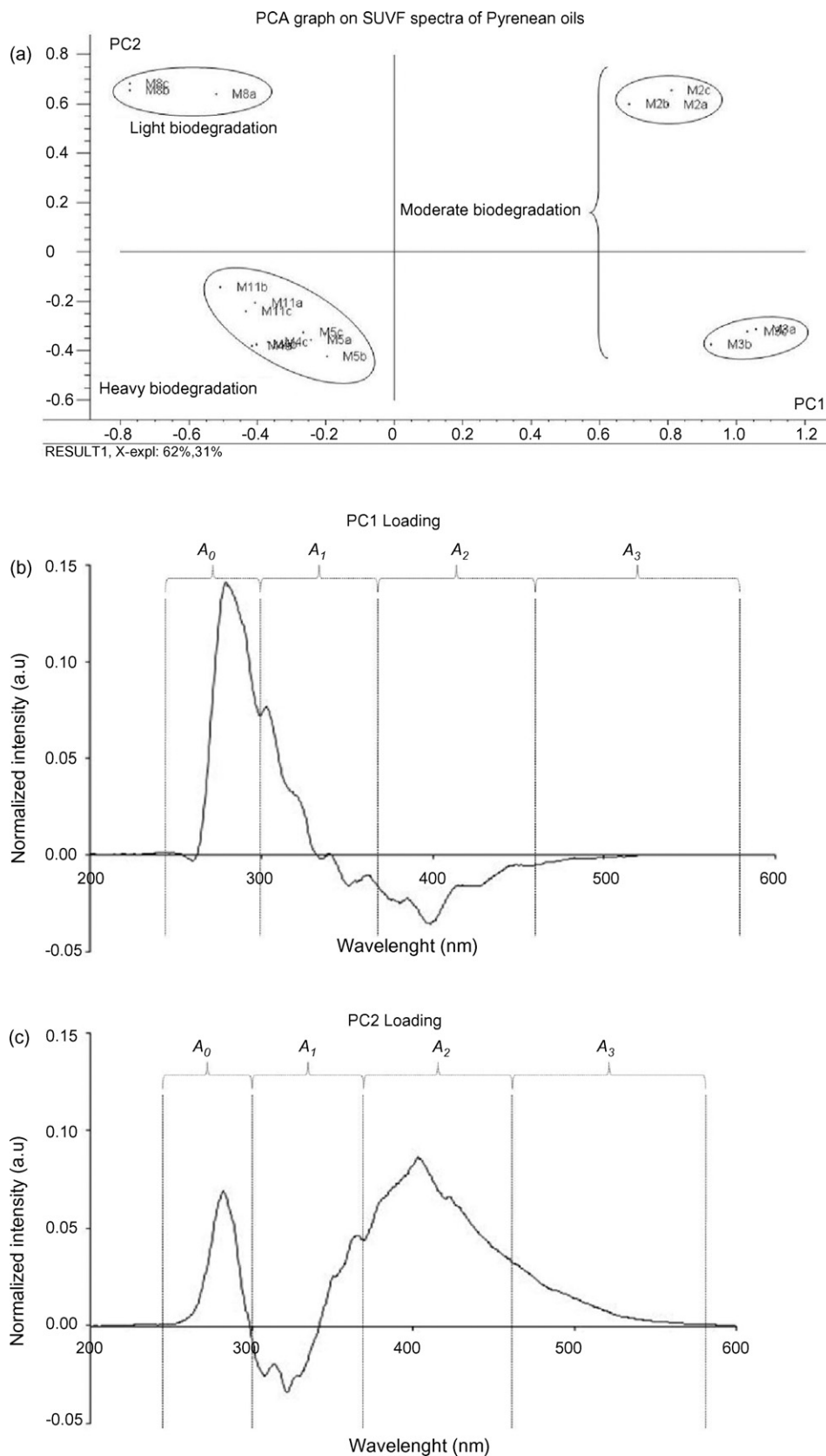
Fig. 4. Pyrenean SUVF PCA scores plot of PC1 vs. PC2 (a) and their associated loadings (b and c).

the negative part of the two loadings) are rich in aromatics with a number of condensed rings superior on two. Their fluorescence intensity is marked between 340 and 480 nm. Their relative abundance is increased because of the low quantity of light aromatics present in deteriorated oils. That confirms the consumption of small aromatic structures in a moderate advanced biodegradation stage. Not altered oils (M8, M2, M3) are located differently on the graph in spite of their similar biodegradation state: the cause of this separation can be explained by a different molecular environment for their small aromatic structures. Thus, their signature in the spectral zone (250–300 nm) is expressed through the first or the second loading. Oil M8, slightly altered, is placed in the negative part of PC1 because it is more differentiated by spectral zone between 350 and 500 nm. This sample expresses its relative abundance of light aromatic species through the second component between 250 and 300 nm. M8 and M2 contain in addition to light polyaromatic hydro-

carbons, molecular structures with three and four condensed aromatic rings.

3.3. SIMPLISMA on spectroscopic data of Brazilian and Pyrenean oils

ATR-FTIR oils spectra (Fig. 5) do not reveal real differences in their chemical composition except for Brazilian oil 619 which presents an oxidized character and for three Pyrenean samples (M4, M5 and M11) containing water. The differentiation of their biodegradation states cannot be done directly from their spectra. Data give only global information on the presence of linear or branched or cyclic alkanes, aromatics, oxygenated compounds or structures with heteroatoms without estimation of the percentage of each compound in oil composition as given by chromatography techniques. More detailed information about their polyaromatic hydrocarbons can be obtained
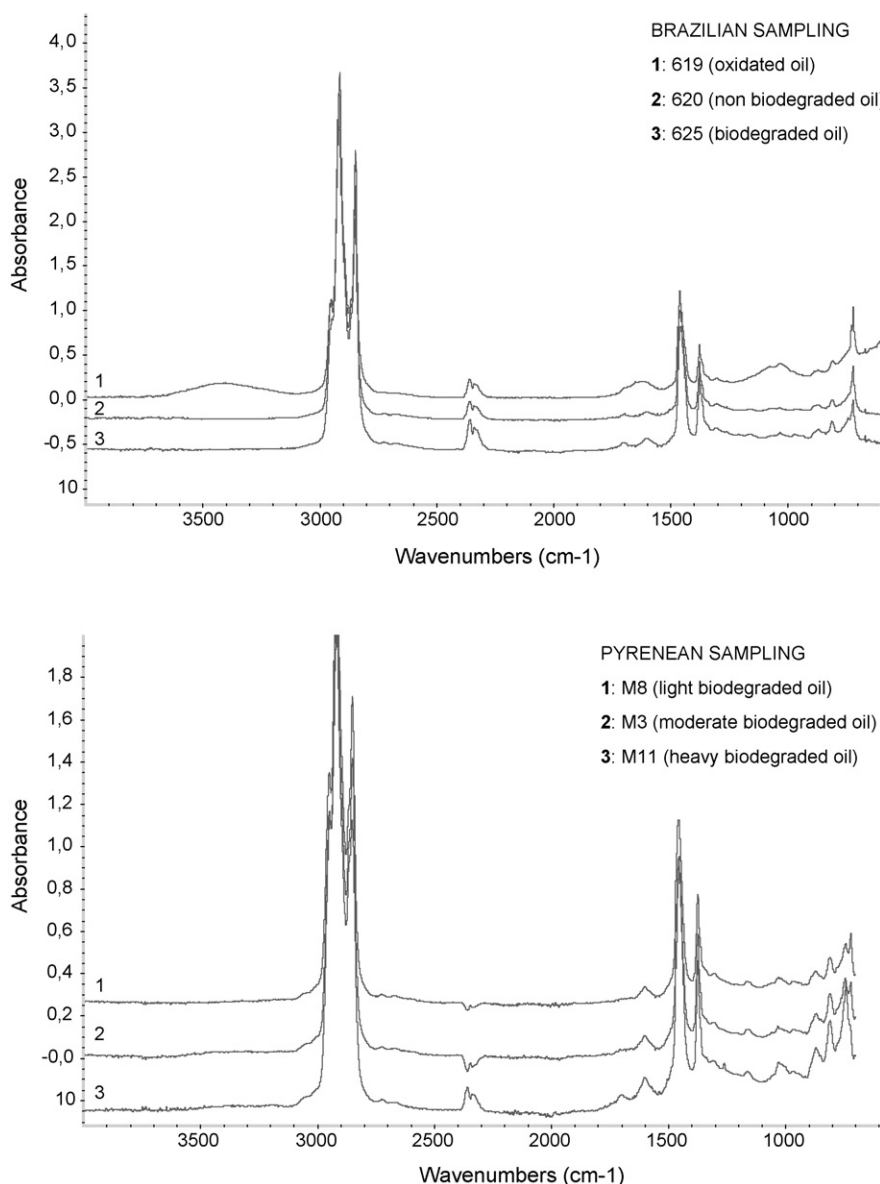
Fig. 5. Some FTIR-ATR spectra of Brazilian and Pyrenean oils.

from synchronous fluorescence technique where indexes are calculated to compare their relative repartition. Thus, to study Brazilian and Pyrenean oils composition in terms of saturated, aromatic and polar fractions, a resolution curve method as SIMPLISMA has been applied on spectroscopic data.

Usually, this multivariate method resolves mixture data into relative concentration profiles and spectra of the pure components present. But in the case of complex system such as petroleum oils, it is impossible to extract the spectral profile of an individual compound in particular when we use IR or SUVF measurements which represent a global signature of a large number of chemical species. That is the reason why we have attributed extracted IR spectra to compounds families regrouping aliphatic or aromatic or functionalized species. In the case of fluorescence, synchronous spectra have been deconvoluted into different extracted spectra representing distinct classes of aromatic compounds.

As well as chromatography technique, the treatment of spectroscopic data by SIMPLISMA has permitted to compare oils chemical composition after a biodegradation process. The relative concentration profile associated to each mathematically extracted spectrum gives us its relative contribution in the reconstruction of the experimental spectrum. Thus, the sum of all resolved spectra pondered by a coefficient called here concentration has to reconstruct original spectrum with an error near. As five FTIR-ATR measurements have recording for each sample, we have obtained (five × number of oils samples) relative concentration values for each resolved spectrum, which have been reported on the graph called "relative concentration profile". For SUVF data, three relative concentration values have been obtained.

3.3.1. FTIR-ATR data

Original spectra of the two origins (Brazilian and Pyrenean) have been reconstructed with four extracted spectra (RRSSQ = 3.2%) presented in Fig. 6. According to the absorption bands present at 2958, 2918, 2848, 1464, 1377, 721 cm^{-1} and their correspondence with IR bands assignments (Table 1), the first spectrum (Fig. 6a) describes various saturated hydrocarbons such as n-alkanes, iso-alkanes and cyclo-alkanes present in the saturated fraction of oils. The second extracted spectrum (Fig. 6b) can be attributed to the present water but also, it can be associated to phenolic, alcoholic and carboxylic derivatives, because of the presence of some large bands which characterize theses species. The third one (Fig. 6c) represents mono- or polycyclic aromatics (1610, 880, 818, 748, 734 cm^{-1}), branched with aliphatic chains or condensed with cyclo-alkanes (2954, 2924, 2854, 1458, 1377 cm^{-1}) and various rings containing sulfur atom (1176, 1035, 970 cm^{-1}). The last spectrum (Fig. 6d) includes all the others structures with aromatic nuclei, alkylated chains and heteroatoms like nitrogen, sulfur and oxygen (1715, 1261, 1103, 1041 cm^{-1}). These NSO compounds, called in the following "polar" structures, could be assimilated to resins and asphaltenes as it is evoked in the petroleum language. In the same time, if we attribute this spectrum to phenols, acids or carbazole, we will not be able to see the vibration of hydroxyl group, because
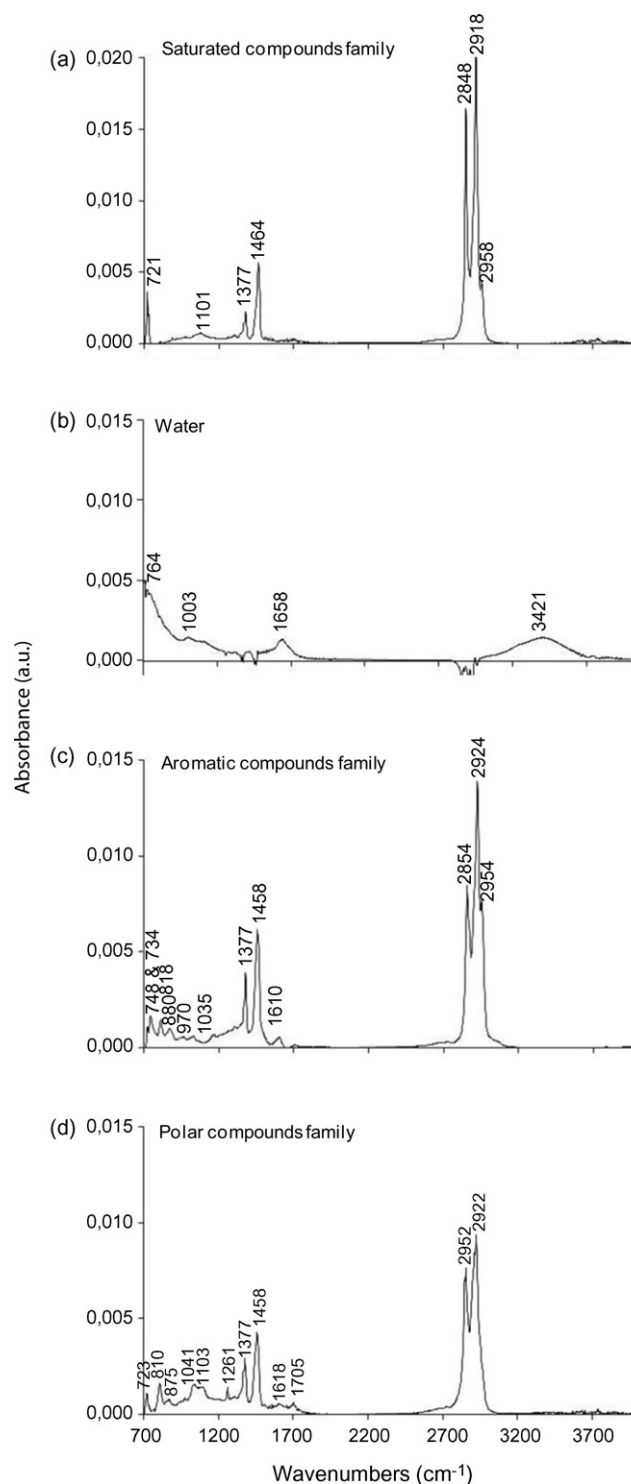
Fig. 6. Mathematical FTIR-ATR spectra extracted by SIMPLISMA approach.

its signal has before been extracted with the bands of water fraction.

After examination of their relative associated concentration profiles describing the relative repartition of these compounds families in the oils composition (Fig. 7), we note that there is a real difference between the Brazilian and Pyrenean samples. Even if we have not exact information on the biodegradation level of Brazilian oils, we can suppose that it is weaker than
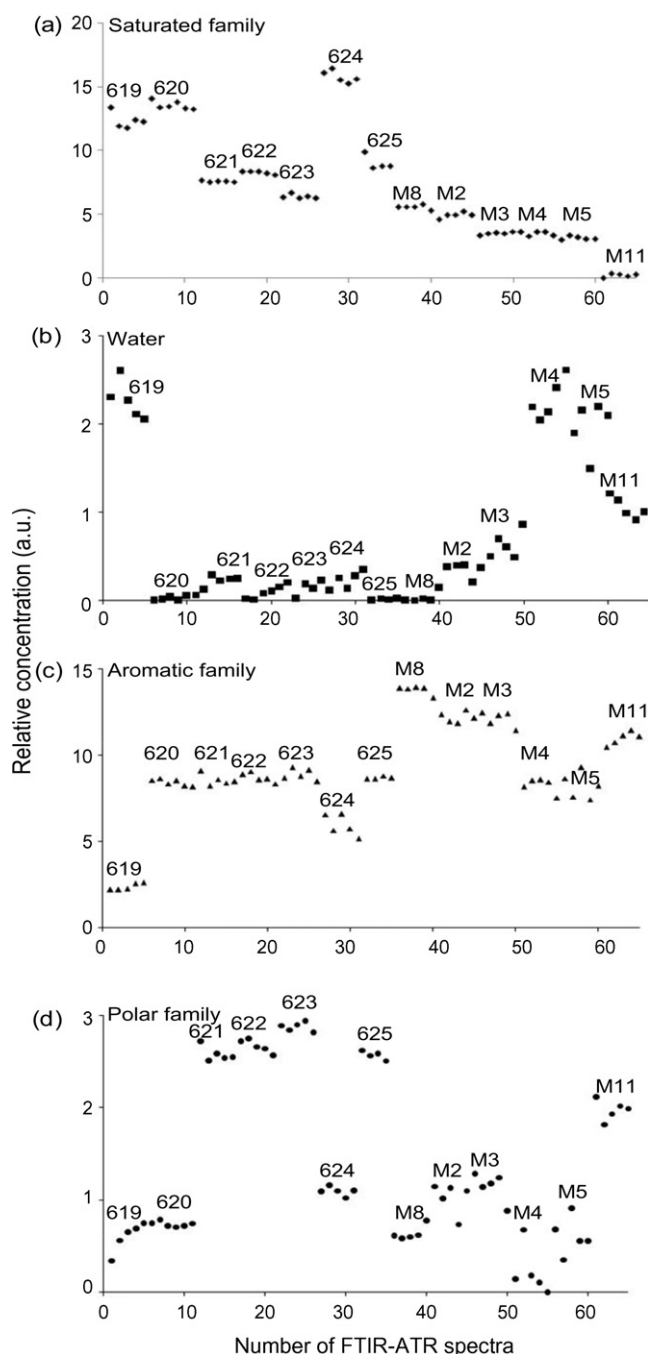
Fig. 7. Relative associated concentration profiles of SIMPLISMA resolved FTIR-ATR spectra.

that of the Pyrenean oils ranged in three–four level according to Peters and Moldowan scale. Indeed the Brazilian samples contain more saturated compounds than their Pyrenean homologues. Their relative concentration is described by the profile 7a, where we can also note that not biodegraded Brazilian oils (620, 624) are the richest in saturated hydrocarbons. For Pyrenean samples, the saturated hydrocarbons rate is predominant for M8 and negligible for M11, which is in good correlation with their biodegradation degree. The profile of the second extracted pure spectrum (Fig. 7b) confirms the water presence (not due to the fact that the apparatus is not purged) in important quantity for Pyrenean oils

(M4, M5) and not negligible for M11 sample. This repartition is in agreement with the environment of theses samples submerged or floating on water pools in the mines. Concerning Brazilian oil 619, the contribution of this resolved spectrum to the reconstruction of the original data is important because it characterizes the polar constituents such as alcohols, ketones or acid derivatives due to the oxidation of this oil. In Fig. 7c, polyaromatic hydrocarbons appear more abundant for the moderate degraded Pyrenean oils M8, M2, M3 and sample M11, the most affected one. They are in weak proportions for the untouched Brazilian ones (619 and 624) and are distributed in the same proportions in the others samples. These compounds are in low rate in altered oils (M4, M5 and M11). This can be explained by the fact that they have been removed from the original oil because of their advanced biodegradation state. The little contribution of aromatics in chemical composition of oil 619 is due to the overlapping of their specific absorption bands with those of the oxidized compounds. In accordance with the alteration state of oils, the last family including the polar structures is very represented in biodegraded oils (relative concentration profile 7d) except for samples 619, M4 and M5. The latter have respectively oxidized structures and water in abundant quantity, already shown the second resolved spectrum "b" and its associated profile.

3.3.2. SUVF data

Original data have been reconstructed (RRSSQ = 2.8%) with three extracted spectra (Fig. 8) with an absorption maximum of which relative position and intensity are in function of the present polycyclic aromatic structures. The first spectrum (Fig. 8a) characterizes the light aromatics with one benzene ring; they mainly fluoresce in spectral zone between 250 and 300 nm. The second one (Fig. 8b) represents mainly the structures with two condensed benzene rings because of the absorption maximum at 340 nm and some structures with three or four fused aromatic rings giving a weaker fluorescence in A2 area. The last one (Fig. 8c) defines all the others polycyclic aromatic hydrocarbons which have a high number of condensed benzene rings. The band pointed at 280 nm corresponds to THF solvent. Generally, peaks indicate which species are present but do not give information on their concentration because each compound has its own fluorescence effectiveness. As we have normalized spectra to unit area to avoid this problem, the associated profiles (Fig. 9) allow us to obtain their relative proportions in oil and to apprehend the influence of the biodegradation on their relative distribution.

In Brazilian sample, light aromatics (Fig. 9a) are more numerous in non-biodegraded oils (620 and 624). Unfortunately, this observation is not confirmed with Pyrenean set. The relative abundance of light aromatics decreases with the biodegradation degree for oils M3, M4, M5 and M11 but samples M8 and M2 present a weaker rate of these structures. Perhaps, these oils have not been submitted to the same bacterial action because of their location sampling (from the gallery ceilings and walls in the mine). About the other polyaromatic hydrocarbons, M8 and M5 samples are rich in structures with two fused benzene rings (Fig. 9b). It is also the case of 619, 620, M2 and M11 oils which also contain highly condensed aromatic species as shown in Fig. 9c.
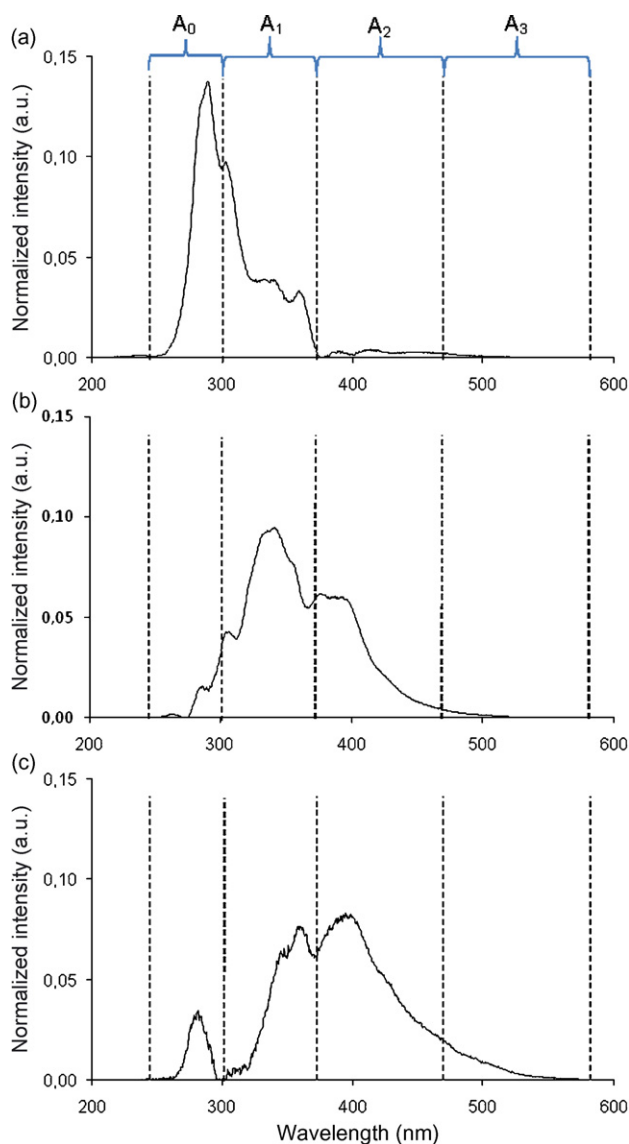
Fig. 8. Mathematical SUVF spectra extracted by SIMPLISMA approach.

Fig. 9. Relative associated concentration profiles of SIMPLISMA resolved SUVF spectra.

3.4. Comparison between spectroscopic and chromatographic techniques

PCA model based on FTIR-ATR data is therefore able to distinguish biodegraded oils at different levels of alteration (light or heavy). Results obtained by SIMPLISMA make it possible to confirm that oils biodegradation involves a consumption of alkanes as it has already been described in literature [44,45]. Previously GC and GC/MS studies [28] which have shown that Brazilian oils codified 619 and 620 are characterized by a dominance of high molecular n-alkanes, pristane much higher than phytane and odd/even n-alkane preference. Oil codified 624, sampled from the same field but entrapped in distinct reservoir sequence, is not affected by biodegradation and has similar structure as 619 and 620 oils. Conversely, 621, 622, 623 and 625 samples are marked by the depletion of n-paraffins and a pronounced unresolved complex mixture which rises above GC baseline, indicating the biodegradation of oils. The interpretation

of the mathematically resolved IR spectra and their associated concentration profiles is in good agreement with GC/MS conclusions because results show a predominance of saturated compounds family in no biodegraded samples of Brazil. Moreover, SIMPLISMA approach reveals an important relative abundance of condensed polyaromatic molecules containing N, S and O atoms, which well traduce their advanced biodegraded state.

FTIR classification of Pyrenean oils is similar to the results obtained by Permanyer and Caja [30], who evoked a relative increase of iso-alkanes rate for the least biodegraded samples. In fact, oil coded M8 (non-biodegraded) is characterized by a maximum content of saturated hydrocarbons by both GC and IR

techniques. Chromatographic analysis of these samples reveal an evolution of alteration process associated to a consumption of *n*-alkanes and iso-cyclo-alkanes to total degradation for samples codified M4 and M11 (most biodegraded). This grading degradation is also clearly demonstrated through extracted concentration profile of saturated compounds family. For chromatography, the progressive diminution of *n*-alkanes is combined to relative increase in the isoprenoids pristane and phytane, not detected by IR measurements because these species are represented by the same extracted spectrum regrouping all aliphatic structures (linear, branched and cyclic ones). No selectivity has been obtained in this case with infrared data.

For aromatic structures, GC/MS measurements have been done only for Pyrenean origin and have been resolved in terms of presence of relative quantity of dimethylphenanthrene, tri-aromatic steroids but all these compounds fluoresce in the same spectral zone between 370 and 460 nm in synchronous excitation–emission mode. GC/MS has shown that bacterial alteration has remained some aromatics such as naphthalene, phenanthrene and alkylbenzene series. Some molecular series disappeared or are temporary concentrated (triaromatic steroids, 1,2,8-trimethylphenantrene) according to the progression of biodegradation until a total consumption in the case of M11 oil (the most altered). Information obtained from fluorescence is a repartition of aromatics versus their condensation degree. An increased biodegradation state is traduced by a decrease of relative abundance of light polycyclic aromatic hydrocarbons for M3, M4, M5 and M11 oils. This evolution has not been observed for oils M8 and M2.

In a general way GC/MS analysis has a high resolving power and is able to separate and identify a large number of individual petroleum hydrocarbons including homologue series and isomers of alkanes and mono- and polycyclic aromatic hydrocarbons. Spectroscopic techniques do not permit to reach detailed chemical composition of oils but only a global knowledge of the present chemical groups. Modifications of saturated alkanes are apparent in GC/MS and FTIR results but no selectivity between linear, branched and cyclic alkanes is obtained by FTIR technique. Nevertheless, an estimation of alkanes loss after biodegradation can be done from concentration profile of aliphatic compounds family extracted by SIMPLISMA approach. The distribution of alkylated polycyclic aromatic compounds, easily studied with GC/MS, is less evident by FTIR analysis because of the overlapping bands; then synchronous excitation–emission fluorescence technique comes to supplement it by differentiating aromatic structures on the basis of the condensation degree of their rings. Resulted oils classification reveals that light aromatics have been removed in the case of a hard biodegradation.

Experimentally, spectroscopic techniques are characterized by the simplicity of samples preparation while GC–MS technique has disadvantages of necessary chromatographic separation procedures before detecting and requirement of expensive instruments. Optical techniques are better suited for rapid data collection with minimal pre-treatments to interpret it. Objectives of chromatographic or spectroscopic techniques are different. GC–MS technique is performed to provide structural information for individual compounds present in oils while spectroscopic techniques are used for a rapid screening tool to investigate similarities and evolution of oils in terms of aliphatic, aromatic and polar character.

4. Conclusion

Spectroscopic techniques associated to chemometric treatment give results in good agreement with conventional geochemical methods (GC, GC/MS) and offer a rapid way to evaluate the petroleum biodegradation. The PCA loadings and SIMPLISMA profiles give a spectroscopic interpretation useful to determine the relative abundance of compounds families characterizing oils according to their bacterial degradation. Thus, FTIR-ATR analysis permits to discriminate oils for which the relative abundance of alkanes decreases in function of their biodegradation state. SUVF measurements success where FTIR technique shows some limits and particularly in the study of aromatic hydrocarbons evolution. The correlation between a fluorescence spectral region in synchronous emission–excitation mode and a type of condensed aromatic ring permits to know if the biodegradation has also affected the "light" aromatic compounds after consuming the alkanes.

The innovating method permits to classify rapidly oils in terms of their biodegradation state and informs us on the structural modifications of oils composition. Results make it possible to consider this analytical methodology as a preliminary study when a rapid screening is required before any detailed investigations in the field of petroleum research.

Acknowledgements

References

[1] L.M. Wenger, C.L. Davis, G.H. Isaksen, SPE Reservoir Evaluat. Eng. 5 (2001) 375–383.
[2] K.E. Peters, J.M. Moldowan, The Biomarker Guide: Interpreting Molecular Fossils in Petroleum and Ancient Sediments, Prentice Hall, Englewood Cliffs, NJ, 1993, pp. 252–255.
[3] K.E. Peters, C.C. Walters, J.M. Moldowan (Eds.), The Biomarker Guide vol. 2: Biomarkers and Isotopes in the Petroleum Exploration and Earth History, Cambridge University Press, 2005.
[4] A. Charrié-Duhaut, E. Grosjean, P. Adam, P. Schaeffer, J. Trendel, D. Dessort, J. Connan, P. Albrecht, Org. Geochem. 38 (2007) 1501–1515.
[5] F. Behar, H.L. de Barros Penteado, F. Lorant, H. Budzinski, Org. Geochem. 37 (2006) 1042–1051.
[6] H.L. de Barros Penteado, F. Behar, F. Lorant, D.C. Oliveira, Org. Geochem. 38 (2007) 1197–1211.
[7] C. Magnier, I. Moretti, J.O. Lopez, F. Gaumet, J.G. Lopez, J. Letouzey, Mar. Pet. Geol. 2 (2004) 195–214.
[8] J.S. Wattson, D.M. Jones, R.J.P. Swannell, A.C.T. van Duin, Org. Geochem. 33 (2002) 1153–1169.
[9] W. Meredith, S.J. Kelland, D.M. Jones, Org. Geochem. 31 (2000) 1059–1073.
[10] C.A. Hughey, S.A. Galasso, J.E. Zumberge, Fuel 86 (2007) 758–768.

[11] L.M.V. Malmquist, R.R. Olsen, A.B. Hansen, O. Andersen, J.H. Christensen, J. Chromatogr. A 1164 (2007) 262–270.

[12] J.H. Christensen, A.B. Hansen, U. Karlson, J. Mortensen, O. Andersen, J. Chromatogr. A 11090 (2005) 133–145.

[13] H. Justwan, B. Dahl, G.H. Isaksen, Mar. Pet. Geol. 23 (2006) 213–239.

[14] H. Napitupulu, L. Ellis, R.M. Mitterer, Indonesia Org. Geochem. 31 (2000) 295–315.

[15] A. Permanyer, L. Douifi, M. Alberdi, C. Rébufa, J. Kister, 8th Latin American Congress on Organic Geochemistry, Colombia, October 20–24, 2002, pp. 111–114.

[16] L.D. Stasiuk, L.R. Snowdon, Appl. Geochem. 12 (1997) 229–241.

[17] H.W. Hagemann, A. Hollerbach, Org. Geochem. 10 (1986) 473–480.

[18] J. Kister, M. Guiliano, C. Largeau, S. Derenne, E. Casadevall, Fuel 69 (1990) 1356–1361.

[19] J. Kister, N. Pieri, R. Alvarez, M.A. Diès, J.J. Pis, Energy Fuels 10 (1996) 948–957.

[20] N. Pieri, Thèse de l'Université d'Aix-Marseille III (1994) 214.

[21] M.D. Guillén, N. Cabo, J. Sci. Food Agric. 80 (2000) 2028–2036.

[22] J. Kister, M. Guiliano, G. Mille, H. Dou, Fuel 67 (1988) 1076–1082.

[23] J. Kister, P. Doumenq, E. Davin, G. Mille, Comptes rendus de l'Académie des Sciences, Paris, 315 (2) (1992) 149–152.

[24] O. Abbas, C. Rébufa, N. Dupuy, A. Permanyer, J. Kister, D.A. Azevedo, Fuel 85 (17/18) (2006) 2653–2661.

[25] O. Abbas, N. Dupuy, C. Rébufa, L. Vrielynck, J. Kister, A. Permanyer, J. Appl. Spectrosc. 60 (3) (2006) 304–314.

[26] J.H. Christensen, G. Tomasi, J. Chromatogr. A 1169 (2007) 1–22.

[27] A. Permanyer, D.A. Azevedo, C. Rébufa, J. Kister, F.T.T. Gonçalves, 9th Latin American Congress on Organic Geochemistry, 2004.

[28] A. Permanyer, D.A. Azevedo, C. Rébufa, J. Kister, F.T.T. Gonçalves, Geogaceta 38 (2005) 139–141.

[29] A. Permanyer, 7th Latin American Congress on Organic Geochemistry, Foz do Iguaçù, 2000, pp. 204–207.

[30] A. Permanyer, M.A. Caja, Geogaceta 38 (2005) 135–138.

[31] G. Mille, J. Kister, J.P. Aune, in: H. Charcosset (Ed.), Part IV: Products of Extraction, Oxydation and Pyrolysis, Elsevier, Amsterdam, 1990, pp. 227–242, Chapter 13.

[32] G. Mille, M. Guiliano, J. Kister, Org. Geochem. 13 (1987) 947–952.

[33] H. Martens, T. Naes, Multivariate Calibration, John Wiley and Sons, New York, 1989.

[34] S. Millar, P. Robert, M.F. Devaux, R.C.E. Guy, P. Maris, Appl. Spectrosc. 9 (1996) 1134–1139.

[35] W. Windig, J. Guilment, Anal. Chem. 63 (1991) 1425–1432.

[36] W. Windig, Chemom. Intell. Lab. Syst. 23 (1994) 71.

[37] D. Bertrand, C.N.G. Scotter, Appl. Spectrosc. 46 (1992) 1420–1425.

[38] G. Mazerolles, M.F. Devaux, E. Dufour, E.M. Qannari, Ph. Courcoux, Chemom. Intell. Lab. Syst. 63 (2002) 57–68.

[39] R. Tauler, A. De Juan, Multivariate Curve Resolution, home page: http://www.ub.es/gesq/mcr/mcr.htm.

[40] R.M. Atlas, Microbiol. Rev. 45 (1981) 180–209.

[41] J.G. Leahy, R.R. Colwell, Microbiol. Rev. 54 (1990) 305–315.

[42] A. Permanyer, D. Dessort, 9th Latin American Congress on Organic Geochemistry, Mérida, México, 2004, p. 2.

[43] O. Abbas, Thèse de l'Université d'Aix-Marseille III (2007).

[44] C. Ratledge, in: R.J. Watkinson (Ed.), Developments in Biodegradation of Hydrocarbons, vol. 1, Applied Science Publishers, London, 1978, pp. 1–46.

[45] J.M. Hunt, Petroleum Geochemistry and Geology, second ed., Freeman W.H. and Company, New York, 1996, p. 743.

Solid-phase extraction and simultaneous determination of trace amounts of sulphonated and azo sulphonated dyes using microemulsion-modified-zeolite and multivariate calibration

Yahya S. Al-Degs [a], Amjad H. El-Sheikh [a], Mohammad A. Al-Ghouti [b],
Bahram Hemmateenejad [c,d], Gavin M. Walker [e,*]

[a] *Chemistry Department, The Hashemite University, P.O. Box 150459, Zarqa, Jordan*
[b] *Industrial Chemistry Center, Royal Scientific Society, P.O. Box 1438, Amman, Jordan*
[c] *Chemistry Department, Shiraz University, Shiraz, Iran*
[d] *Medicinal and Natural Products Chemistry Research Center, Shiraz University of Medical Sciences, Zand Street, Shiraz 71345, Iran*
[e] *School of Chemistry and Chemical Engineering, Queen's University Belfast, David Keir Building, Stranmillis Road, Belfast BT95AG, UK*

Abstract

A simple and rapid analytical method for the determination of trace levels of five sulphonated and azo sulphonated reactive dyes: Cibacron Reactive Blue 2 (C-Blue, trisulphonated dye), Cibacron Reactive Red 4 (C-Red, tetrasulphonated azo dye), Cibacron Reactive Yellow 2 (C-Yellow, trisulphonated azo dye), Levafix Brilliant Red E-4BA (L-Red, trisulphonated dye), and Levafix Brilliant Blue E-4BA (L-Blue, disulphonated dye) in water is presented. Initially, the dyes were preconcentrated from 250 ml of water samples with solid-phase extraction using natural zeolite sample previously modified with a microemulsion. The modified zeolite exhibited an excellent extraction for the dyes from solution. The parameters that influence quantitative recovery of reactive dyes like amount of extractant, volume of dye solution, pH, ionic strength, and extraction–elution flow rate were varied and optimized. After elution of the adsorbed dyes, the concentration of dyes was determined spectrophotometrically with the aid of principle component regression (PCR) method without separation of dyes. The results obtained from PCR method were comparable to those obtained from HPLC method confirming the effectiveness of the proposed method. With the aid of SPE by M-zeolite, the concentration of dyes could be reproducibly detected over the range 25–200 ppb for C-Yellow and L-Blue and from 50 to 250 ppb for C-Blue, C-Red, and L-Red. The multivariate detection limits of dyes were found to be 15 ppb for C-Yellow and L-Blue and 25 ppb for C-Blue, C-Red, and L-Red dyes. The proposed chemometric method gave recoveries from 85.4 to 115.3% and R.S.D. from 1.0 to 14.5% for determination of the five dyes without any prior separation for solutes.
© 2008 Elsevier B.V. All rights reserved.

Keywords: Microemulsions; Solid-phase extraction; Sulphonated and azo sulphonated dyes; Preconcentration; Natural zeolite; Spectral overlap; Multivariate calibration

1. Introduction

Color is an essential property for a variety of industrial products. For example, natural and synthetic dyes are heavily used by the food, pharmaceutical, cosmetic, textile and leather industries [1]. The effluents of these industries are highly colored and disposal of these wastes into natural waters causes damage to the environment [1–2]. Dyes can be classified into three types according to their chemical structure: cationic, nonionic, and anionic [1]. Anionic dyes are the direct, acid and reactive dyes [2–3]. Some classes of dyes are harmful to aquatic life even at lower concentrations [2–3]. It is pointed out that less than 1.0 ppm of dye content causes obvious water coloration [1]. Dye concentrations of 10 ppm up to 25 ppm have been cited as being present in dyehouse effluents [4]. After mixing with other water streams, the concentration of dyes is further diluted. The concentration of dyes could be in the ($\mu g\,L^{-1}$) level in wastewater [5]. In response to concerns regarding the health risks associated with the use of reactive dyes, an increasing number of analytical methods have been developed in recent years for

their determination. Several papers described the applications of new analytical procedures for the detection and determination of anionic and cationic dyes in various matrices such water, wastewater, urine, fish tissue, and animal feed [3,5]. The analysis of textile dyes poses special problems because these products do not belong to one group of chemical compounds, but cover many chemical functionalities with large differences in solubility, volatility, and ionization efficiency. Sulfonated reactive dyes are non-volatile and thermally unstable, and consequently cannot be analyzed by gas chromatography (GC). For this reason, liquid chromatography/mass spectrometry (LC/MS) has been recommended analysis of disperse azo dyes but are not applicable to sulfonated azo dyes [6]. Capillary electrophoresis (CE) is a powerful alternative to classical chromatographic techniques and it can overcome the problems with LC in the separation of sulfonated azo dyes [7]. The simultaneous determination of sulfonated azo dyes was successfully carried out using ion-pair HPLC/UV–vis for analyzing eight dyes [8]. Recently, method development for resolution of highly overlapped spectra has increased exceptionally, because of the availability of powerful instrumentation and robust numerical methods. For example, derivative spectrophotometry [9], H-point standard addition method [10], chemometric methods including classical least squares (CLS), principal-components regression (PCR), net analyte signal (NAS), and partial least squares regression (PLS) [11–13] have been frequently employed to overcome the problems of interference due to spectral overlapping. A limited number of studies have been reported on using multivariate calibration for analysis of multi-component mixtures of reactive dyes [14–16]. As mentioned earlier in this section, reactive dyes are present in the environmental samples at trace levels ($\mu g\,L^{-1}$ levels). Accordingly, the direct quantification of dyes is not possible unless the solute is preconcentrated to be detected by the instrument. One of the current methods that is used to concentrate pollutants that present at trace level is the solid-phase extraction (SPE) [17]. SPE is a widely used sample preparation technique for the isolation and preconcentration of the target analyte(s) which usually present either in solid-phase or liquid-phase. The solid-phase extraction has attracted considerable attention as a preconcentration technique because of its high enrichment efficiencies and it does not require large amount of organic solvent compare to familiar liquid–liquid extraction techniques [17]. SPE is based on the distribution of analyte between an aqueous solution and sorbent by different mechanisms such as: adsorption, co-precipitation, complex formation and other chemical reactions [18]. SPE techniques were effectively applied to quantify heavy metals [19] and organic pollutants [20] that present in solution at trace levels. Many solid surfaces of different properties were tested as solid-phase extractants which includes molecular imprinted polymers [18], fluoroplastic [20], activated carbon [21], and nanotubes activated carbons [22]. A few numbers of solid surfaces were found to be effective for extracting sulphonated dyes from solution [5–7]. Riu et al. have studied the extraction of sulphonated azo dyes using crosslinked polystyrene–divinylbenzene prior their determination by capillary electrophoresis techniques, the obtained recoveries for dyes were in the range 16–80% [5]. It is

known that anionic dyes (dyes having anionic charges) have a poor adsorption on a wide range of adsorbents and this was attributed to the negative charges of the dye [23]. Recently, de Castro Dantas et al. have successfully applied a number of microemulsions for extraction of reactive dyes from synthetic textile wastewater; the extractants were effective and can be used many times for dyes extraction [24]. In a different study, the previous authors have applied microemulsion-modified-diatomite for effective extraction chromium from solution [25]. At the best of the authors' knowledge, there is no available study on using microemulsion or microemulsion-modified adsorbents for preconcentrating and analyzing reactive dyes. The application of microemulsion-modified-zeolite as a solid-phase extractant for reactive dyes is investigated in this work. The studied dyes have a wide application in textile industry and usually present in treated water at trace levels. Effect of experimental conditions such as, extractant mass, pH, and ionic strength on extraction efficiency was investigated using the column method. Desorption of dyes from the solid surface was studied using different desorption agents including: water, 0.1 M HCl, and methanol–H_2O agents. Another aim of this study was to develop a simple procedure for the spectrophotometric determination of ppb levels of reactive dyes in water using microemulsion-modified-zeolite as solid-phase extractant. The figures of merit such as selectivity, sensitivity, and limit of detection (LOD) for the proposed multivariate methods were calculated. Quantitative determination of the five reactive dyes in a synthetic textile wastewater was carried out using the proposed multivariate calibration method and the obtained results were compared with those obtained using ion-pair-HPLC method.

2. Solving Beer's law for multi-component systems using multivariate calibration

The Beer's law model for m calibration standards containing l chemical components with spectra of n digitized absorbances can be presented in matrix notation as [26]

$$\mathbf{A} = \mathbf{CK} + \mathbf{E} \tag{1}$$

Or in matrix form,

$$
\begin{bmatrix}
A_{11} & A_{12} & \dots & A_{1n} \\
A_{12} & A_{22} & \dots & A_{2n} \\
\vdots & \vdots & & \vdots \\
A_{m1} & A_{m2} & \dots & A_{mn}
\end{bmatrix}
=
\begin{bmatrix}
C_{11} & C_{12} & \dots & C_{1l} \\
C_{12} & C_{22} & \dots & C_{2l} \\
\vdots & \vdots & & \vdots \\
C_{m1} & C_{m2} & \dots & C_{ml}
\end{bmatrix}
$$
$$
\times
\begin{bmatrix}
K_{11} & K_{12} & \dots & K_{1n} \\
K_{12} & K_{22} & \dots & K_{2n} \\
\vdots & \vdots & & \vdots \\
K_{l1} & K_{l2} & \dots & k_{ln}
\end{bmatrix}
+
\begin{bmatrix}
E_{11} & E_{12} & \dots & E_{1n} \\
E_{12} & E_{22} & \dots & E_{2n} \\
\vdots & \vdots & & \vdots \\
E_{m1} & E_{m2} & \dots & E_{mn}
\end{bmatrix}
\tag{2}
$$

where $\mathbf{A}$ is the $m \times n$ absorption matrix of calibration spectra, $\mathbf{C}$ the $m \times l$ concentration matrix of components (dyes in this study) concentrations, $\mathbf{K}$ the $l \times n$ matrix of absorptivity

constants or simply the calibration matrix and $\mathbf{E}$ is the $m \times n$ matrix of spectral errors that not fit by the model. The elements of $\mathbf{K}$-matrix can be determined by measuring spectra of individual components; however, this dose not takes into accounts the interactions (or overlapping) between components. In literature, there are many chemometric techniques that can effectively solve Eq. (2) and find the perfect relation between the absorbance and concentration. Among these calibration methods, classical least squares (CLS), principal component regression (PCR), partial least squares (PLS), and Kalman filter (KF) are the most employed in the chemometric research [16]. Determination of dyes concentration in synthetic and real samples using CLS and PCR methods was carried out according to the theories proposed in Refs. [27–30]. Determination of figures of merit like sensitivity, selectivity, and limit of quantification for multivariate calibration was carried out as outlined in Refs. [31–32].

3. Experimental

3.1. Instrumentation and software

The absorbance measurements were obtained using a double beam unicam spectrophotometer (Cary 50 UV–vis spectrophotometer). The UV–vis spectra were recorded over the wavelength range of 200–800 nm and digitized absorbance values were transferred to a Pentium (IV) personal computer for subsequent analysis. Data treatment and chemometric calculations were carried out using MATLAB (version 6.1). The pH measurements were made with a WTW-Inolab (Germany) pH-meter using a companied glass electrode. Shimadzu LC Liquid Chromatograph System with variable wavelength UV–vis detector was used for chromatographic analyses of dyes.

3.2. Characteristics of zeolite and preparation of microemulsion-modified-zeolite (M-zeolite)

Zeolite sample was donated by the Natural Resources Authority (Amman, Jordan). The sample (about 0.25 kg) was crushed and sieved to different particle size ranges (Standard Sieve Apparatus, Endecotts Ltd., London, England). The sieved samples were washed many times with triply deionised water and dried in an oven at 100 °C overnight and was allowed to cool in a desiccator. Extraction tests were conducted on an average size range of 63–125 μm. The mineral constitution of the extractant was determined using X-ray diffraction techniques (PANalytical, ExpertPro, equipped with Xlerator detector). The chemical composition of zeolite (using X-ray fluorescence analysis) was given by the Natural Resources Authority (wt%): SiO$_2$ 56.47%, Al$_2$O$_3$ 19.13%, Fe$_2$O$_3$ 7.13%, CaO 1.10%, MgO 1.53%, K$_2$O 3.22%, Na$_2$O 0.53%, and L.O.I (loss on ignition) 11.41%. Microemulsion was prepared by mixing of 10 wt% surfactant (saponified coconut oil; mostly lauric acid, CH$_3$(CH$_2$)$_{10}$COOH, with some myristic acid, CH$_3$(CH$_2$)$_{12}$COOH;) and 25 wt% aqueous phase (deionised water). Coconut was saponified by standard procedure ASTM D-5558/1995 to form CH$_3$(CH$_2$)$_{10}$COO$^-$Na$^+$. Then the mixture mixed with 40 wt% cosurfactant (isoamyl alcohol) 99% P.A., and 25 wt% oil phase (heavy distillate) [24–25].

Due to the spontaneous formation of microemulsions, they can be prepared in one step by mixing the constituents. The order of mixing of the reagents is not crucial for microemulsion preparation, but it can influence the time required to establish equilibrium [33]. To prepare M-zeolite, 15.0 g of zeolite (63–125 μm) and 25 cm^3 of microemulsions were mixed together under mild agitation for 4 h. Then, the mixture was filtered, washed and dried at 65 °C for 48 h. The microemulsion-modified-zeolite was refered to as M-zeolite throughout the text.

3.3. Chemicals and solutions

Doubly distilled water and high purity reagents were used for all preparations of the standard and sample solutions. Five reactive dyes-which have a wide application in textile industry-were selected, namely; Cibacron Reactive Blue 2, Cibacron Reactive Red 4, Cibacron Reactive Yellow 2, Levafix Brilliant Red E-4BA, and Levafix Brilliant Blue E-4BA. Dyes samples of analytical grade were obtained from Aldrich chemicals. The chemical structures of dyes (in their Na-form) are illustrated in Fig. 1. The employed dyes are widely used in cotton dyeing. Standard stock solutions (1.00×10^3 mg L^{-1}) of reactive dyes were prepared individually by dissolving 0.100 (±0.001) g in doubly distilled water in a 100.0 ml volumetric flask. Dilute solutions were prepared by the appropriate dilution of the stock solution in doubly distilled water. Phosphate buffer was prepared by mixing solutions of 23.0 g of KH$_2$PO$_4$ and 57.7 g of K$_2$HPO$_4$, the volume of the mixture was bringing to 1.0l. The ionic strength of dye solutions was adjusted using pure NaCl. All reagents employed in this research were obtained from Merck Company.

3.4. Extraction studies

A typical solid-phase extraction polyethylene column was packed with 1.0 g of M-zeolite. It was washed three to four times with doubly distilled water. A portion of dyes solution (50–1000 ml) containing 250 ppb of each dye was extracted after pH adjustment to 7.0 ± 0.5 by adding 5 ml of 1.0 M (KH$_2$PO$_4$/NaH$_2$PO$_4$) buffer. The above solutions were passed through the column with a flow rate of 1.0 ml min^{-1}. After that, adsorbed dyes were eluted with 5.0 cm^3 of methanol–H$_2$O (70:30 vol.%) mixture. The concentration of each dye after preconcentration was determined using the proposed multivariate calibration methods or HPLC method. The extraction testes were carried out under controlled flow rates with the aid of 12-port visiprep vacuum manifold (Supelco, USA).

3.5. Preconcentration and analysis of reactive dyes spiked in synthetic wastewater sample

In fact the main chemical compounds that used within dyeing process (and obviously will be discharged with the unreacted dyes) are: tannic acid, chrome alum, sodium chloride, aluminum salt, chromium salt, copper salt, iron salt and sodium carbonate [24]. A synthetic textile wastewater was prepared by spiking tap water with the above chemicals in large amounts and reactive

Fig. 1. The chemical structure of reactive dyes.

Fig. 2. Absorbance spectra of five reactive dyes: (a) zero-order spectra and (b) first-order spectra, each dye at 16.0 ppm, pH: 7.0; [NaCl]: 0.10 M.

3.6. Preparation of calibration and validation sets

Two sets of standard solutions were prepared; the calibration and validation sets. Calibration set was used to build the calibration model, while the effectiveness of the proposed model for prediction was testified in the validation set. Due to the high overlapping between dyes spectra (53–98% overlap, see Table 3) a large number of training samples were necessary to resolve that overlapping. Univariate calibration measurements were carried out to each dye in order to establish the proper concentration ranges for the dyes determination in the mixtures. Solutions of absorbance values higher than 1.0 were diluted. Forty synthetic mixtures (maintained at pH 7.0 using phosphate buffer and ionic strength of 0.10 M NaCl) of reactive dyes were prepared. From these solutions, 25 mixtures were selected as the calibration set and the remaining 15 solutions were kept as validation set. The compositions of calibration and validation sets were presented in Table 1. The design of calibration set was based on five-level fractional factorial designs according to Brereton's procedure [34]. The prediction set was selected randomly. All dyes solutions were scanned over the entire UV–vis range (200–800 nm). The number of experimental points (λ) per spectrum was 151 where the spectrum is subdivided into 4.0 nm intervals. Within this spectral region, maximum spectral information is available as indicated in Fig. 2a. Accordingly, the dimension of calibration absorption matrix (**A**) is 25×151, while the dimension for calibration concentration matrix (**C**) is 15×5 (see Eq. (2)). It is advisable that the concentration ranges of dyes in the validation samples should be within the same space as that in calibration mixtures (Table 1).

dyes in trace amounts. Prior spiking of water sample with reactive dyes, the sample was filtered through a cellulose membrane filter (Millipore) of 0.45 mμ pore size to remove any suspended or undissolved matters. Furthermore, the pH of water samples was adjusted to 7.0 using phosphate buffer. The spiked samples were extracted as described in Section 3.4. The concentrated dyes in the eluted solutions were measured spectrophotometrically over the range 200–800 nm. The obtained digitized data were analyzed by the proposed chemometric calibration methods. HPLC method was used side-by-side with multivariate calibration to determine dyes concentration in spiked wastewater sample after SPE with M-zeolite.

Table 1
Composition of calibration and validation sets

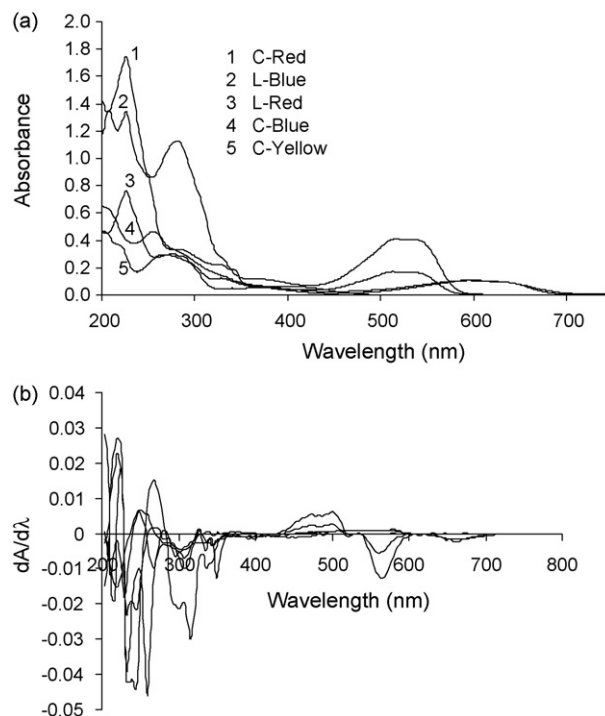| Sample	C-Blue	C-Red	C-Yellow	L-Blue	L-Red
Calibration set[a]					
1	4.5	5.0	5.5	6.0	5.0
2	1.5	1.5	5.5	4.0	8.0
3	1.5	8.5	2.0	10.0	4.0
4	8.0	3.0	2.0	6.0	9.0
5	3.0	8.0	9.0	4.0	6.0
6	8.0	5.0	4.0	4.0	4.0
7	4.5	3.0	9.0	8.0	4.0
8	3.0	3.0	5.5	10.0	7.0
9	3.0	7.0	4.0	8.0	9.0
10	6.0	8.0	4.0	6.0	7.0
11	8.0	7.0	7.0	10.0	6.0
12	6.0	5.0	9.0	10.0	8.0
13	4.5	8.0	7.0	2.0	8.0
14	8.0	8.0	5.5	8.0	2.0
15	8.0	1.5	9.0	2.0	7.0
16	1.5	7.0	9.0	6.0	2.0
17	6.0	1.5	2.0	8.0	6.0
18	1.5	5.0	7.0	8.0	7.0
19	4.5	7.0	2.0	4.0	7.0
20	6.0	7.0	5.5	2.0	4.0
21	6.0	3.0	7.0	4.0	2.0
22	3.0	1.5	7.0	6.0	4.0
23	1.5	3.0	4.0	2.0	6.0
24	3.0	5.0	2.0	2.0	2.0
25	4.5	1.5	4.0	10.0	2.0
Validation set[b]					
26	0	5.0	0	0	5.0
27	6.0	0	6.0	0	0
28	0	5.0	0	5.0	6.0
29	0	0	5.0	5.0	5.0
30	0	0	6.0	0	0
31	7.0	0	0	0	0
32	0	8.0	0	0	0
33	0	0	0	0	7.0
34	0	0	0	9.0	0
35	6.0	8.0	7.0	10.0	9.0
36	6.0	8.0	8.0	3.0	4.0
37	7.0	7.0	7.0	7.0	7.0
38	6.0	9.0	5.0	10.0	8.0
39	4.0	6.0	3.0	8.0	9.0
40	5.0	3.0	8.0	6.0	8.0

[a] Constructed according to five-level fractional factorial designs according to Brereton's procedure [34].
[b] Randomly constructed.

3.7. Determination of sulphonated reactive dyes using ion-pair HPLC methodology

Due to the high polarity of reactive dyes, which results from the polar sulphonated groups as shown in Fig. 1, ion-pair, reverse chromatography was used for separation. In this work, the method described in Ref. [8] was adopted with slight modifications. Effect of pH, mobile phase composition, concentration of ion-pair reagent, and mobile phase flow rate of dyes separation were studied and optimized for the current system. The optimized conditions that used for dyes analysis were: Separation was carried out on a Merck C18, 5 μm size particle and 15 cm × 4.0 mm column using methanol/water as a mobile phase and triethylammonium acetate as the ion-pair reagent. The mobile phase contained 0.003 M triethylammonium acetate with final pH of 5.5. A gradient of methanol from 40 to 65% (from 0 to 5 min) and from 65 to 85% (from 5 to 10 min) at flow rate of 1.0 ml min^{-1} and 20° C was used during separation. Detection at 260 nm was carried out by means of UV detector. The samples of dyes were dissolved in the mobile phase and filtered over a Millipore 0.45 μm. Twenty microliters sample volumes were injected in all experiments.

4. Results and discussion

Separation and determination of sulphonated and azo sulphonated dyes in water and wastewater can be carried out by using different analytical techniques including high performance liquid chromatography (HPLC), liquid chromatography and mass spectrometry (LC–MS), capillary electrophoresis (CE), and gas chromatography and mass spectrometry (GC–MS) [5–7,35–39]. However, these analytical methods usually lengthy and also previous separation and clean-up steps are essential because of spectral and chromatographic overlapping. In fact, only a few research studies have considered the preconcentration and analysis of sulphonated and azo sulphonated dyes in different environmental samples. A summary of these studies was presented in Table 2. As seen from Table 2, a number of solid sorbents such as styrene or polystyrene–divinylbenzene [5–7,35,39–40], strong cation-exchangers [35], and C$_{18}$ sorbents [36–39] have been reported for the enrichment of anionic dyes with different numbers of sulphonated group from dilute solutions prior to their determination by a variety of analytical techniques. Modest recoveries of dyes were reported using polystyrene–divinylbenzene, highly crosslinked polystyrene–divinylbenzene and strong cation-exchange cartridges [5–7,35]. Other kinds of SPE have been employed for sulphonated dyes, such as C$_{18}$ cartridges and columns [36–39] and the recoveries were higher compare to those obtained using other extractants. In fact, more sorbents of higher capacities should be tested for the extraction and preconcentration of anionic sulphonated dyes in various environmental water matrices [5–7]. In this work, microemulsion-modified-zeolite (M-zeolite) has been applied to solve the problem of low recovery of polar anionic dyes. After preconcentration of dyes, multivariate calibration methods such as classical least squares (CLS) and principal component regression (PCR) were applied to determine the individual concentration of dyes without prior separation from the mixture. The advantages of applying multivariate calibration methods were to minimize or eliminate sample preparation tasks and to avoid a preliminary separation step in complex matrices.

4.1. Spectral overlap and importance of multivariate calibration

Fig. 2 shows the zero-order and the first order absorption spectra of reactive dyes. As can be seen in Fig. 2a, an important degree of spectral overlap occurs between the dyes. Moreover, the first-derivative spectra showed a high overlap between dyes

Table 2
Summary of SPE preconcentration–determination methods developed for sulphonated and azo sulphonated dyes

Dye type	Extractant employed	Analytical techniques	Detection limit	Recovery (%)	Application	Ref.
Sulphonated azo dyes	Polystyrene–divinylbenzene and strong cation-exchange cartridges	Micellar electro kinetic capillary chromatography/UV detection	ppb levels	30	Water and soil samples	[35]
Monosulphonated and Disulphonated azo dyes	Highly crosslinked polystyrene–divinylbenzene	Micellar electro kinetic capillary chromatography/UV and MS detection	10–150 ppb	16–80	Groundwater and industrial samples	[5–7]
Monosulphonated azo dyes	C_{18} cartridge	L.C./atmospheric pressure ionization mass spectrometry	20–50 ppb	87–103	Water	[36]
Disulphonated azo dyes	C_{18} column	LC/MS	50 ppb	70–122	Wastewater	[37]
Di, tri, and tetrasulphonated dyes	C_{18} column	Capillary electrophoresis/diode array detection	23–42 ppb	81–121	Wastewater	[38]
Di, tri, and tetrasulphonated dyes	C_{18} column	HPLC/UV	7–28 ppb	–	Water	[39]
Di, tri, and tetrasulphonated and azo sulphonated dyes	Microemulsion modified zeolite	Multivariate calibration/UV detection	15–25 ppb	85–115	Water and wastewater	This work

Table 3
Degree of spectral overlap between dyes spectra as calculated from Eq. (3)[a]

Dye binary system	Degree of overlap (%)
C-Red and L-Blue	64
C-Red and L-Red	98
C-Red and C-Blue	66
C-Red and C-Yellow	53
L-Blue and L-Red	73
L-Blue and C-Blue	96
L-Blue and C-Yellow	54
L-Red and C-Blue	79
L-Red and C-Yellow	56
C-Blue and C-Yellow	58

[a] D-values were calculated over the spectral range 200–800 nm and $\Delta\lambda = 2$ nm.

which may limit the application of spectrophotometric derivative methods for analysis of the current dyes system.

The degree of spectral overlap can be estimated using Eq. (3):

$$D = \frac{\sum k_1 k_2^t}{\sum k_1 k_1^t \sum k_2 k_2^t} \tag{3}$$

$\sqrt{D}$ is a convenient measure of the degree of spectral overlap [27]. k_1 and k_2 are the column vectors of individual component absorptivities. The values of k_1 and k_2 were calculated from the corresponding absorbance values at each wavelength for each pure dye using Beer's law. The degrees of spectral overlap between the studied dyes are given in Table 3. As indicated from Table 3, there is a significant spectral overlap between the bands of dyes. For all systems, the overlap was more than 50%. C-Yellow dye showed the lowest spectral overlap with the other dyes and the lowest overlap was with C-Red (53% overlap). Due to the significant spectral overlapping, it is obvious that the conventional calibration procedures would have a limited application for quantitative determination of dyes in the mixture. Therefore, the simultaneous determination of these dyes requires: (a) the use of a separation technique (like LC, HPLC, and CE) before their determination, or (b) the application of a multivariate calibration technique for the resolution of the complex system. The second option was chosen, owing to its simplicity, rapidity and low cost.

4.2. Optimization of experimental conditions that affecting dyes absorption

Many experimental conditions may affect the absorption characteristics of reactive dyes, among these; pH and ionic strength of solution are the most significant. The influence of pH on dyes absorptivity was studied over a wide pH range (1.0–13.0) and at constant solution ionic strength (0.1 M NaCl). The spectra obtained for C-Red at different pH values are presented in Fig. 3, which shows very small variations in absorption spectra over pH range: 2.0–10.0. The absorption characteristics of the dye have been affected at extreme pH conditions (pH: 1 and 13). The changes in absorption behavior of the dye could be attributed to the hydrolysis or aggregation at these extreme pH conditions. The rest of dyes exhibited a similar spectral behavior which was

Table 4
Analytical characteristics for single-component determination of reactive dyes

Dye	C-Blue	C-Red	C-Yellow	L-Blue	L-Red
$\lambda_{.max}$ (nm)	615.0	530.0	413.0	605.0	525.0
Linearity range (ppm)	1.0–30.0	1.0–30.0	1.0–30.0	1.0–30.0	1.0–30.0
r^2	0.9997	0.9996	0.9994	0.9993	0.9991
Limit of detection[a]	0.31	0.11	0.27	0.35	0.20
Limit of quantification[b]	1.04	0.36	0.91	1.18	0.68

[a] Limit of detection = $3s_B/m$; s_B, standard deviation of blank ($n = 10$); m, slope of calibration.

[b] Limit of quantification = $10s_B/m$; s_B, standard deviation of blank ($n = 10$); m, slope of calibration.
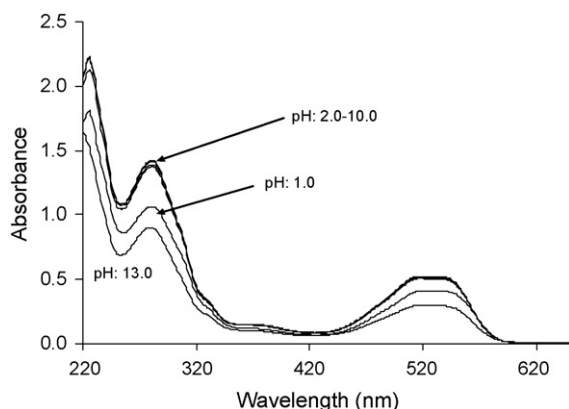

Fig. 3. Influence of solution pH on the absorption characteristics of C-Red (20 ppm and 0.10 M NaCl).

attributed to the structural similarities between dyes (see Fig. 1). The absorption spectra of all dyes were not affected by solution ionic strength over the range of 0.0–1.0 M NaCl. Fig. 4 shows the influence of solution ionic strength on absorption behavior of C-Blue over the wavelength range: 220–800 nm. Based on that, the spectral analyses for all dyes mixtures were recorded at pH: 7.0 and 0.10 M NaCl.

4.3. Univariate calibration

Analytical characteristics for individual determination of reactive dyes were evaluated at the maximum absorption wavelength in the visible region and the results were summarized in Table 4. Optimum linear concentration range for each compound
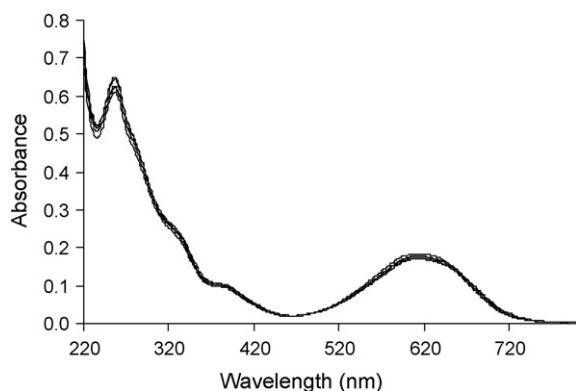
Fig. 4. Influence of solution ionic strength on the absorption characteristics of C-Blue (20 ppm and pH: 7).

was obtained from the Ringbom plot (not shown) concerning each individual calibration giving the following ranges, between 1.3 and 29.0 ppm for C-Blue, C-Red, and C-Yellow and 1.5–28.0 ppm for L-Blue and L-Red. The determination of these concentration ranges are useful in building both calibration and validation sets. As can be noted, the concentrations of dyes used in multi-component mixtures (Table 1) were much lower than their concentrations corresponding to their limit of linearity (~30 ppm); this was made to avoid excessive absorbance of the mixtures [40].

4.4. Effective calibration by CLS and PCR

4.4.1. Selection of the optimum wavelength range

In multi-component spectrophotometric analysis, the optimum wavelength range should be carefully chosen for getting acceptable accuracy and precision in the results. The selection of the optimum wavelengths range can be made using several criteria such as maximum S/N ratio method [41], changeable size moving window [42], and the minimum condition number of the calibration matrix (cond($\mathbf{K}$)) [26]. The last method was adopted in this work due to its rapidity for determination of the optimum wavelength range. In fact, error propagation is important in establishing the optimal wavelength range for quantitation. This error can be represented by the condition number of the calibration matrix, cond($\mathbf{K}$) [26]; a large condition number represents a large error in estimating the analyte concentration as well as a high degree of non-orthogonality in the spectra. Instead of selecting a wavelength range with the best sensitivity, it must be selected with the smallest error amplification, i.e., smallest cond($\mathbf{K}$) [43]. The cond($\mathbf{K}$) value was calculated for a set of different wavelength ranges between 200 and 800 nm, which is the interval where the five reactive dyes present absorbance (see Fig. 2a). The calibration matrix that used in the numerical analysis for estimation of cond($\mathbf{K}$) was the one obtained from Eq. 3, similar results were obtained for cond($\mathbf{K}$) values while using the $\mathbf{K}$ matrix of absorptivities of pure dyes. Table 5 shows the calculated cond($\mathbf{K}$) values for several wavelength ranges. The lowest cond($\mathbf{K}$) value was 14 in the wavelength range 250–650 nm and, therefore, this range was selected for subsequent calculations.

4.4.2. Detecting the outlier(s) in the calibration and validation sets

In chemometric studies, the detection of outlier either in the calibration or in prediction sets can be simply carried out using Mahalanobis distance method [40] or principal component anal-

Table 5
Cond($\mathbf{K}$) values obtained at different wavelength ranges

Wavelength range (nm)	Cond($\mathbf{K}$)
200–800	33
200–300	75
200–400	38
220–700	28
230–680	25
250–550	42
250–650	14
300–600	24
400–800	75
450–650	235

Table 6
Relative error of prediction (REP%) and standard error of prediction (SEP) values estimated for dyes in the validation set

Reactive dye	REP%		SEP(mg l^{-1})	
	CLS	PCR	CLS	PCR
C-Blue	6.5	5.5	2.4	2.0
C-Red	14.4	3.9	3.1	1.0
C-Yellow	5.6	2.9	1.0	0.6
L-Blue	15.4	3.1	2.4	0.8
L-Red	18.4	4.6	2.0	0.8

$F(0.95) = 2.463$.

ysis [44]. Principal component analysis (PCA) was adopted in this work to detect the outlier and also to insure homogeneity between the calibration and validation samples. In outlier determination, the absorbance data matrices of both calibration and prediction samples were separately subjected to principle component analysis. Plotting of the first component factor (PC1) against (PC2) for both sets is shown in Fig. 5. As can be seen in Fig. 5, both calibration and prediction sets are symmetrically fall within the same factor space −0.8 to +0.8 and hence no outlier is present. If any outlier-in any sample in both sets was detected, then that sample should be excluded from numerical analysis.

4.4.3. Determination of reactive dyes in validation samples and figures of merit of the multivariate calibration methods

The determination of the optimum number of factors (h) to be used in the PCR analysis is important to achieve better performance in prediction phase. This allows modeling of the system with the optimum amount of information, avoiding overfitting [40]. To avoid overfitting, leave-one-out cross validation procedure was adopted [11,13]. The obtained optimum number of principal components (h) was 7, which indicate that the variability sources number in the presently studied system exceeds the number of studied analytes (5 analytes). The analytical precision of the CLS and PCR calibration methods was evaluated as the relative error of prediction (REP). REP values were obtained

Fig. 5. Score plots obtained from (PCA) for absorption data matrices of the calibration and validation sets.

from Eq. (4) [13]:

$$REP\% = 100 \times \left[\frac{\sum_{i=1}^{n} (C_{i,\text{pred}} - C_{i,\text{act}})^2}{\sum_{i=1}^{n} (C_{i,\text{act}})^2} \right]^{1/2} \quad (4)$$

where n, C_{pred}, and C_{act} are the total number of validation samples, predicted concentration and the actual concentration of the analyte, respectively. The results in Table 6 showed that the best REP for each dye depends on the calibration method used but, in general, the best results were obtained with the PCR (REP < 10% for all dyes). In order to evaluate whether there are significant differences between the concentrations found for each dye and each calibration method, the F-test (at the 95% confidence level) was employed to compare the standard error of prediction (SEP). SEP values were obtained as [16,40]

$$SEP = \sqrt{\frac{\sum_{i=1}^{n} C_{i,\text{pred}} - C_{i,\text{act}})^2}{n-1}} \quad (5)$$

The values of SEP are given in Table 6. The results showed no significant differences with any of the calibration methods for C-Blue and C-Yellow determination as judged from the F-statistical test. However, PCR method was much better for predicting the concentrations of C-Blue and C-Yellow in the validation set. For the rest of dyes, there were significant differences between PCR and CLS calibration methods. Since the PCR method gave the lowest REP and SEP values, this was the method that adopted for predicting dyes concentrations in real samples. Low selectivity values are associated to unstable estimations of the concentrations and large prediction errors for new samples. Usually, the multivariate selectivity values ranges between zero (complete overlap between analyte and other analytes or interferences) and unity (no or small overlap between analyte and other analytes or interferences) [45]. Higher values of sensitivity are an indication of higher accuracy in determination of the solute. Table 7 shows the selectivity, sensitivity, LOD, linearity range as calculated from the calibration set and the accuracy of measurements as calculated from Eq. 5 for the validation set. In order to take into account all the causes of variability of the method, accuracy in the concentrations was assessed by SEP of a set of n validation samples not included in

Table 7
Values of sensitivity (SEN), selectivity (SEL), and limit of detection (LOD) for dyes determination in the calibration sets and accuracy values (SEP) for dyes determination in validation set

Dye	SEL	SEN	LOD	Linearity range (ppm)	Accuracy (SEP)
C-Blue	0.194	0.0222	0.68	2.3–10	2.0
C-Red	0.154	0.0241	0.62	2.1–10	1.0
C-Yellow	0.422	0.0413	0.42	1.3–10	0.6
L-Blue	0.258	0.0253	0.51	1.7–10	0.8
L-Red	0.188	0.0214	0.82	2.7–10	0.8

the calibration set, which were analyzed in reproducible conditions using PCR calibration method. As indicated from Table 7, C-Yellow is the compound that has the highest selectivity and sensitivity while the rest of dyes have a lower and closer values and this may be attributed to their high spectral overlap. The high sensitivity (0.0413) and selectivity (0.422) obtained for C-Yellow can be attributed to lower spectral overlap with other dyes as reported in Table 3. Moreover, the estimated concentration of C-Yellow should be more accurate than the other dyes. The values of SEP that estimated from the validation set indicated that the most accurate estimation was for C-Yellow dye. Generally, the studied dyes can be simultaneously analyzed with an acceptable degree of accuracy with linearity ranges given in Table 7. The multivariate limits of detection (LOD), ranging between 0.42 and 0.82 ppm for dyes were shown in Table 7. The lower LOD of C-Yellow is expected as this dye has the highest values of SEN and SEL.

4.5. Characterization of the solid-phase extractant

XRD analysis confirmed the presence of philipsite as a major mineral and fassaite as a minor mineral in the adsorbent as indicated in Fig. 6. In fact, the adsorption capacity of anionic dyes on zeolite is limited because of the intrinsic ability of zeolite minerals for attracting positively charged ions. In a different study, Ozdemir et al., have improved the adsorption capacity of a natural zeolite (sepiolite) for anionic dyes after surface treatment with cationic quaternary amines [46]. To examine the changes on the surface of zeolite after modification, both zeolite and M-zeolite were subjected to FTIR analysis. After modification with microemulsion, new peaks appeared at 1565 and 1464 cm^{-1} refers to (COO^{-}) stretch bands and 2929 and
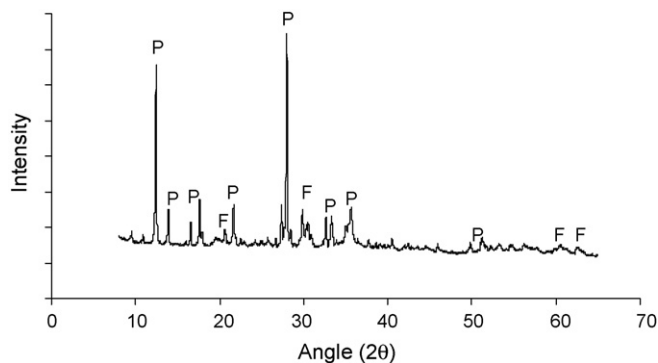
Fig. 6. X-ray diffraction (XRD) scans of natural zeolite. P: Philipsite, F: Fassaite.

2875 cm^{-1} refers to C–H stretching in –CH$_3$ and –CH$_2$– [33]. As a result, a chemisorption occurred by the adsorption of carboxylic acids (saponified coconut oil) on the surface of zeolite to form surface carboxylate groups. In fact, the modification of zeolite with microemulsion makes the surface more hydrophobic and increases the surface ability for dyes extraction.

4.6. Solid-phase extraction of reactive dyes using M-zeolite: optimization of the extraction process

The solid-phase extraction of 20 µg of each dye present in 100 ml of aqueous solution containing 5 ml of 0.5 M phosphate buffer (pH 7.0 ± 0.5) with zeolite and M-zeolite was investigated. M-zeolite exhibits a quantitative enrichment while unmodified zeolite gave an enrichment of 30–50% of dyes which reflects the importance of microemulsion for dyes extraction from solution. Various parameters responsible for offline column preconcentration and elution were systematically optimized. The results of these experiments are summarized in Table 8 and are discussed below briefly. The pH of a set of solutions was adjusted between 2.0 and 10.0 and the general procedure was applied. The solid-phase extraction of C-Blue is constant with a maximum recovery in the pH range 6.0–10.0 (see Table 8). In all subsequent studies, the pH was adjusted to 7.0 ± 0.5 using phosphate buffer. The effect of amount of M-zeolite on the extraction of C-Blue at pH 7.0 was examined in the range 0.5–3.0 g. The results indicate quantitative recoveries of the dye in the range of 1.0–3.0 g of M-zeolite. Hence, 1.0 g of M-zeolite was used in all subsequent experi-

Table 8
Recovery values of C-Blue dye obtained at different experimental variables

pH	2.0	4.0	6.0	7.0	8.0	10.0
Recovery (%)	86.5 ± 0.3	95.6 ± 0.4	>99.9	>99.9	>99.9	>99.9
Amount of M-zeolite (g)	0.5	1.0	1.5	2.0	2.5	3.0
Recovery (%)	90.3 ± 0.2	>99.9	>99.9	99.9	>99.9	>99.9
Extraction flow rate (ml min^{-1})	0.5	1.0	1.5	2.0		
Recovery (%)	>99.9	>99.9	94.0 ± 0.2	66.3 ± 0.2		
Elution flow rate (ml min^{-1})	0.5	1.0	1.5	2.0		
Recovery (%)	>99.9	>99.9	>99.9	>99.9		
Aqueous phase volume (ml)	50	100	250	400	800	1000
Recovery (%)	>99.9	>99.9	>99.9	>99.9	>99.9	>99.9
Enrichment factor[a]	10	20	50	80	160	200

[a] Enrichment factor = volume of sample/volume of eluent.

Table 9
Determination of dyes in different mixtures after preconcentration with M-zeolite using PCR calibration and HPLC methodologies[a]

Mixture	Added (ppb)	PCR Method		HPLC method	
		Found (ppb)	Recovery (±R.S.D)[b]	Found (ppb)	Recovery (±R.S.D)[c]
1					
C-Blue	55.0	63.0	115.3 (14.5)	57.0	104.0 (3.6)
C- Yellow	30.0	32.0	105.7 (6.7)	29.0	97.3 (3.3)
C-Red	60.0	55.0	92.0 (8.3)	63.0	104.8 (5.0)
L-Blue	70.0	67.0	95.4 (4.4)	72.0	102.2 (3.0)
L-Red	80.0	73.0	91.3 (9.0)	82.0	101.4 (2.5)
2					
C-Blue	150.0	128.0	85.4 (14.7)		
C-Yellow	95.0	92.0	96.3 (3.2)		
C-Red	200.0	215.0	108.1 (7.5)		
L-Blue	100.0	106.0	105.4 (6.0)		
L-Red	150.0	135.0	90.3 (10.0)		
3					
C-Blue	90.0	80.0	89.1 (11.1)		
C-Yellow	100.0	99.0	99.2 (1.0)		
C-Red	90.0	85.0	94.6 (5.6)		
L-Blue	0	(2.0)[c]	–		
L-Red	100.0	91.0	90.6 (9.0)		
4					
C-Blue	0	(−3.0)[c]	–	(1.0)[c]	–
C-Yellow	0	(1.0)[c]	–	(2.0)[c]	–
C-Red	80.0	87.0	109.0 (9.0)	82.0	102.2 (2.5)
L-Blue	120.0	115.0	96.2 (4.2)	120.0	99.8 (1.0)
L-Red	70.0	75.0	106.5 (7.1)	69.0	98.4 (1.4)
5					
C-Blue	80.0	71.0	89.3 (11.3)		
C-Yellow	0	(–0.1)[c]	–		
C-Red	0	(0.5)[c]	–		
L-Blue	0	(2.0)[c]	–		
L-Red	90.0	82.0	91.3 (9.0)		

[a] Preconcentration conditions: volume of dyes solution: 250 ml, pH: 7.0, mass of M-zeolite: 1.0 g, and extraction and elution flow rates: 1.0 ml min^{-1}. The water was spiked with: tannic acid, chrome alum, sodium chloride, aluminum chloride, chromium chloride, copper nitrate, iron chloride and sodium carbonate of 200 ppm each.

[b] Average of three trials.

[c] Found content (ppb) when no dye had been added to the mixtures.

ments. The elution of adsorbed C-blue dye was evaluated by using 5.0 ml of various eluting agents including H_2O, 0.1 M HCl, ethanol, methanol–H_2O (70:30 vol.%). Quantitative elution of C-Blue (>99.8%) was obtained with methanol–H_2O and 0.1 M HCl, however, methanol–H_2O mixture was used as eluent in subsequent extraction trials. The influence of flow rate in the range 0.5–2.0 ml min^{-1} on the extraction of C-Blue onto M-zeolite and elution of enriched dye were studied. Up to a preconcentration flow rate of 1.0 ml min^{-1} and an elution flow rate of 2.0 ml min^{-1}, quantitative recoveries were obtained and hence 1.0 ml min^{-1} flow rate was chosen for preconcentration and elution in subsequent studies. Preconcentration factors for a given volume of the sample solution passing through the column depend upon the original sample volume and the volume of eluent solution required to quantitatively elute the dyes retained on the extractant. The recoveries and the enrichment factors for different sample volumes containing 20 µg of each dye are given in Table 8. The preconcentration factor obtained may theoretically be very high if extremely large volumes of sample are pumped

through the column. However, this suffers the obvious drawback of taking a substantial amount of time. An experimental technique is not feasible if it takes several hours to prepare one sample. As a result, a compromise between time and the enrichment factor is necessary. As a result, preconcentration factors of 20–50 are commonplace. In this work, volumes of sample ranging from 100 to 250 ml were used, depending on the analyte and on the enrichment factor required to obtain in a range of concentrations suitable for the sample type. The solid-phase extraction results for the rest of dyes were comparable to those reported in Table 8, therefore, the results were not provided. The linear working ranges for dyes determination (after preconcentration from 250 ml solution) were: 25–200 ppb for C-Yellow and L-Blue and from 50 to 250 ppb for the remaining dyes. The multivariate detection limits of dyes were found to be 15 ppb for C-Yellow and L-Blue and 25 ppb for C-Blue, C-Red, and L-Red dyes. In fact, the SPE preconcentration method developed in the present work enables simple and low cost instrument like spectrophotometer with aid of multivariate calibration meth-
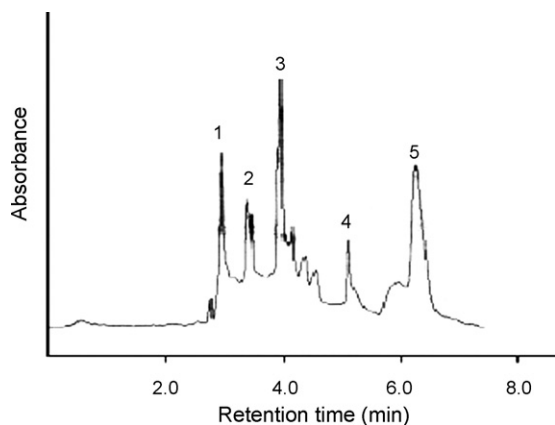
Fig. 7. Ion-pair HPLC separation of reactive dyes mixture on C$_{18}$ column: (1) C-Blue, (2) L-Blue, (3) L-Red, (4) C-Red, and (5) C-Yellow.

ods to analyze water samples containing trace amounts of five sulphonated reactive dyes. The results obtained in this work were summarized in the last row in Table 2 for comparison with more sophisticated instrumental methods that usually employed for sulphonated dyes analysis.

4.7. Simultaneous determination of reactive dyes added to synthetic textile wastewater by multivariate calibration and HPLC methods

Obviously, the next step was to determine how well the proposed multivariate methods do when applied to the analysis of real wastewater containing reactive dyes, considering that fact that the calibration set was designed using standards where other interferences were not accounted. As stated earlier, the main aim of this study was to develop an analytical method with a minimal sample preparation and find a simple analytical method to replace the common analytical methods summarized in Table 2. The proposed method was applied for determination of dyes added to synthetic textile wastewater samples. The determination of reactive dyes in two, three, four and five component mixtures was investigated and the results were summarized in Table 9. In spite of the complexity of sample matrix, the employed chemometric method gave acceptable errors (R.S.D. $\leq$ 10%) for dyes except for C-Blue with errors around 15% (mixtures 1 and 2). It must be emphasized that the high prediction errors obtained for C-Blue in all mixtures are quite reasonable taking into account the high spectral overlap with other dyes and the lower multivariate sensitivity and selectivity values. To validate the proposed PCR calibration method, the dyes that present in real sample were analyzed by ion-pair HPLC methodology. Under the established chromatographic conditions, the five reactive dyes in standard solutions were separated and the obtained resolution times were 3.1, 3.6, 4.2, 5.3, and 6.3 min for C-Blue, L-Blue, L-Red, C-Red and C-Yellow, respectively as shown in Fig. 7. Calibration curves relative to peak area were obtained for each individual dye, with linearity from 1.0 to 15.0 ppm. Analysis of reactive dyes was carried out for mixtures 1 and 4 only and the results were also included in Table 9. Relatively speaking, the chromato-

graphic method gave better results (R.S.D. $\leq$ 5%), furthermore, the determination of C-Blue dye was more accurate using HPLC method. The superiority of HPLC method is expected because the dyes were totally separated before being analyzed, while, in PCR method dyes were determined without separation from the sample matrix. Compare to HPLC method, the proposed PCR regression method was rapid, easy and of low cost for the quantification of sulphonated and azo sulphonated dyes in water using simple UV–vis spectrophotometry. The proposed method could be used for the screening of these dyes in water (e.g., in situ analyses) or as a quantification method in cases where the chromatographic ones cannot be implemented owing to cost limitations, lack of analytical instrumentation.

5. Conclusions

Microemulsion modified zeolite was found to be an effective extractant for concentrating five sulphonated and azo sulphonated dyes from solution. With a preconcentration factor of 50, the five dyes present at concentration range of 20–200 ppb were quantitatively preconcentrated from 250 ml and simultaneously quantified using UV–vis spectrophotometer and a PCR calibration method. No separation was needed for dyes prior their determination. The results obtained from multivariate analysis were fairly comparable to those obtained from HPLC method confirming the effectiveness of the proposed method. With the aid of SPE by M-zeolite, the concentration of dyes could be reproducibly detected over the range 25–200 ppb for C-Yellow and L-Blue and from 50 to 250 ppb for C-Blue, C-Red, and L-Red. The multivariate detection limits of dyes were found to be 15 ppb for C-Yellow and L-Blue and 25 ppb for C-Blue, C-Red, and L-Red dyes. The proposed analytical method gave recoveries from 85.4 to 115.3% and R.S.D. from 1.0 to 14.5% for determination of five dyes.

References

[1] T. Robinson, G. McMullan, R. Marchant, P. Nigam, Biores. Technol. 77 (2001) 247–255.
[2] S. Netpradit, P. Thiravetyan, S. Towprayoon, J. Colloids Interf. Sci. 270 (2004) 255–261.
[3] M. Mottaleb, D. Littlejohn, Anal. Sci. 17 (2001) 429–435.
[4] C. O'Neill, F. Hawkes, D. Hawkes, N. Lourenço, H. Pinheiro, W. Delée, J. Chem. Technol. Biotechnol. 74 (1999) 1009–1018.
[5] J. Riu, I. Schönsee, D. Barceló, C. Ràfols, Trends Anal. Chem. 16 (1997) 405–419.
[6] I. Schönsee, J. Riu, D. Barceló, Quím. Anal. 16 (1997) 243–249.
[7] J. Riu, I. Schönsee, D. Barceló, J. Mass Spectrom. 33 (1998) 653–663.
[8] D. Vaněková, P. Jandera, J. Hrabica, J. Chromatogr. A 1143 (2007) 112–120.
[9] J. Nevado, C. Cabanillas, A. Salcedo, Talanta 42 (1995) 2043–2051.
[10] F. Reig, P. Falcó, Analyst 113 (1988) 1011–1016.

[11] G. Escandar, P. Damiani, H. Goicoechea, A. Olivieri, Microchem. J. 82 (2006) 29–42.

[12] P. Geladi, Spectrochim. Acta B: Atom. Spectrosc. 58 (2003) 767–782.

[13] B. Hemmateenejad, M. Safarpour, A. Mehranpour, Anal. Chim. Acta 535 (2005) 275–285.

[14] S. Şahin, C. Demir, Ş. Güçer, Dyes Pigments 73 (2006) 368–376.

[15] P. Peralta-Zamora, A. Kunz, N. Nagata, R. Poppi, Talanta 47 (1998) 77–84.

[16] P. López-de-Alba, L. López-Martínez, V. Cerdá, Quím. Anal. 20 (2001) 27–63.

[17] M. Korn, J. Andrade, D. de Jesus, V. Lemos, M. Bandeira, W. dos Santos, M. Bezerra, F. Amorim, A. Souza, S. Ferreira, Talanta 69 (2006) 16–24.

[18] E. Birlik, A. Ersöz, A. Denizli, R. Say, Anal. Chim. Acta 565 (2006) 145–515.

[19] K. Suvardhan, K. Kumar, D. Rekha, B. Jayaraj, G. Naidu, P. Chiranjeevi, Talanta 68 (2006) 735–740.

[20] L. Oliferova, M. Statkus, T. Tikhomirova, Z. Baskin, G. Tsizin, J. Anal. Chem. 59 (2004) 841–846.

[21] P. Daorattanachai, F. Unob, A. Imyim, Talanta 67 (2005) 59–64.

[22] Y. Cai, Y. Cai, S. Mou, Y. Yi-qiang Lu, J. Chromatogr. A 1081 (2005) 245–247.

[23] M. El-Barghouthi, A. El-Sheikh, Y.S. Al-Degs, G. Walker, Sep. Sci. Technol. 42 (2007) 2120–2295.

[24] T. de Castro Dantas, L. Beltrame, A. Neto, M. de Alencar Moura, J. Chem. Technol. Biotechnol. 79 (2004) 645–650.

[25] T. de Castro Dantas, A. Neto, M. Moura, Water Res. 35 (2001) 2219–2224.

[26] L. Pérez-Arribas, F. Navarro-Villoslada, M. León-Gonzalez, L. Polo-Díez, J. Chemometr. 7 (1993) 267–275.

[27] H. Goicoechea, A. Olivieri, Talanta 47 (1998) 103–108.

[28] D. Haaland, E. Thomas, Anal. Chem. 60 (1988) 1193–1202.

[29] P. Geladi, B. Kowalski, Anal. Chim. Acta 185 (1986) 1–17.

[30] K. Beebe, R. Kowalski, Anal. Chem. 59 (1987) 1007A–1017A.

[31] A. Lorber, Anal. Chem. 58 (1986) 1167–1172.

[32] A. Espinosa-Mansilla, A. Muñoz de la Peña, F. Salinas, D. González Gómez, Talanta 62 (2004) 853–860.

[33] M. Khraisheh, M. Al-Ghouti, Adsorption 11 (2005) 547–559.

[34] R. Brereton, Analyst 122 (1997) 1521–1530.

[35] W. Brumley, C. Brownrigg, J. Chromatogr. A 646 (1993) 377–389.

[36] A. Bruins, L. Weidolf, J. Henion, W. Budde, Anal. Chem. 59 (1987) 2647–2652.

[37] P. Edlund, E. Lee, J. Henion, W. Budde, Biol. Mass Spectrom. 18 (2005) 233–240.

[38] T. Poiger, S. Richardson, G. Baughman, J. Chromatogr. A 886 (2000) 271–282.

[39] M. Pérez-Urquiza, M. Prat, J. Beltrán, J. Chromatogr. A 871 (2000) 227–234.

[40] P. López-de-Alba, L. López-Martínez, V. Cerdá, J. Amador-Hernández, J. Braz. Chem. Soc. 17 (2006) 715–722.

[41] T. Isaksson, T. Naes, Appl. Spectrosc. 44 (1990) 1152–1158.

[42] Y. Du, Y. Liang, J. Jiang, R. Berry, Y. Ozaki, Anal. Chim. Acta 501 (2004) 183–191.

[43] J. Kalivas, P. Lang, J. Chemometr. 3 (1989) 443–449.

[44] B. Hemmateenejad, M. Akhond, F. Samari, Spectrochim. Acta A: Mol. Biomol. Spectrosc. 67 (2007) 958–965.

[45] R. Boqué, N. Faber, F. Rius, Anal. Chim. Acta 423 (2000) 41–49.

[46] O. Ozdemir, B. Armagan, M. Turan, M. Çelik, Dyes Pigments 62 (2004) 49–60.

Optimization of pressurized liquid extraction (PLE) of dioxin-furans and dioxin-like PCBs from environmental samples

Pedro Antunes[a], Paula Viana[a], Tereza Vinhas[a], J.L. Capelo[b],
J. Rivera[c], Elvira M.S.M. Gaspar[d],*

[a] Reference Laboratory of Environmental Institute, Rua da Murgueira Zambujal, Apartado 7585, Alfragide, 2721-865 Amadora, Portugal
[b] Requimte, Department of Chemistry, Faculty of Science and Technology, New University of Lisbon,
Quinta da Torre, 2825-114 Caparica, Portugal
[c] Instituto de Investigaciones Quimicas y Ambientales,CSIC, Departamento de Ecotecnologías, Laboratorio de Dioxinas,
c/Jordi Girona, 18, 08034 Barcelona, Spain
[d] Department of Chemistry, CQFB-Requimte, Faculty of Science and Technology, New University of Lisbon,
Quinta da Torre, 2825-114 Caparica, Portugal

Abstract

Pressurized liquid extraction (PLE) applying three extraction cycles, temperature and pressure, improved the efficiency of solvent extraction when compared with the classical Soxhlet extraction. Polychlorinated-p-dioxins (PCDDs), polychlorinated dibenzofurans (PCDFs) and dioxin-like PCBs (coplanar polychlorinated biphenyls (Co-PCBs)) in two Certified Reference Materials [DX-1 (sediment) and BCR 529 (soil)] and in two contaminated environmental samples (sediment and soil) were extracted by ASE and Soxhlet methods. Unlike data previously reported by other authors, results demonstrated that ASE using n-hexane as solvent and three extraction cycles, 12.4 MPa (1800 psi) and 150 °C achieves similar recovery results than the classical Soxhlet extraction for PCDFs and Co-PCBs, and better recovery results for PCDDs. ASE extraction, performed in less time and with less solvent proved to be, under optimized conditions, an excellent extraction technique for the simultaneous analysis of PCDD/PCDFs and Co-PCBs from environmental samples. Such fast analytical methodology, having the best cost-efficiency ratio, will improve the control and will provide more information about the occurrence of dioxins and the levels of toxicity and thereby will contribute to increase human health.

1. Introduction

The extreme toxicity of dioxins and furans has made their analysis in environmental samples increasingly important. They are well known as persistent and highly toxic organic pollutants (POPs). Pressurized liquid extraction (PLE, sometimes designated by, accelerated solvent extraction ASE) has been used in the last years with the aim of reducing the solvent consumption and the sample preparation time.

PLE technique [1–3] uses conventional liquid solvents at elevated pressures (10.3–13.8 MPa) and temperatures (40–200 °C)

to extract solid samples quickly, and uses less solvent than the classical Soxhlet procedure. For instance, the Soxhlet technique for the extraction of polychlorinated-p-dioxins (PCDDs) and polychlorinated dibenzofurans (PCDFs) can take over 18 h and uses from 50 to 400 mL. With ASE, a solid sample is enclosed in a stainless steel vessel which is filled with an extraction solvent and heated to temperature. The sample is allowed to statically extract for 5–10 min. Extraction solvents of PLE are commonly used at temperatures that are higher than their respective boiling points and at high pressures to increase the analyte solubilities in solvents. The complete procedure is finished in 15–25 min, using about 15 mL of solvent for a 10 g sample. PLE has been approved by the United States Environmental Protection Agency (USEPA) as proposed Method 3545 [4] which includes polychlorinated biphenyls (PCBs), organochlorine and

organophosphorous pesticides (OCP and OPP), semi-volatiles or BNAs, chlorinated phenoxy herbicides and polycyclic aromatic hydrocarbons (PAHs).

Optimization studies of PLE procedure, such as choice of solvents and temperatures, have been reported [5] because recoveries of POPs from environmental samples depend strongly on these conditions. However, few studies have been done for quantitative and simultaneous extractions of PCDDs, PCDFs and PCBs from environmental samples [5,6]. The main reason is that PLE conditions for each compound are indicated separately by the USEPA method.

This paper reports on, for the first time, PLE optimized conditions for quantitative and simultaneous extraction of PCDDs, PCDFs and dioxin-like PCBs (Co-PCBs) from two Certified Reference Materials DX-1 (sediment) and BCR 529 (soil) and also from two real environmental samples. Unlike data previously reported by other authors, the results indicate that an exhaustive and simultaneous extraction was achieved using *n*-hexane as single solvent at optimized conditions (three cycles, 12.4 MPa and 150 °C) and recoveries were surprisingly high for PCDDs when compared to those obtained using Soxhlet extraction. PLE method is performed in less time and with less solvent than Soxhlet methodology, being an excellent sustainable extraction technique for the simultaneous analysis of chlorinated dioxin-like compounds. The method is a good alternative to European Community needs for information about production and release of organohalogen compounds to the environment.

2. Experimental

2.1. Samples

Two Certified Reference Materials DX-1 (sediment), National Water Research Institute, Canada and BCR-529 (sandy soil), European Commission—Joint Research Center, Institute for Reference Materials and Measurements, Belgium were used in this study. The water content, according to certificate values, were residual (<5%); the organic matter for DX-1 was 3.5% and for BCR-529 was 0.8%. The authors would like to test this method with a previously mentioned Certified Reference Material CRM 0422 [5,6]. However, internationally, this reference corresponds to a fish muscle, instead of a forest soil sample [7].

The real samples are one sediment sample from Castelo de Bode dum, Portugal, and a Portuguese forest soil. The real samples were sieved to particles $\leq 106\,\mu\text{m}$ and lyophilized during 72 h (water content <5%).

2.2. Standards and reagents

PCDD/PCDFs internal standards for extraction (EPA 1613 LCS), PCDD/PCDFs injection standards (EPA 1613 ISS) and PCDD/PCDFs calibration standards (EPA 1613 CSL, CS1–CS5), all in nonane solution, were purchased from Wellington Laboratories (Ont., Canada). Co-PCBs extraction standards (WP–LCS), Co-PCBs injection standards (WP–ISS) and Co-PCBs calibration standards (WP–CS1–CS7), all in
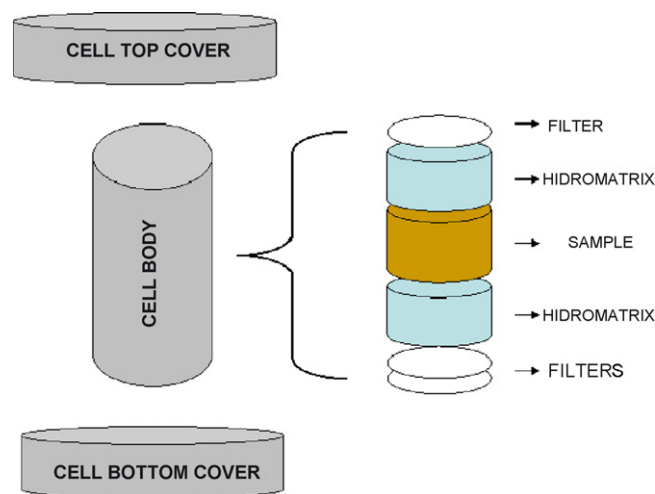
Fig. 1. Packing diagram of the extraction cell of ASE system.

nonane solution, were also purchased from Wellington Laboratories (Ont., Canada). All internal standards are $^{13}\text{C}_{12}$-labelled compounds. All used solvents are from Merck (pesticide grade; Darmstad, Germany). Diatomaceous earth (Hidromatix), ASE PreP DE, is from Dionex (Sunnyvale, CA, USA). Soxhlet cellulose extraction thimbles (30 mm × 80 mm) are from Schleicher & Schuell (Dassel, Germany). Power-prep columns are from Power Prep (Fluid Management System, Waltham, MA, USA); silica (19 cm), basic alumina (11 g, 19 cm) and carbon/celite (0.34 g, 4 cm) column were used.

2.3. Soxhlet extraction

Soxhlet apparatus were used with a cellulose thimble containing 1 or 2 g samples. The extractions were performed with and without copper, following USEPA 1613 Method for PCDD/PCDFs and USEPA Method 1688 for Co-PCBs. Both USEPA methods have similar procedures; the difference is the internal standards. The copper treatment included the addition of copper powder to the sample (1/2) contained in the cellulose thimble. Toluene was used as solvent and the extraction was performed during 48 h. Triplicate extractions were always performed, using ca. 350 mL of toluene. The certified values were based on Soxhlet extraction using toluene as solvent.

2.4. PLE extraction

Pressurized liquid extraction was carried out using a PLE system (ASE 200; Dionex, Sunnyvale, CA, USA) equipped with 33 mL stainless-steel extraction cells. All samples were packed according to Fig. 1 . All samples were placed into the stainless-steel extraction cells prepared with a cellulose filter (Dionex), then a portion (ca. 1/3 of cell's volume) of diatomaceous earth was placed and the sample (ca. 1/3 of cell's volume) was added, enriched with $^{13}\text{C}_{12}$-labelled internal extraction standards. The cell stands by 2 h to incorporate the standards and then were filled with a second portion of diatomaceous earth (ca. 1/3 of cell volume) and closed with a cellulose filter (Dionex, USA). During the process, the material in cell was being compressed

Table 1

Copper and sulphuric acid cleanup effect on Soxhlet extraction and pressurized liquid extraction (PLE) of PCDD/Fs and dioxin-like PCBs (Co-PCBs) from Certified Reference Material DX-1 (sediment).

PCDD/Fs and Co-PCBs isomers (IUPAC number)	DX-1 certificate value (ng kg^{-1})	Soxhlet with Cu$_{(s)}$ and H$_2$SO$_4$ ($n=3$)				Soxhlet without Cu$_{(s)}$ and H$_2$SO$_4$ ($n=3$)			
		Concentration[a] (ng kg^{-1})	Observed/certified value (%)	RSD (%)	Recovery[b] (%)	Concentration[a] (ng kg^{-1})	Observed/certified value (%)	RSD (%)	Recovery[b] (%)
2,3,7,8-TCDF (F1)	89 ± 44	51	58	24	85	32	36	29	103
1,2,3,7,8-PeCDF (F2)	39 ± 14	45	114	18	79	40	101	4.9	88
2,3,4,7,8-PeCDF (F3)	62 ± 32	67	109	9.3	82	81	130	9.0	85
1,2,3,4,7,8-HxCDF (F4)	714 ± 276	669	94	6.2	82	639	90	1.9	96
1,2,3,6,7,8-HxCDF (F5)	116 ± 37	128	110	2.1	72	111	96	7.9	88
2,3,4,6,7,8-HxCDF (F6)	57 ± 36	63	110	4.6	76	56	98	6.6	86
1,2,3,7,8,9-HxCDF (F7)	28 ± 42	48	172	2.1	86	44	156	1.1	91
1,2,3,4,6,7,8-HpCDF (F8)	2397 ± 796	2468	103	2.6	71	2467	103	1.3	67
1,2,3,4,7,8,9-HpCDF (F9)	137 ± 62	157	115	2.1	84	152	111	1.6	69
OCDF (F10)	7122 ± 2406	7669	108	20	–	6362	89	2.4	–
2,3,7,8-TCDD (D1)	263 ± 53	260	99	0.6	81	216	82	0.6	104
1,2,3,7,8-PeCDD (D2)	22 ± 8	28	129	13	79	28	129	2.5	87
1,2,3,4,7,8-HxCDD (D3)	23 ± 7	22	96	5.2	87	25	107	20	85
1,2,3,6,7,8-HxCDD (D4)	77 ± 27	88	114	12	70	75	98	2.4	92
1,2,3,7,8,9-HxCDD (D5)	53 ± 24	41	77	27	–	42	79	4.4	–
1,2,3,4,6,7,8-HpCDD (D6)	634 ± 182	640	101	11	74	654	103	1.0	70
OCDD (D7)	3932 ± 933	4187	106	8.9	69	3904	99	2.4	52
3,4,4′,5-TCB (#81)	–	475	–	7.2	51	421	–	16	103
3,3′,4,4′-TCB (#77)	–	6244	–	2.1	49	6519	–	22	110
2′,3,4,4′,5-PeCB (#123)	–	1377	–	7.1	64	991	–	22	90
2,3′,4,4′,5-PeCB (#118)	–	44670	–	3.4	67	41977	–	13	90
2,3,4,4′,5-PeCB (#114)	–	1939	–	10	60	1902	–	15	93
2,3,3′,4,4′-PeCB (#105)	–	19230	–	6.0	47	23557	–	5.5	96
3,3′,4,4′,5-PeCB (#126)	–	328	–	29	49	206	–	16	116
2,3′,4,4′,5,5′-HxCB (#167)	–	1549	–	4.3	68	1174	–	24	97
2,3,3′,4,4′,5-HxCB (#156)	–	3934	–	5.6	56	3822	–	12	86
2,3,3′,4,4′,5′-HxCB (#157)	–	761	–	12	51	727	–	3.6	91
3,3′,4,4′,5,5′-HxCB (#169)	–	37	–	26	46	16	–	47	95
2,3,3′,4,4′,5,5′-HpCB (#189)	–	410	–	9.0	66	337	–	8.7	85

2,3,7,8-TCDF (F1)	89 ± 44	69	77	16	66	44	49	2.3	94
1,2,3,7,8-PeCDF (F2)	39 ± 14	54	138	12	73	43	111	4.8	73
2,3,4,7,8-PeCDF (F3)	62 ± 32	95	152	42	70	83	134	5.7	73
1,2,3,4,7,8-HxCDF (F4)	714 ± 276	798	112	1.7	66	730	102	2.1	79
1,2,3,6,7,8-HxCDF (F5)	116 ± 37	149	128	0.8	64	133	114	4.4	77
2,3,4,6,7,8-HxCDF (F6)	57 ± 36	84	148	8.5	61	65	114	3.5	77
1,2,3,7,8,9-HxCDF (F7)	28 ± 42	65	230	8.5	60	52	186	2.2	83
1,2,3,4,6,7,8-HpCDF (F8)	2397 ± 796	3328	139	4.1	44	2764	115	2.3	49
1,2,3,4,7,8,9-HpCDF (F9)	137 ± 62	232	169	8.2	41	163	119	3.5	41
OCDF (F10)	7122 ± 2406	7724	108	0.5	-	3401	48	33	–
2,3,7,8-TCDD (D1)	263 ± 53	248	94	1.9	74	272	103	4.2	91
1,2,3,7,8-PeCDD (D2)	22 ± 8	47	215	10	71	64	291	21	74
1,2,3,4,7,8-HxCDD (D3)	23 ± 7	30	131	13	68	23	101	24	82
1,2,3,6,7,8-HxCDD (D4)	77 ± 27	229	297	2.0	63	332	431	7.5	76
1,2,3,7,8,9-HxCDD (D5)	53 ± 24	90	170	14	-	143	269	15	-
1,2,3,4,6,7,8-HpCDD (D6)	634 ± 182	1956	308	0.2	57	2041	322	3.0	63
OCDD (D7)	3932 ± 933	9984	254	2.7	41	8349	212	1.2	45
3,4,4′,5-TCB (#81)	–	600	–	13	45	–	–	–	–
3,3′,4,4′-TCB (#77)	–	6819	–	5.8	54	–	–	–	–
2′,3,4,4′,5-PeCB (#123)	–	1316	–	2.8	72	–	–	–	–
2,3′,4,4′,5-PeCB (#118)	–	46868	–	2.1	71	–	–	–	–
2,3,4,4′,5-PeCB (#114)	–	2364	–	16	65	–	–	–	–
2,3,3′,4,4′-PeCB (#105)	–	20408	–	5.7	66	–	–	–	–
3,3′,4,4′,5-PeCB (#126)	–	283	–	10	58	–	–	–	–
2,3′,4,4′,5,5′-HxCB (#167)	–	1800	–	2.4	72	1361	–	27	87
2,3,3′,4,4′,5-HxCB (#156)	–	4466	–	4.6	67	4208	–	12	88
2,3,3′,4,4′,5′-HxCB (#157)	–	977	–	10	65	906	–	28	86
3,3′,4,4′,5,5′-HxCB (#169)	–	27	–	41	55	34	–	12	41
2,3,3′,4,4′,5,5′-HpCB (#189)	–	487	–	5.1	62	471	–	5.3	85

by hand. Then, the cell was sealed with the top cell cap. The dead volume was lower than 2 mm.

The optimal PLE conditions achieved for extractions were $P = 12.4$ MPa and $T = 150\,^\circ$C, with three (3) extraction cycles. Triplicate extractions were performed without and with copper (added to the sample), using n-hexane and toluene as solvents. The choice of these solvents was based on the USEPA Method 3545A for PCDD/PCDFs and PCBs, which recommends the use of single solvent.

2.5. Cleanup

The cleanup procedures included both possibilities—the treatment without and with sulphuric acid. The treatment with sulphuric acid was done submitting the extracts to three successive extraction steps with 50 mL of concentrated sulphuric acid. During the first extraction the acid stands by 24 h, while the second and third extractions were performed during 3 h. The organic phase was collected and submitted to multi-layered silica/alumina/active carbon columns (Power Prep/FMS apparatus). A gradient elution, using an automatic program, was done. PCDD/PCDFs were retained in the active carbon column, which was first eluted with mixed different solvents and, at the end, was eluted using toluene from the opposite flow direction. Co-PCBs were collected from all columns, using different solvents (dichloromethane/hexane and toluene). The PCDD/PCDFs fraction was concentrated to dryness using a rotary evaporator and a nitrogen stream, and after was diluted with nonane and internal standards (USEPA 1613-ISS solution; 5 μL of each).

The Co-PCBs sub-fraction (mono-ortho-PCBs) resulted from the silica and alumina columns' elution. This sub-fraction was concentrated to dryness using a rotary evaporator and nitrogen stream. A portion of this sub-fraction was combined with the PCDD/PCDFs fraction which contains the non-ortho-PCBs, to constitute the total Co-PCBs fraction [8]. Finally, the diluted $^{13}C_{12}$-labelled injection internal standards WP–ISS were added to each sample to calculate the recoveries of the extraction and cleanup procedures. Table 1 and Fig. 2 shows the dioxin and

furan's recoveries. The cleanup for PCBs with copper and sulphuric acid revealed identical recovery results.

2.6. Determination of PCDD/PCDFs and Co-PCBs

Procedures were done according to USEPA Method 1613 for PCDD/PCDFs and USEPA 1618 for PCBs. HRGC/HRMS (Agilent Technologies 6890 series coupled with a Micromass spectrometer AutoSpec ultima) was used. We achieved GC separation for TetraCDDs/CDFs to HexaCDDs/CDFs, for HeptaCDDs/CDFs to OctaCDDs/CDFs, and for TetraCBs to HeptaCBs, respectively, using a capillary column VF5MS (60 m × 0.25 mm i.d. × 0.25 μm; Varian, Mideelburg, The Netherlands) and a DB Dioxin column (60 m × 0.15 mm i.d. × 0.20 μm; J&W Scientific, Folsom, CA, USA).

Recoveries of the $^{13}C_{12}$-labelled extraction standards were good according to USEPA methods (1613 and 1688), which established the ranges 40–120% for labelled compounds and 80–120% for native compounds (observed value/certified value). Results are shown in Tables 1 and 2.

3. Results and discussion

Soxhlet extractions of CRM (DX-1 and BCR 529) were performed using n-hexane and toluene with and without copper and sulphuric acid. Tables 1 and 2 and Fig. 2 summarize the compound's recoveries. The $^{13}C_{12}$ recoveries are ratios of recovered $^{13}C_{12}$-labelled compound to the spiked $^{13}C_{12}$-labelled compound and recovery of native compounds are ratios of each isomer's concentration to the certified values. It is important to emphasize that certified values are determined using EPA Method 1613, this means Soxhlet extraction procedure using toluene as solvent. We have tried different solvents. Using n-hexane lower recoveries of PCDD/PCDFs and Co-PCBs (<80%) were achieved. Using toluene, a more polar solvent, better recoveries of both PCDD/PCDFs and Co-PCBs were produced. Our Soxhlet's results are in good agreement with those recently published [5].
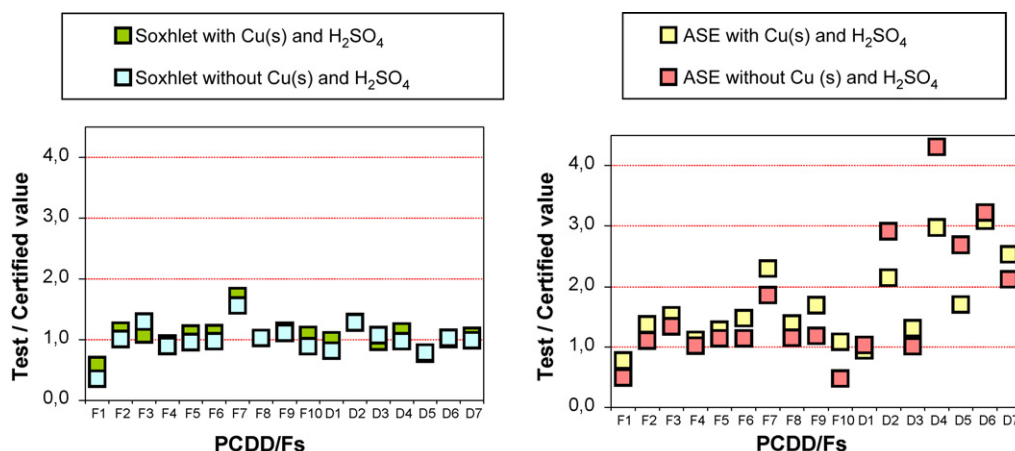

Fig. 2. Graphical visualization of cleanup effect on Soxhlet and ASE extraction procedures of PCDD/Fs from CRM DX-1: F1-F10, polychlorinated dibenzo-furans and D1-D7, polychlorinated dibenzo-dioxins (according to Table 1).

Table 2
Recoveries of PCDD/Fs and dioxin-like PCBs (Co-PCBs) from Certified Reference Materials BCR 529 using Soxhlet and PLE (3 cycles, 12.4 MPa and 150 °C) extractions

PCDD/Fs and Co-PCBs isomers (IUPAC number)	BCR certificate value (ng kg^{−1})	Soxhlet (n = 3)				PLE (n = 3)			
		Concentration[a] (ng kg^{−1})	Observed/certified value (%)	RSD (%)	Recovery[b] (%)	Concentration[c] (ng kg^{−1})	Observed/certified value (%)	RSD (%)	Recovery[b] (%)
2,3,7,8-TCDF (F1)	78 ± 13	–	–	–	–	–	–	–	–
1,2,3,7,8-PeCDF (F2)	140 ± 30	247	176	40	70	203	145	20	68
2,3,4,7,8-PeCDF (F3)	360 ± 70	555	154	5.1	82	460	189	1.0	69
1,2,3,4,7,8-HxCDF (F4)	3400 ± 500	4352	128	9.6	72	6218	198	18	71
1,2,3,6,7,8-HxCDF (F5)	1090 ± 150	1184	109	11	74	1444	150	2.7	62
2,3,4,6,7,8-HxCDF (F6)	370 ± 40	518	140	8.7	73	658	206	11	69
1,2,3,7,8,9-HxCDF (F7)	22 ± 10	–	–	12	–	–	–	12	–
1,2,3,4,6,7,8-HpCDF (F8)	–	13652	–	3.5	–	15171	–	14	–
1,2,3,4,7,8,9-HpCDF (F9)	–	1984	–	2.9	–	2248	–	12	–
OCDF (F10)	–	60674	–	10	–	63556	–	16	–
2,3,7,8-TCDD (D1)	4500 ± 600	3955	88	2.4	75	5507	122	1.8	69
1,2,3,7,8-PeCDD (D2)	440 ± 50	666	151	12	80	3469	635	109	67
1,2,3,4,7,8-HxCDD (D3)	1200 ± 300	1171	98	6.5	68	2058	163	54	71
1,2,3,6,7,8-HxCDD (D4)	5400 ± 900	5041	93	7.2	68	7623	141	30	64
1,2,3,7,8,9-HxCDD (D5)	3000 ± 400	2045	68	2.0	–	2964	99	46	–
1,2,3,4,6,7,8-HpCDD (D6)	–	44920	–	8.4	–	59222	–	17	–
OCDD (D7)	–	245067	–	8.0	–	270657	–	10	–
3,4,4′,5-TCB (#81)	–	782	–	3.1	39	2971	–	5.6	52
3,3′,4,4′-TCB (#77)	–	21846	–	9.3	45	89640	–	26	65
2′,3,4,4′,5-PeCB (#123)	–	3560	–	1.5	46	3301	–	8.0	97
2,3′,4,4′,5-PeCB (#118)	–	29970	–	5.0	47	34366	–	8.5	96
2,3,4,4′,5-PeCB (#114)	–	3728	–	11	44	4517	–	13	93
2,3,3′,4,4′-PeCB (#105)	–	11727	–	0.8	42	14011	–	5.7	90
3,3′,4,4′,5-PeCB (#126)	–	4089	–	1.4	54	6902	–	3.6	78
2,3′,4,4′,5,5′-HxCB (#167)	–	25363	–	15	45	14374	–	4.6	82
2,3,3′,4,4′,5-HxCB (#156)	–	19047	–	2.6	45	19763	–	4.8	79
2,3,3′,4,4′,5′-HxCB (#157)	–	4899	–	5.8	45	3770	–	1.4	77
3,3′,4,4′,5,5′-HxCB (#169)	–	554	–	1.1	58	569	–	10	67
2,3,3′,4,4′,5,5′-HpCB (#189)	–	6124	–	4.0	44	6427	–	1.6	87

[a] Extraction solvent: toluene.

[b] [13]C: labelled compounds.

[c] Extraction solvent: n-hexane.

Table 3
Comparison of Soxhlet and PLE extraction results with literature data [6]

PCDD/Fs isomers	CRM DX-1 (sediment)		CRM 0422 (forest soil) [6][a]	
	Soxhlet with toluene	PLE with *n*-hexane	Soxhlet with toluene	PLE with (1/1) *n*-hexane/acetone
	Observed/certified value (%)	Observed/certified value (%)	Observed/certified value (%)	Observed/certified value (%)
2,3,7,8-TCDF (F1)	58	77	103	77
1,2,3,7,8-PeCDF (F2)	114	138	124	108
2,3,4,7,8-PeCDF (F3)	109	152	114	83
1,2,3,4,7,8-HxCDF (F4)	94	112	116	99
1,2,3,6,7,8-HxCDF (F5)	110	128	104	89
2,3,4,6,7,8-HxCDF (F6)	110	148	118	95
1,2,3,7,8,9-HxCDF (F7)	172	230	107	87
1,2,3,4,6,7,8-HpCDF (F8)	103	139	105	72
1,2,3,4,7,8,9-HpCDF (F9)	115	169	114	107
OCDF (F10)	108	108	117	81
2,3,7,8-TCDD (D1)	99	94	96	83
1,2,3,7,8-PeCDD (D2)	129	215	109	86
1,2,3,4,7,8-HxCDD (D3)	96	131	101	91
1,2,3,6,7,8-HxCDD (D4)	114	297	105	81
1,2,3,7,8,9-HxCDD (D5)	77	170	104	85
1,2,3,4,6,7,8-HpCDD (D6)	101	308	124	96
OCDD (D7)	106	254	92	83

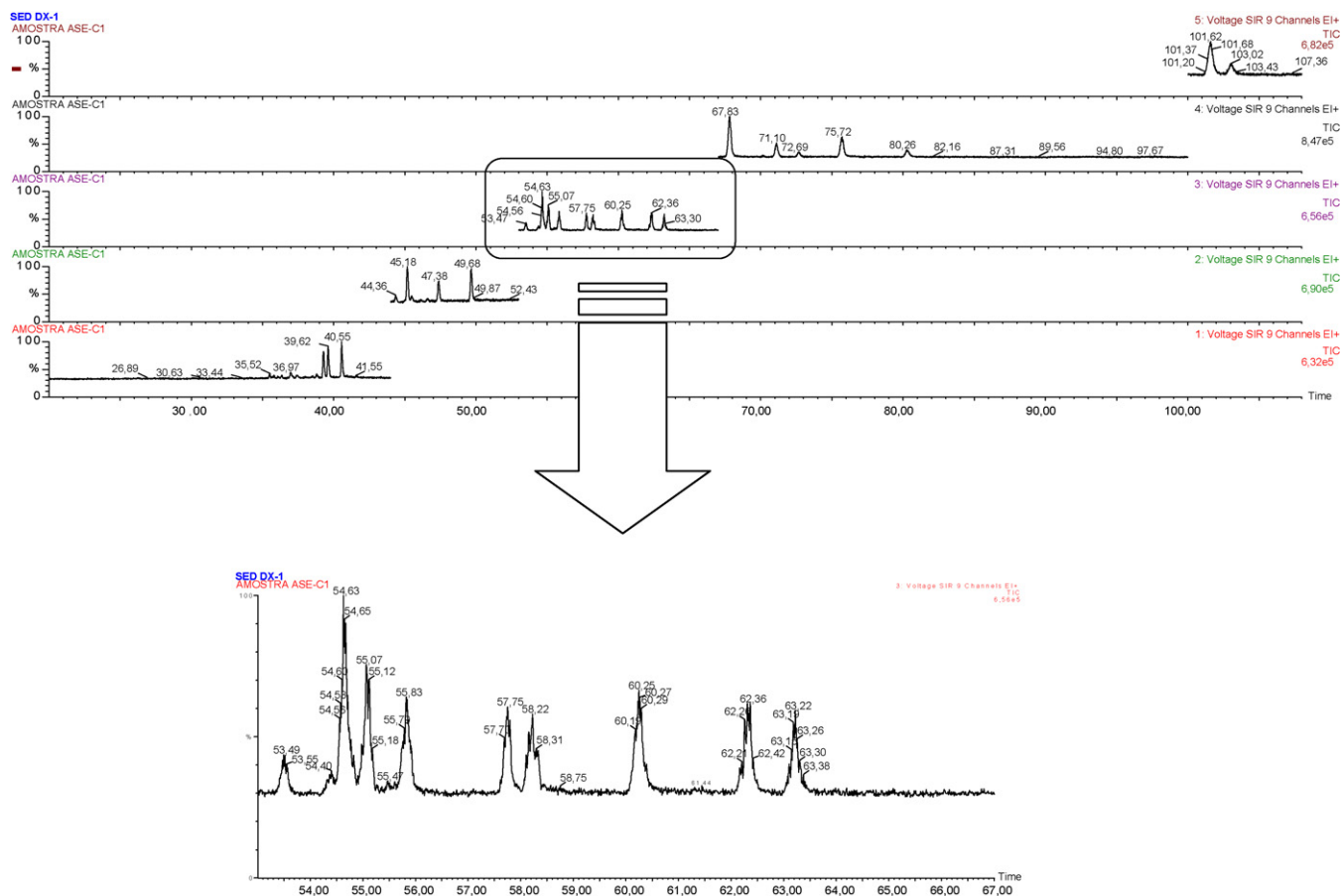[a] Internationally CRM 422 corresponds to a fish muscle [7].

Fig. 3. *n*-Hexane ASE extraction chromatogram from BCR DX-1 sample, using DB-Dioxin column. The specific congeners of PCDDs are shown. Zoom area shows the Hx(6)CDD/Fs.

PLE extractions were done using the same extraction solvents as those used for Soxhlet extractions. Different conditions were tried till the ASE optimal conditions were achieved: three (3) cycles, $P = 12.4$ MPa, $T = 150$ °C. As the solvent recoveries were comparable, due to safety reasons *n*-hexane was considered to be our choice. Recovery results are summarized in Tables 1 and 2. Contrary to our expectations based on the results obtained with Soxhlet methodology, PLE extractions using toluene produced similar recoveries as those using *n*-hexane. During the cleaning step the sample matrix is washed with *n*-hexane. The extraction with *n*-hexane seems to guarantee the uniformity of the process. PLE extraction using *n*-hexane, at described conditions, exhibited the highest "native" recoveries of PCDDs ever reported. These recoveries are comparable to those recently obtained with more polar solvents at different operation conditions by Kiguchi et al. [5,6] (Table 3). The RSDs of both PCDD/PCDFs and Co-PCBs for the PLE extraction using 3 cycles are low. The good recoveries and the low RSDs of PCDD/PCDFs and Co-PCBs may indicate that, at these conditions, exists a strong analyte–matrix interaction.

Some researchers [5,6] have mentioned that several cycles are necessary to achieve satisfactory extraction of PCDD/PCDFs and Co-PCBs from environmental samples. Our results support those findings, proving that PLE using 3 cycles, 12.4 MPa and 150 °C, produce the best native analyte's recoveries already reported. However, Table 3 also shows that using these condi-

tions no mixed solvents are necessary for good extraction of more tightly bounded PCDFs and Co-PCBs, being the PCDDs increasingly recovered from certified reference materials. The Z-score values for PCDD/Fs and Co-PCBs were also determined (data not shown). This parameter is considered to evaluate the performance of the method during the laboratories' accreditation or inter-laboratorial assays and during proficiency testing schemes. For PCDDs, using ASE extraction, the Z-score values were consistently high in all samples, revealing that recovery values are better than those obtained with Soxhlet extraction. As PLE extraction applies temperature and pressure to accelerate extraction processes, the effect was particularly improved with PCDDs using three cycles, showing a good efficiency of *n*-hexane extraction.

Some authors, using different conditions from the ones that are reported in this work, have already demonstrated that PLE is equivalent to classical extraction methods such as Soxhlet [3]. This work proves that using optimized conditions, PLE has higher native dioxin-like compounds' recoveries than Soxhlet methodology. As organic solvents required to extract solid samples using Soxhlet method, represent a large source of waste in the environmental analysis laboratory, PLE proved to be an important alternative extraction procedure for PCDDs and PCDFs from environmental samples.

Figs. 3 and 4 show the DB-Dioxin column chromatograms. It is possible to visualize the comparison of the native recovery of
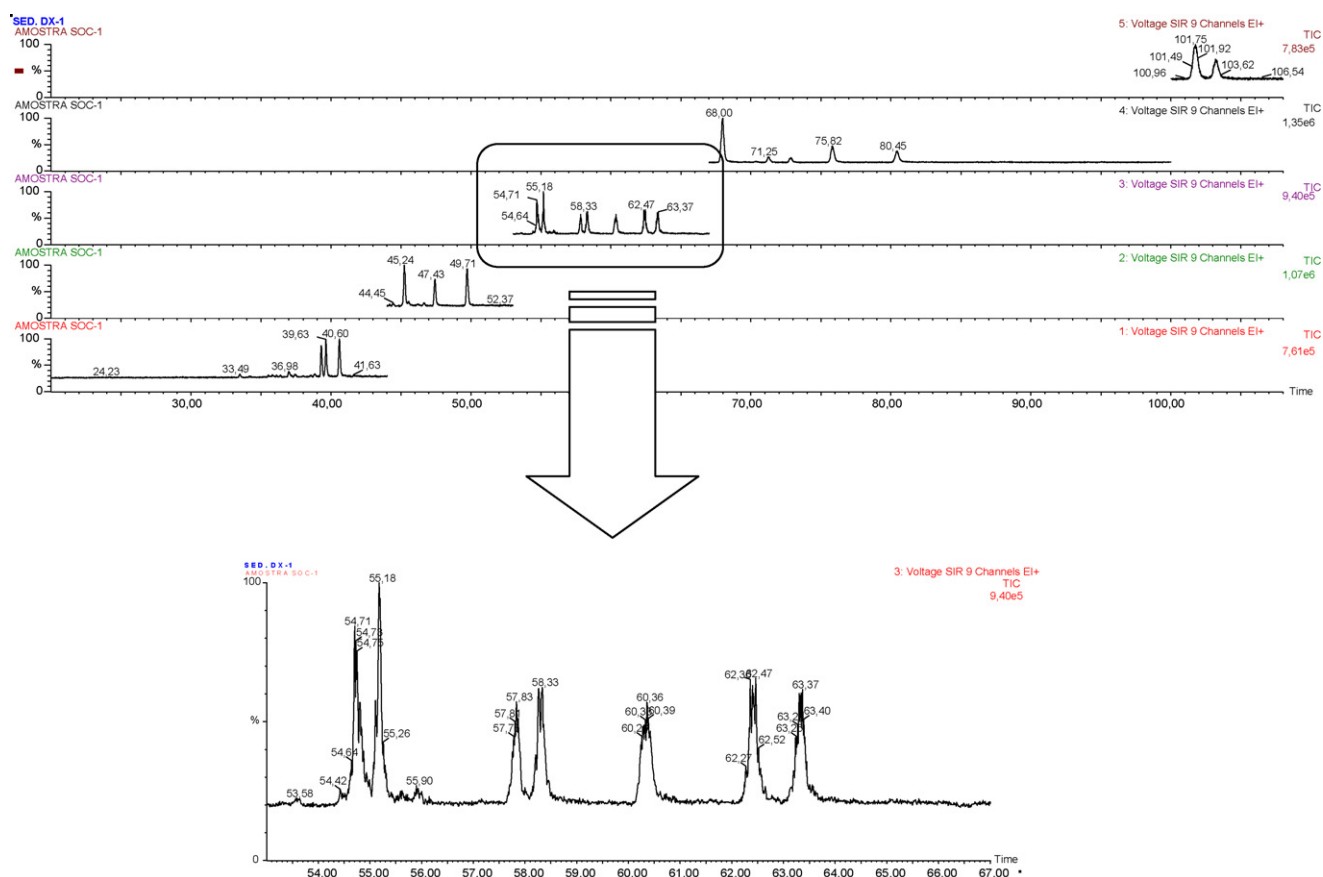

Fig. 4. Toluene Soxhlet extraction chromatogram from BCR DX-1 sample, using DB-Dioxin column. The specific congeners of PCDDs are shown. Zoom area shows the Hx(6)CDD/Fs.

Table 4
Individual WHO–TEF values for risk assessment and native recoveries (WHO–TEQ values) of PCDD/Fs and Co-PCBs using Soxhlet and PLE extraction for two real environmental samples: sediment and forest soil

PCDD/Fs isomers	WHO–TEF[a]	Sediment (TOC = 2.1%)		Forest soil (TOC = 13.8)	
		Soxhlet with toluene (ng WHO–TEQ kg^{-1})	PLE with n-hexane (ng WHO–TEQ kg^{-1})	Soxhlet with toluene (ng WHO–TEQ kg^{-1})	PLE with n-hexane (ng WHO–TEQ kg^{-1})
2,3,7,8-TCDF (F1)	0.1	0.02[b]	0.02[b]	6.4	6.1
1,2,3,7,8-PeCDF (F2)	0.05	0.03[b]	0.03[b]	3.0	3.6
2,3,4,7,8-PeCDF (F3)	0.5	0.25[b]	1.3[b]	63	69
1,2,3,4,7,8-HxCDF (F4)	0.1	0.38	0.34	11	14
1,2,3,6,7,8-HxCDF (F5)	0.1	0.08[b]	0.24[b]	9.7	15
2,3,4,6,7,8-HxCDF (F6)	0.1	0.09[b]	0.24[b]	14	21
1,2,3,7,8,9-HxCDF (F7)	0.1	0.13[b]	0.13[b]	3.8	4.1
1,2,3,4,6,7,8-HpCDF (F8)	0.01	0.12	0.20	4.9	6.2
1,2,3,4,7,8,9-HpCDF (F9)	0.01	0.012[b]	0.012[b]	0.54	0.36
OCDF (F10)	0.0001	0.0044	0.0063	0.051	0.019
2,3,7,8-TCDD (D1)	1	0.5[b]	0.5[b]	6.8	10
1,2,3,7,8-PeCDD (D2)	1	1.2[b]	2.5[b]	43	35
1,2,3,4,7,8-HxCDD (D3)	0.1	0.06[b]	0.06[b]	2.2	2.6
1,2,3,6,7,8-HxCDD (D4)	0.1	0.11[b]	0.11[b]	3.7	4.9
1,2,3,7,8,9-HxCDD (D5)	0.1	0.13[b]	0.13[b]	2.8	2.7
1,2,3,4,6,7,8-HpCDD (D6)	0.01	1.12	1.39	2.2	3.3
OCDD (D7)	0.0001	0.111	0.155	0.073	0.11
	Total	4.35	7.31	176	196
Co-PCBs isomers (IUPAC number)	WHO–TEF[a]	Soxhlet with Toluene (ng WHO–TEQ kg^{-1})	PLE with n-Hexane (ng WHO–TEQ kg^{-1})	Soxhlet with Toluene (ng WHO–TEQ kg^{-1})	PLE with n-Hexane (ng WHO–TEQ kg^{-1})
3,4,4′,5-TCB (#81)	0.0001	0.00039	0.00019	0.010	0.0086
3,3′,4,4′-TCB (#77)	0.0001	0.0037	0.0019	0.18	0.18
2′,3,4,4′,5-PeCB (#123)	0.0001	0.00002[b]	0.00004[b]	0.024	0.090
2,3′,4,4′,5-PeCB (#118)	0.0001	0.0225	0.0129	0.57	0.59
2,3,4,4′,5-PeCB (#114)	0.0005	0.0002[b]	0.0003[b]	0.14	0.18
2,3,3′,4,4′-PeCB (#105)	0.0001	0.0088	0.0038	0.19	0.27
3,3′,4,4′,5-PeCB (#126)	0.1	0.34	0.29	83	76
2,3′,4,4′,5,5′-HxCB (#167)	0.00001	0.00032	0.00012	0.046	0.041
2,3,3′,4,4′,5-HxCB (#156)	0.0005	0.034	0.0125	1.2	1.4
2,3,3′,4,4′,5′-HxCB (#157)	0.0005	0.0001[b]	0.0034	0.29	0.28
3,3′,4,4′,5,5′-HxCB (#169)	0.01	0.001[b]	0.001[b]	1.2	1.4
2,3,3′,4,4′,5,5′-HpCB (#189)	0.0001	0.00001[b]	0.00001[b]	0.068	0.072
	Total	0.41	0.33	87	81

[a] Individual WHO–TEF values for risk assessment [11] are based on the conclusions of the World Health Organization meeting in Stockholm, Sweden, 15–18 June 1997.
[b] The concentration of compounds are below DL or QL.

the specific congeners, according to Tables 1 and 2. Respecting the total of the isomers, it can be seen that PLE is essentially identical to Soxhlet method. Respecting congeners, it was possible to clearly find more isomers in the HxCDD/Fs congener group, using PLE extraction.

Individual WHO–TEF values are mentioned in Table 4. Table 4 also shows WHO–TEQ values of different magnitude for two real samples, sediment and forest soil. The sediment sample exhibited low levels of dioxins/furan and Co-PCBs. The majority of the compounds in this sediment are below the detection limit (DL) and quantification limit (QL) of the method. However, the forest soil sample showed considerable amounts of dioxins/furans and Co-PCBs.

According to literature [9,10] the optimal value of dioxins/furans and Co-PCBs for a soil should be below 5 ng WHO–TEQ kg^{-1}. Values greater than 100 ng WHO–TEQ kg^{-1} are considered relatively high and reduces the possibility of using the soil, due to contamination and level of toxicity. The possible reason for the high values of this sample could be related with the fact that this specific soil belongs to a place used has a trust for electrical components industry (condensers and other electrical components which use oils).

4. Conclusions

As conclusion, PLE, when used at optimal conditions, is a good alternative extraction technique for the simultaneous and quantitative analysis of PCDD/PCDFs and dioxin-like PCBs (Co-PCBs) in solid environmental samples. The average exposure of the European population (8–21 pg/kg body weight) is occasionally higher than the total tolerable weekly intake for dioxins and dioxin-like PCBs [8]. Consequently, there is a driv-

ing force from the European Commission to decrease the overall intake. An important tool to achieve this goal is to increase monitoring (Commission Directive 2002/69/EC). PLE methodology, in this work, proved to be a very good alternative, faster and sustainable analytical methodology for the simultaneous determination of PCDDs, PCDFs and Co-PCBs in environmental samples. The method allowed the simultaneous determination of 29 organohalogen compounds in one single extraction, and can be applied to other kind of matrices, e.g. food. Having the best cost-efficiency ratio, may improve the control and provide more information about the occurrence of dioxins and the levels of toxicity and thereby may contribute to increase human health.

Acknowledgments

References

[1] B.E. Richter, J.L. Ezzell, W.D. Felix, K.A. Roberts, D.W. Later, Am. Lab. (1995) 24.
[2] B.E. Richter, B.A. Jones, J.L. Ezzell, N.C. Porter, N. Avdalovic, C. Pohl, Anal. Chem. 68 (1996) 1033.
[3] B.E. Richter, J.L. Ezzell, D.E. Knowles, F. Hoefler, A.K.R. Mattulat, M. Scheutwinkel, D.S. Waddell, T. Gobran, V. Khurana, Chemosphere 34 (1997) 975.
[4] US Environmental Protection Agency Method 3545A, Pressurized fluid extraction (PFE), EPA SW-846, US Government Printing Office, Washington, DC, November 2000.
[5] O. Kiguchi, T. Kobayashi, K. Saitoh, N. Ogawa, J. Chromatogr. A 1108 (2006) 176, and references cited therein.
[6] O. Kiguchi, K. Saitoh, N. Ogawa, J. Chromatogr. A 1144 (2007) 262.
[7] http://www-naweb.iaea.org/nahu/nmrm/nmrm2003/material/bcr422.htm
[8] S. Sporring, K. Wiberg, E. Björklund, P. Haglund, Combined extraction/cleanup strategies for fast determination of PCDD/Fs and WHO-PCBs in food and feed samples using accelerated solvent extraction, Organohalogen Compd. 60 (2003) 1–4.
[9] A. Basler, Regulatory measures in the Federal Republic of Germany to reduce the exposure of man and the environment to dioxins, Organohalogen Compd. 20 (1994) 567–570.
[10] Communication from the Commission to the Council, the European Parliament and the Economic and Social Committee, 2001, Community Strategy for Dioxins, Furans and Polychlorinated Biphenyls", Commission of the European Communities, COM (2001) 593 Final, Brussels, 24.10.2001, http://eur-lex.europa.eu/LexUriServ/LexUriServ.do?uri=COM:2001:0593:FIN:EN:PDF.
[11] M. Van den Berg, L. Birnbaum, A.T.C. Bosveld, B. Brunström, P. Cook, M. Feeley, J.P. Giesy, A. Hanberg, R. Hasegawa, S.W. Kennedy, T. Kubiak, J.C. Larsen, F.X.R. van Leeuwen, A.K.D. Liem, C. Nolt, R.E. Petersn, L. Poellinger, S. Safe, D. Schrenk, D. Tillit, M. Tysklind, M. Younes, F. Waern, T. Zacharewski, Environ. Health Perspect. 106 (1998) 775.

Ion-selective electrode for aluminum determination in pharmaceutical substances, tea leaves and water samples

M. Arvand *, S.A. Asadollahzadeh

Department of Chemistry, Faculty of Science, Guilan University, P.O. Box 1914, Rasht 0098, Iran

Abstract

A novel ion-selective PVC membrane sensor for Al(III) ions based on 6-(4-nitrophenyl)-2-phenyl-4-(thiophen-2-yl)-3,5-diaza-bicyclo[3.1.0]hex-2-ene (NTDH) as a new ionophore has been prepared and studied. The electrode exhibit a good response for aluminum ion over concentration range of 1.0×10^{-6} to 1.0×10^{-1} mol L^{-1} with a Nernstian slope of 19.6 ± 0.4 mV per decade and low detection limit of 6.3×10^{-7} mol L^{-1}. The best performance was obtained with membrane composition 30% poly(vinyl chloride), 62% acetophenone, 5% oleic acid, 3% ionophore and 2 ml tetrahydrofuran. NTDH-based electrode was suitable for aqueous solutions of pH 3. It has relatively fast response time ($\sim$10 s) and can be used at least for 3 months without any considerable divergence in potentials. The proposed membrane electrode revealed good selectivity for Al(III) ions over a wide variety of other cations. The standard electrode potentials were determined at different temperatures and used to calculate the isothermal coefficient of the electrode. The formation constant and stoichiometry ratio of ionophore–Al(III) complex were calculated at 25 °C by using segmented sandwich membrane method. It was used in non-aqueous solvents and also as indicator electrode in potentiometric determination of Al(III) ions in some real samples.
© 2008 Elsevier B.V. All rights reserved.

Keywords: Potentiometric Al(III) sensor; Poly(vinyl chloride) membrane; Non-aqueous media; Isothermal temperature coefficient; Sandwich method

1. Introduction

Today, aluminum is the most widely used metal in the world after iron. It is used in the manufacture of automobiles, packaging materials, electrical equipments, machinery and building construction. Aluminum is also ideal for beer and soft drink cans and foil because it can be melted and reused. During the last two decades, many studies have focused on the toxicity of aluminum on living systems especially on human beings and it is believed that aluminum plays important roles in the pathology of dialysis disease. Aluminum is also known to cause dementia, anemia, myopathy, bone and joint disease [1–3]. Thus, the determination of aluminum exhibits its extraordinary importance.

The introduction of new ion-selective membrane electrodes has played a fundamental role in the development of potentiometric measurements. The advantages of ISEs over many other methods for cations and anions detections are their easy handling, non-destructive analysis, accuracy, reproducibility, fast relatively response, lower costing, time saving, affectivity and facility in preparation and inexpensive sample preparation.

Ion-selective electrodes (ISEs), especially those with neutral carrier-based solvent polymeric membranes, have been studied for more than three decades, and are now routinely employed for direct potentiometric measurements of various ionic species in environmental, industrial and clinical samples [4,5]. Until now, a large number of ionophores with high selectivity for specific metal ions have been developed for the potentiometric sensors for the determination of the respective metal ions [6–9], but little was published on trivalent ions such as Cr(III) [10], Fe(III) [11], Au(III) [12], Al(III) [13,14], Ce(III) [15] and Bi(III) [16]. On the other hand, these sensors suffer from the disadvantages of narrow working range and significant interferences from some cations (e.g. La^{3+}, Cd^{2+} and Mn^{2+}) [10,15]. In this paper we reported a new ISE for determination of Al(III) ion based on synthesized ligand 6-(4-nitrophenyl)-2-phenyl-4-(thiophen-2-yl)-3,5-diaza-bicyclo[3.1.0]hex-2-ene (NTDH). Our previously works revealed that these types of compounds are the excellent

---

* Corresponding author. Fax.: +98 131 3233262.
   E-mail address: arvand@guilan.ac.ir (M. Arvand).

choice as ionophore for the fabrication of ion sensors due to their peculiar properties [17,18].

2. Experimental

2.1. Reagents and solutions

All reagents used were of analytical reagent grade. High relative molar mass poly(vinyl chloride) (PVC), acetophenone (AP), dibuthyl phthalate (DBP), dibuthyl sebacate (DBS), *o*-nitrophenyl octyl ether (*o*-NPOE), oleic acid (OA), sodium tetraphenylborate (NaTPB), potassium tetrakis(*p*-chlorophenyl)borate (KT*P*ClPB), 2-benzoyl-3-(4-nitrophenyl) aziridine, ammonium bromide, thiophene-2-carbaldehyde, tetrahydrofuran (THF), hydrochloric acid (HCl), ethanol (EtOH), sodium acetate, and chloride or nitrate salts of other cations were obtained all from Merck or Fluka. All solutions were prepared by dissolving the salts in distilled deionized water.

2.2. Apparatus and emf measurements

Potentiometric measurements were carried out with a digital pH/millivoltmeter (Jenway, Model 3305) at laboratory ambient temperature. The emf observations were made relative to a double junction saturated calomel electrode (SCE) with the chamber filled with an ammonium nitrate solution. A silver/silver chloride electrode containing a $3\,mol\,L^{-1}$ solution of KCl was used as the internal reference electrode. The electrode cell assembly of the following type was used:

Ag–AgCl|KCl $\quad$ (3 mol L^{-1})|internal $\quad$ solution, $1.0 \times 10^{-3}\,mol\,L^{-1}$ $\quad$ AlCl$_3$ + $1.0 \times 10^{-3}\,mol\,L^{-1}$ $\quad$ HCl|PVC membrane|test solution|Hg–Hg$_2$Cl$_2$, KCl (saturated).

The reference electrode was obtained from Azar Electrode Company (Urmia, Iran). A digital pH meter (Corning Model 125) was used for measuring pH.

2.3. Preparation of electrode

Typical membrane was constructed by combining various components with ratios as detailed in Table 2. The sensor membrane was prepared with the following composition: the ionophore (m/m, ∼3%), plasticizer AP (m/m, ∼62%), PVC (m/m, ∼30%) and additive OA (m/m, ∼5%) were mixed and the components were dissolved in THF (2 ml). The solvent was evaporated slowly at room temperature until an oily concentrated mixture was obtained. A Pyrex or Teflon tube (3–5 mm i.d. on top) was dipped into the mixture for about 10 s, so that a transparent membrane of about 0.3 mm thickness was formed. The tube was then pulled out from the mixture and hold at room temperature for about 2 h. The tube was then filled with internal filling solution of $1.0 \times 10^{-3}\,mol\,L^{-1}$ of aluminum chloride and $1.0 \times 10^{-3}\,mol\,L^{-1}$ of hydrochloric acid. The electrode was finally conditioned for 24 h by soaking in a $1 \times 10^{-2}\,mol\,L^{-1}$ solution of aluminum chloride.

2.4. Preparation of sandwich membrane

A potentiometric method to determine ionophore-complex formation constants in solvent polymeric membrane phase requires membrane potential measurements on two-layer sandwich membranes, where only one side contains the ionophore. If both membrane segments have the same ionic strength, it is convenient to assume that the activity coefficients for the complexed and uncomplexed ions are approximately equal. In that case, they can be omitted and the complex formation constant is related to the potential as follows [19]:

$$\beta_{ILn} = \left(L_T - \frac{nR_T}{Z_I}\right)^n \exp\left(\frac{E_M Z_I F}{RT}\right) \tag{1}$$

where L_T is the total concentration of ionophore in the membrane segment, R_T is the concentration of lipophilic ionic site additives, n is the ion–ionophore complex stoichiometry, and R, T and F are the gas constant, the absolute temperature, and the Faraday constant. The ion I carries a charge of z_I. This relationship allows for the convenient determination of formation constants of ion–ionophore complexes within the membrane phase on the basis of transient membrane potential measurements on two-layer sandwich membranes can be if ion pairing neglected.

Ion-selective electrode membranes were cast by mixing the recorded membrane components to give a total cocktail mass of 100 mg in 2 ml of THF. The solvent THF allowed to evaporate overnight. A series of disks were cut with a cork borer from the parent membrane. These disks were conditioned overnight in each of metal chloride $0.01\,mol\,L^{-1}$ salt solutions of Al(III), Fe(III), Ce(III) and Cr(III). All membrane electrode potential measurements were performed at laboratory ambient temperature in unstirred salt solution (identical to the conditioning and inner filling solution) versus Hg/Hg$_2$Cl$_2$ reference electrode. Sandwich membrane was made by pressing two individual membranes (ordinary one without ionophore and one with the same components and additional ionophore) together immediately after blotting them individually, dry with tissue paper. The combined segmented membrane was then rapidly mounted into the electrode body and immediately measured. The time required from making the membrane sandwich contact until final membrane potential measurement was less than 1 min.

2.5. Preparation of 6-(4-nitrophenyl)-2-phenyl-4-(thiophen-2-yl)-3,5-diaza-bicyclo[3.1.0]hex-2-en (NTDH)

The 6-(4-nitrophenyl)-2-phenyl-4-(thiophen-2-yl)-3,5-diaza-bicyclo[3.1.0]hex-2-ene (NTDH) used as the ionophore was synthesized according to a previously reported method with some modification in the described procedure [20] and its structure is shown in Scheme 1. All 2-benzoyl-3-(4-nitrophenyl)aziridine (0.536 g, 2 mmol), NH$_4$Br (0.1 g, 1 mmol) and thiophene-2-carbaldehyde (0.2 ml, 0.23 g, 2 mmol) were dissolved in 16 ml of absolute ethanol and stirred at room temperature. The anhydrous gaseous ammonia is gently blown
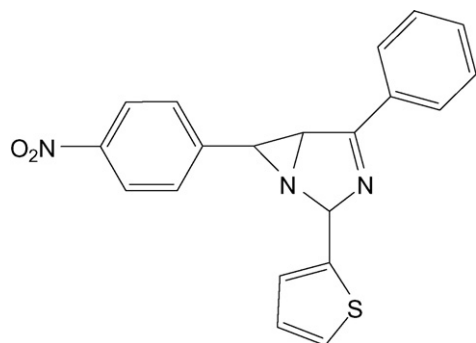
Scheme 1. The structure of 6-(4-nitrophenyl)-2-phenyl-4-(thiophen-2-yl)-3,5-diaza-bicyclo[3.1.0]hex-2-ene (NTDH) used as ionophore.

Fig. 1. Plot of conductivity vs. [NTDH]/[Al^{3+}] in acetonitrile solutions.

Table 1
Formation constants of different M^{n+}-ionophore complexes in acetonitrile

Cation	log K_f
Al^{3+}	5.17 ± 0.11
Ca^{2+}	3.08 ± 0.10
Ba^{2+}	2.76 ± 0.08
Ni^{2+}	1.34 ± 0.13
Zn^{2+}	2.22 ± 0.07
Sn^{2+}	1.23 ± 0.09
Cr^{3+}	2.41 ± 0.13
Mn^{2+}	2.02 ± 0.17
Mg^{2+}	1.53 ± 0.15
Ce^{3+}	2.63 ± 0.12
Pb^{2+}	1.63 ± 0.05
Fe^{3+}	3.16 ± 0.09
Bi^{3+}	2.71 ± 0.15

into the reaction mixture for 6 h. The color of the reaction mixture changes to pink. The reaction mixture was filtered and washed with ethanol. The filtrate was diluted with EtOH and extracted with ether and solvent evaporated and dried in the air and the resulting solid was purified by silica gel column chromatography and recrystallized from ethanol. mp = 177–178 °C, IR (KBr): 3050, 1595, 1508, 1440, 1340, 1010, 970, 880, 790, 760, 740, 700, 690 cm^{-1}, ^{1}H NMR (CDCl$_3$): δ 2.72 (s, 1H), 3.83 (s, 1H), 6.9 (s, 1H), 7.02 (t, J = 4.8 and 3.7 Hz, 1H), 7.17 (d, J = 3.2 Hz, 1H), 7.29 (d, J = 5.2 Hz, 1H), 7.47 (d, J = 8.6 Hz, 2H), 7.53 (t, J = 7.6 and 7.4 Hz, 2H), 7.58 (t, J = 7.3 Hz, 1H), 8.01 (d, J = 7.4 Hz, 2H), 8.21 (J = 8.6 Hz, 2H), ^{13}C NMR (CDCl$_3$): δ 42.90, 58.62, 93.50, 124.22, 126.09, 126.33, 127.50, 127.98, 129.13, 129.43, 131.77, 132.56, 140.95, 145.69, 147.94, 171.49. Exact mass: (M^+) calcd. 361.0885, found 361.0882, UV–vis (EtOH): λ_{max}/(nm) = 285.

3. Results and discussion

3.1. Study of the interaction between 6-(4-nitrophenyl)-2-phenyl-4-(thiophen-2-yl)-3,5-diaza-bicyclo[3.1.0]hex-2-en and Al^{3+} ions in solution phase

In order to obtain evidence concerning the coordination of NTDH with Al^{3+} ion and determination of ionophore to Al^{3+} mole ratio, the values of conductivity of 2.5×10^{-4} mol L^{-1} AlCl$_3$ in acetonitrile solution were monitored as a function of NTDH to Al^{3+} mole ratio at 25 °C. The resulting plot is shown in Fig. 1. It can be seen that, the addition of the NTDH to Al^{3+} solution causes a significant decrease in conductivity, which tends to level off at mole ratio about one. Also, the complexation of NTDH with a number of cations was investigated conductometrically. The formation constant, K_f, of the resulting 1:1 complexes are given in Table 1. It can be seen that, the NTDH with the most stable complex with Al^{3+} ion is expected to act as a highly selective ionophore for preparation of Al^{3+} ion-selective membrane electrodes. Thus, in the next step, the NTDH was used as a potential neutral carrier in construction of PVC-based membrane ion-selective electrodes for aluminum ion.
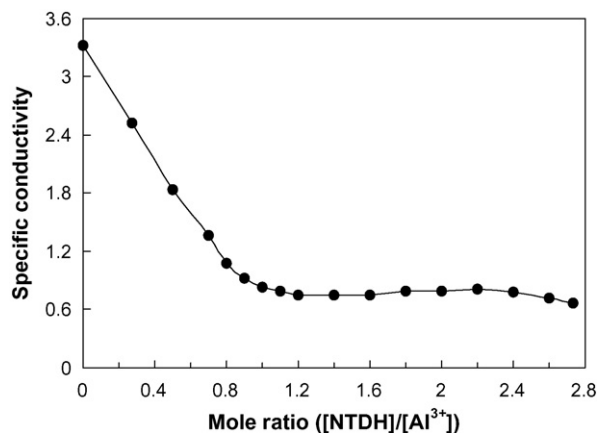
3.2. Effect of membrane composition on the electrode response and calibration curve

At first, before to do any type of optimization the potential responses of various ISEs based on NTDH for each ion separately were obtained and the results are shown in Fig. 2. Among different cations, aluminum ion gives a better character-
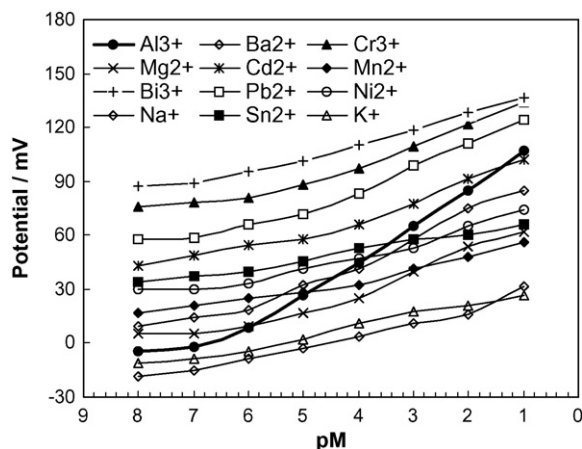

Fig. 2. Potential response of various metal ion-selective electrodes based on NTDH.

Table 2
Optimization of membrane ingredients

No.	Membrane composition (%, w/w)				Slope[a] (mV/decade)	LLLR[b] [M]	LLD[c] [M]
	PVC	Plasticizer	NTDH	Additive			
1	30	62(DBP)	3	5(OA)	13.1 ± 0.6	10^{-5}	1×10^{-5}
2	30	62(DBS)	3	5(OA)	12.1 ± 0.7	10^{-5}	1×10^{-5}
3	30	62(o-NPOE)	3	5(OA)	16.9 ± 0.6	10^{-6}	7×10^{-7}
4	30	62(AP)	3	5(NaTPB)	20.4 ± 0.4	10^{-5}	8×10^{-6}
5	30	62(AP)	3	5(KTpClPB)	17.4 ± 0.5	10^{-5}	7×10^{-6}
6	30	62(AP)	2	5(OA)	18.5 ± 0.4	10^{-4}	6×10^{-5}
7	29	61(AP)	5	5(OA)	15.8 ± 0.5	10^{-5}	5×10^{-6}
8	30	62(AP)	3	5(OA)	19.6 ± 0.4	10^{-6}	6.3×10^{-7}
9	29	58(AP)	3	10(OA)	16.5 ± 0.6	10^{-4}	5×10^{-5}
10	30	62(AP)	0	0(OA)	5.8 ± 0.8	10^{-5}	1×10^{-5}
11	30	62(AP)	3	0(OA)	3.4 ± 0.8	10^{-5}	1×10^{-5}
12	31	62(AP)	0	5(OA)	7.4 ± 0.9	10^{-5}	7×10^{-6}
13	40	52(AP)	3	5(OA)	17.5 ± 0.4	10^{-6}	5×10^{-7}

[a] Mean values of slopes for three replicate measurements.
[b] Lower limit of linear range.
[c] Lower limit of detection.

istic response. The selective electrode exhibited linear responses to the activity of Al^{3+} ions within the concentration range of 1.0×10^{-6} to 1.0×10^{-1} mol L^{-1} AlCl$_3$ with a Nernstian slope of 19.6 ± 0.4 mV per decade and a correlation coefficient of 0.9951 ($n = 10$). Ionophores for use in sensors should have rapid exchange kinetics and adequate complex formation constants in the membrane. Also, they should be well soluble in the membrane matrix and have a sufficient lipophilicity to prevent leaching from the membrane into the sample solution. In addition, the selectivity of the neutral carrier-based ISEs is known to be governing by stability constant of the neutral carrier–ion complex and its partition constant between the membrane and sample solution [21]. It is well known that, not only the nature of ionophore, but also the membrane composition and the properties of plasticizer affect on the sensitivity, selectivity and linearity of ISE [21]. The plasticizer to be used in membrane should exhibit high lipophilicity, have high molecular weight, low tendency for exudation from the polymer matrix, low vapor pressure and high capacity to dissolve the substrate and other additives present in the membrane. Additionally, its viscosity and dielectric constant should be adequate. The nature of plasticizer also influences the mobility of the ionophore molecule, the state of ligand and hence, the response characteristics [21–23]. Therefore, several membrane compositions were investigated by varying the amount and nature of plasticizer (Table 2). It is clear that among several plasticizers including AP, DBP, DBS and o-NPOE used, AP exhibited the best sensitivity (no. 8 in Table 2 and Fig. 3). It is also known that the presence of lipophilic anions in cation-selective membrane electrodes not only diminishes the ohmic resistance [13,24–26] and enhances the response behavior, selectivity, and sensitivity of the membrane electrodes [9,27,28], but also may catalyze the exchange kinetics at the sample–membrane interface [29]. Without such additives, many electrodes do not respond properly toward a cation. However, the response of the proposed Al(III)-selective electrode in the absence of an additional lipophilic anion exchanger may be caused by possi-

ble trace anionic impurities within the PVC used [6,21]. From the data given in Table 2, it is immediately obvious that the nature and amount of additive influences the performance characteristics of the membrane sensor significantly. The use of ionic additives such as different tetraphenyl borate salts and its more lipophilic derivative, tetrakis(p-chlorophenyl)borate (KT$_P$ClPB) also fatty acids such as oleic acid as lipophilic additives is widely reported in the preparation of different ion-selective electrodes [30,31]. Their main role is attributed to the inducing permselectivity to some PVC membrane selective electrodes [21,31]. Addition of 5 mg OA as a lipophilic additive showed better Nernstian response and linear range (no. 8). Tetraphenylborate salts (NaTPB and KT$_P$ClPB) were also investigated as additives. The data given in Table 2 shows that OA is more suitable additive than tetraphenylborate salts. However, increasing the amount of OA shows no beneficial influence on the membrane electrode response, further more the
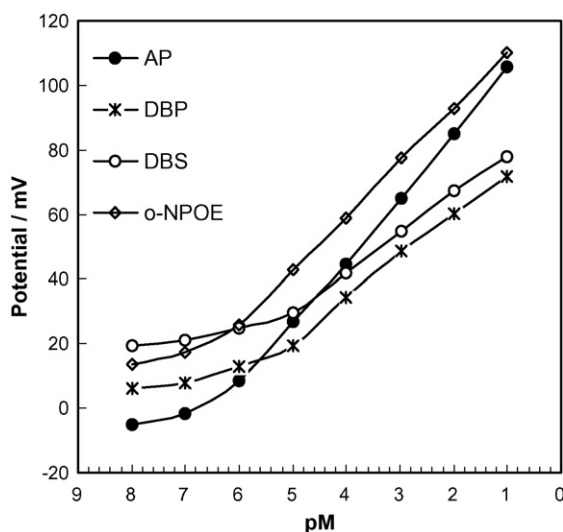

Fig. 3. Effect of plasticizer type on the response of the aluminum ion-selective electrode with 3% (w/w) ionophore.
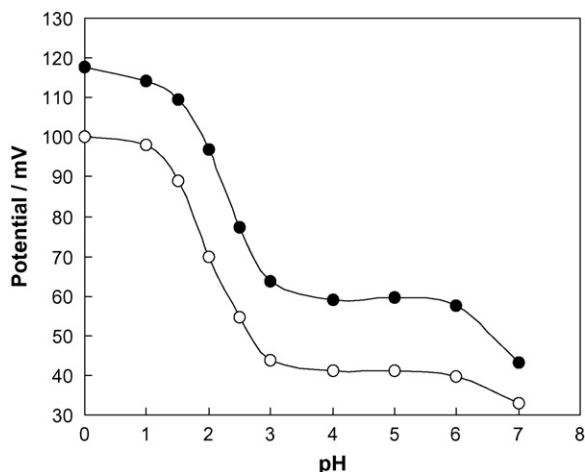
Fig. 4. Effect of pH on the potential response of the aluminum ion-selective electrode at two different concentrations: (●) 1×10^{-3} mol L^{-1} and (○) 1×10^{-4} mol L^{-1} (membrane no. 8).

Fig. 5. Dynamic response time of the membrane electrode for step change in concentration of Al^{3+}: (a) 1.0×10^{-5} mol L^{-1}, (b) 5.0×10^{-5} mol L^{-1}, (c) 1.0×10^{-4} mol L^{-1}, (d) 5.0×10^{-4} mol L^{-1}, (e) 1.0×10^{-3} mol L^{-1} and (f) 5.0×10^{-3} mol L^{-1}.

observed potential was seen to be unstable. Moreover 3 mg of ionophore was chosen as the optimum amount of ionophore in the PVC membrane. Further addition of ionophore (no. 7), however resulted in some decreases in the response of the electrode, most probably due to some inhomogeneities and possible saturation of the membrane [8]. The high amount of the ionophore may also induce strong interactions between polymeric chains and ionophore-preventing mobility of the segments as explained by Hall considering experimental observations of Reinhoudt and coworkers [32]. In general, the thickness and hardness of the membrane depend upon the amount of PVC used. At higher PVC content, the membrane becomes too dense, this makes the transport of cations into the membrane more difficult and results in the increased resistance (no. 13). At lower PVC content, the membrane becomes mechanically weak and swells up easily in aqueous solution. The AP/PVC ratios of 1.3–2.1 were examined. The membrane prepared with an AP/PVC ratio of 2.1 was found to have the highest sensitivity and the widest linear range. Collective results, given in Table 2 indicate that the use of 62% AP in the presence of 30% PVC, 3% ionophore and 5% OA results in the best sensitivity, with a Nernstian slope of 19.6 mV/decade, over a relatively wide dynamic range of Al^{3+} ions and the characteristics performance of the electrode was the best (no. 8). The emf versus pM (Al^{3+}) prepared under optimal composition, indicated a linear range from 1.0×10^{-6} to 1.0×10^{-1} mol L^{-1} with a detection limit of 6.3×10^{-7} mol L^{-1}.

3.3. Effect of pH on membrane electrode response

The potentiometric response of the electrode was found to be sensitive to pH changes. The effect of pH on membrane electrode was examined over the pH range of 0–7 at Al^{3+} ion concentration of 1×10^{-3} to 1×10^{-4} mol L^{-1} and the results are shown in Fig. 4. As can be seen, the potentials are independent of pH in the range 3–6 and the same can be taken as the working pH range of the electrode. At low pH, the potential increased, indicating that the membrane sensor responds to hydrogen ions, while the observed decrease in potential at higher pH values could be due
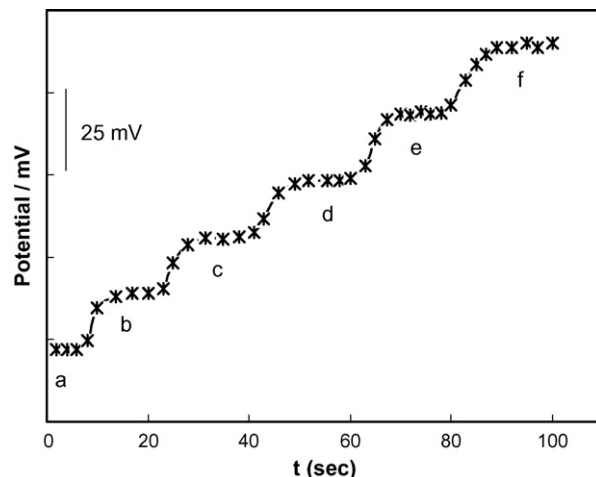
to the formation of some hydroxyl complexes of Al^{3+} in solution. As aluminum hydroxide may precipitate at higher pHs, we used pH 3.0 for subsequent studies by hydrochloric acid–sodium acetate buffer solution (pH 3).

3.4. Equilibration and response time

The response time of an ISE is an important parameter that must be considered if the sensor is going to have any type of practical utility. The dynamic response of ionophore-based ion-selective electrodes has been studied for many years [33,34]. For conventional membrane-based ISEs, the potentiometric response is due to the phase-boundary potential that results at the sample–membrane interface when activity changes occur in either surface layer [35]. The optimum equilibration time for the membrane electrode in 1×10^{-2} mol L^{-1} Al^{3+} solution was found to be 24 h when it starts generating stable and reproducible potential. The static response time required for the proposed Al(III) sensor to reach a potential within ±1 mV of the final equilibrium value was measured after successive immersion in a series of aluminum ion solutions, each one having a five-fold difference in concentration. The electrode has a fast response time of ∼10 s. The potentials were sustained for at least 3 min. The actual potential versus time traces is shown in Fig. 5. Reproducibility of electrode was examined by using six similar constructed electrodes under the optimum conditions. The results showed good reproducibility for proposed electrode. The slope of the electrode response was reproducible over a period of at least 3 months. Therefore the proposed electrode can be used for more than 3 months without a considerable change in its response characteristics towards Al^{3+}.

3.5. Reversibility of the electrode response

To evaluate the reversibility of the electrode, a similar procedure with opposite direction was adopted. The measurements
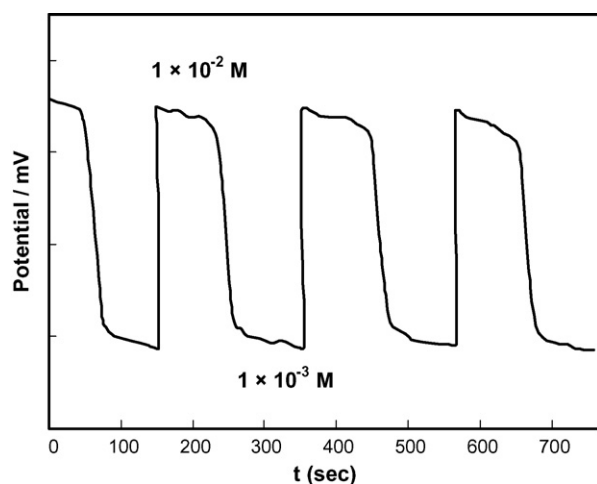
Fig. 6. Reversibility of membrane electrode for Al^{3+} step change of concentration from 1.0×10^{-2} to 1.0×10^{-3} mol L^{-1}.

were performed in the sequence of high-to-low sample concentrations and the results are shown in Fig. 6. It shows that the potentiometric responses of the sensor was reversible and had any memory effect, although the time needed to reach equilibrium values were longer than that of low-to-high sample concentration. Noteworthy, it is well documented that, in the case of high-to-low concentration, the time needed to attain a stable potential is some 100 times larger than that required for the case of low-to-high concentrations (for a 10 times change in the cation concentration) [21].

3.6. Effect of non-aqueous media

The functioning of the electrode was investigated in partially non-aqueous media using acetone–water, methanol–water and ethanol–water mixtures and the results obtained are presented in Table 3. It is observed that in the presence of ethanol, the slope as well as working concentration range is almost constant, while the slope for methanol and acetone decrease. Therefore, the electrode is not suitable for using in methanol–water and

acetone–water mixtures. However, in ethanol–water mixture (up to 20%), there is only a small decrease in slope and working concentration range and hence the electrode can be satisfactorily used in these media with above-mentioned percentages.

3.7. Selectivity coefficients

The selectivity is clearly one of the most important characteristics of a potentiometric sensor, which represents the preference of a sensor for the response to primary ion over other (interfering) ions that are present in the solution. To investigate the selectivity of the membrane electrode proposed, a fixed interfering ion method (FIM) was used [36]. The emf of a cell comprising an ion-selective electrode and a reference electrode (SCE) was measured for solutions of constant activity of the interfering ion (1.0×10^{-2} mol L^{-1}), a_J, and varying activity of the primary ion, a_I. The emf values obtained are plotted versus the logarithm of the activity of the interfering ion. The intersection of the extrapolated linear portions of this plot indicates the value of a_I that is used to calculate $K_{I,J}^{Pot}$ from the following equation:

$$K_{I,J}^{Pot} = \frac{a_I}{a_J^{(z_I/z_J)}} \tag{2}$$

where z is the charge of ion. This equation regardless of its simplicity and ease of use for mono-valance ions gives the results higher than those expected. The selectivity coefficients were evaluated and the results are summarized in Table 4. From Table 4, it is readily seen that the proposed Al^{3+} ion-selective electrode is quite selective with respect to the common cations tested. Table 4 also shows that, for all the diverse ions used, the selectivity coefficients are small enough, indicating that they would not significantly disturb the functioning of the Al^{3+} ion-selective electrode. However, the high selectivity values for the divalent ions like Zn^{2+}, Ca^{2+} and Mg^{2+} are due to the nature of Eq. (2) that apparently gives higher values for the case of divalent ions, which are tested as interferers.

Table 3
Performance of the membrane sensors in partially non-aqueous media

Non-aqueous content (%, v/v)	Slope (mV/decade)	Working concentration range [M]	R^2
Acetone			
5	12.9 ± 1.1	1.0×10^{-6}–1.0×10^{-1}	0.985
10	12.6 ± 1.0	1.0×10^{-6}–1.0×10^{-1}	0.968
15	12.7 ± 0.9	1.0×10^{-6}–1.0×10^{-1}	0.987
20	12.4 ± 1.0	1.0×10^{-6}–1.0×10^{-1}	0.985
Ethanol			
5	18.5 ± 0.7	1.0×10^{-6}–1.0×10^{-1}	0.993
10	18.7 ± 0.7	1.0×10^{-6}–1.0×10^{-1}	0.988
15	18.5 ± 0.5	1.0×10^{-6}–1.0×10^{-1}	0.995
20	18.6 ± 0.6	5.0×10^{-6}–1.0×10^{-1}	0.994
Methanol			
5	11.4 ± 0.8	1.0×10^{-5}–1.0×10^{-1}	0.991
10	10.2 ± 1.1	1.0×10^{-5}–1.0×10^{-1}	0.981
15	10 ± 0.9	1.0×10^{-5}–1.0×10^{-1}	0.979
20	10.3 ± 1.2	1.0×10^{-5}–1.0×10^{-1}	0.978

Table 4
Selectivity coefficient $\left(K_{Al,J}^{Pot}\right)$ of various interfering ions obtained using the electrode conditioned with Al^{3+} in all cases (membrane no. 8)

M^{n+}	$-\log K_{Al,J}^{Pot}$
Cu^{2+}	3.02
Mn^{2+}	2.51
Ni^{2+}	3.01
Pb^{2+}	2.73
Zn^{2+}	2.01
Hg^{2+}	2.54
Ca^{2+}	1.98
Mg^{2+}	2.06
Cd^{2+}	3.12
Ba^{2+}	2.59
Fe^{3+}	2.54
Cr^{3+}	3.07
Ce^{3+}	2.67
Tl^{+}	2.82
K^{+}	3.17
Na^{+}	3.05

3.8. Determination of formation constant of Al(III) complex

Membrane potential values (emf) for the examined metal salt solutions of Al(III), Fe(III), Ce(III) and Cr(III) were determined by subtracting the cell potential for a membrane without ionophore from that of the sandwich membrane. The determined formation constants ($\log \beta_{ILn}$) for the examined different complexes were recorded in Table 5. A careful analysis of the data in Table 5, reveals that Al(III) has significant cation-binding characteristics.

3.9. Effect of temperature

Trend of changes of electrode performance with temperature, at test solution temperatures 10, 15, 20, 25, 30, 35, 40 and 50 °C for the Al(III)-selective electrode was studied. The electrode exhibits good Nernstian behavior in the temperature range (10–40 °C) (Fig. 7). At higher temperatures, the slope of electrode did not show a good Nernstian behavior. This behavior may be due to the following reason: at such high temperatures, the phase boundary equilibrium at the gel layer-test solution interface is disturbed by the thermal agitation of the solution [37].

The standard cell potentials (E_{cell}^0) were determined at different temperatures from the respective calibration plots as the intercepts of these plots at pAl(III) = 0, and were used to deter-

Table 5
Experimental membrane potentials and corresponding ionophore-complex formation constants determined with two segment AP–PVC sandwich membrane

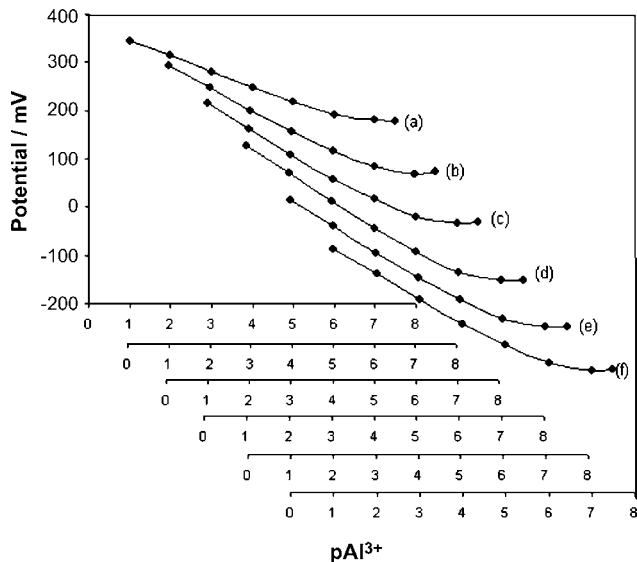| Ion	Membrane potential Δemf (mV)	Formation constant ($\log \beta_{ILn}$)	Selectivity coefficient $\left(-\log K_{Al,J}^{Pot}\right)$
Al(III)	63 ± 0.5	5.36 ± 0.04	–
Fe(III)	27 ± 0.5	3.29 ± 0.02	2.54
Ce(III)	11 ± 0.4	2.86 ± 0.05	2.67
Cr(III)	9.0 ± 0.8	2.45 ± 0.04	3.07

Fig. 7. Calibration graphs for Al^{3+}-selective sensor at test solution temperatures: 10 °C (a), 15 °C (b), 20 °C (c), 25 °C (d), 30 °C (e) and 40 °C (f).

mine the isothermal temperature coefficient (dE^0/dt) of the cell with the aid of the following equation [38]:

$$E_{cell}^0 = E_{cell(25\,°C)}^0 + \left(\frac{dE^0}{dt}\right)_{cell}(t - 25) \tag{3}$$

Plot of E_{cell}^0 versus $(t - 25)$ produced a straight line. The slope of this line was taken as the isothermal temperature coefficient of the cell. It amounts to 0.00076 V/°C. The standard potentials of the reference electrode (Hg/Hg_2Cl_2; KCl (saturated)) were calculated using the following equation:

$$E_{Hg/Hg_2Cl_2}^0 = 0.241 - 0.00066(t - 25) \tag{4}$$

The values of the standard potentials of Al(III)-selective electrode were calculated at the different temperatures from the following relation:

$$E_{reference}^0 + E_{cell}^0 = E_{electrode}^0 \tag{5}$$

A plot of $E_{electrode}^0$ versus $(t - 25)$ gave a straight line. The slope of this line was taken as isothermal temperature coefficient of the Al(III) electrode. It amounts to 0.00061 V/°C. The small values of $(dE^0/dt)_{cell}$ and $(dE^0/dt)_{electrode}$ reveal the high thermal stability of the electrode within the investigated temperature range.

Table 6
Comparison of results from the proposed method and that of AAS

Sample	Aluminum content[a] ($\times 10^{-3}$ mol L^{-1})	
	The proposed method	AAS method
Aluminum Mg syrup	8.1 ± 0.3	8.64 ± 0.12
Tea leave	148.9 ± 2.1 μg/g	146.7 ± 1.8
Mineral water[b]	10.3 ± 0.5	10.1 ± 0.3
Tap water[c]	6.3 ± 0.16	6.15 ± 0.14

[a] Average of four determinations ± S.D.
[b] Vata mineral drinking water, Ardebil, Iran (spiked with 9.5×10^{-3} mol L^{-1} Al^{3+}).
[c] Spiked with 5.9×10^{-3} mol L^{-1} Al^{3+}.

Table 7
Comparison of Al^{3+}-selective electrode based on NTDH with those previously reported in literature

Ionophore	Slope (mV/decade)	pH range	Lifetime	Detection limit (mol L^{-1})	Linear range (mol L^{-1})	Reference
Furil	18.5 ± 0.7	0.5–3.0	2 months	1.3×10^{-7}	1.0×10^{-6}–1.0×10^{-2}	[13]
Bis(5-phenylazo salicylalde-hyde) 2,3-naphthalene diimine	19.3 ± 0.8	3.5–5.0	>2 months	2.5×10^{-6}	5.0×10^{-6}–1.0×10^{-2}	[14]
7-Ethylthio-4-oxa-3-phenyl-2-thioxa-1,2–dihydro-pyrimido[4,5-*d*]pyrimidine	19.5	2.25–3.25	1 month	3.2×10^{-6}	1.0×10^{-5}–1.0×10^{-1}	[40]
Aluminon	29.5	–	2 months	1.0×10^{-6}	1.0×10^{-5}–1.0	[41]
1-Hydroxy-3-methyl-9-xanthen-9-one	20.0 ± 0.2	3–8.5	3 months	6.0×10^{-7}	1.6×10^{-6}–1.0×10^{-1}	[42]
Morin	19.7 ± 0.1	3.5–5	2 months	3.2×10^{-7}	5.0×10^{-7}–1.0×10^{-1}	[43]
6-(4-Nitrophenyl)-2-phenyl-4-(thiophen-2-yl)-3,5-diaza-bicyclo[3.1.0]hex-2-ene	19.6 ± 0.4	3–6	>3 months	6.3×10^{-7}	1.0×10^{-6}–1.0×10^{-1}	Proposed electrode

4. Analytical application

The optimized Al(III) selective electrode was found to work well under laboratory conditions. To assess the applicability of the proposed electrode to real samples, an attempt was made to determine Al(III) in aluminum Mg syrup, tea leave and tap and mineral waters. The samples were pre-treated by a suitable method and analyzed by this method (pH 3) and atomic absorption spectrometry (AAS) [39]. The results are summarized in Table 6. As seen from Table 6, the results determined with the proposed electrode are in good agreement with those obtained by the AAS method. Thus, it can be concluded that, the membrane electrode may have applications in the drug analysis and environmental monitoring of Al(III) ions. Moreover, due to its low detection limit and short response time, the proposed electrode can also be used as a suitable detector in flow injection analysis and ion-chromatography monitoring of Al(III) ions.

5. Conclusion

On the results discussed in this paper, 6-(4-nitrophenyl)-2-phenyl-4-(thiophen-2-yl)-3,5-diaza-bicyclo[3.1.0]hex-2-ene (NTDH) can be considered as a suitable neutral ionophore for construction of a PVC-based membrane selective electrode for the direct determination of Al(III) ion in solution. The inherent advantages of the proposed electrodes are its simple operation, stability, precise results, low cost and direct application to the determination of Al^{3+} ions, wide dynamic range, low detection limit and fast response time. The electrode was successfully applied for the determination of Al^{3+} content in aqueous solutions. It was successfully applied to the determination of Al^{3+} ions in real samples. Table 7 lists linear range, detection limit, lifetime, pH range and slope of some of the Al^{3+}-selective electrodes against proposed solvent polymeric Al^{3+}-selective electrode for comparative purposes [13,14,40–43].

Acknowledgement

References

[1] P.F. Good, C.W. Olanow, D.P. Perl, Brain Res. 593 (1992) 343.
[2] S.W. King, J. Savory, M.R. Willis, Crit. Rev. Clin. Lab. Sci. 13 (1981) 1.
[3] I.S. Parkinson, M.K. Ward, J. Clin. Pathol. 34 (1981) 1285.
[4] S.M. Sabry, A.-A.M. Wahbi, Anal. Chim. Acta 401 (1999) 173.
[5] J. Theresa, Hosick, L. Robin, Ingamells, D. Steven, Machemer, Anal. Chim. Acta 456 (2002) 263.
[6] P. Bühlmann, E. Pretsch, E. Bakker, Chem. Rev. 96 (1998) 1593.
[7] M. Moghimi, M.A. Bagherinia, M. Arvand, M.A. Zanjanchi, Anal. Chim. Acta 527 (2004) 169.
[8] H. Aghaie, M. Giahi, M. Monajjemi, M. Arvand, G.H. Nafissi, M. Aghaie, Sens. Actuators B 107 (2005) 756.
[9] M. Arvand, M.A. Zanjanchi, L. Heydari, Sens. Actuators B 122 (2007) 301.
[10] S. Khalil, A.A. Wassel, F.F. Belal, Talanta 63 (2004) 303.
[11] A. Sil, V.S. Ijeril, A.K. Srivastava, Sens. Actuators B 106 (2005) 648.
[12] J.A. Ortuño, T. Pérez Ruiz, C. Sánchez-Pedreño, Anal. Chim. Acta 185 (1986) 351.
[13] M.F. Mousavi, M. Arvand-Barmchi, M.A. Zanjanchi, Electroanalysis 13 (2001) 1125.
[14] A. Abbaspour, A.R. Esmaeilbeig, A.A. Jarrahpour, B. Khajeh, R. Kia, Talanta 58 (2002) 397.
[15] V.K. Gupta, A.K. Singh, B. Gupta, Anal. Chim. Acta 575 (2006) 198.
[16] S. Kharitonov, J. Pharm. Biomed. Anal. 30 (2002) 181.
[17] M. Arvand, A.M. Moghimi, A. Afshari, N. Mahmoodi, Anal. Chim. Acta 579 (2006) 102.
[18] M.A. Zanjanchi, M. Arvand, A. Islamnezhad, N.O. Mahmoodi, Talanta 74 (2007) 125.
[19] M.M. Shultz, O.K. Stefanova, S.B. Mokrov, K.N. Mikhelson, Anal. Chem. 74 (2002) 510.
[20] N.O. Mahmoodi, M.A. Zanjanchi, H. Kiyani, J. Chem. Res. (2004) 438.
[21] E. Bakker, P. Bühlmann, E. Pretsch, Chem. Rev. 97 (1997) 3083.
[22] X. Yang, N. Kumar, H. Chi, D.D. Hibbert, P.N.W. Alexander, Electroanalysis 9 (1997) 549.
[23] R. Eugster, T. Rosatzin, B. Rusterholz, B. Aebersold, U. Pedrazza, D. Ruegg, A. Schmid, U.F. Spichiger, W. Simon, Anal. Chim. Acta 289 (1994) 1.
[24] D. Amman, E. Pretsch, W. Simon, E. Lindler, A. Bezegha, E. Pungor, Anal. Chim. Acta 171 (1991) 1380.
[25] M. Shamsipur, M.H. Mashhadizadeh, Talanta 53 (2001) 1065.
[26] D. Ammann, E. Pretsch, W. Simon, E. Lindler, A. Bezegh, E. Pungor, Anal. Chim. Acta 17 (1985) 119.
[27] E. Bakker, E. Pretsch, Anal. Chim. Acta 309 (1995) 7.
[28] S. Wakida, T. Masadome, T. Imato, Y. Shibutani, K. Yakabe, T. Shono, Y. Asano, Anal. Sci. 15 (1999) 47.
[29] R. Eugster, P.M. Gehrig, W.E. Morf, U.E. Spichiger, W. Simon, Anal. Chem. 63 (1991) 2285.
[30] U. Schaller, E. Bakker, U.E. Spichiger, E. Pretsch, Anal. Chem. 66 (1994) 391.

[31] M.A. Zanjanchi, M. Arvand, M. Akbari, K. Tabatabaeian, G. Zaraei, Sens. Actuators B 113 (2006) 304.

[32] P.L.H.M. Cobben, R.J.M. Egberink, J.B. Bomer, P. Bergveld, W. Verboom, D.D. Reinhoudt, J. Am. Chem. Soc. 114 (1992) 10573.

[33] E. Lindner, K. Toth, E. Pungor, W.E. Morf, W. Simon, Anal. Chem. 50 (1978) 1627.

[34] W.E. Morf, E. Lindner, W. Simon, Anal. Chem. 47 (1975) 1596.

[35] E. Bakker, P. Bühlmann, E. Pretsch, Talanta 63 (2004) 3.

[36] Y. Umezawa, P. Bühlmann, K. Umezawa, K. Tohda, S. Amemiya, Pure Appl. Chem. 72 (2000) 1851.

[37] S. Khalil, S. Abd El-Aliem, J. Pharm. Biomed. Anal. 27 (2002) 25.

[38] L.I. Antropov, Theoretical Electrochemistry, Mir, Moscow, 1972.

[39] A.D. Eaton, L.S. Glesceri, A.E. Greenberg, Standard Methods for the Examination of Water and Wastewater, American Public Health Association, Washington, 1995, Part 3000, pp. 3–43.

[40] M.B. Saleh, S.S.M. Hassan, A.A. Abdel Gaber, N.A. Abdel Kream, Anal. Chim. Acta 434 (2001) 397.

[41] V. Babenikov, L. Bykova, L. Evsevleeva, J. Anal. Chem. 60 (2005) 866.

[42] A. Yari, L. Darvishi, M. Shamsipur, Anal. Chim. Acta 555 (2006) 329.

[43] V.K. Gupta, A.K. Jain, G. Maheshwari, Talanta 72 (2007) 1469.

A microscale Kjeldahl nitrogen determination for environmental waters

P. Campins-Falco [*], S. Meseguer-Lloret,
T. Climent-Santamaria, C. Molins-Legua

*Departament de Química Analítica, Facultad de Química, Universitat de Valencia, C/ Dr. Moliner 50,
E46100 Burjassot, Valencia, Spain*

Abstract

A microscale Kjeldahl system has been designed which has been homemade reduced. The digestor unit of a macroKjeldahl system and a modified glassware microdistillation unit have been used. The optimal conditions for digestion and distillation have been established for ammonium and methylamine as model compound of organic amino nitrogen. The optimised procedure has been applied to the determination of Kjeldahl nitrogen in water samples. Recoveries near 100% and good precision have been achieved. This procedure combines nitrogen miniaturized system and the use of a selective ion electrode for ammonia detection. The analysis time was reduced 4.8 times and the analysis cost 6.6 times compared with classical procedure. The residues generated have been also markedly minimized. A preconcentration factor of 4 instead of 1.5 obtained by the macroscale design has been achieved.
© 2008 Elsevier B.V. All rights reserved.

Keywords: Microscale; Nitrogen Kjeldahl system; Ammonium and/or organic nitrogen determination; Ammonia electrode; Water samples

1. Introduction

The development of microscale chemistry in laboratory is becoming increasingly popular. Microscale chemistry is performed by using markedly reduced amounts of chemicals, safe and easy making techniques, miniature labware and high-quality skills [1]. These features have been made in response to the need of cutting costs of materials, waste disposal and time. Moreover, these experiments become safer, more environmental friendly, and a change in the psychology of people using chemicals occurs. Thus, microscale chemistry is a laboratory-based green chemistry approach.

Microscale chemistry was originally introduced in the organic chemistry, and later was expanded to inorganic, analytical and environmental chemistry. However a few applications have been developed in the quantitative analytical field [2–4].

The Kjeldahl method is well known as a standard method for nitrogen analysis in environmental waters. Nitrogen is a key nutrient in natural waters, but excessive N inputs lead to eutrophication problems. The main N species in waters are: dissolved inorganic N (ammonium, nitrite and nitrate), dissolved organic N (the largest fraction is made up of amino acids and peptides and it is often called amino N) and particulate organic (due to small organisms: algae, bacteria) and inorganic N [5]. In natural waters, inputs of dissolved organic nitrogen (DON) are largely a result of autochthonous biological processes. Additionally, external sources of DON arise from sewage and industrial effluents, terrestrial run-off and atmospheric deposition [6].

The most employed method for DON analysis is the Kjeldahl wet chemical method [7–11]. This is the reference method established by European Directive [12] concerning to waste water treatment.

The work presented in this paper gives the equipment design for a microscale quantitative analysis of nitrogen by the Kjeldahl method. Kjeldahl method in its macroscale style (more than 100 mL sample and digestion flasks from 500 to 800 mL) has been adapted to microscale by changing the digestion tubes and the distillation system. The ammonium content in the distilled solution obtained is measured with an ammonia selective electrode. Applicability of the designed microscale system is demonstrated for water samples. Advantages of the proposed equipment are compared to macroscale and outlined to microscale Kjeldahl equipments existing in the market (http://www.labconco.com).

---

[*] Corresponding author.
E-mail address: pilar.campins@uv.es (P. Campins-Falco).

2. Experimental

2.1. Reagents

All solutions were prepared in deionised water produced in a NANOpure Water System (Millipore Iberica, Madrid, Spain) and all reagents were of analytical grade. Stock standard solutions of ammonium were prepared by dissolving ammonium chloride (Probus, Barcelona, Spain) in nanopure water (100 or 1000 mg/L). Standards solutions with variable amounts of ammonium were obtained by dilution. Methylamine (MA) (Sigma, St. Louis, MO, USA) solutions were prepared in the same way. Potassium sulphate (Prolabo, Fontenay, France), sulphuric acid (Fluka Chemie, Steinheim, Switzerland), sodium hydroxide (J.T. Baker, Deventer, Holland) and potassium sulphate/copper sulphate Kjeltab (Merck, Darmstadt, Germany) were used in the digestion and distillation steps.

2.2. Apparatus

A homemade flask of 25 mL was used for sample digestion (Fig. 1a) and distillation (Fig. 1b) instead of commercial Kjeldahl flasks of 500–800 mL (classical). The typical digestion block (Tecator Digestion system 6, 1007 Digestor (Höganäs, Sweden) (Fig. 1c), that allows to process up to six samples simultaneously, was used. A homemade collector tubes of 15 mL were used for the distillation step. Fig. 2a shows the general view of the distillation unit.

2.3. Procedure

Twenty millilitres of standard solution or water samples were placed in the digestion tube, and 0.75 g of the potassium sulphate/copper sulphate Kjeltab and 0.75 mL of concentrated sulphuric acid, were added. The tubes were placed on the Kjeldahl digestor, previously heated at 370 °C. Heating was kept until white fumes appeared (approximately 10 min), then

the digestion was continued for 15 min. The digestion residue obtained was cooled and diluted up to 6.5 mL with nanopure water. The distillation was performed after the addition of 3.5 mL of sodium hydroxide (12.5 M). Distilled ammonia was picked up on 1.5 mL of 0.04N sulphuric acid up to 4.5 mL. Collected solutions were diluted up to 5 mL. A 0.1 mL of 10 M sodium hydroxide was added to 2.5 mL of the distillation solution and then, the Kjeldahl nitrogen was measured by ammonia selective electrode. All the measurements were performed at room temperature in triplicate.

3. Results and discussion

3.1. Optimization of the digestion and distillation steps

Fig. 1 compares the dimension of the homemade flask of 25 mL and the commercial flasks of 500–800 mL. Commercial flask for the micro method have 100 mL.

As can be seen in Fig. 2a, beside the reduction of the digestor flask and the collector tube, the distillation unit was also reduced in a factor approximately of three, respect the typical distillatory unit. An enlarged picture of the collector tube can be seen in Fig. 2b.

The digestion and the distillation steps were optimised by separated. For the distillation step, 5 mL of sample containing ammonium at different concentration levels were distilled and picked on sulphuric acid (1.5 mL, 0.04N) up to 5 mL. A fraction of 2.5 mL was alkalinised (0.1 mL NaOH 10 M) in order to performing the potential measurement. The recoveries obtained for ammonium in the distillation step calculated from the calibration graph of the ammonium standard solutions without distillation, E (mV) = 7.025–65.967 log C, r^2 = 1, were 110 ± 18 (n = 3). No influence of sulphuric acid and the digestion reagent was observed in the ammonium recoveries in the distillation step, the found recoveries were: 108 ± 3 (n = 3), 110 ± 18 (n = 3) and 95 ± 7 (n = 3) for ammonium standard containing 2.5 mg/L of ammonium in sulphuric acid, standard distilled and picked on
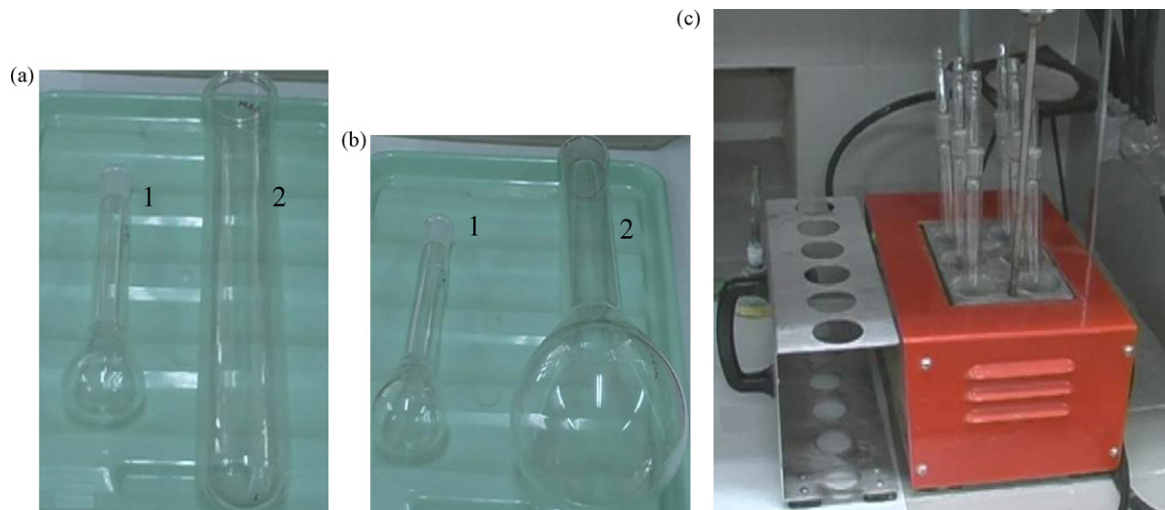

Fig. 1. Flasks used in (a) digestion step and (b) distillation step. (1, microKjeldahl designed system; 2, macroKjeldahl reference system). (c) Digestion block.
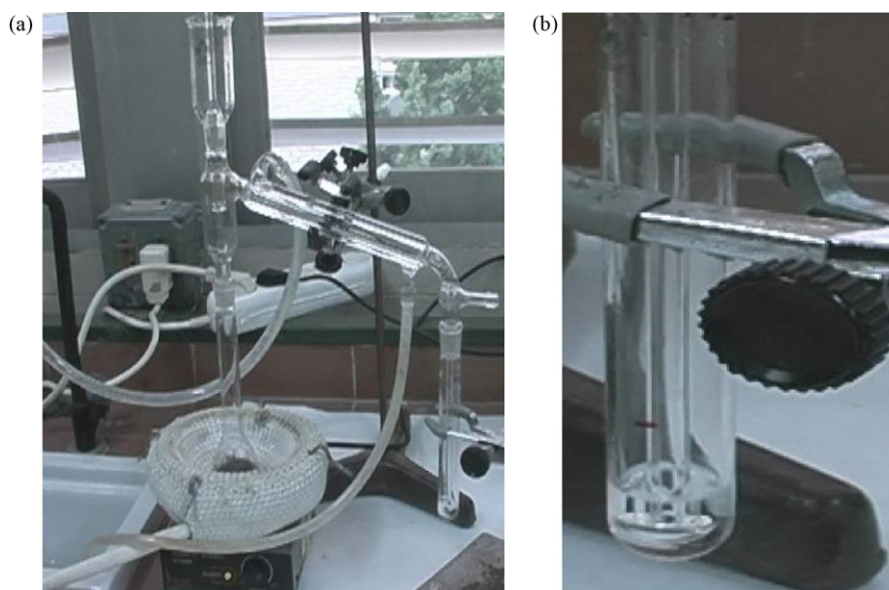
Fig. 2. (a) Microdistillation device and (b) enlarged picture of the collector unit.

sulphuric acid and standard plus digestion reagent distilled and picked on sulphuric acid, respectively.

For the digestion step, different sample volumes (5, 15, 20 and 25 mL) fortified with ammonium or/and organic amine (methylamine was used as model compound for organic amino nitrogen) at different initial concentration levels (2–10 mg/L NH_4^+) were digested and distilled according to the procedure described above. Fig. 3 shows the results obtained, similar recoveries and near 100% were obtained for ammonium and methylamine by using different sample volumes. An aliquot of 20 mL was selected in order to reach low ammonium concentrations. Digestion times were assayed up to 30 min, but no more than 15 min at 370 °C were needed to obtain a good recovery. The digestion residue obtained was dissolved in 6.5 mL of water and alkalinised with NaOH (3.5 mL, 12.5 M) in order to be distilled.

3.2. Analysis of real samples

The proposed procedure has been applied to different real water samples; the ammonium concentration found is shown in Table 1. In order to evaluate the accuracy of the procedure, the samples were fortified with ammonium and recoveries were near 100% in all cases as can be seen in Table 1, being the mean value 108 and the rsd 16%. Also confirmation studies based on the application of different measurement procedures and macroKjeldahl were carried out. Irrigation water was analysed by the validated *o*-phthaldialdehyde/*N*-acetyl-L-cysteine (OPA/NAC) method for ammonium [11] after macroKjeldahl treatment, the found concentration was $1.5 \pm 0.2(s)$ ($n = 3$). River water *a* was analysed by the chemiluminescence method
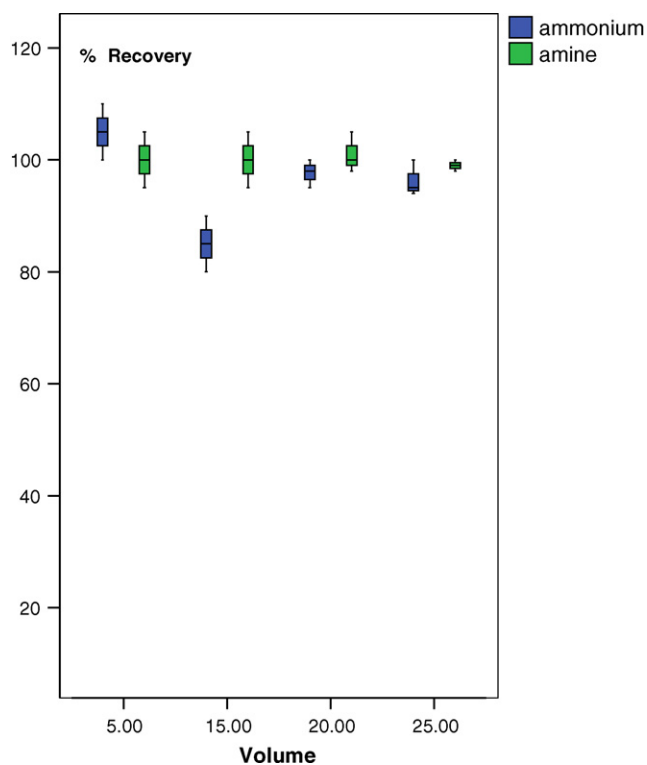

Fig. 3. Ammonia and amine % recoveries box plots ($n = 3$) by using different standard volumes in the digestion step. Final concentration in all cases 10 mg/L (as NH_4^+).

Table 1
Found ammonium concentration in different real samples (non-spiked and spiked) after microKjeldahl procedure

Sample	Found NH_4^+ (mg L^{-1})	
	Non-fortified	% Recovery in fortified sample (2.5 mg L^{-1})
Irrigation water	1.32 ± 0.06	103
Residual water	10.7 ± 0.05	136
Tap water	<LD	89
River water *a*	0.6 ± 0.1	110
River water *b*	<LD	100

Table 2
Comparison of the different conditions employed with the reference macroKjeldahl system and the designed microKjeldahl system

Steps	Reference macrokjeldahl	Designed microkjeldahl
Digestion		
Kjeldahl flask (mL)	500–800 mL	25 mL
Sample volume	100 mL	20 mL
H_2SO_4 (18 M)	10.0 mL	0.75 mL
K_2SO_4	10.5 g	0.75 g of Kjeltab
$CuSO_4$	1.4 g	
Distillation		
NaOH (12.5 M)	40 mL	3.5 mL
H_2SO_4 (0.04N)	25 mL	1.5 mL
Distilled solution volume	65 mL	4.5 mL
Ammonia measurement	ISE	ISE
Total time	2 h	25 min
Total cost per sample	€ 1.26	€ 0.19

described in Ref. [13] and the estimated concentration was 0.6 ± 0.1 ($n = 3$). The values obtained by the proposed method are inside the corresponding confidence intervals calculated from the validated procedures and then, the results are statistically similar.

In Table 2 are detailed the different steps and conditions involved in the designed microKjeldahl procedure, and are compared to the reference macroKjeldahl procedure. As can be seen, by using the designed microscaled procedure a reduction of laboratory hazards can be achieved because the amounts of chemical reagents used in laboratory experiments are markedly reduced. This system reduced disposal cost per sample by a factor of 6.6 times and time of analysis by a factor of 4.8 times. Besides, higher sensitivity can be reached due to the preconcentration factor, 4 instead of 1.5 obtained by the macroscale design. This system has the advantage of using the macro digestion unit of the conventional Kjeldahl system, avoiding a new investment.

4. Conclusions

In this paper has been shown how is possible to reduce the size of the macroKjeldahl system and the sample volume without losses of sensitivity in the nitrogen Kjeldahl determination and using the macrodigestor. By using this equipment, the procedure is faster, cheaper, more environmental friendly, easier to handle and efficient and accurate in the application to real water samples at the same levels of concentrations than macroKjeldahl system. Compared to other microscale Kjeldahl equipment existing in the market (http://www.labconco.com), both have the advantage of use small samples, however the commercial system are recommended for samples with relatively high amounts of nitrogen and uses 100 mL flasks and microdigestor and microdistillator specially designed.

Acknowledgements

References

[1] J. Skimer, Microscale chemistry. Experiments in miniature, RSC, 1998.
[2] V. Kumar, P. Courie, S. Haley, J. Chem. Educ. 69 (1992) A213.
[3] M.M. Singh, C.B. McGowan, R.M. Pike, Z. Szafran, J. Chem. Educ. 77 (2000) 625.
[4] J.N. Richardson, M.T. Stauffer, J.L. Henry, J. Chem. Educ. 80 (2003) 65.
[5] T.P. Burt, A.L. Heathwaite, S.T. Trudgill, Nitrate: Processes, Patterns and Management, John Wiley & Sons, New York, 1993.
[6] E.-S.A. Badr, E.P. Achterberg, A.L. Tappin, S.J. Hill, C.B. Braungardt, Trends Anal. Chem. 22 (2003) 819.
[7] K. Cameron, C. Madramootoo, A. Crolla, C. Kinsley, Water Res. 37 (2003) 2803.
[8] S.E. Tsiouris, A.P. Mamolos, K.L. Kalburtji, D. Alifrangis, Agric. Ecosyst. Environ. 89 (2002) 117.
[9] S.H. Ensign, M.A. Mallin, Water Res. 35 (2001) 3381.
[10] V.P. Aneja, B. Bunton, J.T. Walker, B.P. Malik, Atmos. Environ. 35 (2001) 1949.
[11] S. Meseguer-Lloret, J. Verdú-Andrés, C. Molins-Legua, P. Campíns-Falcó, Talanta 65 (2005) 869.
[12] Directive 91/271/CEE, Official Journal L 135 of May 30, 1991, pp. 0040–0052.
[13] S. Meseguer-Lloret, C. Molins-Legua, J. Verdú-Andrés, P. Campíns-Falcó, Anal. Chem. 78 (2006) 7504.

High performance liquid chromatography–mass spectrometry analysis for rat metabolism and pharmacokinetic studies of lithospermic acid B from danshen

Liang Cui [a], Wan Chan [a], Jian-Lin Wu [a], Zhi-Hong Jiang [b],
Kelvin Chan [c], Zongwei Cai [a,*]

[a] *Department of Chemistry, Hong Kong Baptist University, Kowloon, Hong Kong SAR, China*
[b] *School of Chinese Medicine, Hong Kong Baptist University, Kowloon, Hong Kong SAR, China*
[c] *Pharmacy Department, School of Applied Sciences, University of Wolverhampton, United Kingdom*

Abstract

Metabolism and pharmacokinetic studies on rat were conducted for lithospermic acid B, one of the components from *Radix Salviae Miltiorrhizae* (danshen) that shows many bioactivities. Liquid chromatography–electrospray ionization mass spectrometry method was applied for the determination of lithospermic acid B and its metabolites in samples from *in vitro* and *in vivo* metabolism studies. Rat plasma samples collected after intravenous administration were analyzed for obtaining pharmacokinetic data of lithospermic acid B. Four *O*-methylated metabolites, namely one monomethyl-, two dimethyl- and one trimethyl-lithospermic acid B, were detected when lithospermic acid B was incubated in rat hepatic cytosol. These four metabolites were also detected in rat bile, plasma and feces samples after intravenous administration of lithospermic acid B. The *in vitro* and *in vivo* results indicate that the methylation is the main metabolic pathway of lithospermic acid B. The danshen component and its methylated metabolites were excreted to rat bile and feces.
© 2008 Elsevier B.V. All rights reserved.

Keywords: LC–MS; Drug metabolism and pharmacokinetics; Rat; Lithospermic acid B; Danshen

1. Introduction

Radix Salviae Miltiorrhizae (danshen) is one of the most widely used traditional Chinese herbs. The herb has been officially listed in the Chinese Pharmacopeia for the treatment of menstrual disorders, menorrhalgia, insomnia, menostasis, blood circulation diseases and other cardiovascular diseases. Components in danshen can be grouped into two major classes: the lipid-soluble diterpenoid quinones and the water-soluble phenolic acid. In the past, research was focused mainly on lipophilic diterpenoids or tanshiones that have been considered to be the major active constituents [1–4]. In recent years, however, the water-soluble components that are mainly caffeic acid derivatives have attracted increasing attention due to their various pharmacological activities [5–8]. Among them,

lithospermic acid B (or salvianolic acid B, Fig. 1) that is a tetramer condensate of caffeic acid is the most abundant in aqueous extracts of *Salvia* species [9,10]. Lithospermic acid B has been shown to possess strong effects on antioxidative and free radical scavenging, on protecting renal dysfunction, hepatitis, uremia and lung fibrosis, and on improving blood circulation [11–21].

Recently, several studies on the pharmacokinetics of lithospermic acid B in dogs have been conducted with experiment of intravenous administration. A liquid chromatography–tandem mass spectrometry (LC–MS/MS) method was used to detect plasma concentrations of lithospermic acid B [22,23]. The obtained pharmacokinetic parameters indicated that lithospermic acid B was distributed and eliminated quickly in the beagle dogs. Pharmacokinetic characteristics of lithospermic acid B in rats after oral and intravenous administration were also investigated by using HPLC-electrochemical detection (ECD) to determine the plasma concentrations of lithospermic acid B, and extremely low systemic bioavailability in rats was found

* Corresponding author. Tel.: +852 34117070; fax: +852 34117348.
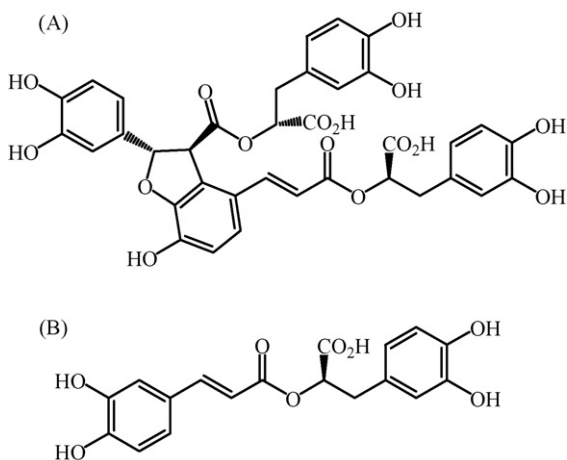*E-mail address:* zwcai@hkbu.edu.hk (Z. Cai).

Fig. 1. Chemical structures of lithospermic acid B (A) and the internal standard rosmarinic acid (B).

[24]. Extensive metabolism, wide distribution and poor absorption might be the main reasons of poor bioavailability. Rat metabolism study of lithospermic acid B by using hepatic cytosol has been reported [25]. Four major metabolites were isolated from bile sample extract after the intravenous administration of lithospermic acid B to rat and identified as *meta-O*-methylated products.

Liquid chromatography/mass spectrometry (LC/MS) has shown to be a powerful and reliable analytical approach to study active components in Chinese medicines, including their metabolism and pharmacokinetics [26–32]. Although LC coupled with triple–quadrupole MS has been widely used in pharmacokinetics study because its multiple reaction monitoring (MRM) technique provides high sensitivity for quantification, LC coupled with ion trap MS is becoming a useful technique for drug metabolites detection and identification. This is because the ion trap can effectively produce full-scan mass spectra while still offering high sensitivity [33] and the MS^n capability of ion trap MS also provides additional information for structural elucidation of the metabolites. In this paper, a LC/ion trap MS method was developed and successfully applied for the plasma pharmacokinetic study of lithospermic acid B in rats after the intravenous administration of the danshen component. Both *in vivo* and *in vitro* metabolism study was supported by LC–MS and MS/MS analysis. Four methylated metabolites of lithospermic acid B were detected not only in rat bile samples, but also in the rat feces and plasma samples.

2. Experimental

2.1. Materials

Lithospermic acid B and the internal standard rosmarinic acid (RA) with purity of 98% (Fig. 1) were provided by the School of Chinese Medicine, Hong Kong Baptist University. HPLC-grade acetonitrile was purchased from Acros Organics (NJ, USA). Water was produced by Milli-Q Ultra-pure water system. Rat liver cytosol fraction was prepared from the liver of Wister rat.

S-adenosyl-L-methionine (SAM) chloride and all other reagents (analytical grade) were purchased from Sigma (St. Louis, MO, USA).

2.2. In vitro incubation

Stock solution of lithospermic acid B was prepared in water at a concentration of 12.5 mM. Twenty microliters of the stock solution was added to 480 μL of 0.1 mM potassium phosphate buffer (pH 7.4) containing 2 mM SAM and 6 mM $MgCl_2$. The mixture was shaken for 5 min for equilibration in a water bath at 37 °C. The incubation was then initiated by adding a 500-μL rat liver cytosol and 0.1 mM phosphate buffer into the above mixture. The final concentration of lithospermic acid B, SAM and $MgCl_2$ were 0.25, 1 and 3 mM, respectively. The incubation was carried over 3 h at 37 °C. Aliquots of 100 μL of the incubation mixture were collected at 0, 5, 10, 20, 30, 45, 90, 120 and 180 min and the reaction was quenched by adding each aliquot into 200 μL of acetonitrile. The samples were vortex-mixed, placed in ice for 5 min and centrifuged at $14,000 \times g$ for 10 min. An aliquot of 10 μL was injected onto the HPLC column for LC–MS or $LC–MS^n$ analyses. Control incubations were carried out either without rat liver cytosol or without SAM.

2.3. Intravenous and oral administration

Lithospermic acid B was dissolved in saline containing 0.9% sodium chloride. Blood samples from three male SD rats (body weight 200–220 g) were obtained at specific time points after an intravenous dose (20 mg/kg). For each animal, the right jugular vein was cannulated 24 h prior to the administration of lithospermic acid B. Blood samples were withdrawn into heparinized tubes at 5, 10, 20, 30, 45, 60, 90, 120, 180, 240 and 360 min after the intravenous administration. The blood was then centrifuged at $8200 \times g$ for 10 min and 200 μL plasma was collected. A plasma sample (200 μL) and 20 μL of the internal standard were added to a test tube and mixed with 32 μL formic acid/water (1:3, v/v). Then 3 mL ethyl acetate was added to each tube. Extraction was performed by vortex mixing the tubes for 1.5 min, followed by centrifugation at $16,000 \times g$ for 2 min. The organic layer was transferred to a clean test tube and dried under a flow of nitrogen gas at 30 °C. The residue was reconstituted in 100 μL of methanol. After centrifugation at $16,000 \times g$ for 2 min, a volume of 20 μL of the supernatant was introduced into the LC–MS system. Oral administration of lithospermic acid B (20 mg/kg) was also conducted on two rats. The aqueous solution of the danshen active component in 5% b-cyclodextrin was given to each rat within 1 min. Blood samples were obtained after the oral administration and prepared for the LC–MS analysis by using the same procedure described above.

2.4. Bile sample collection

Three male Sprague–Dawley rats (body weight 200–220 g) were fasted overnight but with access to water before exper-

iments. Under the anesthesia with diethyl ether, bile fistulas of the rats were cannulated with polyethylene tubing for collection of bile. The bile was collected at 2 h intervals for 12 h after a single intravenous dose (8 mg/kg) of lithospermic acid B in saline. A 1 mL portion of bile was adjusted to pH 3 with 0.1% H_3PO_4 and centrifuged at $14,000 \times g$ for 10 min. The supernatant was applied to a preconditioned Waters Sep-Pak C_{18} cartridge. The column was washed with water, and the metabolites were eluted with methanol. An aliquot of 10 μL of the methanol solution was injected onto the HPLC column for analyses.

2.5. Feces and urine sample collection

Three male Sprague–Dawley rats (body weight 200–220 g) were fasted overnight but with access to water before experiments. Rat feces and urine were collected from 0 to 48 h after a single intravenous dose (8 mg/kg). One gram feces sample of each rat was homogenized and extracted with methanol. The sample extract was dried and the residue was dissolved in 1 mL methanol. After centrifugation at $10,000 \times g$ for 10 min, an aliquot of 10 μL of the supernatant was injected onto the HPLC column for analyses. A 5 mL portion of urine was adjusted to pH 3 with 0.1% H_3PO_4 and centrifuged at $14,000 \times g$ for 10 min. The supernatant was applied to a preconditioned Waters Sep-Pak C_{18} cartridge. The column was washed with water, and the metabolites were eluted with methanol. An aliquot of 10 μL of the methanol solution was injected onto the HPLC column for analyses.

2.6. LC–MS analysis

HPLC experiment was carried out on Agilent HP1100 series HPLC system equipped with degasser, binary pump, diode array detector and auto-sampler (San Francisco, USA). The liquid chromatography was performed on a reversed phase column (Phenomenex, Gemini, C_{18}, 150 mm × 2.1 mm, 5 μm) at a flow rate of 0.2 mL/min. The HPLC mobile phases consisted of 0.2% formic acid solution (A) and acetonitrile containing 0.2% formic acid (B). The gradient for metabolism studies started at 95% A, 5% B for 5 min, followed by a linear increase of solvent B to 70% within 30 min. This condition of 70% B was maintained for 5 min and then decreased to 5% B and equilibrated for 10 min before the injection of the next sample.

The ESI-MS analysis was performed on an Esquire 400 ion-trap mass spectrometer (Bruker-Daltonics, Bremen, Germany) with an ESI interface. The mass spectrometer was operated at negative ion mode at an ionization voltage of −4500 V and source temperature of 350 °C. Nitrogen was used as nebulizer gas at 36 psi and drying gas at a flow rate of 8 L/min. Helium was used as the collision gas for the tandem mass spectrometric experiments. Fragmentation was induced with resonant excitation amplitude of 1.0–1.2 V, following isolation of the ion of interest over a given mass window of 4 Da. The MS^n experiments were performed using an ion charge control (ICC) facility to automatically adjust the accumulation time as the ion abundance changed.

2.7. Calibration curves and quality control samples

An internal standard calibration method using matrix-matched standards was used for the quantitative analyses. Standard stock solution of lithospermic acid B and RA were individually prepared in methanol at 1.0 mg/mL and serially diluted to make the working solutions with methanol. All stock and working solutions were stored at −20 °C until use. Calibration standards and quality control (QC) samples were prepared by spiking 20 μL of working solutions, 20 μL of the internal standard and 32 μL formic acid/water (1:3, v/v) into 200 μL blank plasma. The resulted concentrations of lithospermic acid B in calibration standards were 0.25, 0.5, 1.0, 2.5, 5, 10, 25, 40 and 50 μg/mL. QC samples were obtained with lithospermic acid B concentrations of 0.5, 10.0 and 40 μg/mL. The calibration standards and QC samples were extracted with ethyl acetate and prepared under the same conditions as the test samples.

3. Results and discussion

3.1. Extraction recovery and stability

The extraction recovery was determined by comparing the peak area of lithospermic acid B in plasma samples that had been spiked with the danshen component prior to extraction to that of lithospermic acid B added in blank plasma extract. The results showed that the extraction recoveries of lithospermic acid B were in the range of 70–75% at concentrations of 0.5, 10 and 40 μg/mL. The extraction recovery of the internal standard was $83.7 \pm 3.6\%$.

The stability of lithospermic acid B in rat plasma was investigated under a variety of storage and process conditions. The concentration variations found after three cycles of freezing and thawing were within ±9% of nominal concentrations, indicating no significant substance loss during repeated thawing and freezing. After storage at ambient temperature for 24 h, lithospermic acid B showed a good stability evidenced from that the responses varied no more than ±8% at all concentrations studied.

3.2. Accuracy and precision

Accuracy and precision of the method were determined by replicate analyses of QC samples at three concentrations, by performing the complete analytical runs on the same day and also on three consecutive days. The intra-day and inter-day precisions were less than 10% for each QC level of lithospermic acid B. The accuracy, determined from QC samples, was within ±10% for each QC level. The results are summarized in Table 1.

3.3. Assay specificity

The specificity of the method was demonstrated by comparing the LC–MS chromatograms for lithospermic acid B and the I.S. obtained from the analyses of a drug-free rat plasma sample, a spiked plasma sample and a plasma sample collected 30 min after the intravenous administration. No significant peak

Table 1
Accuracy and precision results for lithospermic acid B in rat plasma (3 days, 5 replicates per day)

Spiked levels (μg/mL)	Mean measured concentration (μg/mL)	Relative error (%)	Intra-day R.S.D. (%)	Inter-day R.S.D. (%)
0.50	0.45	−9.8	6.7	8.2
10.0	9.84	−1.6	8.7	5.6
40.0	36.7	−8.2	5.2	10.1

interference with the analytes was observed in the drug-free rat plasma.

3.4. Linearity of calibration curves and limit of quantitation

Linear calibration curve with correlation coefficients greater than 0.99 were obtained in the concentration ranges 0.25–50 μg/mL in 200 μL of plasma for lithospermic acid B. The limit of quantitation (LOQ), defined as the lowest concentration analyzed with accuracy within ±10% and a precision ≤15%, was 0.15 μg/mL in 200 μL of plasma. The limit of detection (LOD), defined as the lowest concentration at which the analytical assay can reliably differentiate analyte LC peaks from background levels (S/N > 3), was 0.01 μg/mL in 200 μL of plasma. The LOQ and LOD of a reported LC–MS/MS method on a triple–quadrupole mass spectrometer to detect plasma concentrations of lithospermic acid B in the beagle dogs were 10 and 1.0 ng/mL, respectively [23]. Although multiple-reaction-monitoring (MRM) technique on a triple–quadrupole mass spectrometer is more sensitive than the ion trap mass spectrometer for the quantitative analysis, the current method is sensitive enough to detect plasma concentrations of lithospermic acid B in rats and to obtain its pharmacokinetics parameters. Meanwhile, ion trap mass spectrometry can simultaneously offer information about potential unknown metabolites because of the full-scan MS detection, i.e., a wide range of masses can be trapped and accumulated over an extended period of time. For quadrupole mass spectrometric analysis, the samples have to be reanalyzed by a full-scan MS technique for the detection and identification of metabolites.

3.5. Pharmacokinetic studies of lithospermic acid B

The calibration curve was used for the determination of lithospermic acid B concentrations in the plasma samples collected after the intravenous administration to support the rat pharmacokinetic study. The plasma concentrations of lithospermic acid B at each time point were determined, and the data obtained from three rats were averaged. Fig. 2 shows mean plasma concentration–time curves of lithospermic acid B after the intravenous dose of 20 mg/kg to the SD rats. The corresponding pharmacokinetic parameters ($T_{1/2}$, AUC_{0-t}, and $AUC_{0-\infty}$) are presented in Table 2. The mean AUC_{0-t} value was 9.94 μg h/mL in the current study, which was different from what reported previously [24]. The reason of the difference might be due to the usage of different rat species.

Large values of V_d (8.93 L/kg) and CL (2.01 L/h/kg) were observed, suggesting that rapid distribution and metabolism of lithospermic acid B in tissues and organs might have occurred.
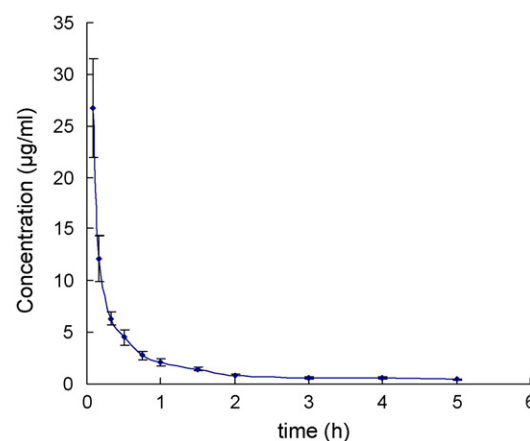

Fig. 2. Mean plasma concentration profiles of lithospermic acid B after the intravenous administration at 20 mg/kg to SD rats ($n = 3$).

Extensive metabolism and wide distribution of lithospermic acid B was also reported previously [24,25]. It was suggested that poor absorption of lithospermic acid B contributed to the extremely low systemic bioavailability and the excretion of unchanged lithospermic acid B in bile and urine was extremely low. These statements were supported by our data obtained from the oral dosing experiments. Lithospermic acid B was not detected in the plasma samples collected at each time point between 0 and 6 h after the oral administration at 20 mg/kg, with the LOD of 0.01 μg/mL for the current LC–MS method. Therefore, the oral experiment results indicated the poor absorption or extensive metabolism of lithospermic acid B, both of which may contribute to its low bioavailability.

3.6. In vivo metabolites identification

Four metabolites, along with lithospermic acid B, were detected in rat bile samples collected from 0 to 2 h. Fig. 3 shows the extracted $[M − H]^-$ ion chromatograms for lithospermic acid B at m/z 717 (A, retention time 25.8 min), one monomethy-

Table 2
Pharmacokinetic parameters of lithospermic acid B (20 mg/kg) after intravenous administrations to three rats (mean ± S.D.)

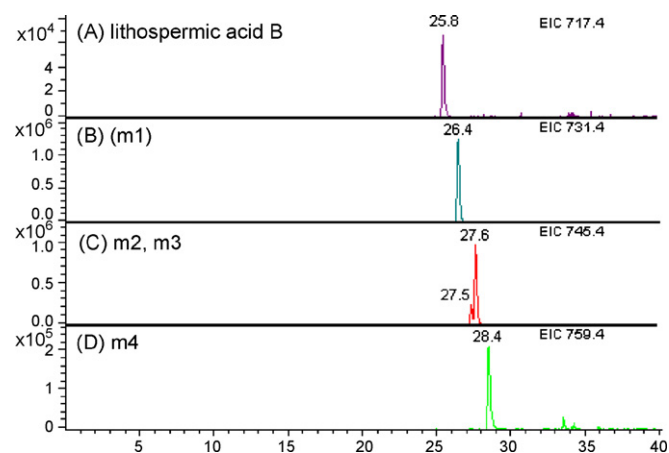| Parameter	Value
$t_{1/2}$ (h)	3.07 ± 0.42
k_e (1/h)	0.23 ± 0.03
AUC_{0-t} (μg h/mL)	9.94 ± 0.36
$AUC_{0-\infty}$ (μg h/mL)	11.82 ± 0.74
MRT (h)	2.36 ± 0.34
V_d (L/kg)	8.93 ± 0.87
CL (L/h/kg)	2.01 ± 0.07

Fig. 3. Extracted ion chromatograms for the $[M - H]^-$ ions of lithospermic acid B at m/z 717 (A), the monomethylated metabolite (M1) at m/z 731 (B), the dimethylated metabolites (M2, M3) at m/z 745 (C), and the trimethylated metabolite (M4) at m/z 759 (D) that were detected in rat bile samples collected 0–2 h after the intravenous administration of lithospermic acid B with a dosage of 8 mg/kg.

lated metabolite (M1) at m/z 731 (B, retention time 26.4 min), two dimethylated metabolites (M2, M3) at m/z 745 (C, retention time 27.5 and 28.6 min), and one trimethylated metabolite (M4) at m/z 759 (D, retention time 28.4 min). The molecular weights of the four metabolites were 14, 28, 28 and 42 mass units higher than lithospermic acid B, indicating that the four metabolites might be monomethyl-, dimethyl-, and trimethyl-lithospermic acid B, respectively. Methylation appeared to be the major metabolic pathways of lithospermic acid B in the rat.

LC–MS and MS/MS analyses in negative ESI mode were used to detect and confirm the detection of the methylated metabolites. The MS/MS spectra of lithospermic acid B and its four metabolites were shown in Fig. 4. The major fragment ions in the MS/MS spectrum of lithospermic acid B at m/z 519 and m/z 321 were interpreted as the cleavage of the ester bond and the loss of one and two of the right part chain (the $C_6H_3(OH)_2CH_2CH(OH)COOH$ moiety), respectively. Compared with the MS/MS spectrum of the $[M - H]^-$ ion of metabolite M1 with that of the parent compound, the major fragment ions were at m/z 533 and m/z 335, both of which are 14 mass unit higher that those of lithospermic acid B, indicated that the methylation occurred on one of the phenolic hydroxyl group on A or B ring. However, since there are four hydroxyl group on A and B ring, the exact methylation position could not be determined. Similarly, the exact methylation position of metabolite M2 to M4 could not be determined.

These four methylated metabolites, together with the unchanged lithospermic acid B were also detected in rat feces samples collected from 0 to 12 h after an intravenous dose with a dosage of 8 mg/kg, indicating lithospermic acid B and its methylated metabolites were excreted into rat bile and feces, instead of urine. Metabolites M1 to M3 could also be detected in rat plasma samples after an intravenous dose at 20 mg/kg.

No hydroxylated products, glucuronide or sulfate conjugates of lithospermic acid B were found in rat bile, feces, urine and plasma samples under the current sample preparation and
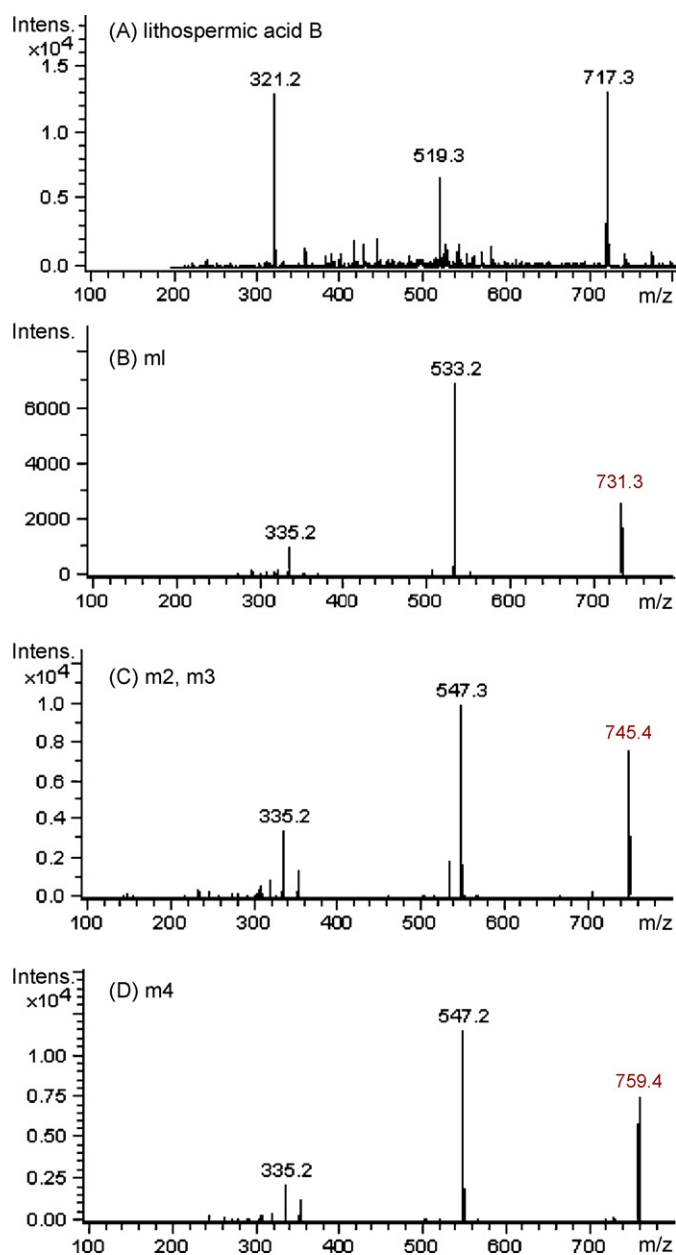

Fig. 4. MS/MS spectra of $[M - H]^-$ ions of lithospermic acid B (A), the monomethylated metabolite M1 (B), the dimethylated metabolites M2 and M3 (C), and the trimethylated metabolite M4 (D) that were detected in rat bile samples collected 0–2 h after the intravenous administration of lithospermic acid B with a dose at 8 mg/kg.

LC–MS conditions. The observation on lithospermic acid B metabolism is clearly different from the metabolic pathways of rosmarinic acid, the dimmer of caffeic acid that are also major lipid-soluble components of danshen [34]. In addition to methylation, major metabolism of rosmarinic acid included sulfate conjugation and subsequent cleavage of the ester bond to produce caffeic acid and the metabolites of caffeic acid [34].

3.7. In vitro metabolites identification

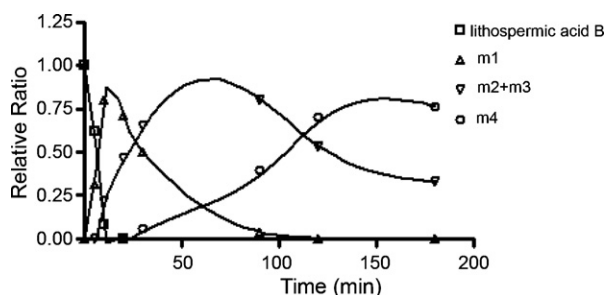*In vitro* metabolism study of lithospermic acid B was conducted by using rat liver cytosol. The danshen component

Fig. 5. Mean concentration profiles of lithospermic acid B and its metabolites when the medicinal component was incubated with rat hepatic ($n = 3$).

disappeared quickly when incubated with rat liver cytosol for a prolonged period (more than 20 min) and four metabolites, corresponding to M1 to M4 in bile and feces samples, were detected. The incubation curves in Fig. 5 show the results that are in agreement with the proposed metabolic pathways of lithospermic acid B. These *in vitro* results also support the statement that rapid and extensive metabolism of lithospermic acid B may contribute to the low bioavailability of the danshen component in rats.

4. Conclusions

Pharmacokinetic parameters of lithospermic acid B was obtained from the LC–MS analysis of the plasma samples collected after the intravenous administration to three SD rats at 20 mg/kg. Four methylated metabolites of lithospermic acid B were detected in rat bile, feces and plasma samples. The metabolite identification was consistent with the results from the *in vitro* incubation of lithospermic acid B with rat hepatic cytosol. The pharmacokinetic and drug metabolism study suggested that methylation might be the major metabolic pathways of lithospermic acid B in rats. The identification of these metabolites may provide important information regarding the bioactive forms of lithospermic acid B and its pharmacological mechanisms. As both of the *in vitro* and *in vivo* results indicated that lithospermic acid B was rapidly and extensively metabolized to its methylated metabolites, investigation on whether the metabolites might exert some pharmacological activities would be of interest.

Acknowledgements

References

[1] L.N. Li, Pure Appl. Chem. 70 (1998) 547.
[2] H.M. Chang, K.P. Cheng, T.F. Choang, H.F. Chow, K.Y. Chui, P.M. Hon, J. Org. Chem. 55 (1990) 3537.
[3] Y. Liang, Y.M. Yang, S.L. Yuan, Chin. Tradit. Herbal Drugs 31 (2000) 304.
[4] G.L. Tian, Y.B. Zhang, T.Y. Zhang, F.Q. Yang, I. Yoichiro, J. Chromatogr. A 904 (2000) 107.
[5] Y. Takako, H.Y. Chung, H. Oura, G.I. Nonaka, I. Nishioka, Jpn. J. Nephrol. 31 (1989) 1091.
[6] T. Tanaka, S. Morimoto, G. Nonaka, I. Nishioka, Y. Takako, H.Y. Chung, H. Oura, Chem. Pharm. Bull. 37 (1989) 340.
[7] Y. Lu, L.Y. Foo, Phytochemistry 59 (2002) 117.
[8] G. Du, Acta Pharm. Sin. 30 (1995) 184.
[9] R. Kasimu, K. Tanaka, Y. Tezuka, Z.N. Gong, J.X. Li, P. Basnet, T. Namb, S. Kadota, Chem. Pharm. Bull. 46 (1998) 500.
[10] P. Hu, G.A. Luo, Z. Zhao, Z.H. Jiang, Chem. Pharm. Bull. 53 (2005) 677.
[11] T.N. Ly, S. Makoto, R. Yamauchi, J. Agric. Food Chem. 54 (2006) 3786.
[12] D.Y. Soung, S.H. Rhee, J.S. Kim, J.Y. Lee, H.S. Yang, J.S. Choi, T. Yokozawa, Y.N. Han, H.Y. Chung, J. Pharm. Pharmacol. 55 (2003) 1427.
[13] D.G. Kang, H. Oh, E.J. Sohn, T.Y. Hur, K.C. Lee, K.J. Kim, T.Y. Kim, H.S. Lee, Life Sci. 75 (2004) 1801.
[14] X.J. Wu, Y.P. Wang, W. Wang, W.K. Sun, Y.M. Xu, L.J. Xuan, Acta Pharmacol. Sin. 21 (2000) 855.
[15] T. Yokozawa, T.W. Lee, H.Y. Chung, H. Oura, G. Nonaka, I. Nishioka, J. Pharm. Pharmacol. 42 (1990) 712.
[16] K. Kamata, M. Noguchi, M. Nagai, Gen. Pharmacol. 25 (1994) 69.
[17] K. Hase, R. Kasimu, P. Basnet, S. Kadota, T. Namba, Planta Med. 63 (1997) 22.
[18] T. Yokozawa, E. Dong, H. Oura, H. Kashiwagi, G. Nonaka, I. Nishioka, Nephron 75 (1997) 88.
[19] W. Wang, Y.P. Wang, W.K. Sun, Y.M. Xu, L.J. Xuan, Acta Pharmacol. Sin. 21 (2000) 859.
[20] W.B. Luo, Y.P. Wang, Acta Pharmacol. Sin. 22 (2001) 1135.
[21] K.K. Au-Yeung, D.Y. Zhu, K.O.Y.L. Siow, Biochem. Pharmacol. 62 (2001) 483.
[22] X.C. Li, C. Yu, W.K. Sun, G.Y. Liu, J.Y. Jia, Y.P. Wang, Acta Pharmacol. Sin. 25 (2004) 1402.
[23] X.C. Li, C. Yu, W.K. Sun, G.Y. Liu, L.J. Xuan, Y.P. Wang, J. Pharm. Biomed. Anal. 38 (2005) 107.
[24] Y. Zhang, T. Akao, N. Nakamura, C.L. Duan, M. Hattori, X.W. Yang, J.X. Liu, Planta Med. 70 (2004) 138.
[25] Y. Zhang, T. Akao, N. Nakamura, M. Hattori, X.W. Yang, C.L. Duan, J.X. Liu, Drug Metab. Dispos. 32 (2004) 752.
[26] Z. Cai, T.X. Qian, R.N.S. Wong, Z.H. Jiang, Anal. Chim. Acta 492 (2003) 283.
[27] T.X. Qian, Z. Cai, R.N.S. Wong, Z.H. Jiang, Rapid Commun. Mass Spectrom. 19 (2005) 3549.
[28] S.A. Chan, S.W. Lin, K.J. Yu, T.Y. Liu, M.R. Fuh, Talanta 69 (2006) 952.
[29] J.L. Wu, L.P. Yee, Z.H. Jiang, Z. Cai, Talanta 73 (2007) 656.
[30] H.X. Chen, Y. Chen, H. Wang, P. Du, F.M. Han, H.S. Zhang, Talanta 67 (2005) 984.
[31] J.H. Chen, F.M. Wang, F.S.-C. Lee, X.R. Wang, M.Y. Xie, Talanta 69 (2006) 172.
[32] H.-L. Lee, C.Y. Wang, S. Lin, D.P.H.T. Hsieh, Talanta 73 (2007) 76.
[33] Z. Cai, A.K. Sinhababu, S. Harrelson, Rapid Commun. Mass Spectrom. 14 (2000) 1637.
[34] T. Nakazawa, K. Ohsawa, J. Nat. Prod. 61 (1998) 993.

Quantum dot nanocrystals having guanosine imprinted nanoshell for DNA recognition

Sibel Emir Diltemiz [a], Rıdvan Say [a,b], Sibel Büyüktiryaki [b],
Deniz Hür [a], Adil Denizli [c], Arzu Ersöz [a,*]

[a] Department of Chemistry, Anadolu University,
Eskişehir, Turkey
[b] BİBAM (Plant, Drug and Scientific Researches Center), Anadolu University, Eskişehir, Turkey
[c] Department of Chemistry, Hacettepe University, Ankara, Turkey

Abstract

Molecular imprinted polymers (MIPs) as a recognition element for sensors are increasingly of interest and MIP nanoparticles have started to appear in the literature. In this study, we have proposed a novel thiol ligand-capping method with polymerizable methacryloylamido-cysteine (MAC) attached to CdS quantum dots (QDs), reminiscent of a self-assembled monolayer and have reconstructed surface shell by synthetic host polymers based on molecular imprinting method for DNA recognition. In this method, methacryloylamidohistidine-platinium (MAH-Pt(II)) is used as a new metal-chelating monomer via metal coordination-chelation interactions and guanosine templates of DNA. Nanoshell sensors with guanosine templates give a cavity that is selective for guanosine and its analogues. The guanosine can simultaneously chelate to Pt(II) metal ion and fit into the shape-selective cavity. Thus, the interaction between Pt(II) ion and free coordination spheres has an effect on the binding ability of the CdS QD nanosensor. The binding affinity of the guanosine imprinted nanocrystals has investigated by using the Langmuir and Scatchard methods, and experiments have shown the shape-selective cavity formation with O6 and N7 of a guanosine nucleotide ($K_a = 4.841 \times 10^6$ mol L^{-1}) and a free guanine base ($K_a = 0.894 \times 10^6$ mol L^{-1}). Additionally, the guanosine template of the nanocrystals is more favored for single stranded DNA compared to double stranded DNA.
© 2007 Elsevier B.V. All rights reserved.

Keywords: Quantum dots; Nanoshell sensor; Molecularly imprinted polymers; Deoxtribo nucleic acid (DNA) recognition; Photoluminescence

1. Introduction

Molecular imprinting provides a promising technique for designing synthetic receptors that possess the molecular recognition properties of biological systems and is a method for making selective binding sites in synthetic polymers using molecular template [1]. The selectivity of the polymer depends on various factors like the size and the shape of the cavity and rebinding interactions. Covalent interactions [2], non-covalent interactions [3–5], electrostatic interactions [6] and metal ion coordination [7,8] can be exploited to organize the functional monomers around the template. The molecular imprinted polymers (MIPs) have been applied to the realization of recognition and specificity to biomaterials for bioseparations, diagnostic assays, biosensors, and biocatalysis. MIPs have also been employed in efforts to synthesize materials for biosensor application.

On the other hand, semiconductor nanocrystal quantum dots (QDs) have been explored as fluorescent biological labels, due to their photostable, size-tunable, narrow bandwidth photoluminescence and chemically functionalizable surfaces [9–12].

Organic fluorescent dyes have been used for analyte detection in molecular imprinting process [13,14]. But better results can be obtained from inorganic semiconductor nanoparticles. Due to its broad excitation spectra, which is effective to whole spectrum of colors, emission without red tailing and photodegradation stability of QDs make them more effective as fluorescent labels [15].

Composite nanomaterials, containing polymer host, have several advantages [16,17]. Such nanocomposites are facile fabrication of luminescent bodies for display and other applications via coatings of them. These obviously require consideration of factors like, long shelf life of the coating solution, uniform monodispersity of the sulphide nanoparticles in the solution as also relatively long life of the nanoparticles without degradation, e.g., agglomeration and oxidation [18].

QDs consist of an inorganic nanoparticle that is surrounded by a layer of organic ligands. This organic ligand shell dictates the surface chemistry of the QDs. Ligand-exchange with various thiol-containing ligands has been extensively studied [19,20]. Aqueous phase synthesis and functionalization with biomolecules of QDs, i.e., CdS nanocrystals, would provide a convenient, economic, biocompatible and environmental friendly alternative to the labor intensive method of organic phase synthesis, i.e., CdSe which have surfaces that readily oxidized when exposed to water [11].

Additionally, in terms of strength, specificity and directionality, the metal coordination interaction is more like a covalent interaction than hydrogen bonding or electrostatic interactions in water [7]. These features make metal coordination as a promising binding mode preparing highly specific templated polymers for recognition sites of DNA, via the arrangements of metal coordinating ligands on CdS nanocrystals which have polymerizable ligand.

Recently, the combination of nanoparticles and MIPs has been applied in selective sensing detection. Only a few applications of nanoparticle/MIPs have been reported [15,21,22].

In this study, we have proposed a novel thiol ligand-exchange method with polymerizable methacryloylamidocysteine (MAC) of CdS QDs to capped by organic layer, reminiscent of a self-assembled monolayer and have reconstructed surface shell by synthetic host polymers based on molecular imprinting method for DNA recognition. MAH-Pt(II) was used as a new metal-chelating monomer via metal coordination-chelation interactions and guanosine templates of DNA. We have combined semiconductor nanotechnology with MIP that the ability of guanosine to chelate of platinum (II) ion of methacryloylamidohistidine (MAH) monomer to create reminiscent ligand-exchange (LE) assembled monolayer for DNA recognition, because the Pt(II) primarily interacts with the guanine base of DNA [23]. Synthesis, characterization and specificity of the QD nanoshell sensor based on guanosine imprinted polymer have been reported in this work.

2. Experimental

2.1. General methods

Methacryloyl chloride was supplied by Aldrich and used as received. L-histidine methyl ester dihydrochloride and L-cysteine methyl ester hydrochloride were supplied from Acros Organics. Ethylene glycol dimethacrylate (EDMA) was obtained from Fluka A.G., distilled under reduced pressure in the presence of hydroquinone inhibitor and stored at 4 °C until use. Azobisisobutyronitrile (AIBN) was also obtained from Fluka.

Platinum(II) chloride was supplied from Sigma Chem Co. (St. Louis, MO, USA). All other chemicals were of reagent grade and were purchased from Merck AG. All water used in the experiments was purified using a Barnstead NANOpure ultrapure water system. All MALDI-TOF/MS mass spectra were acquired on a Voyager Biospectrometry STR Workstation/the system utilizes a pulsed nitrogen laser, emitting 337 nm. The acceleration voltage was set to 20 kV and the delay time was 100 ns. Mass analysis was carried out in positive reflector mode and delayed extraction mode applied. α-cyano-4-hydroxycinnamic acid (CHCA) matrix solution was used. 10 mg CHCA solved in 1:1, 1 mL of 0.1% TFA solution and acetonitrile. 2 μL sample solution was mixed with 18 μL of a 10 mg mL^{-1} solution of CHCA in acetonitrile/0.1% TFA. This preparation (1 μL) was placed onto a MALDI-sample plate and allowed to dry.

Solid-state NMR samples were packed into 7 mm zirconia rotors. ^{13}C CP-MAS NMR spectra were obtained at a base frequency of 75.48 MHz on a Bruker AVANCE 300 spectrometer and the pulse sequence used a delay (D1) and acquisition time (AQ) of 5.0 and 0.042 s, respectively, a spectral width of 24038.46 Hz, 2 K data points and 256 scans.

The transmission emission microscopy (TEM) images of nanocrystals were acquired on a FEI-Tecnai™ G^2 Sprit transmission electron microscope (20–120 kV). Sample preparation was consisted of drop coating the QDs onto carbon-coated copper grids and air-dried.

2.2. Preparation of functional and metal-chelate monomers

The role of ligand-exchange monomers is to assist the creation of the specific binding cavity after the polymerization situated within the cavity in an optimal size and shape position for rebinding. Histidine-functional monomer and metal-chelate monomer, MAH and MAH-Pt(II), respectively, were synthesized according to the previously published procedures [24,25]. MAH-Pt(II) metal-chelate monomer was characterized with MALDI-TOF/MS (Fig. 1a). The ion peaks at 441 and 445 *m/e* confirms that MAH-Pt-(H$_2$O)$_2$ metal-chelate monomer structure was produced exactly. Furthermore, Pt-N vibration bands at 552 and 441 cm^{-1} in FTIR spectrum shows that Pt(II) was incorporated into MAH structure (Fig. 1b).

Ligand-exchange monomer, MAH-Pt(II)-guanosine, [MAH-Pt(II)-Gu], was preorganized using MAH-Pt(II) and template guanosine [25]. MAH-Pt(II) (0.25 mmoL) and guanosine (0.25 mmoL) were dissolved in 3.0 mL ethanol and the solution was stirred for 20 min until precipitation begins.

Methacryloylamidocysteine (MAC) was used for forming the reminiscent of self-assembled monolayer of near surface of QD and was synthesized and characterized according to the following procedure [26].

2.3. Preparation of guanosine imprinted nanoshell sensor

For CdS synthesis, 0.01 M of Cd(OAc)$_2$·2H$_2$O solution (6 mL) was prepared with ethanol. Solution was stirred continuously for 30 min in nitrogen ambient. Sodium sulfide (0.01 M,
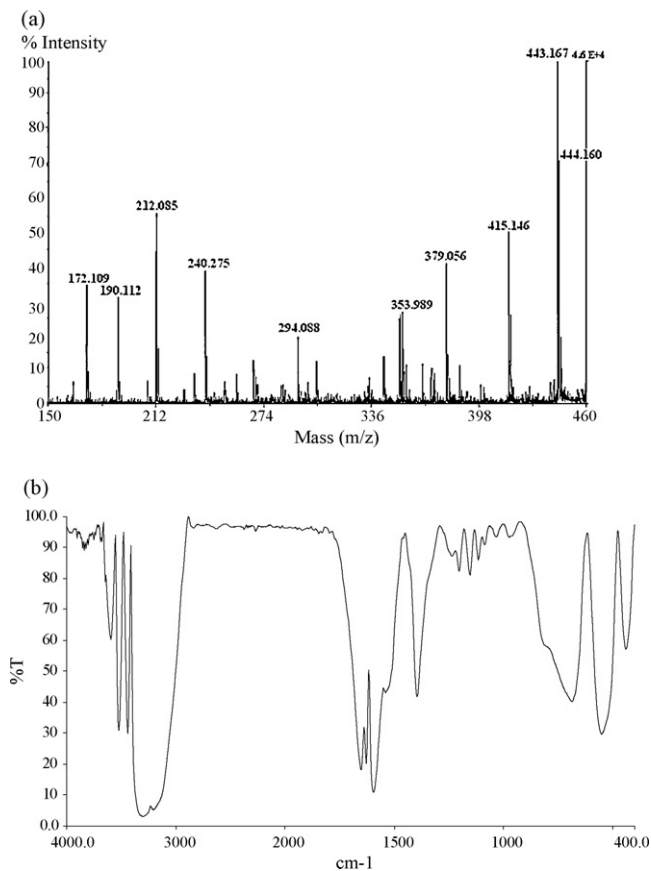
Fig. 1. (a) MALDI-TOF/MS spectrum of metal-chelate monomer (2 μL MAH-Pt(II) solution was mixed with 18 μL of a 10 mg mL^{-1} solution of CHCA in acetonitrile/0.1% TFA. The acceleration voltage was set to 20 kV and the delay time was 100 ns) and (b) FTIR spectrum of MAH-Pt(II).

Fig. 2. Schematic representation of nanoshell based on guanosine template reconstruction on CdS/QD.

6 mL) was slowly added, stirred under nitrogen ambient for 30 min and then centrifuged to collect precipitate. It was washed in double distilled water and dried in air. The entire synthesis was carried out at room temperature [27].

CdS nanocrystals were immersed in ethanol containing MAC (0.2 mg) for 30 min in order to introduce methacryloyl groups onto the surface of CdS nanocrystals. The nanocrystals were then washed with ethanol and deionized water for 10 min to remove the excess of thiol groups. A stable self-assembled monolayer of MAC was formed onto the nanocrystal surfaces after all these steps.

For the synthesis of guanosine recognized nanoshell/polymer nanocrystals, methacryloyl-activated nanocrystals were immersed in the reaction mixture containing the metal-chelate (MAH-Pt(II)/Gu) monomer (0.05 mmol) in methoxyethanol, EDMA cross-linking monomer (0.4 mmol) and 1 mol% of the initiator (AIBN) of the radical polymerization in ethanol. This solution was transferred into the dispersion medium placed in a magnetically stirred (at a constant stirring rate of 600 rpm) glass polymerization reactor. The reactor temperature was kept at 60 °C for 48 h. After polymerization, guanosine nanoshells having CdS nanocrystals were separated from the polymerization medium. The residuals (e.g., unconverted monomer, initiator, etc.) were removed by cleaning procedure.
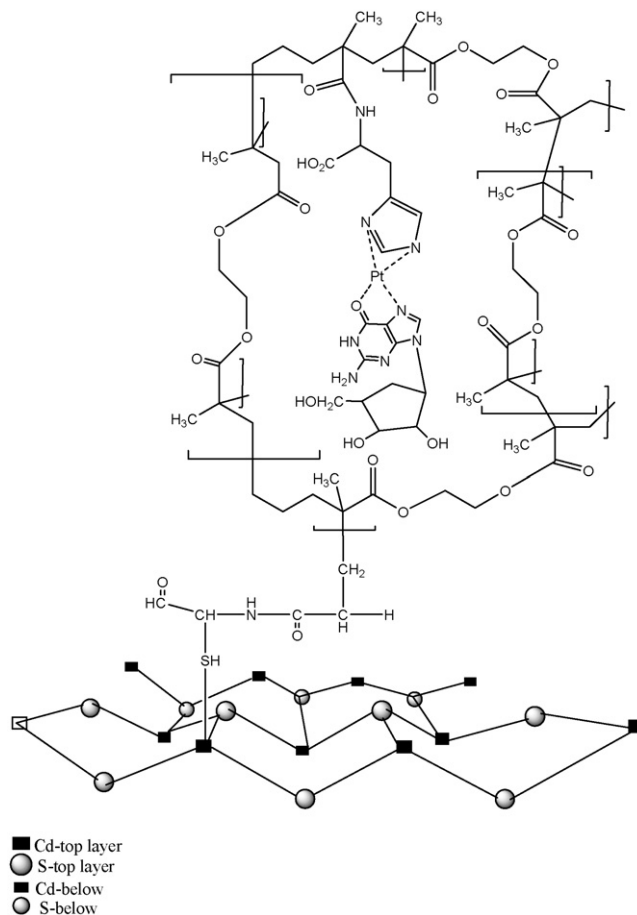
The resulting nanocrystals were treated with 15 mL 1.0 M of KOH solution in ethanol for 24 h to remove the templates. This procedure was repeated two times.

The functional metal-chelate monomer, MAH-Pt(II), was chose to interact guanosine and to make metal-complexing polymeric receptors for selective binding of guanosine and analogues. Metal-chelate monomer and guanosine molecule was mixed through preorganization and this preorganization complex defines the size and direction of the chemical interactions of the guanosine imprinted cavity to prepare synthetic guanosine receptor of CdS/QD (Fig. 2).

2.4. Evaluation of nanoshell QDs luminescence

The sensing capability and specificity of the guanosine memory having CdS nanoshell sensor were further explored by introducing guanosine as a template molecule. The interactions with guanine, ss-DNA, ds-DNA and adenosine were studied using fluorescence (measurements) spectrophotometer. The guanosine imprinted nanoshell CdS/QDs showed a high separation between the excitation and emission wavelengths, simplifying fluorescence measurements, recorded photoluminescence spectra using spectrofluorometer (RF-5301 PC, Shimadzu Japan). Guanine, guanosine, ss-DNA, ds-DNA sam-
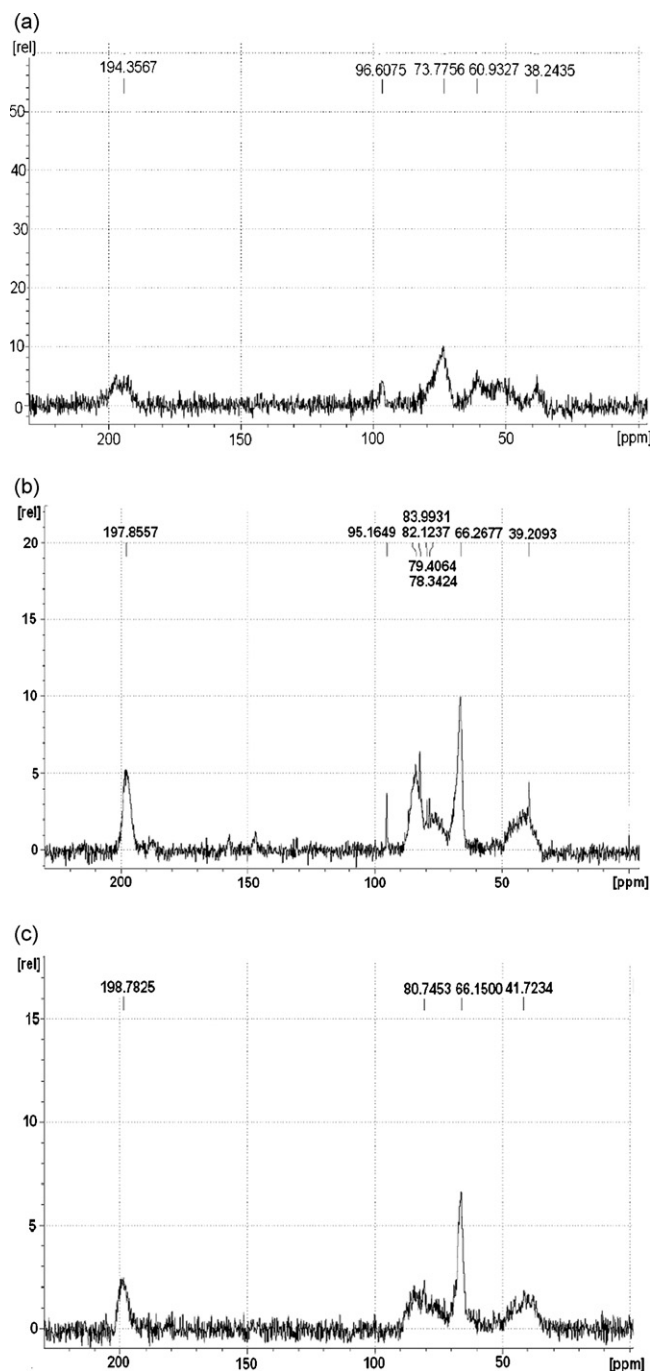
Fig. 3. The ^{13}C CP-MAS NMR spectra of (a) CdS-MAC; (b) before and (c) after the removal of template of the guanosine imprinted nanoshell (7.04 T, 75.43 MHz and 256 scans).

ples and the CdS/QD nanosensors were excited at 300 nm, and emission was recorded at 600 nm.

3. Results and discussion

3.1. ^{13}C solid-state NMR and TEM characterization of nanoshell sensors

The ^{13}C CP-MAS NMR spectra of MAC capped CdS nanoparticles and CdS-MIP core-shell nanoparticles (with guanosine template and without template) are shown in Fig. 3a–c. We have compared the ^{13}C CP-MAS NMR spectra of CdS-MAC (Fig. 3a) before (Fig. 3b) and after (Fig. 3c) the removal of template of the guanosine imprinted nanoshell. In Fig. 3a, the peak at 194.4 ppm is due to the carbonyl group of cysteine and resonance at 198 ppm signal is due to the carbonyl of methacryloyl group. On the other hand, signals at 60.9 and 73.8 ppm in Fig. 3a are due to the methine and methylene carbons of methacryloyl groups, respectively. In addition, the resonance at 50 ppm CA and the resonance at 38.2 ppm CB of cysteine were observed.

As far as the guanosine template polymer is concerned, the peaks at 60.9 and 73.8 ppm were disappeared as the incorporation of MAH (Fig. 3b). The appearance of histidine resonances CA and CB in the region of 66.3–79.4 ppm, guanosine resonances C4′, C1′ and C3′ in the region of 88.0–82.1 ppm and particularly increase of the signal around 200 ppm shows incorporation of cross-linker EDMA into polymer at high ratio.

After guanosine (template) was removed from CdS/QD nanoshell, disappearance of peaks in the range of 88.0–82.0 ppm revealed to the guanosine memory of nanoshell (Fig. 3c).

The incorporation of MAC into CdS/QD from the binding site of thiolate groups was supported by the observation of peak at 41.7 ppm, the conservation of MAH-Pt groups which were binded to them observed in the region of 81.0–66.0 ppm and the formation of cross-linked MIP based core/shell QD by the existence of peak around 199 ppm. This is the first ^{13}CP-MAS NMR description of these types of the structure in the literature.

TEM images for CdS nanoparticles having MAC monolayer before and after the removal of guanosine template are shown in Fig. 4. Fig. 4a shows a typical image for the prepared MAC-capped CdS nanoparticles. The shape of the nanoparticles is close to spherical, aggregated and with average size about 35 nm. The shape of the CdS-MIP nanoparticles with guanosine template is like spherical, more aggregated because of polymerization with average size about 46 nm (Fig. 4b). Fig. 4c shows CdS-MIP nanoparticles without guanosine template after methanolic KOH treatment. The shape of these nanoparticles is close to spherical and aggregated look like to MAC-capped CdS nanoparticles and with average size about 45 nm.

3.2. Measurement of binding interactions of molecularly imprinted nanoshell sensor via photoluminescence

The selective binding ability and detection of guanosine, guanine, ss-DNA, ds-DNA and adenosine with the CdS nanoshell sensor were studied with fluorescence spectroscopy, and the results were given in Fig. 5. Guanosine, guanine and ss-DNA additions caused significant increases in fluorescence intensity because they induced photoluminescence emission from CdS nanocrystals through the specific binding to the recognition sites of the cross-linked nanoshell polymer matrix.

The fluorescence intensity of the guanosine imprinted CdS/QD nanoshells can be enhanced by guanosine and our analogues. The enhancement of fluorescence intensity is proportional to guanosine concentration.
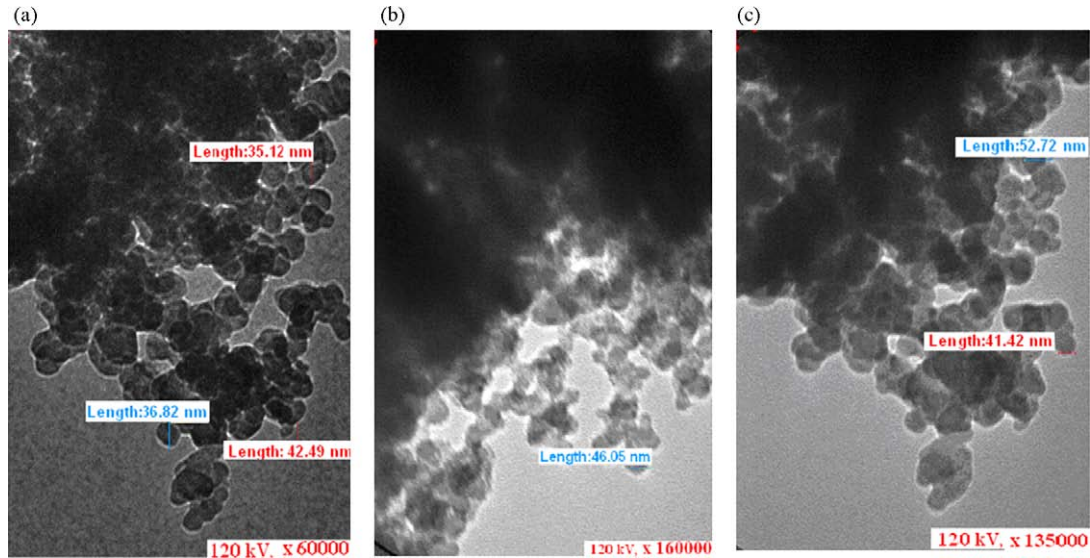
Fig. 4. TEM images of (a) MAC-capped CdS nanoparticles; (b) CdS-MIP nanoparticles and (c) CdS-MIP nanoparticles without guanosine template.

The rates at which the fluorescence changes are concentration-dependent with maximum changes occurring at $400\,\mu g\,L^{-1}$ concentration of guanosine and guanine. Guanosine imprinted nanocrystal were treated with adenosine in order to check whether the nanoshell has any effect on recognition process (Fig. 5). This control experiment (with adenosine) did not show a significant change in fluorescence intensity. This result clearly indicates that the change of fluorescence intensity is due to specific binding between guanosine structural analogues and guanosine memory having nanocrystal.

The fluorescence intensity correlates with the amount of guanosine analogues bounded to the nanoshell having CdS nanocrystal in the cases of incubating the guanosine imprinted nanoshell sensor with the guanosine, guanine, ss-DNA and ds-DNA aqueous solution.

As can be seen in Fig. 5, fluorescence intensity increased with the initial concentration of guanosine and its analogues. In order to reach the "saturation", the initial concentration of guanosine and its analogues were increased. It was observed that the amount of binding increased with the initial concentration of guanosine and its analogues.

The affinity constants of guanosine and its analogues to the nanoshell sensor can be estimated from the thermodynamic analysis of the fluorescence intensity as a function of the guanosine and structural analogues concentration based on Scatchard analysis [28,29] and Langmuir isotherm [30].

If we consider a binding equilibrium scenario such as:

$$G + QDS \underset{k^{-1}}{\overset{k}{\rightleftharpoons}} [G - QDS] \tag{1}$$

where G and QDS represent guanosine and its structural analogues in solution and guanosine imprinted polymeric nanoshell having nanocrystal, and G-QDS is the guanosine-nanocrystal bound complex. A Scatchard relationship can be obtained using the following equation.

$$\frac{I}{C_o} = \frac{I_{max}}{K_D - (I/K_D)} \tag{2}$$

where K_D is the equilibrium dissociation and I is the fluorescence intensity.

A plot of I versus I/C will give a straight line and the equilibrium binding constants calculated as $K_a = 1/K_D$ were given in Table 1.

The validity of the Langmuir isotherm can be tested by determining the affinity constant by measuring the fluorescence intensities at equilibrium with different bulk concentrations (Fig. 5). Langmuir relationship can be obtained using the following equation:

$$\frac{C_o}{I} = \frac{1}{I_{max}b} + \frac{C_o}{I_{max}} \tag{3}$$

The results obtained from the linearized form of the Langmuir isotherm, by plotting C_o/I as a function of C_o, and the Scatchard analysis findings were compared in Table 1.

The binding affinity of the guanosine imprinted nanocrystals was investigated using the Langmuir and Scatchard methods. K_a and I_{max} values for the specific interaction between the template-
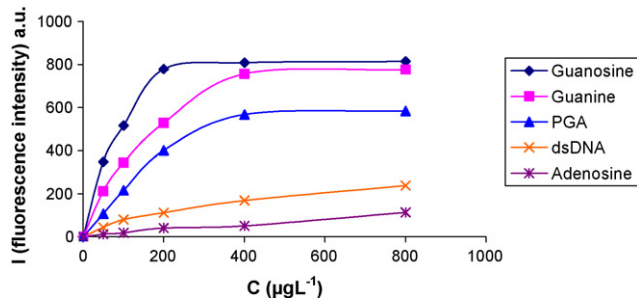

Fig. 5. The effect of concentration of guanosine and analogues on the change of the fluorescence of the guanosine imprinted CdS/QD nanosensor (Sensor Specificity Adsorption Isotherm, excitation at 300 nm, and emission at 600 nm).

Table 1
Comparison of Langmuir and Scatchard analysis for guanosine imprinted nanocrystals

Rebound molecules	Langmuir K_a (L µg^{-1})	I_{max} (a.u.)	Scatchard, K_a (L µg^{-1})	I_{max} (a.u.)
Guanosine	1.71×10^{-2}	909.1	1.06×10^{-2}	1011
Guanine	5.92×10^{-3}	1000	5.0×10^{-3}	1053
Polyguanylic acid	3.81×10^{-3}	833.3	1.6×10^{-3}	1525
ds-DNA	2.86×10^{-3}	333.3	3.2×10^{-3}	313.8
Adenosine	8.82×10^{-4}	250.0	0.9×10^{-3}	250.7

imprinted polymer of the nanocrystal and the template itself were determined by Langmuir isotherms and Scatchard's plots.

The Langmuir adsorption model assumes that the molecules are adsorbed at a fixed number of well-defined sites, each of which is capable of holding only one molecule. These sites are also assumed to be energetically equivalent, and distant from each other so that there are no interactions between molecules adsorbed on adjacent sites. According to the correlation coefficients of isotherms, Langmuir adsorption model is most favorable for guanosine and guanine (R^2: 0.995 and R^2: 0.989, respectively) and Langmuir model was found to be applicable in interpreting guanosine and analogues adsorption guanosine imprinted CdS/QD. The comparison of the association constants, K_a, and the apparent maximum number of recognition sites, I_{max} values, are presented in Table 1. As seen from Table 1, in general magnitude of K_a (4.841×10^6, 3.0×10^6 mol L^{-1}, based on Langmuir and Scatchard analysis, respectively) is due to the accessibility of guanosine template molecules. Some template cavities formed during imprinting process were stayed inside the polymer matrix of the nanoshell.

The K_a and I_{max} values estimated from Scatchard analysis are very close to the Langmuir analysis data and guanosine templated sites of nanocrystals are highly selective to the guanosine recognition sites. So the association constants based on Scatchard analysis for the binding of guanosine and guanine to MIP nanosensor are 3.0×10^6 and 0.76×10^6 mol L^{-1}, respectively. Maximum fluorescence intensity of ligand-exchange interaction sites for guanosine and guanine, I_{max}, are 1011 and 1053, respectively. The value of K_a suggests that affinity of the binding sites is very strong.

3.3. Recognition selectivity of guanosine imprinted nanoshell sensor

Molecular imprinting with guanosine gives a cavity that is selective for guanosine and its analogues. For various nucleotide the oligomers serving as DNA models, the highest binding affinity was found between N7 of guanine and platinum [23]. The guanosine can simultaneously chelate to Pt(II) metal ion and fit into the shape-selective cavity. So, this interaction between Pt(II) ion and free coordination spheres has an effect on the binding ability of the CdS/QD nanosensor. Experiments have shown that shape-selective cavity formation with O6 and N7 of a guanosine nucleotide ($K_a = 4.84 \times 10^6$ mol L^{-1}) and a free guanine base ($K_a = 0.894 \times 10^6$ mol L^{-1}) can contribute with natural antibodies; however, single stranded DNA (poly(guanidylic acid),

$K_a = 3.81 \times 10^{-3}$ L µg^{-1}) is more favored than DNA double helix (2.86×10^{-3} L µg^{-1}) for shape-selective cavity formation. This can be explained that most of the retained MAH-Pt(II) memory binding sites bonds two neighboring N7-coordinated guanosine nucleotides on the same DNA strand.

4. Conclusion

We have developed a novel chemical preparation method for methacryloyl based self-assembled monolayer and to make up imprinting polymer via ligand-exchange of guanosine on CdS/QD nanoshell. The guanosine imprinted MAH-Pt(II)-EDMA copolymer is expected to bind guanosine and its analogues for DNA sensing. The results showed that the fluorescence enhancement effect could be attributed to the high complexation geometric shape affinity (or guanosine memory) between guanosine molecules and guanosine cavities on to CdS/QD nanoshells. In conclusion, the guanosine imprinted nanoshell sensor has been gaining widespread recognition as a sensor for guanosine and its analogues because the imprinting methods create a nanoenvironment based on the shape of the cavity memorial, the size and the positions of functional groups that recognizes the imprinting molecule guanosine based on ligand-exchange imprinting methods. Nanoshell sensor having guanosine templates responses to the concentration of the guanosine and its analogues through fluorescence intensity enhancement.

Our results not only demonstrate that guanosine detection is achieved using CdS/QD nanoshell, but that they can also be used to assay target DNA sequencing. Guanosine imprinted CdS/QD nanoshells can recognize and bind the guanosine molecules. Likewise, CdS/QD nanocrystals containing MAH-Pt-guanosine can also be used in the mutagenic studies and for the detection of DNA defects.

Moreover, as a result of the reaction between guanine molecule and methylazonium cation or ethylmethyl sulphanate, alkylies of these compounds are bound from O6 site of guanine and usually guanine–thymine pair interaction is formed instead of guanine–cytosine interaction [31]. In the same way, in MAH-Pt-guanine monomer which has presented in this study, in the end of the interaction between Pt(II) and O6 site of guanine and usually guanine–thymine pair interaction is formed instead of guanine–cytosine interaction and this metal-chelate monomer can be used in both solid phase systems and nanoparticles. Thus, ODs can also be used for both molecular recognition based on the hybridization of nucleic acid strands and mutagenesis.

Acknowledgments

References

[1] B. Sellergren, Anal. Chem. 66 (1994) 1578.
[2] M.J. Whitcombe, M.E. Rodriquez, P. Villar, E.N. Vulfson, J. Am. Chem. Soc. 117 (1995) 7105.
[3] O. Ramstrom, L.I. Andersson, K. Mosbach, J. Org. Chem. 58 (1993) 7562.
[4] D.A. Spivak, K.J. Shea, Macromolecules 31 (1998) 2160.
[5] R. Say, Anal. Chim. Acta 579 (2006) 74.
[6] B. Sellergren, K.J. Shea, J. Chromatogr. 654 (1993) 31.
[7] P.K. Dhal, F.H. Arnhold, Macromolecules 25 (1992) 7051.
[8] M. Andaç, R. Say, A. Denizli, J. Chromatogr. B 811 (2004) 119.
[9] M. Bruchez Jr., M. Maronne, P. Gin, S. Weiss, A.P. Alivisatos, Science 281 (1998) 2013.
[10] W.C.W. Chan, S. Nie, Science 281 (1998) 2016.
[11] J.O. Winter, T.Y. Liu, B.A. Korgel, C.E. Schmidt, Adv. Mater. 13 (2001) 1673.
[12] J.O. Winter, N. Gomez, S. Gatzert, C.E. Schmidt, B.A. Korgel, Colloid Surf. A 254 (2005) 147.
[13] P. Turkewitsch, B. Wandelt, G.D. Darling, W.S. Powell, Anal. Chem. 70 (1998) 2025.
[14] C.I. Lin, A.K. Joseph, C.K. Chang, Y.D. Lee, Biosens. Bioelect. 20 (2004) 127.
[15] C.I. Lin, A.K. Joseph, C.K. Chang, Y.D. Lee, J. Chromatogr. A 1027 (2004) 259.
[16] J. Yang, H. Lin, Q. He, L. Ling, C. Zhu, F. Bai, Langmuir 17 (2001) 5978.
[17] L. Qi, H. Colfen, M. Antionetti, Nanoletters 1 (2001) 61.
[18] B. Bhhattacharjee, D. Ganguli, S.J. Chadhuri, Nanoparticle Res. 4 (2002) 225.
[19] C. Bruchez, H. Mattoussi, J.M. Mouro, E.R. Goldman, G.P. Anderson, V.C. Sundar, F.V. Mikulec, M.G. Bawendi, J. Am. Chem. Soc. 122 (2000) 12142.
[20] K. Sungjee, G.B. Moungi, J. Am. Chem. Soc. 125 (2003) 14652.
[21] A.B. Kharitonov, A.N. Shipway, I. Willner, Anal. Chem. 71 (1999) 1441.
[22] J. Matsui, K. Akamatsu, S. Nishiguchi, D. Miyoshi, H. Nawafune, K. Tamaki, N. Sugimato, Anal. Chem. 76 (2004) 1310.
[23] W. Kaim, B. Schwederski, Bioinorganic Chemistry: Inorganic Elements in the Chemistry of Life, John Wiley, 1994, pp. 369.
[24] R. Say, E. Birlik, A. Ersöz, F. Yılmaz, T. Gedikbey, A. Denizli, Anal. Chim. Acta 480 (2003) 251.
[25] A. Ersöz, A. Denizli, A. Özcan, R. Say, Biosens. Bioelect. 20 (2005) 2197.
[26] A. Denizli, R. Say, B. Garipcan, S. Emir, A. Karabakan, S. Patır, Sep. Purif. Technol. 30 (2003) 3.
[27] S.K. Kulkarni, A.S. Ethiraj, S. Kharrazi, D.N. Deobagkar, D.D. Deobagkar, Biosens. Bioelect. 21 (1) (2005) 95.
[28] P.Y. Tsoi, J. Yang, Y.T. Sun, S.F. Sui, M.S. Yang, Langmuir 16 (2000) 6590.
[29] M. Yang, P.Y. Tsoi, C.W. Li, J. Zhao, Sens. Actuators B 115 (2006) 428.
[30] B. Persson, K. Stenhag, P. Nilsson, A. Larsson, M. Uhlen, P.A. Nygren, Anal. Biochem. 246 (1997) 34.
[31] F. Marchesi, M. Turriziani, G. Tortorelli, G. Avvisati, F. Torino, L. De Vecchis, Pharmacol. Res. 56 (2007) 275.

Homogeneous immunoassay based on aggregation of antibody-functionalized gold nanoparticles coupled with light scattering detection

Baoan Du, Zhengping Li[*], Yongqiang Cheng

College of Chemistry and Environmental Science, Hebei University, Baoding 072002, PR China

Abstract

A universal platform of homogeneous noncompetitive immunoassay, using human immunoglobulin (IgG) as a model analyte, has been developed. The assay is based on aggregation of antibody-functionalized gold nanoparticles directed by the immunoreaction coupled with light scattering detection with a common spectrofluorimeter. In phosphate buffer (pH 7.0) solution, the light scattering intensity of the gold nanoparticles functionalized with goat-anti-human IgG can be greatly enhanced by addition of the human IgG. Based on this phenomenon, a wide dynamic range of $0.05–10\,\mu g\,ml^{-1}$ for determination of human IgG can be obtained, and the detection limit can reach $10\,ng\,ml^{-1}$. The proposed immunoassay can be accomplished in a homogeneous solution with one-step operation within 10 min and has been successfully applied to the determination of human IgG in serum samples, in which the results are well consistent with those of the enzyme-linked immunosorbent assay (ELISA), indicating its high selectivity and practicality. Therefore, the gold nanoparticle-based light scattering method can be used as a model to establish the general methods for protein assay in the fields of molecular biology and clinical diagnostics.
© 2008 Elsevier B.V. All rights reserved.

Keywords: Immunoassay; Light scattering; Gold nanoparticles

1. Introduction

Owing to the high specificity and sensitivity, immunoassays have been rapidly developed since they were introduced in the early 1960s. Immunoassays always play a major role in clinical diagnostics and biochemical studies, and become increasingly important to monitor drugs in biological samples and hazardous materials in the environment [1–3]. Most of the current immunoassays are performed in a heterogeneous format, such as the standard method of enzyme-linked immunosorbent assay (ELISA) due to the advantages of low background, wide dynamic range, and high specificity. However, the heterogeneous immunoassays have a fundamental weakness that they usually need a long dwell time due to several cycles of consecutive binding and washing steps [4]. There is an increasing need for homogeneous immunoassays without any separation steps, especially in the field of clinical diagnostics because of their simplicity, ease of automation, and high throughput. To date, several methods for homogeneous immunoassays, such as fluorescence polarization [5,6], fluorescence resonance energy transfer (FRET) [7], surface plasmon resonance (SPR) [8], and bioluminescence resonance energy transfer (BRET) [4,9] have been proposed. However, most of homogeneous immunoassays are less sensitive than their heterogeneous counterparts because of their high background. Recently, a highly sensitive homogeneous immunoassay has been explored based on enzymatic complementation systems, because the sensitive substrates, such as bioluminescent substrates, can be used to detect the immune complexes in the systems. But they need sophisticated recombinant technology [1,10].

A new colorimetric detection scheme for homogeneous immunoassay has been developed based on aggregation of gold nanoparticles functionalized with protein antigens [11]. The gold nanoparticle-based assay offered several advantages over conventional fluorophore-based assays with respects to simple preparation, easy readout, good stability and resist-photobleaching. However, the main disadvantage of this approach is its low sensitivity (with a detection limit

* Corresponding author. Fax: +86 312 5079403.
  E-mail address: lzpbd@mail.hbu.edu.cn (Z. Li).

of $1 \mu g \, ml^{-1}$ anti-protein A). The sensitivity of the gold nanoparticle-based immunoassays can be improved with scanometric method [12], surface enhanced Raman scattering [13,14], surface plasmon resonance [15,16], chemiluminescence detection [17,18], and bio-bar-code amplification [19]. But all these methods need to perform the immunoassay on the heterogeneous formats with multiplex binding and washing steps. They are too complicated and too tedious to be carried out in routinely clinic diagnoses and medical purpose.

In this paper, a sensitive homogeneous immunoassay has been developed by using antibody-functionalized gold nanoparticle as probes coupled with a light scattering detection. Light scattering detection has been used in the latex immunoassay, which is based on agglutination, by reaction with an antigen, of calibrated latex particles coated with a specific antibody. However, the high light scattering background produced by micrometer-sized latex particles leads to the low sensitivity and poor precision. Rosenweig and Yeung have developed a highly sensitive latex immunoassay with laser scattering detector [20] in which the latex particles coated with a antibody need to be separated by the capillary electrophoresis from the aggregates of the latex particles produced by the immunoreaction. A gold nanoparticle-based Hyper-Rayleigh scattering (nonlinear light scattering) immunoassay has been explored, in which $10 \mu g \, ml^{-1}$ human immunoglobulin (IgG) can be detectable [21]. Recently, Jiang et al. have also reported the resonance light scattering (RLS) immunoassays with gold nanoparticle labels for detection of fibrinogen [22], apolipoprotein A1 and apolipoprotein B [23], in which the gold nanoparticles labeled on the antibodies can be released from the immunoreactions and the released gold nanoparticles aggregate in the action of PEG 4000 solution. However, the RLS immunoassays have a narrow dynamic range and need the ultrasonic incubation for the immunoreactions. Herein, we found that the light scattering background of the suspensions of gold nanoparticles coated with antibodies is very low. The great enhancement of light scattering originated from the aggregate formation by the immunoreaction can be observed when microamounts of the antigen is directly mixed with the gold nanoparticles. The proposed immunoassay can be performed with one-step operation in homogeneous solution and the light scattering can be easily measured by using a common spectrofluorimeter equipped with a 150 W high pressure Xenon lamp. By using human IgG as a model analyte, a wide dynamic range of $0.05–10 \mu g \, ml^{-1}$ was achieved and as low as $10 \, ng \, ml^{-1}$ human IgG can be detected. Compared with the nanoparticle-based Hyper-Rayleigh scattering method, ~1000-fold improvement in the sensitivity was obtained.

2. Experimental

2.1. Instruments

A F-4500 spectrofluorimeter (Hitachi, Japan) equipped with a $0.5 \, cm \times 0.5 \, cm$ quartz cell was used to measure the light scattering spectra. A WH-861 vortex mixer (Huangjin Instrumental Co., Jiangsu, China) was used to blend the solutions. A thermo-

static water bath (Liaota, China) that can control the temperature at $0.1 \, °C$ intervals was used to perform the immunoreactions. A pHS-3C digital pH meter (Shanghai Weiye Instrument plant, Shanghai, China) was used to measure the pH values of the solutions. The TEM images of the colloidal gold were acquired on a JEM-1200EX II transmission electron microscope (JEOL, Japan).

2.2. Reagents

Tetrachloroauric acid ($HAuCl_4 \cdot 4H_2O$) was obtained from Sinopharm Group Chemical Reagent Co. (Shanghai, China). Human IgG, goat-anti-human IgG, rabbit IgG, goat IgG and bovine serum albumin (BSA) were purchased from Xin Jing Ke Biotechnology Co. Ltd. (Beijing, China). The HRP-labeled goat-anti-human IgG solution (Xin Jing Ke biotechnology Co. Ltd., Beijing, China) contains $2.0 \, mg \, ml^{-1}$ HRP and $4.0 \, mg \, ml^{-1}$ goat-anti-human IgG in $0.01 \, mol \, l^{-1}$ sodium phosphate-buffered saline including 0.05% Tween 20 (PBS-T, pH 7.4). The 1:400 dilution of the HRP-labeled goat-anti-human IgG solution with PBS-T was used as the work solution for the ELISA test. *O*-Phenylenediamine (OPD) (Sigma Co.) was served as the substrate of HRP. The OPD solution ($0.4 \, mg \, ml^{-1}$) was prepared by dissolving 10.0 mg OPD in 6.1 ml $0.1 \, mol \, l^{-1}$ citric acid solution, and then adding 6.4 ml $0.2 \, mol \, l^{-1} \, Na_2HPO_4$ solution and 12.5 ml deionized distilled water. $40 \, \mu l$ 30% H_2O_2 was added in the OPD solution immediately prior to use. The human serum (provided by Hebei University Hospital) was used as the samples to evaluate the reliability of the proposed immunoassay.

Deionized distilled water was used throughout. All other reagents were of analytical reagent grade and used as purchased without further purification.

2.3. Preparation of colloidal gold nanoparticles and gold nanoparticles coated with goat-anti-human IgG

Gold nanoparticles were prepared according to literature [24] with slight modification. Briefly, after boiling a 100 ml of the 0.01% $HAuCl_4$ solution, 3.5 ml of 1.0% trisodium citrate solution was quickly added with vigorous stirring. Boiling was continued for 7 min. The solution color turned to ruby. After the solution was naturally cooled to room temperature, it was filtered through a $0.20 \, \mu m$ membrane filter and then diluted to 100 ml and adjusted the pH value to 9.0 with K_2CO_3. The TEM image showed that the average diameter of the gold nanoparticles was about 13 nm (Fig. 1A).

1 ml of $0.5 \, mg \, ml^{-1}$ goat-anti-human IgG, (10% more than the minimum amount, determined by a flocculation test according to literature [18]) was added to 4.5 ml of pH-adjusted colloidal gold solution ($10^{-4} \, g \, ml^{-1}$, calculated by $HAuCl_4$) with being agitated and incubated in room temperature for 1 h. The resulting bio-conjugate was centrifuged at 12,000 rpm for 30 min. The oily ruby sediment was washed by $0.01 \, mol \, l^{-1}$ phosphate buffer (pH 7.0) and then resuspended with 5 ml the $0.01 \, mol \, l^{-1}$ phosphate buffer and the bio-conjugate solution was stored at 4 °C. The 10-fold dilution of the bio-conjugate
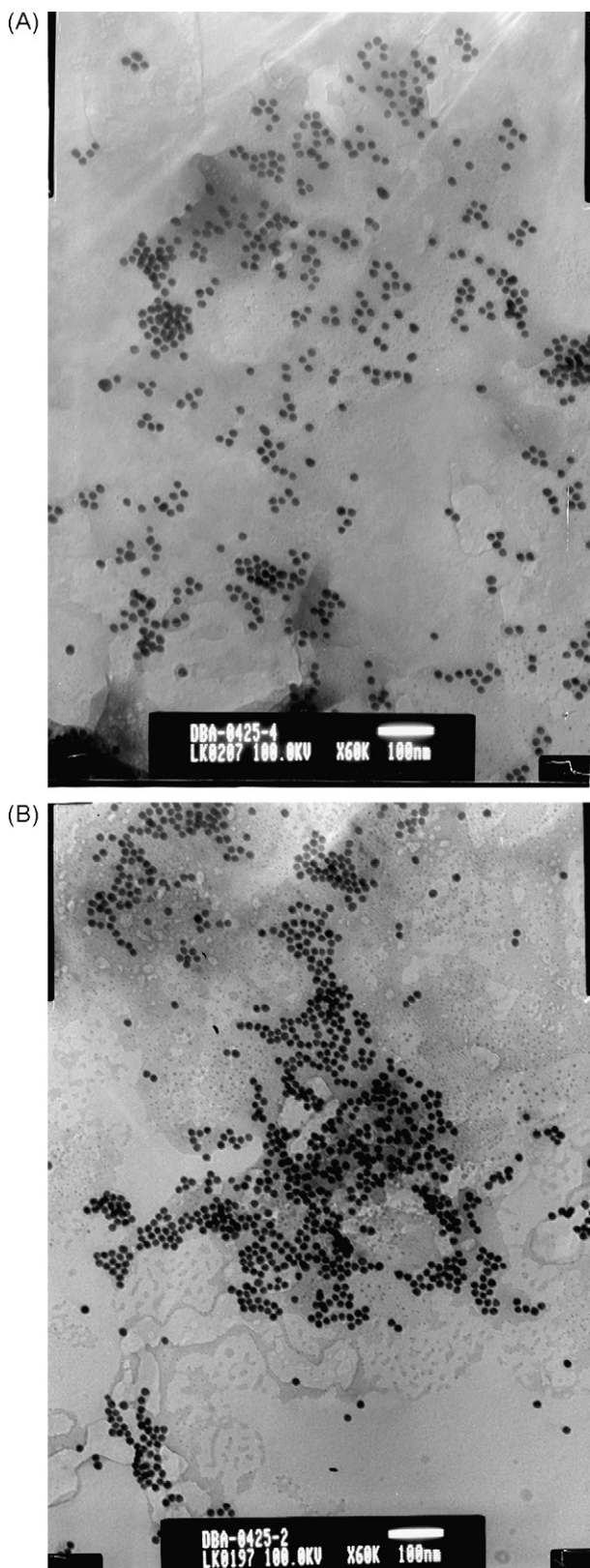
(A)

(B)

Fig. 1. (A) The TEM image of the gold nanoparticles. (B) TEM image of the aggregates of the gold nanoparticles coated with goat-anti-human IgG by addition of human IgG. The immunoreaction was carried out in $10\,mmol\,l^{-1}$ phosphate-buffered solution (pH 7.0) containing $1.0\,mmol\,l^{-1}$ NaCl, the reaction time is 10 min at room temperature. The concentration of human IgG is $0.3\,\mu g\,ml^{-1}$.
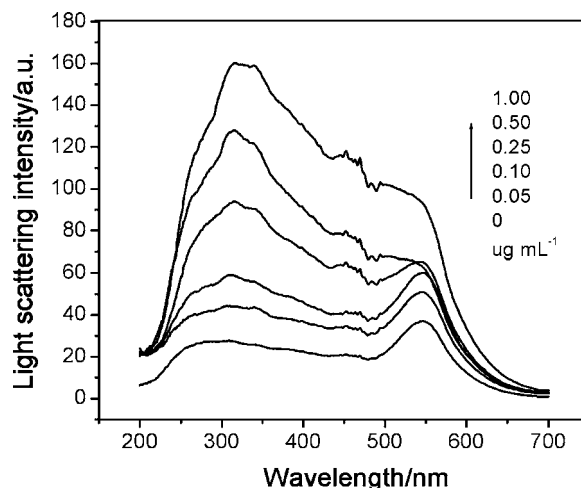

Fig. 2. Light scattering spectra of the gold nanoparticles coated with goat-anti-human IgG in the absence and in the presence of the human IgG at different concentration. The assay was carried out in $10\,mmol\,l^{-1}$ phosphate-buffered solution (pH 7.0) containing $1.0\,mmol\,l^{-1}$ NaCl, the reaction time is 10 min at room temperature.

solution with $0.01\,mol\,l^{-1}$ phosphate buffer (pH 7.0) was used as working solution to perform the immunoassay. The same batch of gold nanoparticles modified with goat-anti-human IgG was used throughout the total assay process to eliminate possible deviations between batches.

2.4. Standard procedures for immunoassay

Under the ambient temperature, 2 ml working solution of gold nanoparticles modified with goat-anti-human IgG was added to the dry 5 ml test tubes. Then a series of dilutions of human IgG or diluted serum samples were pipetted using micro-syringes into the test tubes. Afterward, the NaCl concentration was adjusted to $1.0\,mmol\,l^{-1}$. The mixtures were blended by the WH-861 vortex mixer and incubated for 10 min at room temperature. Utilizing F-4500 spectrofluorimeter, the light scattering spectra were measured and recorded by scanning synchronously the excitation and emission monochromators at the same wavelength (namely, $\Delta\lambda = 0$) from 200 to 700 nm.

In this study, ELISA was used as the standard method to test the reliability of the proposed immunoassay for the determination of human IgG serum samples. The ELISA test procedures were the same as our previous work [18].

3. Results and discussion

3.1. Spectral characteristics of light scattering

The light scattering spectra of the gold nanoparticles coated with goat-anti-human IgG in the absence and in the presence of human IgG at different concentrations are presented in Fig. 2. The gold nanoparticles show two weak light scattering peaks located at 284 and 547 nm, respectively. The light scattering intensity can be greatly enhanced in the wavelength range of 250–600 nm when a small amount of human IgG is mixed with the gold nanoparticles.

The gold nanoparticles with an average diameter of about 13 nm is well monodispersed in solution (Fig. 1A). The light scattering of the gold nanoparticle dispersion should be considered as only Rayleigh scattering because the diameter of the gold nanoparticles is about less than 1/20 of the wavelength of incident light. So the light scattering intensity is very weak. By using an uncorrected spectrofluorimeter equipped with a high-pressure Xenon lamp, the Rayleigh light scattering spectrum of an aqueous solution generally has a maximum light scattering at about 300 nm and then the light scattering intensity gradually decreases with increasing incident light wavelength [25]. According to the RLS theory of Pasternack and Collings [26], the RLS effect is observed as increased light scattering intensity at or near the wavelength of absorption of aggregated chromophores. The gold nanoparticles, as the aggregates of Au atoms, have a maximum absorption at 520 nm originated from their surface plasma oscillation, the light scattering peak at 547 nm of the gold nanoparticles can therefore be characterized as a RLS peak. When human IgG is mixed with the gold nanoparticles coated with the antibody, as shown in Fig. 1B, the gold nanoparticles aggregate to form larger particles through the immunoreaction and the light scattering (including both Rayleigh scattering and RLS) can be greatly enhanced.

Interestingly, it is worth noting that the RLS peak disappears when the concentration of human IgG is greater than $0.25\,\mu g\,ml^{-1}$. It is likely due to that the size of aggregates of the gold nanoparticles directed by the immunoreactions at higher antigen concentration exceeds the range to produce RLS [25,26]. On the other hand, gold nanoparticles in different size can scatter light at different wavelength and show different color [27]. However, it can be seen from Fig. 2 that the maximum light scattering wavelength except the RLS peak has only little red-shift from 315 to 350 nm with increasing the concentration of the human IgG, which means that the light scattering of the gold nanoparticle aggregates in different size resulted from different concentration of human IgG has no great wavelength selectivity. Therefore, the great enhancement of light scattering induced by the immunoreaction cannot be simply explained by increased size of the aggregates of the gold nanoparticles, probably because the aggregates formed in a network structure are still water-soluble in the solution.

The great enhancement of light scattering induced by the aggregation of the gold nanoparticles can be elucidated by Einstein's fluctuation theory for light scattering. In the aggregation area of gold nanoparticles, the gold nanoparticle concentration would be much greater than that of the surrounding solution. In other words, the aggregation of the gold nanoparticles directed by immunoreaction can lead to the great concentration fluctuation of the gold nanoparticles in the solution, which can consequently induce the great enhancement of light scattering according to Einstein's fluctuation theory. Therefore, the light scattering is very sensitive to detect the aggregation of gold nanoparticles in a solution, as well as the human IgG concentration.

One can also see from Fig. 2 that the immunoassay has a narrow dynamic range by measuring the RLS. However, the light scattering intensities in the wavelength range of 250–500 nm
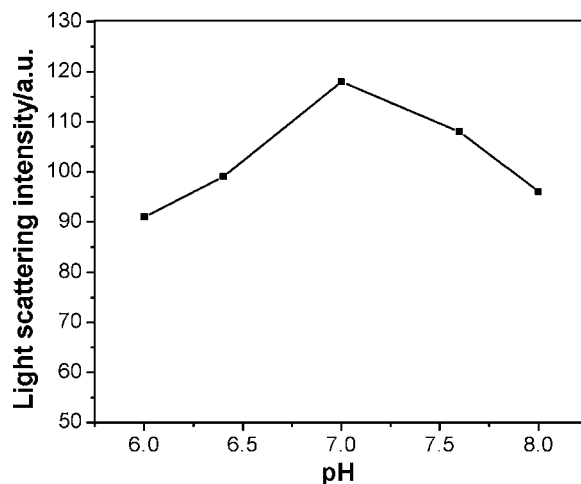

Fig. 3. The pH effect on the aggregation performance. Human IgG concentration is $0.5\,\mu g\,ml^{-1}$, $10\,mmol\,l^{-1}$ phosphate-buffered solutions containing $1.0\,mmol\,l^{-1}$ NaCl at different pH were used. The immunoreaction time is 10 min at room temperature. The intensity of the scattering light was measured at 350 nm.

increase with increasing the human IgG concentrations in a wide range. In this paper, 350 nm is chosen as the measuring wavelength for the light scattering immunoassay in order to obtain high sensitivity and wide dynamic range.

3.2. pH dependence

Both the immunoreaction and the aggregation of the gold nanoparticles involve charged species and electrostatic interaction [20]. The pH value of the solution would affect the charge distribution of antigen and antibody and on the surface of the nanoparticles, which consequently affect the aggregation of the gold nanoparticles directed by the immunoreaction and the light scattering intensity of the aggregates. The pH effect on the light scattering intensity is investigated in the pH range of 6.0–8.0. As shown in Fig. 3, the light scattering intensity of the aggregates of the gold nanoparticles resulted from the immunoreaction peaks at pH 7.0. Therefore, pH 7.0 is chosen as being optimum for subsequent work.

3.3. Effect of ionic strength on the immunoaggregation

Generally, the bare gold nanoparticles are easy to aggregate by addition of electrolytes due to charge screening effect [28]. As shown in Fig. 4, the light scattering of the gold nanoparticles coated with goat-anti-human IgG is weak and stable when NaCl concentration is less than $20\,mmol\,l^{-1}$, indicating that the gold nanoparticles are monodispersed in lower electrolyte concentration. But the light scattering increases sharply resulted from the aggregation of the gold nanoparticles when the NaCl concentration is greater than $20\,mmol\,l^{-1}$. It also can be seen from Fig. 4 that the light scattering produced by the immunoaggregation firstly keeps a constant when NaCl concentration is less than about $2.0\,mmol\,l^{-1}$. Then the light scattering decreases with increasing the NaCl concentration and keeps low intensities until the NaCl concentration is greater than $20\,mmol\,l^{-1}$.
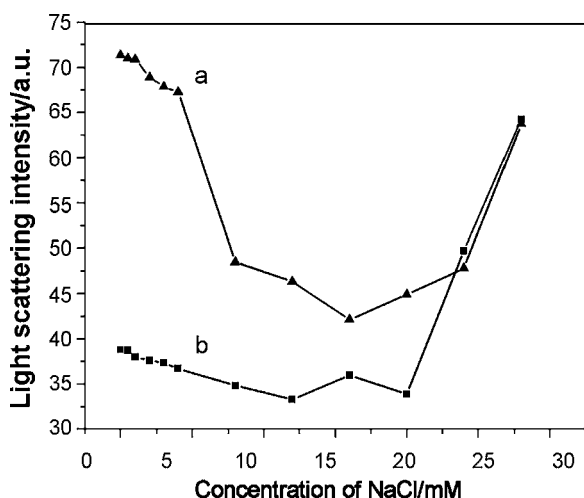
Fig. 4. Effect of NaCl concentration on the light scattering intensity of (a) gold nanoparticles coated with goat-anti-human IgG mixed with human IgG ($0.3\,\mu g\,ml^{-1}$) and (b) gold nanoparticles modified with goat-anti-human IgG. The immunoreaction was carried out in $10\,mmol\,l^{-1}$ phosphate-buffered solution (pH 7.0) at room temperature for1 0 min. The intensity of the scattering light was measured at 350 nm.

It is likely that the higher ionic strength can make the proteins (antigen and antibody) to denaturalize, which is unfavorable to the immunoreaction and further affects the immunoaggregation. Remembering that there already exists $10\,mmol\,l^{-1}$ phosphate used in the buffer, therefore, the phosphate buffer (pH 7.0) containing $1.0\,mmol\,l^{-1}$ NaCl is used to control the ionic strength in the solution for the immunoassay.

3.4. Effect of the incubation time on the immunoaggregation

The effect of the incubation time on the immunoaggregation is investigated by monitoring the light scattering immediately after mixing the gold nanoparticles coated with goat-anti-human IgG and human IgG. As shown in Fig. 5, the light scattering intensity can immediately reach its maximum when the solutions are mixed at the ambient temperature. However, it is unstable when the incubation time is less than 10 min because of the blending operation with the vortex mixer. Then the light scattering intensity becomes stable after 10 min and remains a constant at least within 60 min. Meanwhile, the light scattering intensity of the gold nanoparticles coated with goat-anti-human IgG in the absence of human IgG keeps a constant at low intensity in the period. The results express that immunoaggregation is fast and the stability of the light scattering signals is practical for the immunoassay.

3.5. Specificity

The specificity of the proposed immunoassay is evaluated by detecting the light scattering signals arising from human IgG. The gold nanoparticles coated with goat-anti-human IgG are used for the immune recognition and goat IgG, rabbit-IgG, and BSA are served as contrast reagents. The results in Table 1 show that a well-defined light scattering signal is observed from the
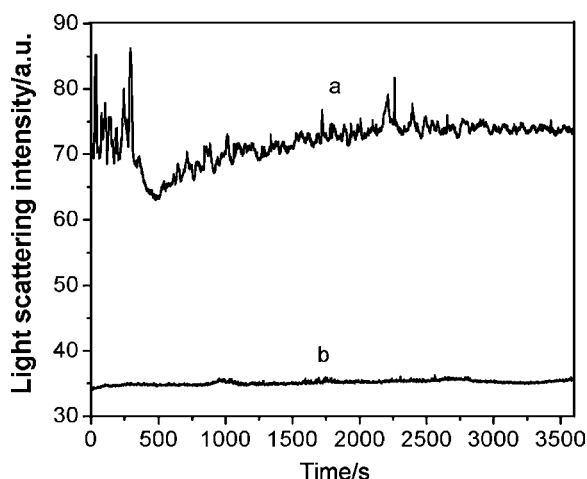

Fig. 5. Effect of the incubation time on the light scattering intensity of (a) gold nanoparticles coated with goat-anti-human IgG and human IgG ($0.3\,\mu g\,ml^{-1}$) and (b) gold nanoparticles modified with goat-anti-human IgG. The immunoreaction was carried out in $10\,mmol\,l^{-1}$ phosphate-buffered solution (pH 7.0) containing $1.0\,mmol\,l^{-1}$ NaCl at room temperature. The intensity of the scattering light was measured at 350 nm by using the time-scan model of F-4500 spectrofluorimeter.

human IgG, while light scattering intensity of goat IgG, rabbit-IgG, and BSA are less than 5.0%. The results indicate that the gold nanoparticles coated with goat-anti-human IgG can specifically recognize the human IgG and the specificity of the gold nanoparticle-based immunoassay has an acceptable level.

3.6. Analytical performance

Under the optimized experimental conditions mentioned above, the relationship between the light scattering intensity and the concentration of human IgG is investigated. As presented in Fig. 6, the dynamic range for determination of the human IgG concentration from 0.05 to $10\,\mu g\,ml^{-1}$ is obtained. At higher concentration, the sensitivity decreases due to the blocking of the active sites in the immunoreaction process. The detection limit (3σ, $n = 11$) is estimated to be $10\,ng\,ml^{-1}$ (i.e., $\sim0.16\,nM$). A series of eleven repetitive measurements of $0.05\,\mu g\,ml^{-1}$ human IgG are used for estimating the precision and the relative standard deviation (R.S.D.) is 2.3%, indicating an acceptable level of the precision for the immunoassay.

3.7. Analytical application

To evaluate the reliability and applicability of the proposed immunoassay to clinical diagnostics, a series of human serum samples are analyzed simultaneously with the proposed method

Table 1
Specificity of the proposed aggregate-based immunoassay

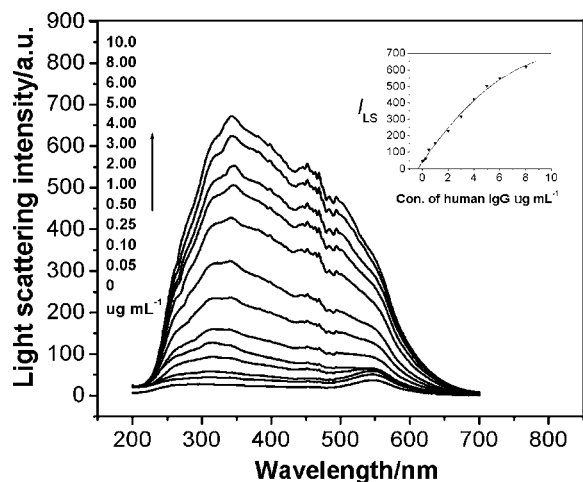| Analytes ($8\,\mu g\,ml^{-1}$)	Relative light scattering intensity (average, $n = 3$)
Human IgG	100
BSA	1.6
Goat IgG	3.4
Rabbit IgG	3.6

Fig. 6. Calibration curve of scattering light intensity vs. concentration of human IgG. The immunoreaction was carried out in 10 mM phosphate-buffered solution (pH 7.0) containing $1.0 \, mmol \, l^{-1}$ NaCl at room temperature for 10 min. The intensity of scattering light was measured at 350 nm.
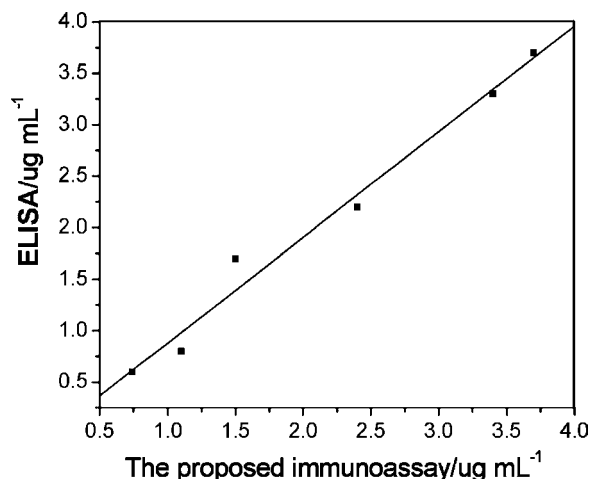

Fig. 7. Correlation between ELISA and the proposed gold nanoparticle-based immunoassay.

and ELISA. As shown in Fig. 7, a good correlation of determination results of human IgG in the serum samples between the proposed method and ELISA is obtained. The correlation equation is $y = -0.15 + 1.03x$ (where y and x are the determination results of ELISA and the proposed method, respectively), and the correlation coefficient $r = 0.9910$.

4. Conclusion

In this contribution, a homogenous noncompetitive immunoassay has been developed based on the aggregation of antibody-functionalized gold nanoparticles by using a simple light scattering technique. The proposed method can be characterized with obvious advantages in aspects of: (1) one-step operation and short assay time (10 min); (2) high sensitivity and specificity in the homogenous immunoassay; (3) use of a common spectrofluorimeter available in ordinary laboratories; (4) easy preparation and good stability of the gold

nanoparticle labels. The method is more rapid and sensitive than the other homogeneous immunoassays. The simple operation can avoid the multiple steps of immunoreactions and washings in the heterogeneous immunoassays and consequently keep away from the errors and deviations caused inevitably by those multiple steps. The proposed method can be successfully applied to the determination of human IgG in serum samples. Therefore, we believe that the proposed immunoassay has great potential for protein assay in the fields of molecular biology and clinical diagnostics.

Acknowledgments

References

[1] I.A. Darwish, A.M. Mahmoud, A.A. Al-Majed, Talanta 72 (2007) 1322–1328.
[2] T. Pulli, M. Hoyhtya, H. Soderlund, K. Takkinen, Anal. Chem. 77 (2005) 2637–2642.
[3] A. Bromberg, R.A. Mathies, Anal. Chem. 75 (2003) 1188–1195.
[4] R. Arai, H. Nakagawa, K. Tsumoto, W. Mahoney, I. Kumagai, H.H. Ueda, T. Nagamune, Anal. Biochem. 289 (2001) 77–81.
[5] G.I. Hatzidakis, A.M. Tsatsakis, E.K. Krambovitis, A. Spyros, S.A. Eremin, Anal. Chem. 74 (2002) 2513–2521.
[6] M.L.S. Martinez, M.P.A. Caballos, S.A. Eremin, A.G. Hens, Talanta 72 (2007) 243–248.
[7] G. Wang, J. Yuan, X. Hai, K. Matsumoto, Talanta 70 (2006) 133–138.
[8] R. Pei, X. Cui, X. Yang, E. wang, Talanta 53 (2000) 481–488.
[9] Y. Yamakawa, H. Ueda, A. Kitayama, T. Nagamune, J. Biosci. Bioeng. 93 (2002) 537–542.
[10] N. Komiya, H. Ueda, Y. Ohiro, T. Nagamune, Anal. Biochem. 327 (2004) 241–246.
[11] N.T.K. Thanh, Z. Rosenzweig, Anal. Chem. 74 (2002) 1624–1628.
[12] C.M. Niemeyer, B. Ceyhan, Angew. Chem. Int. Ed. 40 (2001) 3685–3688.
[13] D.S. Grubisha, R.J. Lipert, H.Y. Park, J. Driskell, M.D. Porter, Anal. Chem. 75 (2003) 5936–5943.
[14] Y.C. Cao, R. Jin, J.M. Nam, C.S. Thaxton, C.A. Mirkin, J. Am. Chem. Soc. 125 (2003) 14676–14677.
[15] A.J. Haes, R.P. Van Duyne, J. Am. Chem. Soc. 124 (2002) 10596–10604.
[16] J.C. Riboh, A.J. Haes, A.D. Mcfarland, C.R. Yanzon, R.P. Van Duyne, J. Phys. Chem. B 107 (2003) 1772–1780.
[17] A. Fan, C. Lau, J. Lu, Anal. Chem. 77 (2005) 3238–3242.
[18] Z.P. Li, Y.C. Wang, C.H. Liu, Y.K. Li, Anal. Chim. Acta 551 (2005) 85–91.
[19] J.M. Nam, C.S. Thaxton, C.A. Mirkin, Science 301 (2003) 1884–1886.
[20] Z. Rosenweig, E.S. Yeung, Anal. Chem. 66 (1994) 1771–1776.
[21] C.X. Zhang, X. Wang, Z.M. Tang, Z.H. Lu, Anal. Biochem. 320 (2003) 136–140.
[22] Z.L. Jiang, S.J. Sun, A.H. Liang, C.J. Liu, Anal. Chim. Acta 571 (2006) 200–205.
[23] Z.L. Jiang, S.J. Sun, A.H. Liang, W.X. Huang, A.M. Qin, Clin. Chem. 52 (2006) 1389–1394.
[24] K.C. Grabar, R.G. Freeman, M.B. Hommer, M.J. Natan, Anal. Chem. 67 (1995) 735–743.
[25] R.F. Pasternack, C. Bustamante, P.J. Collings, A. Giannetto, E.J. Gibbs, J. Am. Chem. Soc. 115 (1993) 5393–5399.
[26] R.F. Pasternack, P.J. Collings, Science 269 (1995) 935–939.
[27] J. Yguerabide, E.E. Yguerabide, Anal. Biochem. 262 (1998) 137–156.
[28] C.A. Mirkin, Inorg. Chem. 39 (2000) 2258–2272.

Flow-batch technique for the simultaneous enzymatic determination of levodopa and carbidopa in pharmaceuticals using PLS and successive projections algorithm

Marcos Grünhut [a], María E. Centurión [a,*], Wallace D. Fragoso [b], Luciano F. Almeida [b], Mário C.U. de Araújo [b], Beatriz S. Fernández Band [a]

[a] *Department of Chemistry, Universidad Nacional del Sur, 8000, Bahía Blanca, Buenos Aires, Argentina*
[b] *Department of Chemistry, Universidade Federal da Paraíba, João Pessoa, Brazil*

Abstract

An enzymatic flow-batch system with spectrophotometric detection was developed for simultaneous determination of levodopa [(*S*)-2 amino-3-(3,4-dihydroxyphenyl)propionic acid] and carbidopa [(*S*)-3-(3,4-dihydroxyphenyl)-2-hydrazino-2-methylpropionic acid] in pharmaceutical preparations. The data were analysed by univariate method, partial least squares (PLS) and a novel variable selection for multiple lineal regression (MLR), the successive projections algorithm (SPA). The enzyme polyphenol oxidase (PPO; EC 1.14.18.1) obtained from *Ipomoea batatas* (L.) Lam. was used to oxidize both analytes to their respective dopaquinones, which presented a strong absorption between 295 and 540 nm. The statistical parameters (RMSE and correlation coefficient) calculated after the PLS in the spectral region between 295 and 540 nm and MLR-SPA application were appropriate for levodopa and carbidopa. A comparative study of univariate, PLS, in different ranges, and MLR-SPA chemometrics models, was carried out by applying the elliptical joint confidence region (EJCR) test. The results were satisfactory for PLS in the spectral region between 295 and 540 nm and for MLR-SPA. Tablets of commercial samples were analysed and the results obtained are in close agreement with both, spectrophotometric and HPLC pharmacopeia methods. The sample throughput was 18 h^{-1}.
© 2007 Elsevier B.V. All rights reserved.

Keywords: Flow-batch; Polyphenol oxidase; Levodopa; Carbidopa; PLS; MLR-SPA

1. Introduction

Levodopa [(*S*)-2 amino-3-(3,4-dihydroxyphenyl)propionic acid] is a precursor of the neurotransmitter dopamine used in the treatment of Parkinson's disease. It is a progressive neurological disorder that occurs when the brain fails to produce enough dopamine. This condition causes tremor, muscle stiffness or rigidity, slowness of movement and lost of balance.

Dopamine cannot be administered directly because it does not cross the blood brain barrier readily. Therefore, its precursor levodopa is given orally, which is easily absorbed through the bowel, there, the dopamine is formed by the action of the decarboxylase. High levels of dopamine also cause adverse reactions such as nausea, vomiting and car-

diac arrhythmias. Usually, the peripheral decarboxylation of levodopa in extracerebral tissues is associated with an inhibitor of peripheral aromatic-ʟ-amino acid decarboxilase, such as carbidopa [(*S*)-3-(3,4-dihydroxyphenyl)-2-hydrazino-2-methylpropionic acid]. Thus, the importance of the presence of carbidopa (CBD) together with levodopa (LVD) makes that the dopamine levels can be controlled properly. Also, it was observed that the side effects are reduced [1,2].

In order to achieve better curative effect and lower toxicity, it is very important to control the content of levodopa and carbidopa in pharmaceutical tablets. The most frequently analytical technique, used in quality control analyses of pharmaceutical products, is high-performance liquid chromatography (HPLC). However, this technique is expensive, labour-intensive task, time consuming and produces chemical waste.

The polyphenol oxidase (PPO; EC 1.14.18.1) is an enzyme widely distributed in the nature. This enzyme catalyses the oxidation of LVD and CBD to the corresponding dopaquinone

which is converted to leucodopachrome by a rapid and spontaneous auto-oxidation. Then, the leucodopachrome is oxidized to its corresponding dopachrome. This kind of chemical reaction, where the dopachrome was formed, is produced with both analytes LVD and CBD and the products of both reactions present a strong absorption in the UV–vis spectra [3–5].

LVD and CBD determinations are commonly carried out by using high-performance liquid chromatography (HPLC) [6–8], capillary electrophoresis (CE) [9] and chemometrics-assisted spectrophotometric method [10]. Fatibello-Filho et al. [11] have published a paper on the FI spectrophotometric determination of LVD and CBD applying univariate calibration and using polyphenol oxidase. However, the mixture of both analytes shows a serious spectral overlapping, after the chemical reaction with the enzyme. Moreover, such flow manifold requires significant changes in their physical assemblies when it is necessary to analyse samples with a large variation of analyte concentration and/or physical–chemical properties.

Automated micro batch (AMBA) proposed by Sweileh and Dasgupta [12,13], and flow-batch analysers (FBA) proposed, developed and first named by Araújo et al. [14] constitute an excellent alternative to automate the quality control of pharmaceutical products because they are systems very flexible and versatile (multi-task characteristic). With AMBA or FBA, it is possible to work in wide analyte concentration range as well as to implement different analytical processes [14–25] without significant alterations on the physical configurations of the analyser. All these may be accomplished just by changing the operational parameters in their control software. These analysers have been used to implement several analytical procedures such as: liquid–liquid extraction [12], distillation of volatile analyte [13], kinetic approach [13], titrations [14,15], analyte addition [16,17], internal standard [18], screening analysis [19], exploitation of concentration gradients [20], on-line matching of pH [21] and salinity [22] and sample digestion [23].

FBA and AMBA combine favorable characteristics of both flow (FA) and batch analysers (BA). As in FA, the transportation of reagents, samples or other solutions are carried out in a flow mode, and, as in BA, the sample processing is carried out into a mixing chamber (MC). In AMBA, an injecting loop is used on the sampling stage (as in FA), while in FBA the sample amounts are added into the MC by controlling the ON switching time of one solenoid valve. As most of the FA, FBA and AMBA also present good precision and accuracy, high sample throughput and low contamination, consumption, manipulation of reagents and samples, cost per analysis and waste liberation for the environment, etc. Moreover, these analysers present high sensitivity because the physical and chemical equilibria inherent to the analytical processes may be attained and the dispersion and/or dilution of the samples may be negligible. In another hand, the analytical signal measurements can be performed in flow cells or directly inside MC and the multicommutation [24,25] may be used in order to manipulate the fluids in a simultaneous and/or in an intermittent way.

The application of multivariate calibration methods, such as multiple linear regression (MLR), principal component regression (PCR) and partial least squares (PLS), to the spectrometric data may require the use of variable selection for constructing well-fitted models. Several authors have presented theoretical and empirical evidence supporting the use of variable selection to improve the predictive ability of PCR, PLS [26–28] and, principally, MLR models. MLR yields models which are simpler and easier to interpret than PCR and PLS, since these calibration techniques perform regression on latent variables, which do not have physical meaning. In another hand, MLR calibration is more dependent on the spectral variables selection. To overcome this problem, Araújo et al. proposed a novel variable selection strategy for MLR calibration, which uses the "successive projections algorithm" (SPA) to minimize collinearity problems [29,30]. SPA is a forward selection method which operates on the instrumental response. The number of variables to be selected can be optimized in order to maximize model prediction capability [29].

The aim of the present work was to propose a chemometric-assisted flow-batch method for the simultaneous spectrophotometric determination of levodopa and carbidopa in medicaments. The method was based on the enzymatic oxidation of LVD and CBD with PPO obtained from a natural source (*Ipomoea batatas* (L.) Lam), in phosphate buffer medium (pH 7.0).

2. Experimental

2.1. Apparatus and software

Centrifugation of extracts was performed in a refrigerated-automatic Sigma centrifuge. The spectrometric measurements were carried out by using a Hewlett-Packard model 8453 UV-visible diode array spectrophotometer with a Hellma flow cell (inner volume of 18 μL). A model 713 Metrohm pHmeter was used to carry out the pH measurements.

SPA and MLR calculations and pre-selection were performed using programs developed in our own laboratory with the MATLAB®, Version 5.3 high-level programming language. The UNSCRAMBLER® chemometrics software (CAMO A/S), Version 9.5, was used for PLS calculations.

2.2. Reagents and solutions

All reagents were of analytical grade. To prepare all solutions ultra pure water (18 MΩ) was used.

A $0.1 \, mol \, L^{-1}$ phosphate buffer solution (pH 7.0) was prepared. $0.05 \, mol \, L^{-1}$ catechol stock solution used as substrate for enzymatic activity determination was prepared by dissolving 0.1375 g of catechol (Anedra) in 25 mL of the buffer solution.

Stock solutions of LVD (Saporiti) and CBD (Saporiti) of $0.800 \, mg \, mL^{-1}$ and $0.400 \, mg \, mL^{-1}$ respectively were prepared in medium of phosphate buffer. All stock solutions were protected from light and stored at 4 °C. The working standard solutions were prepared by adequate dilutions of the stock solutions in medium of phosphate buffer.

Dowex 1×8 100–200 mesh (Fluka) strong basic, quaternary ammonium anion exchange resin was used as a protective and stabiliser agent in the sweet potato extract preparation. A 0.015%

m/v sodium azide (Sigma) solution was added to the extract as an antimicrobial agent in order to increase its lifetime.

Sweet potato roots (*I. batatas* (L.) Lam.) purchased in local supermarkets, were washed, hand-peeled, chopped and frozen at $-18\,^{\circ}\text{C}$ before use.

The drug samples containing the pharmaceutical preparations Lebocar® (Pfizer, Searle) and Parkinel® (Bagó) were purchased in a local pharmacy. These preparations are presented in the form of tablets, with a nominal content of 250 mg of LVD and 25 mg CBD (Lebocar® and Parkinel® A) or 100 mg of LVD and 25 mg CBD (Lebocar® and Parkinel® B) and excipients until arriving at the weight of approximately 400 and 230 mg per tablet, respectively. In this work, both preparations (A and B) were analysed.

A solution containing different excipients as microcrystalline cellulose, maize starch, magnesium stearate and colloidal anhydride silica (Saporiti) was prepared in adequate proportions in a buffer phosphate medium.

2.3. Methods

2.3.1. Extraction of PPO of sweet potato root

An amount of 25 g of *I. batatas* previously frozen was cut into small pieces and placed in a liquefier and added 100 mL of $0.1\,\text{mol}\,\text{L}^{-1}$ phosphate buffer (pH 7.0) and 2.5 g of resin. It was homogenized for 3 min in a temperature range of 4–6 °C. The homogenate was rapidly filtered through two layers of cheesecloth and centrifuged at 15,000 rpm for 60 min, at 4 °C. The resulting supernatant was separated and stored at $-18\,^{\circ}\text{C}$ in a freezer with previous addition of 0.015% sodium azide solution. This crude extract was then used as an enzymatic source in the flow-batch procedure.

2.3.2. Measurement of PPO activity

The PPO activity in the crude extract was determined. The *o*-quinones were obtained when 0.2 mL of PPO was mixed with 2.8 mL of $0.05\,\text{mol}\,\text{L}^{-1}$ catechol and buffer phosphate to 5.0 mL. The classical spectrometric method was used for the absorption measurements of the *o*-quinones at 410 nm.

One unit of PPO activity is defined as the amount of enzyme that causes an increase of 0.001 absorbance units per minute, under the conditions described above [31].

2.3.3. Preparation of the calibration and validation sets

A calibration set of nine samples was prepared following a central composite design with three central point replicates. The concentration ranges were from 0.057 to 0.553 mg mL^{-1} of LVD and from 0.021 to 0.070 mg mL^{-1} of CBD (Fig. 1). The component ratios were selected considering the usual LVD/CBD relationship in the commercial pharmaceutical products, i.e., from 4:1 to 10:1.

To evaluate the predictive capacity of the model of calibration, a validation set with eight mixtures were prepared in concentrations comprised within those of calibration.
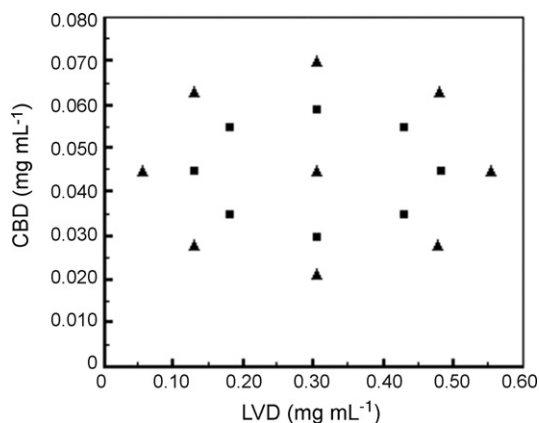

Fig. 1. Calibration (▲) and validation (■) concentrations of LDV and CBD corresponding to proposed experimental design.

2.3.4. Sample preparation

Ten tablets of each commercial pharmaceutical preparation were weighed, finely powered and homogenized, and a suitable amount of the obtained powder was weighed and dissolved in 100 mL of phosphate buffer. Then, it was filtered on-line by passing through a tubular cotton filter in the flow-batch system.

2.3.5. Flow-batch system

A schematic flow diagram of the proposed flow-batch analyser is shown in Fig. 2. Six Cole Parmer three-way solenoid valves were used: five of them (V_{LVD}, V_{CBD}, V_S, V_{BS} and V_{PPO}) to send the flows of LVD, CBD, sample, buffer solution and PPO towards mixing chamber (MC), respectively. The sixth valve ($V_{MC/W}$) was used to select the stream flowing of mixture coming from the MC or water, through the flow-cell. A Pentium 166 MHz microcomputer furnished with a laboratory-made parallel interface card was used to control the peristaltic pump and valves and to perform the acquisition and treatment of data. The software was developed in Labview® 5.1 graphic language. An electronic actuator (EA) increased the power of the microcomputer signal in order to control the valves.

A Minipuls 3 Gilson peristaltic pump, equipped with six pumping channels was used. Six Tygon® tubes of 1.29 mm i.d. were used. A home-made mixing chamber (MC) of 2 mL was constructed in Teflon®. The lines linking the valves V_{LVD}, V_{CBD}, V_S, V_{BS} and V_{PPO} to MC and $V_{MC/W}$ to detector were implemented as short as possible using 0.8 mm i.d. Teflon® tubing.

2.3.6. Flow-batch procedure

One step inherent to flow-batch technique implementation is to obtain the signals that are used to correct the responses for volume changes or the flow-rates of the channels and then performing the calibration and subsequent sample analysis. This step can be easily implemented through the procedure described by Almeida et al. [16]. As the ratio between the flow rates of two channels has varied into a range of 1.00–1.10, it was necessary to apply a correction factor on the timing control of the delivered volumes in some channels.

Before starting the procedure, all solutions in their respective channels were pumped and recycled towards their flasks (Fig. 2).
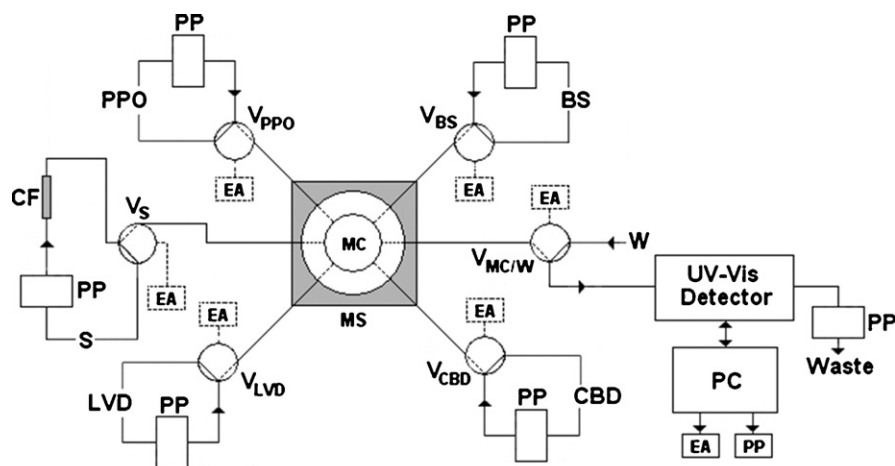
Fig. 2. Diagram of the flow-batch system at initial configuration. BS: buffer solution; CBD; carbidopa; CF: cotton filter; EA: electronic actuator; LVD: levodopa; MC: mixing chamber; MC/W: commutation MC/water; MS: magnetic stirrer; PC: microcomputer; PP: peristaltic pump; PPO: polyphenol oxidase; S: sample; V: solenoid valves; W: water. The arrows and the dotted lines indicate the direction of the fluids and the control lines, respectively.

After, each valve was switched ON during a time interval of 3 s and the solutions were pumped towards MC in order to fill the channels between the V_{LVD}, V_{CBD}, V_S, V_{BS} and V_{PPO} valves and MC. Right after, $V_{MC/W}$ was switched ON and the excess of the solutions into MC was aspirated to waste during 5 s. This operation, denominated "fill channels", consumed a total time interval of 8 s and it was always accomplished when the solution in each channel was changed.

The MC cleaning was carried out by switching ON V_{BS} valve for a time interval enough to assure the total emptying of the MC after finishing the operation. The system was cleaned always between measurements and the stirrer was ON during all the steps. After performing the filling channels and cleaning procedures, the system was ready to carry on the preparation of the standard solutions.

To perform the construction of the calibration or validation sets all the valves were initially switched OFF, so that the LVD, CBD, sample, buffer and PPO were continuously pumped into their channels, returning to their respective recipients. For the acquisition of the baseline, a blank solution was yielded by switching ON the V_{BS} and V_{PPO} valves for suitable times (t_{BS} and t_{PPO}) and afterwards it was aspirated towards the spectrophotometer. The valves V_{LVD}, V_{CBD}, V_S

and V_{BS} were then simultaneously switched ON during previously defined time intervals for each valve (t_{LVD}, t_{CBD}, t_S and t_{BS}) and aliquots of each fluid were pumped towards the MC. Soon after, the V_{PPO} valve was switched ON and the reaction started (time 0 s of the reaction). Then the mixture was homogenised for 12 s and aspirated towards the spectrophotometer, by switching ON $V_{MC/W}$ for 20 s allowing the fulfilling of the flow cell. After that, the flow was stopped switching OFF the $V_{MC/W}$ valve. The delay time was 51.5 s and the stopped flow time was 128.5 s (for more details see Section 3) for each point of the calibration/validation sets and samples. Then, the spectra corresponding to each mixture yielded was recorded for posterior chemometric treatment by using PLS and MLR-SPA models. This procedure was repeated for each standard solution and sample, varying only the t_{LVD}, t_{CBD}, t_S and t_{BS} values.

In the experimental design of the multivariate calibration, the total volume that was added into MC was the same in all points of the calibration/validation sets in order to maintain the constant matrix composition or matrix effect, avoiding inaccurate results [32]. Thus, t_S and t_{PPO} were always the same and, while t_{LVD} and t_{CBD} increased, t_{BS} decreased (and vice versa).

Table 1
System operation schedule

Flow rate (mL min^{-1})	V_{LVD} 2.20	V_{CBD} 2.09	V_S 2.25	V_{BS} 2.18	V_{PPO} 2.30	$V_{MC/W}$ 2.30
Valve switching time intervals (s)						
Filling channels	3	3	3	3	3	5
Wash system						
(a) MC filling	0	0	0	47	0	0
(b) MC empting	0	0	0	0	0	50
Blank	0	0	0	27.5	19.5	0
Calibration	1.3–12.5	3.8–12.6	0	5.7–19.7	19.5	0
Validation	2.9–10.9	5.4–10.6	0	8.2–17.4	19.5	0
Samples	0	0	13.3	13.8	19.5	0
Delay (MC to spectrophotometric cell)	0	0	0	0	0	20

Table 2
Optimum values of chemical variables and flow-batch parameters

	Optimum value
Chemical variables	
Enzymatic activity (UE)	1200
Buffer concentration (mol L^{-1})	0.1
pH	7.0
Flow-batch parameters	
(a) Volume (mL)	
Sample	0.50
Buffer	0.50
Enzyme	0.75
Total volume	1.75
(b) Time (s)	
Delay	51.5
Mixture	12
Stopped-flow	128.5
Total analyses[a]	200

[a] Include times are not described in this table.

In Table 1 is summarized the schedule of procedures and the respective switching ON times of the valves to carry on the complete analysis.

2.3.7. Optimization of the reaction time

In order to obtain the optimum reaction time for the oxidation of LVD and CBD with PPO, a kinetic study was carried out. Thus, 1200 units of PPO reacted in phosphate buffer medium (pH 7) with the mixtures corresponding to the calibration and validation sets. The spectra were registered at each 60 s and during 600 s.

3. Results and discussion

3.1. Enzymatic activity

The crude extract was obtained from different commercial sweet potato roots along 2 months. The mean of enzymatic activity and the standard deviation ($n = 4$) was 4511 ± 287 UE mL^{-1}. When the extract was stored at $-18\,^{\circ}$C, these values did not vary along 1 month. Therefore, the conditions for obtaining crude extract were satisfactory.

3.2. Optimization of chemical variables and flow-batch parameters

In Table 2 are presented the optima values to chemical variables. The enzymatic activity was optimized in order to obtain the optimum spectral values for PLS and MLR-SPA models, so we tested between 1000 and 2000 UE. The selected value was 1200 UE.

In the case of the buffer solution, the working pH was established according to literature results at 7.0 (0.1 mol L^{-1} phosphate buffer) [33].

Optima values for flow-batch parameters are also shown in Table 2. The optimization was performed by using the univariate method and selected as a compromise between sensitivity and reproducibility of the analytical signals. The MC was
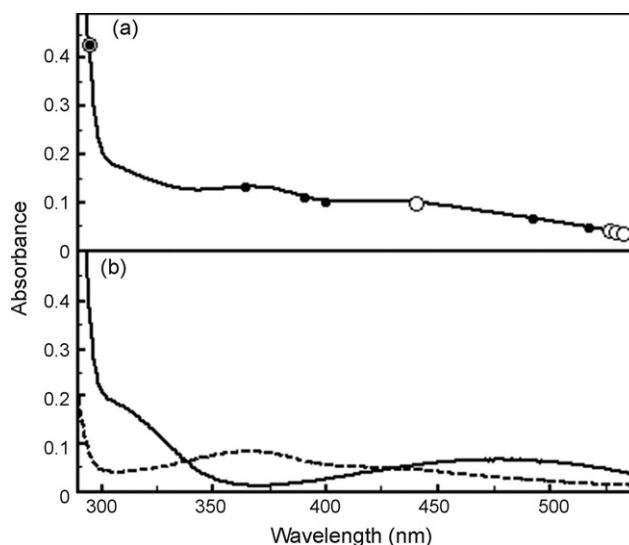

Fig. 3. (a) Spectra of LVD + CBD (0.305 mg mL^{-1} to LVD and 0.045 mg mL^{-1} to CBD). (b) Spectra of LVD (0.305 mg mL^{-1}, solid line) and CBD (0.045 mg mL^{-1}, dashed line). The circles indicate the selected variables by MLR-SPA: (○) corresponding to LVD and (●) corresponding to CBD.

proper enough because a good mixture between the enzyme and the substrate was obtained. Besides, the flow-batch system performed the automatic preparation of the calibration and validation samples, reducing significantly the total time of analyses and the reagents–sample consumption. The sample throughput was 18 h^{-1}.

3.3. Selection of the spectral features

Both compounds are oxidized in the presence of PPO enzyme which produces o-quinones that have a strong absorption in the UV–vis region. In spite of the structural similarity between the analytes, different products are obtained from the enzymatic reaction. In Fig. 3b is shown the spectra of LVD and CBD when they were oxidized by PPO. It can be observed that LVD and CBD present a strong absorption around 480 and 360 nm, respectively. However, the mixtures of the analytes present serious overlapping spectra after the reaction with PPO (Fig. 3a). Therefore, the traditional methods need strictly to use a separation technique before the determination. Besides, the resolution result is more complex, taking into account that CBD is a minor constituent in the commercial pharmaceutical preparations. Nevertheless, there are some spectral differences that can be useful for multivariate calibration methods. To both analytes, the spectral region between 295 and 540 nm was selected as suitable for the analysis. Additionally, the bands of more intense absorption for the respective analytes (450–540 nm to LVD and 340–390 nm to CBD) have also been used. In all cases, the data points were taken every 1 nm.

3.4. Optimization of the time reaction

The absorption of the chromophores increased significantly over the time studied. The criterion to choose the optimum reaction time was based on the lowest RMSEV obtained in the

Table 3
Results obtained from the application of PLS-1, MLR-SPA and univariate model

Analytes	Figures of merit	Models			
		PLS-1		MLR-SPA	Univariate
LVD	Selected variables (nm)	295–540	450–540	295, 441, 527, 530, 533	500
	Number of factors	3	1	–	–
	SEN (mL mg^{-1})	1.370	1.327	0.406	0.106
	LOD (mg mL^{-1})	0.0165	0.0165	0.131	0.218
	Calibration				
	Concentration range (mg mL^{-1})			0.057–0.553	
	RMSE[a] (mg mL^{-1})	0.0047	0.0657	0.0252	0.0565
	Correlation	0.9995	0.9077	0.9876	0.9594
	Validation				
	Concentration range (mg mL^{-1})			0.129–0.481	
	RMSEV (mg mL^{-1})	0.0272	0.0959	0.0095	0.1073
	Correlation	0.9939	0.6779	0.9981	0.6957
	Prediction of real samples				
	RMSEP (mg mL^{-1})	0.0074	0.0681	0.0100	0.0662
CBD	Selected variables (nm)	295–540	340–390	295, 364, 391, 400, 493, 518	360
	Number of factors	2	2	–	–
	SEN (mL mg^{-1})	15.6	3.567	1.566	1.871
	LOD (mg mL^{-1})	0.0014	0.0022	0.040	0.015
	Calibration				
	Concentration range (mg mL^{-1})			0.021–0.070	
	RMSE[a] (mg mL^{-1})	0.0033	0.0041	0.0035	0.0039
	Correlation	0.9774	0.9645	0.9779	0.9801
	Validation				
	Concentration range (mg mL^{-1})			0.030–0.059	
	RMSEV (mg mL^{-1})	0.0030	0.0036	0.0020	0.0046
	Correlation	0.9932	0.9935	0.9916	0.9734
	Prediction of real samples				
	RMSEP (mg mL^{-1})	0.0034	0.0074	0.0038	0.0082

[a] RMSECV for PLS-1 or RMSEC for SPA-MLR and univariate.

prediction of samples of the validation set when PLS and MLR-SPA regression was applied to the spectral data to each time studied.

In conclusion, 180 s seems to be the optimum time for the simultaneous determination of LVD and CBD.

3.5. Interference study

An interference study was done by us and their results were recently published [34]. In this work a solid mixture of microcrystalline cellulose, maize starch, magnesium stearate, and colloidal anhydride silica was prepared in the amounts present in the analysed commercial samples. We demonstrated that the presence of excipients did not interfere in the spectral region (295–540 nm) used for the determination of both analytes.

3.6. Analytical performance

3.6.1. Application of univariate method

A study using univariate calibration was carried out selecting a maximum absorption of 500 nm to LVD and 360 nm to CBD, as was published by Fatibello-Filho et al. [11]. The results of predictions and figures of merit for these models were not satisfactory, as can be seen in Table 3.

3.6.2. Application of PLS and MLR-SPA

Previous to the application of the PLS and MLR-SPA methods, the data set was smoothed by using the moving average algorithm with an overall window size of 3 points. Then, the smoothed data set and their concentrations were mean centred.

3.6.2.1. PLS models.

The PLS models were developed in the PLS-1 mode where the regression was carried out for each independent variable individually.

The calibration model and its performance was evaluated by leaving one out cross-validation, in which each sample was left out once, and its concentration was estimated by a model built with the remaining samples. The number of significant factors has been chosen as the lower number whose mean square error of prediction by cross-validation (MSECV) was not significantly different from the lowest MSECV value.

For an easier comparison and interpretation of the obtained results, the root mean square error (RMSE), which is an estimate of the absolute error of prediction for the calibration (with cross-validation) and validation sets of each analyte, were calculated. To both, the optimum spectral region and number of latent variables for the PLS-1 algorithm, as well as the statistical parameters: root mean square error of cross-validation (RMSECV) and the correlation coefficients are summarized in Table 3. Also, the validation set containing eight lab-made sam-

ples was analysed by the proposed procedure. The statistical validation results are summarized in Table 3. The RMSECV value for cross-validation and RMSEV values for validation set were reasonably low for both LVD and CBD when the spectral region 295–540 nm was used. The region 340–390 nm for CBD supplied correlations to the model, and the RMSECV and RMSEV were identical to those obtained in the region 295–540 nm. However, for LVD the region 450–540 nm presented a model having worse parameters.

Table 3 also gives other important statistical parameters such as the sensitivities (SEN) and detection limits (LOD). SEN for a given analyte k has been defined as

$$SEN_k = \frac{1}{||\mathbf{b}_k||}$$

where $||\cdot||$ indicates the Euclidean norm and $\mathbf{b}_k$ is the vector of final regression coefficients appropriate for component k, which can be obtained by any multivariate method. In another hand, the limit of detection is

$$LOD_k = 3.3||\boldsymbol{\delta r}||||\mathbf{b}_k||$$

In this expression, $||\boldsymbol{\delta r}||$ indicates the instrumental noise.

The LODs and SENs obtained for LVD, when PLS was applied in the two studied regions, 295–540 nm and 450–540 nm, were comparable and satisfactory. However, for CBD the results were better when PLS was applied in the region 295–540 nm (Table 3).

3.6.2.2. MLR-SPA model. MLR-SPA uses a calibration (Xcal) and a validation (Xval) set consisting of instrumental response data and parameter values measured by a reference method (*y*). The essence of SPA consists of projection operations carried out on the calibration matrix. A detailed explanation of the projection operations is given elsewhere [29,30]. Starting from each of the *J* variables (columns of Xcal) available for selection, SPA builds an ordered chain of *K* variables where each element is selected in order to present the least collinearity with the previous ones. The collinearity between variables is assessed by the correlation between the respective column vectors of Xcal. It is worth to point out that, according to this selection criterion, no more than *K* variables can be included in the chain [29,30]. It is possible to extract *K* subsets of variables from each of the J chains constructed by using one up to *K* elements in the order in which they were selected. Thus, a total of $J \times K$ subsets of variables can be formed. In order to choose the most appropriate subset $J \times K$, MLR models are built using the calibration samples set and compared in terms of the root mean square error obtained for the validation samples set.

Table 3 presents selected variables and the figures of merit for models constructed with MLR-SPA. The selected variables are also shown in Fig. 3a. In Fig. 3 it can verify that the selected variables for SPA agree with the regions of higher absorbance for each analyte. Thus, CBD appears to be better predicted if absorptions at 364, 391 and 400 nm are included, while LVD is better predicted if absorptions at 295, 527, 530 and 533 nm are considered. However, some variables outside these regions are important and have also been identified by SPA. For example, the
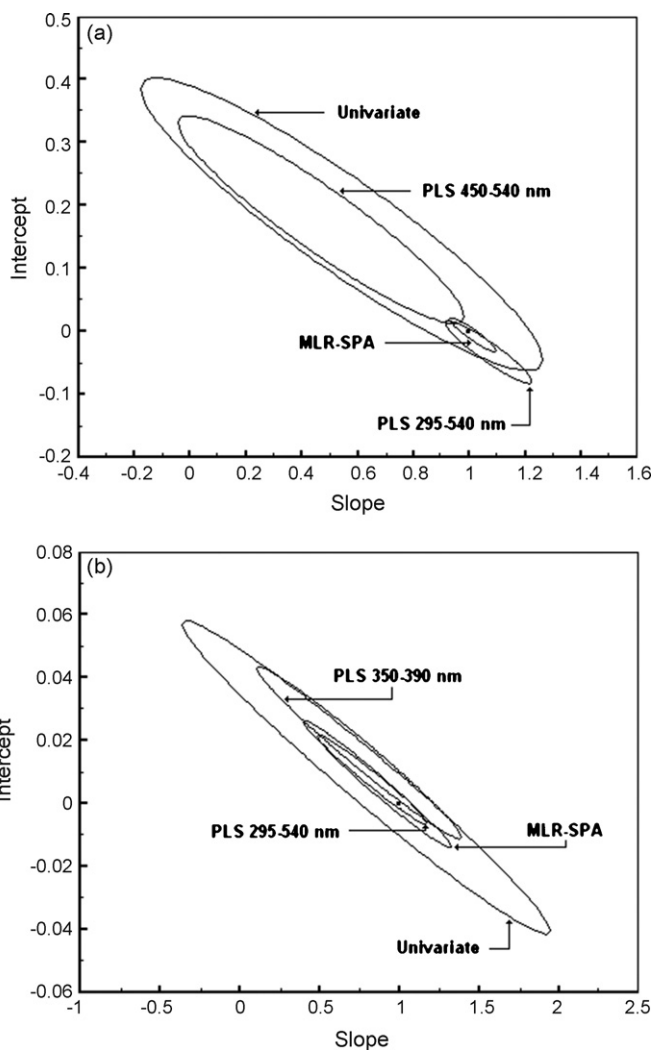

Fig. 4. Elliptical joint confidence regions for the slope (*b*) and intercept (*a*) corresponding to regressions of actual concentrations vs. univariate, PLS and MLR-SPA predicted concentrations for: (a) LVD and (b) CBD. The point marks the theoretical point ($a = 0$, $b = 1$).

absorption of LVD at 295 nm was also selected for CBD model. We believe that this must be the way in which SPA solves the spectral overlapping. The regression coefficient at 295 nm in the CDB model was negative, corroborating this assumption.

The LOD and SEN obtained for LVD and CBD when MLR-SPA was applied are shown in Table 3. The model supplied a higher LOD and a lower SEN than PLS model for both, LVD and CBD.

3.6.2.3. Comparative study of chemometric models. In order to get further insight into the precision ability of both chemometric methods herein analysed, linear regression analysis of actual concentration values versus PLS and MLR-SPA predictions was applied. The estimated intercept and slope (*a* and *b*, respectively) were compared with their ideal values of 0 and 1 using the elliptical joint confidence region (EJCR) test, in this case by using an ordinary least squares fitting (OLS) of the actual versus the simultaneously 12 predicted values for each method (8 of the validation sets more 4 real samples) by each

Table 4
Determination of LVD and CBD in pharmaceutical preparations

	Nominal (mg per tablet)		Pharmacopeia (mg per tablet)			Proposed method (mg per tablet)					
			HPLC		$\lambda = 280$ nm	PLS-1 (295–540 nm)			MLR-SPA		
	LVD	CBD	LVD	CBD	LVD + CBD	LVD	CBD	LVD + CBD	LVD	CBD	LVD + CBD
Sample											
Lebocar® A	250	25	235 (2)	24 (1)	276 (2)	238 (1)	24 (1)	262 (1)	237 (1)	23 (1)	260 (1)
Lebocar® B	100	25	104 (1)	25 (1)	123 (1)	100 (2)	23 (1)	123 (2)	100 (1)	23 (1)	123 (1)
Parkinel® A	250	25	243 (1)	23 (1)	272 (2)	242 (1)	25 (1)	267 (1)	249 (2)	24 (1)	273 (2)
Parkinel® B	100	25	87 (1)	21 (1)	122 (1)	92 (2)	21 (1)	113 (2)	94 (1)	22 (1)	116 (1)
t calculated[a]						0.3	0.3	2.4	1.2	0.9	1.35
t critical[b]							3.18			3.18	
n							4			4	

Significance test (t-test) for comparison between pharmacopeial and proposed methods. The samples were analysed for triplicate. Standard deviations are in parenthesis.

[a] For LVD and CBD: HPLC vs. proposed method and for LVD + CBD: spectrophotometric vs. proposed method.

[b] Tabulated 95% confidence limit.

analyte, as recommended by Martinez et al. [35]. The ellipses that contain the theoretical point ($a = 0$, $b = 1$) are indicative that proportional and constant errors are not present. On the other hand, the size of the joint confidence region for a given level of significance α depends directly on the estimate of the experimental error $\hat{s}^2$. In this way, when few experimental data are available, the values of $\hat{s}^2$ are usually overestimated. This increase in uncertainty is due to the lack of information inherent to a small number of data pairs, or in some cases, to the lack of fit of the experimental data to the OLS regression line. In these cases, the joint confidence region is oversized [35]. Fig. 4(a) and (b) shows the EJCR plots for the four studied chemometric-assisted methods. As can be seen, PLS in the region 295–540 nm and MLR-SPA presents an excellent predictive ability to both LVD and CBD, compared with the other studied chemometrics methods.

3.6.3. Application to real samples

The proposed method was used for the simultaneous determination of LVD and CBD in pharmaceutical preparations. Table 4 shows a comparative study of the obtained results of the following methods: flow-batch method (with spectral data analysed by PLS in the region 295–540 nm and MLR-SPA) and pharmacopeial methods (the spectrophotometric at 280 nm [36] and the HPLC [37]).

It is important to say that, for all analysed samples, the obtained concentrations for both analytes by proposed methods were in close agreement with those obtained by HPLC. On another hand, the obtained concentrations, when PLS and MLR-SPA were applied, were used to calculate the total concentrations (LVD + CBD), in order to compare with the results obtained from the spectrophotometric method.

Results of significance test (test "t") for comparison between proposed methods and pharmacopeial methods are shown in Table 4. Additionally, the root mean square error of prediction (RMSEP) and the correlation coefficients for PLS-1 and MLR-SPA models are present in Table 3.

The repeatability expressed as the relative standard deviation (R.S.D. %) was 1.3% for LVD and 2.1% for CBD when PLS-1 was applied and 3.6% for LVD and 3.7% for CBD when MLR-SPA was applied ($n = 4$).

4. Conclusion

The simultaneous spectrophotometric enzymatic determination of LVD and CBD in pharmaceutical preparations is feasible using absorption spectral data with PLS in the region 295–540 nm and MLR-SPA. Both multivariate calibration models solved successfully the serious spectral overlapping in mixtures with high ratios of LVD/CBD concentrations (10/1; 4/1). A relatively small calibration set, based on the central composite design, was required. MLR-SPA models have been constructed with five wavelengths for LVD and six for CBD and presented results of prediction with performance comparable to PLS models.

The proposed system improved the analytical signal and allowed the automatic preparation of calibrations and validation samples and this was an important advantage. The excipients were retained successfully in the cotton filter and did not interfere in the determination.

Precise and accurate results were obtained based on the estimation of figures of merit. The validation was done on real samples against the official methods of the pharmacopeia.

The proposed flow-batch method is of low cost and fast, it can be useful as a possible alternative method for the quality control analysis of these pharmaceutical preparations.

References

[1] A. Goodman-Hilman, T. Rall, A. Nier, P. Taylor, The Pharmacological Basis of Therapeutics, McGraw-Hill, New York, 1996.

[2] A. Osol, Remington's Pharmaceutical Science, Mach Publishing, Easton, PA, 1975.

[3] H.S. Mason, in: F.F. Nord (Ed.), Advanced in Enzymology, vol. XVI, Interscience, New York, 1955, p. 164.

[4] J. Vachtenheim, J. Duchon, B. Matous, Anal. Biochem. 146 (1985) 405.

[5] I. Behbahani, S.A. Miller, D.H. O'Keefe, Microchem. J. 47 (1993) 251.

[6] K.A. Sagar, M.R. Smyth, J. Pharm. Biomed. Anal. 22 (2000) 613.

[7] A. Tolokán, I. Klebovich, K.K. Balogh-Nemes, G. Horvai, J. Chromatogr. Biomed. Appl. 698 (1997) 201.

[8] S. Husain, R. Sekar, R. Nageswararao, J. Chromatogr. A 687 (1994) 351.

[9] S. Fanali, V. Pucci, C. Sabbioni, M.A. Raggi, Electrophoresis 21 (2000) 2432.

[10] P.C. Damiani, A.C. Moschetti, A.J. Rovetto, F. Benavente, A.C. Olivieri, Anal. Chim. Acta 543 (2005) 192.

[11] O. Fatibello-Filho, I. Da Cruz Vieira, Analyst 122 (1997) 345.

[12] J.A. Sweileh, P.K. Dasgupta, Anal. Chim. Acta 214 (1988) 107.

[13] J.A. Sweileh, J.L. Lopez, P.K. Dasgupta, Rev. Sci. Instrum. 59 (1988) 2609.

[14] R.S. Honorato, M.C.U. Araujo, R.A.C. Lima, E.A.G. Zagatto, R.A.S. Lapa, J.L.F. Costa Lima, Anal. Chim. Acta 396 (1999) 91.

[15] R.S. Honorato, M.C.U. Araujo, R.A.C. Lima, E.A.G. Zagatto, Anal. Chim. Acta 416 (2000) 231.

[16] L.F. Almeida, V.L. Martins, E.C. Silva, P.N.T. Moreira, M.C.U. Araujo, Anal. Chim. Acta 486 (2003) 143.

[17] L.F. Almeida, V.L. Martins, E.C. Silva, P.N.T. Moreira, M.C.U. Araujo, J. Braz. Chem. Soc. 14 (2003) 249.

[18] J.E. da Silva, F.A. da Silva, M.F. Pimentel, R.S. Honorato, V.L. da Silva, B.S.M. Montenegro, A.N. Araújo, Talanta 70 (2006) 522.

[19] R.A.C. Lima, S.R.B. Santos, R.S. Costa, G.P.S. Marcone, R.S. Honorato, V.B. Nascimento, M.C.U. Araujo, Anal. Chim. Acta 518 (2004) 25.

[20] E.P. Medeiros, E.C.L. Nascimento, A.C.D. Medeiros, J.G.V. Neto, E.C. da Silva, M.C.U. Araujo, Anal. Chim. Acta 511 (2004) 113.

[21] R.S. Honorato, J.M.T. Carneiro, E.A.G. Zagatto, Anal. Chim. Acta 441 (2001) 309.

[22] J.M.T. Carneiro, A.C.B. Dias, R.S. Honorato, E.A.G. Zagatto, Anal. Chim. Acta 455 (2002) 327.

[23] R.S. Honorato, M.T. Carneiro, E.A.G. Zagatto, J. Anal. Chem. 368 (2000) 496.

[24] B.F. Reis, M.F. Giné, E.A.G. Zagatto, J.L.F.C. Lima, R.A. Lapa, Anal. Chim. Acta 293 (1994) 129.

[25] P.C.A. Jerônimo, A.N. Araujo, M. Montenegro, C. Pasquini, I.M. Raimundo, Anal. Bioanal. Chem. 380 (2004) 108.

[26] C.H. Spiegelman, M.J. Mc Shane, M.J. Goetz, M. Motamedi, Q.L. Yue, G.L. Coté, Anal. Chem. 70 (1998) 35.

[27] H.C. Goicoechea, A.C. Olivieri, J. Chemom. 17 (2003) 338.

[28] R. Leardi, M.B. Seasholtz, R.J. Pell, Anal. Chim. Acta 461 (2002) 189.

[29] R.K.H. Galvão, M.F. Pimentel, M.C.U. Araújo, T. Yoneyama, V. Visani, Anal. Chim. Acta 443 (2001) 107.

[30] M.C.U. Araújo, T.C.B. Saldanha, R.K.H. Galvão, T. Yoneyama, H.C. Chame, V. Visani, Chemom. Intell. Lab. Syst. 57 (2001) 65.

[31] E.J. Lourenço, J.S. Leão, V.A. Neves, J. Sci. Food Agric. 52 (1990) 249.

[32] J.H. Kalivas, Talanta 34 (1987) 899.

[33] I. da Cruz Vieira, O. Fatibello-Filho, Anal. Chim. Acta 366 (1998) 111.

[34] M. Grünhut, M.E. Centurión, B.S. Fernández Band, Anal. Lett. 40 (2007) 2016.

[35] A. Martinez, J. Riu, O. Busto, J. Guasch, F.X. Rius, Anal. Chim. Acta 406 (2000) 257.

[36] United States Pharmacopeia National Formulary XXI, US Pharmacopeia Convention, Rockville, MD, 1985.

[37] British Pharmacopeia, The Stationery Office Ltd., Norwich, 1998.

Enhanced spectrofluorimetric determination of aflatoxin B1 in wheat by second-order standard addition method

Javad Hashemi [a], Gholamreza Asadi Kram [b], Naader Alizadeh [a,*]

[a] *Department of Chemistry, Faculty of Science, Tarbiat Modares University, P.O. Box 14115-175, Tehran, Iran*
[b] *Department of Biochemistry, Rafsanjan Faculty of Medicine, Rafsanjan, Iran*

Abstract

Determination of aflatoxin B1 (AFB1) in wheat has been accomplished by enhanced spectrofluorimetry in combination with second-order standard addition method (EF-SOSAM). The adopted strategy combined the use of parallel factor analysis (PARAFAC) for extraction of the pure analyte signal and the standard addition method, for a determination in the presence of matrix effect caused by wheat matrix. The method is based on the enhanced fluorescence of AFB1 by β-cyclodextrin in 10% (w/w) methanol–water solution. After sample treatment and without any extended cleanup steps and derivatization process, four standard additions were performed for each sample. A specific PARAFAC model was built from three-way arrays formed by excitation–emission spectra and 5 measurements (sample plus 4 additions). The scores related to AFB1 were used for a linear regression in the standard addition method. Two naturally contaminated wheat and spiked wheat samples containing AFB1 in the range 0–18 $\mu g\,kg^{-1}$ were analyzed by EF-SOSAM and compared with HPLC results. EF-SOSAM analysis of spiked wheat samples gave a good correlation with spiked values ($R^2 > 0.990$). The limit of detection of method was 0.9 $\mu g\,kg^{-1}$ for the determination of AFB1 in wheat samples.
© 2008 Elsevier B.V. All rights reserved.

Keywords: Aflatoxin B1; Wheat; β-Cyclodextrin; Enhanced spectrofluorimetry; Second order advantage; Parallel factor analysis

1. Introduction

Aflatoxins produced by *Aspergillus flavus* molds were first detected in the late 1960s [1–3]. Different forms of aflatoxin, including B1 (Scheme 1), B2, G1, and G2, are found in many forms of human foods, cereals, grains, and peanut products and are known for their toxicity and carcinogenicity [3–6]. Various studies suggested a link of aflatoxin exposure with an increased occurrence of liver and lung cancer [7]. Some recent studies, however, submit that the aflatoxins may not be the cause for these cancers in humans [8,9]. Aflatoxin B1 (AFB1), the most toxic compound in this series, has been found to be one of the most potent carcinogens occurring naturally and it was classified as Group I human carcinogen by the International Agency for Research on Cancer (IARC) in 1987. The occurrence of aflatoxins in food has been recognized as potential threat to human health, either caused by direct contamination via grains and grain products or by "carry over" of mycotoxins and their metabolites in animal tissues, milk and meat after intake of contaminated feedstuffs. There exist a great number of reports that suggest intoxication of humans by the consumption of aflatoxins contaminated agricultural products. Epidemiological studies have shown that aflatoxins exposure is associated with increased risk of hepatocellular carcinoma, particularly in combination with hepatitis B virus. The potency of aflatoxins appears to be significantly enhanced in individuals with hepatitis B infection. Additionally, the food contamination by aflatoxins causes serious economic losses. Due to their frequent occurrence and their severe toxicity, guidelines and tolerance levels of aflatoxins have been set in several countries. Wheat is susceptible to these fungi infections through its growth, harvest, transport and storage [10]. Iran has set a maximum residue limit of 5 $\mu g\,kg^{-1}$ for AFB1 in wheat for imports [11].

Various methods for the determination of aflatoxins in grains include TLC [12], fluorescence polarization assay [13], HPLC [14,15], radioimmunoassay (RIA) [16] ELISA [17], and fiber-optic based immunoassays [18]. Whereas chromatographic methods require extended cleanup steps and derivatization after

---

* Corresponding author. Fax: +98 21 8006544.
  E-mail address: alizaden@modares.ac.ir (N. Alizadeh).
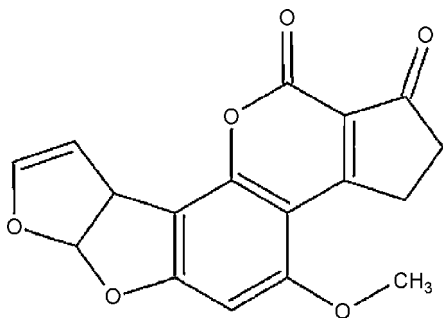
Scheme 1. Structure of the AFB1.

extraction in order to get rid of interfering substances, commercially available ELISAs require enzymatic reactions and washing and separation of bound and free label.

The use of spectrofluorimetry analysis in natural sample such as blood, urine, foods, cereals, grains, and peanut products is made difficult by the complexity of matrices which show a great variety of natural fluorescent compounds whose spectra often overlap the analyte signal. This situation demands tedious separation steps to enable the analyte determination [19]. Fluorescence spectrum of AFB1 shows an emission maximum at 433 nm and an excitation maximum at 362 nm [1].

Recently we demonstrated that the inclusion within cyclodextrins yields a significant enhancement to the molecular fluorescence of AFB1 [20]. In present work, β-cyclodextrin was used as a fluorescence enhancer for increasing the sensitivity of method.

Recently we reported determination of AFB1 in pistachio by normal and synchronous spectrofluorimetry in combination with some multivariate calibration methods and derivative techniques [1].

In some multivariate calibration models addition of new constituent(s) is not allowed during analysis. If there is any new constituent, recalibration will be necessary [21]. In case of multi-way data, it is possible to handle unknown interferences as part of the calibration. Several methods have been developed involving both generalized rank annihilation methods [22] and PARAFAC [23].

PARAFAC is a generalization of PCA to higher order data, which presents unique solution independent of rotation (uniqueness), a great advantage for modeling spectroscopic data [19,23]. In particular, the mathematical model of PARAFAC is coherent with the nature of fluorescence data. When the fluorescence of a sample is measured at several emission wavelengths for several excitation wavelengths, an excitation–emission matrix (EEM) is obtained. Also a sample set is measured at similar conditions, a three-way array is obtained, which must show a *tri-linear* behavior. This is in spite of the presence of noise, scatter (Rayleigh and Raman) and other phenomena such as *n*-order diffraction [19]. This behavior turns chemometric three-way methods, such as PARAFAC [24] and multi-way partial least square (N-PLS) [25] suitable for fluorescence data analysis. The structural basis of PARAFAC can be given by the following equation:

$$x_{ijk} = \sum_{f=1}^{F} a_{jf} c_{if} b_{kf} + e_{ijk} \tag{1}$$

where x_{ijk} represent the fluorescence intensity measured for the ith sample at the excitation wavelength j and emission wavelength k; a_{jf} and c_{if} are the molar absorption coefficient at the excitation wavelength j and the concentration of the fth fluorophore in the sample i, respectively; b_{kf} is the relative emission coefficient of the fth fluorophore at the wavelength k; and finally e_{ijk} represents the residues of the model. A crucial step in the PARAFAC analysis is the choice of the appropriate number of the factors for which no absolute criterion is introduced. This choice can be made based on the variance accounted for the model, the chemical knowledge of the system, split-half methods [26] or the recently proposed core consistency diagnostic (CORCONDIA) [27]. Due to the easiness of generating *tri-linear* data, molecular fluorescence has probably been the subject of a major number of PARAFAC applications found in the literature [28–30].

Chemical analysis can be further complicated by matrix effects [21]. The sensitivity of the response depends on the matrix composition and quantitative predictions based on pure standards may be affected by differences in the sensitivity of the response of the analyte both in the presence and absence of chemical matrix. The standard addition method can be used to compensate for such matrix effects. The standard addition method is well known among analytical chemists and its description can be found in many standard books [31,32]. This method is applied to univariate data as a means of overcoming matrix effects that change the analyte signal. This method imposes two constraints on the instrumental response, namely:

(1) It should have a linear dependence on the increase of the analyte concentration.
(2) It should be zero when the analyte concentration is zero.

In 1979, Saxberg and Kowalski published an extension of standard addition method to multivariate data, named generalized standard addition method (GSAM) [33]. GSAM requires that the analyte and the interferences be sequentially added in the sample. This relaxes the constraint that the analytical method must be fully selective to the analyte of interest. However, reliable results cannot be obtained if an uncalibrated source of instrumental signal is present. Therefore, in the absence of every species included in the calibration model, the instrumental response must be zero in all channels. In 1995, Booksh et al. published another extension of standard addition method, in this case for multi-way data named second-order standard addition method (SOSAM) [34]. SOSAM can be summarized in three steps:

(1) Tri-linear decomposition is applied for decomposition of a third-order data array. The correct number of factors used

Table 1
Comparison of AFB1 analyses of naturally contaminated and spiked wheat samples using EF-SOSAM and HPLC

Wheat sample no.	HPLC (μg kg^{-1})[a]	Added (μg kg^{-1})	Standard addition values (μg kg^{-1})	Found by present method (μg kg^{-1})[b]	Recovery (%)
1	0.7 ± 0.1	0.0	1.0, 2.0, 2.9, 3.8	Below the LOD	–
2	0.7 ± 0.1	5.4	2.0, 3.8, 5.7, 7.4	5.4 ± 0.2	89
3	0.7 ± 0.1	18.0	1.9, 3.7, 5.4, 7.1	17.3 ± 0.1	93
4	0.1 ± 0.1	0.0	2.0, 3.8, 5.7, 7.4	1.3 ± 0.3	–
5	0.1 ± 0.1	10.6	2.0, 3.8, 5.7, 7.4	9.7 ± 0.3	91

[a] HPLC analysis by AOAC standard method [37].
[b] Standard deviation of three replications.

in the decomposition should correspond to the number of analytes plus the interferences.

(2) The loading matrix of the mode corresponding to the sample composition should contain, in their columns, the information related to analyte and interference concentrations.

(3) The values of the identified column, corresponding to the analyte concentrations in the sample and after each addition, are used in a linear regression, in the same way as in univariate standard addition.
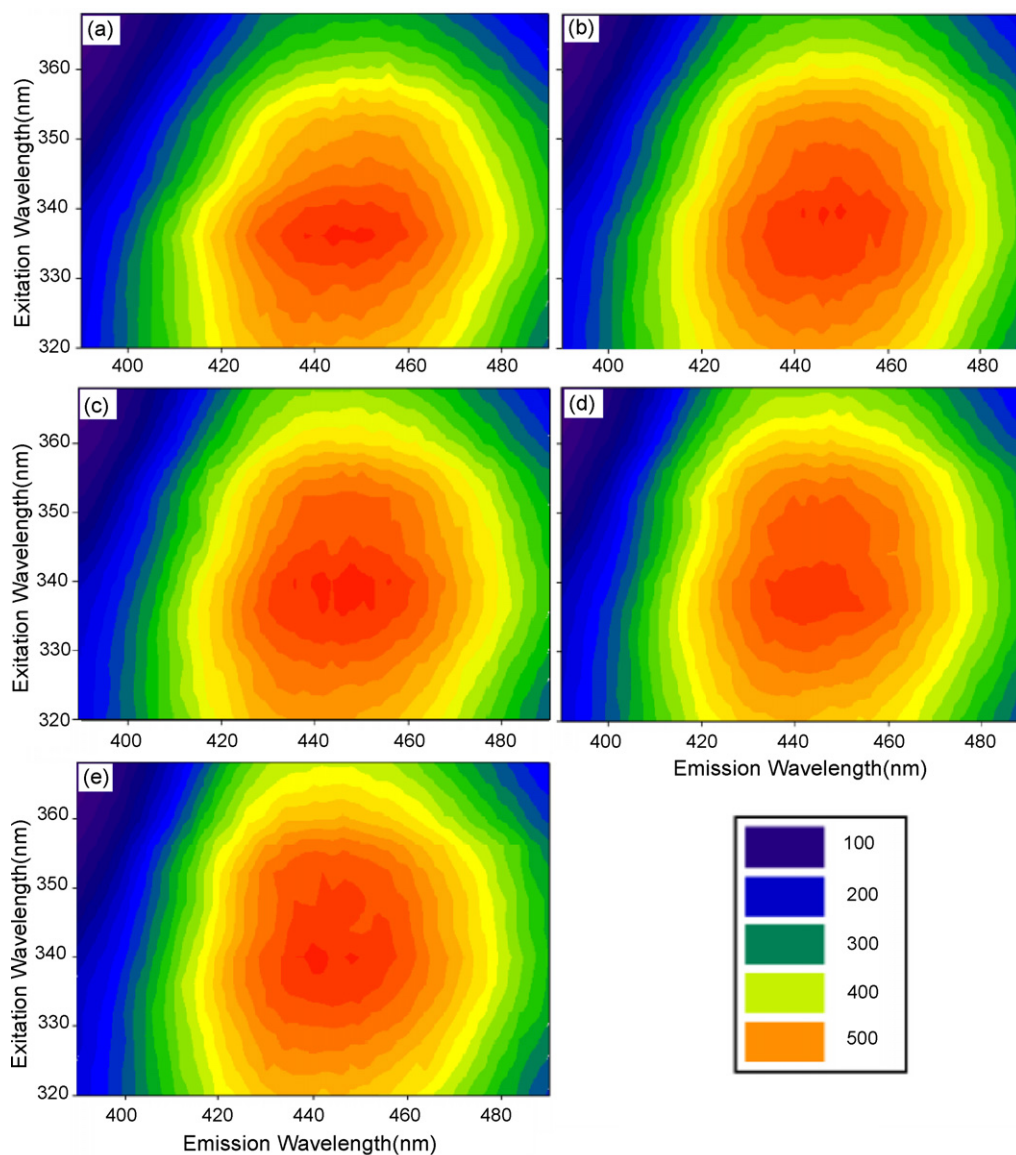

Fig. 1. Contour plots (excitation–emission) for an original wheat sample (no. 5, Table 1) and four AFB1 standard additions; (a) the original sample, (b) plus 2.0 μg kg^{-1}, (c) plus 3.8 μg kg^{-1}, (d) plus 5.7 μg kg^{-1}, (e) plus 7.4 μg kg^{-1}.

Table 2
Interference effect of AFG1 on AFB1 determination in wheat samples

AFB1 concentration ($\mu g \, kg^{-1}$)	Added AFG1 ($\mu g \, kg^{-1}$)	AFB1 score	Change in score (%)	Prediction error ($\mu g \, kg^{-1}$)
1.0	0.0	0.1184	−11.60	−0.1
1.0	2.5	0.1047		
2.0	0.0	0.1911	−5.93	−0.1
2.0	2.5	0.1798		
2.9	0.0	0.2713	+5.51	+0.2
2.9	2.5	0.2863		
4.6	0.0	0.4826	−2.52	−0.1
4.6	2.5	0.4704		

In this work we developed a simple, fast, and sensitive method for determination of AFB1 in complex matrix of wheat samples by using fluorescence data (EEM) in combination with SOSAM. The proposed method does not require immunoaffinity column, extended cleanup steps and derivatization process.

2. Experimental

2.1. Reagents and samples

All the reagents used were of analytical grade. The purity of the organic solvent (methanol and chloroform), from Merck, was checked via fluorescence prior to use. Aflatoxins, B1, G1, and β-cyclodextrin were purchased from Sigma. Double-distilled water was used throughout. Stock standard solution of AFB1 was prepared by dissolving 5 mg in 50 mL of methanol. Other AFB1 solutions were prepared by diluting the stock solution in methanol. The concentration of AFB1 solution was established by following an AOAC official method 971.22 [35]. UV spectrum of the solution was scanned from 200 to 500 nm against methanol as a reference solvent, and the concentration was calculated using molecular absorptivity (ε) of 21,500 at wavelength of maximum absorption, $\lambda_{max} = 360$ nm. Each solution was protected from light by aluminum foil and kept at 4 °C.

Two wheat flour samples that were harvested in the summer of 2006 were purchased from markets of Isfahan province (Isfahan, Iran).

Since AFB1 is toxic and carcinogenic, all used laboratory ware were soaked in a 10% solution of household bleacher for 30 min before disposal. A fume hood was used; gloves, protective clothing, and eyewear were worn.

2.2. Apparatus and software

The fluorescence spectra were recorded by a Varian Eclipse spectrofluorimeter equipped with a thermostated cell compartment. The excitation and emission slits were both maintained at 10 nm. The scan rate of the monochromators was maintained at 1200 nm/min for the acquisition of three-dimensional excitation–emission spectra. All measurements were performed in a 400 μL, 10 mm quartz cells at 27 ± 0.1 °C. Absorption spectra were obtained using a Sinco (model UVS-2100) UV–visible

spectrophotometer. HPLC analysis were carried out on a Waters 1525 chromatographic system by Food Control Laboratory of Medicine Kerman University, Iran, with the following conditions: mobile phase, combine 600 mL of water with 300 mL of methanol and 200 mL of acetonitrile, add 0.12 g of potassium bromide and 350 μL of nitric acid (4 M), sonicate for at least 10 min or filter through glass fiber filter to remove air bubbles; column was a stainless steel Nova-Pak column (25 cm × 4.6 mm i.d.) of octadecylsilane C18 (4 μm); flow rate, 0.8 mL/min; fluorescence detector (Waters 2475), emission at 440 nm, excitation at 360 nm; samples were run in triplicate.

The data were treated in MATLAB Version 7.1. The PARAFAC calculations were carried out with the N-way toolbox for MATLAB Version 2.14 (Rasmus Bro & Claus Andersson, Copenhagen University, DK-1958 Frederiksberg, Denmark, www.models.kvl.dk/source/nwaytoolbox).

2.3. Procedure

2.3.1. Sample treatment

In order to prepare each wheat sample, amount of 5 g wheat flour was placed in a 50 mL falcon centrifuge tube, and 0.50 g ammonium acetate was added. Then samples were extracted two times with 10 mL of 80% (w/w) methanol/water. Extraction time was 60 min and the mixture was shaked in each step. Extracts were centrifuged at 2500 rpm for 2 min, immediately after each extraction step. The extract was filtered through folded filter paper. Obtained solution was transferred into a separation funnel. Then 30 mL distilled water and 5 g NaCl was added to the solution and it was extracted twice with 5 mL chloroform. The chloroform phase was evaporated to dryness under a flow of nitrogen at room temperature. The dry residues were dissolved in 0.50 g methanol and followed by addition of 4.50 g water and 0.5 g NaCl. The obtained colloidal solution was centrifuged at 4000 rpm for 2 min. Then 0.0227 g β-cyclodextrin was added to 2.0 mL of obtained clear solution. The final solution was used as a sample for taking fluorescence spectra. The standards and samples were protected from direct light during all procedures.

2.3.2. Optimization of chemical variables and method parameters

Chemical variables were studied to obtain the best measurement conditions and maximum fluorescence sensitivity for AFB1. The influence of pH on the fluorescence intensity of AFB1 in the presence of β-cyclodextrin was also studied, changing the pH by adding HCl and NaOH. The fluorescence intensity of AFB1 is nearly constant at pH values between 3 and 10 and because of this we did not use any buffer for controlling the pH of medium.

The AFB1 is sparingly soluble in water, so it is necessary to use methanol for increasing its solubility. In this way the effect of methanol content in the medium was investigated by preparing samples of AFB1 and cyclodextrin, while varying the methanol percentage between 1 and 20% (v/v). The fluorescence intensity due to AFB1 decreases when the methanol percentage in the medium increases. Because of this reason, it is necessary to use
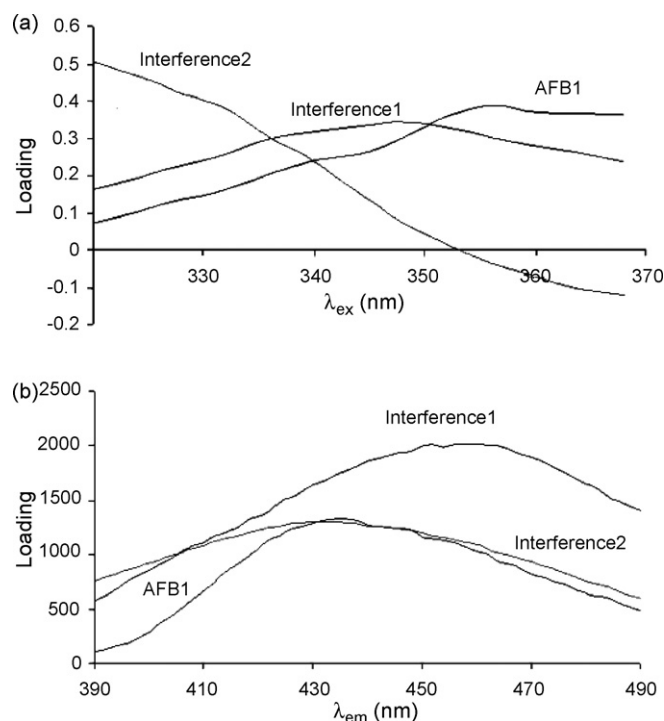
Fig. 2. The PARAFAC loadings related to excitation (a) and emission (b) modes.

a minimum methanol content for dissolving AFB1 in concentration lesser than $20 \, \mu g \, kg^{-1}$, so 10% (w/w) methanol–water solvent was used in this work. In the above-mentioned chemical conditions, in order to avoid the presence of Rayleigh scattering, the EEMs were then recorded in restricted excitation and emission wavelength ranges. All the fluorescence spectra were obtained in the excitation range from 320 to 368 nm (step 4 nm) and in the emission range from 390 to 490 nm (step 2 nm). In these intervals, maximum spectral information was obtained and the prediction error is lowest.

2.3.3. Second-order standard addition method

In order to perform second-order standard addition method, $400 \, \mu L$ of each sample was transferred to a $(400 \, \mu L, 10 \, mm)$ quartz cell and then an excitation–emission spectrum was recorded for it. After this, in four steps different amounts of AFB1 were added to sample and after each addition an excitation–emission spectrum was recorded, so that finally five excitation–emission spectra for each sample were available.

3. Results and discussion

Fig. 1 shows the contour plots of EEM for an original wheat sample (no. 5, Table 1) plus four standard additions. The fluorescence contour plots of EEM demonstrate that the addition of AFB1 concentration increases the fluorescence signal in the region of maximum signal for AFB1 ($\lambda_{ex} \approx 360$ nm and $\lambda_{em} \approx 430$ nm). Furthermore, the red circles with high signal are trending toward given region.

The PARAFAC models were constructed from three-way arrays assembled with 5 measurements, 51 emission wavelengths in the range of 390–490 nm (step 2 nm) and 13 excitation
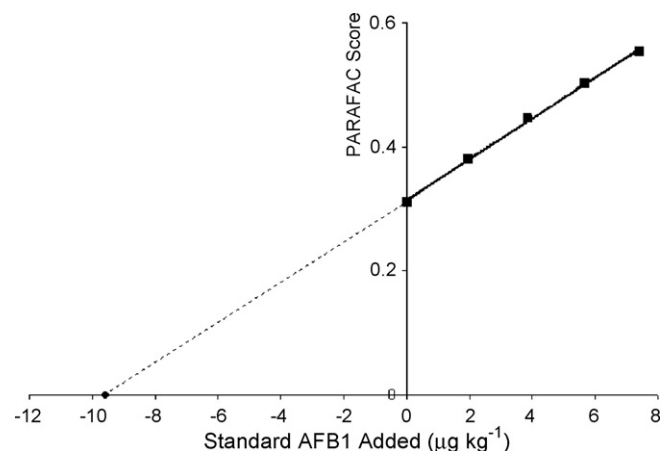

Fig. 3. Standard addition graph (scores vs. AFB1 concentration) for sample no. 5, Table 1.

wavelengths in the range of 320–368 nm (step 4 nm). In all cases, three factors and no constraints were used and the models accounted for more than 99.90% of the total data variance. It was verified that models without constraints provided results with lower errors than models under non-negativity constraints. The *tri-linear* consistency of each model was evaluated by CORCONDIA [27]. Modeling of the standard addition data sets with two-component models resulted in high values for CORCONDIA test (100%) but low model fit. When a three-component model was tried, a relatively good model fit (99.8%) was found with a lower value for the CORCONDIA test (61–83%) and provided prediction errors significantly lower than the models built with two factors. Attending to the appreciate increase in the model fit from the two to three-component models, and lower prediction errors of three-component models, three-component models seem more adequate to predict AFB1 concentration.

The PARAFAC loadings related to excitation and emission modes are shown in Fig. 2a and b, respectively. As can be seen in Fig. 2a the maximum loading relative to excitation mode for AFB1 is about 357 nm that shows a blue shift relative to standard AFB1 solution. The presence of this spectral shift and a non-zero response when the analyte concentration is zero, makes SOSAM a good selection for AFB1 determination in wheat matrix.

The loadings related to sample mode (scores) were used for calibration through a linear regression ($R^2 > 0.990$ and S.D. < 0.3 over the range of 0–18 $\mu g \, kg^{-1}$ of AFB1). A sample of standard addition graph (scores vs. AFB1 concentration) is shown in Fig. 3. These loadings are equivalent to the filtered signal free of interferences. The determinations were carried out in a situation of variable total volume with continuous variation of standard and the consequent analyte dilution was taken into account [36].

AFB1 was analyzed in two naturally contaminated wheat samples and three spiked wheat samples by mentioned EF-SOSAM. The spiked wheat samples were prepared from sample nos. 1 and 4 (Table 1) before other sample treatments (mentioned in Section 2.3.1), therefore these samples were similar to naturally contaminated samples. Each determination was repeated three times for all wheat samples (spiked and non-spiked sam-
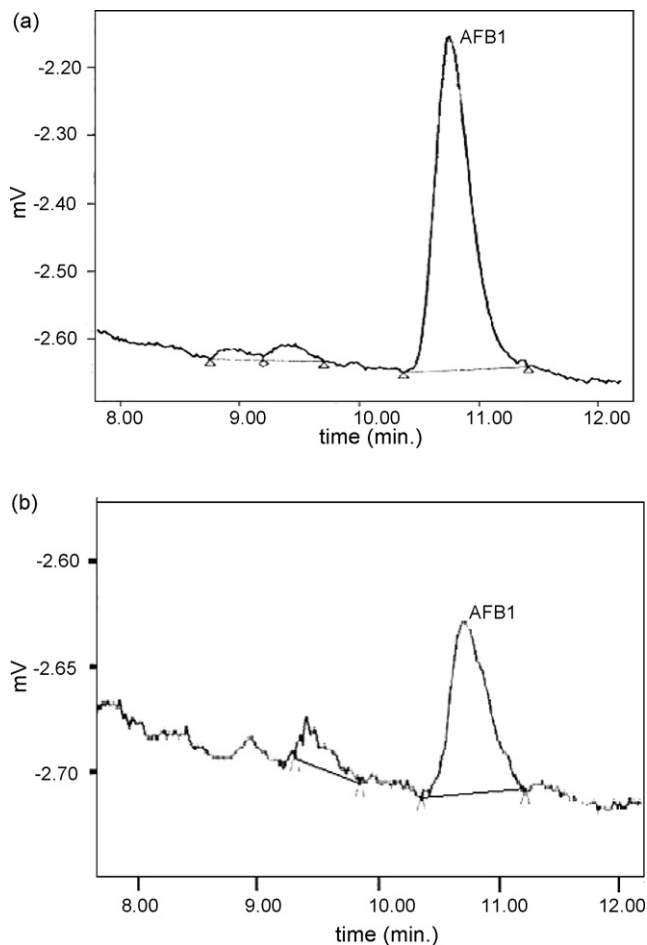
Fig. 4. HPLC chromatograms for analysis of AFB1 in two naturally contaminated wheat samples, (a) sample no. 1 and (b) sample no. 4 of Table 1.

ples) and sample preparation steps were done separately for each repetition. The results of two naturally contaminated wheat samples were compared with HPLC method [37] and results are shown in Table 1 together with the results obtained from EF-SOSAM. The chromatograms of two naturally contaminated wheat samples with fluorimetric detection are shown in Fig. 4. The correlation coefficients (R^2) of the standard addition lines were more than 0.990. The worst result in Table 1 was obtained for a sample with low AFB1 content (sample no. 4) showing a positive absolute error of prediction. The AFB1 content of mentioned sample is lower than LOD of the method (see below paragraph) and in this concentration level, the AFB1 signal is completely superimposed by the signal of the matrix background. According to negative errors for most samples, these can be ascribed to the efficiency of about 90% for sample treatment step. Taking the above discussion in account, the recoveries of add-found tests will increase to about 100% and the errors will decrease to maximum 2.5%.

The limit of detection (LOD) can be estimated according to Eq. (2).

$$LOD = 3\sigma(0) \tag{2}$$

The term $\sigma(0)$ is the standard deviation in the concentration estimated for three blank samples free of AFB1. The calculated LOD of AFB1 for this method was $0.9\,\mu g\,kg^{-1}$.

The occurrence of aflatoxin G1 (AFG1) in wheat has been recognized as most occurring after AFB1 in wheat samples [10]. Therefore the interference effect of AFG1 on determination of AFB1 in wheat samples was investigated by addition of different amounts of AFG1 to wheat samples (with known amounts of AFB1) and monitoring changes in values of AFB1 scores (Table 2). The prediction errors were obtained lower than $0.2\,\mu g\,kg^{-1}$, therefore AFG1 does not act as a serious interference in AFB1 determination.

4. Conclusion

This work demonstrated that the combination of enhanced fluorescence excitation/emission measurements with PARAFAC and standard addition method turned possible the determination of AFB1 in a complex matrix such as wheat. The values obtained (average of three replicates) by the proposed method (Table 1) are statistically comparable to that obtained with the HPLC method. These results suggest that the presence of the AFG1 in wheat cause no serious interference when applying the proposed method (Table 2). The LOD of method was low enough ($0.9\,\mu g\,kg^{-1}$) to control the AFB1 level in wheat samples. The proposed method is, a simple, fast, inexpensive (not require immunoaffinity column, extended cleanup steps and derivatization process) and sensitive method for determination of AFB1 in complex matrix of wheat samples by using fluorescence data (EEM) in combination with SOSAM. This application was only a limited example for the potent chemometric strategy in the food analysis fields. Other applications on this field and other fields, such as biochemical, environmental and agronomical analysis can also be imagined.

References

[1] M. Aghamohammadi, J. Hashemi, G.A. Kram, N. Alizadeh, Anal. Chim. Acta 582 (2007) 288.
[2] P.M. Newbern, W.H. Butler, Cancer Res. 29 (1969) 236.
[3] T. Asao, G. Buchi, M.M. Abdel-kader, S.B. Chang, E.L. Wick, G.N. Wogan, J. Am. Chem. Soc. 87 (1965) 882.
[4] P. Sizaret, C. Malaveille, R. Montesano, C. Frayssinet, J. Natl. Cancer Inst. 69 (1982) 1375.
[5] J.J. Langone, H.V. Vunakis, J. Natl. Cancer Inst. 56 (1976) 591.
[6] T.C. Campbell, L. Stoloff, J. Agric. Food Chem. 22 (1974) 1006.
[7] O.C. Georggiett, J.C. Muino, H. Montrull, N. Brizuela, S. Avalos, R.M. Gomez, ReV. Fac. Cien. Med. UniV. Nac. Cordoba 57 (2000) 95.
[8] L. Stoloff, Regul. Toxicol. Pharmacol. 10 (1989) 272.
[9] S.H. Henry, F.X. Bosch, T.C. Troxell, P.M. Bolger, Science 286 (1999) 2453.

[10] B. Giray, G. Girgin, A.B. Engin, S. Aydın, G. Sahin, Food Control 18 (2007) 23.
[11] G. McMullen, Australian Postharvest Technical Conference, 1998, p. 61.
[12] J. Stroka, E. Anklam, J. Chromatogr. A 904 (2000) 263.
[13] M.S. Nasir, M.E. Jolley, J. Agric. Food Chem. 50 (2002) 3116.
[14] E. Papp, K. Otta, G. Záray, E. Mincsovics, Microchem. J. 73 (2002) 39.
[15] W. Shim, Z. Yang, J.S. Kim, J.Y. Kim, S. Kang, W. Gun-Jo, Y. Chung, S. Eremin, D. Chung, J. Microbiol. Biotech. 17 (2007) 1629.
[16] A. Korde, U. Pandey, S. Banerjee, H.D. Sarma, S. Hajare, M. Venkatesh, A.K. Sharma, M.R.A. Pillai, J. Agric. Food Chem. 51 (2003) 843.
[17] A.Y. Kolosova, W. Shim, Z. Yang, S.A. Eremin, D. Chung, Anal. Bioanal. Chem. 384 (2006) 286.
[18] C.M. Maragos, V.S. Thompson, Nat. Toxins 7 (1999) 371.
[19] M.M. Sena, M.G. Trevisan, R.J. Poppi, Talanta 68 (2006) 1707.
[20] M. Aghamohammadi, N. Alizadeh, J. Lumin. 127 (2007) 575.
[21] M. Bahram, R. Bro, Anal. Chim. Acta 584 (2007) 397.
[22] E. Sanchez, B.R. Kowalski, Anal. Chem. 58 (1986) 496.
[23] R. Bro, Multi-way Analysis in the Food Industry, Ph.D. Thesis, University van Amsterdam, 1998.
[24] R. Bro, Chemometr. Intell. Lab. 38 (1997) 149.
[25] R. Bro, J. Chemometr. 10 (1996) 47.
[26] M.M. Reis, D.N. Biloti, M.M.C. Ferreira, F.B.T. Pessine, G.M. Teixeira, Appl. Spectrosc. 55 (2001) 847.
[27] R. Bro, H.A.L. Kiers, J. Chemometr. 17 (2003) 274.
[28] L.C. Silva, M.G. Trevisan, R.J. Poppi, M.M. Sena, Anal. Chim. Acta 595 (2007) 282.
[29] A.M. de la Pena, N.M. Dıez, D.B. Gil, A.C. Olivieri, G.M. Escandar, Anal. Chim. Acta 569 (2006) 250.
[30] J.A. Arancibia, G.M. Escandar, Talanta 60 (2003) 1113–1121.
[31] D.A. Skoog, D.M. West, F.J. Holler, Fundamentals of Analytical Chemistry, seventh ed., Saunders College Publishing, Orlando, 1997.
[32] D.C. Harris, Quantitative Chemical Analysis, fifth ed., WH Freeman and Company, New York, 1999.
[33] B.E.H. Saxberg, B.R. Kowalski, Anal. Chem. 51 (1979) 1031.
[34] K. Booksh, J.M. Henshaw, L.W. Burgess, B.R. Kowalski, J. Chemometr. 9 (1995) 263.
[35] Official Method of Analysis of AOAC International, Official Method 971. 22, 17th ed., AOAC Int., Gaithersburg, MD, 2002.
[36] M. Bader, J. Chem. Educ. 57 (1980) 703.
[37] Official Methods of Analysis of AOAC International, 17th ed., vol. 2, Gaithersburg, 2000, p. 35.

Partial least-squares analysis of time decay data for Eu(III)–tetracycline complexes Simultaneous luminescent determination of tetracycline and oxytetracycline in bovine serum

Gabriela A. Ibañez [*]

*Departamento de Química Analítica, Facultad de Ciencias Bioquímicas y Farmacéuticas,
Universidad Nacional de Rosario and Instituto de Química Rosario (IQUIR), Consejo Nacional de
Investigaciones Científicas y Técnicas (CONICET), Suipacha 531, Rosario S2002LRK, Argentina*

Abstract

A simple and sensitive methodology to simultaneously quantify tetracycline and oxytetracycline in bovine serum samples is described. The method combines the advantages of the lanthanide-sensitized luminescence (i.e., sensitivity and selectivity) with partial least-squares (PLS) analysis, and requires no previous separation steps. Due to the strong overlapping of emission and excitation spectra of the analytes and their europium complexes, the luminescence decay curve (intensity of luminescence vs. time) of analyte–Eu complex was selected to resolve mixtures of tetracycline and oxytetracycline. Partial least-squares uses the luminescence decay as discriminatory parameter and regresses the luminescence versus time onto the concentrations of standards. Using a 16-sample aqueous calibration set, 10 validation samples, 11 spiked serum bovine samples and a blank of serum were studied. The analyte recoveries from serum samples ranged from 87 to 104% for tetracycline and from 94 to 106% for oxytetracycline. The results obtained by the developed method were statistically comparable to those obtained with high performance liquid chromatography.
© 2008 Elsevier B.V. All rights reserved.

Keywords: Tetracyclines; Lanthanide-sensitized luminescence; Europium; Partial least-squares; Bovine serum

1. Introduction

Tetracycline (TC) and oxytetracycline (oxy-TC) are antibiotics of the tetracycline group, which possess a wide range of antimicrobial activity against Gram-positive and Gram-negative bacteria. In addition to the employment of tetracyclines (TCs) in humans, there is an ever-increasing use of them for therapeutic veterinary purposes, to maintain the health of animals intended for human consumption, and to enhance the productivity of the farming industry [1,2]. To decrease the resistance in new strains, unnecessary usage of TCs should be minimized. One way of achieving this goal is to decrease their consumption, and this requires monitoring methods for TCs residues in sam-

ples such as blood serum, urine, milk, egg and animal tissues [1].

The fluorescent properties of TCs and all of their chelates formed with different metal ions have been extensively studied [2]. On the other hand, it is well established that TCs can be sensitively detected using europium-sensitized luminescence both in solid supports [3,4] and micellar solutions [5–9]. TCs present several coordination sites, being the β-diketone group the main portion which can act as bidentate ligand to form six-membered rings with metal ions such as Eu(III). The stoichiometry of the Eu(III)–TC chelates was reported as 1:1 [6,7]. TCs excited at about 392 nm undergo intersystem crossing to their triplet state, and the associated energy is transferred to the 4f level to the europium ion, which yields a characteristic line-type band at about 615 nm. This luminescence signal is proportional to the tetracycline concentration, and this fact has been employed for the direct individual determination of tetracyclines in sev-

* Tel.: +54 341 4372704; fax: +54 341 4372704.
  E-mail address: gibanez@fbioyf.unr.edu.ar.

eral samples (serum, milk, etc.) with a very low detection limit (10 ng mL^{-1}) [5]. The use of a synergistic ligand to form ternary complexes, such as ethylenediaminetetraacetic acid (EDTA) or trioctylphosphine oxide (TOPO) and surfactants such as Triton X-100, cetyltrimethylammonium chloride (CTACl), or dodecyl-sulfate sodium salt (SDS), allows the sensitivity to increase, due to a luminescence signal enhancement. The synergistic ligand removes water molecules from the coordination sphere of the lanthanide ion, a fact that is deleterious to lanthanide emission. In addition, the micellar environment protects the Eu(III)–TC chelate against non-radiative processes [4,5]. Analytical methods such as high performance liquid chromatography (HPLC) and flow injection analysis (FIA) employing sensitized Eu(III) luminescence as detection system have been reported [10].

Most methods for the determination of TCs use HPLC [11–17], thin layer chromatography [18,19], capillary electrophoresis (CE) [20–22], FIA [23–25] coupled to CE [26], microbiological assay [27–29], immunoassay [30,31], stopped flow mixing [5,32] have also been employed. Other methodologies based on titrimetry [33] and differential-pulse polarography [34] have been described. Spectrofluorometric methods with pre-treatment have been used in the past [35,36] but they involve tedious prior extraction steps. As alternative to these methods, spectrofluorometric techniques combined with multivariate calibration have been proposed [1,2] to individually quantify TCs. Besides separative methods such as chromatography and CE, only few methods have been described for the simultaneous determination of TCs [3,32]. It is noteworthy that methods based on native fluorescence of TCs have not been reported for their simultaneous analysis. An explanation to this fact lies in the strong overlapping between the fluorescence excitation and emission spectra of TC and oxy-TC in aqueous solution, which in principle precludes the application of multivariate calibration of spectroscopic data for the resolution of these mixtures. Even powerful three-way methods based on fluorescence matrices may fail because of the high degree of collinearity between TC and oxy-TC spectra. Cruz Ortiz and co-workers have compared different calibration models (zero, first and second order signal) to individually quantify TCs (TC, chlor-TC or oxy-TC) at a fixed level of the other TCs as interference [2]. On the other hand, the emission spectra of the lanthanide–analyte systems are not useful for analyte resolution, because they correspond to the lanthanide ion. Owing to this fact, we have selected the luminescence decay curve as analytical signal to resolve mixtures of TC and oxy-TC. Recently, a method using photochemically induced fluorescence signals combined with both first- and second-order multivariate calibration have been reported to quantify a mixture of three TCs in surface water samples [37,38].

Multivariate calibration methods are being successfully applied to instrumental data of a variety of sources, mainly spectroscopic, in order to construct predictive models for the determination of mixtures of compounds in several fields [39]. In recent years, multivariate calibration methods have also been applied to the analysis of kinetic [40–42], chromatographic [39,43] and electrochemical data [39]. However, only in few cases these methods have been applied to the analysis of time-resolved data. We can mention the simultaneous determination

of human albumin and γ-globulin with 5As-EDTA-Eu(III) complexes employing partial least-squares (PLS) [44]. In a previous work, Alava-Moreno et al. proposed a procedure for analysing mixtures of tetracyclines based on the differences in decay rates by using the Kalman filtering algorithm to process the decay data [3]. It is important to mention that in these previous works the determination of the analytes were not performed in complex matrices. PLS is the most popular regression method for multicomponent analysis due to the performance of its calibration models, the availability of software and the easiness of its implementation [39]. The use of PLS for chemical applications was initiated by Joreskog and Wold [45], and the number of references has increased extensively in recent years [46–48].

PLS is a multivariate regression technique, which has been successfully applied to many analytical systems and shows several important advantages: (1) it employs full spectral data, a feature critical for the resolution of complex multi-analyte mixtures; (2) analytical procedures can be carried out in a short time, usually with no sample clean-up or physical separation; and (3) its calibration models ignore the concentrations of other components except a selected analyte in the studied samples [39]. PLS involves a two-step procedure: (1) calibration, where the relationship between vectorial data such as spectra and reference component concentrations is established from a set of standard samples, and (2) prediction, in which the calibration results are employed to estimate the component concentrations in unknown samples [49]. In the PLS-1 version, all model parameters are optimized for the determination of each analyte at a time. During the model-training step, the calibration data are decomposed by an iterative algorithm, which correlates the data with the calibration concentrations using a so-called 'inverse' model [50]. This provides a set of regression coefficients to be applied to a new sample. Before calibration, however, the optimum number of latent variables should be selected in order to avoid over-fitting, by applying the leave-one-out cross-validation method described by Haaland [50] (see Section 3).

In this paper, a simple and sensitive method for the simultaneous determination of TC and oxy-TC in bovine serum samples, combining the advantages of lanthanide-sensitized luminescence and PLS analysis with no previous separation steps, is described. This study is performed on time decay data (intensity of luminescence vs. time) due to the strong overlapping of emission and excitation spectra discussed above. It is important to emphasize that the calibration samples were prepared without serum addition and employing only 16 calibration samples; however the proposed method shows good results even in complex matrices such as bovine serum. With the purpose of validating the developed method, TCs were also quantified by HPLC.

2. Experimental

2.1. Instrumentation and software

For the decay curve measurements, an SLM Aminco Bowman Series 2 luminescence spectrometer, equipped with 7 W Xenon pulse lamp and connected to a PC microcomputer with AB2 software which runs on the OS2 operating system was used.

Instrumental parameters were: delay time 30 μs, gate time 10 μs, minimum flash period 5 ms, λ_{exc} 390 nm, λ_{em} 616 nm, band pass 8 nm, photomultiplier tube (PMT) sensitivity 510 mV.

All decay curves were measured in random order with respect to analyte concentrations, and those corresponding to the calibration set were recorded in different days with respect to the validation set and spiked serum samples. Data were saved in ASCII format, and transferred to a PC Sempron AMD microcomputer for subsequent manipulation by the PLS program. PLS was applied with the program MVC1 [51] written in MATLAB 6.0, and freely available on the Internet at www.chemometry.com. The program is based on a previously described algorithm [50,52]. Sigmaplot 9.0 software was used for regression analysis and treatment of data.

HPLC was carried out on a liquid chromatograph equipped with a Waters (Milford, MA, USA) 515 HPLC pump and a variable-wavelength UV–vis detector measuring at 362 nm. A Rheodyne injector with a 200.0 μL loop was employed to spread the sample onto a Zorbax SB C18 column (5 μm average particle size, 150 mm × 4.6 mm i.d.).

2.2. Reagents

All chemicals used were of analytical reagent grade. For the luminometric measurements, tetracycline and oxytetracycline stock solutions (200 mg L^{-1}) were prepared weighing the required amount of the corresponding compounds (tetracycline and oxytetracycline hydrochlorides from Sigma) and dissolved in doubly distilled water. Water was chosen to prepare the stock solutions because organic solvents could affect the fluorescence intensity. Due to the lower stability of the analytes in the aqueous solutions, they must be prepared daily.

A stock solution of europium(III) (1.20×10^{-2} M) was prepared from europium(III) nitrate pentahydrate (Fluka). A 6.60×10^{-3} M stock solution of EDTA was prepared by dissolving the appropriate amount of reagent in doubly distilled water. Finally, a 5% (w/v) solution of CTACl and a Tris [tris(hydroxymethyl)-aminomethane] buffer solution (0.05 M, pH 9.0) were also used. CTACl and Tris were purchased from Fluka and Merck, respectively.

For HPLC determinations, tetracycline and oxytetracycline stock solutions (1000 mg L^{-1}) were prepared by weighing the required amount of the corresponding compounds (tetracycline and oxytetracycline hydrochlorides) and dissolving them in HPLC-grade methanol (Merck). The reagents for the mobile phase were HPLC-grade acetonitrile (Merck) and an aqueous solution containing both oxalic acid 0.01 M (oxalic acid dihydrate, Mallinckrodt) and sodium decanesulfonate 0.005 M (Fluka).

2.3. Luminometric procedure

Experimental conditions to obtain an adequate analytical signal [pH, concentration of Eu(III), and nature and concentration of surfactant and co-ligand] were selected according to the literature [8]. Thus, the final concentrations of Eu(III) and EDTA, used as co-ligand, were fixed at 1×10^{-4} M. CTACl was employed

Table 1
Calibration set for applying the PLS-1 method and the corresponding calibration statistical parameters

Number of calibration sample	Tetracycline (mg L^{-1})	Oxytetracycline (mg L^{-1})
1	0	0
2	0.050	0
3	0.111	0
4	0.171	0
5	0	0.045
6	0.050	0.045
7	0.111	0.045
8	0.171	0.045
9	0	0.106
10	0.050	0.106
11	0.111	0.106
12	0.171	0.106
13	0	0.166
14	0.050	0.166
15	0.111	0.166
16	0.171	0.166
Factors	2	2
Sensor range (μs)	30–350	30–350
RMSE[a] (mg L^{-1})	5.0×10^{-3}	7.9×10^{-3}
REP[b]	6.10	9.90
R^{2}[c]	0.994	0.984
SEN (mg^{-1} L)	26.5	12.3
γ[d] (mg^{-1} L)	469	216
$1/\gamma$ (mg L^{-1})	2.13×10^{-3}	4.63×10^{-3}
SEL	0.27	0.26
LOD[e] (mg L^{-1})	6.5×10^{-3}	1.5×10^{-2}

[a] $RMSE = \left[(1/I) \sum_1^I (c_{act} - c_{pred})^2 \right]^{1/2}$ where I is the number of calibration samples.

[b] $REP = (100 = RMSE)/\bar{C}$ where $\bar{C}$ is average concentration of the component for the I calibration samples.

[c] $R^2 = 1 - \sum_1^I (c_{act} - c_{pred})^2 / 1 - \sum_1^I (c_{act} - c_{pred})^2$.

[d] $\gamma = SEN/sy$, where sy is instrumental noise.

[e] $LOD = 3 \times sy/SEN$.

as surfactant being its final concentration 0.5% (w/v) and pH was kept at 9 employing Tris buffer.

To resolve the mixtures of TC and oxy-TC, a calibration set was constructed by preparing 16 calibration samples following a full factorial design. Table 1 shows the composition of the binary mixtures used in the calibration set. A validation set with 10 randomized validation samples was prepared with the concentrations of TC and oxy-TC reported in Table 2.

Calibration and validation solutions were prepared as follows: aliquots of standard solutions of TC and oxy-TC were simultaneously placed in a 5.00 mL volumetric flask. Appropriate amounts of stock solutions of CTACl, EDTA and Eu(III) were then added, and finally Tris buffer solution was added to the mark in order to obtain final concentrations of 0.5% (w/v) CTACl, and 1×10^{-4} M EDTA and Eu(III).

2.4. Serum samples

To consider the possible variation of the serum samples components, six different bovine sera were spiked at different concentration levels than those used for calibration, following a random design. The set constituted of eleven serum samples

Table 2
Prediction result and statistical analysis for the simultaneous determination of TC and oxy-TC in validation set using PLS-1 method

	Tetracycline (mg L^{-1})[a]		Oxytetracycline (mg L^{-1})[a]	
	Actual	Predicted	Actual	Predicted
	0.060	0.065 (4)	0.106	0.108 (5)
	0.084	0.082 (1)	0	N.D.
	0.121	0.123 (7)	0.144	0.148 (8)
	0.135	0.136 (2)	0.051	0.058 (8)
	0	N.D.	0.098	0.102 (2)
	0.146	0.15 (1)	0.155	0.15 (1)
	0.090	0.096 (5)	0.070	0.068 (4)
	0.036	0.039 (2)	0.139	0.137 (6)
	0.126	0.125 (5)	0.080	0.082 (2)
	0.065	0.068 (1)	0.126	0.133 (1)
RMS[b]/REP[c]	4.9×10^{-3}/5.7		6.8×10^{-3}/6.7	
R^{2d}	0.988		0.978	

[a] Experimental standard deviation from duplicate sample analysis between parentheses.

[b] RMSE $= \left[(1/I)\sum_1^I (c_{act} - c_{pred})^2\right]^{1/2}$, where I is the number of validation samples.

[c] REP $= (100 \times$ RMSE $/\bar{C}$ where $\bar{C}$ is average concentration of the component for the I calibration samples.

[d] $R^2 = 1 - \sum_1^I (c_{act} - c_{pred})^2 / \sum_1^I (c_{act} - c_{pred})^2$.

and a blank of serum was prepared as follows: aliquots of aqueous stock solutions of both TC and oxy-TC were simultaneously placed in 2.00 mL flasks and sera were added to each flask in order to obtain final concentrations in the range 1–5 mg mL^{-1}. These values widely cover the normal concentrations of both compounds in serum [53]. A volume of 167 μL of a given serum, previously spiked with TC and oxy-TC, was transferred to a 5.00 mL volumetric flask, appropriate amounts of stock solutions of CTACl, EDTA and Eu(III) were added and then Tris buffer solution incorporated to the mark in order to obtain final concentrations of 0.5% (w/v) CTACl, and 1×10^{-4} M EDTA and Eu(III).

2.5. Chromatographic procedure

A calibration set was prepared in the range 0–2.2 mg L^{-1} for both analytes. Serum samples were treated as follows: 1.00 mL of a given spiked serum sample (obtained as described in Section 2.4.) was added with 2.00 mL of oxalic acid dissolved in acetonitrile, vortexed for 5 min, and then centrifuged (10 min at $2500 \times g$). A volume of 1.00 mL of supernatant was transferred to a 1.00 mL volumetric flask, and was partially evaporated (until 1/4 of the original volume) with a stream of N$_2$. It was then filled to the mark with mobile phase. This solution was filtered through a 0.45 μm nylon membrane filter and 200.0 μL were injected into the HPLC column. The chromatographic separation was accomplished in 400 sec under isocratic conditions, using a 18:82 mixture of acetonitrile and an aqueous solution of both oxalic acid and sodium decanesulfonate as mobile phase [17,54,55]. The flow rate was maintained at 1 mL/min. The retention times for the analytes were 345 s (TC) and 260 s (oxy-TC).
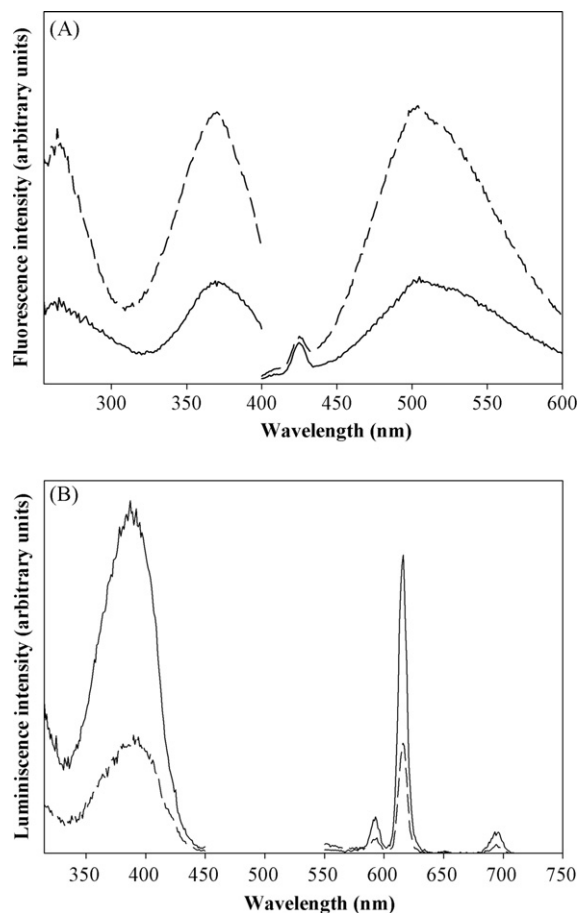

Fig. 1. Excitation and emission luminescence spectra for: (A) TC ($C_{TC} = 2.25$ mg mL^{-1}) (solid line) and oxy-TC ($C_{oxy-TC} = 7.80$ mg mL^{-1}) (dashed line) at pH 9.0, PMT sensitivity = 700 V; (B) Eu(III)–TC complex (solid line) and Eu(III)–oxy-TC complex (dashed line) in the following experimental conditions: Eu(III) $= 1 \times 10^{-4}$ M, EDTA $= 1 \times 10^{-4}$ M, CTACl $= 0.5\%$ (w/v), pH 9.0, $C_{TC} = 0.500$ mg mL^{-1}, $C_{oxy-TC} = 0.500$ mg mL^{-1}. Instrumental parameters: delay time = 30 μs, gate time = 10 μs, minimum flash period = 5 ms, band pass = 8 nm, PMT sensitivity = 500 mV.

3. Results and discussion

The high degree of overlapping between the fluorescence excitation and emission spectra of TC and oxy-TC and their europium complexes in aqueous solution discourages the application of multivariate calibration of fluorescence data for the resolution of this mixture, due to the apparent lack of selectivity. Fig. 1A shows the excitation and emission spectra of TC and oxy-TC solutions at pH 9 and Fig. 1B displays the excitation and emission spectra of TC and oxy-TC europium complexes under the studied experimental conditions. As explained above, these spectra cannot be employed to analyse mixtures of TCs, and the luminescence decay curve was selected to resolve them.

If the lanthanide–analyte complexes exhibit dissimilar lifetimes, and thus different luminescence decay curves, the latter may be used as discriminatory parameters to resolve the mixture of analytes. The lifetimes of the studied systems were measured, and the values obtained were 50 and 80 μs for the Eu(III) complexes of oxy-TC and TC, respectively. The value for the TC–Eu(III) system is in agreement with the literature
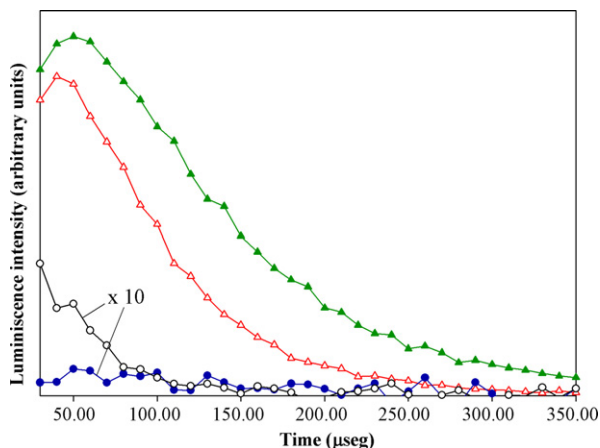
Fig. 2. Luminescence decay curve for TC–Eu(III) (filled green triangles), oxy-TC–Eu(III) (open red triangles), a blank sample (filled blue circles) and a typical unspiked serum sample (open black circles) in the following experimental conditions: Eu(III) = 1×10^{-4} M, EDTA = 1×10^{-4} M, CTACl = 0.5% (w/v), pH 9.0. For the decay curves containing each analyte, $C_{TC} = 0.111$ mg mL^{-1} and $C_{oxy-TC} = 0.106$ mg mL^{-1}. Instrumental parameters: delay time = 30 μs, gate time = 10 μs, minimum flash period = 5 ms, λ_{exc} = 390 nm, λ_{em} = 616 nm, band pass = 8 nm, PMT sensitivity = 510 mV (For interpretation of the references to color in this figure legend, the reader is referred to the web version of the article.).

one [8]. Fig. 2 shows the luminescence decay curve of both analyte–Eu(III) systems and also of a blank sample. With the aim of determining if the lifetime differences may discriminate the analytes, a set of calibration and validation samples was prepared and analysed by PLS. In order to build multivariate calibration models for TC and oxy-TC determination, decay curves were recorded for all samples. No additional advantage was obtained by selecting data ranges, and thus the entire decay curve was processed. Using these curves, partial least-squares at the PLS-1 level coupled to leave-one-out cross-validation was then performed in order to estimate the number of optimum latent variables in each case, using Haaland and Thomas criterion [50]. The optimum number of factors is estimated by computing the ratios $F(A) = \text{PRESS}(A < A^*)/\text{PRESS}(A)$ [where $\text{PRESS} = \Sigma(c_{i,\text{act}} - c_{i,\text{pred}})^2$ is the predicted error sum of squares, $c_{i,\text{act}}$ and $c_{i,\text{pred}}$ indicate the actual and predicted concentration for the ith sample, A is a trial number of factors and A^* corresponds to the minimum PRESS], and by selecting the number of factors leading to a probability of less than 75% that $F > 1$. This analysis led to the conclusion that the latter number is two for both calibrations, which allows PLS to explain more than 99% of the observed variance in the calibration data.

Table 1 summarizes the optimum number of factors for each analyte, the optimal regions used in calibration and the statistical parameters of calibration: squared correlation coefficient (R^2), relative error of prediction (REP) and root mean square error (RMSE), which provide an indication of the quality of fit of all calibration data. The calculated figures of merit for both analytes: sensitivity (SEN), analytical sensitivity (γ), its inverse $1/\gamma$, selectivity (SEL) and limit of detection (LOD) are also shown in Table 1. It is important to mention that the proposed method has a low detection limit for both analytes in the order of ng mL^{-1}, comparable to those reported in previous methods

Table 3
Prediction results for TC and oxy-TC in spiked serum samples using PLS-1 method

Actual	Predicted[a]		
	PLS	HPLC	d[b]
Tetracycline (mg L^{-1})			
1.80	1.72(5) [95.6]	1.7(2) [94.4]	−0.02
4.71	4.8(1) [101.7]	4.64(7) [99]	−0.16
1.38	1.20(5) [87]	1.33(5) [96.4]	0.13
1.95	1.79(5) [91.8]	1.8(2) [92.3]	0.01
2.54	2.37(4) [93.3]	2.35(1) [92.5]	−0.02
4.04	4.1(1) [101.5]	4.06(2) [100.5]	−0.04
0	N.D.	N.D.	–
4.22	4.4(4) [104.3]	4.2(1) [99.5]	−0.2
3.62	3.7(2) [102.2]	3.6(1) [99.4]	−0.1
2.85	2.8(2) [98.2]	2.78(3) [97.5]	−0.02
3.91	4.0(3) [102.3]	3.94(1) [100.8]	−0.06
0	N.D.	N.D.	–
Oxytetracycline (mg L^{-1})			
2.84	3.02(7) [106.3]	2.88(2) [101.5]	−0.14
1.47	1.46(8) [99.3]	1.50(5) [102]	0.04
2.24	2.2(1) [98.2]	2.1(1) [93.8]	−0.10
0	N.D.	N.D.	–
2.12	2.0(1) [94.3]	2.2(1) [103.8]	0.2
2.48	2.5(2) [100.8]	2.5(1) [100.8]	0
4.70	4.8(2) [102]	4.8(2) [102]	0
2.84	2.80(1) [98.6]	2.80(7) [98.6]	0
4.44	4.4(1) [99.1]	4.44(3) [100]	0.04
4.04	4.0(1) [99]	3.92(1) [98]	−0.08
3.60	3.6(3) [100]	3.74(6) [103.9]	0.14
0	N.D.	N.D.	–

N.D.: not detected, concentration of analyte below detection limit.
[a] The values are informed according to the experimental standard deviation from triplicate sample analysis (between parentheses). The recoveries (in square brackets) are based on the amount added to a serum free of studied drugs.
[b] Differences between predicted values by HPLC and PLS.

involving lanthanide-sensitized luminescence [4,5,8] and other methodologies such as HPLC and CE [13,22].

Table 2 shows the prediction results and the statistical analysis corresponding to the validation set (binary mixtures). They indicate that the present method is accurate in what concerns binary mixtures, as suggested by the good validation RMSE and REP values.

With the aim of evaluating the proposed method in real samples, the luminescence decay curve was recorded for a typical bovine serum sample, showing no serious interferences with the analyte signals (Fig. 2). Therefore, six bovine serum samples were spiked with both analytes and analyzed with the described method. The values obtained, summarised in Table 3, indicate that the proposed method yields good results concerning the simultaneous determination of both analytes in serum samples, with good recoveries between 87 and 104% for TC and from 94 to 106% between oxy-TC.

In order to assess the accuracy of the method, linear regression analysis of HPLC versus PLS found concentration values of both compounds was applied. The estimated intercept and slope (a and b, respectively) were compared with their ideal values of
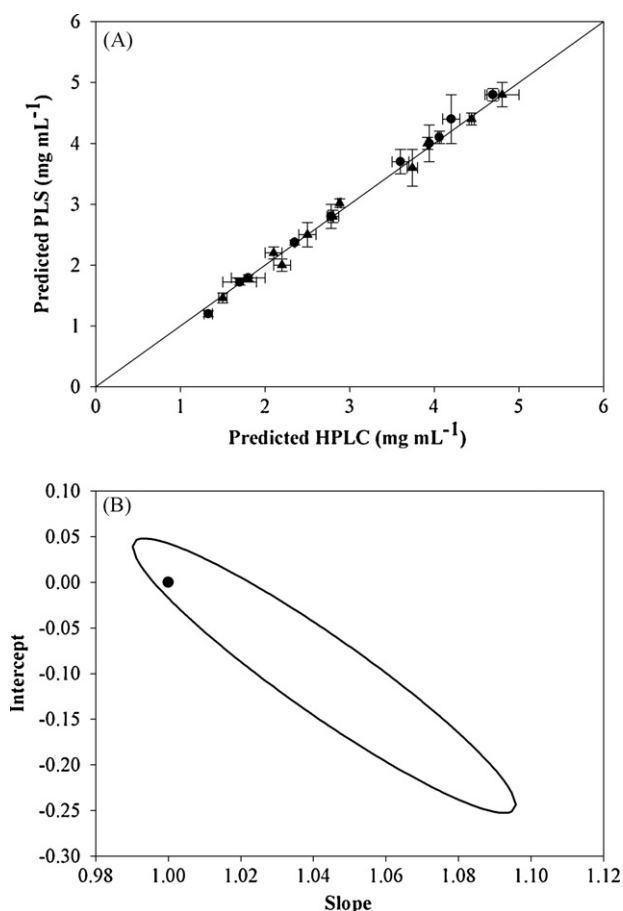
Fig. 3. (A) Plot of the TC (●) and oxy-TC (♦) concentrations predicted in spiked serum samples by the proposed PLS method, as a function of the concentrations predicted by HPLC. Error bars indicate the standard deviations of the triplicate sample analysis (see Table 2). The solid line is the perfect fit. (B) Elliptical joint region (at 95% confidence level) for the slope and intercept of the weighted least-squares regression of the data shown in plot (A). The circle marks the theoretical ($a = 0$, $b = 1$) point.

0 and 1 using the elliptical joint confidence region (EJCR) test [56] (Fig. 3). As can be seen, the EJCR contains the theoretical ($a = 0$, $b = 1$) point, concluding that the proposed approach yields statistically comparable results with HPLC in serum samples. In addition, the PLS results were also compared with those provided by the reference technique using a paired t-test statistics. This test compares the experimental t value $t_{exp} = (\bar{d}\sqrt{n}/s)$ [$\bar{d}$ is mean of d (Table 3), n the number of pairs of values and s the standard deviation of d] with the critical value of t [57]. The critical value at 95% confidence level with 9 degrees of freedom is 2.26 and t_{exp} are 1.65 and 0.303 for TC and oxy-TC, respectively. The comparison of these values reveals no significant differences between both methods.

It is important to mention that the PLS calibration was performed without serum addition. Therefore, the components present in serum samples do not appear to constitute serious interferences to the developed method (Fig. 2). In conclusion, the proposed method allows the simultaneous determination of TC and oxy-TC without pre-treatment (separation or masking) in complex matrices such as bovine serum samples, even when the matrix was not incorporated in the calibration step. Most of the

methods described to quantify TCs in complex matrices (serum, milk) involve deproteinization [4,9,13] or include the matrix in the calibration [5,8,11]. Even HPLC or CE may require tedious pre-treatment steps, which can affect the recovery and increase the time of analysis [13,22].

4. Conclusions

The simultaneous determination of tetracycline and oxytetracycline in serum samples was performed using luminescence decay curves of analyte–Eu(III) complexes in the presence of EDTA as synergistic ligand and CTACl as surfactant. A first-order multivariate calibration method (PLS-1) was applied to these time decay data. Two validation sets of synthetic mixtures and spiked bovine serum samples were studied. The results showed that PLS-1 is a good alternative to the simultaneous determination of TC and oxy-TC in serum samples based on the difference in the lifetimes of their europium(III) complexes. The proposed method shows an improvement in simplicity and speed with respect to those currently employed for the simultaneous determination of TCs. In addition, the results obtained in serum samples were statistically comparable to those obtained by the HPLC reference method.

Although the usefulness of the present method has been shown using two representative tetracycline components, TC and oxy-TC, it could be easily extended to the simultaneous determination of other TCs. Only differences between their lifetimes are necessary to resolve the problem if first-order multivariate calibration methods, such as PLS, are applied.

An alternative of the proposed method could be the use of second-order methods employing excitation-time decay matrix data.

References

[1] H.C. Goicoechea, A.C. Olivieri, Anal. Chem. 71 (1999) 4361.
[2] I. García, L. Sarabia, M. Cruz Ortiz, Anal. Chim. Acta 501 (2004) 193.
[3] F. Alava-Moreno, Yi-Ming. Liu, M.E. Díaz-García, A. Sanz-Mendel, Microchim. Acta 112 (1993) 47.
[4] R.C. Rodríguez-Díaz, M.P. Aguilar-Caballos, A. Gómez-Hens, Anal. Chim. Acta 494 (2003) 55.
[5] P. Izquierdo, A. Gómez-Hens, D. Pérez-Bendito, Anal. Chim. Acta 292 (1994) 133.
[6] L.M. Hirschy, E.V. Dose, J.D. Winefordner, Anal. Chim. Acta 147 (1983) 311.
[7] J. Georges, S. Ghazarian, Anal. Chim. Acta 276 (1993) 401.
[8] N. Arnaud, J. Georges, Analyst 126 (2001) 694.
[9] M.C. Mahedero, D. Bohoyo, F. Salinas, T. Ardila, D. Airado, B. Roldán, J. Pharm. Biomed. Anal. 37 (2005) 1101.

[10] T.J. Wentzell, L.M. Collette, D.T. Dahlen, S.M. Hendrickson, L.W. Yarmaloff, J. Chromatogr. B: Biomed. Sci. Appl. 433 (1988) 149.

[11] S.W. Yang, J.M. Cha, K. Carlson, J. Chromatogr. A 1097 (2005) 40.

[12] G.H. Wan, H. Cui, H.S. Zheng, J. Zhou, L.J. Lui, X.F. Yu, J. Chromatogr. B: Anal. Technol. Biomed. Life Sci. 824 (2005) 57.

[13] C.R. Anderson, H.S. Rupp, W.H. Wu, J. Chromatogr. A 1075 (2005), 23 and references therein.

[14] W.C. Andersen, J.E. Roybal, S.A. Gonzales, S.B. Turnipseed, A.P. Pfenning, L.R. Kuck, Anal. Chim. Acta 529 (2005) 145.

[15] F.N. Zhao, X.Z. Zhang, Y.R. Gan, J. Chromatogr. A 1055 (2004) 109.

[16] B. Loetanantawong, C. Suracheep, M. Somasundrum, W. Surareungchai, Anal. Chem. 76 (2004) 2266.

[17] J.W. Fritz, Y. Zuo, Food Chem. 105 (2007) 1297.

[18] K. Ng, S.W. Linder, J. Chromatogr. Sci. 41 (2003) 460.

[19] A. Crecelius, M.R. Clench, D.S. Richards, V. Parr, J. Chromatogr. A 958 (2002) 249.

[20] J.J. Pesek, M.T. Matyska, T. Bloomquist, G. Carlon, J. Liquid Chromatogr. Relat. Technol. 28 (2005) 3015.

[21] S.L. Wei, L. Liu, J.F. Zhao, G.H. Deng, Fenxi Shiyanshi 22 (2003) 52.

[22] H. Oka, Y. Ito, H. Matsumoto, J. Chomatogr. A 882 (2000) 109.

[23] A. Townshend, W. Ruengsitagoon, C. Thongpoon, S. Liawruangrath, Anal. Chim. Acta 541 (2005) 105.

[24] N. Wangfuengkanagul, W. Siangproh, O. Chailapakul, Talanta 64 (2004) 1183.

[25] X.W. Zheng, Y. Mei, Z.J. Zhang, Anal. Chim. Acta 440 (2001) 143.

[26] L. Nozal, L. Arce, B.M. Simonet, A. Rios, M. Valcarcel, Anal. Chim. Acta 517 (2004) 89.

[27] A.L. Myllyniemi, L. Nuotio, E. Lindfors, H. Korkeala, Analyst 129 (2004) 265.

[28] T. Pellinen, G. Bylund, M. Virta, A. Niemi, M. Karp, J. Agric. Food Chem. 50 (2002) 4812.

[29] A.L. Myllyniemi, L. Nuotio, E. Lindfors, R. Rannikko, A. Niemi, C. Backman, Analyst 126 (2001) 641.

[30] L. Okerman, K. de Wasch, J. van-Hoof, W. Smedts, J. AOAC Int. 86 (2003) 236.

[31] D.S. Aga, R. Goldfish, P. Kulshrestha, Analyst 128 (2003) 658.

[32] P. Izquierdo, A. Gómez-Hens, D. Pérez-Bendito, Anal. Lett. 27 (1994) 2303.

[33] S.A. Nabi, E.S.M. Abu-Nameh, M.I.H. Helaleh, J. Pharm. Biomed. Anal. 17 (1998) 357.

[34] E. Pinilla-Gil, L. Calvo-Blazquez, R.M. García-Monco-Carra, A. Sánchez-Misiego, Fresenius Z. Anal. Chem. 335 (1989) 1002.

[35] H. Poiger, C. Schalatter, Analyst 101 (1976) 808.

[36] W. Chang, Y. Zhao, Y. Ci, L. Hu, Analyst 117 (1992) 1377.

[37] R. Santiago Valverde, M.D. Gil García, M. Martínez Galera, H.C. Goicoechea, Anal. Chim. Acta 562 (2006) 85.

[38] R. Santiago Valverde, M.D. Gil García, M. Martínez Galera, H.C. Goicoechea, Talanta 70 (2006) 774.

[39] G.M. Escandar, P.C. Damiani, H.C. Goicoechea, A.C. Olivieri, Microchem. J. 82 (2006) 29.

[40] A. Muñoz de la Peña, A. Espinosa-Mansilla, M.I. Acedo Valenzuela, H.C. Goicoechea, A.C. Olivieri, Anal. Chim. Acta 463 (2002) 75.

[41] A. Afkhami, N. Sarlak, A. Zarei, Talanta 71 (2007) 893.

[42] P.C. Damiani, A.C. Moschetti, A.J. Rovetto, F. Benavente, A.C. Olivieri, Anal. Chim. Acta 543 (2005) 192.

[43] E. Fornal, P. Borman, C. Luscombe, Anal. Chim. Acta 570 (2006) 267.

[44] H. Goicoechea, B.C. Roy, M. Santos, A.D. Campiglia, S. Mallik, Anal. Biochem. 336 (2005) 64.

[45] K.G. Joreskog, H. Wold, System Under Indirect Observations, North Holland, Amsterdam, The Netherlands, 1982.

[46] A. Safavi, H. Abdollahi, R. Mirzajani, Spectrochim. Acta A 63 (2006) 196.

[47] B. Nadler, R.R. Coffman, J. Chemomether. 19 (2005) 45.

[48] Z. Rezaei, B. Hemmateenejad, S. Khabnadideh, M. Gorgin, Talanta 65 (2005) 21.

[49] H. Martens, T. Naes, Multivariate Calibration, Wiley, Chichester, 1989.

[50] D.M. Haaland, E.V. Thomas, Anal. Chem. 60 (1988) 1193.

[51] A.C. Olivieri, H.C. Goicoechea, F.A. Iñón, Chemom. Intell. Lab. Syst. 73 (2004) 189.

[52] H.C. Goicoechea, A.C. Olivieri, Trends Anal. Chem. 19 (2000) 599.

[53] H.D. Mercer, L.D. Rollins, G.G. Carter, R.P. Gural, D.W.A. Bourne, L.W. Dittert, J. Pharm. Sci. 66 (1977) 1198.

[54] C.R. White, W.A. Moats, K.L. Kotula, J. AOAC Int. 76 (1993) 549.

[55] AOAC Official Methods of Analysis, 23, Chlortetracycline, Oxytetracycline, and Tetracycline in Edible Animal Tissues, Liquid Chromatographic Method, AOAC International, Gaithersburg, MD, USA, 2000.

[56] A.G. González, M.A. Herrador, A.G. Asuero, Talanta 48 (1999) 729.

[57] J.N. Miller, J.C. Miller, Statistics and Chemometrics for Analytical Chemistry, 4th. ed., Prentice Hall, Upper Saddle River, NJ, USA, 2002, pp. 45–51.

The separation of aluminum(III) ions from the aqueous solution on membrane filter using Alizarin Yellow R

Kazuaki Ihara [a],[*], Shin-Ichi Hasegawa [b], Kunishige Naito [a]

[a] *Department of Materials Science, Faculty of Engineering, Ibaraki University, Hitachi, Ibaraki 316-8511, Japan*
[b] *National Institute for Materials Science, Tsukuba, Ibaraki 305-0047, Japan*

Abstract

The membrane filtration was examined as an effective and selective method for collection of Al(III) ions from aqueous solutions using Alizarin Yellow R, one of a pH-indicator, as a precipitating reagent. For preparation of aqueous solutions without precipitate or turbidity, a non-ionic surfactant, Triton X-100, was used as a solubilizing reagent for insoluble materials. Three metal ions, Al(III), V(III) and Cu(II) ions, were able to be collected as yellow-orange precipitates from aqueous solutions controlled in a range of pH 4–7, pH 4–9, and pH 5.5–12, respectively, on a membrane filter by filtration under suction. Hydrogen peroxide and *o*-phenanthroline were found to be capable of masking V(III) and Cu(II) ions in a range of pH 5.5–8 in which Al(III) ions were collected. This membrane filtration was applied to selective separation and determination of Al(III) ions in tap water.
© 2008 Elsevier B.V. All rights reserved.

1. Introduction

Although analytical instruments have been greatly improved in sensitivity and accuracy, a convenient pretreatment method of analytical samples has been necessary to be developed for determination of a trace amount of minor constituents. In determination of impurities contained in alloys or highly pure metals, an effective pretreatment method for separation and/or concentration of impurities from major components is usually required to avoid their chemical and physical interferences in quantitative determinations. Such a pretreatment method includes a liquid–liquid extraction, a precipitation, an adsorption and an ion-exchange method. In the method containing or forming solid particles, separation of the abundant component is often accompanied with some loss of the minor constituents. And the liquid–liquid extraction method has a major disadvantage that a large amount of an organic solvent is wasted. A membrane filtration, utilized for the microorganism analysis and for dialysis of drinking water, was recently proposed as a new technique

without such disadvantages for separation and concentration of metal complexes and ion-pairs [1–7,13,14]. If the metal ions were directly collected in the form of metal complexes or ion-pairs on a membrane filter from an aqueous solution by filtration, this membrane filtration can be used as a convenient separation and concentration technique for pretreatment of analytical samples.

A reagent used as a scavenger does not always require high sensitivity for determination of metal ions and would rather be easily separated from metal ions by a simple operation in the specimen preparation for determination after the membrane filtration. We selected salicylic acid and its derivatives as such a reagent. In a previous paper [8], Chromazurol B, one of triphenylmethane dyes with functional groups similar to those of salicylic acid, was successfully used for collection of Fe(III) ions. In the present study, Alizarin Yellow R, one of azo dyes with a salicylic acid structure, was examined whether this reagent was able to collect effectively some metal ions on a membrane filter from an aqueous solution by filtration under suction. Alizarin Yellow R is occasionally used as a pH indicator [9] and rarely as a metallochromic indicator [10] because this indicator and its metal complex have similar color in their aqueous solutions. If the metal complex were able to be separated from the indicator

remained in excess, this metal complex can be utilized for photometric determination of the metal ion. Furthermore, Alizarin Yellow R itself can be easily separated from metal ions by precipitation or extraction into an organic solvent such as benzene from a strongly acidic aqueous solution. Thus, this reagent may be used not only as a separating reagent but also as a determining reagent.

2. Experimental

2.1. Apparatus

A Hitachi U-2000 spectrophotometer was used for measuring absorption spectra of aqueous solutions and their filtrates, and absorbance at a fixed wavelength. A Hitachi-Horiba F-16 pH/ion meter equipped with a combined glass electrode was used to measure pH of the solutions. An Analytik Jena ZEEnit700 atomic absorption spectrophotometer was used for direct determination of aluminum ions in tap water.

2.2. Reagents

Alizarin Yellow R (Tokyo Kasei Kogyo Co. Ltd., Tokyo, Japan) for a pH indicator was used without further purification. Other chemical reagents were of analytical reagent grade. A commercially available hydrophilic surface-modified polytetrafluoroethylene (PTFE) membrane filter, Omni pore filter (Millipore, pore size 0.2 μm; 25 mm in diameter; 80 μm of thick), was used. pH buffers used are as follows: 2-morpholinoethanesulfonic acid (MES)–HCl–NaOH (pH 3–8), *N*-cyclohexyl-2-aminoethanesulfonic acid (CHES)–NaOH (pH 8–10), and NaCl–NaOH (pH 10–13).

2.3. Procedure

2.3.1. Examination of collection of metal ions

Two cubic centimeters of a 7.50×10^{-4} mol dm^{-3} solution of Alizarin Yellow R and 1.9 cm^3 of a 8.00×10^{-3} mol dm^{-3} solution of Triton X-100 were added to 1.50 cm^3 or the desired volume of a 1.00×10^{-3} mol dm^{-3} solution of each metal ion. This solution was diluted to 50 cm^3 after adding a pH buffer for adjusting to pH 3.00–13.00 by occasional agitation. A fixed volume (20 or 30 cm^3) of thus prepared aqueous solutions were filtered through a membrane filter held in a glass-made filter holder set onto a glass-made bell jar under suction with an aspirator. Absorption spectra and absorbance at a wavelength of 400 nm were measured for the original solution (the initial solution before filtration) and the filtrate, and then, the pH values were measured for both solutions. The collection of the metal ion on the membrane filter was evaluated based on a difference in absorbance between the original solution and the filtrate.

For examining the mole ratio of Al(III) to Alizarin Yellow R in a Al(III)–Alizarin Yellow R complex deposited on a membrane filter, the complex collected as precipitate on the membrane filter was dissolved in 5 cm^3 of DMSO, decomposed by adding a small amount of 6 mol dm^{-3} hydrochloric acid. After diluting this solution to 50 cm^3 with distilled water, Alizarin Yellow R

was extracted into benzene and determined by measurement of absorbance of the benzene layer at a wavelength of 370 nm. Using an aqueous layer after this extraction, Al(III) ions was determined as an Al(III)–Chromazurol S complex by measuring absorbance at a wavelength of 546 nm.

Determination of Al(III) ions in tap water by the graphite-furnace atomic absorption spectrophotometry was conducted according to the guidelines described in the public notice no. 216 of Ministry of Health, Labour and Welfare of Japan.

2.3.2. Quantitative examination of collection of Al(III) ions

Twenty or 30 cm^3 of tap water sample or a 0.5 cm^3 of a 1.00×10^{-4} mol dm^{-3} solution of a foreign metal ion was mixed with 2.5 cm^3 of a 0.01×10^{-3} mol dm^{-3} aqueous solution of *o*-phenanthroline, 1.0 cm^3 of a 0.3% hydrogen peroxide solution, 1.9 cm^3 of a 8.00×10^{-3} mol dm^{-3} Triton X-100 solution, 1.5 cm^3 of a 1.00×10^{-3} mol dm^{-3} solution of Alizarin Yellow R and 0.5 cm^3 of a 1.00×10^{-4} mol dm^{-3} Al(III) solution if necessary. This solution was diluted to 50 cm^3 or 100 cm^3 (for tap water sample) with distilled water after adjusting to pH 5.4–5.5 with MES–NaOH buffer solution, and then a fixed volume (15 cm^3) of this diluted solution was filtered through a membrane filter under suction. Yellow-orange solid precipitate collected on the membrane filter was dissolved in 5 cm^3 of DMSO and diluted to 50 cm^3 with distilled water. Absorbance of this aqueous dimethylsulfoxide solution was measured at a wavelength of 443 nm. The concentration of Al(III) ions was estimated by using a calibration curve prepared under the same conditions.

3. Results and discussion

Alizarin Yellow R, an organic reagent with the structure combining nitrobenzene and salicylic acid through a diazo group, was usually used as a pH indicator. This reagent can be expected to react with a metal ion through the same functional groups as those of salicylic acid to form a metal complex, but analytical applications of this reagent have been rarely studied. In a low pH region, this reagent itself deposits in a free acid form from aqueous solutions, so that a non-ionic surface-active agent Triton X-100 was utilized for solubilizing such insoluble material. In a preliminary experiment, Alizarin Yellow R itself was not collected as solid precipitate on a membrane filter from Triton X-100 added aqueous solutions. An addition of Triton X-100 was confirmed to prevent a free acid species of Alizarin Yellow R from deposition from an aqueous solution, as was expected.

3.1. Examination of Alizarin Yellow R as a metal scavenger

Then, we first examined whether the metal ion was effectively collected as precipitate of a metal–Alizarin Yellow complex on a membrane filter from aqueous solutions by the membrane filtration for Mg(II), Al(III), Ca(II), V(III), Fe(II), Fe(III), Co(II), Ni(II), Cu(II), Zn(II), Ga(III), Rb(I), Bi(III), Ag(I), Mo(VI) and In(III). The original solution was prepared at the same concentrations for each metal ion, Alizarin Yellow R and Triton X-100,
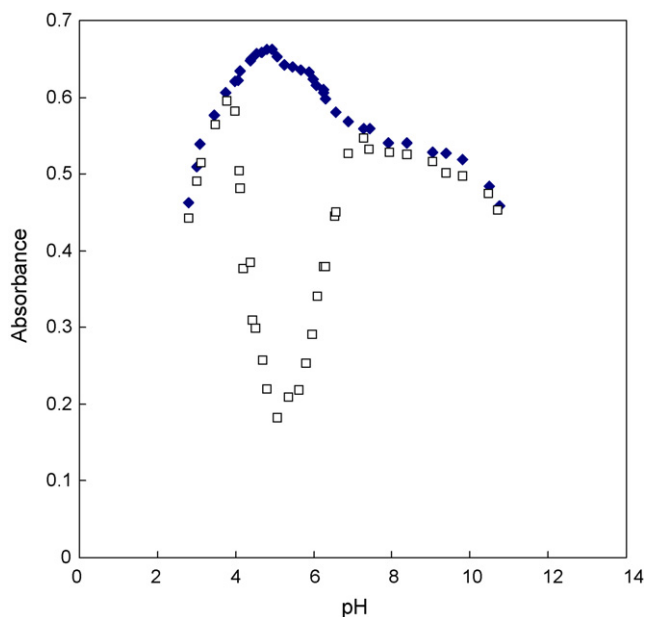
Fig. 1. pH-Dependence of the absorbance ($\lambda = 400$ nm) of the Alizarin Yellow R solution containing Al(III) ions and the filtrate: (♦) the original solution; (□) the filtrate. Concentration of Alizarin Yellow R: 3.00×10^{-5} mol dm^{-3}; concentration of Al(III): 3.00×10^{-5} mol dm^{-3}; concentration ratio of Triton X-100 to Alizarin Yellow R: 10.

Fig. 2. Effect of hydrogen peroxide in the absorbance ($\lambda = 400$ nm) of the Alizarin Yellow R solution containing V(III) ions and the filtrate: (♦) the original solution in the absence of hydrogen peroxide; (□) the filtrate in the absence of hydrogen peroxide; (▲) the original solution in the presence of hydrogen peroxide; (○) the filtrate in the presence of hydrogen peroxide; Concentration of Alizarin Yellow R: 3.00×10^{-5} mol dm^{-3}; concentration of V(III): 3.00×10^{-5} mol dm^{-3}; concentration of hydrogen peroxide: 4.00×10^{-4} mol dm^{-3}; concentration ratio of Triton X-100 to Alizarin Yellow R: 10.

by controlling pH to the desired value by adding pH buffers. Yellow-orange colored precipitate was found to deposit on the membrane filter by filtration under suction for Al(III), V(III) and Cu(II). Chen et al. reported that Alizarin Yellow R reacted with Fe(III) to form a 1:3 Fe(III)–Alizarin Yellow R complex with absorption maximum at a wavelength of 520 nm in the presence of cetyltrimethylammonium bromide [11]. We considered that Fe(III) ions did not react with Alizarin Yellow R in the absence of a quaternary ammonium ions under the present conditions. Recently, Denizli et al. reported a removal method of Al(III) with Alizarin Yellow-attached magnetic poly(2-hydroxyethyl methacrylate) beads [12]. Then, we examined suitable masking methods of Cu(II) and V(III) ions for selective separation of Al(III) ions by the membrane filtration using Alizarin Yellow R as a collecting agent.

We first examined pH effect on collecting Al(III) ions from aqueous solutions containing Al(III) ions, Alizarin Yellow R and Triton X-100. Fig. 1 shows pH-dependence of absorbance of the original solution containing Al(III) ions, Alizarin Yellow R and Triton X-100, and its filtrate. Both solutions showed different absorbance in the pH region of 4.0–7.0, where yellow-orange precipitate deposited on a membrane filter by filtration under suction. No precipitate was collected on a membrane filter out of this pH range by this membrane filtration. Comparing the pH-absorbance curve of the above original solution with that of aqueous solution of Alizarin Yellow R with Triton X-100, Al(III) ions were found to react with Alizarin Yellow R to form a Al(III)–Alizarin Yellow R complex in the original solution in this pH range capable of collecting yellow-orange precipitate on a membrane filter. These results indicate that the Al(III)–Alizarin Yellow R complex formed in the original solu-
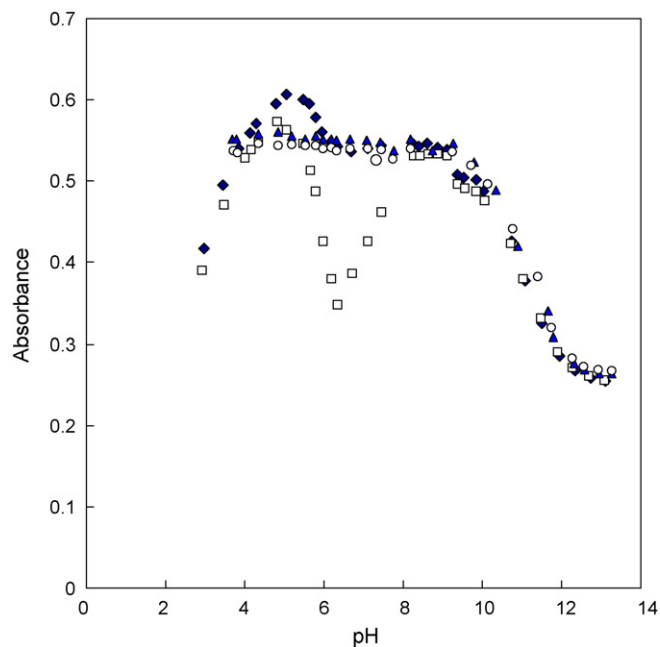
tion deposited completely as solid precipitate on the membrane filter by filtration under suction.

In Fig. 2, pH-dependence of absorbance of the original solution containing V(III) ions with Alizarin Yellow R and Triton X-100 in the absence and in the presence of hydrogen peroxide and their filtrates. In the absence of hydrogen peroxide, the original solution and its filtrate showed different absorbance in the pH region of 4.5–9, where yellow-orange precipitate deposited on a membrane filter by filtration under suction. In this case, V(III) ions were considered to react with Alizarin Yellow R to form a V(III)–Alizarin Yellow complex in the pH range capable of collecting yellow-orange precipitate on a membrane filter because absorbance of the original solution was different from that of the aqueous solution of Alizarin Yellow R with Triton X-100 in this pH range. However, Al(III) ions were also collected on a membrane filter in this pH region. We examined use of hydrogen peroxide as an effective masking reagent of V(III) ions. The pH-absorbance curves of the original solution adding hydrogen peroxide and its filtrate were almost coincident with that of an aqueous solution of Alizarin Yellow R itself in the whole pH range under study. Furthermore, a peak of the pH-absorbance curve observed at a pH of 4.0–6.4 for the original solution in the absence of hydrogen peroxide disappeared by adding hydrogen peroxide. These observations indicate that the formation of a V(III)–Alizarin Yellow R complex was completely inhibited with hydrogen peroxide under the applied condition.
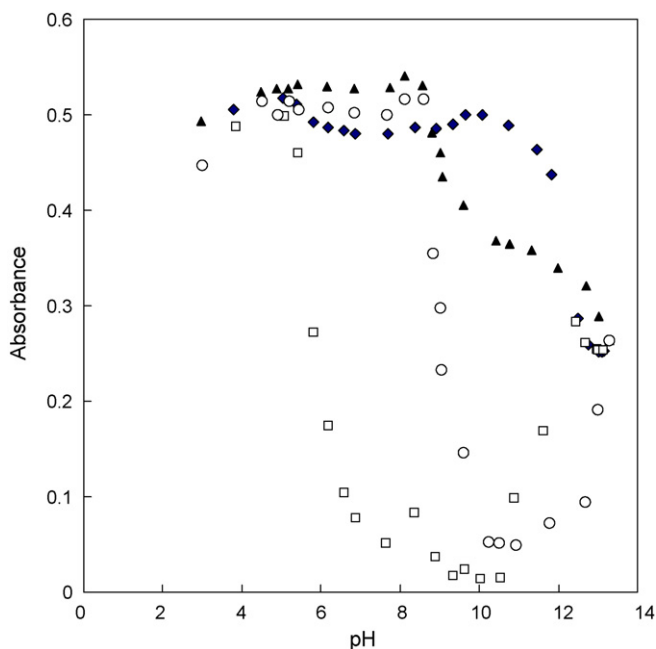
Fig. 3. Effect of *o*-phenanthroline in the absorbance ($\lambda = 400$ nm) of the Alizarin Yellow R solution containing Cu(II) ions and the filtrate: (♦) the original solution in the absence of *o*-phenanthroline; (□) the filtrate in the absence of *o*-phenanthroline; (▲) the original solution in the presence of *o*-phenanthroline; (○) the filtrate in the presence of *o*-phenanthroline; concentration of Alizarin Yellow R: 3.00×10^{-5} mol dm^{-3}; concentration of Cu(II): 3.00×10^{-5} mol dm^{-3}; concentration of *o*-phenanthroline: 4.00×10^{-4} mol dm^{-3}; concentration ratio of Triton X-100 to Alizarin Yellow R: 10.

Fig. 3 shows that absorbance of the original solution containing Cu(II) ions with Alizarin Yellow R and Triton X-100 was different from the filtrate in the pH range of 5.0–12.5, where yellow-orange precipitate deposited on a membrane filter by filtration under suction. A slight difference in absorbance between the original solution and an aqueous solution of Alizarin Yellow R with Triton X-100 suggests formation of a Cu(II)–Alizarin Yellow R complex in the pH range under study. Since this wide pH range overlapped with the pH range capable of collecting Al(III) or V(III), this interference of Cu(II) ions should be avoided by a suitable method for the selective collection of Al(III) ions by this membrane filtration. Addition of *o*-phenanthroline resulted in a large decrease of the pH range for collecting yellow-orange precipitate of a Cu(II)–Alizarin Yellow R complex on a membrane filter, from 5.0–12.5 to 8.0–12.5, that is, Cu(II) ions were not able to deposit on a membrane filter in the presence of *o*-phenanthroline by controlling the pH of aqueous solutions in a pH range from 5.0 to 8.0. These results indicate that selective collection of Al(III) ions can be made by controlling pH at 5–8 in the presence of hydrogen peroxide and *o*-phenanthroline even when V(III) and Cu(II) ions coexist with Al(III) ions in an aqueous solution.

3.2. Quantitative examination

We tried to dissolve the precipitate in a polar organic solvent such as acetone, ethanol, *N,N*-dimethylformamide and dimethylsulfoxide (DMSO) in order to determine Al(III) ion and Alizarin Yellow R in the precipitate collected on a membrane filter. Dimethylsulfoxide was found to be the best organic solvent for dissolving the precipitate. At the most 5 cm^3 of this solvent was required for complete dissolution of solid precipitate collected on a membrane filter and preventing from reprecipitation of a Al(III)–Alizarin Yellow R complex from an aqueous DMSO solution by dilution with distilled water. A thus-dissolved Al(III)–Alizarin Yellow R complex was able to be easily decomposed by adding hydrochloric acid. Alizarin Yellow R was readily recovered by extraction into benzene and Al(III) ions remained in an aqueous layer. Thus-separated Alizarin Yellow R and Al(III) ions can be easily determined photometrically by using the benzene extract and by color development with Chromazurol S, respectively. For the precipitate collected around pH 5.6, a mole ratio of Al(III) to Alizarin Yellow R was found to be 1:2, that is, Al(III) ions were collected as a 1:2 Al(III)–Alizarin Yellow R complex on a membrane filter by this membrane filtration. This result does not agree with the estimation of Denizli et al. [12]. When solid precipitate collected on a membrane filter was dissolved in 5 cm^3 of DMSO and diluted with distilled water to 50 cm^3, a good linear relationship was observed between absorbance of this aqueous DMSO solution and a concentration of Al(III) ions in the original solution. This linear relationship was always observed with a slightly different slope when pH was varied, and when hydrogen peroxide and *o*-phenanthroline were added into the original solution. This linear relationship may be utilized as a calibration curve for determination of Al(III) ions. From the above Section 3, we decided the following conditions as the optimum condition for collection of Al(III) ions: a metal concentration 1.50×10^{-6} mol dm^{-3}, a concentration of Alizarin Yellow R 3.00×10^{-5} mol dm^{-3}, a concentration of Triton X-100 3.00×10^{-4} mol dm^{-3}, pH of the original solution 5.4–5.5, and an addition of 1.0 cm^3 of 0.3% hydrogen peroxide for masking V(III) ions and 1.0 cm^3 of a 0.01 mol dm^{-3} solution of *o*-phenanthroline for masking Cu(II) ions. We tried to confirm whether Al(III) ions were selectively collected or not by the membrane filtration using Alizarin Yellow R as a collecting reagent under the above condition. Tables 1 and 2 show a recovery of Al(III) ions in the absence and in the presence of *o*-phenanthroline and hydrogen peroxide, respectively. From these results showing a complete collection of Al(III) from aqueous solutions, *o*-phenanthroline and hydrogen peroxide as masking reagents were found to gave no interference in quantitative determination of Al(III) by this membrane filtration. When an added amount of hydrogen peroxide was precisely controlled, a recovery of Al(III) ions was kept almost the same. We concluded that Alizarin Yellow R was able to be used as a selective collecting reagent for Al(III) ions in the presence of *o*-phenanthroline and hydrogen peroxide when some foreign ions were simultaneously present.

Table 3 shows effects of foreign metal ions and some common anions on the determination of Al(III). Relative error was calculated for the Al(III) concentration observed in the presence of a foreign metal ion or a common anion. Four foreign metal ions, Ga(III), In(III), Ag(III) and Mo(VI), were found to obstruct severely determination of Al(III) when these metal

Table 1
Results of the determination of Al(III) ions

Absorbance (443 nm)	C_{Al} ($\times 10^{-6}$ mol dm^{-3})	Recovery (%)
1.073	1.53	102
1.078	1.54	103
1.061	1.51	101
1.075	1.53	102
1.070	1.52	102
Mean value 1.071	1.53	102

Al(III): 1.50×10^{-6} mol dm^{-3}; Alizarin Yellow R: 6.00×10^{-6} mol dm^{-3}; Triton X-100: 3.00×10^{-4} mol dm^{-3}; pH 5.5.

Table 2
Results of the determination of Al(III) ions

Absorbance (443 nm)	C_{Al} ($\times 10^{-6}$ mol dm^{-3})	Recovery (%)
0.751	1.02	102
0.726	9.85	98
0.748	1.02	102
0.748	1.01	101
0.750	1.02	102
Mean value 0.744	1.01	101

Al(III): 1.00×10^{-6} mol dm^{-3}; Alizarin Yellow R: 3.00×10^{-6} mol dm^{-3}; Triton X-100: 3.00×10^{-4} mol dm^{-3}; o-Phenanthroline: 5.00×10^{-4} mol dm^{-3}; hydrogen peroxide: 1.76×10^{-3} mol dm^{-3}; pH 5.5.

ions were present at a concentration 50 times higher than that of Al(III) ions, but to have little effect at the same concentration as that of Al(III) ions. For the other metal ions, no effect could be practically observed even when adding 50 times in excess since an average of Al(III) ions recovery were estimated as 101.7%. Further, little effect was observed on determination of Al(III) ions even when nitrate, sulfate and acetate were present at a concentration of 0.1 mol dm^{-3}. Thus, we considered that this membrane filtration method was available for determination of Al(III) ions present at a trace level. Then we applied this method for determination of Al(III) ions in tap water. No precipitation was found to be collected on a membrane filter when using only tap water as a sample. This fact suggests that the concentration limit is present for collection of an Al(III)–Alizarin Yellow R complex as precipitate in this method. This concentration limit was considered to be required for the formation of colloidal particles of an Al(III)–Alizarin Yellow R complex with the suitable size. Then we added a known amount of Al(III) ions to tap water sample so as to control the concentration of Al(III) ions suitable for collection of Al(III) ions on a membrane filter by filtration. From the above Section 3, the Al(III) concentration after dilution was decided as about 1×10^{-6} mol dm^{-3} where Al(III) ions were completely collected on a membrane filter by filtration. Table 4 shows the result obtained by the membrane filtration method associated with a standard addition method along with the result observed by the graphite-furnace atomic

Table 3
Effect of foreign metal ion and some common anion on the determination of Al(III)

Foreign metal ions	Adding form	Concentration ($\times 10^{-6}$ mol dm^{-3})	Al(III) concentration ($\times 10^{-6}$ mol dm^{-3})		Relative error (%)
			Added	Found (%)	
Bi(III)	BiCl$_3$	50	1.00	1.03	3.3
Co(II)	CoCl$_2$	50	1.00	1.01	0.98
Cu(II)	CuCl$_2$	50	1.00	1.03	3.0
Fe(II)	FeCl$_2$	50	1.00	1.00	0.33
Fe(III)	Fe(ClO$_4$)$_3$	50	1.00	1.05	4.9
Ca(II)	(CH$_3$COO)$_2$Ca	50	1.00	1.04	3.6
Mg(II)	MgCl$_2$	50	1.00	0.94	−5.6
Ni(II)	NiCl$_2$	50	1.00	1.01	0.98
Rb(I)	RbCl	50	1.00	1.01	0.66
V(III)	VCl$_3$	50	1.00	1.02	2.0
Zn(II)	ZnCl$_2$	50	1.00	1.05	4.6
Ga(III)	GaCl$_3$	50	1.00	0.45	−65
		1.0	1.00	1.01	1.0
In(III)	InCl$_3$	50	1.00	0.47	−63
		1.0	1.00	0.99	−1.0
Ag(I)	AgNO$_3$	50	1.00	0.48	−62
		1.0	1.00	0.99	−0.8
Mo(VI)	(NH$_4$)$_6$Mo$_7$O$_{24}$	50	1.00	0.51	−60
		1.0	1.00	0.97	−2.6

Anions	Adding form	Concentration ($\times 10^{-6}$ mol dm^{-3})	Al(III) concentration ($\times 10^{-6}$ mol dm^{-3})		Relative error (%)
			Added	Found	
Nitrite	NaNO$_3$	0.1	1.00	0.97	−3.3
Sulfate	NaHSO$_4$	0.1	1.00	1.04	3.9
Acetate	CH$_3$COONa	0.1	1.00	1.00	0.30

Alizarin Yellow R: 3.00×10^{-6} mol dm^{-3}; Triton X-100: 3.00×10^{-4} mol dm^{-3}; o-Phenanthroline: 5.00×10^{-4} mol dm^{-3}; hydrogen peroxide: 1.76×10^{-3} mol dm^{-3}; pH 5.5.

Table 4
Determination of Al(III) in tap water

	Sample volume taken (cm^3)	Al(III) (µg)		Al(III) in sample (ng cm^{-3})
		Added[a]	Found	
Present method	20.0	0.0	0.0	–
	20.0	2.70	2.99	1 ± 0.6 (n = 5)
	30.0	2.70	3.10	14 ± 0.6 (n = 5)
GF-AAS	–	–	–	17 ± 0.3 (n = 5)

Alizarin Yellow R: 3.00×10^{-6} mol dm^{-3}; Triton X-100: 3.00×10^{-4} mol dm^{-3}; *o*-Phenanthroline: 5.00×10^{-4} mol dm^{-3}; hydrogen peroxide: 1.76×10^{-3} mol dm^{-3}; pH 5.5 (MES–NaOH).
[a] Added as an internal standard.

absorption spectrophotometry. The concentration of Al(III) ions in tap water observed by the present method were very similar to that found by the graphite-furnace atomic absorption spectrophotometry. This result indicates that the present membrane filtration method using Alizarin Yellow R as a collecting reagent can be applicable for determination of Al(III) ions in a trace level without any concentration method.

3.3. Mechanism of collection of a metal complex on a membrane filter

When using several sheets of membrane filter, solid precipitate was observed to deposit only on a top side of a membrane filter in contact with an aqueous solution and not on the remaining membrane filters. Since a whole of the first membrane filter was not dyed, a Al(III)–Alizarin Yellow R complex was not penetrated into a filter body. This result indicates that a Al(III)–Alizarin Yellow R complex did not pass through the membrane filter. This idea was supported by the fact that a colored solution was not obtained by rinsing the remaining membrane filters with dimethylsulfoxide (DMSO). By scanning electron microscopic observation, the network consisting of fine fibers constructed narrow channels in the membrane filter and solid precipitate was first formed on such fine fibers, then gradually blocked such narrow channels and finally covered membrane surface in contact with a clear aqueous solution. Furthermore, a Tyndall phenomenon was observed on an aqueous solution containing Al(III) ions with Alizarin Yellow R and Triton X-100 by applying a light beam from a laser pointer, but not or weakly on the filtrate of this solution. This fact suggests that colloidal particles showing such Tyndall phenomenon were removed by the membrane filtration in a similar manner as the ordinary filtration of solid particles suspension through a filter paper.

4. Conclusion

(1) Aluminium(III), V(III) and Cu(II) ions were found to deposit as solid precipitate of their Alizarin Yellow R com-

plexes on a membrane filter in the presence of Triton X-100 by filtration under suction. In this membrane filtration, Al(III) ions were separated from V(III) ions by using hydrogen peroxide and Cu(II) by using *o*-phenanthroline as a masking reagent in the range of pH 5.0–8.0.

(2) Some foreign metal ions and common anions gave little effect on collection of Al(III) ions by using Alizarin Yellow R in the presence of hydrogen peroxide and *o*-phenanthroline under the optimum conditions. And Ga(III), In(III), Ag(I) and molybdate ions, showing large inhibiting effect when present at a 50-fold higher concentration, were allowed to be present at the same concentration of Al(III) ions(1.0×10^{-6} mol dm^{-3}).

(3) This membrane filtration was able to be applied to determination of a trace amount of Al(III) ions in tap water.

(4) A possible mechanism was briefly discussed for collection of an Al(III)–Alizarin Yellow R complex on a membrane filter by this membrane filtration considering that the complex dispersed as colloidal particles in aqueous solution and by scanning electron microscopic observation of membrane filter surface.

References

[1] K. Goto, S. Taguchi, Anal. Sci. 9 (1993) 1.
[2] S. Taguchi, H.-F. Sun, N. Hata, I. Kasahara, Bunseki Kagaku 49 (2000) 941.
[3] M. Taga, M. Kan, Bull. Chem. Soc. Jpn. 62 (1989) 1482.
[4] M. Taga, M. Kan, F. Komatsu, S. Tanaka, H. Yoshida, Anal. Sci. 5 (1989) 219.
[5] M. Kan, T. Nasu, M. Taga, Anal. Sci. 5 (1989) 707.
[6] M. Kan, T. Nasu, M. Taga, Anal. Sci. 7 (1991) 87.
[7] M. Kan, H. Sakamoto, T. Nasu, M. Taga, Anal. Sci. 7 (1991) 913.
[8] K. Ihara, S. Hasegawa, K. Naito, Anal. Sci. 19 (2003) 265.
[9] T.R. Williams, M. Lautenschleger, Talanta 10 (1963) 804.
[10] S.D. Goswmi, B.M. Patel, B. Patel, J. Inst. Chem. (India) 55 (1983) 145.
[11] Y.S. Chen, M. Sha, Z.X. Chen, Hauxue Shiji 8 (1986) 365;
    Y.S. Chen, M. Sha, Z.X. Chen, Chem. Abstr. 106 (1987) 148563.
[12] A. Denizli, R. Say, E. Oiskin, React. Funct. Polym. 55 (2003) 99.
[13] M. Soylak, U. Divrikli, L. Elci, M. Dogan, Talanta 56 (2002) 565.
[14] I. Narin, M. Soylak, Anal. Chim. Acta 493 (2003) 205.

Quantification of components in overlapping peaks from capillary electrophoresis by using continues wavelet transform method

Long Jiao[a], Suya Gao[a], Fang Zhang[b], Hua Li[a,*]

[a] Institute of Analytical Science, Northwest University, Xi'an 710069, China
[b] National Defence Key Laboratory for SRTP, The Research Institute 213 of CNGC, Xi'an 710061, China

Abstract

The application of continues wavelet transform (CWT) for resolving overlapping peaks from capillary electrophoresis (CE) is described. Overlapping peaks can be resolved easily by transforming experimental signals into their wavelet coefficients. The proposed method was applied for the determination of benzoic acid and salicylic acid in overlapping peaks from CE. The composition of the two acids in Zuguangsan, a traditional Chinese patent medicine, was determined. The quantification results are satisfactory. CWT has been shown to be a practicable approach for resolving overlapping peaks and for quantitative determining coeluted compounds in overlapping peaks from CE. The quantification results obtained from CWT were compared with those obtained from numerical differentiation method. CWT has been shown prior to numerical differentiation method for processing experimental signals which contain noise.
© 2008 Elsevier B.V. All rights reserved.

Keywords: Capillary electrophoresis; Continues wavelet transform; Overlapping peaks; Benzoic acid; Salicylic acid

1. Introduction

Capillary electrophoresis is a powerful and highly efficient separation technique applied throughout the field of chemistry. However, searching for optimal separation conditions is generally a time-consuming and tedious procedure. When the physical separation of analytes is not accomplished, resolving these compounds is still possible by using chemometric methods [1,2].

In general, electrophoretic data acquired from different electrophoresis system can be grouped under two sorts: first-order and second-order data [3]. Different data may have different mathematical properties, which should be taken into account before selecting a given method for processing and interpretation. The derivative of electropherogram is usually employed to resolve overlapping peaks from first-order data [2,4,5]. Numerical differentiation method is generally used to calculate the derivative of electropherogram. However, numerical differentiation is a method which is easily influenced by noise. Only when

electropherograms are smooth profiles can satisfactory resolution results be obtained [4]. Artificial neural network (ANN) [6–9] and partial least-squares (PLS) [10,11] has also been applied to processing first-order data and quantify components in unresolved peaks. The two methods require constructing a sufficiently representative calibration set of samples, which should span all the variability expected in unknown samples. A model trained by fewer samples cannot promise the accuracy of quantification results [2,3]. In addition, the selection of parameters for ANN and PLS is some complex. Therefore, quantifying components in overlapping peaks with ANN or PLS is time-consuming and labor-intensive. As for processing second-order data, many second-order chemometric methods have been developed, including evolving factor analysis [12], windows factor analysis [13], heuristic evolving latent projections [14–16] and alternating least-squares [17–21], etc. Some methods have been applied to CE [16,19–21]. These second-order methods are not suitable for processing first-order data.

Wavelet transform (WT) is a high-performance signal processing technique, which has been widely applied throughout the analytical chemistry [22–26]. The application of WT to resolving overlapping signals has been reported [27–36]. Especially, Shao and Ma [30] has demonstrated the practicability of using

---

* Corresponding author. Tel.: +86 29 88302942; fax: +85 29 88303448.
  E-mail address: huali@nwu.edu.cn (H. Li).

WT, including discrete wavelet transform (DWT) and CWT, for resolving overlapping peaks in first-order signals. DWT has been successfully used to the quantification of components in overlapping peaks [27]. However, CWT has not been applied to quantifying components in unresolved peaks. Therefore, this work investigates the application of CWT to the quantitative determination of coeluted compounds in overlapping peaks from CE. The overlapping electrophoretic peaks of benzoic acid and salicylic acid were resolved with CWT. The composition of the two acids in Zuguangsan, a traditional Chinese patent medicine, was then determined. Satisfactory quantification results were obtained, which demonstrate that CWT is a practicable method for quantifying coeluted compounds and for resolving overlapping peaks in first-order electropherograms. Moreover, the quantification results obtained from CWT and those from numerical differentiation method were compared. CWT has been shown to be prior to numerical differentiation method for processing experimental electropherograms which contain noise.

2. Theory

WT is a mathematical tool, which can be used to decompose a signal in terms of elementary contributions called wavelets. The WT can be described as

$$W_f(a, b) = \int_{-\infty}^{+\infty} f(t)\psi_{a,b}^*(t)\mathrm{d}t \tag{1}$$

where $f(t)$ is a signal and * represents the complex conjugate. $W_f(a,b)$ is called the wavelet coefficients. $\Psi_{a,b}(t)$ is the wavelet function; a and b is called scale parameter and translation parameter, respectively. For CWT algorithm, the scale parameter, $a \in N$ (N denotes positive integer) [30–33].

CWT can be employed as a differentiation and smoothing procedure of $f(t)$ [30], because CWT can be denoted as follows:

$$W_f(a, b) = a^n \frac{\mathrm{d}^n}{\mathrm{d}t^n}(f^*\theta_a)(b) \tag{2a}$$

$$\theta_a(t) = \frac{1}{a}\theta\left(\frac{t}{a}\right) \tag{2b}$$

where * denotes the operator of convolution and n is the vanishing moment of the wavelet function. $\theta(t)$ is a function with fast decay and whose integral is a nonzero constant, namely, $\theta(t)$ satisfies the condition of a smoothing function. According to Eq. (2), CWT through a wavelet function with n vanishing moments is equivalent to the calculation of the nth order derivative of $f(t)$ smoothed by $\theta(t)$.

One of the applications of CWT is resolving overlapping peaks in analytical signals. The resolution capability of CWT is controlled by the scale parameter. CWT only can resolve overlapping peaks under some scales. In general, the resolution capability has a decreasing tendency with the increase of the scale [30]. Small scale can give better resolution of overlapping peaks. As for *gaus2* function, the resolution capability of CWT decreases with the increase of the scale. Only if the scale is smaller than a certain value can overlapping peaks be

baseline resolved. Naturally, this value is different for different signals and it can be experimentally determined according to their wavelet coefficients. When CWT is used to resolve overlapping peaks, it can suppress the noise in signals simultaneously since a smoothing procedure is involved in it. The smoothing efficiency of CWT is also controlled by the scale parameter, which can be regarded as the size of the smoothing window. The larger the scale parameter is used, the smoother signals will be obtained. In addition, CWT is a linear operation, which makes it a practicable tool for quantitative analysis [33].

3. Experimental

3.1. Reagents and solutions

All solutions were prepared with twice distilled water. The background electrolyte solution consists of 20.00 mM borate, 30.00 mM sodium dodecyl sulfate (SDS), and 4% methanol (all are analytical-reagent grade and purchased from Xi'an Chemical Factory, Shannxi, China) and was adjusted at pH 9.8. The Zuguangsan (Suizhou Medicine Corporation, Hubei, China) was resolved in methanol–water solution (4:1) and so was each pure analyte of benzoic acid and salicylic acid (all are analytical-reagent grade and purchased from Xi'an Chemical Factory). Eleven mixture samples were prepared by mixing the standard samples of benzoic acid and salicylic acid and employed as standards. The concentrations of the two acids in each mixture are shown in Table 1.

3.2. Instrument

A HPCE-01 capillary electrophoresis system with DD2000 ultraviolet detector was used (Shandong Chemical Industry Research Institute, Shandong, China). Fused-silica capillaries (Refine Chromatography, Yongnian, Hebei, China) of 75 μm ID with an effective length of 47 cm and a total length of 55 cm were used. The data were obtained with a compatible computer by using N2000 chromatography data station software (Intelligent Information Engineering Institution of Zhejiang University, China). All the data were obtained at the wavelength of 250 nm at regular steps of 0.1 s during the electrophoresis process.

Table 1
Concentration of benzoic acid and salicylic acid in each mixture

Samples	Benzoic acid (mg mL^{-1})	Salicylic acid (mg mL^{-1})
M1	8.0	0.0
M2	7.2	0.8
M3	6.4	1.6
M4	5.6	2.4
M5	4.8	3.2
M6	4.0	4.0
M7	3.2	4.8
M8	2.4	5.6
M9	1.6	6.4
M10	0.8	7.2
M11	0.0	8.0

3.3. CE procedure

Prior to the everyday experiment, the capillary was sequentially rinsed with 0.1 M NaOH, water, and 1 M HCl, each for 10 min. Between runs, the capillary was rinsed with water for 5 min and with the background electrolyte solution for 5 min. The sample was injected by gravity for 10 s (height 10 cm). The components in Zuguangsan were separated at 16 kV for 15 min. The capillary was thermostated at 25 °C. The sample of Zuguangsan was subjected to three replicate CE runs, generating three electropherograms.

3.4. Data simulation

All the simulated signals are overlapping peaks of two-component mixtures. Each single peak was simulated with the Gaussian function:

$$peak = h \exp\left(\frac{-(x - p)^2}{g}\right) \tag{3a}$$

where h, p and g are, respectively, the height, position and width of a simulated peak. Each simulated signal was generated by combining two single peaks which was indicated as peak A and peak B:

$$s = peak_A + peak_B \tag{3b}$$

where s denotes the simulated signals. The noisy signals were generated by adding random noise to simulated noise-free signals obtained from Eq. (3). The noise being added was simulated using Eq. (4) [31]:

$$noise_x = \frac{(0.5 - Rand)}{SNR} max \tag{4}$$

where SNR is signal-to-noise ratio (SNR); max is the maximal value of a simulated signal, and Rand is a random number between 0 and 1.

3.5. Software

All computations were performed with Matlab7.0 for Windows on a PC.

4. Results and discussion

Although many wavelet functions can be used to run CWT, in practice, a wavelet function from Gaussian basis functions is suitable for processing simulated signals generated with Gaussian function and electrophoretic peaks which commonly are Gaussian peaks. In this work, *gaus2* wavelet function was used.

4.1. Simulated signal

4.1.1. Quantitative relationship between simulated peaks and resolved peaks

To investigate the relationship between the areas of raw simulated peaks (peak A and B) and the areas of CWT resolved peaks
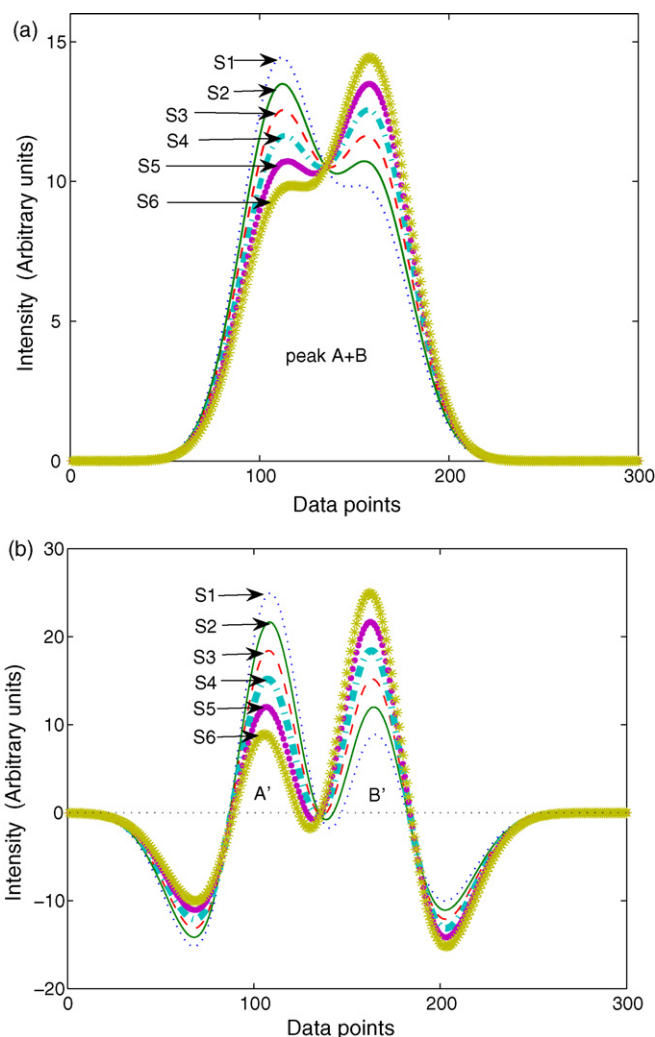

Fig. 1. (a) A group of simulated signals (S1–S6 denotes the six simulated signals); and (b) their wavelet coefficients. (Scale: $a = 21$).

(indicated as peak A′ and peak B′) a group of noise-free signals were simulated and processed with CWT. The simulated signals (S1–S6) and their wavelet coefficients (W_f) are displayed in Fig. 1. Clearly, separated peaks (peak A′ and B′) were obtained through the transform procedure. It is found that the areas of resolved peaks are linearly dependent on the areas of simulated peaks. Here, the x-axis was used as baseline of resolved peaks to calculate the peak areas. Fig. 2 illustrates the linear relationship between the areas of resolved peaks and those of simulated peaks. The relationship is the basis of quantitative analysis with CWT.

4.1.2. Selection of the scale parameter

For noise-free signals, scale parameter has no influence on the linear relationship between simulated and resolved peaks [32,33]. Areas of resolved peaks are always linearly dependent on the areas of corresponding simulated peaks. According to the theory, CWT merely can resolve overlapping peaks completely under some scales. Hence, when processing noise-free signals, selecting a scale under which overlapping peaks can be baseline resolved is the only requirement for the employment of CWT.
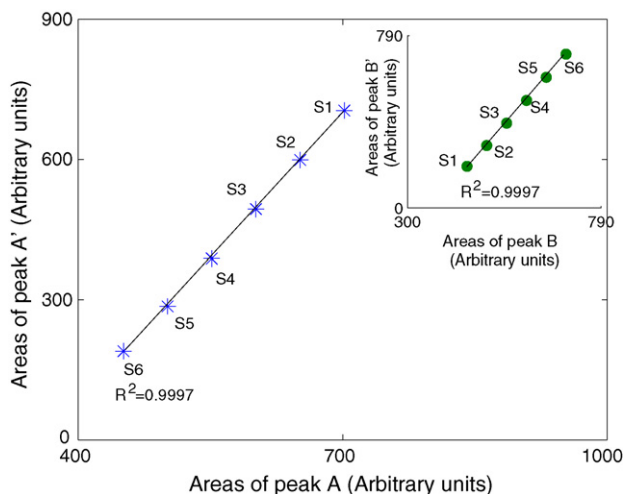
Fig. 2. Resolution results of the simulated signals shown in Fig. 1a. (Scale: $a = 21$).

On the other hand, scale parameter has a great influence on the resolution results when processing noisy signals. According to the theory, CWT can simultaneously resolve overlapping peaks and suppress the noise in signals. And the effect of noise suppressing is controlled by the scale parameter. In general, using larger scale can smooth signals better. If the scale being used is too small, noise might not be suppressed satisfactorily and quantitative analysis might be hindered. However, because the resolution capability of *gaus2* decreases with the increase of the scale, using too large scale is also impracticable. If the scale is too large, overlapping peaks will not be baseline resolved. To illustrate the influence of the scale parameter on the resolution

of noisy signals, Fig. 3 exhibits a simulated noisy signal and its wavelet coefficients under three different scales. Clearly, the wavelet coefficients curve in Fig. 3b is corrupted by noise. It is inaccurate to do quantitative analysis with the curve. The curve in Fig. 3d is smooth, whereas the overlapping peak is not baseline resolved. The curve in Fig. 3c is evidently smoother than the one in Fig. 3b, and the baseline separation of the overlapping peak has been achieved.

Because the scale parameter has a great influence on the resolution results of CWT, an appropriate scale should be selected when processing noisy signals in order to get a reasonable and satisfactory result. A simple strategy was used here to select the scale. The strategy is selecting the maximal scale from the scales under which overlapping peaks can be baseline resolved to run CWT. In this way, the noise in signals can be suppressed to the greatest extent when the overlapping peaks have been baseline resolved. To investigate the practicability of the strategy, CWT was applied to four groups of simulated noisy signals, which were generated by adding different level noise (SNR = 50, 30, 20 and 10, respectively) to the noise-free signals shown in Fig. 1a. In this case, the overlapping peaks can be baseline resolved when the scale parameter $a \leq 21$. According to the proposed strategy, the scale of 21 should be used to run CWT. Then, CWT was carried out under the scales of 21, 17, 13 and 9, respectively. The resolution results are shown in Table 2. As was expected, the best result was obtained under the scale of 21. The proposed strategy has been demonstrated practicable for processing simulated noisy signals.

In addition, this case also demonstrates that CWT can be applied to processing noisy signals without other noise filtering procedures. Numerical differentiation method cannot be
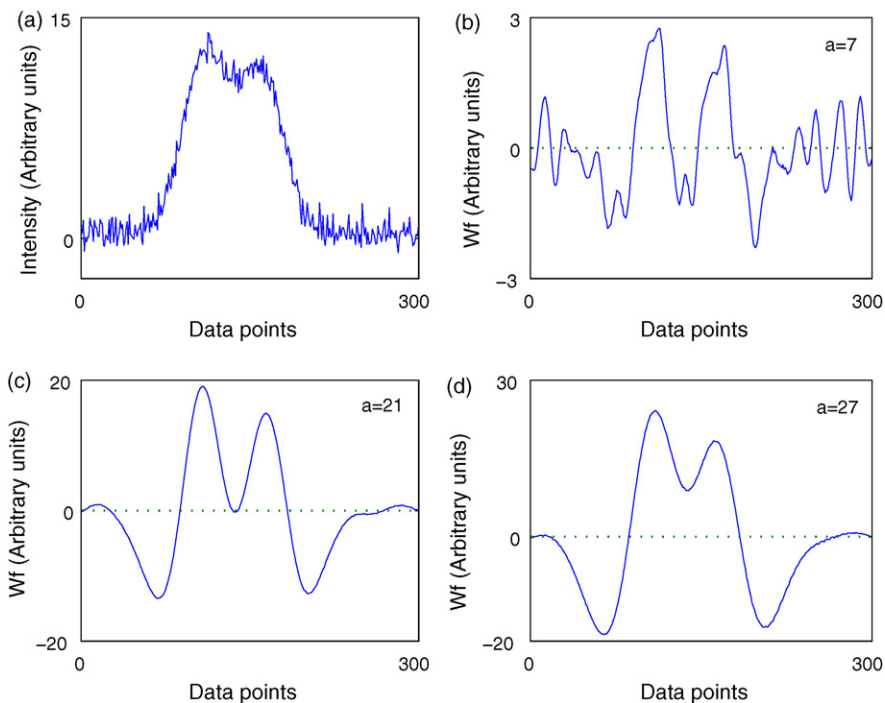

Fig. 3. A simulated noisy signal (SNR = 20) generated by adding noise to S1 (shown in Fig. 1a); and its wavelet coefficients under three different scales.

Table 2
Quantitative resolution results of simulated noisy signals

Peak	SNR	R^2			
		$a = 21^a$	$a = 17$	$a = 13$	$a = 9$
A	50	0.9992	0.9982	0.9974	0.9957
	30	0.9986	0.9976	0.9955	0.9906
	20	0.9983	0.9944	0.9848	0.9462
	10	0.9896	0.9810	0.9752	–[b]
B	50	0.9986	0.9973	0.9959	0.9932
	30	0.9975	0.9966	0.9950	0.9907
	20	0.9963	0.9939	0.9888	0.9746
	10	0.9942	0.9888	0.9830	–[b]

R^2 denotes the correlation coefficients between the areas of simulated peaks and the areas of resolved peaks.

[a] a is the scale parameter of CWT.

[b] The areas of resolved peaks cannot be calculated due to the existence of noise.

employed to process these noisy signals without filtering the noise by other approaches. Obviously, processing noisy signals with CWT is simpler and easier than by using numerical differentiation method.

4.2. Quantification of benzoic acid and salicylic acid in Zuguangsan

Benzoic acid and salicylic acid are two main components in Zuguangsan. The electropherogram of Zuguangsan obtained under the separation conditions described in Section 3.3 is shown in Fig. 4a. Obviously, the two acids cannot be separated completely by using CZE technique under the described separation conditions.

4.2.1. Resolving overlapping peaks with CWT

CWT was employed to resolve the overlapping peaks of the two acids from raw experimental data. In this case, the overlapping peaks can be baseline resolved when $a \le 16$. According to the strategy proposed in Section 4.1.2, the best resolution
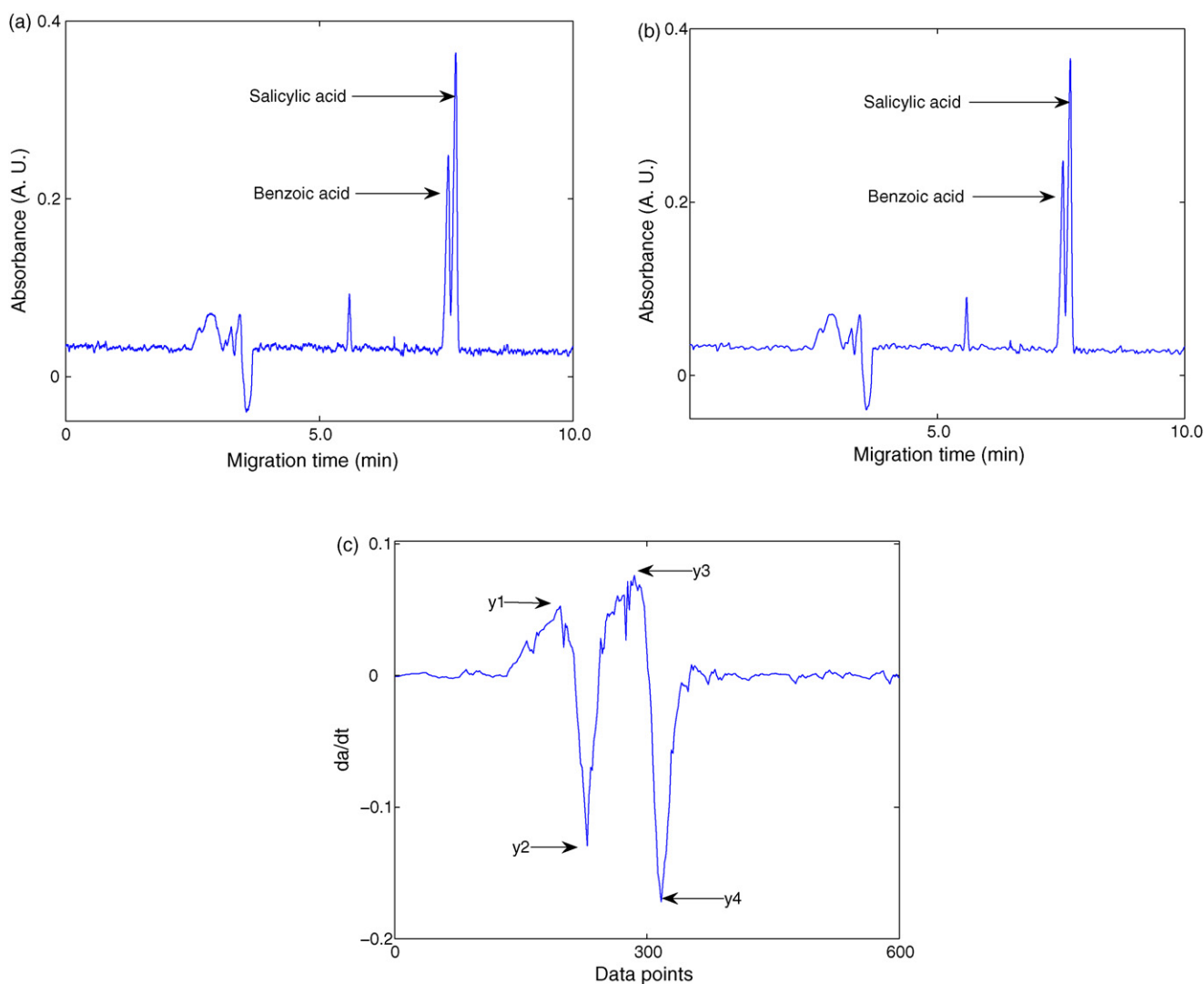

Fig. 4. (a) Electropherogram of Zuguangsan; (b) denoised electropherogram of Zuguangsan; (c) first derivative of the electropherogram shown in Fig. 4b.

Table 3
Correlation coefficients between the concentrations of benzoic acid and salicylic acid and their resolved peak areas under different scales

Compounds	R^2			
	$a = 16$[a]	$a = 14$	$a = 12$	$a = 10$
Benzoic acid	0.9444	0.9440	0.9429	0.9413
Salicylic acid	0.9625	0.9594	0.9569	0.9540

R^2 denotes the correlation coefficients between the concentrations of the two acids in the standard samples and their resolved peak areas.

[a] a is the scale parameter of CWT.

Table 4
Calibration equations and correlation coefficients of the three models

Compounds	Models	Calibration equations	R^2
Benzoic acid	Model 1	$y = 2.593x - 0.5408$	0.9444
	Model 2	$y = 2.587x - 0.4634$	0.9438
	Model 3	$y = 0.0638x - 0.0187$	0.9265
Salicylic acid	Model 1	$y = 2.853x - 0.5828$	0.9625
	Model 2	$y = 2.850x - 0.5181$	0.9618
	Model 3	$y = 0.0422x + 0.0464$	0.9401

results should be obtained under the scale of 16. To investigate the practicability of the strategy for processing experimental signals, CWT was carried out under the scales of 16, 14, 12 and 10, respectively. Table 3 displays the correlation coefficients between the concentrations of the two acids in the standard samples and their resolved peak areas. As was expected, the largest R^2 was obtained under the scale of 16. The proposed strategy is demonstrated practicable in processing experimental signals.

Then, a calibration model (Model 1) was built by using the concentrations of the two acids and their resolved peak areas obtained under the scale of 16. The calibration equations are shown in Table 4. Table 5 displays the quantification results of the two acids. The relative quantification error for benzoic acid and salicylic acid is 0.28% and 0.93%, respectively. For the two acids, the relative standard deviation (R.S.D.) in the three replicates CE runs is 5.48% and 6.61%, respectively. CWT has been shown to be suitable for processing experimental signals which contain noise.

In addition, another calibration model (Model 2) was built by using the denoised electropherograms, which are obtained by DWT method [37] (wavelet function: db4). Fig. 4b shows the denoised electropherogram of Zuguangsan. CWT was also carried out under the scale of 16. The quantification results of this model are shown in Table 5 also. As shown in Table 5, there is no apparent difference in the accuracy of quantification results between Model 1 and Model 2. It demonstrates that CWT can be used to process experimental electropherograms without filtering the noise.

In this case, the two calibration models were built with 11 standard samples in order to obtain more accurate models. In practice, fewer standard samples are also adequate to build a correct calibration model. That is to say, quantifying coeluted compounds in overlapping electrophoretic peaks, fewer standard samples are required by the proposed approach than by ANN and PLS.

4.2.2. Resolving overlapping peaks with numerical differentiation method

In this section, the first derivative of the electropherograms was calculated with numerical differentiation method in order to resolve the overlapping peaks of the two acids. To obtain an acceptable resolution results, the derived electropherograms were calculated from the denoised electropherograms obtained in Section 4.2.1. According to the literatures [2,4], the differences between maximum and minimum in derived electropherograms ($y1$–$y2$) and ($y3$–$y4$), as shown in Fig. 4c, are linearly dependent on the concentrations of the two acids. Then, a calibration model (Model 3, shown in Table 4) was built and the concentrations of the two acids in Zuguangsan were calculated. The quantification results are described in Table 5.

Obviously, the quantification results of CWT are better than those of numerical differentiation method. Probably, the residual noise in the electropherograms lowers the accuracy of numerical differentiation method. More accurate quantification results might be obtained using other denoising algorithm. However, it is time-consuming and tedious to search for a satisfactory denoising result suitable for resolving overlapping peaks with numerical differentiation method.

Table 5
Quantification results of benzoic acid and salicylic acid

	Concentrations (mg g^{-1})					RE[c] (%)	R.S.D.[d] (%)
	True	Calc1[a]	Calc2	Calc3	Average[b]		
Benzoic acid							
Model 1		114.3	113.3	103.3	110.3	0.28	5.48
Model 2	110.0	113.2	112.2	102.3	109.2	0.73	5.52
Model 3		93.63	104.2	94.46	97.43	11.4	6.03
Salicylic acid							
Model 1		190.1	171.0	168.9	176.6	0.93	6.61
Model 2	175.0	189.0	170.1	167.8	175.7	0.38	6.63
Model 3		161.6	158.0	157.9	159.2	9.04	1.33

[a] Calc1, Calc2, Calc3 denote the calculated concentration of three replicate CE runs, respectively.

[b] Average is the average concentration of three calculated concentrations.

[c] RE denotes the relative error.

[d] R.S.D. is the relative standard deviation of three calculated concentrations.

5. Conclusion

The application of continues wavelet transform to resolving overlapping peaks from CE is described. CWT was employed to resolve simulated overlapping peaks and experimental overlapping peaks of benzoic acid and salicylic acid from CE. The overlapping peaks can be resolved by transforming original signals into their wavelet coefficients. By resolving their overlapping peaks, the composition of benzoic acid and salicylic acid in Zuguangsan was determined, although the two acids were not separated by CE. CWT was shown to be a practicable approach for resolving overlapping peaks and for quantitative determining coeluted compounds in overlapping peaks from CE. In addition, CWT can enhance the resolution of overlapping peaks and simultaneously suppress the noise in signals. Consequently, processing noisy signals with CWT is simpler and easier than by numerical differentiation method.

Acknowledgement

References

[1] J.W. Jorgenson, K.D. Lukacs, Anal. Chem. 53 (1981) 1298.
[2] F. Zhang, H. Li, Electrophoresis 26 (2005) 1692.
[3] M. Escandar, N.K.M. Faber, H.C. Goicoechea, A.M. de la Pena, A.C. Olivieri, R.J. Poppi, Trends Anal. Chem. 26 (2007) 752.
[4] V. Dohnal, H. Li, M. Farková, J. Havel, Chirality 14 (2002) 509.
[5] A.A. Fasanmade, A.F. Fell, Anal. Chem. 6 (1989) 720.
[6] Y.X. Zhang, H. Li, A.X. Hou, J. Havel, Talanta 65 (2005) 118.
[7] Y.X. Zhang, H. Li, J. Havel, Chin. J. Anal. Chem. 32 (2004) 673.
[8] Y.X. Zhang, H. Li, A.X. Hou, J. Havel, Chemom. Intell. Lab. Syst. 82 (2006) 165.
[9] G. Bocaz-Beneventi, R. Latorre, M. Farková, J. Havel, Anal. Chim. Acta 47 (2002) 452.
[10] R.M. Latorre, J. Saurina, S. Hernandez-Cassou, J. Chromatogr. A 871 (2000) 331.
[11] J.L. Beltrán, E. Jiménez-Lozano, D. Barrón, J. Barbosa, Anal. Chim. Acta 501 (2004) 137.
[12] H. Gampp, M. Maeder, C.J. Meyer, A.D. Zuberbuehler, Talanta 32 (1985) 1133.
[13] E.R. Malinowski, J. Chemom. 6 (1992) 29.
[14] O.M. Kvalheiml, Y.Z. Liang, Anal. Chem. 64 (1992) 936.
[15] P.V. van Zomeren, H. Darwinkel, P.M.J. Coenegracht, G.J. de Jong, Anal. Chim. Acta 487 (2003) 155.
[16] H. Li, J.R. Hou, K. Wang, F. Zhang, Talanta 70 (2006) 336.
[17] R. Tauler, D. Barcelo, Trends Anal. Chem. 12 (1993) 319.
[18] R. Tauler, B. Kowalski, S. Fleming, Anal. Chem. 65 (1993) 2040.
[19] H. Li, F. Zhang, J. Havel, Electrophoresis 24 (2003) 3107.
[20] F. Zhang, H. Li, Chemom. Intell. Lab. Syst. 82 (2006) 184.
[21] R.M. Latorre, J. Saurina, S. Hernandez-Cassou, Electrophoresis 21 (2000) 563.
[22] X.G. Shao, A.K.M. Leung, F.T. Chau, Acc. Chem. Res. 36 (2003) 276.
[23] C.X. Ma, X.G. Shao, J. Chem. Inf. Comput. Sci. 44 (3) (2004) 907.
[24] M. Cocchi, C. Durante, G. Foca, A. Marchetti, L. Tassi, A. Ulrici, Talanta 68 (2006) 1505.
[25] R.N.F. dos Santos, R.K.H. Galvao, M.C.U. Araujo, E.C. da Silva, Talanta 71 (2007) 1136, J.D.
[26] Qiu, LiangF R.P., X.Y. Zou, J.Y. Mo, Talanta 61 (2003) 285.
[27] X.G. Shao, W.S. Cai, P.Y. Sun, M.S. Zhang, G.W. Zhao, Anal. Chem. 69 (1997) 1722.
[28] X.G. Shao, W.S. Cai, P.Y. Sun, Chemom. Intell. Lab. Syst. 431 (1998) 147.
[29] X.G. Shao, W.S. Cai, Z.X. Pan, Chemom. Intell. Lab. Syst. 45 (1999) 249.
[30] X.G. Shao, C.X. Ma, Chemom. Intell. Lab. Syst. 69 (2003) 157.
[31] X.Q. Lu, H.D. Liu, Z.H. Xue, Q. Zhang, J. Chem. Inf. Comput. Sci. 44 (2004) 1228.
[32] S.G. Wu, L. Nie, J.W. Wang, X.Q. Lin, L.Z. Zheng, L. Rui, J. Electroanal. Chem. 508 (2001) 11.
[33] L. Nie, S.G. Wu, J.W. Wang, L.Z. Zheng, X.Q. Lin, L. Rui, Anal. Chim. Acta 450 (2001) 185.
[34] Y.Q. Zhang, J.Y. Mo, T.Y. Xie, P.X. Cai, X.Y. Zou, Anal. Chim. Acta 437 (2001) 151.
[35] S.S. Khaloo, A.A. Ensafi, T. Khayamian, Talanta 71 (2007) 324.
[36] E. Dinç, A. Özdemir, D. Baleanu, Talanta 65 (2005) 36.
[37] D. Jouan-Rimbaud, B. Walczak, R.J. Poppi, O.E. de Noord, D.L. Massart, Anal. Chem. 69 (1997) 4317.

ELSEVIER

Online preconcentration for the determination of lead, cadmium and copper by slotted tube atom trap (STAT)-flame atomic absorption spectrometry

Gokce Kaya [a], Mehmet Yaman [b],*

[a] *Adiyaman University, Sciences and Arts Faculty, Department of Chemistry, Adiyaman-Turkey*
[b] *Firat University , Sciences and Arts Faculty, Department of Chemistry, Elazig-Turkey*

Abstract

An online sensitivity enhancement by using atom trapping in flame atomic absorption spectrophotometry was examined for increasing the residence time of the analyte atoms in the light path. For this purpose, various parameters of quartz tubes of the slotted tube atom trap were tested. The studied parameters include the internal diameter, the length of the upper slot and the wall thickness of quartz tube. The best sensitivities as high as 7-fold, 13-fold and 3-fold enhancement were achieved by the tubes having an internal diameter of 6 mm, an upper slot length of 1.0 cm and the wall thickness of 1.5 mm for lead, cadmium and copper, respectively. The limits of quantitation were found to be 30 ng mL^{-1} for Pb and 3 ng mL^{-1} for Cd and 30 ng mL^{-1} for Cu by the optimized method. The achieved technique was applied to determine the concentrations of Pb, Cd and Cu in different plant leaves taken around cement and textile industries.
© 2008 Elsevier B.V. All rights reserved.

Keywords: The sensitivity improvement; Flame atomic absorption spectrometry; Lead; Cadmium; Copper; Plant leaves

1. Introduction

Humans are exposed to Cd, Pb and Cu by food intake and inhaling air which is polluted by environmental conditions and industrial emissions. The accumulation of these metals in human body can have middle and long-term health risks and can adversely affect the physiological functions.

For a long time, it is known that lead is toxic for brain, kidney and reproductive system and can also cause impairment in intellectual functioning, infertility, miscarriage and hypertension. Several studies have shown that lead exposures in school-aged children can significantly reduce IQ and has been associated with aggressive behavior, delinquency and attention disorders. Due to its malleability, low melting point, and ability to form compounds, Pb has been used in hundreds of products such as pipes, solder, brass fixtures, crystal, paint, cable, ceramics, and batteries [1]. As a result, populations in, at least, 100 countries are still exposed to air pollution with lead in spite of banning the usage of lead in gasoline.

Cd competes with Zn for binding sites and can therefore interfere with some of Zinc's essential functions. Thus, it may inhibit enzyme reactions and utilization of nutrients. Cd can generate free radical tissue damage because it may be a catalyst to oxidation reactions. Furthermore, excessive Cd exposure can cause renal damage, reproduction problems, cardiovascular diseases and hypertension. There are several sources of human exposure to Cd, including employment in primary metal industries, production of certain batteries, some electroplating processes and consumption of tobacco products [2]. Consequently, it was reported by International Agency Research on Cancer (IARC) that through inhalation cadmium could cause lung cancer in humans and animals [3].

Copper is a necessary element as a component of more than 30 enzymes including superoxide dismutase (SOD), caeruplasmin, cytochrome oxidase, ascorbate oxidase and tyrosinase in the human body. On the other hand, Cu has adverse effects on human health at its high concentrations. Furthermore, *in vitro* studies have shown that cancer cells in a high copper environment find it easy to proliferate into tumor. It was reported that copper is a well known pro-oxidant and may participate in metal-catalyzed peroxidation of lipids as similar to iron [4].

Recently, increased attention is paid to the use of plant parts such as leaves, shoots and barks as biomonitors. In the most

* Corresponding author. Fax: +90 4242330062.
  E-mail addresses: kayag232@hotmail.com (G. Kaya),
myaman@firat.edu.tr (M. Yaman).

used expression, biomonitoring may be defined as the use of bioorganism or biomaterials to obtain information on certain compounds in biosphere. The advantages of using of biomonitors for environmental surveillance lie in the lower cost as compared to direct methods of pollution measurement, since no collecting or measuring equipment has to be installed and protected against vandalism. If the biomonitors are widely distributed and occur frequently enough they can be used over large areas for recording and evaluating heavy-metal inputs. Furthermore, they make it possible to identify sources of emissions and verify the overland transportation of individual elements. As a result, many plant species are useful for biomonitoring atmospheric deposition of pollutants [5].

The World Health Organization (WHO) [6] established provisional tolerable weekly intakes (PTWIs) of Cd and Pb of 0.007 and 0.025 mg kg^{-1} body weight, respectively, for all human groups. Therefore, analytical techniques with high sensitivity are required for detection of these metals. These techniques include electrothermal atomic absorption spectrometry (ETAAS), inductively coupled plasma-atomic emission spectrometry (ICP-AES), anodic stripping voltammetry (ASV), differential-pulse polarography (DPP), and inductively coupled plasma-mass spectrometry (ICP-MS).

It is well known that the flameless atomic absorption spectrometry is a more sensitive technique than flame atomic absorption spectrometry (FAAS). However, relative to the later technique, flameless AAS has some disadvantages such as its high cost, slowness and greater proneness to interferences [7]. Although, effective chemical modifiers, background correction systems, improved furnace and platform designs and careful optimization of temperature programs were used to remove the interferences [8], it is still widely studied in relation to the interferences in this field of flameless AAS [9]. If both of these methods can be used, FAAS should be preferred to flameless AAS because FAAS is faster, cheaper and does not require expert operators.

Therefore, there are continuing efforts to enhance the sensitivity of FAAS despite its being the mature analytical (many believe "over the hill") technique. These efforts can be classified as offline and online methods. The offline methods include the most of preconcentration methods such as liquid–liquid extraction, adsorption, precipitation, solid phase extraction [10–13] except their several special applications. The sensitivity of FAAS is limited by several factors. The analyte atoms generated in the flame pass rapidly and continuously through the measurement zone during sample aspiration. A further limitation is the poor efficiency of the nebulizer/burner system. A maximum of 10% of the aspirated sample solution reaches the flame. The sensitivity can be improved if the atomic vapor has been constrained to remain in the light path for a long time. In a review article, Matusiewicz recently discussed in detail the techniques examined for this purpose [14]. Among these methods, atom-trapping technique is designed in two different shapes: the slotted quartz tube and the water-cooled silica tube. Although these techniques that can be called as online methods were firstly described 25 years ago [15], it is evident that the scientific literature on this topic has increased recently [14]. The water-cooled silica sys-
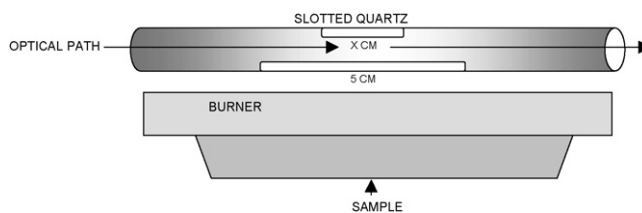

Fig. 1. Schematic diagram of the STAT.

tem, in addition to having the advantage of being more sensitive to improvement than the slotted quartz tube, has the disadvantage of needing a very large volume of a sample due to the longer aspiration times as long as 2 min for one measurement [16–18]. In another application of atom trapping technique, the re-volatilization of analytes using organic solvent in a more concentrated form into the atomizer system was studied [19]. However, this technique has also the disadvantages mentioned above for the water-cooled silica system as well as the possible imprecise measurements.

Keeping atoms in the optical path with the so-called slotted-tube atom trap (STAT) system, as illustrated in Fig. 1, has been found to be more popular recently [14,21]. Because quartz has a sufficiently high melting point and a low thermal expansion coefficient, it has been chosen as the material for the atom trap. The sensitivity improvement is attributed to the increased residence time of the analyte atoms in the light path due to slower flame speed in STAT. Furthermore, the more stable chemical environment due to homogenous temperature in quartz tube enhances the numbers of neutral atoms, thereby increasing the sensitivity. In the STAT system, a double-slotted quartz tube with the length of the upper slot shorter than that of the lower slot is installed above the burner and placed into the flame gases and analyte atoms using pneumatic nebulizer system (Fig. 1). The optimization of the slotted tube using various designs and parameters, such as exit holes, tube length and tube materials, was reviewed in detail [14]. In that review [14], it was also reported that the achieved improvements in the sensitivity were in the range of 2- to 5-fold. In recent times, 10-, 6- and 3-fold improvements in the sensitivities of Cd, Pb and Cu were achieved by using the tube having the diameter of 6.0 mm, the upper slot length of 2.3 cm, the tube length of 12 cm and the lower slot length of 5 cm, respectively [20,21].

In other studies [22–26], cadmium, lead and Cu concentrations in the biological and environmental samples, such as human urine, fruits, milk, soil and water, were determined by using direct FAAS-STAT and/or together with preconcentration methods. In those studies, 2.5- and 5-fold improvements in the sensitivity of FAAS were achieved for lead and cadmium using the STAT having a diameter of 8 mm and an upper slot of 4 cm, respectively.

In this study, the length of the upper slot, the internal diameter and the wall thickness of quartz tube in STAT were systematically changed in order to improve the sensitivity of FAAS. The obtained best conditions were applied to the determinations of Cd, Pb and Cu concentrations in the plant leaves taken around

industrial areas such as cement factory and textile industry to examine their biomonitoring possibilities.

2. Experimental

2.1. Apparatus and reagents

An ATI UNICAM 929 Model flame atomic absorption spectrophotometer (FAAS) equipped with ATI UNICAM hollow cathode lamps (HCL) was used for the metal determinations. The acetylene–air flame in FAAS in which the optimal conditions were studied is provided in the manufacturer's instructions for the spectrophotometer. A domestic microwave oven (Kenwood) was used for the digestion of the tissues. The STAT was used to improve the sensitivity of FAAS.

Unless stated otherwise, all chemicals used were of analytical-reagent grade. During all analytical work, double-distilled water was used. All glass apparatus were kept permanently full of $1 \, mol \, L^{-1}$ nitric acid when not in use. In the digestion procedures, concentrated nitric acid (65%, Merck) and hydrogen peroxide (35%, Merck) were used. Stock solutions of the metals ($1000 \, mg \, L^{-1}$) were prepared by dissolving their nitrate salts in $1.0 \, mol \, L^{-1}$ nitric acid.

To assess the reliability of measurements, some samples were analyzed by PerkinElmer Elan 9000 inductively coupled plasma-mass spectrometry (ICP-MS) at ACME Analytical Labs in Canada.

2.2. Changes made on the STAT

Various changes on quartz tubes were studied to enhance the sensitivity. These changes included the internal diameter, the length of the upper slot, the wall thickness of quartz tube and the length of tube. Among the other suspected factors, lower slot length depends on the slot of the burner. Hence, it is obvious that the change in its length has not improved the sensitivity. The height of the tube over the burner was always adjusted to obtain a maximum absorbance. The studied quartz tube can be used only in the flame of the acetylene–air mixture. The changes made on the quartz tubes are given in Table 2. In all designs, the length of the lower slot was 50 mm.

2.3. Sampling and sample preparation

The studied plant leaves including *Ficus carica*, *cherry*, *apple*, *Punica granatum*, *Prunus domestica*, *maize*, *Morus* L., *cedrus and pieca* were obtained around Gaziantep city and transferred to laboratory in plastic bag. The samples were washed with tap water and then rinsed with distilled water. After drying at $70 \, °C$, 0.5 g of samples were transferred into flask (Pyrex) and digested by using dry or/and microwave (MW) ashing methods.

2.4. Dry ashing

The dried samples were heated gradually in a furnace at $200 \, °C$ for 15 min, at $300 \, °C$ for 10 min, at $400 \, °C$ for 10 min, and ashed at $480 \, °C$ for 4 h.
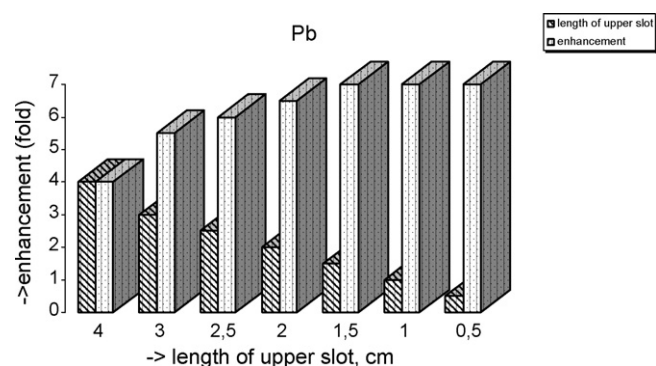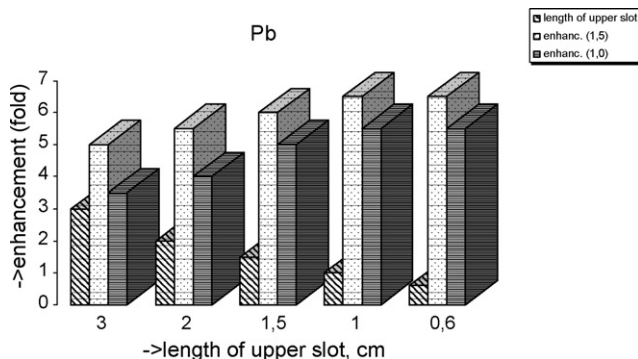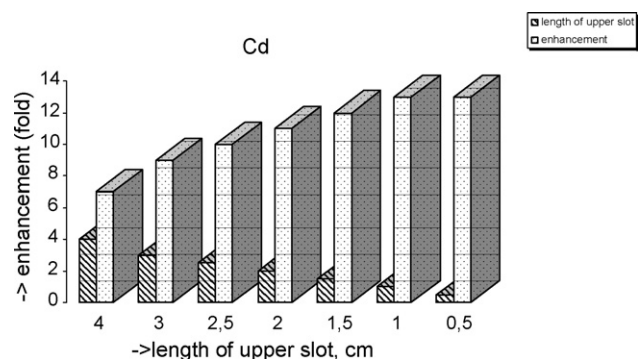

Fig. 2. The sensitivity enhancements for Pb depending on the changes in length of upper slot, using tube length of 12 cm and thickness of 1.5 mm.

The mixture of concentrated nitric acid/hydrogen peroxide (1/1) (3 mL for 1 g of dried samples) were added to the ashed sample and heated up to drying. This procedure was repeated. After cooling, 3 mL of $1 \, mol \, L^{-1}$ nitric acid was added and centrifuged, if necessary. The clear solutions were measured by FAAS and STAT-FAAS for metal determinations. The blank digests were carried out in the same way.

2.5. Microwave (MW) ashing

To assess the losses of the studied metals in dry digestion procedure, some samples were also digested by using MW energy. Approximately 0.2 g of dried samples was transferred into Teflon bomb and 1 mL of the mixture of HNO_3/H_2O_2 was added. The bomb was closed, placed inside the microwave oven, and microwave radiation was carried out for 3 min at 450 W. After a 4-min cooling period and adding 1 mL of the same acid mixture, the microwave radiation was repeated for 3 min. After cooling, the digest was diluted to 3 mL by adding $0.1 \, mol \, L^{-1} \, HNO_3$. The solution was centrifuged, if necessary. The clear solution was measured by FAAS and STAT-FAAS for metal determinations. Blank digests were carried out using the same procedures.

3. Results and discussion

It is known that the enhancement in the sensitivity of FAAS is importantly dependent on the flow rate of the aspirated solution. In this study, the speed of the aspirated solution was measured as 1 mL/11 s. Table 1 shows the obtained results for various designs of quartz tube together with the applied changes. The effect of parameters, such as, the internal diameter and the wall thickness of the tube, length of the upper slot and length of the tube on the improvement of sensitivity were examined. The observed improvements in the sensitivity can be summarized as follows.

Figs. 2–5 were obtained from the data given for Pb and Cd in Table 1. As it can be seen from these Figures, the sensitivity enhancement depending on the lengths of the upper slot is found significantly higher than that on the other parameters. Moreover, more improvements in the sensitivities are obtained using the tube having length of 12 cm as compared with the length of 11 cm. The sensitivity enhancement depending on tube length is higher in Cd than in Pb. Finally, higher enhancement in the

Table 1
The obtained improvements in the sensitivity of Pb, Cd and Cu by using STAT-FAAS

Diameter of tube (mm)	Length of upper slot (cm)	Length of tube (cm)	Enhancement in sensitivity		
			Pb	Cd	Cu
6[a]	4	12	4	7	1
6[a]	3	12	5.5	9	2
6[a]	2.5	12	6	10	2
6[a]	2	12	6.5	11	3
6[a]	1.5	12	7	12	3
6[a]	1	12	7	13	3
6[a]	0.5	12	7	13	3
5[a]	3	12	5	10	1
5[a]	2	12	5	12	1
5[a]	1	12	6	13	1
5[a]	0.5	12	6	13	1
6[a]	3	11	5	8	2
6[a]	2	11	5.5	9	3
6[a]	1.5	11	6	10	3
6[a]	1	11	6.5	11	3
6[a]	0.6	11	6.5	11	3
6[b]	3	11	3.5	6	1
6[b]	2	11	4	7	2
6[b]	1.5	11	5	8	2
6[b]	1	11	5.5	9	2
6[b]	0.6	11	5.5	9	2
L of Q as ng mL^{-1} with direct FAAS			200	40	80

The lengths of the lower slot are 5 cm.
[a] Tube thickness is 1.5 mm.
[b] Tube thickness is 1.0 mm.

Fig. 3. The sensitivity enhancements for Pb depending on the changes in length of upper slot and thickness of 1.5 mm, using tube length of 11 cm.

Fig. 4. The sensitivity enhancements for Cd depending on the changes in length of upper slot, using tube length of 12 cm and thickness of 1.5 mm.
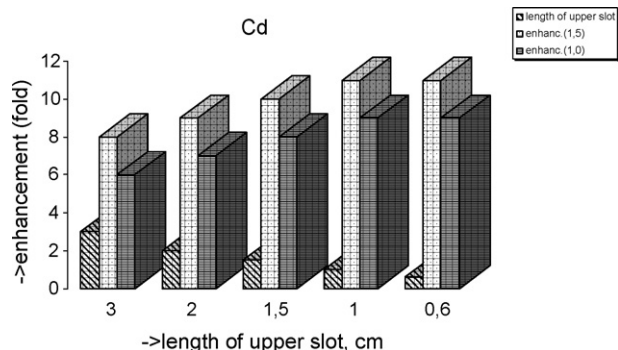
Fig. 5. The sensitivity enhancements for Cd depending on the changes in length of upper slot and thickness of 1.5 mm, using tube length of 11 cm.

sensitivity of lead and cadmium are observed using the tube thickness of 1.5 mm, as compared with the tube of 1.0 mm. This can be attributed to the more numbers of neutral atoms in the more stable chemical environment due to the homogenous temperature, in the tube thickness of 1.5 mm. As it can be seen from Table 1, the sensitivity is not improved much when the tube has the diameter of less than 6 mm for both of Pb and Cd. This result can be related to the diameter of light, which is larger than 5 mm, particularly in entrance of the tube. As a result, the determination of Pb and Cd concentrations as low as 30 and 3 μg L^{-1} were achieved by the modified STAT-FAAS method in which the tube had the length of 1.0 cm and the diameter of 6 mm in the upper slot.

The obtained calibration graphs for Pb by using different designed tubes were given in Fig. 6, and the calibration curves were found to be linear in the given ranges. The equations of the calibration curves for Pb without STAT and with most sensitive STAT are as follows:

$Y = 0.0468X + 0.5342 R^2 = 0.9995$ for Pb without STAT (200–2000 ng mL^{-1}).
$Y = 0.3056X - 0.0734 R^2 = 0.9999$ for Pb with most sensitive STAT (30–400 ng mL^{-1}).
$Y = 0.3042X + 38.93 R^2 = 0.9997$ for Pb using standard additions (0.0–400 ng mL^{-1}), respectively.

The obtained calibration graphs for Cd by using different designed tubes were given in Fig. 7, and the calibration curves were found to be linear in the given ranges. The equations of the calibration curves for Cd without STAT and with most sensitive STAT are as follows:

$Y = 0.2437X + 0.214 R^2 = 1.0000$ for Cd without STAT (40–800 ng mL^{-1}).
$Y = 3.1284X + 0.3547 R^2 = 0.9999$ for Cd with most sensitive STAT (3.0–40 ng mL^{-1}).
$Y = 3.1074X + 31.288 R^2 = 0.9996$ for Cd using standard additions (0.0–40 ng mL^{-1}), respectively.

As it can be seen from the data for Cu in Table 1, the sensitivity enhancement depending on the lengths of the upper slot is found higher. Moreover, higher enhancement in the Cu
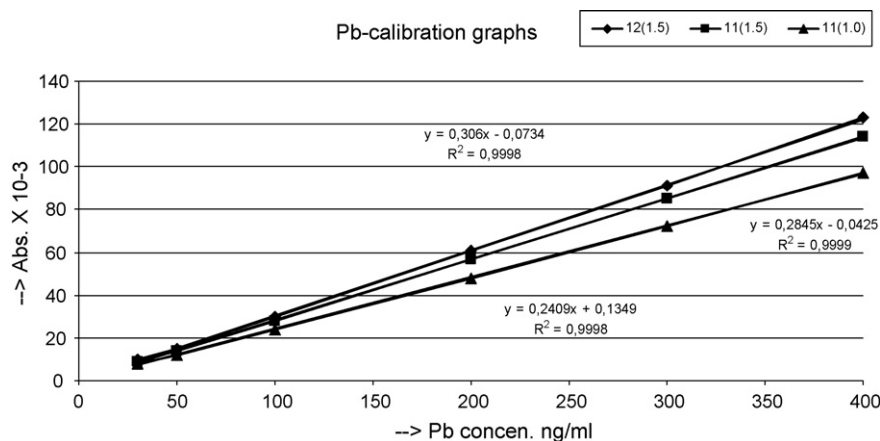
Fig. 6. The obtained calibration graphs for Pb using tubes having diameter of 6.0 mm, length of upper slot of 1.0 cm. The terms 12 (1.5); length of tube: 12.0 cm and tube thickness: 1.5 mm, 11 (1.5); length of tube: 11.0 cm and tube thickness: 1.5, 11 (1.0); length of tube: 11.0 cm and tube thickness: 1.0.

sensitivity is observed using the tube thickness of 1.5 mm, in comparison to the tube of 1.0 mm, similar to Pb and Cd. The sensitivity is decreased much when the tube has the diameter of less than 6 mm for Cu unlike Pb and Cd. This result can be attributed to the diameter of light of copper HCL lamp, which is larger than 5 mm, particularly at the entrance of the tube.

The calibration graphs together with standard additions graph for Cu by using the designed tubes including the length of upper slot of 1.0 cm, the length of tube of 11.0 cm were examined, and the calibration curves were found to be linear in the given ranges. The equations of these curves for Cu are as follows:

$Y = 0.102X – 0.2 R^2 = 0.9999$ for Cu without STAT (100–1000 ng mL^{-1}).

$Y = 0.318X - 0.3902 R^2 = 0.9999$ for Cu with most sensitive STAT (30–400 ng mL^{-1}), by using tube thickness of 1.5 mm.

$Y = 0.2234X - 0.3171 R^2 = 0.9999$ for Cu with STAT (30–400 ng mL^{-1}), by using tube thickness of 1.0 mm.

$Y = 0.3173X + 41.646 R^2 = 0.9997$ for Cu using standard additions (0.0–400 ng mL^{-1}).

As a result, the determinations of Cu concentrations as low as 30 μg L^{-1} were achieved by the modified STAT-FAAS method in which the tube had the length of 1.0 cm, the diameter of 6 mm in the upper slot and the wall thickness of 1.5 mm.

The main advantages of the STAT-FAAS compared to the conventional FAAS lie in the increased sensitivity and in the reduction of potential interferences because the former technique allows greater dilution of the sample. Devitrification of the slotted quartz tube was prevented by aspirating of a 1% (m/v) lanthanum solution. As a result, the service life of quartz tube was increased. On the other hand, it was observed that the service life of the quartz tube was related to the wall thickness of the tubes. The measurements more than 100 cycles can be done using the tube having a wall thickness of 1.5 mm.

3.1. Analytical performance

Levels of Pb, Cd and Cu in the reagent blanks in the total analytical steps were found to be 8.0, 0.5 and 3.5 ng mL^{-1} with standard deviations (s) of 1.0, 0.1 and 0.7 ng mL^{-1}, respectively. Therefore, the detection limit, defined as three times of the s values of blanks, was calculated as 3.0, 0.3 and 2.1 ng mL^{-1}. Limit
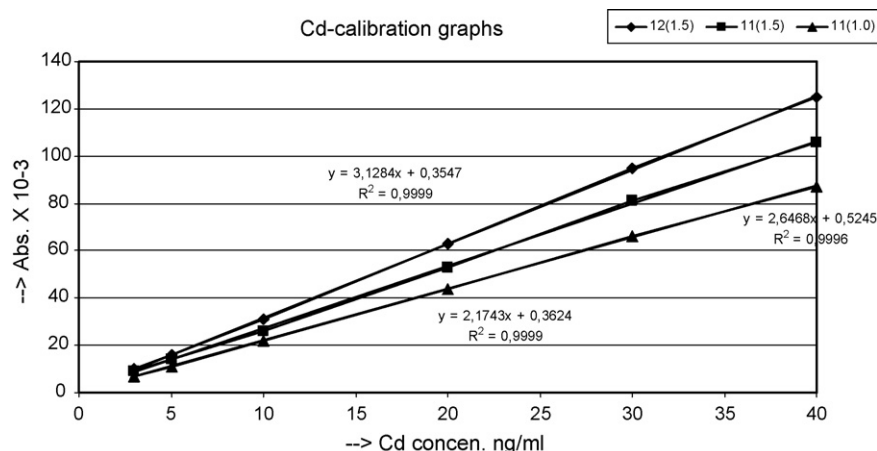

Fig. 7. The obtained calibration graphs for Cd using tubes having diameter of 6.0 mm, length of upper slot of 1.0 cm. 12 (1.5): length of tube: 12.0 cm, tube thickness: 1.5 mm, 11 (1.5): length of tube: 11.0 cm, tube thickness: 1.5, 11 (1.0): length of tube: 11.0 cm, tube thickness: 1.0.

Table 2
The observed metal concentrations in plant leaves taken from around Gaziantep cement and textile industries

Plant	Pb (mg kg^{-1})		Cd (µg kg^{-1})		Cu (mg kg^{-1})	
	Cement (ICPMS)	Textile (ICPMS)	Cement (ICPMS)	Textile (ICPMS)	Cement (ICPMS)	Textile (ICPMS)
Cedrus libani	7.6 ± 0.9	1.3 ± 0.3 (1.3 ± 0.2)	39 ± 8	50 ± 5 (46 ± 4)	3.0 ± 0.4	2.4 ± 0.5 (2.8 ± 0.4)
Picea		1.1 ± 0.2 (1.0 ± 0.2)		23 ± 4 (20 ± 2)		2.5 ± 0.3 (2.3 ± 0.2)
N. Oleander	2.1 ± 0.5 (1.8 ± 0.3)	2.1 ± 0.3 (2.3 ± 0.3)	66 ± 12 (61 ± 5)	56 ± 6 (52 ± 5)	8.2 ± 1.0 (8.7 ± 1.0)	3.7 ± 0.5 (4.0 ± 0.7)
Aesculus	11 ± 2 (10 ± 1)		41 ± 8 (46 ± 7)		5.8 ± 1.0 (6.2 ± 0.9)	
Morus L.	0.8 ± 0.2	2.4 ± 0.4 1.9 ± 0.2[a]	11 ± 4	18 ± 2 19 ± 5[a]	4.8 ± 0.5	3.3 ± 0.3 3.5 ± 0.3[a]
Eriobotrya Japonica	4.0 ± 0.5 (3.4 ± 0.5)	2.3 ± 0.2 (2.7 ± 0.4)	176 ± 26 (200 ± 32)	367 ± 44 (394 ± 40)	2.8 ± 0.5 (3.2 ± 0.4)	4.0 ± 0.6 (4.4 ± 0.5)
Rosa canina		1.5 ± 0.4 (1.8 ± 0.1)		40 ± 5 (46 ± 8)		3.2 ± 0.4 (3.6 ± 0.2)
Prunus domestica	6.7 ± 1.2		7 ± 2		4.0 ± 0.8	
Punica granatum	6.8 ± 0.8	3.5 ± 0.6	44 ± 6	36 ± 4	4.7 ± 0.6	3.0 ± 0.2
Cydonia oblonga	4.4 ± 0.3 (4.4 ± 0.4)		112 ± 13 (103 ± 10)		5.3 ± 0.5 (5.9 ± 0.8)	
Ficus carica	3.0 ± 0.2	2.5 ± 0.6	30 ± 5	32 ± 4	2.5 ± 0.3	1.7 ± 0.2
Juglans	5.0 ± 0.4	2.5 ± 0.4 (2.9 ± 0.3)	18 ± 4	25 ± 7 (28 ± 6)	2.8 ± 0.5	3.3 ± 0.6 (3.7 ± 0.5)
Apple		2.6 ± 0.4 2.9 ± 0.5[a]		31 ± 7 33 ± 7[a]		2.7 ± 0.3 2.5 ± 0.1[a]
Armena		2.4 ± 0.4 2.3 ± 0.3[a]		24 ± 2 18 ± 3[a]		3.3 ± 0.1 3.3 ± 0.2[a]
Prunus		2.9 ± 0.7 (3.3 ± 0.6)		10 ± 2 (9 ± 4)		5.4 ± 1.0 (6.0 ± 0.6)
SRM-Tomato leaves-1573a	–		Certified 1520 ± 40	Found 1495 ± 25	Certified 4.70 ± 0.14	Found 4.5 ± 0.12

The values in parenthesis are obtained by using ICP-MS.

[a] These values are obtained by using MW ashing.

of quantitation for Pb, Cd and Cu were found as 200, 40 and 80 for direct FAAS and 30, 3 and 30 ng mL^{-1} for the best conditions of sensitivity. For total analytical procedure containing the digestion procedure, the relative standard deviations measured for concentrations of 100, 20 and 80 ng mL^{-1} of Pb, Cd and Cu were found as 5, 3 and 4%, respectively ($n = 8$).

The accuracy of the method was studied by examining the Standard Reference Material-Tomato Leaves-1573a. The results were given in Table 2. It can be seen that the recovery values for Cd and Cu in Tomato Leaves-1573a was found as 96 and 98%, respectively.

In addition, the plant leaves containing the highest concentrations of Pb and/or Cd and/or Cu were analyzed by using both direct conventional FAAS and the STAT-FAAS. The obtained results using STAT-FAAS were compared with those obtained from the direct conventional FAAS. It was observed that the results obtained from STAT-FAAS were agreed with the results obtained from the conventional FAAS, at least 95%. In addition, the recoveries of Pb, Cd and Cu from the plant leaves fortified with the Pb, Cd and Cu were used to test of the accuracy of the modified method. The concentrations of Pb, Cd and Cu spiked to the samples are in the range of 100–300, 10–30 and 40–60 ng mL^{-1}, respectively. It was found that at least 96% of Pb, Cd and Cu added to the plant leaves were recovered. The effect of contamination was eliminated by subtracting the obtained values for blanks. In addition, to overcome the enhancement or suppression due to the presence of major components of the leaves matrix, calibration solutions were performed within the sample matrix itself. On the other hand, the standard additions method for the determination of Pb, Cd and Cu in the plant samples was examined. As described above, the slopes of the calibration curves were compared with the slopes obtained by the standard additions method. These results indicate the absence of chemical interferences, because the slopes of calibration curves and standard additions are identical for three studied elements. Therefore, the calibration graphs were used to determine Pb, Cd and Cu in the studied plant samples. The optimized method was applied to the determination of lead, cadmium and copper

in different plant leaves using the quartz tube having the best conditions described above.

Finally, it is observed that there is not a significant difference between the data (Table 2) obtained by FAAS and ICP-MS methods using *t*-test at confidence level of 90% for the studied metals. Similarly, Pb, Cd and Cu concentrations in plant samples were found to be in acceptable limits by using dry ashing in considering *t*-test at confidence level of 90% as compared with the MW ashing results. No losses of Pb and Cd in dry ashing can be attributed to the differences in matrices [11].

3.2. Application

Lead, Cd and Cu concentrations in the leaves of various plants are summarized in Table 2. As it can be seen that lead concentration (dw) ranges from 0.8 to 11 µg g^{-1} for the cement factory area and 1.1–3.5 µg g^{-1} for the textile industry area. This variation may be depending on varying uncontaminated and polluted areas by cement factory. The authors generally determined the metal concentrations in plants to evaluate atmospheric pollution [5,27,28]. From Table 2, Pb concentrations in the leaves of *Cedrus libani* taken around cement factory were found to be higher about five times than in the textile area.

Cd concentrations in leaves of *E. Japonica* and *Cydonia oblonga* plants were found to be 10-fold higher than in those other plants taken around cement factory. As a result, the leaves of these two plants can be used as biomonitors for environmental Cd pollution. Higher Cd concentration (367 ng g^{-1}) in *E. Japonica* leaves taken around textile industry than in those other plants taken from the same area, and in the same plant taken around cement factory also support this conclusion. The observed Cu concentrations in the studied plant leaves are in acceptable limits.

4. Conclusions

It has been demonstrated that the optimized technique can be used for the determination of ultratrace concentrations of

Pb, Cd and Cu in analytical samples. The proposed method has some advantages such as high speed, less risk of contamination, low cost and easy manufacturing of the required quartz tube. Although the achieved improvement is modest (7-fold for Pb, 13-fold for Cd and 3-fold for Cu), the modified online method has much importance in comparison with the other offline enrichment techniques such as adsorption or extraction because of its simplicity and instantly applicability.

Finally, the sensitivity between the FAAS and flameless AAS for some elements such as lead and cadmium is bridged gradually via the atom trap in FAAS. In this study, the sensitivity improvement, which has not been obtained so far by STAT, has been achieved for Pb and Cd by using very simple modifications in the STAT. The limits of quantitation were found to be $30 \, \text{ng} \, \text{mL}^{-1}$ for Pb, $3 \, \text{ng} \, \text{mL}^{-1}$ for Cd and $30 \, \text{ng} \, \text{mL}^{-1}$ for Cu. The required volume of sample for this method is less in comparison with other enrichment methods; i.e., only 0.9 mL of solution is sufficient for three metal determinations.

References

[1] Sjs. Flora, J. Environ. Biol. 23 (1) (2002) 25.
[2] G.F. Nordberg, Biometals 17 (5) (2004) 485.
[3] IARC, Cadmium and cadmium compounds, in: IARC Monographs on the Evaluation of Carcinogenic Risks to Humans, France, vol. 58, Beryllium, Cadmium, Mercury, and Exposures in the Glass Manufacturing Industry, IARC, Lyon, 1993.
[4] M. Yaman, Curr. Med. Chem. 13 (21) (2006) 2513.
[5] A. Mulgrew, P. Williams, Biomonitoring of air quality using plants, Air Hygiene Report No 10, Berlin, Germany, WHO CC, 165 pp., 2000.
[6] WHO (World Health Organization), Fifty-Third report of the Joint FAO/WHO Expert Committee on Food Additives, WHO Technical Report Series 896, Geneva, Switzerland, 2000.
[7] M. de, G. Pereira, M.A.Z. Arruda, Microchim. Acta 141 (2003) 115.
[8] H.M. Ortner, E. Bulska, U. Rohr, G. Schlemmer, S. Weinbruch, B. Welz, Spectrochim. Acta B 57 (2002) 1835.
[9] A.B. Volynsky, Spectrochim. Acta B 53 (12) (1998) 1607.
[10] B.F. Senkal, M. Ince, E. Yavuz, M. Yaman, Talanta 72 (2007) 962.
[11] M. Yaman, S. Gucer, Analyst 120 (1995) 101.
[12] M. Yaman, G. Kaya, Anal. Chim. Acta 540 (2005) 77.
[13] F.A. Aydin, M. Soylak, Talanta 72 (1) (2007) 187.
[14] H. Matusiewicz, Spectrochim. Acta B 52 (12) (1997) 1711.
[15] R.J. Watling, Anal. Chim. Acta 97 (1978) 395.
[16] A.A. Brown, D.J. Roberts, K.V. Kahokola, J. Anal. At. Spectrom. 2 (1987) 201.
[17] H. Matusiewicz, R. Sturgeon, V. Luong, K. Moffatt, Fresenius. J. Anal. Chem. 340 (1991) 35.
[18] H.W. Sun, L.L. Yang, D.C. Zhang, J. Anal. At. Spectrom. 11 (1996) 265.
[19] D. Korkmaz, S. Kumser, N. Ertas, M. Mahmut, O.Y. Ataman, J. Anal. At. Spectrom. 17 (2002) 1610.
[20] M. Yaman, I. Akdeniz, Anal. Sci. 20 (2004) 1363.
[21] M. Yaman, Anal. Biochem. 339 (2005) 1.
[22] M. Yaman, J. Anal. At. Spectrom. 14 (1999) 275.
[23] M. Yaman, Y. Dilgin, S. Gucer, Anal. Chim. Acta 410 (1–2) (2000) 119.
[24] M. Yaman, Y. Dilgin, Atom. Spectrosc. 23 (2) (2002) 59.
[25] M. Yaman, N. Cokol, Atom. Spectrosc. 25 (4) (2004) 185.
[26] M. Yaman, Spectrosc. Lett. 34 (2001) 763.
[27] M. Singh, P. Goel, A.K. Singh, Environ. Monit. Assess. 107 (1–3) (2005) 101.
[28] B. Wolterbeek, Environ. Pollut. 120 (2002) 11.

Erratum

Erratum to "Coated graphite-epoxy ion-selective electrode for the determination of chromium(III) in oxalic medium" [Talanta 63 (2) (2004) 303–307]

S. Khalil *, A.A. Wassel, F.F. Belal

Teachers College at Riyadh, Department of Chemistry, Riyadh, Saudi Arabia

Available online 1 April 2008

This article has been retracted at the request of the Talanta Editors-in-Chief.

After publication this article was discovered to have been plagiarized from an earlier work by Orlando Fatibello-Filho, Marcos Fernando de Souza Teixeira, Alexandre Zambon Pinto, presented in their paper '*Coated graphite-epoxy ion-selective electrode for the determination of iron*(III) *in oxalic medium*', published in Analytical Letters 30 (1997) 417–427. We very much regret this error, and offer our apologies to Professor Fatibello-Filho and his co-workers.

Development of an SPME–GC–MS/MS procedure for the monitoring of 2-phenoxyethanol in anaesthetised fish

Eva Klimánková [a], Kateřina Riddellová [a,*], Jana Hajšlová [a], Jan Poustka [a],
Jitka Kolářová [b], Vladimír Kocourek [a]

[a] *Institute of Chemical Technology, Faculty of Food and Biochemical Technology,*
Department of Food Chemistry and Analysis, Technická 3, 166 28 Prague 6, Czech Republic
[b] *University of South Bohemia in České Budějovice, Research Institute of Fish Culture and Hydrobiology Vodňany (USB RIFCH),*
Zátiší 728/II, 389 25 Vodňany, Czech Republic

Abstract

2-Phenoxyethanol (ethylene glycol monophenyl ether, $C_8H_{10}O_2$) is a promising anaesthetic agent used in fisheries and aquaculture. The aim of this study was to develop a fast and easy method to determine 2-phenoxyethanol residue levels in fish tissue and blood plasma, and, subsequently, to use the method to monitor the dynamics of 2-phenoxyethanol residues in fish treated with anaesthetic.

We developed a new procedure that employs solid phase microextraction (SPME) of the target analyte from the sample headspace followed by gas chromatography–mass spectrometry (GC–MS). Both sample handling, aimed at maximum transfer of 2-phenoxyethanol into the headspace, and SPME–GC–MS conditions were carefully optimised. Using a divinylbenzene/Carboxen/polydimethylsiloxane (PDMS/CAR/DVB) fiber for 60 min sampling at 30 °C and an ion trap detector operated in MS/MS mode, we obtained detection (LOD) and quantification (LOQ) limits of 0.03 and 0.1 mg kg^{-1} of sample, respectively. The method was linear in a range of 0.1–250 mg kg^{-1} and, depending on the sample matrix and spiking level, a repeatability (expressed as relative standard deviation, R.S.D.) of between 3% and 11% was obtained.

1. Introduction

Anaesthetic agents are routinely used in aquaculture to allow the performance of disruptive procedures. They reduce the injuries and stress caused to fish in their handling; although, on certain occasions, anaesthesia itself may evoke a stress response or immunodepression [1,2,6,8]. Modern fish anaesthetics should meet a number of general requirements; in particular, high solubility of the substance, rapid effect, wide margin of safety, spontaneous recovery of fish and no residue. At the same time, the anaesthetics should be harmless to both fish and human beings, as well as to the environment.

Among the many anaesthetic agents used, 2-phenoxyethanol (ethylene glycol monophenyl ether, $C_8H_{10}O_2$) is considered to be highly suitable for aquacultural practices because of its easy synthesis, low price, bactericidal and fungicidal properties, and rapid action, together with the fast and uneventful recovery of the fish to which it is administered. Despite these advantages, 2-phenoxyethanol has not yet been approved for use in fish intended for human consumption. With no maximum residue limit (MRL) having yet been set, use of this promising anaesthetic agent remains illegal according to EEC Regulation 2377/90 [3].

To the best of our knowledge, existing papers are primarily concerned with the mode of action of anaesthetic agents used by fish biologists. Some comparative studies on the efficacy of anaesthetic chemicals have also been published, together with information about their effects on biochemical profile of blood [4–8]. However, because more data is required if

---

* Corresponding author. Tel.: +420 220 443 218; fax: +420 220 443 186.
E-mail address: katerina.riddellova@vscht.cz (K. Riddellová).

2-phenoxyethanol is to be registered, our research encompassed the investigation of its acute toxicity, the histological examination of fish tissue and the determination of 2-phenoxyethanol residue levels in treated fish.

None of the aforementioned papers reported on analytical strategies applicable to the determination of anaesthetic residues in treated fish. To enable 2-phenoxyethanol analysis in experimental samples (fish tissue and blood plasma), we developed a new procedure that employs solid phase microextraction (SPME) [9,10] to sample the target analyte from the matrix headspace, followed by gas chromatography–mass spectrometry (GC–MS) to detect it. Subsequently, this method was used to monitor the dynamics of 2-phenoxyethanol residues in fish treated with anaesthetic.

2. Experimental

2.1. Chemicals and materials

A standard of 2-phenoxyethanol [CAS No. 56257-90-0] (p.a. standard for GC) was supplied by Sigma–Aldrich (Czech Republic). Stock solution I ($40\,g\,L^{-1}$) of 2-phenoxyethanol was prepared in ethyl acetate (Merck, Czech Republic) and stored at $+4\,^{\circ}C$ prior to use. Every day, fresh stock solution I was prepared. Working standards in ethyl acetate were prepared from stock solution I at concentrations in a range of $0.03–18\,g\,L^{-1}$.

SPME fibers coated with: (i) divinylbenzene/Carboxen/polydimethylsiloxane ($50/30\,\mu m$ StableFlex, PDMS/CAR/DVB), (ii) polyacrylate ($85\,\mu m$, PA) and (iii) carbowax/divinylbenzene ($65\,\mu m$, CW/DVB) were supplied by Sigma–Aldrich (Czech Republic). Prior to use, all fibers were conditioned in accordance with the manufacturer's recommendations. Each day, before analysis of the samples began, short thermal "cleaning" of the fibers in a GC injector ($30\,min$ at $250\,^{\circ}C$) was performed, together with a blank run, to verify that no extraneous compounds were desorbed from the fiber.

Ten millilitres headspace vials (Sigma–Aldrich, Czech Republic) were cleaned by sonication: $20\,min$ in water with detergent, followed by $20\,min$ in distilled water, and finally by $20\,min$ in re-distilled acetone (Penta, Czech Republic). After heating at $220\,^{\circ}C$ for $4\,h$, the clean vials were covered with aluminium foil and stored. To verify that no interfering compounds were desorbed from the vial or chemicals, in each sample sequence a blank run from an empty vial was performed, together with analysis of a reagent blank sample.

Ultrapure water was obtained from a Milli-Q water purification system (Milipore, Germany).

An HS 250 basic device (IKA Laboratortechnik, Germany) was used to homogenize samples prior to SPME.

2.2. Fish samples

Anaesthetic treatment of fish was carried out by our project partner, the Institute of Fish Culture and Hydrobiology Vodňany.

Experimental fish were exposed to anaesthetic in a bath containing $0.30\,mL$ of 2-phenoxyethanol per $1\,L$ (dissolved in water at $10\,^{\circ}C$). After exposure, the fish were transferred to a bath containing clean water. To investigate the dynamics of 2-phenoxyethanol residues in both fish tissue and blood plasma, the fish were sampled at various purification times following their treatment and subsequent transfer to clean water.

Fish tissue was collected from back musculature at different sampling times: $10\,min$; $24\,h$; 7, 14, 21 and 28 days. Anaesthetised fish samples were analysed together with control samples, i.e. fish not exposed to anaesthetic. Six to 11 fish were collected at each sampling time.

Blood plasma was obtained by centrifuging the blood (taken from a tail fin) in a cooled centrifuge ($4\,^{\circ}C$, $837 \times g$). The samples were collected from three fish (A–C) both before and after anaesthetic treatment with 2-phenoxyethanol. Two samples of blood were collected at each sampling time: immediately after exposure; $15\,min$; 1, 4 and $24\,h$.

All samples were maintained at $-16\,^{\circ}C$ until analysis began.

2.3. Sample preparation

2.3.1. Samples for method optimisation

Tissue samples from fish not exposed to 2-phenoxyethanol were used to develop and characterize the SPME method.

Spiked samples without matrix modification were prepared as follows: $5\,\mu L$ of working standards was added to $2\,g$ of ground fish tissue to obtain a final spiking level of $3–382\,mg\,kg^{-1}$.

Subsequently, several alternative matrix modifications were tested: (i) $2\,g$ of either spiked tissue or tissue with incurred residue was transferred into a $10\,mL$ headspace (HS) vial, to which $2\,mL$ of ultrapure water was then added; (ii) $2\,g$ of tissue with incurred residue was ground with $2\,g$ of sodium sulphate; (iii) $2\,g$ of tissue with incurred residue was ground with $2\,g$ of sodium sulphate and then immersed in $3\,mL$ of ultrapure water in a $10\,mL$ HS vial.

All modified samples were shaken vigorously for $20\,min$ prior to SPME analysis.

2.3.2. Real samples of anaesthetised fish

Fish muscle tissue: $2\,g$ of frozen sample was ground with $2\,g$ of sodium sulphate and then immersed in $3\,mL$ of ultrapure water in a $10\,mL$ HS vial. The sample was vigorously shaken for $20\,min$ prior to SPME analysis.

Fish blood plasma: $0.5\,g$ of sample was weighed into a $10\,mL$ HS vial and analysed.

2.4. Optimised SPME procedure

Samples prepared according to the procedure described in Section 2.3.2 were incubated for $5\,min$ at $30\,^{\circ}C$ prior to automated SPME. The extraction was carried out using a divinylbenzene/Carboxen/polydimethylsiloxane ($50/30\,\mu m$ StableFlex, PDMS/CAR/DVB) fiber for $60\,min$ at $30\,^{\circ}C$. One minute desorption of the analyte took place in the injection port of the gas chromatograph, which was maintained at $250\,^{\circ}C$. The fiber was kept inside the GC injector port until the end of the GC run ($30\,min$).

Table 1
MS/MS conditions

Parameter	Range tested
Precursor ions	94, 138
Daughter ions	77.1, 94.1
Isolation window	0.5, 1, 2
Excitation voltage	1, 5, 10

2.5. GC–ITMS conditions

Automated HS-SPME of 2-phenoxyethanol was performed using a CombiPal multipurpose sampler (CTC Analytics, USA) connected to a GC–ITMS system consisting of a Trace GC 2000 gas chromatograph (Thermo Quest, USA) equipped with a PTV injector (liner volume 95 μL), digital pressure flow control (DPFC) and an ion trap mass spectrometric detector POLARIS Q (Finnigan, USA). An HP-Innowax capillary column (30 m length × 0.25 mm i.d., coated with 0.25 μm film, Agilent, USA) was employed to separate the extracted compounds. The initial oven temperature of 45 °C was maintained for 1 min, before being increased to 225 °C at a rate of 3 °C min^{-1}, and subsequently to 275 °C at 10 °C min^{-1} (total GC run time was 30 min). The injector was operated in a splitless mode with a 1 min sampling time (splitless period). The injection port, the transfer line and the ion source temperatures were set at 250, 275 and 200 °C, respectively. The detector was operated in electron ionisation mode (70 eV) using either Segment Scan (MS spectra recorded in a range of m/z 35–520) or MS/MS mode. The tested range of optimised parameters is summarised in Table 1.

The data was processed using XCALIBUR software, version 1.2.2 (Finnigan, USA).

3. Results and discussion

SPME as an innovative, solvent free technique [9,10] has become widely used in the analysis of flavours and fragrances [11–15], pharmaceutics [16] and contaminants in environmental [17,18], food and biological matrices [19,20].

Our choice of this technique for the extraction of 2-phenoxyethanol from fish samples was based on the ability of SPME to concentrate analytes, as well as on the need for simple sample handling.

To develop the procedure, parameters influencing the SPME process, such as fiber selection, extraction time, extraction temperature and matrix modification were first optimised. In addition to the use of Segment Scan operation mode, MS/MS [21–23] mode was also applied to increase the sensitivity of MS determination. The optimisation steps are described in detail below.

3.1. Optimisation of SPME method

To obtain high sensitivity and good repeatability of determination, HS-SPME, as an equilibrium technique, requires careful optimisation. Consequently, the main factors influencing the whole analytical process were investigated.

Because of the complex character of the analysed samples, headspace sampling was the only SPME mode considered. To avoid any potential change to the sample matrix caused by elevated temperatures, the decision to keep the sorption temperature at 30 °C was made at the beginning of our study. This, together with the fact that 2-phenoxyethanol is a relatively polar compound (log K_{ow} = 1.16) with relatively low vapour pressure (0.07 mmHg at 25 °C), makes the optimisation of headspace sampling difficult, but by no means impossible.

To identify the fiber most efficient for analyte extraction, three commercially available SPME fibers (PA, PDMS/CAR/DVB, CW/DVB), with different stationary phase selectivities, were evaluated. A fish tissue (unmodified) spiked at a level of 33 mg kg^{-1} served as the sample in these fiber testing experiments. All extractions were performed under the same conditions (60 min sorption at 30 °C). Unsatisfactory extraction efficiency results (based on detector response, i.e. signal to noise ratio comparison) were obtained using PA and CWX/DVB fibers. The mixed PDMS/CAR/DVB fiber produced the best results, and was therefore employed in our subsequent experiments.

Experiments focusing on the dynamics of 2-phenoxyethanol extraction were conducted with 5, 15, 30, 40 and 60 min extraction times at 30 °C. The experiments were carried out using samples of fish tissue spiked at a level of 1 mg kg^{-1}. The results obtained are shown in Fig. 1. The amount of extracted analyte increased continuously over the course of the extraction time range. To maintain laboratory sample throughput at an acceptable level, no further increase in extraction time was considered. The extraction time of 60 min was chosen for further analyses.

3.2. Sample preparation and modification

Initially, sample preparation for SPME analysis consisted solely of the grinding of fish tissue. However, relatively poor repeatability of 2-phenoxyethanol determination (relative standard deviation, R.S.D. = 25%, n = 5, level of 50 mg kg^{-1}) was obtained; most likely as a result of the differing water content of the analysed samples. In addition, the method sensitivity was too low (LOQ 1 mg kg^{-1}). These results indicated that more atten-
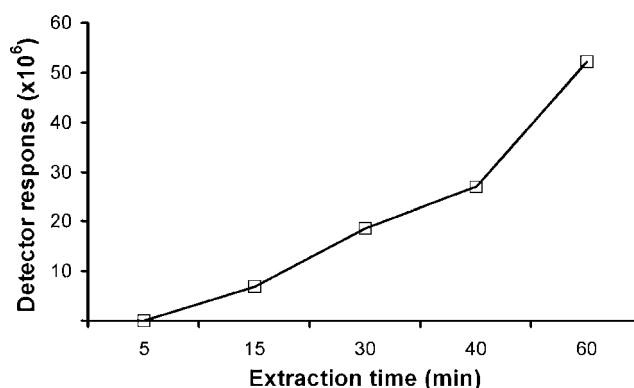

Fig. 1. Dynamics of 2-phenoxyethanol extraction.

Table 2
Comparison of relative responses of 2-phenoxyethanol in unmodified and modified samples

Sample	Without modification	Addition of water	Addition of sodium sulphate	Addition of sodium sulphate and water
Incurred residues	100%[a]	66% 10%	166%	100%[b]
Spiked sample	100%[a]	–	371%	

[a] Response of 2-phenoxyethanol in unmodified fish sample represents 100%.
[b] Response of 2-phenoxyethanol in fish sample ground with sodium sulphate and immersed in water represents 100%.

tion must be paid to the sample preparation step, and especially to unifying the water content of the samples. A well-known way of achieving this involves desiccating a sample by mixing it with a drying agent, such as sodium sulphate. Together with this method, the opposite approach, involving the addition of an excessive amount of water to the samples, was also investigated in our study.

To lower the LOQ and improve the repeatability of the method, several matrix modifications were tested: fish tissue immersed in ultrapure water; fish tissue ground with sodium sulphate; fish tissue ground with sodium sulphate and then immersed in ultrapure water. All modified samples were shaken vigorously for 20 min prior to SPME analysis.

For the experiments encompassing matrix modification, we used fish tissue samples spiked at a level of 40 mg kg^{-1}, as well as samples with incurred residues of 2-phenoxyethanol (fish after anaesthetic treatment, the level 100 mg kg^{-1}).

A comparison of the results obtained from these experiments is summarised in Table 2.

The addition of water always reduced the amount of 2-phenoxyethanol extracted. Conversely, grinding with sodium sulphate resulted in responses approximately 1.5 (166%)–3.5 (371%) times higher than the responses obtained for the unmodified samples. This result shows that homogenisation of a sample with sodium sulphate (i.e. simultaneous disintegration and drying of the sample) improves method sensitivity.

The difference between the increase in analyte response in the samples with incurred residues (166%) and the samples spiked with standard solution (371%) proves that dissimilar transitions to the headspace above the solid sample occurred. This can be a problem when the standard addition method (which involves spiking a matrix with a standard solution) is used for quantification.

Despite the fact that our earlier results indicated a possible reduction in the amount of 2-phenoxyethanol extracted following water addition, in an attempt to unify analyte transition, we also decided to test samples immersed in water after being ground with sodium sulphate. As can be seen from Table 2, the negative influence of water addition was not an issue in the case of these samples, for which 2-phenoxyethanol response was 10 times higher than for the samples only immersed in water.
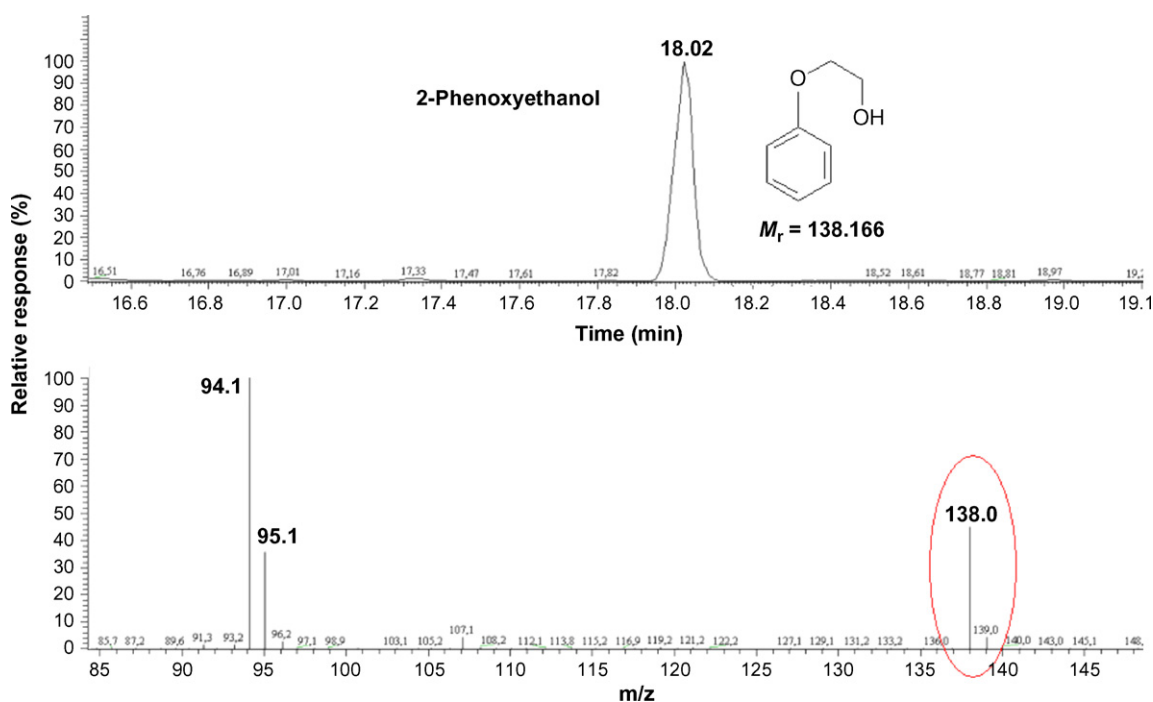

Fig. 2. Chromatogram and mass spectrum (Segment Scan) obtained by injection of standard of 2-phenoxyethanol in ethyl acetate (injection corresponds to 50 μg).
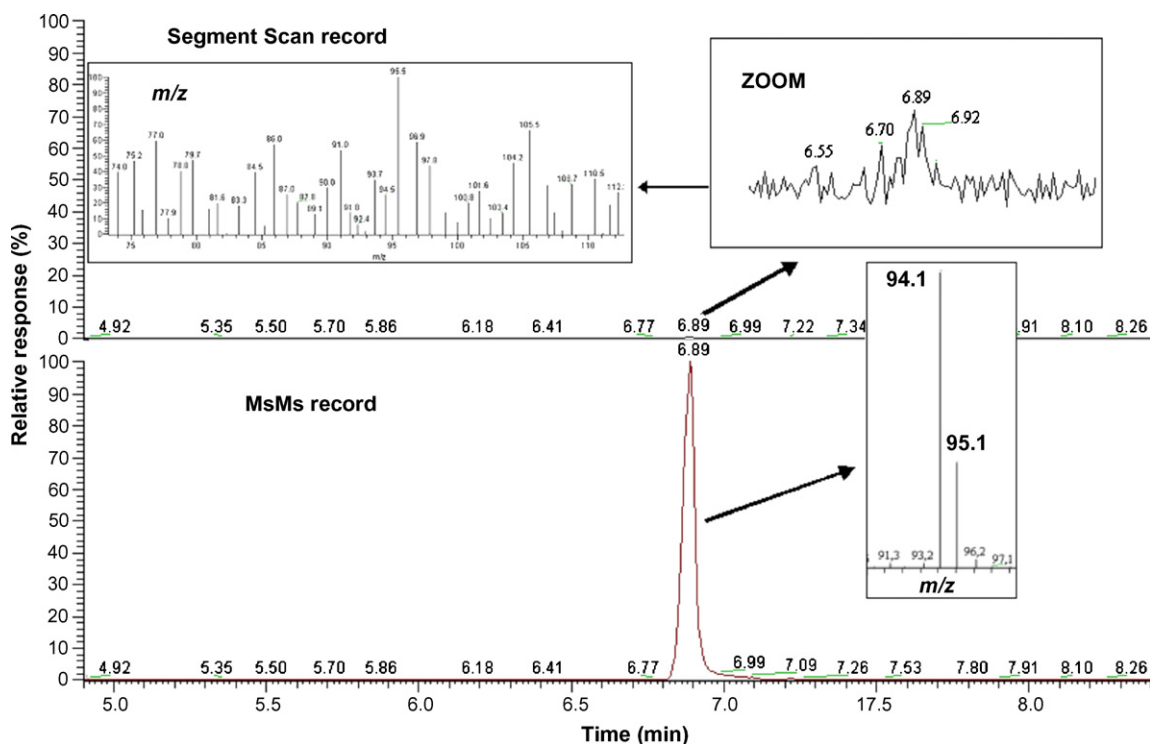
Fig. 3. Comparison of chromatograms obtained by Segment Scan and MS/MS detection modes. Sample of fish tissue spiked at a level of 0.36 mg kg^{-1}.

The blood plasma samples, having a completely different character, did not require any matrix modification, and were analysed immediately after being weighed into 10 mL glass vials.

3.3. Optimisation of MS detection

In addition to optimising the sample preparation strategy, the need to improve the sensitivity of the MS detection method was also addressed. The sensitivity of the ion trap detector was optimised by running it in MS/MS detection mode (rather than in the originally used Segment Scan single-MS mode) and by adjusting the relevant parameters (selection of precursor ion, excitation voltage, isolation window).

The spectra of 2-phenoxyethanol obtained in single-MS mode (EI, 70 eV) showed two major ions (m/z 94 and 138) in different ratios (see Fig. 2).

To achieve good selectivity of the MS/MS detection method, the m/z 138 ion (rather than the most abundant, but lower mass and, therefore, less selective m/z 94 ion) was selected for further optimisations. Evaluation of sensitivity was based on a comparison of the signal to noise ratios for these particular experiments. The best results were obtained with the following parameters: isolation window m/z 0.5; excitation voltage 1.0; excitation time 15 ms; medium excitation energy with the first product ion m/z 74 and the last product ion m/z 114.

The sensitivities of the Segment Scan and MS/MS modes are compared in Fig. 3. After fragmentation in MS/MS mode, the daughter ions m/z 94 and 95 were obtained (see zoom in MS/MS chromatogram). In comparison with Segment Scan mode (LOQ as high as 1 mg kg^{-1}), method sensitivity improved by one order

of magnitude with the use of MS/MS detection mode (LOQ 0.1 mg kg^{-1}).

3.4. Method validation

Once the final SPME and MS detection conditions (see Sections 2.4 and 3.3) were optimised, validation of the developed HS-SPME–GC–MS/MS procedure was carried out in terms of linearity range, repeatability and sensitivity.

Repeatability was determined by performing five replicate analyses and expressed as a relative standard deviation. R.S.D. values of 11% and 3% were, respectively, achieved for fish tissue samples spiked at 40 mg kg^{-1} and samples containing incurred residues (100 mg kg^{-1}). The method was linear within a range of 0.1–150 mg kg^{-1}, with a regression coefficient of
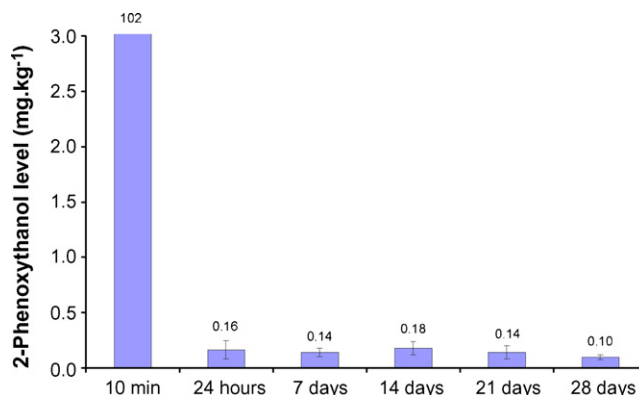

Fig. 4. Dynamics of 2-phenoxyethanol in fish tissue.

Table 3
Levels of 2-phenoxyethanol in tissue of rainbow trout

Purification time following anaesthetic treatment	Content in analysed sample (mg kg^{-1})												
	1	2	3	4	5	6	7	8	9	10	11	Average	R.S.D. (%)
10 min	120.18	100.16	88.95	116.65	98.69	95.73	105.34	116.01	94.24	97.01		101.88	10
24 h	0.33	0.25	0.24	0.17	0.19	0.10	0.11	0.10	0.10	0.13	0.14	0.16	36
7 days	0.19	0.15	0.18	0.12	0.20	0.12	0.11	0.10				0.14	27
14 days	0.26	0.27	0.17	0.12	0.14	0.14	0.11	0.15				0.18	39
21 days	0.18	0.17	0.23	0.14	<LOQ	0.10	0.16	0.14				0.14	41
28 days	<LOQ	0.12	<LOQ	0.13	<LOQ	<LOQ						0.10	24

Six to 11 samples were collected at each sampling time.

Table 4
Levels of 2-phenoxyethanol in fish blood samples

Sample	Code	Content in analysed sample (mg kg^{-1}) (% of initial content)			
		A	B	C	Average
Control sample (before anaesthetic treatment)	P1	–	–	–	–
Immediately after anaesthetic treatment	P2	254.6 (100)	252.1 (100)	137.1 (100)	214.6 (100)
15 min	P3	14.0 (5.5)	34.6 (13.7)	43.1 (31.5)	30.6 (14.3)
1 h	P4	12.8 (5.0)	5.6 (2.2)	14.7 (10.7)	11 (5.1)
4 h	P5	1.7 (0.7)	1.0 (0.4)	2.0 (1.5)	1,6 (0.7)
24 h	P6-a	1.4 (0.5)	0.8 (0.3)	0.9 (0.6)	1.0 (0.5)
24 h	P6-b	1.4 (0.6)	0.7 (0.3)	0.9 (0.6)	1.0 (0.5)

Samples from three fish were collected at each sampling time.

$r^2 = 0.9996$. An LOQ of 0.1 mg kg^{-1} was achieved in MS/MS detection mode.

An R.S.D. value of 10% was achieved for blood plasma samples containing incurred residues (level 250 mg kg^{-1}), and the method was linear within a range of 0.1–250 mg kg^{-1} ($r^2 = 0.9993$).

3.5. Dynamics of 2-phenoxyethanol in anaesthetised fish

The analytical procedure described above was used to analyse residues of 2-phenoxyethanol in fish tissue and blood plasma with the aim of monitoring its dynamics after anaesthetic treatment. As described in Section 2 (see Section 2.2), two groups
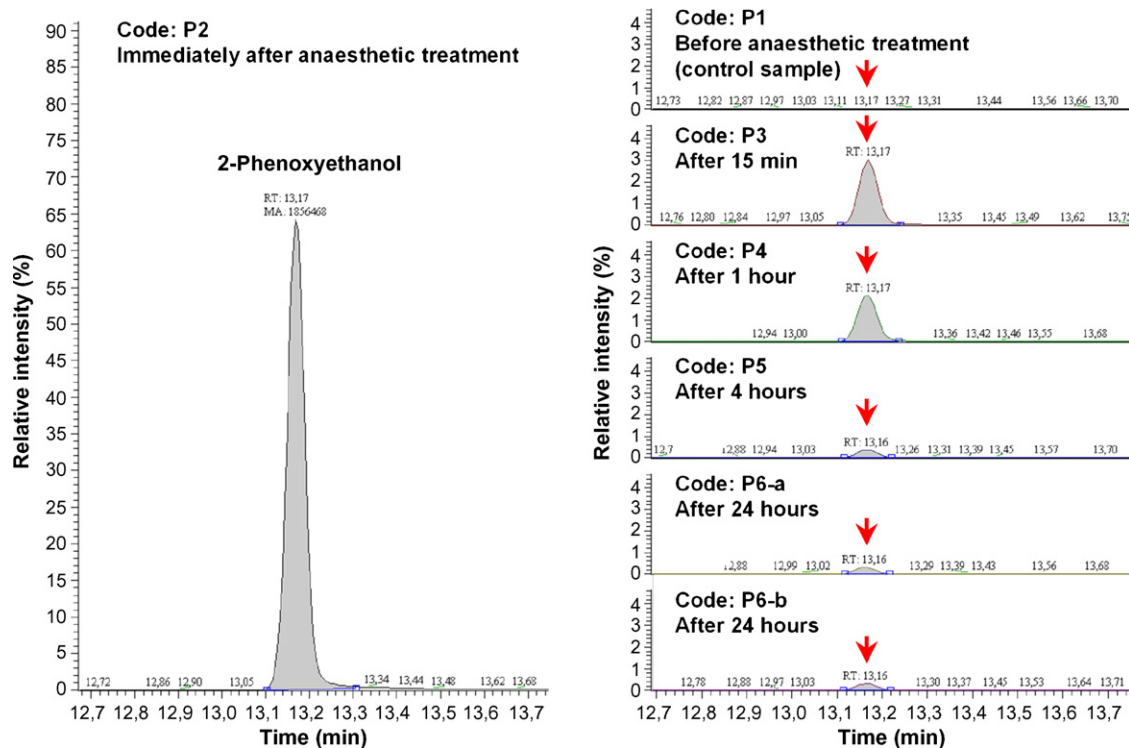

Fig. 5. Chromatograms of fish blood plasma samples taken from fish before and after anaesthetic treatment.

of samples, control fish and fish exposed to 2-phenoxyethanol, were studied.

3.5.1. Fish muscle tissue

At each sampling time, 6–11 samples were collected and analysed. The levels of 2-phenoxyethanol found in the analysed samples are summarised in Fig. 4 and Table 3.

No residues of 2-phenoxyethanol were detected in the control samples (fish not exposed to anaesthetic treatment). All fish samples collected 10 min after anaesthetic treatment showed high levels of 2-phenoxyethanol, with the mean being 102 mg kg^{-1}. Within the first 24 h after treatment, residue levels dropped remarkably to 0.16 mg kg^{-1}. This level remained more or less constant until the 28th day of purification, at which time a further slight decrease to 0.10 mg kg^{-1} was observed.

3.5.2. Blood plasma samples

At each sampling time, either one or two blood plasma samples were collected from three fish. The levels of 2-phenoxyethanol found in the analysed samples are summarised in Table 4 and Fig. 5.

During the first 15 min, a rapid decrease in 2-phenoxyethanol residue levels (down to 5–31% of the initial content) was observed. After 4 h, 2-phenoxyethanol content ranged from 1 to 2 mg kg^{-1} (0.4–1.5% of the original content) in all three analysed fish, and subsequently remained unchanged for the following 20 h. Twenty-four hours after anaesthetic treatment the mean residual amount of 2-phenoxyethanol in fish blood was 1 mg kg^{-1}, representing 0.5% of the initial amount detected immediately after anaesthetic treatment.

4. Conclusions

An SPME–GC–MS/MS method for the quantitative determination of 2-phenoxyethanol in fish tissue and blood plasma samples was developed with the aim of achieving the lowest possible LOD. Several parameters influencing both the SPME procedure and the MS detection method were optimised. The best results were obtained using a PDMS/CAR/DVB fiber for 60 min extraction of 2-phenoxyethanol from the sample headspace at 30 °C. Matrix modification proved to be the crucial step in achieving good method repeatability and sensitivity. In particular, fish tissue should be both ground with sodium sulphate and immersed in water prior to SPME analysis. (This procedure does not apply to blood plasma samples, which can be analysed without matrix modification.) The optimised headspace SPME–GC–MS/MS procedure resulted in both a low detection limit (LOD 0.03 mg kg^{-1}) and a low quantification limit (LOQ 0.1 mg kg^{-1}) for 2-phenoxyethanol in both tested biological materials.

The applicability of our method was proven by analyses of fish samples collected at different times following anaesthetic treatment. Significant reductions in 2-phenoxyethanol residue levels in both fish muscle tissue and blood plasma were observed during the first 24 h after treatment. These promising results support the registration of 2-phenoxyethanol as an anaesthetic agent in fish intended for consumption.

References

[1] H. Tsantilas, A.D. Galatos, F. Athanassopoulou, JHVMS 56 (2005) 130.
[2] P.L. Munday, S.K. Wilson, J. Fish Biol. 51 (1997) 931.
[3] Regulation (EEC) No. 2377/90, Council Regulation (EEC) No. 2377/90 of 26 June 1990 laying down a Community procedure for the establishment of maximum residue limits of veterinary medicinal products in foodstuffs of animal origin (OJ No. L 67 of 7.3.1997, p. 1).
[4] H. Tsantilas, A.D. Galatos, F. Athanassopoulou, N.N. Prassinos, K. Kousoulaki, Aquaculture 253 (2006) 64.
[5] C.C. Mylonas, G. Cardinaletti, I. Sigelaki, A. Polzonetti-Magni, Aquaculture 246 (2005) 467.
[6] J. Velisek, Z. Svobodova, V. Piackova, L. Groch, L. Nepejchalova, Vet. Med. Czech. 50 (2005) 269.
[7] J. Ortuno, M.A. Esteban, J. Meseguer, Vet. Immunol. Immunopathol. 89 (2002) 29.
[8] J. Velisek, Z. Svobodova, Acta Vet. Brno 73 (2004) 379.
[9] J. Pawliszyn, Theory and Practice, Wiley, New York, 1997.
[10] C.L. Artur, J. Pawliszyn, Anal. Chem. 62 (1990) 2145.
[11] V. Romeo, M. Ziino, D. Giuffrida, C. Condurso, A. Verzera, Food Chem. 101 (2007) 1272.
[12] T. Čajka, J. Hajšlová, J. Cochran, K. Holadová, E. Klimánková, J. Sep. Sci. 30 (2007) 534.
[13] T. Čajka, J. Hajšlová, LC GC Eur. 20 (2007) 25.
[14] M.C. Diaz-Maroto, M.S. Peréz-Coello, M.D. Cabezudo, Chromatographia 55 (2002) 723.
[15] R.A. Pérez, T. Navarro, C. de Lorenzo, Flav. Frag. J. 22 (2007) 265.
[16] X. Fu, Y. Liao, H. Liu, Anal. Bioanal. Chem. 381 (2005) 75.
[17] R. Stiles, I. Yang, R.L. Lippincott, E. Murphy, B. Buckley, J. Sep. Sci. 30 (2007) 1029.
[18] K. Holadová, G. Prokůpková, J. Hajšlová, J. Poustka, Anal. Chim. Acta 582 (2007) 24.
[19] F. Bianchi, M. Careri, M. Musci, A. Mangia, Food Chem. 100 (2007) 1049.
[20] S. Guillot, L. Peytavi, S. Bureaul, R. Boulangerc, J.-P. Lepoutred, J. Crouzeta, S. Schorr-Galindoa, Food Chem. 96 (2006) 147.
[21] J.J. Ramos, B. Gómara, M.A. Fernández, M.J. González, J. Chromatogr. A 1152 (2007) 124.
[22] B. Gómara, M.A. Fernández, M.J. González, L. Ramos, J. Sep. Sci. 29 (2005) 123.
[23] C. Zwiener, L. Kronberg, Fresenius J. Anal. Chem. 371 (2001) 591.

Application of multivariate analysis to the screening of molecularly imprinted polymers (MIPs) for ametryn

A.R. Koohpaei [a,1], S.J. Shahtaheri [b,*], M.R. Ganjali [c], A. Rahimi Forushani [d], F. Golbabaei [a]

[a] *Department of Occupational Health, School of Public Health, Medical Sciences, University of Tehran, Tehran, Iran*
[b] *Department of Occupational Health, School of Public Health, Center for Environmental Research, Medical Sciences/University of Tehran, Tehran, Iran*
[c] *Center of Excellence in Electrochemistry, Endocrine & Metabolism Research Center, University of Tehran, Tehran, Iran*
[d] *Department of Biostatistics, School of Public Health, Medical Sciences, University of Tehran, Tehran, Iran*

Abstract

Among the solid-phase extraction (SPE) techniques, a novel system for a triazine herbicide named ametryn, has been developed based on a molecular imprinted polymer (MIP) phase. Through this method, the synthesis of the complementary to ametryn MIP was accomplished and the factors influencing its efficiency have been optimized. Through the optimization process, the type and the amounts of functional monomer and solvents, template amount, cross-linker, initiator as well as the polymerization temperature were considered to be evaluated. Based on the obtained results, the optimum conditions for the efficient polymerized sorbent, considering the recovery efficiency were solvent: acetonitrile, 6.41 mL; monomer: methacrylic acid, 5.41 mmol; template: 1.204 mmol; cross-linker: 27.070 mmol; initiator: 2.03 mmol; temperature: 40.86 °C. The optimum molar ratio among the template, monomer and cross-linker for ametryn was 1:4.49:22.48. The reversed-phase HPLC-UV was used for the ametryn determination, using an isocratic solvent delivery system (acetonitrile: H_2O, 60:40), flow-rate of 0.8 mL min^{-1} and a UV wavelength of 220 nm. In line with the obtained results, using central composite design (CCD) can increase the precision and accuracy of synthesis and optimization of MIP to ametryn and possibly other similar analogues.
© 2008 Elsevier B.V. All rights reserved.

Keywords: Molecular imprinted polymers; Solid-phase extraction; Central composite design; Herbicides; Triazine; Ametryn

1. Introduction

The most widely used group of herbicides, since their discovery in the 1950s, is triazines including ametryn, atrazine, simazine, cyanazine and propazine. Triazinic herbicides were considered as systemic toxicants, causing a variety of acute health effects. On the other hand, the analysis of herbicides, in order to monitor, assess, evaluate and control their effects in the environment, is one of the most important fields in analytical chemistry [1]. In occupational and environmental assessment, a large number of samples are needed. Consequently, inexpensive and rapid analytical techniques are required [2]. In some efforts to reduce the cost, time and use of organic solvents in the organic trace analysis, many researchers have developed miniature methods, requiring fewer sample amounts and thus, less extracting solvents to carry out their analyses. In addition, new approaches such as solid-phase extraction (SPE), supercritical fluid extraction (SFE), accelerated solvent extraction (ASE) and solid-phase microextraction (SPME) using polymer-coated fibers have been investigated, demonstrating more promising approaches in the environmental analysis [3]. Other approaches, which are gaining popularity for the sample clean-up, include the immunoaffinity chromatography [4–6] and the molecular imprinting polymers (MIPs).

In the MIP technique, functional monomers and cross-linkers are polymerized in the presence of a template molecule, which is followed by the template removal from the resultant polymer network to leave a template-fitted cavity. The molecular imprinting technology is less expensive than the antibody production and may offer an alternative when the cost of the antibody production is prohibitive or the antibody performance is a problem.

---

* Corresponding author. Tel.: +98 91 21779019; fax: +98 21 88951390.
E-mail address: shahtaheri@tums.ac.ir (S.J. Shahtaheri).
[1] Present address: Department of Occupational Health, Qom University of Medical Sciences, Qom, Iran.

In addition, the molecular imprinted polymers are highly resistant to the organic solvent effects, unlike antibodies (or other biological receptors). Subsequently, the molecular imprints may have applications to the analysis of highly lipophilic compounds (such as PCBs or pesticides) either in a sample clean-up step or in a detection method [7]. The molecular imprinted polymers for triazinic herbicides have been a subject of many investigations in the recent years with interesting application in chemical analysis [8–11]. MIPs are used for SPE and chromatographic separation [1,12–18].

For a general use of the molecular imprinting technology, the class of the imprintable compounds needs to be extended and the existing recognition elements need to be improved in order to meet the requirements in the given application. The large number of compositional (monomers, cross-linkers, porogenic solvents, template to monomer ratios, etc.) and operational (initiation method, polymerization temperature and time) variables, present even in a relatively simple MIP preparation, coupled with the fact that they are dependent with each other, make it an extremely difficult task to optimize an MIP. In this development, a key factor is the identification and the optimization of the main factors, affecting the material structure and the molecular recognition properties.

The procedural optimization can be achieved in a traditional trial and error manner or with the assistance of chemometrics. Even using combinatorial methods under the best conditions, a few of the compositional variables can be explored. The complexity of these problems makes the application of chemometric methods an ideal opportunity for the design and the evaluation of the MIPs [19]. The chemometric approach is based on the use of an optimum set of experiments (experimental design), which allows the simultaneous variation of all the studied experimental factors [20]. Rather than making every combination in an *n*-dimensional matrix, these methods allow one to vary multiple parameters simultaneously. The utilization of the multivariate analysis of the 'response factor' (e.g. fractional binding of the template) in the polymers, which are synthesized and screened, allows the optimum polymer composition to be predicted. This approach has recently been used in several studies successfully. Navarro-Villoslada et al. [21] used this approach to optimize six key factors in the MIP preparation for the bisphenol A polymers. In that research, the polymers were synthesized as mini-MIPs and screened by HPLC, leading to a rapid and cost-effective identification of the optimized polymers. Kempe and Kempe [22] synthesized beaded polymers by suspension polymerization in mineral oil for their multivariate study and, then, screened for rebinding by radioligand counting methods. In this way, a more extensive screening became feasible and more sophisticated response parameters could be defined, if required using, e.g. competitive binding formats. Davies et al. [23] applied chemometrics to the optimization of highly selective and group selective polymers for sulphonamides. To achieve this aim, they used more sophisticated response factors, based on a multi-analyte competition assay, to estimate the rebinding ability of the synthesized polymers and to select the optimum sulphonamide structures to use as template and for the rebinding studies. The chemometric optimizations of

the template/monomer/cross-linker ratios led to the polymers that demonstrated either specificity or group selectivity depending on the experimental design. This methodology can open a new approach for the synthesis of tailor-made phases, called MIPs.

The aim of this work was the optimization of the main factors, affecting the material structure and the molecular recognition properties of the molecular imprinting polymers by a chemometric approach. Triazinic herbicide ametryn was chosen as the model system of this study. The triazinic herbicides are suitable models for these studies because they are relatively inexpensive and stable. As a consequence, the gram quantities necessary in a typical reaction can be handled without extraordinary precautions.

2. Experimental

2.1. Reagents

Ametryn, with greater than 98.2% purity, was obtained from Riedel-de-Häen (Seelze, Germany), 4-vinylpyridine, methacrylic acid (MAA, functional monomer) [79-41-4] and ethylene glycol dimethacrylate (EGDMA, co-monomer) [97-90-5] were purchased from the Merck Company, Germany. 2,2′-Azobisisobutyronitrile (AIBN, initiator) [78-67-1] was obtained from the Acros Company, USA. All solvents (acetic acid, acetonitrile, dichloromethane and methanol) were of analytical reagent grade (Merck, Germany). Ultra pure water was obtained from a Purite Purification System. Stock standard solutions ($1\,\mathrm{g\,L^{-1}}$) were prepared by weighing the solutes, their dissolution in acetonitrile and their storage at $-18\,^{\circ}\mathrm{C}$. The standard solutions were obtained with the dilution of the stock solutions in acetonitrile.

2.2. Equipment

All measurements were performed by a reversed-phase HPLC system from the Knauer Company (Germany), consisting of a K-1001 series high-pressure pump, a K-2006 photo diode-array detector and a VS injection valve, equipped with a 20-μL loop. The analytes were separated on a Chromolith Performance RR-C_{18}e 100 mm × 4.6 mm i.d. (Merch KGa A, Germany) and column guards (Chromolith Guard Cartridge Kit RP-C_{18}e and 5 cm × 4.6 mm i.d., 5 μm), using isocratic elution as follows: 60% acetonitrile and 40% purified water. Ametryn was monitored at 220 nm and quantified with external calibration using the peak area measurements ($R^2 = 0.9998$). Each sample was repeated three times to assure the chromatogram reproducibility. The flow-rate was set at $0.8\,\mathrm{mL\,min^{-1}}$. The system was linked with a LaserJet 1200 series printer for recording the chromatograms, using a 1456-1 Chromogate Data System, Version 2.55. For the polymer synthesis, the used apparatus included soxhlets and a heater unit, a liquid extraction unit (S&S, Germany), a reactor heater system (Memmert, Germany), a nitrogen supply system, an ultrasonic shaker (Tecna-6, Italy), a syringe-filtration unit (FH-0.45 μm, Millipore Corp., USA), PTFE filters (0.2 μm, Sartorius, Germany),

an oven (Memmert, Germany) and a shaker (Innova 4000). The amount of reagents was measured, using a digital balance (Sartorius-2024, Germany) for milligram quantities or less. The quantitative liquid transfers were performed with a pipette (Socorex, Germany).

2.3. Preliminary polymer preparation

In this study, non-covalent bulk polymerization was employed, as one of the successful molecular imprinting protocols [15,24], to obtain glassy polymer blocks to be used as powder after being crushed, ground and sieved. The preliminary molecularly imprinted polymers as center points of the experimental design were prepared as follows: 1-mmol ametryn and 4-mmol MAA were added to a 25-mL glass tube and, afterwards, the mixture was left for 5 min. Subsequently, EDMA (20 mmol), AIBN (2 mmol) and 5-mL acetonitrile were added. The mixture was purged with nitrogen for 5 min and the glass tube was sealed under this atmosphere. It was then placed at a thermostated water bath at 55 °C to start the polymerization process. After 24 h, the tube was broken, the obtained polymer was ground and sieved, and the particles with sizes between 50 and 105 μm were collected. The template was removed by soxhlet extraction using a two-step procedure (methanol:acetic acid washing (9:1, v/v) 18 h as a first step and methanol washing for 6 h as a second step). This procedure was optimized in this study to generate MAA-based binding sites complementary to ametryn. Finally, the produced powder was stored in desiccators. Furthermore, non-imprinted polymers were obtained following the same procedure without the addition of the template molecule. Safety precautions were considered during the preparation of the polymerization mixture, the grinding and the extraction of the polymer. These steps were performed in a safety cabinet, because they involve the handling of the toxic compounds: methacrylic acid, ethylene glycol dimethacrylate and 2,2′-azobisisobutyronitrile.

2.4. Qualitative optimization of the solvents and functional monomers

In order to select the best solvent and functional monomers, a screening plan was performed and through this approach, four experiments were designed (Table 1), namely as ametryn 1 to ametryn 4 (AME_1, AME_2, AME_3 and AME_4). The imprinted polymers were synthesized and examined (except for the solvents and functional monomers), following the same procedure with the preliminary molecularly imprinted polymers.

2.5. Experimental design approach

The factorial design requires fewer measurements than the classical one-at-a-time experiment to give the same precision. At the same time, it detects and estimates any interaction between the factors, which the classical experiment cannot do. The order of the running experiments was restrictedly randomized to eliminate the possible bias (restricted factor was the polymerization temperature) [25]. The standard approach to the analysis of the experimental design data is to evaluate a list of the main and interaction effects supported by an ANOVA table, indicating which effects are significant [20]. The Minitab, Release 14 for windows statistical software package was used for data manipulation [26]. At the first stage of the experimental design, six factors were selected as potentially affecting the rebinding efficiency. These factors can be the compositional variables, such as the amounts of functional monomer, template, cross-linker, porogen or solvent of polymerization, as well as the operational variables such as the initiator and polymerization temperature. Consequently, a two-level full factorial design of 2^6 was utilized following a linear and quadratic model, containing squared terms. This design involved sixty-four basic experiments, undertaken in random order plus four central points. The values, corresponding to the high (+), low (−) and central (0) points for each factor, are shown in Table 2. At the second stage, a central composite design (CCD) was used with three different α values (1.414, 2, 2.449) in order to assess the α effects on the experimental design result, adding twelve star points to the above 2^6 factorial design. Therefore, 80 runs for each α state were selected or totally 240 runs. For each run in the experiments, non-imprinted polymers (NIPs) were obtained. Table 2 lists the α values given to each factor.

2.6. Equilibrium-rebinding experiments

After the soxhlet extraction and the template removal from the polymer structure, the synthesized polymer was placed at a thermostated oven at 70 °C for 2 h. Afterwards about 1 g of the polymer particles was placed at a beaker, containing a 100 ng mL^{-1} ametryn solution. Finally, the mixture was placed in a digital shaker (100 rpm, 25 °C, for 5 h optimized in this study) and, then, filtered by syringe filter unit (FH-0.45 μm, Millipore Corp., USA). The analyte concentrations in the final solution, representing the analyte amount bound to the polymer, were determined by HPLC-UV as described above. The unbound analyte amount to the polymer was obtained by subtracting the analyte bound amount to the polymer from that of the initial analyte loaded to the polymer.

Table 1
Screening plan for the qualitative optimization of the ametryn molecularly imprinted polymer synthesis

Solvent	Dichloromethane		Acetonitrile	
Functional monomer	4-Vinylpyridine	Methacrylic acid	4-Vinylpyridine	Methacrylic acid
Designed polymer	AME_1	AME_2	AME_3	AME_4

Table 2
Factor levels in the experimental designs

Variable	Low (−)	High (+)	Central (0)	$\alpha = 1.414$		$\alpha = 2$		$\alpha = 2.449$	
				Axial (−α)	Axial (+α)	Axial (−α)	Axial (+α)	Axial (−α)	Axial (+α)
Temperature (°C)	45	65	55	40.86	69.14	35	75	30.51	79.49
Template (mmol)	0.75	1.25	1	0.646	1.353	0.5	1.5	0.387	1.612
Initiator (mmol)	1	3	2	0.586	1.314	0	4	0	4.449
Cross-linker (mmol)	15	25	20	12.93	27.07	10	30	7.775	32.245
Solvent (mL)	4	6	5	3.586	6.414	3	7	2.551	7.449
Monomer (mmol)	3	5	4	2.586	5.414	2	6	1.551	6.449

3. Results

In order to achieve the optimum chromatographic conditions for the ametryn analysis, variables including, the mobile phase composition, UV wavelength, injection volume and mobile phase flow-rate were optimized. Fig. 1 shows the ametryn chromatogram detected at 220 nm (two injections repeatedly).

3.1. Template removing optimization

After the preliminary polymer preparation mentioned earlier, in order to optimize the template removal, the template was removed by soxhlet extraction using a two-step washing procedure. At the first step, the template was washed by 200-mL methanol:acetic acid (100:0, 99:1, 95:5 and 9:1 (v/v)) for 12, 16, 18, 20 and 24 h. For the second step, washing with 200 mL of methanol took place for 2, 4, 6, 8, 10 and 12 h, after each washing at the first step. The ultimate obtained results are illustrated in Fig. 2.
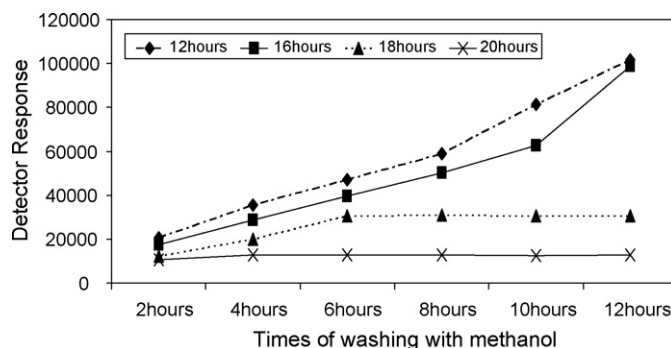
Fig. 2. Template removal with methanol:acetic acid (9:1, v/v).

Table 3
The rebinding mean percentages of ametryn on the MIP vs. the NIP in the rebinding optimization procedure ($N = 3$)

Time (h)	Recovery on the MIP (mean ± S.D.)	Recovery on the NIP (mean ± S.D.)
1	41.494 ± 0.29	1.25 ± 0.07
2	47.45 ± 0.35	3.36 ± 0.3
3	71.18 ± 0.21	5.346 ± 0.12
4	79.19 ± 0.23	7.413 ± 0.09
5	87.50 ± 0.27	8.48 ± 0.25
6	87.12 ± 0.14	8.38 ± 0.31
7	87.29 ± 0.19	8.375 ± 0.47

3.2. Equilibrium-rebinding experiments optimization

After the template removal optimization, a procedure for optimizing the rebinding experiments was selected. In this procedure, 1 g of the polymer particles was placed in a beaker containing a solution of 100 ng mL^{-1} of ametryn in a digital

Fig. 1. The HPLC chromatogram of ametryn at the concentration of 100 ng mL^{-1}. Mobile phase, 60% acetonitrile and 40% purified water, flow-rate: 0.8 mL min^{-1}, injection volume: 20 μL, the analytical column: performance RR-C$_{18}$e 100 mm × 4.6 mm i.d. (Merch KGa A, Germany) and column guards (Chromolith Guard Cartridge Kit RP-C$_{18}$e and 5 cm × 4.6 mm i.d., 5 μm). UV detection at 220 nm, the ambient temperature was used for the chromatographic system.
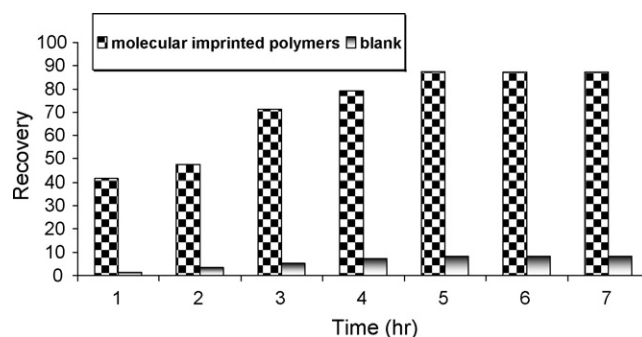
Fig. 3. Effect of the selected times on the rebinding of MIP vs. NIP in the rebinding optimization procedure ($N = 3$).
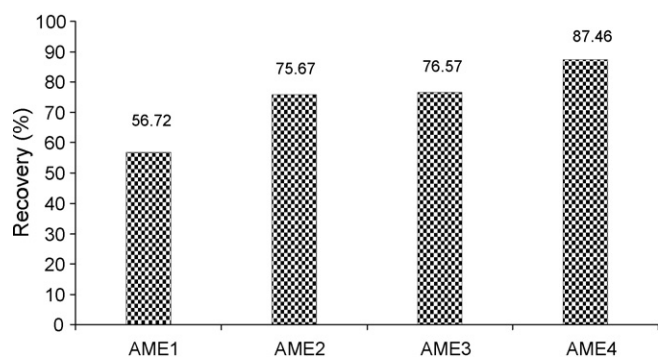
Fig. 4. Rebinding of ametryn to the MIP with different functional monomers and solvents ($N = 5$).
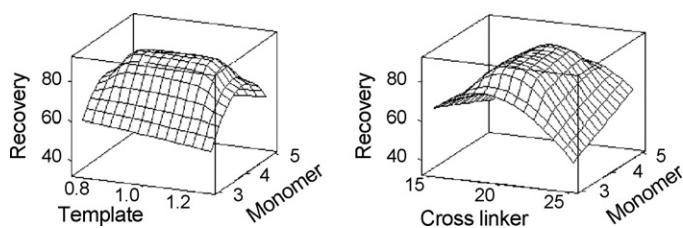

Fig. 5. Response surfaces estimated (recovery%) for atrazine using the central composite design obtained by plotting (a) template (mmol) *vs.* functional monomer (mmol) and (b) cross-linker (mmol) *vs.* functional monomer (mmol).

shaker (100 rpm, 25 °C) for 1–7 h. Each time the analyte concentrations in the final solution were determined by HPLC-UV as mentioned earlier. The results of this equilibrium optimization have been shown in Table 3 and Fig. 3.

3.3. Qualitative optimization of the molecularly imprinted polymer

As mentioned in the previous section, ametryn was the template molecule; MAA and 4-vinylpyridine were used as functional monomers, while acetonitrile and dichloromethane were utilized as porogens. The results of this library have been shown in Fig. 4.

3.4. Quantitative optimization of the molecularly imprinted polymer

When the number of independent variables is small, then overlying the response surfaces and choosing the optimum conditions constitute a simple and usually highly effective method.

Table 4 exhibits the type of optimization design chosen in this work and the so-called response surface model: the central composite design, where the axial points are located on the sphere surrounding the two-level factorial design. The obtained results are summarized in Tables 5 and 6.

The data in Tables 5 and 6 were evaluated by ANOVA at the 5% significance level. The data indicate that, in most cases, interactions took place between principal factors (Table 7). This means that the respective response hypersurfaces in the multi-dimensional factorial space are considerably curved in the domain of the experimental design, *i.e.* the influence of one factor on the optimization parameter depends on the values of all the other factors. For instance, Fig. 5 depicts the response surface plots for ametryn, where the response surface curvature and factor interactions are evident. These data can also be presented by main effects plot (Fig. 6) and interaction effects plot (Fig. 7).

4. Discussion

The phenomenon of selective recognition resulting from polymer imprinting and the associated polymer recognition properties has been observed and reported in great detail. Despite the popularity in the literature published within the past decades,

Table 4
The experimental designs for ametryn

Run	A	B	C	D	E	F	Run	A	B	C	D	E	F	Run	A	B	C	D	E	F	Run	A	B	C	D	E	F
1	0	0	0	0	0	0	21	−	+	+	−	+	+	41	+	−	−	−	+	+	61	+	+	+	−	+	−
2	0	0	0	0	0	0	22	−	+	−	+	+	+	42	+	+	−	−	+	−	62	+	−	+	+	−	+
3	−	−	+	−	+	+	23	−	−	−	−	−	−	43	+	−	+	+	−	−	63	+	−	−	+	+	−
4	−	+	+	−	−	+	24	−	+	−	+	−	+	44	+	+	−	+	+	+	64	+	−	−	−	−	−
5	−	+	−	−	−	+	25	−	−	−	+	+	+	45	+	+	−	−	+	+	65	+	−	+	−	−	+
6	−	−	+	−	−	+	26	−	−	+	+	+	−	46	+	−	+	−	+	−	66	+	−	+	−	−	−
7	−	−	+	+	+	+	27	−	+	−	+	+	−	47	+	+	−	+	+	−	67	0	0	0	0	0	0
8	−	+	−	−	+	+	28	−	−	−	−	−	+	48	+	+	+	−	−	−	68	0	0	0	0	0	0
9	−	+	+	−	−	−	29	−	−	+	−	+	−	49	+	−	−	−	+	−	69	+α	0	0	0	0	0
10	−	+	+	+	+	−	30	−	−	−	−	+	−	50	+	+	+	−	−	+	70	−α	0	0	0	0	0
11	−	+	−	+	−	−	31	−	−	+	−	−	−	51	+	−	+	+	+	−	71	0	+α	0	0	0	0
12	−	+	−	−	−	−	32	−	+	+	+	−	−	52	+	−	−	+	−	−	72	0	−α	0	0	0	0
13	−	+	+	−	+	−	33	−	−	−	+	+	−	53	+	+	+	−	+	+	73	0	0	+α	0	0	0
14	−	+	+	+	+	+	34	−	−	−	−	+	+	54	+	−	−	+	−	+	74	0	0	−α	0	0	0
15	−	−	−	+	−	+	35	+	+	−	−	−	+	55	+	+	+	+	+	−	75	0	0	0	+α	0	0
16	−	−	+	+	−	−	36	+	+	+	+	−	−	56	+	−	+	+	+	+	76	0	0	0	−α	0	0
17	−	−	−	+	−	+	37	+	+	−	+	−	−	57	+	+	−	+	−	+	77	0	0	0	0	+α	0
18	−	−	+	+	−	+	38	+	−	−	+	+	+	58	+	+	+	+	+	+	78	0	0	0	0	−α	0
19	−	+	−	−	+	−	39	+	+	+	+	−	+	59	+	+	−	−	−	−	79	0	0	0	0	0	+α
20	−	+	+	+	−	+	40	+	−	+	−	+	+	60	+	−	−	−	−	+	80	0	0	0	0	0	−α

Factor A: temperature; factor B: template; factor C: initiator; factor D: cross-linker; factor E: solvent; factor F: functional monomer.

Table 5
Mean equilibrium rebinding on the molecular imprinted and the non-imprinted polymers in the full factorial design model

Run	Recovery (mean, N=5)		Run	Recovery (mean, N=5)		Run	Recovery (mean, N=5)		Run	Recovery (mean, N=5)		Run	Recovery (mean, N=5)		Run	Recovery (mean, N=5)	
	MIP	NIP		MIP	NIP		MIP	NIP		MIP	NIP		MIP	NIP		MIP	NIP
1	87.34	8.41	13	59.78	10.59	25	54.40	10.29	37	43.40	15.49	49	76.37	17.45	61	51.29	12.55
2	87.47	8.28	14	89.64	10.63	26	47.57	35.56	38	46.45	12.31	50	41.38	14.52	62	46.37	11.59
3	64.44	12.48	15	52.59	9.47	27	55.42	11.30	39	57.27	16.44	51	41.71	37.33	63	38.37	35.38
4	48.52	12.41	16	45.43	34.67	28	57.24	11.86	40	56.52	14.33	52	35.35	36.49	64	72.36	17.56
5	47.52	12.58	17	43.28	34.78	29	81.68	15.52	41	53.32	16.29	53	41.49	13.41	65	52.29	14.47
6	60.53	12.60	18	54.28	9.28	30	82.67	15.81	42	51.58	12.44	54	44.58	11.37	66	73.59	17.44
7	61.34	8.52	19	59.67	10.43	31	81.25	15.48	43	37.52	36.49	55	50.36	13.51	67	87.45	8.41
8	47.75	17.56	20	65.57	14.63	32	53.38	13.61	44	80.28	13.52	56	53.36	10.55	68	87.44	8.56
9	57.44	8.33	21	49.70	11.33	33	46.31	33.29	45	39.23	19.27	57	73.51	17.55			
10	58.52	11.34	22	88.48	11.64	34	61.45	14.28	46	73.46	17.46	58	81.34	12.52			
11	51.75	13.60	23	80.58	15.62	35	39.60	14.34	47	47.49	13.55	59	47.46	10.55			
12	55.62	8.92	24	80.44	15.37	36	45.49	15.66	48	49.46	10.31	60	49.34	13.37			

the selectivity of MIP mechanisms and their rational control has not entirely been recognized and still is under question. Therefore, there is the need to optimize the extraction procedure more detailed. This becomes apparent in contributions as published by Martin-Esteban in 2001. It was found that, after imprinting a polymer against the drug tamoxifen for solid-phase extraction purposes, a control polymer imprinted against propanol exhibited greater affinity for tamoxifen than the tamoxifen imprinted polymer despite the obvious differences in the molecular structure of the template molecules. Such irregularities necessitate detailed study and analysis of the MIP systems prior to a more widespread acceptance as a facile analytical technique [27]. As already stated, the first step in the MIP preparation involves the prearrangement of the template and the used monomer. The applied temperature as well as the employed template, monomer, cross-linker and solvent (porogen) are obviously the key parameters for the achievement of a successful selective MIP [28]. Since all the mentioned parameters have a strong influence on the overall MIP performance in terms of affinity, selectivity, loading capacity, etc., their proper selection (qualitative and quantitative) will ensure that polymers with appropriate properties are obtained for a particular application. As it has been mentioned in Section 2.3, in order to start the optimization process by an experimental design approach, a preliminary polymer synthesis was designed. In general, a template–monomer molar ratio of 1:4 provides enough stability for the formed complex, assuring the achievement of the desired imprint effect. As a consequence, this ratio was selected as a start point for optimization process. From the results given in Fig. 3, it was deduced that NIP was not capable of binding a relatively high degree of ametryn in comparison with the ametryn MIPs. This indicated that the MIPs might have not rebound a large ametryn amount through non-specific binding interactions.

It should be noted that generally there are some problems associated with the use of MIPs in analytical separations, such as leakage of the imprinted molecules. The leakage of the imprinted molecules during the elution stage was evident on several occasions, which led to an uncertainty in the concentration determination. For that reasons, each method development at one stage must confirm the absence of interference from the bleeding template species. One approach to circumvent this problem is the polymer heat-treatment, accompanied with excessive washes under strong washing conditions [29]. This treatment is claimed to greatly reduce or even eliminate the template bleeding from the MIP phase. Therefore, a two-step washing procedure (methanol:acetic acid and methanol), based on soxhlet extraction, was optimized in this study to generate MAA-based binding sites complementary to ametryn. Soxhlet extraction is easy to handle, however, involves large volumes of solvent and takes 6–24 h [30,31]. In accordance with many authors, the results showed that by using methanol:acetic acid (9:1, v/v) 18 h and methanol 6 h as the template washing regime, the template would be removed completely from the polymer structure (Fig. 2) [32].

In order to select properly the functional monomer and solvent, as it is displayed in Table 1, a screening library was obtained. From Fig. 4, it could be concluded that AME_4 pre-

Table 6
Mean equilibrium rebinding on the molecular imprinted and the non-imprinted polymers in the star points of central composite design model ($N = 5$)

Run	$\alpha = 1.414$		Run	$\alpha = 2$		Run	$\alpha = 2.449$	
	Recovery (mean ± S.D.)			Recovery (mean ± S.D.)			Recovery (mean ± S.D.)	
	MIP	NIP		MIP	NIP		MIP	NIP
69	77.60 ± 0.06	9.67 ± 0.08	69	45.53 ± 0.07	15.22 ± 0.01	69	35.40 ± 0.05	25.41 ± 0.07
70	89.46 ± 0.09	8.42 ± 0.03	70	–	–	70	–	–
71	86.54 ± 0.05	8.33 ± 0.02	71	85.37 ± 0.04	8.48 ± 0.07	71	84.31 ± 0.03	8.58 ± 0.05
72	59.56 ± 0.06	8.36 ± 0.02	72	43.46 ± 0.10	8.24 ± 0.07	72	32.35 ± 0.06	8.40 ± 0.05
73	85.33 ± 0.03	12.55 ± 0.05	73	84.42 ± 0.05	14.42 ± 0.07	73	84.40 ± 0.02	15.27 ± 0.06
74	75.47 ± 0.09	9.16 ± 0.01	74	–	–	74	–	–
75	85.27 ± 0.02	17.84 ± 0.01	75	79.30 ± 0.02	25.70 ± 0.01	75	70.28 ± 0.01	30.52 ± 0.06
76	61.57 ± 0.10	9.33 ± 0.05	76	52.53 ± 0.06	9.43 ± 0.02	76	45.51 ± 0.04	9.49 ± 0.05
77	88.54 ± 0.05	8.51 ± 0.06	77	81.70 ± 0.05	10.27 ± 0.03	77	75.53 ± 0.07	11.40 ± 0.03
78	71.47 ± 0.05	11.54 ± 0.05	78	65.32 ± 0.05	12.59 ± 0.09	78	54.35 ± 0.08	13.51 ± 0.05
79	80.38 ± 0.05	13.45 ± 0.04	79	79.28 ± 0.06	14.22 ± 0.01	79	61.59 ± 0.03	25.40 ± 0.08
80	70.37 ± 0.02	14.19 ± 0.00	80	54.29 ± 0.01	17.32 ± 0.05	80	38.28 ± 0.04	24.48 ± 0.07

sented the highest specificity by binding nearly 11%, as much of its closest member in the library (AME$_3$). The right selection of functional monomers is important in molecular imprinting, because the interaction with functional groups affects the affinity of MIPs. MIPs have mainly been synthesized by the non-covalent approach, using methacrylic acid as the functional monomer and ethylene glycol dimethacrylate as the cross-linker monomer. In general, acidic functional monomers (such as MAA) are normally used for the basic template, whereas 4-vinylpyridine (4-VP) and methacrylamide are used for the acidic templates [24].

Ametryn contains functional groups, being able to form cyclic hydrogen bonds with MAA. These bonds are one of the strongest non-covalent interactions and have proved the basis of some of the most successful MIPs in the literature. Nevertheless, some authors chose other functional monomers such as 4-VP and methacrylamide [24]. It has been demonstrated that MIPs offer the highest selectivity, if for the MIP preparation; the samples were dissolved in the used porogen [33]. Based on analysis considerations, in the qualitative optimization of the solvents and functional monomers, equilibrium-rebinding experiments were conducted with the aid of acetonitrile. Therefore, the highest rebinding was observed in AME$_4$ (where acetonitrile and MAA were used). Acetonitrile has been found to be a suitable mobile phase solvent for low to medium-polar templates, such as triazines with p$K_a = 1$–4 and log $P_{ow} = 1.7$–3.4, presumably due to its weak hydrogen-bonding capacity and, subsequently, its limited ability to compete for the hydrogen-bonding sites. Furthermore, it solvates the methacrylate polymer backbone well and it is polar enough to dissolve a large number of compounds [34]. On the other hand, the morphology was influenced by the properties of the porogen, since the swelling of the polymers is dependent on the surrounding medium [35]. Thus, the swelling is most pronounced in chlorinated solvents, such as dichloromethane, as compared with solvents like acetonitrile. This swelling behavior may lead to changes in the three-dimensional configuration of the functional groups, taking part in the recognition in the sites resulting in poorer binding capacity, as it was observed in AME$_2$ as in comparison with AME$_4$.

Generally, α or the star points indicator in the experimental design should be chosen between 1 and $\sqrt{K}$ (K is the input

Table 7
The estimated response surface regression coefficients for the mean equilibrium rebinding on the molecular imprinted polymer[a]

Term	Coefficient	S.E. coefficient	T	P-value	Term	Coefficient	S.E. Coefficient	T	P_{value}
Constant	87.71	1.654	53.008	0.001	A × C	0.010	1.24	0.008	0.994
Temperature (A)	−5.60	0.86	−6.45	0.001	A × D	0.05	1.24	0.038	0.969
Template (B)	0.44	0.86	0.52	0.605	A × E	0.008	1.24	0.006	0.995
Initiator (C)	0.87	0.86	1.01	0.316	A × F	−0.077	1.24	−0.061	0.951
Cross-linker (D)	−1.24	0.86	−1.44	0.156	B × C	−1.39	1.24	−1.12	0.266
Solvent (E)	3.55	0.86	4.12	0.001	B × D	17.41	1.24	13.97	0.001
Monomer (F)	1.21	0.86	1.41	0.163	B × E	1.28	1.24	1.027	0.309
A × A	−4.32	3.31	−1.3	0.198	B × F	6.87	1.24	5.52	0.001
B × B	−14.80	3.29	−4.49	0.001	C × D	−0.44	1.25	−0.34	0.729
C × C	−7.45	3.30	−2.25	0.321	C × E	1.17	1.25	0.93	0.352
D × D	−14.43	3.31	−4.35	0.001	C × F	−0.38	1.25	−0.308	0.760
E × E	−7.84	3.31	−2.37	0.021	D × E	2.32	1.25	1.85	0.070
F × F	−12.47	3.31	−3.77	0.001	D × F	16.59	1.25	13.22	0.001
A × B	−0.14	1.24	−0.11	0.912	E × F	1.53	1.25	1.22	0.227

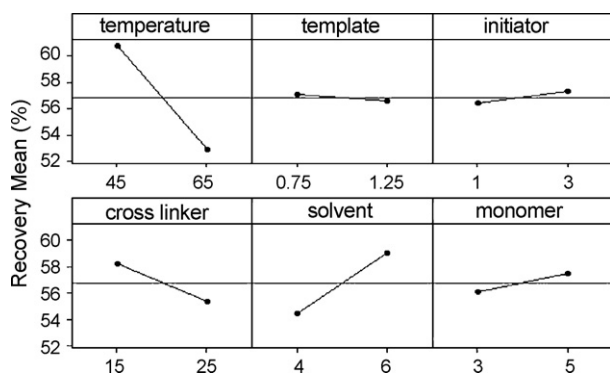[a] $S = 5.035$, $R^2 = 93.6\%$, R^2 (adj) $= 90.3\%$. The analysis was done using coded units.
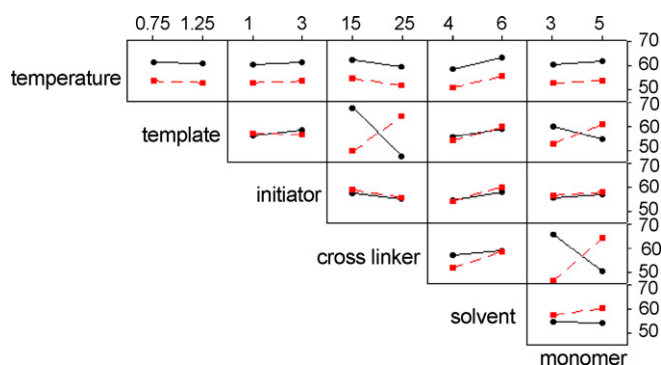
Fig. 6. Main effects plot in the factorial 2^6 design.

The designed 80 MIPs in the CCD had differing physical characteristics, ranging from extremely hard to much softer MIPs that contained lowest cross-linking ratios. Even the polymer in the run numbers 70 (without initiator) and run numbers 74 (very low temperature) were not successfully synthesized (Table 6). In agreement with Fig. 6, in the studied ranges, except temperature and solvent, other factors did not exhibit any statistically significant trend under the linear effect mode, when considered as main isolated factors ($P \leq 0.05$). The temperature values were selected between 30.51 and 79.49 °C. Temperature produced a negative influence. The present results indicated that the polymerization temperature played a crucial role in the performance of the synthesized material. It is believed from the earlier reported studies that the polymer affinity and specificity were significantly improved by optimizing the polymerization temperature [36]. Usually, lower temperature values will stabilize the template–functional monomers complexes [37]. It must be noted that the polymerization temperature also affects the polymerization process and the polymer structure, influencing the quality and the quantity of the MIPs recognition sites. It should be noted that 40.86 °C was the lowest level that has been predicted by central composite design results as theoretical optimum. It means that, the lowest possible level temperature must be selected. Therefore, it was decided to set the temperature at the lowest possible level of 55 °C to avoid the binding sites degradation.

factors in coded units) and rarely outside this range [25]. As a result, in order to evaluate the effects of the α values on the model, three α values, i.e., $\sqrt{2}$, $\sqrt{4}$ and $\sqrt{6}$ (K equals to 6) were chosen. According to the one-way ANOVA test, it was revealed that the differences between the α values were not significant ($P = 0.756$). In line with the resulting data in Table 7, the linear effects of the temperature and the solvent along with the quadratic effects of the template, cross-linker, solvent and the functional monomer on the mean equilibrium rebinding were significant. Also, the R^2 (adj) value was 90.3%, meaning that the six studied factors could explain 90.3% of the variation in the equilibrium-rebinding percentage. The results of the central composite design were validated using ANOVA. The P-value for the model (0.001) was lower than the critical value of the significance set, below 0.05. The R^2 value for a valid model is 0.6 or greater. For this model, the R^2 was 0.806, indicating that the made predictions would be reasonably accurate. The variation domain for each factor defines the parameter space within which the variable can change. For this reason, the selection of the variation domain was based on prior experiments. The molar values for the monomer were selected between 1.551 and 6.449. It was thought that using values lower than 2; it would create binding sites of insufficient opportunity for the template interaction. Conversely, the use of high values for the template would produce binding sites with too many points for the template interactions, resulting in the lack of specificity. Also, the molar values for the cross-linker were selected between 7.775 and 32.245.

As it has been reported, the optimization of the amount porogen is important for the recognition ability and the other MIP properties, such as surface area, swelling capacity and pore volume. Normally, the hydrogen-bonding capacity of the porogens played a significant role in the recognition properties of the materials [38]. The porogen values in the model were selected between 2.551 and 7.449 mL. Regarding the results of Table 7, among the linear effects, the most crucial variables were the temperature and the solvent used in the polymerization as well as among quadratic effects, the effects of the template, cross-linker, solvent and functional monomer were significant ($P \leq 0.05$) (solvent is also identified as a crucial variable when it is treated as quadratic term). Also, in agreement with Fig. 7, it can be derived that the interaction between the template, cross-linker and monomer (B × D, B × F and D × F) was significant ($P \leq 0.05$). According to the obtained results, it was revealed that the molar relationship between the functional monomer and the template was found to be important with respect to the number and quality of the MIP recognition sites. The low monomer:template (M/T) ratios led to less than optimal complexation on account of insufficient functional monomer. On the contrary, when the M/T ratios were too high, non-selective binds were yielded [39]. Furthermore, it was considered that, the application of high molar ratio for the cross-linker would produce an MIP, lacking the flexibility to allow the rapid mass transfer of the rebind analyte to and from the binding site. On the contrary, an MIP, formed with low molar ratios for the cross-linker, would not possess the mechanical strength to retain the binding site memory. Based on the result of ANOVA (Table 7), it can be concluded that, central composite design approach is useful in predicting an optimum

Fig. 7. Interaction effects plot in the factorial 2^6 design.

template:monomer:cross-linker (T:M:C) ratio for the production of an efficient ametryn MIP. By combining the response surfaces and based on the response optimizer data (weight of one and importance of one), it was finally possible to suggest the optimum conditions to be adopted in the MIP synthesis for ametryn, *viz.*, theoretical optimum temperature 40.86 °C, porogen 6.410 mL, cross-linker 27.070 mmol, initiator 2.03 mmol, monomer 5.41 mmol and template 1.204 mmol. The response surface model displayed the optimum template:monomer:cross-linker ratio, presented in Fig. 5. The predicted optimal T:M:C molar ratio for an ametryn MIP was 1:4.49:22.48.

5. Conclusion

MIP applications in the industrial and environmental fields are still rare, although they have become more common in the recent years. The new MIP studies are mainly based on developing imprinted polymers for new target analytes of biological and environmental interest. MIPs may be limited by their low yield of specific binding sites, so in some cases these polymers have low sample load capacity and high non-specific binding. For this reason, studies currently being developed involve the optimization of the MIP synthesis in order to improve the capacity and/or the selectivity of the MISPE sorbents. Chemometrics is frequently employed for analytical method optimization and it is believed that the central composite design could prove beneficial for aiding the MIP development, such as the prediction of an optimum template:monomer:cross-linker ratio together with the optimization of the temperature and the amount of solvent and initiator for the production of an ametryn MIP, capable of rebinding the highest ametryn capacity.

Future works may also consider using different parameters. For example, different types of functional monomer, cross-linker and solvent could be compared for their respective rebind performances. Other factors like type of initiator, polymerization techniques and type of cross-linker could also be incorporated into the factorial and central composite design. However, limitation on the number of factors is essential, as the number of experiments required for modeling will increase proportionally. Finally, in reference with other works [23], this study has shown that chemometrics can be used as a rational approach to the MIP optimization.

Acknowledgements

References

[1] J. Matsui, M. Okada, M. Tsuruoka, T. Takeuchi, Anal. Commun. 34 (1997) 85.
[2] M. Siemann, L.I. Andersson, K. Mosbach, J. Agric. Food Chem. 44 (1996) 141.
[3] J.F. Lawrence, C. Menard, M.C. Hennion, V. Pichon, F. Legoffic, N. Durand, J. Chromatogr. A 752 (1996) 147.
[4] J. Dalluge, T. Hankemeier, R.J.J. Veruls, U.A.T. Brinkman, J. Chromatogr. A 830 (1999) 377.
[5] S.J. Shahtaheri, P. Kwasowski, D. Stevenson, Chromatographia 47 (1998) 453.
[6] S.J. Shahtaheri, M.F. Katmeh, P. Kwasowski, D. Stevenson, J. Chromatogr. A 697 (1995) 131.
[7] M.T. Muldoon, L.H. Stanker, J. Agric. Food Chem. 43 (1995) 1424.
[8] J. Matsui, K. Fujiwara, S. Ugata, T. Takeuchi, J. Chromatogr. A 889 (2000) 25.
[9] C. Cacho, E. Turiel, A. Martin-Esteban, C. Perez-Conde, C. Camara, Anal. Bioanal. Chem. 376 (2003) 491.
[10] C. Cacho, E. Turiel, A. Martin-Esteban, C. Perez-Conde, C. Camara, J. Chromatogr. B 802 (2004) 347.
[11] E. Turiel, C. Perez-Conde, A. Martin-Esteban, Analyst 128 (2003) 137.
[12] J. Matsui, Y. Miyoshi, O. Doblhoff-Dier, T. Takeuchi, Anal. Chem. 67 (1995) 4404.
[13] M.T. Muldoon, L.H. Stanker, Anal. Chem. 69 (1997) 803.
[14] J. Olsen, P. Martin, I.D. Wilson, Anal. Commun. 35 (1998) 13.
[15] T. Takeuchi, D. Fukuma, J. Matsui, Anal. Chem. 71 (1999) 285.
[16] F. Lanza, B. Sellergren, Anal. Chem. 71 (1999) 2092.
[17] B. Bjarnason, L. Chimuka, O. Ramstrom, Anal. Chem. 71 (1999) 2152.
[18] I. Ferrer, F. Lanza, A. Tolokan, V. Horvath, B. Sellergren, G. Horvai, D. Barcelo, Anal. Chem. 72 (2000) 3934.
[19] A.G. Mayes, M.J. Whitcombe, Adv. Drug Deliv. Rev. 57 (2005) 1742.
[20] A.M. Carro, J.C. Cobas, J.B. Rodriguez, R.A. Lorenzo, R. Cela, J. Anal. At. Spectrom. 14 (1999) 1867.
[21] F. Navarro-Villoslada, B. San Vicente, M.C. Moreno-Bondi, Anal. Chim. Acta 504 (2004) 149.
[22] H. Kempe, M. Kempe, Macromol. Rapid Commun. 25 (2004) 315.
[23] M.P. Davies, V.D. Biasi, D. Perrett, Anal. Chim. Acta 504 (2004) 7.
[24] N. Masque, F. Marce, F. Borrull, Trends Anal. Chem. 20 (9) (2001) 477.
[25] C.F. Jef wu, M. Hamada, Experiments: Planning, Analysis, and Parameter Design Optimization, 1st ed., John Wiley and Sons Inc., New York, NY, 2000.
[26] A.R. Jamshidian, M. Nourizad, Design and Analysis of Experiments with Minitab 14, 1st ed., Arkan Publications, Tehran, Iran, 2004.
[27] J.O. Mahony, K. Nolan, M.R. Smyth, B. Mizaikoff, Anal. Chim. Acta 534 (2005) 31.
[28] A. Martin-Esteban, Fresenius J. Anal. Chem. 370 (2001) 795.
[29] L.I. Andersson, J. Chromatogr. B 739 (2000) 163.
[30] V. Camel, Trends Anal. Chem. 19 (2000) 229.
[31] J.R. Dean, Trends Anal. Chem. 19 (2000) 553.
[32] R. Carabias-Martinez, E. Rodriguez-Gonzalo, E. Herrero-Hernandez, Anal. Chim. Acta 559 (2006) 186.
[33] F. Chapuis, V. Pichon, F. Lanza, S. Sellergren, M.C. Hennion, J. Chromatogr. A 999 (2003) 23.
[34] B. Sellergren, Trends Anal. Chem. 18 (1999) 164.
[35] O. Ramstrom, R.J. Ansell, Chirality 10 (1998) 195.
[36] Y. Lu, C. Li, X. Wang, P. Sun, X. Xing, J. Chromatogr. B 804 (2004) 53.
[37] L.A. Andersson, R. Muller, G. Vlatakis, K. Mosbach, Proc. Natl. Acad. Sci. U.S.A. 92 (1995) 4788.
[38] L. Wu, K. Zhu, M. Zhao, Y. Li, Anal. Chim. Acta 549 (2005) 39.
[39] H.S. Andersson, J.G. Karlsson, S.A. Piletsky, A.C. Koch-Schmidt, K. Mosbach, I.A. Nicholls, J. Chromatogr. A 848 (1999) 39.

Utilization of optimized BCR three-step sequential and dilute HCl single extraction procedures for soil–plant metal transfer predictions in contaminated lands

Jana Kubová, Peter Matúš*, Marek Bujdoš, Ingrid Hagarová, Ján Medved'

Comenius University in Bratislava, Faculty of Natural Sciences, Geological Institute, Mlynská dolina 1, 842 15 Bratislava 4, Slovakia

Abstract

The prediction of soil metal phytoavailability using the chemical extractions is a conventional approach routinely used in soil testing. The adequacy of such soil tests for this purpose is commonly assessed through a comparison of extraction results with metal contents in relevant plants. In this work, the fractions of selected risk metals (Al, As, Cd, Cu, Fe, Mn, Ni, Pb, Zn) that can be taken up by various plants were obtained by optimized BCR (Community Bureau of Reference) three-step sequential extraction procedure (SEP) and by single $0.5\,mol\,L^{-1}$ HCl extraction. These procedures were validated using five soil and sediment reference materials (SRM 2710, SRM 2711, CRM 483, CRM 701, SRM RTH 912) and applied to significantly different acidified soils for the fractionation of studied metals. The new indicative values of Al, Cd, Cu, Fe, Mn, P, Pb and Zn fractional concentrations for these reference materials were obtained by the dilute HCl single extraction. The influence of various soil genesis, content of essential elements (Ca, Mg, K, P) and different anthropogenic sources of acidification on extraction yields of individual risk metal fractions was investigated. The concentrations of studied elements were determined by atomic spectrometry methods (flame, graphite furnace and hydride generation atomic absorption spectrometry and inductively coupled plasma optical emission spectrometry). It can be concluded that the data of extraction yields from first BCR SEP acid extractable step and soil–plant transfer coefficients can be applied to the prediction of qualitative mobility of selected risk metals in different soil systems.
© 2008 Elsevier B.V. All rights reserved.

Keywords: Optimized BCR three-step sequential extraction; Dilute HCl single extraction; Reference materials; Soils and plants; Prediction of phytoavailability; Atomic spectrometry

1. Introduction

The soil–plant transfer of risk metals is a part of chemical element cycling in the nature [1]. It is a very complex process governed by several factors, both natural and affected by man. Soil is the main source of the elements for the plants both as nutrients and pollutants and its conditions plays a crucial role in environmentally significant metal behaviour [2]. In natural environments the surface soil layer elements concentrations are a function of litter inputs and the parent material. The dry and wet depositions which enrich the canopies of the trees and surface soils, cause high elements concentrations in the overground plant parts and in the soils [3]. The impact of heavy metal pollution on the ecosystems due to anthropogenic activities like smelting or mining as well as atmospheric deposition has been frequently investigated [4,5]. If the soils contain high contents of heavy metals and suffer from serious acid deposition, it can obviously wonder about the consequences for the ecosystem [6]. Some authors indicated that bioavailability, mobility and activity of heavy metals in the soils with a certain deposit of them, mostly due to cation exchange with H^+, Ca^{2+}, Mg^{2+}, K^+ and NH_4^+, are coming from acid deposition [7]. Acid deposition has become one of the most important factors resulting in environment acidification [8]. Predicting the impact of a contamination event on the environment requires information about the pollutant mobility pattern. The soil properties, metal speciation and plant species, especially soil–plant interactions, determine the bioavailability of soil metals [9,10].

Various one-step extraction methods are frequently used for bioavailability evaluation because of simplicity and ease of the

---

* Corresponding author. Tel.: +421 260296290; fax: +421 260296290.
E-mail address: matus@fns.uniba.sk (P. Matúš).

operation [11–15]. However, no method has been recognized as the general approach for prediction of the bioavailability [16]. The common features of these extraction procedures have been focused only on metal fractions associated with certain soil geochemical phases, but almost all have ignored biological soil reactions which determine the metal speciation, transformation, plant uptake and accumulation, thus determining overall metal bioavailability. The phytoavailability of heavy metals in polluted soils was studied by some authors using of various single extractions [17–19] and transfer factors [19].

The use of sequential extraction procedures (SEP) in soil analysis as a complement to single extractions has increased in last time [20–22]. They are applied to the soils contaminated by various pollution sources, such as irrigation with wastewater [23,24], industry [25], mining [26–28] and smelting [29] activity, automobile emissions [30], sewage sludge addition [31,32] and accidental spill [33]. The use of leaching approach based on sequential extractions can help to elucidate the relative contribution of mixed pollution sources and may aid in the predictions of trace elements mobility. Among the variety of SEPs described in literature, the three-step scheme proposed by the BCR (Community Bureau of Reference) [34] and its optimized version [35] have become very popular during recent years and their application has increased lately [36–41]. These studies showed a good interlaboratory reproducibility for Cd, Cr, Cu, Ni, Pb and Zn for all three extraction steps and the suitability of the optimized BCR scheme for the fractionation of these metals in contaminated soil samples.

Some studies were published about the comparison of HCl single and BCR sequential extraction procedures. Madrid et al. [42] estimated the extractibility of potentially toxic metals (Cu, Pb and Zn) in urban soils by both methods. Ahumada et al. [43] obtained significant positive correlations between the results from HCl single and BCR sequential extraction procedures for copper and lead in the soils from mining and agricultural zone. Larner et al. [44] compared BCR SEP with single HCl extraction for fractionation of 12 metals (Cd, Sb, Pb, Al, Cr, Mn, Fe, Co, Ni, Cu, Zn, As) in CRM NIST 2711.

The aim of the present study was to evaluate the adequacy of optimized BCR SEP and single extraction with dilute HCl for the prediction of the soil pollutants effects affected by different anthropogenic sources of the acidification in a terrestrial ecosystems. These procedures were used after their validation to obtain the distribution of both the major (Al, Fe, Mn) and trace (As, Cd, Cu, Ni, Pb, Zn) risk metals in the soils with various levels and types of the contamination. The element contents in individual soil fractions and in the plants growing on studied localities were determined by atomic spectrometry methods (flame, graphite furnace and hydride generation atomic absorption spectrometry and inductively coupled plasma optical emission spectrometry).

2. Experimental

2.1. Soil and plant sample sites description

The acid soil and plant samples were collected from different locations of Slovakia reflecting the various chemical and physical soil characteristics as well as different types of atmospheric deposition.

Locality A: The first sampling site was situated near open quartzite mine Šobov (Banská Štiavnica, central Slovakia) where a large amount of pyrophyllite-pyrite gangue rock was excavated and deposited on the dump. Intensive pyrite oxidation in the mining dump produces extremely acid water which attacks minerals and causes a higher migration rate of various risk elements and the degradation of the soil and the meadow vegetation [45]. The main mineral composition of soil samples was published in our previous work [28].

Locality B: The second sampling site was situated in the part of National park of the Low Fatra called Lúčanská Fatra where the highest point is the top of Vel'ká Lúka—1476 m above the sea level. The mountain range core is formed by granitoid rocks, the bigger part, however, is made from rocks of the envelope and sheet units, especially dolomites and limestones. The park is rich of flora and fauna. The studied acid soil profile was collected from the higher level of the Vel'ká Lúka locality. The source of its acidity is the podzolization process which is connected with great rainfall, percolating regime and acid vegetation (e.g. dwarf pine, blueberry, grass) where their decomposition products are acidifying the whole soil profile.

Locality C: The third sampling site was situated in the region of Pezinok which is famous for its important ore deposits in the Malé Karpaty Mts. It is geologically built by crystalline rocks of polymetamorphic pelitic-psammitic rocks, basalts and their tuffs, and granitoids. The soil samples were collected from the dump site of Sb ore deposit situated on the south-eastern side of the mountains above the city of Pezinok. Mining and dressing of Sb deposits have significantly contributed to Sb and As contamination of soils, sediments and waters [45,46]. Concentrations of these metals do not only exceed limits of geochemical anomalies and limits of contamination but the remediation is needed in this area because the pollution extends up to the borders of Pezinok city.

2.2. Soil samples

Before the analysis the soil samples were air-dried, sieved through a 2 mm sieve and milled in an agate pot to the fine powder which was used for the chemical analysis. Some of important soil characteristics, listed by individual sampling locality, are shown in Table 1. The sample set exhibits a different soil properties and organic matter content with a narrow range of pH values. The pH measurements in sample suspensions (v/w ratio = 2.5/1) were done after 2 h mixing of soil samples with redistilled water (pH (H_2O)) and 1 mol L^{-1} KCl solution (pH (KCl)) by the standard potentiometric method. The electrical conductivity (EC) measurements in sample suspensions (v/w ratio = 5/1) were done after 2 h mixing of soil sample with redistilled water by the standard conductometric method. The total organic carbon (TOC) concentrations in soil samples were determined by the wet combustion of organic matter with a mixture of $K_2Cr_2O_7$ and H_2SO_4. The nonconsumed dichromate was titrated with $FeSO_4$.

Table 1
Some characteristics of studied soil samples (pH, TOC, EC and sulphate concentration values from three replicates)

Locality	Soil depth (cm)	pH (H₂O)	pH (KCl)	TOC (%)	EC (µS cm⁻¹)	Sulphate (g kg⁻¹)	Soil type	The main sources of acidification
A	0–20	2.99	2.81	4.66	902	9.29	Acid sulphatic earth	Weathered product of pyritized quartzite (dump material)
B	0–20	3.40	2.84	35.9	117	6.25	Histo-humic Podzol	Podzolization process, anthropogenic acid atmospheric inputs, acid vegetation
C	0–20	3.51	3.13	5.37	200	16.6	Fluvi-eutric Gleysol	Sulphide oxidation, mine waters with high concentration of Fe, SO_4^{2-}, As and Sb

2.3. Plant samples

Plant samples were collected together with the soil sampling. They included dominant or typical species which had grown in the sampling area. Before the analysis the plant root, stem, leaf and fruit samples were separated, carefully rinsed in redistilled water, air-dried and cut in small pieces.

Locality A (Šobov)—grass *Festuca Rubra* (root and stem) with higher natural resistance to unfavourable conditions of the environment.

Locality B (Vel'ká Lúka)—blueberry *Vaccinium Myrtillus* L. (root, stem, leaf and fruit), long wearing plant included to semi-bush with dual creeper twigs which have root forming possibility.

Locality C (Pezinok)—blackberry *Rubus fruticosus* (root, stem, leaf), deciduous semi-bush. It occurs on the light forest localities and it requires the humus soils with soft humidity.

2.4. Reference materials

Four soil reference materials (RMs; SRM 2710, SRM 2711, CRM 483, SRM RTH 912), one sediment RM (CRM 701) and two plant RMs (CRM GBW 07603 and CRM GBW 07604) listed in Table 2 were used for the validation of decomposition procedures applied to the samples for the determination of total soil and plant concentrations of studied elements. Listed soil RMs were used also for the validation of sequential and single extractions applied to soil samples for the fractionation of studied metals.

2.5. Determination of total content

Total concentrations of studied elements (Al, As, Ca, Cd, Cu, Fe, K, Mg, Mn, Ni, P, Pb, Zn) in soil samples were determined after their decomposition by acid mixture of $HF + HNO_3 + HClO_4 + H_2O_2$ in open system at 200 °C. Total concentrations of studied elements in plant samples were determined after their decomposition by acid mixture of $HF + HNO_3$ in an autoclave at 160 °C. For As determination the soil and plant samples were decomposed with HNO_3 in an autoclave at 160 °C.

2.6. Sequential extraction

The optimized BCR three-step sequential extraction procedure (BCR SEP); first acid extractable step: extraction with 0.11 mol L⁻¹ acetic acid (v/w ratio = 40/1, 16 h extraction time), second reducible step: extraction with 0.5 mol L⁻¹ NH₂OH·HCl in 0.05 mol L⁻¹ HNO₃ (v/w ratio = 40/1, 16 h extraction time), third oxidizable step: digestion with conc. H₂O₂ at 85 °C followed by extraction with 1 mol L⁻¹ ammonium acetate adjusted to pH 2.0 by conc. HNO₃ (v/w ratio = 50/1, 16 h extraction time) [35] was applied to soil samples. The soil samples were consecutively shaken with these agents at given conditions and obtained suspensions were centrifuged (2500 × g) for 20 min.

2.7. Single extraction

The soil samples were shaken with 0.5 mol L⁻¹ HCl (v/w ratio = 20/1) for 1 h and obtained suspensions were centrifuged (2500 × g) for 20 min [26–28].

Table 2
The reference materials used in this study

Reference material	Description
SRM 2710 (NIST)	Highly contamined soil collected from the top of pasture land along Silver Bow Creek in the Butte, Montana area
SRM 2711 (NIST)	Moderately contamined agricultural soil collected in the till layer of a wheat field, Montana area
CRM 483 (BCR)	Sewage sludge amended soil collected from Great Billings Sewage farm, Northampton
CRM 701 (BCR)	Freshwater sediment collected from lake Orta, Piemonte
SRM RTH 912 (WEPAL)	Loess soil from a forest in Switzerland
CRM GBW 07603 (NRCCRM)	Bush branches and leaves collected from an arid area, Qinghai province
CRM GBW 07604 (NRCCRM)	Leaves of poplar collected from Beijing

NIST, National Institute of Standards and Technology, USA. BCR, Institute for Reference Materials and Measurements or Standards, Measurements and Testing Programme, EU. WEPAL, Wageningen Evaluating Programs for Analytical Laboratories, Netherlands. NRCCRM, National Research Centre for Certified Reference Materials, China.

Table 3
Dilute HCl-fractional and total concentration values from three replicates (mean ± standard deviation) of selected studied elements in used reference materials

RM	Al (mg kg^{-1})	Cd (mg kg^{-1})	Cu (mg kg^{-1})	Fe (mg kg^{-1})	Mn (mg kg^{-1})	P (mg kg^{-1})	Pb (mg kg^{-1})	Zn (mg kg^{-1})
SRM 2710								
HCl	1844 ± 14	15.3 ± 0.2	2281 ± 12	4074 ± 14	3422 ± 6	604 ± 11	4610 ± 14	2471 ± 16
Total	64180 ± 290	22.4 ± 0.1	2888 ± 4	33390 ± 320	9750 ± 60	1096 ± 14	5664 ± 11	7114 ± 42
Total[a]	64400 ± 800	21.8 ± 0.2	2950 ± 130	33800 ± 1000	10100 ± 400	1060 ± 150	5532 ± 80	6952 ± 91
Extraction yield (%)	2.87	70.2	77.3	12.1	33.9	57.0	83.3	35.5
SRM 2711								
HCl	1876 ± 138	35.0 ± 0.5	59.2 ± 0.6	1210 ± 141	328 ± 6	515 ± 16	1036 ± 8	117 ± 7
HCl[b]	2106 ± 65	34.6 ± 0.7	58.3 ± 0.7	1428 ± 22	366 ± 4	NA	855 ± 6	109 ± 1
Total	65270 ± 250	42.4 ± 0.3	110 ± 1	28590 ± 160	583 ± 9	691 ± 2	1120 ± 4	381 ± 2
Total[a]	65300 ± 900	41.7 ± 0.3	114 ± 2	28900 ± 600	638 ± 28	860 ± 70	1162 ± 31	350 ± 5
Extraction yield (%)	2.87	83.9	51.9	4.19	51.4	59.9	89.2	33.4
CRM 483								
HCl	2530 ± 42	31.6 ± 0.5	288 ± 12	6691 ± 83	156 ± 4	7990 ± 947	403 ± 1	874 ± 37
Total	31000 ± 800	36.5 ± 0.6	343 ± 1	26700 ± 500	270 ± 8	9376 ± 44	521 ± 5	1006 ± 10
Total[c]	NA	36.4 ± 2.8	362 ± 12	NA	NA	NA	501 ± 47	987 ± 37
Extraction yield (%)	8.17	86.6	84.0	25.1	57.6	85.2	77.3	86.9
CRM 701								
HCl	1767 ± 13	10.3 ± 0.1	216 ± 4	6434 ± 11	283 ± 0.6	1767 ± 13	129 ± 1	365 ± 1
Total	71470 ± 150	12.6 ± 0.3	279 ± 0.6	38580 ± 290	689 ± 10	2212 ± 39	156 ± 2	476 ± 2
Total[a]	75706 ± 500[d]	(11.7 ± 1.0)	(275 ± 13)	38598 ± 629[d]	774 ± 77[d]	2620 ± 87[d]	(143 ± 6)	(454 ± 19)
Extraction yield (%)	2.47	88.0	78.5	16.7	41.1	79.9	90.2	80.4
SRM RTH 912								
HCl	2300 ± 10	1 ± 0.04	91.3 ± 1.6	1084 ± 8	442 ± 6	38.9 ± 0.7	46.5 ± 0.4	244 ± 3
Total	59800 ± 600	1.67 ± 0.3	120 ± 2	33400 ± 200	692 ± 2	698 ± 9	72.5 ± 1	405 ± 4
Total[a]	64200 ± 11160	1.26 ± 0.35	127 ± 12	36600 ± 6200	792 ± 88	659 ± 94	73.4 ± 17.4	410 ± 53
Extraction yield (%)	3.58	79.4	71.9	2.96	55.8	5.90	63.4	59.5
CRM GBW 07603								
Total	2014 ± 142	0.42 ± 0.02	6.28 ± 0.26	1022 ± 46	60.1 ± 4.2	1018 ± 46	41.5 ± 2.3	50.9 ± 2.6
Total[a]	2000 ± 200	(0.38)	6.6 ± 0.4	1070 ± 40	61 ± 3	1000 ± 30	47 ± 2	55 ± 2
CRM GBW 07604								
Total	1002 ± 42	0.29 ± 0.03	8.9 ± 0.6	284 ± 14	41.5 ± 3.1	1748 ± 52	1.66 ± 0.15	35.1 ± 2.4
Total[a]	1040 ± 50	0.32 ± 0.05	9.3 ± 0.5	274 ± 10	45 ± 2	1680 ± 40	1.5 ± 0.2	37 ± 1

NA, not available. Extraction yields of dilute HCl-fractional metal concentrations were calculated from certified or indicative (SRM 2710, SRM 2711, CRM 701, SRM RTH 912) and own (CRM 483, CRM 701) total metal concentration values.

[a] Certified and (indicative) values from RM certificates.
[b] Informative values for 4 h single extraction with 1 mol l^{-1} HCl from Larner et al. [44].
[c] Informative values for pseudototal *aqua regia* concentrations obtained by the ISO Norm 11466 from Rauret et al. [47].
[d] Informative values for pseudototal *aqua regia* concentrations obtained by the ISO Norm 11466 from Guevara-Riba et al. [48].

2.8. Instrumentation

Flame atomic absorption spectrometry (FAAS) was used for determination of Ca, Cd, Cu, Fe, K, Mg, Mn, Ni, Pb and Zn using a PerkinElmer Model 1100 spectrometer (USA) with air-acetylene flame. Graphite furnace atomic absorption spectrometry (GF AAS) was used for determination of Cd, Ni and Pb at low concentration levels using a PerkinElmer Model 3030 Zeeman (USA). Inductively coupled plasma optical emission spectrometry (ICP OES) was used for determination of Al, P and some other elements using a Kontron Model Plasmakon S 35 sequential spectrometer (Germany). The concentration of Al was measured also by FAAS using a PerkinElmer Model 5000 spectrometer (USA) with nitrous oxide-acetylene flame. The concentration of As was measured by hydride generation atomic absorption spectrometry (HG AAS) using a PerkinElmer Model 1100 spectrometer (USA) equipped with an HG-2 continuous-flow hydride generator (Czech Republic) and an electrically heated quartz tube.

3. Results and discussion

3.1. Validation of decomposition procedures and single and sequential extractions

The decomposition procedures for determination of total concentrations of studied elements in soil and plant samples were validated by seven soil, sediment and plant RMs (Table 2). The reliability of these procedures was tested for eight (Al, Cd, Cu, Fe, Mn, P, Pb, Zn) from thirteen studied elements using of certified, indicative and informative values of total element contents in used RMs (Table 3). The certified and indicative values of total element contents were taken from the certificates of given RMs. The informative values of pseudototal *aqua regia* (obtained according to ISO Norm 11466) concentrations were taken from the papers of Rauret et al. [47] and Guevara-Riba et al. [48]. On the basis of the accordance of these data with own results the accuracy of obtained results can be considered as very good. The precision of measured data was satisfactory.

The single extraction procedure with $0.5 \, mol \, L^{-1}$ HCl was validated by its application to soil and sediment RMs (Table 2). The dilute HCl-fractional concentrations of seven (Al, Cd, Cu, Fe, Mn, Pb, Zn) from nine studied metals and phosphorus determined in five RMs are listed in Table 3. The precision of obtained results was good for all eight elements (the most of R.S.D. values is less than 5%). The efficiency of this procedure was tested on SRM 2711 with informative values for single $1 \, mol \, L^{-1}$ HCl extraction by Larner et al. [44]. In spite of two times higher HCl concentration and four times longer extraction time used in cited work, the obtained results for Cd, Cu and Zn give a very good conformity with published informative values. The different extraction conditions cause that own results for other metals except Pb are lower than informative values. The highest difference was found for Fe (15%) and Pb (21%). The lowest extraction yields of dilute HCl were achieved for Al and Fe, the highest ones for Cd, Cu and Pb.

The optimized BCR SEP specific fraction precision and accuracy were tested for six (Al, Cu, Fe, Mn, Pb, Zn) from nine studied metals by the soil and sediment RMs (SRM 2710, SRM 2711, CRM 483, CRM 701) in previously published work [27]. For Al the precision, repeatability and accuracy of optimized BCR SEP was evaluated by using of fourteen soil, sediment and rock RMs including also above mentioned four RMs [26,28,49,50]. The BCR SEP specific fraction precision was acceptable, the most of relative standard deviation (R.S.D.) values calculated from four replicates for all BCR SEP steps were less than 10% for all six metals [27]. The BCR SEP specific fraction repeatability which was tested only on SRM 2710 for Al [28,50] was also acceptable, the grand mean R.S.D. values calculated from results of BCR SEP performed in our laboratory five times within 2 years were less than 10% for all BCR SEP steps. The accuracy of optimized BCR SEP for the specific fractions of Cu, Pb and Zn ranged from 3 to 15% of certified or informative values for all BCR SEP steps. More variable results were observed for Al and Fe. The highest differences were found in the case of Mn [27].

3.2. Total concentrations of the elements

The determined total contents of macronutrients and studied risk metals concentrations in the investigated samples of topsoils and plants are given in Tables 4 and 5.

The low Ca and Mg soil contents on locality A are related with the main mineral composition of soil samples and type of the anthropogenic activity. The primary reason of low soil pH on this locality is an acid sulphatic weathering and low humus content which cause not only the degradation of these soils but the lost of meadow vegetation as well [27,45]. The low pH values indirectly influence accessibility of Ca^{2+}, Mg^{2+} and K^+ ions because in exchangeable positions they are replaced by Al^{3+} ions. In case of phosphorus it can be fixed on Fe and Al in acid medium. Chemical data which indicate important losses of exchangeable Ca, Mg and K are associated with low soil pH and increase of exchangeable Al. At soil pH < 4.5 aluminium is accumulated to root system as well as to overgrown parts and it reduces root accretion and evolution what is reflected in inhibition of the synthesis of some substances important for plant growth [52]. In plant tissues the aluminium is bounded in organic macromolecules (proteins, polynucleotides) and it can cause the changes in polypeptides states which have the important function of plant tolerance on metal impact by so-called stress polypeptide production [53,54]. The negative impact of liberated aluminium is manifested by high concentration of phytoavailable aluminium which strongly affects the meadow ecosystem at examined study site. Original dominant grassland on this locality was replaced by grass *Festuca Rubra* which is very resistant to extreme unfavourable properties of the environment. The total contents of Cu and Pb are slightly higher than the A limit maximum allowable concentration (MAC) values for Slovakian agricultural soils. The Dutch limits A, B and C based on background values were adopted in the definition of MAC values [51]. The higher concentrations of Cu and Pb are connected with the occurence of polymetallic ores in this local-

Table 4
Selected chemical data of soil and plant samples—macronutrients content values from three replicates (mean ± standard deviation)

Locality	Sample	Ca (mg kg^{-1})	Mg (mg kg^{-1})	K (mg kg^{-1})	P (mg kg^{-1})
	Soil	1180 ± 23	4020 ± 60	19900 ± 300	1050 ± 32
A	Grass root	919 ± 19	632 ± 10	1590 ± 30	1000 ± 31
	Grass stem	1280 ± 15	882 ± 12	25260 ± 400	2403 ± 75
	Soil	1980 ± 25	7300 ± 109	2300 ± 40	817 ± 35
	Blueberry root	1405 ± 22	438 ± 8	1890 ± 30	263 ± 10
B	Blueberry twig	8283 ± 125	1180 ± 10	3970 ± 40	715 ± 30
	Blueberry leaf	7826 ± 120	2218 ± 32	11070 ± 220	964 ± 32
	Blueberry fruit	2465 ± 38	1240 ± 10	11800 ± 200	1570 ± 62
	Soil	20180 ± 220	25600 ± 400	11860 ± 220	930 ± 42
C	Blackberry root	4590 ± 70	1250 ± 30	3110 ± 50	736 ± 38
	Blackberry twig	5900 ± 60	1370 ± 30	10590 ± 220	965 ± 35
	Blackberry leaf	12600 ± 200	4710 ± 60	16470 ± 300	1395 ± 42

ity. These metals and Cd, Ni, Zn as well are affecting the plant root growth and they cause the changes in plant photosynthetic apparatus namely in pigments. In the central tissues they are not localized excessively [55,56].

The low contents of Ca, K and P were determined in the soils from locality B (Table 4) which can be classified as Histo-Humic Podzol on granitic and metamorphic rocks. These naturally acid soils can contain also larger amounts of free Al, Fe and Mn. The source of this acidity originates from the process of soil podzolization which is connected with high rainfalls, water system on this locality and acid vegetation, which decomposition products acidify whole soil profile and long-haul acid deposit transfers as well. According to Ulrich theory [57] the specific neutralization reactions run all in the soils are depending on ion occurrence in soil solution. By this theory it can be distinguished the buffering system of carbonates, silicates, exchangeable cations, aluminium/iron and iron. If the soil loading by acid deposits exceeds the specific buffering capacity of given system, the soil is acidified and degraded to other buffering system. In the extremely acidified stadium (pH < 3.8) the neutralization reactions of aluminium proceed sharing the iron hydroxides and organic complexes formation. By subsequent decrease of pH value below 3.2 the buffering reactions are shifting to the phase of neutralization reactions for iron only. The action of acids presented or incoming to the system is attenuated by the dissolving of iron oxides and releasing of Fe cations migrating in the profile. Thus the clay fraction can be destroyed, the soil life is drastically restricted and the organic matter is accumulated on the soil surface as raw humus. The organic matter fraction is represented by the living and dying off plants and animal organisms which produce the different acid types. The important components of soil humus are the acids too. Hydrogen of their functional groups is capable of the exchangeable reactions with basic cations and thus loose hydrogen acidifies the soil solution. On the other hand the humic and fulvic acids can prevent the acidification, e.g. they generate the water insoluble Ca and Mg humates and fulvates which keep from floating and losses of these ions from the soils. They can also create aluminium complexes and the increased content of organic matter in the soil decreases not only the exchangeable Al concentration at given pH but it decreases the total acidity as well. Metal con-

centrations in the upper soil horizon on locality B exceed the A limit MAC levels for Slovakian agricultural soils by 7 times for As, 28 times for Cu, 11 times for Pb, 1.3 times for Zn, the B limit MAC levels by 6 times for As, 10 times for Cu, 6 times for Pb and the C limit MAC levels by 4 times for As, 2 times for Cu and 1.5 times for Pb, respectively (Table 5). Iron exceeds the statistical value of anomalous concentration in top horizons of Slovakian soils by 1.3 times. The high accumulation of these metals in soil surface can be derived not only from natural processes but from heavy atmospheric contamination with industrial smelting activity as well. The evidence for atmospheric pollution arises from the fact that the concentration of these metals in individual deeper soil horizons are much more lower (10–100 times).

Mining and dressing of the ore deposits characterized by antimonite, pyrite-pyrrhotite and arsenopyrite mineralization have significantly contributed to As, Cu, Ni, Zn and Pb soil contamination in the locality C. Concentrations of these metals exceed the A limit MAC values for Slovakian agricultural soils (6 times for As, 1.1 times for Cd, 2 times for Cu and Ni and 1.5 times for Zn) and B and C limit MAC values (6 and 3.7 times for As) but also recommended limits of contamination in this area (1.5 times for Fe). In the immediate vicinity of pyrite pile the intensive acidification is arising, however, it has only the local range. In the short distance from pile the concentration of Ca and Mg increases but the phosphorus content remains low due to high Fe content presence. The increased concentrations of risk metals (Table 5) in the soils occurred on the locality C are the significant hazard for soil utilization by agricultural activity and close urban agglomeration as well.

3.3. Soil–plant metal transfer study

The soil–plant transfer coefficients were calculated from ratio of the metal total plant concentration to metal total concentration in corresponding top soil horizon where plant had grown to establish a relative sequence of analyzed metals mobility on the examined localities. The results listed in Table 6 and Fig. 1 are in accord with contemporary knowledges and they affirm the plant roots ability to intake the risk metals presented in exchangeable forms in soil solutions. These metals enter to the plants not only through the plant root system but also their bioaccessibility from

Table 5
Selected chemical data of soil and plant samples—risk metals concentration values from three replicates (mean ± standard deviation)

Locality	Sample	Al (mg kg⁻¹)	As (mg kg⁻¹)	Cd (mg kg⁻¹)	Cu (mg kg⁻¹)	Fe (mg kg⁻¹)	Mn (mg kg⁻¹)	Ni (mg kg⁻¹)	Pb (mg kg⁻¹)	Zn (mg kg⁻¹)
A	Soil	58950 ± 1470	18.9 ± 0.8	0.30 ± 0.02	37 ± 0.8	32730 ± 980	163 ± 1.3	5.3 ± 0.25	99.4 ± 2.5	92.5 ± 2.2
	Grass root	2870 ± 100	1.73 ± 0.08	0.4 ± 0.035	21.7 ± 0.5	10740 ± 250	62.9 ± 1.1	1.7 ± 0.07	9.6 ± 0.62	64.5 ± 1.6
	Grass stem	990 ± 40	0.66 ± 0.03	<0.05	4.7 ± 0.3	513 ± 11	458 ± 5	2.45 ± 0.08	<2.5	29.5 ± 0.8
B	Soil	23430 ± 380	195 ± 6	0.618 ± 0.04	1004 ± 25	74800 ± 1500	346 ± 2	6.9 ± 0.22	890 ± 18	176 ± 4
	Blueberry root	550 ± 22	1.08 ± 0.05	0.215 ± 0.022	94.3 ± 2.2	614 ± 15	303 ± 1	0.65 ± 0.04	125.3 ± 3.5	64.5 ± 2
	Blueberry twig	200 ± 18	1.03 ± 0.04	0.3 ± 0.02	12.7 ± 0.8	146 ± 7	1342 ± 16	0.7 ± 0.04	7.2 ± 0.6	94 ± 1.8
	Blueberry leaf	275 ± 22	0.91 ± 0.04	0.242 ± 0.025	9.73 ± 0.8	169 ± 5	1084 ± 14	0.63 ± 0.05	3.2 ± 0.25	15.8 ± 0.5
	Blueberry fruit	51.5 ± 3	<0.005	<0.05	16.1 ± 1.1	63.7 ± 2.3	380 ± 3	<0.5	<2.5	28.1 ± 0.6
C	Soil	52980 ± 1500	186 ± 4	0.854 ± 0.05	72.3 ± 2	87710 ± 1580	524 ± 16	72 ± 2.2	48.7 ± 1.8	210 ± 4
	Blackberry root	904 ± 36	2.47 ± 0.12	0.844 ± 0.055	9.2 ± 0.7	2199 ± 47	134 ± 1	10.1 ± 0.2	4.59 ± 0.36	82.5 ± 2.5
	Blackberry twig	411 ± 20	1.82 ± 0.08	0.482 ± 0.038	5.69 ± 0.42	463 ± 12	197 ± 3	4.05 ± 0.28	<2.5	95.2 ± 2.2
	Blackberry leaf	903 ± 42	3.74 ± 0.11	0.4 ± 0.035	8.1 ± 0.66	977 ± 20	807 ± 11	7.05 ± 0.35	<2.5	77.5 ± 1.6
MAC A[a]		[103800]	29	0.8	36	[56200]	[2230]	35	85	140
MAC B[a]			30	5	100			100	150	500
MAC C[a]			50	20	500			500	600	3000

[a] Maximum allowable concentration (MAC) with limits A, B and C for risk elements in top horizons of agricultural soils of Slovakia (Declaration No. 531/1994-540) [46]; data in square brackets are statistical values of anomalous concentration of elements in top horizons of Slovakian soils [46].

atmospheric deposition through the overground parts, mainly plant leaves, is relatively significant. The absorption through the plant leaves is composed of two fundamental phases. The first one is nonmetabolic cuticular penetration which is regarded as the important way of risk metals input to the plants. The second phase is responsible to ions transport through the plasmatic membranes inwards to protoplasma cells. Like the metals intake by root system also the metals absorption by leaves they can be transfered to another plant tissues where their excess is stored. The rate of risk metal transport among the individual tissues mostly depends on plant bodies, their age and given metal properties [58].

The soil–plant transfer coefficient data in Table 6 and more illustrative diagram in Fig. 1 with the same data normalized separately for each one from three sampling localities regardless of the plant part allow to assess the plant intake intensity, phytoavailability and phytoaccumulation of studied metals for each examined site (A, B and C) individually. The results show that Mn, Cd and Zn are the most phytoavailable from all nine studied metals in all three ecosystems. These metals are significantly absorbed and accumulated by almost all given plants and their individual parts. Manganese is characterized by the highest soil–plant transfer coefficients (normalized for 100%) and the highest phytoaccumulation (the Mn soil–plant transfer coefficients range from 25 to 388%) from all studied metals for all examined ecosystems. In contrast to this fact Al, As, Pb and Fe are mostly inert to the plant ability to take up these metals at given pH value in spite of the finding that both As and Pb occur in the soils on sampling sites at very high concentration levels which exceed all three limit MAC values (A, B and C) for Slovakian agricultural soils.

The extraction yield data in Table 7 and more illustrative diagram in Fig. 2 with the first three BCR SEP steps sum and HCl extraction yields normalized separately for each one from three sampling localities regardless of the metal and the extraction procedure allow to assess the soil distribution and mobility of studied metals for each examined site (A, B and C) individually. Sums of the results obtained from first three BCR SEP steps represent so-called mobilizable fractions of given metals. These data for all studied metals except As are related to the results from dilute HCl single extraction [27]. On the basis of extraction yields from both used procedures it can be concluded that Cd and Cu are the most mobile metal from all nine studied metals in all three ecosystems. Cadmium is characterized by the highest extraction yields of BCR SEP mobilizable fractions (normalized for 100%) from all studied metals for all examined ecosystems. In contrast to this fact As is mostly inert to the leaching by both used extraction methods.

From previous findings it is obvious that from all studied metals only cadmium has the attributes of high phytoavailability and phytoaccumulation and it simultaneously disposes of considerable soil mobility in the ecosystem as well. Since Cd is very toxic the environmental risk assessment of this metal on all three examined localities is needed under such conditions. For the other studied metals with the actual contents above the A limit MAC values (e.g. Pb in A and B localities, Zn in B and C, Ni in C and Cu in all localities, see Table 5) the calculated trans-

Table 6
Soil–plant transfer coefficients in% (calculated from the ratio of the metal total plant concentration to metal total concentration in corresponding top soil horizon where plant had grown)

Locality	Sample	Al	As	Cd	Cu	Fe	Mn	Ni	Pb	Zn
A	Grass root	4.87	9.15	133	58.6	32.8	38.7	32.1	9.65	69.7
	Grass stem	1.68	3.49	<16.7	12.7	1.57	281	46.2	<2.52	31.9
B	Blueberry root	2.35	0.55	34.8	9.39	0.82	87.6	9.42	14.1	36.6
	Blueberry twig	0.85	0.53	48.5	1.26	0.20	388	10.1	0.81	53.4
	Blueberry leaf	1.17	0.47	39.2	0.97	0.23	313	9.13	0.36	8.98
	Blueberry fruit	0.22	<0.0026	<8.09	1.60	0.085	110	<7.25	<0.28	16.0
C	Blackberry root	1.71	1.33	98.8	12.7	2.51	25.6	14.0	9.43	39.3
	Blackberry twig	0.78	0.98	56.4	7.87	0.53	37.6	5.63	<5.13	45.3
	Blackberry leaf	1.70	2.01	46.8	11.2	1.11	154	9.79	<5.13	36.9

fer coefficients are lower than Cd. This fact can be explained by the lower phytoavailability and phytoaccumulation of these metals.

In certain conditions the studied plants can be remark as the bioanalytical tools for in situ separation of phytoavailable metals species directly in the ecosystem and the calculated soil–plant transfer coefficients represent the yields of such bioseparations. They express the ratio of partial soil metal concentration separated by the plants (represented by total plant metal concentration) to total soil metal content. In this case the studied plants can be considered for the long-term extraction medium. Also the analyte phytoaccumulation can play the important role in such phytoseparations what it is reflected by the soil–plant transfer coefficients higher than 100%. Therefore the calculated soil–plant transfer coefficients can be compared with the extraction yield data of all steps and their sums of optimized BCR SEP and single extraction by dilute HCl applied to soil samples and listed in Table 7. Nine diagrams in Fig. 3 with the same

data normalized separately for each one from nine studied metals regardless of the extraction procedure and the plant part are more illustrative.

Aluminium (Fig. 3a) is the most abundant metal in the soils. At low pH values it can be toxic. Almost all used conventional extraction procedures offer higher extraction yields than soil–plant transfer coefficient data for Al. Aluminium is predominantly bound to the residual BCR SEP fraction (72–94%, calculated by difference) of soil samples but its significant amounts are released also from reducible (locality A) and oxidizable (locality B) phases in second and third steps of BCR SEP. Further, the sizes of Al oxidizable soil fractions and sums of acid extractable and oxidizable soil fractions are consistent with the soil–plant transfer coefficients of plant root samples for all three localities. Aluminium data obtained from first acid extractable step of BCR SEP are in good agreement with the extraction yields of dilute HCl single extraction. In acid soil conditions the negatively impact of liberated Al is manifested by relatively high
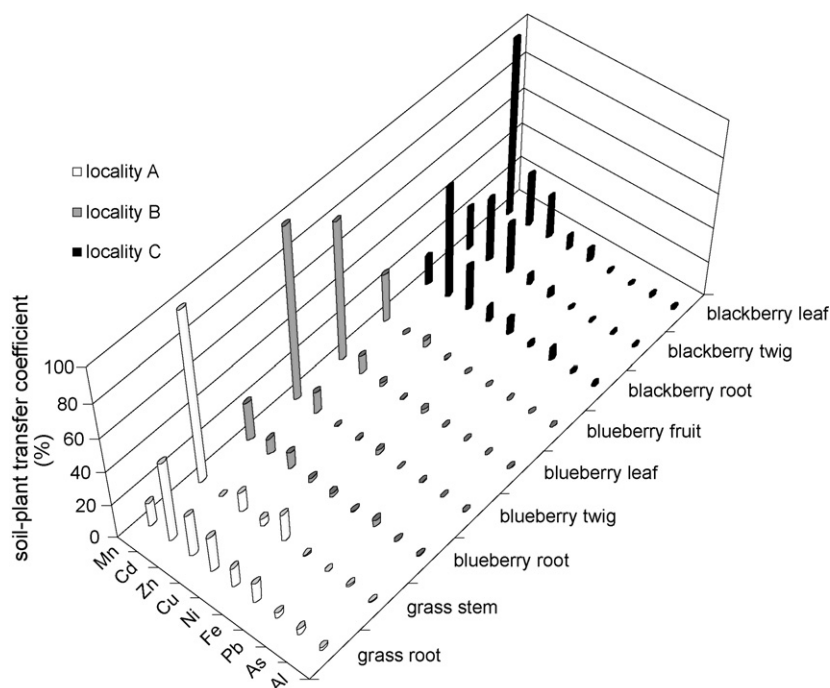
Fig. 1. Distribution of the soil–plant transfer coefficients normalized separately for each one from three sampling localities regardless of the plant part.

Table 7
Extraction yields (%) of optimized BCR SEP and single extraction with 0.5 mol L^{-1} HCl

Locality	Extraction procedure	Al	As	Cd	Cu	Fe	Mn	Ni	Pb	Zn
A	BCR SEP step 1	0.22	<0.21	98.3	8.22	0.70	5.13	19.6	1.43	10.2
	BCR SEP step 2	12.5	<0.21	<6.66	14.7	18.9	20.9	5.28	5.88	2.9
	BCR SEP step 3	2.51	<0.21	<6.66	27.2	9.07	26.8	49.1	<2.52	25.1
	BCR SEP steps 1 + 2	12.7	<0.21	98.3	22.9	19.6	26.0	24.9	7.31	13.1
	BCR SEP steps 1 + 2 + 3	15.2	<0.21	98.3	50.1	28.7	52.8	74.0	7.31	38.2
	HCl	1.16	3.12	29.7	26.4	12.3	8.47	12.8	1.35	12.5
B	BCR SEP step 1	4.59	0.35	34.0	3.52	0.05	6.42	7.54	0.36	11.3
	BCR SEP step 2	6.12	<0.21	48.5	16.4	6.45	3.61	12.8	16.1	12.2
	BCR SEP step 3	17.4	<0.21	18.6	52.2	17.1	20.5	64.5	24.0	20.7
	BCR SEP steps 1 + 2	10.7	0.35	82.5	19.9	6.50	10.0	20.3	16.5	23.5
	BCR SEP steps 1 + 2 + 3	28.1	0.35	101.1	72.1	23.6	30.5	84.8	40.5	44.2
	HCl	6.67	1.72	38.8	61.8	5.25	11.3	12.2	16.8	24.1
C	BCR SEP step 1	1.76	0.24	24.8	1.55	0.22	0.78	2.11	<4.11	1.50
	BCR SEP step 2	1.33	<0.21	46.8	3.82	7.49	2.18	0.89	12.7	0.65
	BCR SEP step 3	2.63	<0.21	18.4	10.4	4.68	3.34	5.69	<5.13	7.11
	BCR SEP steps 1 + 2	3.09	0.24	71.6	5.37	7.71	2.96	3.00	12.7	2.15
	BCR SEP steps 1 + 2 + 3	5.72	0.24	90.0	15.8	12.4	6.30	8.69	12.7	9.25
	HCl	1.36	0.99	9.37	8.33	5.46	1.29	1.14	5.26	2.10

concentrations of phytoavailable Al at all examined localities [59–61].

Arsenic (Fig. 3b) is toxic metal which may be passively insoluble forms taken up by the plants but on the studied localities it is mostly associated with the particulate contamination (total soil As contents exceed all three limit MAC values on both B and C localities) as it is demonstrate with the sequential extraction procedure. The optimized BCR SEP offered only low efficiency is not suitable for As distribution assessment in the soils because its behaviour is significantly different from other monitored metals. A special sequential extraction protocols are needed to discriminate between As bound in low soluble mineral phases and adsorbed or co-precipitated in the precipitates arising mainly from iron hydroxides and oxohydroxides [62,63].

The dilute HCl single extraction is more suitable for our purpose but it offers only less selective results.

Cadmium (Fig. 3c) is one of the most toxic and mobile metals in the soils thus its input to the plants is more intensive. It has the highest mobility in the acid soils (pH < 5.5) and this fact is evidenced also in Table 6 by calculated soil–plant transfer coefficients expression. The Cd input to the plants can proceed through the leaves (atmospheric deposit) or by root system intake from soil solution. On the locality A the transfer coefficient value calculated for plant roots exceeds 100% (the content of soil Cd is lower than plant Cd value), on the locality C it is close to 100% (Table 6). Our results confirm the literature data that in the root system as far as 90% of total Cd plant content can be often present (A and C localities). Considering its high mobility in the plant,
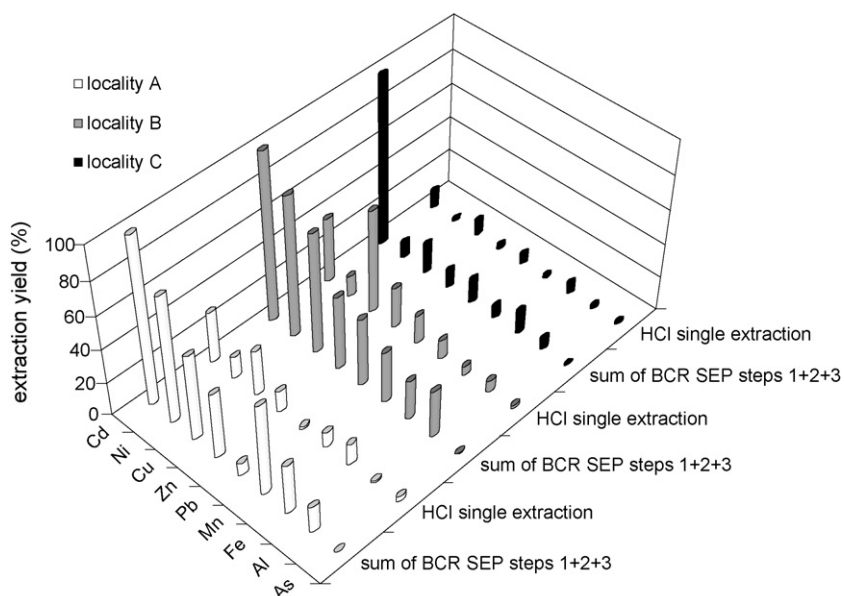
Fig. 2. Distribution of the extraction yields normalized separately for each one from three sampling localities regardless of the metal and the extraction procedure.

Cd can be transported to another plant tissues (stems, twigs, leaves, flowers and fruits) and it can unfavourably influence the agriculture commodity cultivated on acid soils. It seems that from used extraction procedures only the first step of BCR SEP and dilute HCl single extraction are of greater relevance.

Copper (Fig. 3d) has the very important biological functions in plant evolution as significant micronutrient. However increased concentrations of Cu in plant tissues can be exhibited by its phytotoxic influences. In the soils from both B and C localities, when the total Cu contents exceed the MAC values for Slovakian agricultural soils (see Table 5). But the increased contents of phytoavailable Cu in the soils did not cause its higher concentrations in overground plant biomass. The extrac-

tion yield data from individual extraction procedures are not completely consistent with obtained soil–plant transfer coefficients for all examined localities. It seems that all steps of optimized BCR SEP as well as dilute HCl single extraction have the low selectivity considering the Cu phytoavailability assessment on examined localities. Third BCR SEP oxidizable fraction and sum of first three BCR SEP fractions contain highest concentrations of Cu which is probably bound on organic or sulphidic compounds. Further, the third BCR SEP step releases the similar amounts of Cu from all soil samples as the dilute HCl single extraction.

Iron (Fig. 3e) can be also considered for important plant micronutrient. But at higher levels it can be toxic. Its total con-
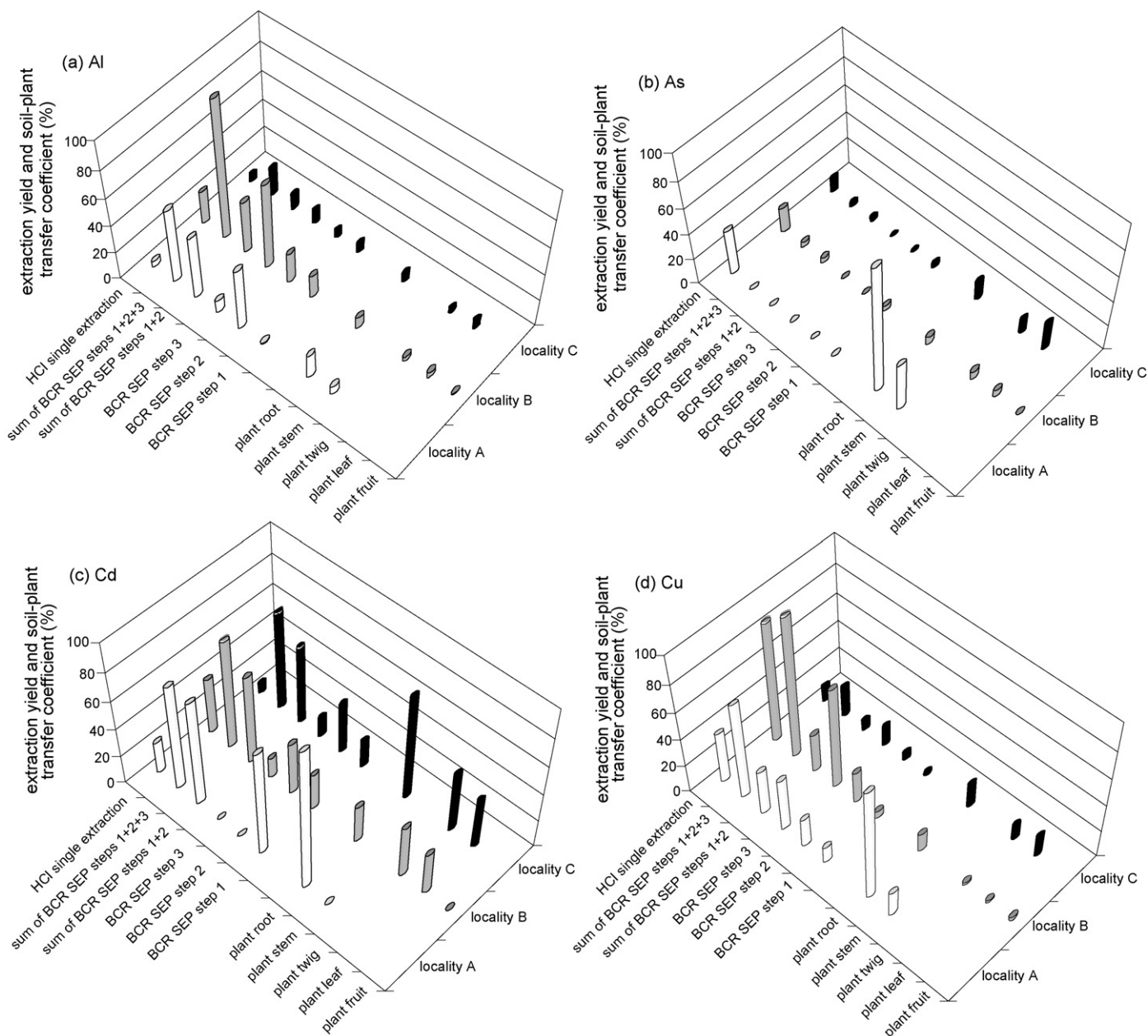
Fig. 3. (a–i) Distribution of the extraction yields and the soil–plant transfer coefficients normalized separately for each one from nine studied metals regardless of the extraction procedure and the plant part.
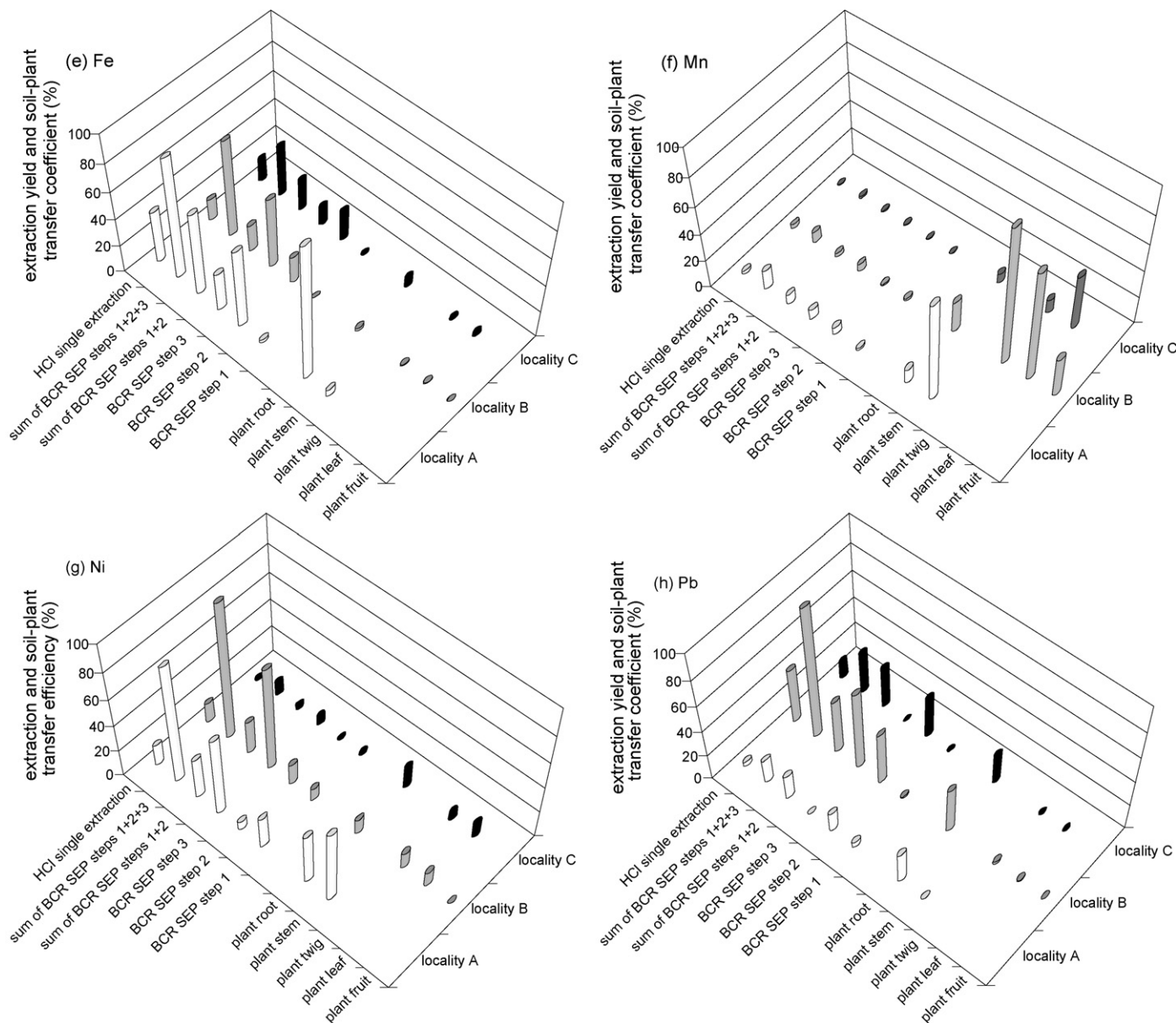
Fig. 3. (*Continued*)

tents in the soils from localities B and C are higher than the anomalous concentrations in top horizons of Slovakian soils (Table 5). But calculated soil–plant transfer coefficients for individual plant parts as well as the values of extraction yield of first BCR SEP acid extractable step are very low what pointed out that the content of phytoavailable Fe and its soil–plant mobility are very low. On the contrary, the Fe transfer coefficients for plant roots, second BCR SEP reducible step, sums of first two and three BCR SEP steps and dilute HCl single extraction are highest for the samples from locality A where Fe total soil concentration does not exceed the anomalous concentration. This fact can be caused by the lowest pH value of soil sample on locality A.

Manganese (Fig. 3f) is an ubiquitous metal in the earth crust. It is characterized by essential but at higher concentration also by toxic effects. The highest soil–plant coefficients were found for overground plant parts on all three examined localities. The Mn concentrations in almost all overground plant tissues (grass stems, blueberry twigs and both blueberry and blackberry leaves) are much higher than in relevant root and soil samples (see Table 5). The considerable phytoaccumulation of Mn in these overground plant tissues on all localities A, B and C was observed. It is expressed by soil–plant coefficients ranged from 110% for blueberry fruit to 388% for blueberry twigs (see Table 6). Similarly like in the case of Cd the atmospheric contamination by Mn can be predicted. The extraction yield data for used extraction procedures are very low compared with obtained soil–plant coefficients. Only first BCR SEP acid extractable step and dilute HCl single extraction procedures can be considered in limited extent for reliable methods for the separation of phytoavailable Mn species taken up by plant root system on given localities.
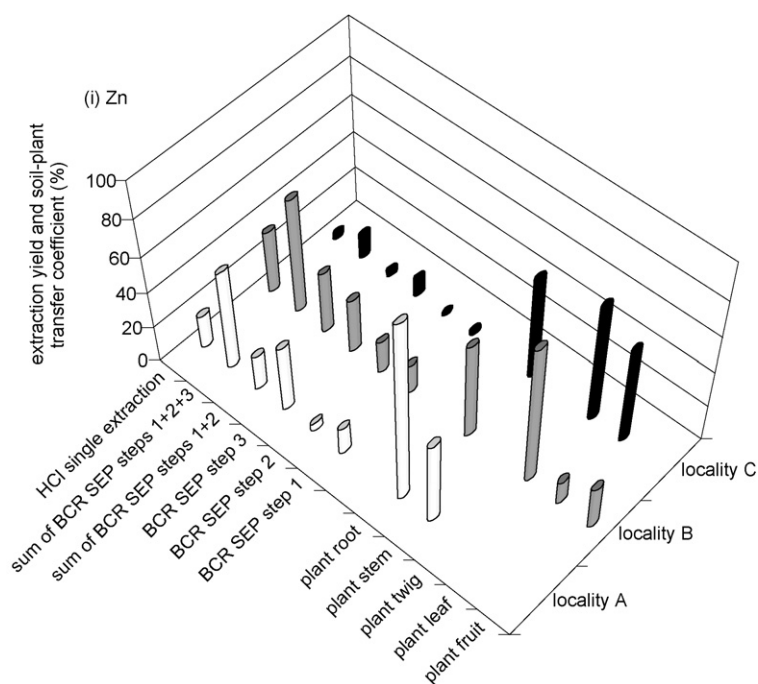
Fig. 3. (*Continued*).

Nickel (Fig. 3g) is toxic for the organisms at elevated levels but its trace amounts are required for several biological processes. It seems that Ni is evenly distributed among all plant parts within each locality. Similarly like in the case of Cu the highest amounts of Ni are leached by third BCR SEP oxidizable step which yields are related to the dilute HCl single extraction yields for all soil samples.

Lead (Fig. 3h) is a nonspecific toxic metal which inhibits many enzymatic activities that regulate a normal biological functioning. Since the Pb concentrations in the soils from A and B localities are higher than the permissible limit MAC values it could be expected that its contents in overground plant biomass will be higher as well. However Pb is one of the least mobile metals in the soils. Only that fraction of Pb total soil content is phytoavailable which is present in the soil solution. The other Pb species are heavily inaccessible to the plants. Up to 90% of total Pb plant concentrations are present in root systems on all localities (see Table 5). The low Pb mobility in the soil confirms also our results from BCR SEP when no more than 13% of Pb total soil content are in the mobilizable forms (except the locality B, see Table 7). The lower mobility of Pb can be related to sulphate content in the soils from localities A and C (Table 1). The calculated transfer coefficients show that the Pb plant intake intensities are very low on all examined localities.

Zinc (Fig. 3i) is an essential metal for plant nutrition but at increased content it may be toxic. In the soils from localities B and C when the total Zn contents slightly exceed the A limit MAC values (see Table 5). The increased contents of available Zn soil forms did not cause their higher concentrations in overground plant biomass. The highest concentration and soil–plant coefficient for Zn were obtained for grass root sample from locality A, similarly like in the case of Al, As, Cd, Cu and Fe. The third BCR SEP oxidizable step and dilute HCl

single extraction procedures offer the highest extraction yield data. Further, the dilute HCl single extraction gives the results related to data obtained in first acid extractable step of BCR SEP.

In our previous works [27] the high correlation between dilute HCl extractable amounts of some metals (Al, Cu, Fe, Mn, Pb, Zn) in the soils and their amounts obtained using the sum of all three steps of BCR SEP was found. Thus the dilute HCl single extraction can supersede more labour BCR SEP. This approach can be utilized as a simple, rapid and cost-effective tool for the monitoring of contaminated areas. The presented results confirm the fitness of this procedure only for standard fractionation of these metals in soil samples but this technique is not suitable for the study of soil–plant mobility. The first BCR SEP acid extractable step is much suitable for this purpose. This fact is also indicated by the correlation between first BCR SEP step extraction yields and soil–plant root transfer coefficients for all studied metals and the localities A and C ($R = 0.7701$ and $R = 0.8539$, respectively).

4. Conclusions

The partitioning of major and trace risk metals in acid soils contaminated by different sources by optimized BCR three-step SEP allowed to predict the relative mobility of these metals in examined ecosystems. Moreover the results from this study can be utilized for qualitative transfer metal mobility prediction in soil–plant systems on examined localities as well. The relative mobility of the considered metals can be well predicted in general when comparing the yields of the first step of BCR SEP with calculated soil–plant transfer coefficients. Based on these results it could be classified the relative mobility of studied metals in different soil systems. However for quantitative and more

reliable estimation of the metal phytoavailability this approach requires to complete this study by other soil parameters.

Acknowledgements

References

[1] D.C. Adriano, Trace Elements in Terrestrial Environments, Biogeochemistry, Bioavailability and Risks of Metals, second ed., Springer, New York, 2001.
[2] A. Kabata-Pendias, Geoderma 122 (2004) 143.
[3] F. De Nicola, G. Maisto, A. Alfani, Sci. Total Environ. 311 (2003) 191.
[4] X. Li, I. Thornton, Appl. Geochem. 16 (2001) 1693.
[5] B. Liao, A. Guo, A. Probst, J.L. Probst, Geoderma 127 (2005) 91.
[6] L. Hernandez, A. Probst, J.L. Probst, E. Ulrich, Sci. Total Environ. 312 (2003) 195.
[7] A. Probst, A. El Ghmari, D. Aubert, B. Fritz, R. McNutt, Chem. Geol. l70 (2000) 203.
[8] L. Boruvka, V. Podrazsky, L. Mladkova, I. Kunes, O. Drabek, Soil Sci. Plant Nutr. 51 (2005) 745.
[9] O. Mestek, K. Volka, Chem. Listy 87 (1993) 795.
[10] J. Makovnikova, G. Barancikova, P. Dlapa, K. Dercova, Chem. Listy 100 (2006) 424.
[11] V.J.G. Houba, T.M. Lexmond, I. Novozamsky, J.J. van der Lee, Sci. Total Environ. 178 (1996) 21.
[12] M. Sager, Accredit. Qual. Assur. 4 (1999) 299.
[13] D. Remeteiova, E. Krakovska, E. Smincakova, J. Tomko, V. Vojtekova, Chem. Pap. 57 (2003) 188.
[14] L. Boruvka, O. Drabek, Plant Soil Environ. 50 (2004) 339.
[15] D. Remeteiova, E. Smincakova, K. Florian, Microchim. Acta 156 (2007) 109.
[16] S. Sauve, W.A. Norwell, M. McBride, W. Hendershot, Environ. Sci. Technol. 34 (2000) 291.
[17] Obrador, J.M. Alvarez, L.M. Lopez-Valdivia, D. Gonzalez, J. Novillo, M.I. Rico, Geoderma 137 (2007) 432.
[18] A.K. Gupta, S. Sinha, J. Hazard. Mater. 149 (2007) 144.
[19] K. Chojnacka, A. Chojnacki, H. Gorecka, H. Gorecki, Sci. Total Environ. 337 (2005) 175.
[20] Ch. Gleyzes, S. Tellier, M. Astruc, Trac-Trend. Anal. Chem. 21 (2002) 451.
[21] A. Sahuquillo, A. Rigol, G. Rauret, Trac-Trend. Anal. Chem. 22 (2003) 152.
[22] V. Vojtekova, E. Krakovska, Chem. Listy 100 (2006) 1096.
[23] I. Ahumada, J. Mendoza, E. Navarrete, L. Ascar, Commun. Soil Sci. Plant Anal. 30 (1999) 507.
[24] L.J. Cajuste, J. Cruz-Diaz, C. Garcia-Osorio, J. Environ. Sci. Health A 35 (2000) 1141.
[25] V. Vojtekova, E. Krakovska, D. Mackovych, D. Remeteiova, J. Tomko, Chem. Pap. 57 (2003) 179.
[26] P. Matus, J. Kubova, M. Bujdos, V. Stresko, J. Medved, Anal. Bioanal. Chem. 379 (2004) 96.
[27] J. Kubova, V. Stresko, M. Bujdos, P. Matus, J. Medved, Anal. Bioanal. Chem. 379 (2004) 108.
[28] P. Matus, J. Kubova, M. Bujdos, J. Medved, Anal. Chim. Acta 540 (2005) 33.
[29] A. Vanek, L. Boruvka, O. Drabek, M. Mihaljevic, M. Komarek, Plant Soil Environ. 51 (2005) 316.
[30] P.K. Lee, J.C. Touray, Water Res. 32 (1998) 3425.
[31] R. Canet, F. Pomares, F. Tarazona, M. Estela, Commun. Soil Sci. Plant Anal. 29 (1998) 697.
[32] I. Walter, G. Cuevas, Sci. Total Environ. 226 (1999) 113.
[33] M. Pueyo, J. Sastre, E. Hernandez, M. Vidal, J.F. Lopez-Sanchez, G. Rauret, J. Environ. Qual. 32 (2003) 2054.
[34] A.M. Ure, P. Quevauviller, H. Muntau, B. Griepink, Int. J. Environ. Anal. Chem. 51 (1993) 135.
[35] G. Rauret, J.F. Lopez-Sanchez, A. Sahuquillo, R. Rubio, C.M. Davidson, A.M. Ure, P. Quevauviller, J. Environ. Monit. 1 (1999) 57.
[36] G.E.M. Hall, G. Gauthier, J.C. Pelchat, P. Pelchat, J.E. Vaive, J. Anal. Atom. Spectrom. 11 (1996) 787.
[37] M.D. Ho, G.J. Evans, Anal. Commun. 34 (1997) 363.
[38] R.A. Sutherland, F.M.G. Tack, Anal. Chim. Acta 454 (2002) 249.
[39] K.F. Mossop, C.M. Davidson, Anal. Chim. Acta 478 (2003) 111.
[40] V. Vojtekova, D. Mackovych, E. Krakovska, Microchim. Acta 150 (2005) 261.
[41] E.D. van Hullebusch, S. Utomo, M.H. Zandvoort, P.N.L. Lens, Talanta 65 (2005) 549.
[42] F. Madrid, R. Reinoso, M.C. Florido, E.D. Barrientos, F. Ajmone-Marsan, C.M. Davidson, L. Madrid, Environ. Pollut. 147 (2007) 713.
[43] I. Ahumada, P. Escudero, L. Ascar, J. Mendoza, P. Richter, Commun. Soil Sci. Plant Anal. 35 (2004) 1615.
[44] B.L. Larner, A.J. Seen, A.T. Townsend, Anal. Chim. Acta 556 (2006) 444.
[45] O. Lintnerova, V. Sucha, V. Stresko, Geol. Carpath. 50 (1999) 395.
[46] J. Veselsky, J. Forgac, S.Y. Mejeed, Mineralia Slov. 28 (1996) 209.
[47] G. Rauret, J.F. Lopez-Sanchez, A. Sahuquillo, E. Barahona, M. Lachica, A.M. Ure, C.M. Davidson, A. Gomez, D. Luck, J. Bacon, M. Yli-Halla, H. Muntau, P. Quevauviller, J. Environ. Monit. 2 (2000) 228.
[48] A. Guevara-Riba, A. Sahuquillo, R. Rubio, G. Rauret, Sci. Total Environ. 321 (2004) 241.
[49] J. Kubova, P. Matus, M. Bujdos, J. Medved, Anal. Chim. Acta 547 (2005) 119.
[50] P. Matus, J. Kubova, M. Bujdos, J. Medved, Talanta 70 (2006) 996.
[51] J. Curlik, P. Sefcik, Geochemical Atlas of the Slovak Republic, Part V: Soils, Ministry of the Environment of the Slovak Republic, Bratislava, 1999.
[52] B. Brazdovicova, G. Vizarova, T. Zatkalikova, Biologia 49 (1994) 899.
[53] K.C. Snowden, R.C. Gardner, Plant Physiol. 103 (1993) 855.
[54] G. Vizarova, K. Bacigalova, L. Tamas, Czech Mycol. 54 (2003) 261.
[55] A. Pavlovic, E. Masarovicova, K. Kralova, J. Kubova, Bull. Environ. Contam. Toxicol. 77 (2006) 763.
[56] P. Castaldi, G. Garau, P. Melis, Fresenius Environ. Bull. 13 (2004) 1322.
[57] B. Ulrich, M.E. Summer (Eds.), Soil Acidity, Springer, Berlin, 1991.
[58] A. Kabata-Pendias, H. Pendias, Trace Elements in Soils and Plants, third ed., CRC Press, Boca Raton, 2001.
[59] P. Matus, J. Kubova, J. Inorg. Biochem. 99 (2005) 1769.
[60] P. Matus, J. Kubova, Anal. Chim. Acta 573/574 (2006) 474.
[61] P. Matus, J. Inorg. Biochem. 101 (2007) 1214.
[62] B. Daus, H. Weiss, R. Wennrich, Talanta 46 (1998) 867.
[63] M. Bauer, C. Blodau, Sci. Total Environ. 354 (2006) 179.

Erratum

Erratum to "Development of novel reactions for the simple and sensitive spectrophotometric determination of vanadium in various samples" [Talanta 71 (2) (2007) 588–595]

K. Suresh Kumar [b], K. Suvardhan [b], L. Krishnaiah [b], D. Rekha [b], K. Kiran [a], K. Janardhanam [a], B. Jayaraj [c], P. Chiranjeevi [b],*

[a] *Department of Environmental Sciences, S.V. University, Tirupati 517 502, Andhra Pradesh, India*
[b] *Environmental Monitoring Laboratory, Department of Chemistry, S.V. University, Tirupati 517 502, Andhra Pradesh, India*
[c] *Department of Mathematics, S.V. University, Tirupati 517 502, Andhra Pradesh, India*

This article has been retracted at the request of the Editors-in-Chief.

Considerable concern was raised about the research purportedly conducted at Sri Venkateswara University, India with the alleged involvement of Professor P. Chiranjeevi. Questions were raised as to the volume of publications, the actual capacity (equipment, orientation and chemicals) of the laboratory in which Professor Chiranjeevi worked, the validity of certain of the research data identified in the articles, the fact that a number of papers appear to have been plagiarized from other previously published papers, and some aspects of authorship.

Professor Chiranjeevi was given the opportunity to respond to these allegations. Thereafter, a committee was constituted by the University to look into these allegations. Based on the enquiry committee report, we have been informed by the head of the Department of Chemistry at Sri Venkateswara University that the university authorities have taken disciplinary action against Professor Chiranjeevi, as the university considers that there are grounds for such action.

Therefore, based on the results of this investigation, the Editors-in-Chief are retracting this article.

An LC–MS method for the determination of pharmaceutical compounds in wastewater treatment plant influent and effluent samples

C. Lacey [a], G. McMahon [b], J. Bones [b], L. Barron [b], A. Morrissey [c], J.M. Tobin [a],*

[a] School of Biotechnology, Dublin City University, Dublin 9, Ireland
[b] School of Chemical Sciences, Dublin City University, Dublin 9, Ireland
[c] Oscail, Dublin City University, Dublin 9, Ireland

Abstract

Pharmaceuticals are continually introduced into the environment as a result of industrial and domestic use. In recent years they have emerged as environmental pollutants. An analytical method has been developed allowing for simultaneous detection and identification of 20 pharmaceutical compounds from various therapeutic classes using solid phase extraction (SPE) followed by liquid chromatography-electrospray ionisation mass spectrometry (LC–MS/MS). The limits of detection and limits of quantitation for the method were in the ng/L–μg/L range. The method was applied to influent and effluent samples from three wastewater treatment plants (WWTPs). Fifteen compounds were identified in the sample matrix with salicylic acid and ibuprofen being the most abundant at 9.17 and 3.20 μg/L respectively.
© 2008 Elsevier B.V. All rights reserved.

Keywords: LC–MS/MS; Pharmaceuticals; Wastewater treatment plant

1. Introduction

Pharmaceuticals and personal care products have traditionally received little attention as potential environmental pollutants. However, in recent years there has been an increase in the number of publications reporting the level of contamination from these sources in the environment [1–3]. Although their toxicity to aquatic and terrestrial organisms is relatively unknown a number of reported investigations has shown that pharmaceutical compounds pose a real threat to the environment [4,5]. Diclofenac for example which is frequently detected in aquatic matrices, has been found to have adverse effects in both rainbow trout and vultures. Diclofenac accumulates, with a concentration factor of up to 2732, in the liver of rainbow trout and causes histopathological alterations in both the kidneys and gills [6]. In vulture populations this drug has been shown to cause renal failure and has resulted in a population decline in Pakistan [4]. This highlights the potential danger to both terrestrial and aquatic life. Moreover, it underlines the latent risk to humans.

Wastewater treatment plants (WWTPs) have been identified as a major point source of pharmaceuticals and personal care products entering the environment as they receive continuous inputs of these compounds either as the parent compound or as an array of metabolites [7]. Removal efficiencies in WWTPs are often low, for example, removal rates for carbamazepine in a German WWTP was 7% while the average removal rate for the 14 compounds investigated was 65% [8]. Compounds not removed are released to receiving water bodies in WWTP effluent streams.

Both the number of pharmaceutical compounds licensed for human use and their annual consumption have increased dramatically over the past number of years. In Ireland, the number of compounds licensed for human use by the Irish Medicines Board increased by 942 to approximately 6000 in 2005 [9]. These compounds and their metabolites may potentially enter the environment. Despite this there is no monitoring of the level of contamination caused by such pollutants in most Irish waters to date.

For these reasons the aim of this work was to develop a sensitive analytical method for the detection of 20 compounds, from a variety of therapeutic classes, in wastewater streams. The range of analytes chosen includes compounds found on the Irish

Table 1
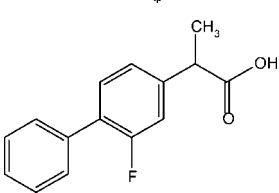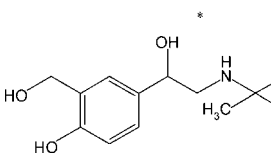Therapeutic class, structure and pK_a value for analytes
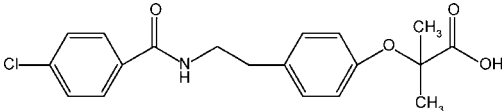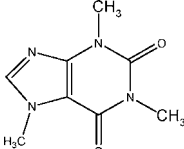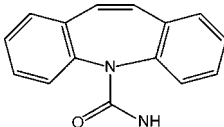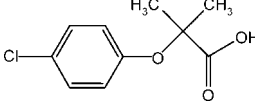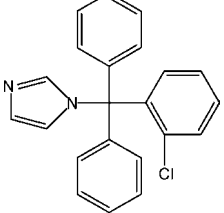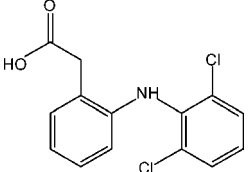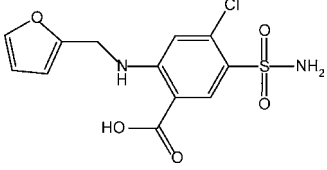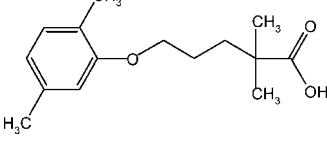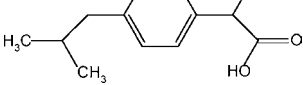
Compound	Therapeutic class	Chemical structure	CAS No.	pK_a	Ref.
Bezafibrate	Antilipemic		41859-67-0	3.6	[22]
Caffeine	CNS stimulant		58-08-2	14.0	[17]
Carbamazepine	Anti convulsant		298-46-4	13.9	[17]
Clofibric acid	Antilipemic		882-09-7	3.2	[23]
Clotrimazole	Antifungal agent		23593-75-1	6.1	[17]
Diclofenac	Anti-inflammatory		15307-79-6	4.2	[22]
Flurbiprofen	Anti-inflammatory		5104-49-4	4.3	[22]
Furosemide	Loop diuretic		54-31-9	3.9	[17]
Gemfibrozil	Lipid regulating agent		25812-30-0	4.8	[24]
Ibuprofen	Anti-inflammatory		31121-93-4	4.3	[22]

Table 1 (*Continued*)
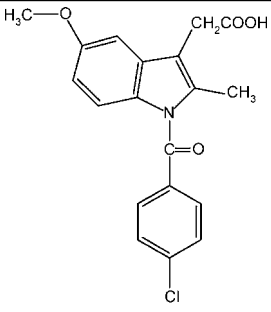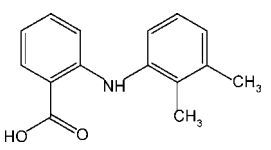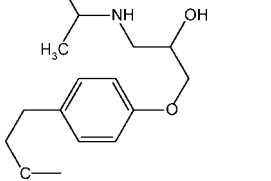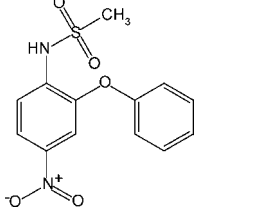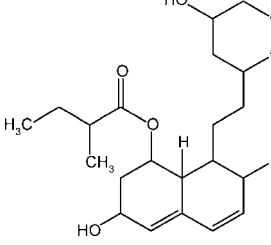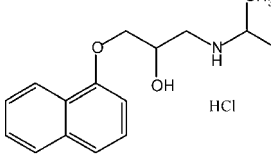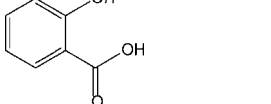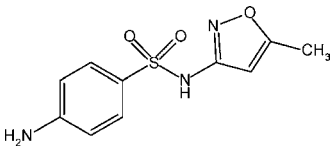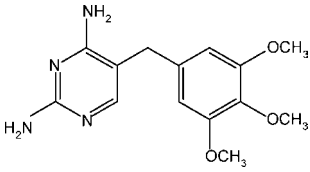
Compound	Therapeutic class	Chemical structure	CAS No.	pKa	Ref.
Indomethcin	Anti-inflammatory		53-86-1 4.5	4.5	[17]
Mefenamic acid	Anti-inflammatory		61-68-7	4.2	[17]
Metoprolol	Beta blocker		56392-17-7	9.4	[22]
Nimesulide	Anti-inflammatory		51803-78-2	6.5	[25]
Pravastatin	Cholesterol lowering Statin		81131-70-6	4.7	[27]
Propranolol hydrochloride	Beta blocker		318-98-9	9.5	[22]
Salbutamol	Beta$_2$ agonist		18559-94-9	9.2	[26]
Salicylic acid	Analgesic/aspirin metabolite		69-72-7	3.5	[17]

Table 1 (*Continued*)

Compound	Therapeutic class	Chemical structure	CAS No.	pK_a	Ref.
Sulfamethoxazole	Antibiotic		723-46-6	1.8, 5.6	[22]
Trimethoprimm	Antibacterial agent		738-70-5	3.2	[22]

top 100 most frequently prescribed compounds for 2004 and compounds regularly reported in the literature [20]. A diverse range of non-steroidal anti-inflamatories, beta-blockers, antibiotics, anti-convulsants, antilipemics, lipid regulating agents, diuretics, CNS stimulants and anti convulsants was included in the list of chosen analytes (Table 1). An array of methods including LC–MS, GC–MS, CE–MS and more recently immunoanalytical techniques such as ELISA assays have been utilised for the detection and quantification of pharmaceutical compounds in environmental matrices [10–12]. Reversed phase chromatography is used extensively for the analysis of pharmaceuticals in wastewater and surface water samples and was therefore chosen for this work due to its applicability to a wide range of compounds, including polar, thermo-labile compounds [13–15]. The use of mass spectrometry as a detector following LC separation allows not only quantitation of the analytes but identification also. This LC–MS/MS method was validated and applied to influent and effluent samples collected at three wastewater treatment plants in the greater Dublin area.

2. Materials and methods

2.1. Chemicals and reagents

Methanol, acetonitrile, water, LC–MS Chromosolv acetonitrile with 0.1% ammonium acetate and LC–MS Chromosolv water with 0.1% ammonium acetate were purchased from Sigma–Aldrich (Steinham, Germany) and were either of HPLC grade or LC–MS grade. Dichlorodimethylsilane and toluene were purchased from Sigma–Aldrich. Pharmaceutical standards were of a high purity ≥95%. Trimethoprim and caffeine were obtained from Fluka (Buchs, Switzerland). Bezafibrate, flurbiprofen, indomethcin, ibuprofen sodium salt, mefenamic acid, gemfibrozil, salbutamol, sulfamethoxazole, furosimde, carbamazepine, nimesulide, salicylic acid, propranolol hydrochloride, clofibric acid, diclofenac sodium salt, Metoprolol tartrate salt, pravastatin sodium and clotrimazole were purchased from Sigma–Aldrich.

Stock 1000 μg/mL solutions of each analyte were prepared in HPLC grade methanol or water depending on solubility and stored at 4 °C in the dark for increased stability. Working solutions, containing the 20 analytes, were prepared as required from stock solutions and stored at 4 °C in the dark.

Strata-X cartridges (200 mg/6 ml) used for solid phase extraction were purchased from Phenomenex (United Kingdom). Other cartridges used for initial investigations included Supelco C_8 (500 mg/3 mL), Supelco C_{18} (500 mg/3 mL), Waters Oasis HLB (200 mg/6 mL), Varian Focus (20 mg/3 mL), Merck LiChrolut-EN (200 mg/3 mL). Glass microfibre filters were purchased from Whatman (United Kingdom).

2.2. Glassware preparation

All glassware used was silanised by rinsing them thoroughly with a 10% (v/v) solution of dichlorodimethylsilane in toluene followed by two toluene rinses and then two methanol rinses. This was to prevent adsorption of pharmaceutical residues to the glassware.

2.3. Sample collection

Influent and effluent samples were collected from three wastewater treatment plants in the greater Dublin area. Amber glass bottles were used to collect 24 h composite samples from each site. Each bottle was filled to the top to reduce headspace and transported to the laboratory. Samples were stored at 4 °C until analysed. All samples were analysed within 72 h.

2.4. Method development

A Varian inert 9012 solvent delivery system, a Dynamax automatic sample injector model AI-200 and a Varian 9050 variable length UV–vis detector was used for the development of the standard HPLC separation. Resolution was achieved using a 150 mm × 4.6 mm end-capped Sunfire C_{18} 3.5 μm reversed phase HPLC column (Waters, Ireland). The optimal mobile phase was a gradient of 0.1% ammonium acetate in water (pH 6.2) and 0.1% ammonium acetate in acetonitrile at a flow rate of 1 mL/min. A 20 μL injection volume was employed for this assay. Absorbance was monitored at 270 nm, which was determined to be the optimum wavelength in preliminary studies performed on a scanning spectrometer.

Various sorbents including Strata-X cartridges (200 mg/6 mL), Supelco C$_8$ (500 mg/3 mL), Supelco C$_{18}$ (500 mg/3 mL), Waters Oasis HLB (200 mg/6 mL), Varian Focus (20 mg/3 mL), Merck LiChrolut-EN (200 mg/3 mL) were investigated for sample pretreatment and analyte preconcentration. Samples were first filtered through Whatman glass fibre filters to remove any solid particulates and adjusted to pH 4 using sulphuric acid. Samples were then divided into aliquots of 500 mL for solid phase extraction (SPE). A Phenomenex extraction manifold was use for SPE. Cartridges were first conditioned with 6 mL of methanol followed by 6 mL of water (HPLC grade). Following this samples were percolated over the cartridge under vacuum at a pressure of −10 kPa. The sorbent was washed with 5 mL of water after sample addition and dried under vacuum for 30 min. The sorbent was then eluted with 10 mL of methanol, dried under a stream of nitrogen and reconstituted in 0.5 mL of methanol.

LC-ESI-MS/MS analysis was performed using an Agilent 1100 LC system (Agilent Technologies, Palo Alto, CA, USA) coupled to a Bruker Daltonics Esquire-LC ion trap MS with an electrospray ionisation interface at atmospheric pressure (Bruker Daltonics, Coventry, UK). A Waters Sunfire, narrow bore, 150 mm × 2.1 mm C$_{18}$ column with 3.5 μm particle size was used for separation. A flow rate of 0.3 mL/min and an injection volume of 10 μL were employed. The LC-ESI-MS/MS system was controlled using Agilent Chemstation version A.06.01 and Bruker Daltonics Esquire Control version 6.08. Bruker Daltonics Data analysis software was used for data analysis.

As a number of compounds were to be analysed in the same separation, gradient elution allowed for a reduced run time. Mixtures of methanol, acetonitrile and water with ammonium acetate and formic acid were examined in varying ratios for mobile phase composition. The final combination was a gradient from 100% A to 100% B where A contained 20:80 acetonitrile:water with 0.1% ammonium acetate (v/v) at pH 6.2 and B contained 80:20 acetonitrile:water with 0.1% ammonium acetate (v/v). The total run time was 55 min including 10 min re-equilibration time.

MS conditions were optimised separately. Standard solutions of each analyte were directly infused, using a Cole Parmer 74900 series syringe pump (Cole Parmer, Vernon Hills, IL, USA), into the mass spectrometer at a flow rate of 300 μL/h. MS conditions were automatically optimised using Bruker Esquire software for each analyte. An average of the recorded parameters was used as the final focusing and ionisation parameters. The precursor peak with the greatest intensity was fragmented using tandem MS and the most abundant product ion was chosen for monitoring of the tandem MS signal. Extracted ion chromatograms for each product ion resulting from LC–MS/MS analysis were used for both quantitation and peak identity confirmation.

2.5. Method validation

The SPE recovery of analytes was determined in WWTP influent and effluent sample matrices. Samples were spiked with a mixed standard and extracted using Strata-X cartridges in triplicate. The concentration recovered was compared to the initial spiking concentration. Blank samples (unspiked influent and effluent samples) were also extracted to determine the concentration of analytes present in the sample before spiking which was included in the calculation.

Linearity, sensitivity (limits of detection (LOD) and limits of quantitation (LOQ)), repeatability and reproducibility were established to determine the accuracy and precision of the overall SPE-LC-ESI-MS/MS method. Six replicate samples were spiked to a concentration of 1.40 μg/L of each analyte using a mixed standard solution containing 2 mg/L (of each analyte). Influent and effluent samples were similarly spiked to give six concentrations of each analyte ranging from 0.60 to 2.80 μg/L and analysed. Linearity was determined between the peak area and concentration using regression analysis. LODs were defined as the lowest observable concentration giving a signal to noise ration of 3:1 while LOQs as the concentration resulting in a signal to noise ratio of 10:1. Both were calculated based on repeated injections ($n = 6$) of a low level standard.

3. Results and discussion

3.1. Sample pretreatment

Analyte recoveries from six commercially available solid phase extraction cartridges were investigated initially. Recoveries in excess of 100% were calculated for some analytes. This may be as a result of variances in the matrix as a real sample matrix was used for this investigation (see Section 3.3). Strata-X yielded the highest average recovery for the analytes investigated and was used for further investigations. An extraction pH of 4 was used as it had been shown previously to give optimum recovery for similar compounds [16].

3.2. Liquid chromatography tandem mass spectrometry

A Sunfire C$_{18}$, 150 mm × 2.1 mm column with a 3.5 μm particle size was used for chromatographic separations. Separation was initially monitored using UV detection. A wavelength of 270 nm was selected following an initial wavelength scan, as this gave the optimum response across the range of analytes. A series of different mobile phases including methanol and acetonitrile as the organic phase and water with ammonium acetate or formic acid added was investigated. A simple gradient of 20–80% acetonitrile with 0.1% ammonium acetate in both the aqueous and organic phase gave satisfactory separation of the 20 analytes (see Fig. 1a and b).

Over the course of the separation two analytes were found to co-elute, nimesulide and flurbiprofen, at 22.3 and 22.5 min respectively. Caffeine and trimethoprim also have close retention times of 2.0 and 2.1 min. Due to the complexity of the sample matrix and presence of matrix components UV detection was not sensitive enough for the quantitation of analytes and therefore MS detection was used.

Mass spectrometry parameters were optimised by direct infusion of standards for each analyte individually. Precursor ions for each analyte, $[M-H]^-$, $[M-COOH]^-$ and $[M+H]^+$ ions were selected in negative and positive mode respectively. Product ions were determined under MS/MS conditions and are shown
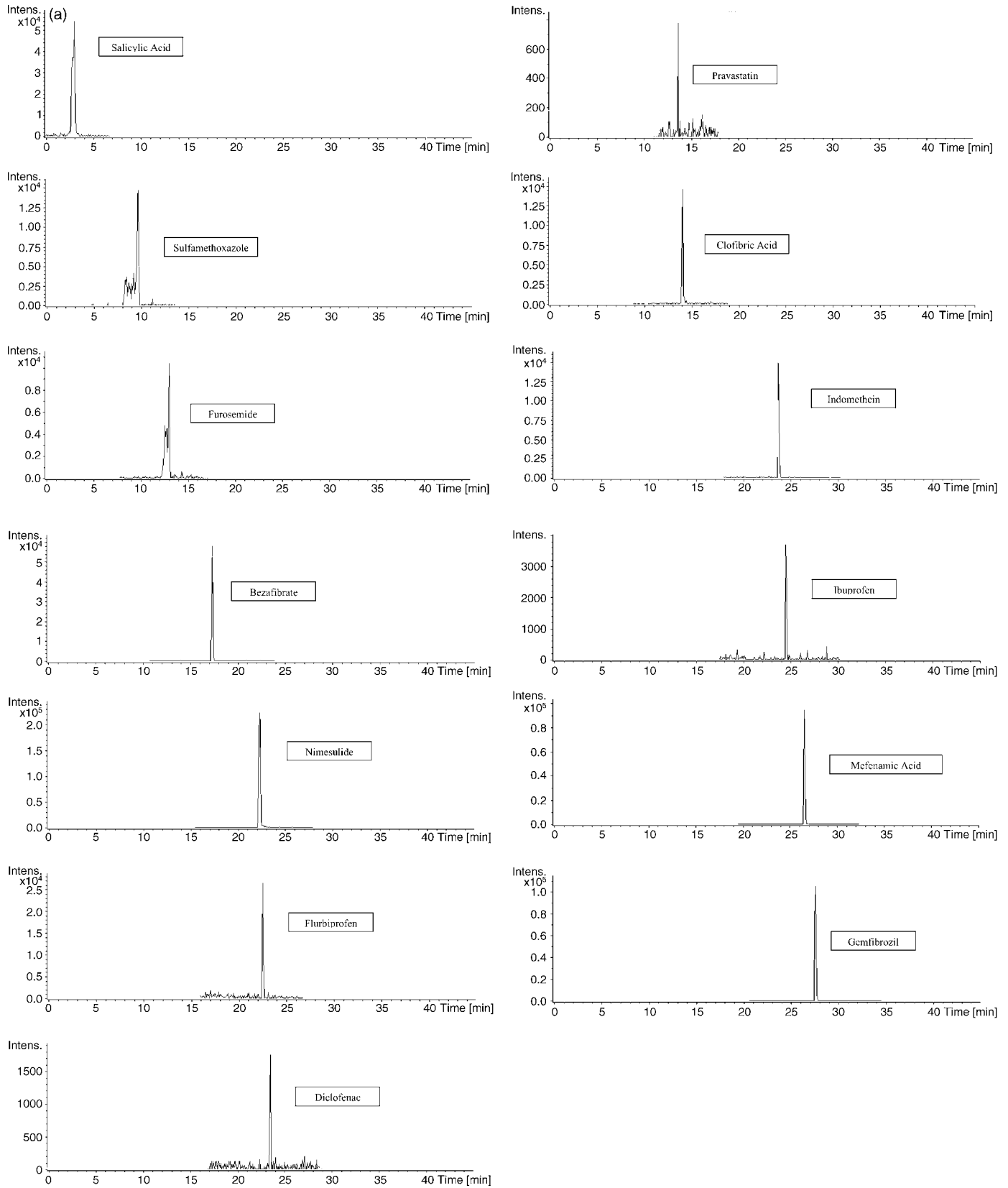
Fig. 1. (a) Chromatograms of a 5 μg/mL standard in influent matrix analysed using negative ionisation. (b) Chromatograms of a 5 μg/mL standard in influent matrix analysed using positive ionisation.
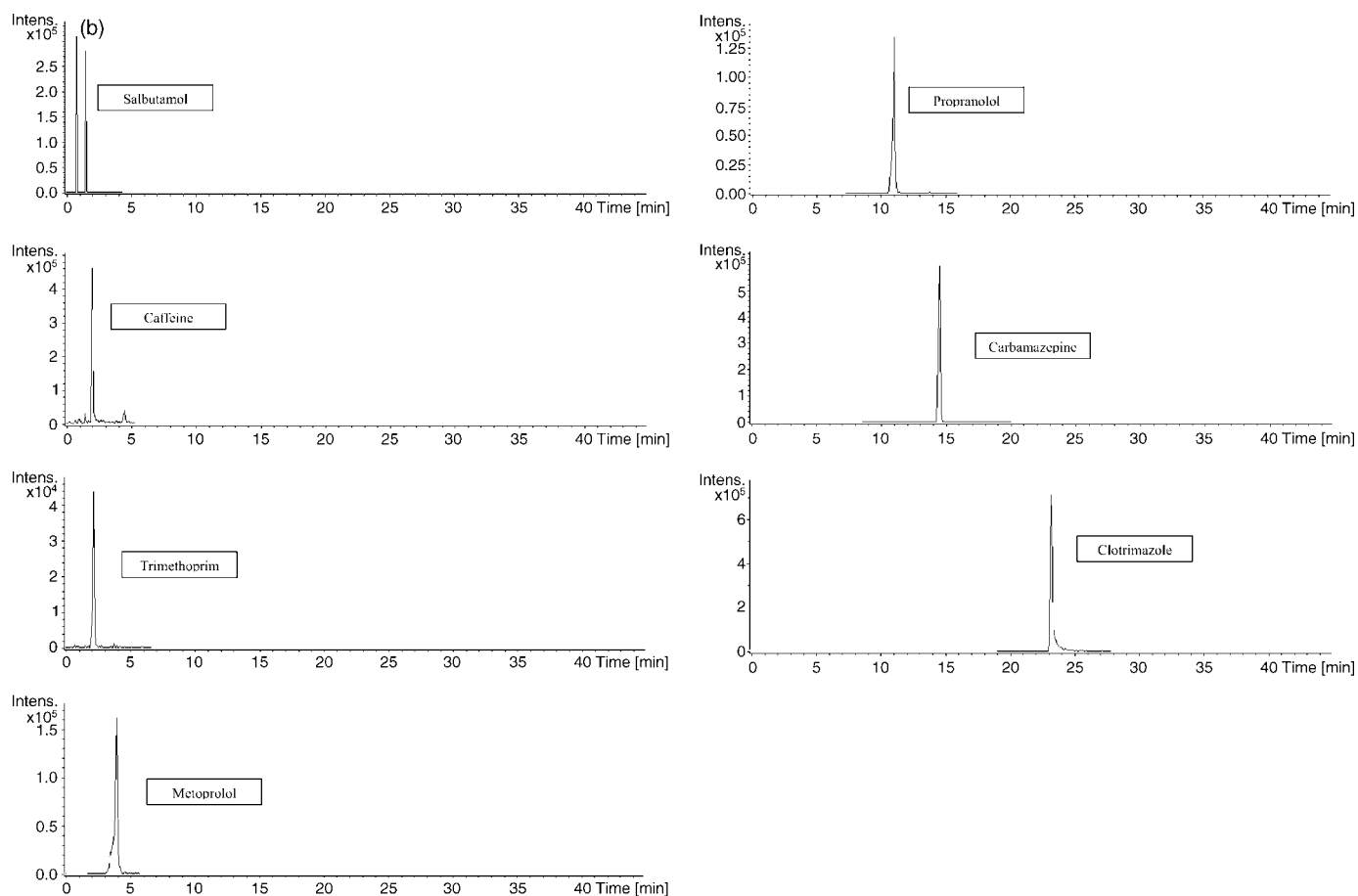
Fig. 1. (*Continued*).

in Table 2. No product ions were observed for salicylic acid, flurbiprofen or sulfamethoxazole in negative mode ionisation. Caffeine also yielded no fragmentation ion in positive mode ionisation. Monitoring of these compounds was consequently restricted to the precursor ions.

3.3. Method validation

The method was validated in both influent and effluent sample matrices and validation data are presented in Tables 1–3. Linearity was determined using regression analysis between the area ratios and concentration. Correlations of $R^2 > 0.9$, with the exception of Ibuprofen, were obtained over a concentration range 0.60–2.90 μg/L (Table 3).

Limits of detection and quantitation (LOD and LOQ) were defined as the concentration yielding a signal to noise ratio of 3:1 and 10:1 respectively. The results are presented in Table 3 and show that the LOD ranged from 0.002 to 0.855 μg/L in the influent and 0.001 to 2.478 μg/L in effluent samples. LOQ ranged from 0.005 to 2.850 μg/L in influent samples and 0.003 to 2.478 μg/L in effluent samples. The precision of the overall method was determined from six replicates of low-level spiked samples, 1.40 μg/L. Precision varied by less than 20% in most cases with the exception of ibuprofen as outlined in Table 3.

Table 2
Retention time and ions for LC–MS/MS monitoring

	R_t (min)	Formula	Precursor ion	Product ion
Negative ionisation				
Salicylic acid	3.0	$C_7H_6O_3$	137	–
Sulfamethoxazole	9.7	$C_{10}H_{11}N_3O_3S$	252	–
Furosemide	13.0	$C_{12}H_{11}ClN_2O_5S$	329	285
Pravastatin	13.6	$C_{23}H_{36}O_7$	423	321
Clofibric acid	14.1	$C_{10}H_{11}ClO_3$	213	127
Bezafibrate	17.3	$C_{19}H_{20}ClNO_4$	360	274
Nimesulide	22.3	$C_{13}H_{12}N_2O_5S$	307	229
Flurbiprofen	22.5	$C_{15}H_{13}FO_2$	199	–
Diclofenac	23.5	$C_{14}H_{11}Cl_2NO_2$	250	214
Indomethcin	23.7	$C_{19}H_{16}ClNO_4$	312	297
Ibuprofen	24.5	$C_{13}H_{18}O_2$	205	159
Mefenamic acid	26.5	$C_{15}H_{15}NO_2$	240	196
Gemfibrozil	27.5	$C_{15}H_{22}O_3$	249	121
Positive ionisation				
Salbutamol	0.8/1.5	$C_{13}H_{21}NO_3$	240	195
Caffeine	2.0	$C_8H_{10}N_4O_2$	194	–
Trimethoprim	2.1	$C_{14}H_{18}N_4O_3$	291	230
Metoprolol	4.0	$C_{15}H_{25}NO_3$	268	159
Propranolol	11.0	$C_{16}H_{21}NO_2$	260	183
Carbamazepine	14.5	$C_{15}H_{12}N_2O$	237	194
Clotrimazole	23.1	$C_{22}H_{17}ClN_2$	277	165

Table 3
Linearity and detection and quantitation limits of the method

	Linearity (R^2)	LOD (µg/L)		LOQ (µg/L)	
		Influent	Effluent	Influent	Effluent
Salicylic acid	0.9864	0.028	0.115	0.093	0.383
Furosemide	0.9205	0.094	0.109	0.313	0.365
Pravastatin	0.9371	0.072	0.047	0.239	0.156
Clofibric acid	0.9813	0.222	0.335	0.740	1.118
Bezafibrate	0.9854	0.033	0.050	0.112	0.150
Nimesulide	0.9655	0.002	0.001	0.005	0.003
Flurbiprofen	0.9907	0.743	0.489	2.478	1.629
Diclofenac	0.9972	0.855	0.743	2.850	2.478
Sulfameth	0.9799	0.072	0.166	0.241	0.553
Indomethcin	0.9712	0.263	0.238	0.877	0.792
Ibuprofen	0.8558	0.228	–	0.760	–
Mefenamic	0.9222	0.020	0.004	0.060	0.013
Gemfibrozil	0.9749	0.026	0.010	0.086	0.032
Caffeine	0.9894	0.280	0.138	0.934	0.460
Trimethoprim	0.9126	0.171	0.020	0.570	0.067
Metoprolol	0.9831	0.633	0.097	2.111	0.324
Propranolol	0.9618	0.007	0.017	0.022	0.057
Carbamazepine	0.9951	0.010	0.004	0.034	0.013
Salbutamol	0.9558	0.008	0.155	0.027	0.518
Clotrimazole	0.9932	0.010	0.004	0.034	0.013

Variability in precision has been shown to increase with the level of sample matrix, therefore the precision data were seen as acceptable [17].

Due to the complexity of the sample matrix ESI-MS analysis may be subject to signal suppression or enhancement as a result of other components in the sample. To quantify the level of ion suppression in both influent and effluent samples a sample was extracted and then spiked with a standard solution (to 2 µg/L of each analyte) and compared to a standard mixture. Blank samples, with no spike were also analysed to determine the level of target compounds present in the sample prior to spiking. Any enhancement or suppression in the signal obtained from the spiked sample over the standard solution was due to matrix components. Signal suppression was observed for all analytes detected by positive mode MS whereas in negative mode MS the level of suppression was greater in the effluent sample for a number of compounds (furosemide, pravastatin, clofibric acid, diclofenac, ibuprofen and sulfamethoxazole). Propranolol (88.7% in influent), salbutamol (77% in effluent) and ibuprofen (77.6 and 72.0% in influent and effluent respectively) were the most affected by signal suppression. Ion enhancement effects due to matrix compounds were also exhibited for five analytes (furosemide, bezafibrate, sulfamethoxazole, mefenamic acid and trimethoprim) with an average ion enhancement of 23%. Standard addition was employed in subsequent samples to minimize the effect of ion suppression or enhancement on quantitation of analytes (Table 4).

3.4. Application to real wastewater treatment plant samples

The method was applied to measure the level of pharmaceutical contamination in influent and effluent samples from three WWTPs in the greater Dublin area. The population equiv-

alents of the WWTPs are 60,000, 90,000 and 1.7 million and the effluent discharges to an estuary, a river and a bay respectively. Twenty-four hour composite samples were collected from each WWTP. Results obtained are summarised in Table 5 and show that 15 of the 20 target analytes were detected. Five analytes were present at quantifiable concentrations in the influent samples collected. Salicylic acid and ibuprofen had maximum concentrations of 9.172 and 3.204 µg/L respectively. Aspirin, of which the primary metabolite is salicylic acid, was the most frequently prescribed product in Ireland in 2004 [7,20]. Aspirin and

Table 4
Reproducibility of the method and ion suppression due to matrix

	%R.S.D.		%Ion suppression	
	Reproducibility	Repeatability	Influent	Effluent
Salicylic acid	15.6	1.4	<5	56.3
Furosemide	18.2	0.1	−48.7	10.7
Pravastatin	13.9	4.7	15.6	27.5
Clofibric acid	14.4	4.9	15.6	29.7
Bezafibrate	13.7	3.5	−2.9	<5
Nimesulide	8.1	5.0	18.5	<5
Flurbiprofen	13.5	1.1	60.5	37.2
Diclofenac	5.8	3.4	23.7	27.7
Sulfamethoxazole	8.0	1.0	−60.3	33.8
Indomethcin	11.4	2.5	11.8	44.2
Ibuprofen	34.7	9.0	77.6	72.0
Mefenamic acid	5.3	0.2	−2.7	25.8
Gemfibrozil	17.7	3.7	45.6	<5
Caffeine	4.7	10.2	28.3	5.4
Trimethoprim	8.7	4.0	38.2	−1.3
Metoprolol	14.5	2.4	52.8	39.1
Propranolol	6.6	5.3	88.7	32.7
Carbamazepine	3.6	2.6	37.7	23.0
Salbutamol	8.4	2.0	<5	77.0
Clotrimazole	6.3	4.4	43.9	25.8

Table 5
Range of concentrations of pharmaceuticals detected in influent and effluent samples

Analyte	Minimum–maximum concentration	
	Influent samples	Effluent samples
Salicylic acid	0.351–9.172	<0.115
Furosemide	<0.313–0.490	nd
Pravastatin	<0.072–<0.239	nd
Clofibric acid	<0.222–<0.740	nd
Bezafibrate	nd	nd
Nimesulide	<0.002–0.441	<0.003–0.45
Flurbiprofen	nd	nd
Diclofenac	nd	<0.743–<2.478
Sulfamethoxazole	nd	<0.166–<0.553
Indomethcin	<0.263–< 0.877 <0.238–<0.792	
Ibuprofen	<0.760–3.204	nd
Mefenamic	nd	0.540–1.050
Gemfibrozil	<0.026–<0.086	<0.032–0.330
Caffeine	nd	nd
Trimethoprim	<0.171–<0.57	<0.067–0.36
Metformin	nd	nd
Metoprolol	nd	nd
Propranolol	nd	nd
Carbamazepine	nd	0.163–0.881
Salbutamol	nd	nd
Clotrimazole	<0.034–0.232	0.034–0.475

ibuprofen are both analgesics which are also available without prescription. Both salicylic acid and ibuprofen were not detected in effluent samples suggesting that they were removed during the treatment process. This is in keeping with other studies where high removal rates of these compounds were observed [18,19]. Furosemide, nimesulide and clotrimazole were also present in measurable concentrations in influent samples. Furosemide appeared to be completely removed over the treatment process while the concentration of nimesulide remained constant and clotrimazole increased (Table 3). Pravastatin, clofibric acid, indomethcin, gemfibrozil and trimethoprim were also identified in influent samples however their concentrations were below the LOQ. Diclofenac, sulfamethoxazole, mefenamic acid and carbamazepine were not detected in influent samples but were present in the corresponding effluent samples. The absence of compounds in the influent may be due to the compounds being present as a conjugated metabolite in the influent which is cleaved to release the parent compound during the treatment process. This is consistent with findings in the case of sulfamethoxazole, for example, where it has been shown that only 10% of the administered dose of sulfamethoxazole is excreted as the parent compound and approximately 50% as the metabolite N^4-acetylsulfamethoxazole [21,22].

4. Conclusion

A SPE-LC-MS/MS method was developed for simultaneous analysis of 20 analytes from a variety of therapeutic classes with different physical and chemical properties. A single SPE method was devised for the extraction and preconcentration of all analytes from both influent and effluent samples. Analysis was performed using LC–MS/MS in both positive and nega-

tive ionisation modes. Detection limits of individual analytes for the overall method were in the ng/L–µg/L range. The final method was used to analyse samples taken from three WWTP in which 15 analytes were detected. This illustrates the suitability of this method for monitoring the presence of pharmaceutical contamination in both influent and effluent waters.

References

[1] R. Hirsch, T.A. Ternes, K. Haberer, A. Mehlich, F. Ballwanz, K.-L. Kratz, J. Chromatogr. A 815 (1998) 213.
[2] D.W. Koplin, E.T. Furlong, M.T. Meyer, E.M. Thurman, S.D. Zaugg, L.B. Barber, H.T. Buxton, Environ. Sci. Technol. 36 (2002) 1202.
[3] M. Petrovic, M.D. Hernando, M.S. Diaz-Cruz, D.J. Barcelo, Chromatogr. A 1067 (2005) 1.
[4] J.L. Oaks, M. Gilbert, M.Z. Virani, R.T. Watson, C.U. Meteyer, B.A. Ridesut, H.L. Shivaprasad, S. Ahmed, M.J.I. Chaudhry, M. Arshad, S. Mahmood, A. Ali, A.A. Khan, Nature 427 (2004) 630.
[5] K. Fent, A.A. Weston, D. Caminada, Aquat. Toxicol. 76 (2006) 122.
[6] J. Schwaiger, H. Ferling, U. Mallow, H. Wintermayr, R.D. Negele, Aquat. Toxicol. 68 (2004) 141.
[7] C.G. Daughton, T.A. Ternes, Environ. Health Perspect. 107 (1999) 907.
[8] T.A. Ternes, Water Res. 32 (1998) 3245.
[9] IMB, 2005, Annual report, http://www.imb.ie/publication.asp?nav=2,38,95&todo=show.
[10] W. Giger, A.C. Alder, E.M. Golet, H.-P.E. Kohler, C.S. Mc Ardell, E. Molnar, H. Siegrist, M.J.-F. Suter, Chimia 57 (2003) 485.
[11] S. Castiglioni, R. Bagnati, D. Calamari, R. Fanelli, E.J. Zuccaato, Chromatogr. A 1092 (2005) 206.
[12] A. Deng, M. Himmelsbach, Q.Z. Zhu, S. Frey, M. Sengl, W. Buchberger, R. Niessner, D. Knopp, Environ. Sci. Technol. 37 (2003) 3422.
[13] R. Lindberg, P.-A. Jarnheimer, B. Olsen, M. Johansson, M. Tysklind, Chemosphere 57 (2004) 1479.
[14] M.J. Hilton, K.V. Thomas, J. Chromatogr. A 1015 (2003) 129.
[15] T. Heberer, J. Hydro. 266 (2002) 175.
[16] J. Bones, K.V. Thomas, P.N. Nesterenko, B. Paull, Environ. Anal. Chem. 86 (2006) 487.
[17] J. Bones, K. Thomas, P.N. Nesterenko, B. Paull, Talanta 70 (2006) 1117–1128.
[18] N. Lindqvist, T. Tuhkanen, L. Kronberg, Water Res. 39 (2005) 2219.
[19] M. Richardson, J.J. Bowron, Pharm. Pharmacol. 37 (1985) 1.
[20] Health Service Executive: Financial and Statistical Analysis of Claims and Payments, 2004. http://www.hse.ie/en/Publications/HSEPublicationsNew/Index/PrimaryCommunityContinuingCarePCCCLHO/#d.en.4786.
[21] T.A. Ternes, A. Joss, Human Pharmaceuticals, Hormones and Fragrances: The Challenge of Micropollutants in Urban Water Management, IWA, London, UK, 2006.
[22] S. Babic, A.J.M. Horvat, D.M. Pavlovic, M. Kastelan-Macan, TrAC, Trends Anal. Chem. 26 (2007) 1043.
[23] T. Scheytt, P. Mersmann, R. Lindstadt, T. Heberer, Water, Air, Soil Pollut. 165 (2005) 3.
[24] J.N. Brown, N. Paxeus, L. Forlin, D.G. Joakim Larsson, Environ. Toxicol. Phar. 24 (2007) 267.
[25] M.P. Alves, A.L. Scarrone, M. Santos, A.R. Pohlmann, S.S. Guterres, Int. J. Pharm. 341 (2007) 215.
[26] Y. Yamini, C.T. Reimann, A. Vatanara, J.A. Jonsson, J. Chromatogr. A 1124 (2006) 57.
[27] D. Kobayashi, T. Nozawa, K. Imai, J.-I. Nezu, A. Tsuji, I. Tamai, J. Pharmacol. Exp. Ther. 306 (2003) 703.

Validation of a new method using the reactivity of electrogenerated superoxide radical in the antioxidant capacity determination of flavonoids

Carine Le Bourvellec [a], Didier Hauchard [b], André Darchen [c],
Jean-Louis Burgot [a], Marie-Laurence Abasq [a,*]

[a] *Laboratoire de Chimie Analytique URU-337, Faculté de Pharmacie, Université de Rennes 1, Avenue du Professeur Léon Bernard, 35043 Rennes Cedex, France*
[b] *Equipe MaCSE, UMR CNRS 6226, Laboratoire Sciences Chimiques de Rennes, Ecole Nationale Supérieure de Chimie de Rennes, Avenue du Général Leclerc, 35700 Rennes, France*
[c] *Equipe MI-CDR, UMR CNRS 6226, Laboratoire Sciences Chimiques de Rennes, Ecole Nationale Supérieure de Chimie de Rennes, Avenue du Général Leclerc, 35700 Rennes, France*

Abstract

This article lays out a new method to measure the antioxidant capacity of some flavonoids. The methodology developed is based on the kinetics of the reaction of the antioxidant substrate with the superoxide radical ($O_2^{\bullet-}$). A cyclic voltammetric technique was used to generate $O_2^{\bullet-}$ by reduction of molecular oxygen in aprotic media. In the same experiment the consumption of the radical was directly measured by the anodic current decay of the superoxide radical oxidation in the presence of increasing concentrations of antioxidant substrate. The method was statistically validated on flavonoid monomers and on the standard antioxidants: trolox, ascorbic acid and phloroglucinol. The linear correlations between the anodic current of $O_2^{\bullet-}$ and the substrate concentration allowed the determination of antioxidant index values expressed by the substrate concentration needed to consume 30% (AI_{30}) and 50% (AI_{50}) of $O_2^{\bullet-}$ in given conditions of oxygen concentration and scanning rate. The fidelity of the method was examined intraday and interlaboratories.
© 2008 Elsevier B.V. All rights reserved.

Keywords: Antioxidant capacity; Cyclic voltammetry; Flavonoids; Superoxide radical

1. Introduction

Oxidative stress which arises in biologic systems leads to cellular death, contributes to faster aging and is responsible of pathology of many human diseases, like cancer, development of neurodegenerative or cardiac disorders [1]. It is associated with or leads to the generation of reactive oxygen species (ROS) including free radicals [2] which are strongly implicated in the pathophysiology of diseases [3,4]. In humans, defense system which protects against such oxidative damage includes endogenous enzymes like superoxide dismutase, glutathione peroxidase, catalase and non-enzymatic system as low molecular antioxidants and vitamins [5]. It is well known that many polyphenol compounds are brought by human nutrition and may act as exogenous molecules taking part in the antioxidant defense system of the organism [6]. Their antioxidant capacity is defined as the capability of a compound to protect against oxidative degradation [7]. The mechanisms involved in the antioxidative actions of polyphenol compounds are described as scavenging capacity, metal chelating capacity, reducing capacity, enzyme inhibition and gene expression regulation [2].

Various methods have been developed to measure the *in vitro* antioxidant capacity of polyphenol compounds, phytochemicals and extracts although bioavailability, absorption, metabolism and pharmacokinetics must all be considered before attempting to extrapolate *in vitro* activity to the human *in vivo* situation. These methods are usually classified into two categories depending on the chemistry involved: (i) hydrogen atom transfer (HAT) methods which quantify a hydrogen atom capacity and (ii) electron transfer (ET) methods which measure an antioxidant reducing capacity. Details on the procedures and the chemistry of these methods are extensively reviewed in the literature [7–14].

---

* Corresponding author. Tel.: +33 2 23 23 48 95; fax: +33 2 23 23 49 12.
E-mail address: marie-laurence.abasq@univ-rennes1.fr (M.-L. Abasq).

Owing to the different reactions occurring in an antioxidant process, an antioxidant substrate may be fully characterized by complementary methods [7–14]. Consequently, as it has been pointed out, data of antioxidant capacities arising from different methods cannot be correlated, particularly when the chemistry involves different radical or oxidant sources. As a pertinent example, hydroxytyrosol which is a polyphenol from olive oil reacts with hydrogen peroxide but not with superoxide anion [15].

Among the radicals involved into the HAT and ET methods, peroxyl radicals ROO$^\bullet$, DPPH$^\bullet$ and ABTS$^{\bullet+}$ are the most frequently used. The peroxyl radicals appear as interesting reactants because of their existence *in vivo* as ROS. Another ROS biologically relevant radical is the superoxide radical $O_2^{\bullet-}$ and some methods were developed to determine specifically the superoxide scavenging capacity. These assays are based on its generation by photochemistry of by using an enzymatic system and the inhibition reaction by the antioxidant substrate is usually measured by spectrophotometry, fluorescence or EPR techniques [7,12,14,16]. Electrochemical techniques for the generation of $O_2^{\bullet-}$ by reduction of dissolved oxygen in aprotic solvents is also a convenient method since no by-product are generated. $O_2^{\bullet-}$ is a long-lived species in aprotic media and the procedure is easy to carry out [17,18]. Moreover, cyclic voltammetry is adequate to follow reaction of electrogenerated $O_2^{\bullet-}$ with substrate. This was already described for some sulfur amino acids [19], esters [20], antioxidative agent [21] and drugs [22–24] but no protocol was really developed and statistically validated. Moreover,

to our knowledge the interaction with polyphenol compounds following this methodology has not been reported yet. Electrochemistry approaches are also of special advantage in evaluation of antioxidant properties regarding the reducing capacity of a substrate by measuring the oxidation potential of the substrates, the studies on this subject has been reviewed recently [25].

In this work we report the procedure and the validation of an electroanalytical method of the *in vitro* antioxidant capacity determination of polyphenol compounds in a polar aprotic media. The methodology is based on the kinetic study by cyclic voltammetry of the interaction of the antioxidant substrate with superoxide anion radical $O_2^{\bullet-}$. The validation of the method was statistically performed on some flavonoid compounds (Fig. 1) and the standard antioxidants trolox, ascorbic acid and phloroglucinol.

2. Experimental

2.1. Reagents

Commercially available chemicals were used without any further purification. The *N,N*-dimethylformamide extra dry ([H$_2$O] $\leq$ 0.005%, stored over molecular sieve 3 Å) and the tetrabutylammonium hexafluorophosphate Bu$_4$NPF$_6$ of electrochemical grade were purchased from Fluka Chemie. Flavonoid monomers: (−)-epicatechin was purchased from Aldrich, phlorizin dihydrate from Fluka, quercetin dihydrate and rutin were purchased from Sigma Chemical
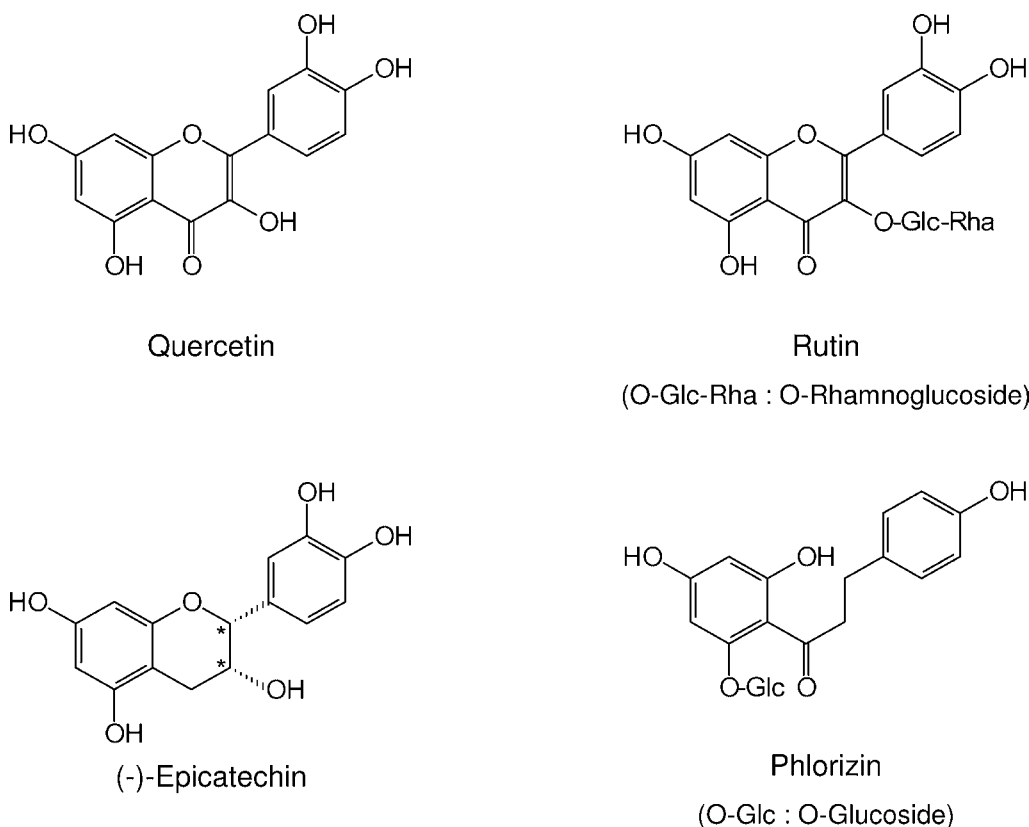

Fig. 1. Chemical structure of the flavonoids investigated.

Co. Standard antioxidants: ascorbic acid and trolox ((±)-6-hydroxy-2,5,7,8-tetramethylchroman-2-carboxylic acid) were purchased from Acros Organics, phloroglucinol dihydrate (1,3,5-trihydroxybenzene·2H$_2$O) was purchased from Aldrich.

2.2. Equipment

Cyclic voltammetry experiments were performed on a dual potentio-galvanostat PGSTAT100 in laboratory 1 or a PGSTAT30 in laboratory 2 (Autolab instrument, Eco Chemie B.V., Utrecht, The Netherlands). All measurements were carried out on a three-electrode thermostated cell. A glassy carbon disk working electrode (diameter 2 mm), a platinum wire counter electrode and a reference electrode, Ag/AgCl in EtOH saturated by LiCl, were used for all electrochemical experiments. The reference electrode was separated from the solution by a salt bridge containing 0.5 M Bu$_4$NPF$_6$ in DMF. The glassy carbon disk working electrode was polished using silicon carbide 4000 paper with a LaboPol-5 (Struers, Ballerup, Denmark), washed with distilled water and then dried. For all measurements, the temperature was maintained at $20 \pm 0.02\,^{\circ}$C with a Julabo heating circulator MP-5 (Julabo, Seelbach, Germany).

2.3. Method

2.3.1. Cyclic voltammetry of oxygen

10 mL of an extra-dry DMF solution containing the supporting electrolyte 0.1 M Bu$_4$NPF$_6$ was saturated by dry air during 10 min. In these conditions the solubility of oxygen was assumed to be 0.94×10^{-3} M, this value corresponding to a partial pressure of 0.2 bar [26]. The cyclic voltammogramm (CV) of the oxygen reduction was then recorded at a scan rate 0.1 V s^{-1}. The initial potential was fixed at 0 V vs. Ag/AgCl. The scanning potential was reversed at −0.9 V vs. Ag/AgCl.

2.3.2. Cyclic voltammetry of oxygen in the presence of antioxidant substrate

A stock solution of the flavonoid monomer or the standard antioxidant was prepared at about 2.5×10^{-2} M. Aliquots of the stock solution were successively added to the 10 mL oxygen solution in order to get an antioxidant substrate concentration in the range (0–2.50 mM). After each aliquot addition, CV of the oxygen solution was recorded at a scan rate 0.1 V s^{-1}.

2.3.3. Statistical evaluation of the method

The statistical analysis of the results was performed according to the well-recognized analytical parameters established by the official compendiums, scientific literature and Pharmacopeias. Analysis of variance and linear correlations tests were performed using the AVA V3-1 qualilab software package. A maximum risk of 5% of the measures outside the acceptance limits was considered statistically significant. Two independent laboratories, two equipments and two operators were involved in the statistical evaluation of the method.
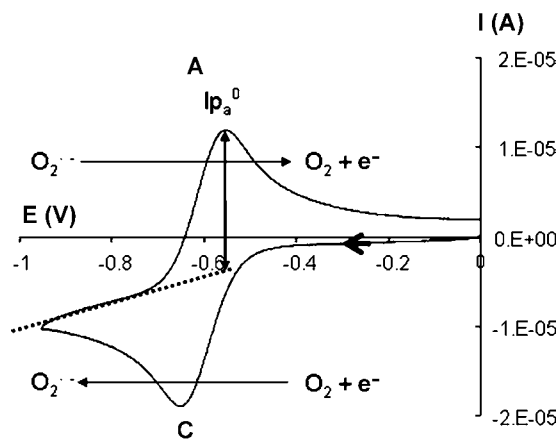

Fig. 2. Cyclic voltammogram of oxygen at a steady glassy carbon disk electrode in DMF/0.1 M Bu$_4$NPF$_6$. Scan rate 0.1 V s^{-1}.

3. Results and discussion

3.1. Electrogeneration of superoxide radical

Cyclic voltammetry technique [27] is used to generate the superoxide radical O$_2^{\bullet -}$ in the diffusion layer of a glassy carbon electrode by the one-electron reduction of molecular oxygen in DMF media (Fig. 2; peak C). The presence of the radical O$_2^{\bullet -}$ is easily detected by its anodic oxidation current measured at the electrode during the reverse scan (Fig. 2; peak A). The reduction of O$_2$ is a reversible reaction and it is known that O$_2^{\bullet -}$ radical is stable in aprotic media and dismutation does not occur during the time scale of the cyclic voltammetry in DMF solution [17,18]. Consequently, it is a convenient way to generate O$_2^{\bullet -}$ without enzyme systems and to study its reaction with a molecule or an extract provided the substrate is not active in the potential range of the reduction of oxygen. Interferences restrictions have been related in the article of Arnao concerning the radicals DPPH$^{\bullet}$ and ABTS$^{\bullet +}$ and the spectrophotometric detection [28]. In voltammetric detection, the substrate has not to be active in the potential range of the couple molecular oxygen/superoxide anion in order to avoid interference or a complex interpretation of the data. Fortunately, this was observed in this study despite the phenols are reducing agents. Indeed, the investigated substrates were oxidized at positive potentials.

In the development of the procedure, the CV was firstly recorded in the absence of the substrate to determine the current value $I_{p_a}^o$ as the anodic peak current of O$_2^{\bullet -}$ oxidation (Fig. 2). $I_{p_a}^o$ is directly related to the O$_2^{\bullet -}$ concentration at the electrode surface and depends on the solubility of oxygen in DMF and the experimental parameters chosen to record the CV.

Clearly it is important that the $I_{p_a}^o$ value is determined in identical conditions for each experiment. It means that the time scale of the CV and the electrode surface have to be the same. The time scale was controlled by the scan rate 0.1 V s^{-1} and the potential range was from 0 to −0.9 V vs. Ag/AgCl. The precision was determined on the $I_{p_a}^o$ value over a period of 3 months and gave a relative standard deviation of 2.14% for interdays values (RSD$_r$) and of 2.21% for interlaboratories values (RSD$_R$) ($n = 18$). These
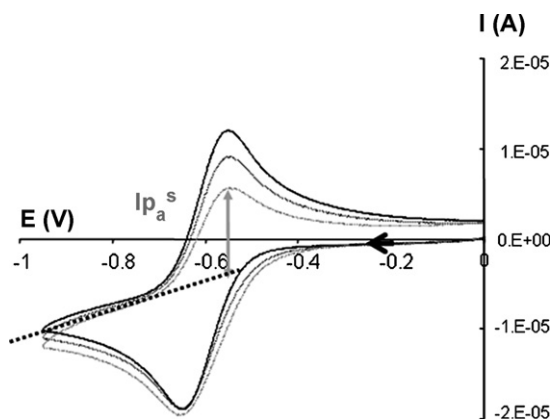
Fig. 3. Cyclic voltammograms of O_2 reduction in the presence of increasing concentrations of phloroglucinol at a steady glassy carbon disk electrode in DMF/0.1 M Bu$_4$NPF$_6$. Scan rate 0.1 V s^{-1}. Phloroglucinol concentrations: (———) 0 mM; (———) 0.49 mM; (———) 1.64 mM.
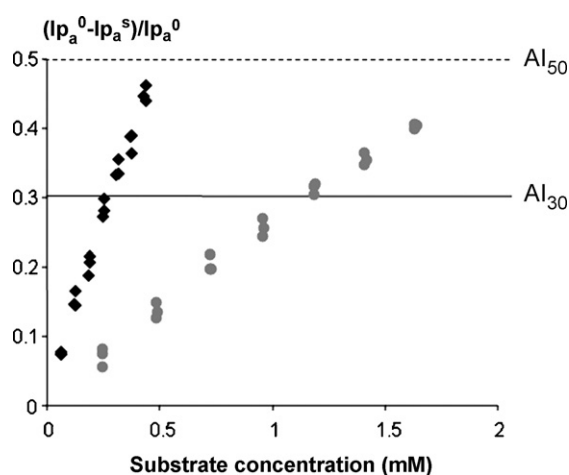

Fig. 4. Dimensionless parameter related to the decrease of superoxide anodic current *vs.* the substrate concentration in the linear range (data reported for analysis over 3 days) ((●) trolox; (♦) quercetin).

results show a good precision on the $I_{p_a}^o$ value and consequently on the solubility of atmospheric oxygen in DMF which was a key point in the validation of the method.

3.2. Electrochemical behavior of oxygen in the presence of an antioxidant substrate

The CV of the O_2 reduction was recorded in the presence of a flavonoid monomer or a standard antioxidant with a view to evaluating the antioxidant capacity of the molecule looking at its reactivity toward $O_2^{\bullet-}$. The increase of the antioxidant substrate concentration leads to a decrease of $O_2^{\bullet-}$ anodic peak current ($I_{p_a}^S$) while the intensity of O_2 cathodic current is not significantly modified as shown in Fig. 3 in the case of phloroglucinol. The decrease of the anodic peak current of $O_2^{\bullet-}$ suggests that the polyphenol substrate reacts irreversibly with $O_2^{\bullet-}$. For each antioxidant compound, a series of $I_{p_a}^S$ values is determined from the CVs recorded for increasing antioxidant concentrations (Fig. 3). All antioxidant substrates exhibited a similar effect upon the O_2 reduction.

At higher concentrations of some antioxidant substrates, a not-well defined reduction peak was observed at a potential more positive than the oxygen reduction peak. We could not attribute this peak to the reduction of an acidic hydrogen since the working electrode was vitreous carbon and not platinum [19]. The concentration range where we observed a significant additional peak was not within the linear range used in the determination of the antioxidant capacity values (Section 3.3.2).

The electrochemical behavior of oxygen may be summarized by the following Eqs. (1)–(3) where AH represents a flavonoid compound or a standard antioxidant. After the reversible reduction of oxygen (1) the electrogenerated superoxide anion reacts with AH (2) leading to products which are not electroactive in the scanned potential range. For this reaction we can follow the hypothesis of an H atom transfer (3) leading to radical A$^\bullet$, which may be a phenoxy radical, and to the conjugated base of hydrogen peroxide [29–31].

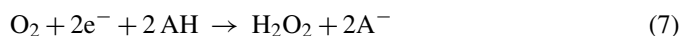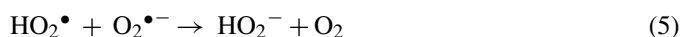Literature reports that some proton donating substrates [17,22,32,33] increase the cathodic current of oxygen from a
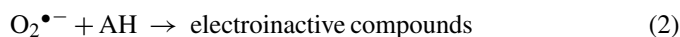
one-electron to a two-electron reduction. The mechanism may be described by a first proton transfer (4) followed by electron transfer (5). With a second proton transfer (6) the overall reaction is a two-electron reduction of oxygen (7). In our experimental conditions we did not observe with flavonoid substrates the increase of oxygen current reduction which is expected in the hypothesis of a proton donating mechanism. Moreover, during the reverse scan until 0.6 V *vs.* Ag/AgCl we never observed an anodic peak which could be attributed to the oxidation of a phenoxide (A$^-$) arising from the proton transfer (4). So our observations suggest that the flavonoid compounds reacted with superoxide radical as H atom donors, as already reported with other methods [29–31].

$$O_2 + e^- \leftrightarrows O_2^{\bullet-} \tag{1}$$

$$O_2^{\bullet-} + AH \rightarrow \text{electroinactive compounds} \tag{2}$$

$$O_2^{\bullet-} + AH \rightarrow O_2H^- + A^\bullet \tag{3}$$

$$O_2^{\bullet-} + AH \rightarrow HO_2^\bullet + A^- \tag{4}$$

$$HO_2^\bullet + O_2^{\bullet-} \rightarrow HO_2^- + O_2 \tag{5}$$

$$HO_2^- + AH \rightarrow H_2O_2 + A^- \tag{6}$$

$$O_2 + 2e^- + 2AH \rightarrow H_2O_2 + 2A^- \tag{7}$$

3.3. Development and statistical evaluation of the method

The $I_{p_a}^o$ and $I_{p_a}^S$ values were determined as described above. The consumption of $O_2^{\bullet-}$ was expressed by a dimensionless parameter $(I_{p_a}^o - I_{p_a}^S)/I_{p_a}^o$ which was plotted *vs.* the substrate concentration (Fig. 4). When the antioxidant concentration increased, the calculated values for $(I_{p_a}^o - I_{p_a}^S)/I_{p_a}^o$, were out of the straight line. These points were not represented in Fig. 4.

3.3.1. Linearity

The linearity of response was studied statistically for each molecule to establish an antioxidant capacity value in the adequate linear range (Table 1). The statistical analysis was performed using the ANOVA regression analysis option of the AVA

Table 1

Characteristic parameters for the regression equation for standard antioxidants and flavonoids monomers

Compounds	Linear range (mM)	Slope	y-Intercept	r^2
Standard antioxidants				
Trolox	0.25–1.63	0.239	0.020	0.995
Phloroglucinol	0.25–1.22	0.262	0.037	0.995
Ascorbic acid	0.10–0.75	0.740	0.031	0.987
Flavonoid monomers				
Phlorizin	0.25–1.65	0.275	0.026	0.993
Rutin	0.20–0.90	0.405	0.024	0.991
Epicatechin	0.10–0.50	0.761	0.034	0.994
Quercetin	0.05–0.45	0.976	0.025	0.994

Fig. 5. Histogram of AI_{50} and AI_{30} values ($n=9$). (■): AI_{50} (mM); (□): AI_{30} (mM); (⊤): standard deviation of interday values.

V3-1 program. A value of $p < 0.05$ was considered statistically significant.

Data for linearity of $(I_{p_a}^o - I_{p_a}^S)/I_{p_a}^o$ vs. the substrate concentration were determined three times (one time a day) (Table 1). A linear correlation was found for each substrate in a given concentration range which is dependent on the reactivity of the substrate toward superoxide. Correlation coefficients, intercepts, slopes and linear range for the calibration data are given in Table 1 from a minimum of five-point linear plot with three replicates. All statistical tests performed by AVA V3-1 were validated except for the intercept test. The key point in this study was to demonstrate a linear interval in the current decay allowing the determination of antioxidant capacity values.

3.3.2. Antioxidant capacity

Under the same experimental conditions, the kinetics of the reaction between the antioxidant substrate and superoxide radical anion may be expressed by the slopes of straight lines (Fig. 4). These slope values are gathered in Table 1. For example, the standard trolox is four times less reactive than the flavon-3-ol quercetin. Instead of these slopes we preferred characterize the reactivity of antioxidant substrates by an antioxidant index AI. By analogy with the inhibiting concentration of antioxidant (IC),

we determined two indexes AI_{30} and AI_{50} by the concentration in mM of antioxidant substrate needed to consume superoxide radical as revealed by a current decrease, respectively 30% and 50% of the initial anodic current $I_{p_a}^o$ ($AI = (I_{p_a}^o - I_{p_a}^S)/I_{p_a}^o = 0.3$ or 0.5) (Fig. 4).

Fig. 4 shows that AI_{30} is within the linear interval response whether the AI_{50} value is an extrapolated value. With this antioxidant characterization, more the AI values are low, more the substrate has an antioxidant capacity toward superoxide.

3.3.3. Precision on the AI_{30} and AI_{50} values

Data are listed in Table 2 and are expressed as mean and confidence interval of AI_{30} and AI_{50} values. The precision on the AI_{30} and AI_{50} values calculated as relative standard deviation (RSD%) was obtained in two levels: interdays RSD_r (three analysis for three days) and interlaboratories RSD_R (two laboratories, two equipments, two operators, three days, three analysis a day, the third day values were determined in lab2) (Table 2). All linear correlations used for the determination of the antiox-

Table 2

Precision data concerning the AI_{50} and AI_{30} values

Compounds		AI (mM) ($n=9$)	Confidence interval (mM)	Interday RSD_r (%)	Interlaboratory RSD_R (%)
Standard antioxidants					
Trolox	AI50	1.97	[1.92–2.02]	3.4	3.3
	AI30	1.14	[1.10–1.17]	4.8	4.2
Phloroglucinol	AI50	1.77	[1.71–1.83]	2.1	4.4
	AC30	1.01	[0.98–1.05]	2.9	4.7
Ascorbic acid	AI50	0.64	[0.60–0.68]	5.9	7.4
	AI30	0.37	[0.35–0.39]	7.2	8.5
Flavonoid monomers					
Phlorizin	AI50	1.69	[1.66–1.71]	1.8	1.9
	AI30	0.98	[0.95–1.01]	3.3	3.6
Rutin	AI50	1.24	[1.20–1.29]	3.2	5.0
	AI30	0.72	[0.69–0.74]	3.4	5.5
Epicatechin	AI50	0.63	[0.61–0.65]	4.4	4.9
	AI30	0.35	[0.33–0.36]	4.6	5.8
Quercetin	AI50	0.46	[0.45–0.48]	4.1	4.0
	AI30	0.27	[0.26–0.28]	4.8	5.4

idant values were obtained from independent stock solutions of the antioxidant substrate. The relative standard deviations were <5% for the AI_{50} values except for the ascorbic acid substrate whether the AI_{30} values showed higher relative standard deviations.

3.3.4. Comparison in the antioxidant capacity of the different substrates

Histogram of Fig. 5 shows the decrease of the antioxidant capacity of the substrates from quercetin to trolox. Our results follow the same order of antioxidant capacity values given in the literature with independent methods for these molecules [34–38]. There is a general agreement that in flavonoid monomers the structural features that favors the radical scavenging activity is (i) the degree of hydroxylation (the *ortho*-diphenolic structure in the B ring and the 3-OH group on the C ring) and (ii) the 2,3-double bond in conjugation with a 4-oxo function in the C ring. These criteria are related to the stabilization by conjugation of the phenoxy intermediate obtained after the H-abstraction scavenging reaction [34–38]. In the flavonoid series, the flavon-3-ol quercetin, which is the most active ($AI_{50} = 0.46$ mM), fulfils all the conditions whether the dihydrochalcone phlorizin ($AI_{50} = 1.69$ mM) does not have these structural characteristics.

Ascorbic acid, a well-known antioxidant, exhibits the same antioxidant capacity than the flavan-3-ol epicatechin. The other standard antioxidants, trolox and phloroglucinol, are the less active substrates which we studied.

4. Conclusion

The electrochemical method described developed in this study allows the determination of an *in vitro* antioxidant capacity value of some flavonoid monomers and standard molecules.

The cyclic voltammetry technique is well-appropriated for the measurement of the antioxidant capacity of phenol substrate toward superoxide radical. Indeed the generation of the radical and the measurement of its consumption are conducted at the same electrode. An important requirement of the method is that the antioxidant substrate is not electroactive in the same potential range where the oxygen reduction occurs.

Superoxide is electrogenerated by the one-electron reduction of dioxygen and therefore its generation involves neither enzymes nor chelating metals as it is usually used in the methods testing the superoxide scavenging capacity. Consequently this method measures specifically the radical scavenging effect toward superoxide whether the other methods cannot discriminate possible synergic actions of the antioxidant activity of polyphenols [38].

Acknowledgements

References

[1] J.L. Mark, Science 238 (1987) 1352–1353.
[2] B. Halliwell, J. Gutteridge, Free Radicals in Biology and Medicine, 3rd ed., Oxford Science Publications University Press, Oxford, 2003.
[3] J.D. Lambeth, Free Radic. Biol. Med. 43 (2007) 332–347.
[4] J.M.C. Gutteridge, Free Radic. Res. Commun. 19 (1993) 141–158.
[5] B. Halliwell, Nutr. Rev. 52 (1994) 253–263.
[6] P-.G. Pietta, J. Nat. Prod. 63 (2000) 1035–1042.
[7] D. Huang, B. Ou, R.L. Prior, J. Agric. Food Chem. 53 (2005) 1841–1856.
[8] G. Cao, R.L. Prior, Clin. Chem. 44 (1998) 1309–1315.
[9] E.N. Frankel, A.S. Meyer, J. Sci. Food Agric. 80 (2000) 1925–1941.
[10] C. Santos-Buelga, G. Williamson, Methods in Polyphenol Analysis, Royal Society of Chemistry, Cambridge, 2003.
[11] V. Roginsky, E.A. Lissi, Food Chem. 92 (2005) 235–254.
[12] R.L. Prior, X. Wu, K. Schaich, J. Agric. Food Chem. 53 (2005) 4290–4302.
[13] N. Hermans, P. Cos, L. Maes, T. De Bruyne, D. Vanden Berghe, A.J. Vlietinck, L. Pieters, Curr. Med. Chem. 14 (2007) 417–430.
[14] Antioxidant measurement and applications, ACS Symposium Series 956, in: F. Shahidi, C.-T. Ho (Eds.), Oxford University Press (2007).
[15] Y. O'Dowd, F. Driss, P. My-Chan Dang, C. Elbim, M.A. Gougerot-Pocidalo, C. Pasquier, J. El-Benna, Biochem. Pharmacol. 68 (2004) 2003–2008.
[16] N. Saint-Cricq de Gaulejac, C. Provost, N. Vivas, J. Agric. Food Chem. 47 (1999) 425–431.
[17] D.T. Sawyer, Oxygen Chemistry, Oxford University Press, Oxford, 1991, p. 27.
[18] D. Vasudevan, W. Wendt, J. Electroanal. Chem. 192 (1995) 69–74.
[19] G. Feroci, A. Fini, Inorg. Chim. Acta 360 (2007) 1023–1031.
[20] R.D. Webster, A.M. Bond, J. Chem. Soc. Perkin Trans. 2 (1997) 1075–1080.
[21] T. Araki, H. Kitaoka, Chem. Pharm. Bull. 49 (2001) 541–545.
[22] M.E. Ortiz, L.J. Nunez-Vergara, J.A. Squella, J. Electroanal. Chem. 519 (2002) 46–52.
[23] S. Bollo, J. Jara-Ulloa, S. Finger, L.J. Nunez-Vergara, J.A. Squella, J. Electroanal. Chem. 577 (2005) 235–242.
[24] M.L. Abasq, J.L. Burgot, M.O. Christen, A. Darchen, S. Dervout, Proceedings of the 11th International Biennial Meeting of the Society for Free Radical Research, Paris, France, 2002, pp. 575–578.
[25] A.J. Blasco, A.G. Crevillen, M.C. Gonzales, A. Escarpa, Electroanalysis 19 (2007) 2275–2286.
[26] C. Dapremont-Avignon, P. Calas, A. Commeyras, C. Amatore, J. Fluorine Chem. 51 (1991) 357–379.
[27] D.H. Evans, K.M. O'Connell, R.A. Petersen, M.J. Kelly, J. Chem. Educ. 60 (1983) 290–293.
[28] M.B. Arnao, Trends Food Sci. Technol. 11 (2000) 419–421.
[29] S.V. Jovanovic, S. Steenken, M. Tosic, B. Marjanovic, M.G. Simic, J. Am. Chem. Soc. 116 (1994) 4846–5485.
[30] J.P. Hu, M. Calomme, A. Lasure, T. De Bruyne, L. Pieters, A. Vlietinck, D.A. Vanden Berghe, Biol. Trace Elem. Res. 47 (1995) 327–331.
[31] N. Cotelle, P. Hapiot, J. Pinson, C. Rolando, H. Vézin, J. Phys. Chem. B 109 (2005) 23720–23729.
[32] C.P. Andrieux, P. Hapiot, J.M. Savéant, J. Am. Chem. Soc. 109 (1987) 3768–3775.
[33] C.M. Collins, C. Sotiriou-Leventis, M.T. Canalas, N. Leventis, Electrochim. Acta 45 (2000) 2049–2059.
[34] C.A. Rice-Evans, N.J. Miller, G. Paganga, Free Radic. Biol. Med. 20 (1996) 933–956.
[35] D. Rosch, M. Bergmann, D. Knorr, L.W. Kroh, J. Agric. Food Chem. 51 (2003) 4233–4239.
[36] O. Firuzi, A. Lacanna, R. Petrucci, G. Marrosu, L. Saso, Biochim. Biophys. Acta 1721 (2005) 174–184.
[37] D. Villaño, M.S. Fernandez-Pachon, A.N. Troncoso, M.C. Garcia-Parrilla, Anal. Chim. Acta 538 (2005) 391–398.
[38] S.A.B.E. Van Acker, D.-J. van den Berg, M.N.J.L. Tromp, D.H. Griffionen, W.P. van Bennekom, W.J.F. van der Vijgh, A. Bast, Free Radic. Biol. Med. 20 (1996) 331–342.

A method to determine quercetin by enhanced luminol electrogenerated chemiluminescence (ECL) and quercetin autoxidation

Rong Lei, Xiao Xu, Fei Yu, Na Li [*], Hu-Wei Liu [**], Kèan Li

Key Laboratory of Bioorganic Chemistry and Molecular Engineering of Ministry of Education, College of Chemistry and Molecular Engineering, Peking University, Beijing 100871, China

Abstract

Quercetin greatly enhanced luminol electrochemiluminescence of quercetin in alkaline solution. When the concentration of luminol was $0.1 \, \mathrm{mol \, L^{-1}}$, the detection limit for quercetin was $2.0 \times 10^{-8} \, \mathrm{mol \, L^{-1}}$ with a linear range from 1.0×10^{-7} to $2 \times 10^{-5} \, \mathrm{mol \, L^{-1}}$. The pH and buffer substantially affected ECL intensity. Quercetin was autoxidized in alkaline aqueous solution. The rate of autoxidation of quercetin in various pH buffers and borate concentrations were measured. Borate was found to inhibit quercetin autoxidation and compromise quercetin enhancement effect on luminol ECL to some extent. Two final autoxidation products were identified with LC–MS methods. Autoxidation process was associated with enhancement of ECL intensity. The ROS generated during quercetin autoxidation enhanced the ECL intensity.
© 2008 Elsevier B.V. All rights reserved.

Keywords: Luminol; Electrogenerated chemiluminescence; Quercetin; Autoxidation

1. Introduction

Quercetin is one of the most widely studied flavonoids due to its very high antioxidant activity, thus free radical-related diseases such as cardiovascular diseases (CVD3) and cancer can be prevented by consumption of quercetin-rich diets [1–3]. However, quercetin may act as a cytotoxic prooxidant after its metabolic activation to semiquinone and quinoidal product accompanied by superoxide ($O_2^{\bullet -}$) and hydrogen peroxide [4,5]. Hodnick et al. [6] reported that autoxidation of quercetin in physiological conditions could generate reactive oxygen species (ROS) such as superoxide, hydrogen peroxide and free radicals (e.g. $^{\bullet}OH$ and semiquinone) [7]. Tournaire et al. [8] reported that the final products in quercetin oxidation were 2,4,6-trihydroxylbenzaldehyde and 3,4-dihydroxybenzoic acid, and that these compounds may also have antioxidant activity [9]. Therefore, developing a method which involves free radicals for detection of quercetin and its degradation/metabolic products would be helpful for understanding the mechanism related to *in vivo* metabolic activation.

The commonly used methods for determination of quercetin and its degradation products are UV–vis spectrophotometry [10–13], mass spectrometry (MS) [14–19] and electrochemical methods [20]. Chemiluminescence [21–24] has been used to evaluate the antioxidant activity of flavonoids. Electrogenerated chemiluminescence (ECL) has been a useful analytical method, which involves the generation of the luminescent species of the excited state on the electrode surface as well as producing luminescent species via chemical reaction. Enhanced $Ru(bpy)_3^{2+}$ ECL by quercetin was observed in our previous study [25]. Compared with $Ru(bpy)_3^{2+}$ ECL system, luminol ECL system offers a lower oxidizing potential and less expensive reagent. Most of the reported applications of luminol ECL are related to ROS [26,27], including hydrogen peroxide, superoxide radicals ($O_2^{\bullet -}$), hydroxyl radical ($^{\bullet}OH$) and HO_2^-. Since ROS are involved in the oxidation of quercetin, luminol ECL was expected to detect quercetin. Pyrogallol [28] was reported to enhance luminol ECL in alkaline solution, but catechol derivatives [29], tannic acid [30], dopamine [31,32] quenched luminol ECL. There are few reports on the direct analysis of quercetin with enhanced luminol ECL. In this study, the quercetin enhancement of luminol ECL was investigated. Quercetin autoxidation was studied to evaluate the correlation with its enhancement effect of luminol ECL. HPLC–MS was used to identify the autoxidation of degradation products.

* Corresponding author. Tel.: +86 10 62761187; fax: +86 10 62751708.
** Corresponding author. Tel.: +86 10 62754976; fax: +86 10 62751708
E-mail addresses: lina@pku.edu.cn (N. Li), hwliu@pku.edu.cn (H.-W. Liu).

2. Experimental

2.1. Chemicals and reagents

All reagents were of analytical grade except acetonitrile that was HPLC grade. Quercetin (3,5,7,3′,4′-pentahydroxyflavone), rutin (5,7,3′,4′-tetrahydroxyflavone-3-rutinoside), morin (3,5,7,2′,4′-pentahydroxyflavone), 3-hydroxyl flavonol and luminol (5-amino-2,3-dihydrophtalazine-1,4-dione) were purchased from Aldrich Chemical Co. (Milwaukee, WI). α-Phenyl-*N-tert*-butylnitrone (PBN) (>99.0%) was synthesized by Prof. Yang Liu's Group, Institute of Chemistry, Chinese Academy of Science (Beijing, China). Ethanol, methanol, glacial acetic acid, sodium carbonate and sodium hydrogen carbonate were purchased from Beijing Chemicals Co. (Beijing, China). HPLC-grade acetonitrile was purchased from Dima Technology (Hong Kong, China). Boric acid, borax and sodium hydroxide were purchased from Chemical Regent Factory (Beijing, China). Double deionized water (conductivity: $0.083 \, \mu S \, cm^{-1}$) was used throughout the study. Luminol stock solution ($10 \, mmol \, L^{-1}$) was prepared in $0.05 \, mol \, L^{-1}$ NaOH solution. Quercetin stock solution ($2 \, mmol \, L^{-1}$) was prepared in acetonitrile. The stock solutions were stored in dark at $4 \,°C$. Working solutions were prepared by diluting the stock solution with buffer immediately before the experiment unless indicated otherwise.

2.2. Physical measurements and instrumentation

ECL experiments were performed on MPI-B multi-channel data-analysis system (MPI-B, Xi'an Remax Electronic Science Tech. Co. Ltd, China) with potentiostat, digitalized flow-injection system and photo-multiplier tube (PMT). Cells for flow-injection analysis (FIA) were made in our laboratory using reported thin-layer design [33,34]. Two solid PTFE 0.1 mm thick spacers were sandwiched between the working electrode and the optical glass disk, creating a $40 \, \mu L$ flow-cell volume. For FIA, a $60 \, \mu L$ sample loop was used. All connections in the flow-injection system were constructed with 0.8 mm internal diameter PTFE tubing. The PMT voltage was set at 600 V for photon collection. The working electrode was a glassy carbon (GC) electrode ($\phi = 4 \, mm$). Prior to each experiment, the GC electrode was polished sequentially with 5 and $0.5 \, \mu m$ alumina slurry to obtain a mirror surface, sonicated to remove particulates and rinsed with deionized water. An Ag/AgCl/KCl ($1 \, mol \, L^{-1}$) reference electrode was used for all measurements. A stainless steel tube served as the auxiliary electrode as well as the outlet of flow cell.

A Hitachi UV-3010 spectrophotometer with a quartz cell (optical path length at 1 cm) (Hitachi, Japan) was used for UV–vis absorption measurement. A measured volume of quercetin stock solution was diluted with selected buffer solution to a desired concentration. Then UV–vis spectrum of the diluted quercetin solution was measured immediately at $25 \,°C$. For autoxidation analysis, the spectroscopy was recorded consecutively at a time interval of 180 s.

A Hitachi F-4500 fluorescence spectrophotometer (Hitachi, Japan) combined with a potentiostat and three-electrode system was used for the ECL spectrum measurement. Spectral recording and cyclic voltammetric scans were conducted simultaneously with spectral scan rate at $6 \, nm \, s^{-1}$ and cyclic voltammetric scan rate at $0.2 \, V \, s^{-1}$ from −0.125 to 0.650 V.

LC–ESI/MS analysis was performed using an Agilent 1100 series LC system (Agilent Technologies, Palo Alto, CA, USA), equipped with an autosampler and diode-array detector (DAD), on-line coupled to Trap XCT ion trap MSD mass spectrometer (Agilent) equipped with a ESI source operating in negative or positive ion mode. A ZORBAX Extended C-18 column ($150 \, mm \times 4.6 \, mm$, particle size $5 \, \mu m$; Agilent) was used for the separation at $25 \,°C$ under isocratic elution with acetonitrile/water (35/65, 0.5% acetic acid) as mobile phase at $0.5 \, mL \, min^{-1}$. The quercetin solution with initial concentration of $20 \, \mu mol \, L^{-1}$ in pH 10, $0.12 \, mol \, L^{-1}$ carbonate buffer was neutralized before injection with $1.69 \, mol \, L^{-1}$ acetic acid. The injection volume was $10 \, \mu L$ and the DAD spectra were recorded from 225 to 450 nm. The effluent from DAD was introduced into the mass spectrometer without splitting.

The parameters for fragmentation experiment with ESI source were: 50.0 psi nebulizer pressure; $8.0 \, L \, min^{-1}$ nitrogen drying gas flow rate at $325 \,°C$. The Agilent ultra-scan mode was utilized in the range of *m/z* 50–400. MSn experiments were carried out with AutoMSn operation modes.
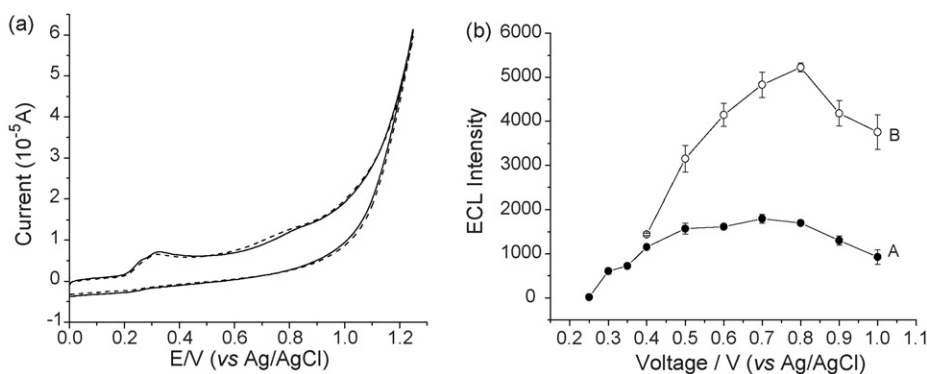

Fig. 1. (a) Cyclic voltammograms of $0.1 \, mmol \, L^{-1}$ luminol in the absence of quercetin (- - -) and in the presence of $0.005 \, mmol \, L^{-1}$ quercetin (—) in $0.12 \, mol \, L^{-1}$ carbonate buffer pH 9.9 with scan rate at $50 \, mV \, s^{-1}$. (b) ECL intensity of $0.1 \, mmol \, L^{-1}$ (●) and 0.1–0.01 $mmol \, L^{-1}$ quercetin (○) as a function of applied voltage in $0.12 \, mol \, L^{-1}$ pH 9.9 carbonate buffer. Carrier solution, $0.12 \, mol \, L^{-1}$ KCl; flow rate, $1.1 \, ml \, min^{-1}$.
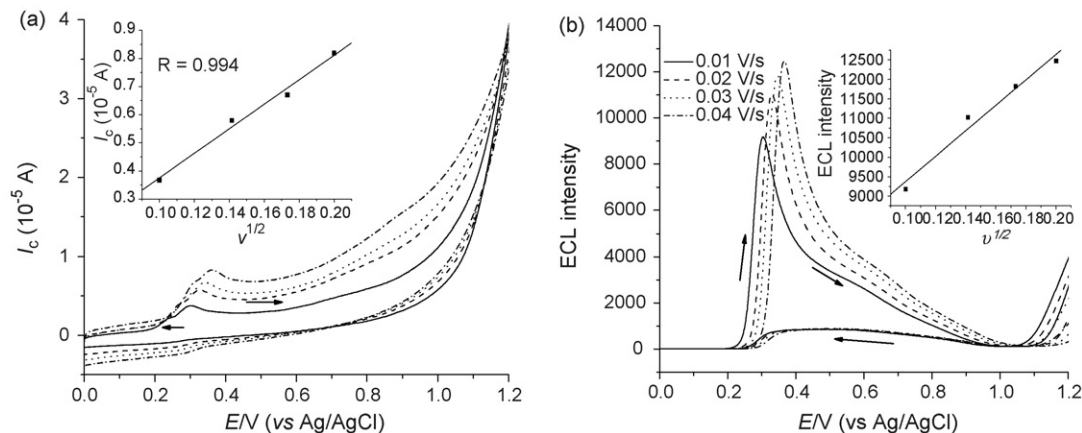
Fig. 2. Cyclic voltammograms (a) and corresponding ECL emission (b) of 0.1 mmol L^{-1} luminol–0.005 mmol L^{-1} quercetin system at varied scan rates in 0.12 mol L^{-1} pH 9.9 carbonate buffer. The insets are plots of peak current (a) and ECL intensity (b) vs. square root of scan rate.

3. Results and discussion

3.1. Voltage applied to ECL measurement

Cyclic voltammograms (Fig. 1a) of quercetin and luminol showed that both luminol and quercetin had an oxidation peak between 0.2 and 0.4 V vs. Ag/AgCl. Comparing the two voltammograms, it was concluded that quercetin contributed to the first oxidation potential at about 0.26 V, and luminol was the second oxidation potential at about 0.32 V [35]. As is shown in the inset of Fig. 2, the anodic peak currents for luminol (a) and corresponding ECL emission intensity (b) increased linearly with the square root of the scan rate, which demonstrated that the electrode reaction was controlled by diffusion [36,37].

The enhancement of quercetin on luminol ECL started to increase when applied voltage was greater than 0.40 V and reached maximum at 0.8 V (Fig. 1b). At voltage greater than 0.80 V, this enhancement decreased with increasing potential.

3.2. Buffer effect on ECL emission

In FIA–ECL experiments, the reagent blank signal and luminol–quercetin signal were affected by the type and pH of buffer.

In NaOH media, the pH was adjusted with either 0.05 mol L^{-1} HCl or 0.05 mol L^{-1} NaOH. The supporting electrolyte was 0.12 mol L^{-1} KCl. The ECL signals for luminol continuously increased as the pH increased. In the presence of quercetin, ECL increased dramatically from pH 10.4 and to a plateau at pH 10.7. For carbonate buffer medium, pH was adjusted by mixing sodium carbonate with sodium bicarbonate at varied ratios to give a constant 0.12 mol L^{-1} concentration. Luminol ECL signal was low at pH from 8.5 to 9.5 and increased linearly with pH from 9.5 to 11.5. Distinct enhanced ECL was observed initially at pH 8.5 and increased to a plateau at pH 9.9. Collectively, the enhanced ECL reached maximum at pH 9.9 and descended thereafter. Because ECL enhancement was greater in carbonate media than in NaOH–KCl media, pH 9.9 carbonate was chosen in the following study. It was reported

[38] that maximum ratio of enhanced ECL signal of epinephrine to reagent blank and optimal reproducibility could be achieved when borax was the carrier stream. Furthermore, polyphenol formed a complex with borax [39,40]. Inspired by these publications, ECL of luminol–quercetin system in borate buffer was investigated. The pH of borate solution was adjusted with boric acid or sodium hydroxide to keep the 0.03 mol L^{-1} concentration constant; however, no enhanced ECL was observed in the borate buffer system. To elucidate borate effect, ECL of luminol–quercetin system was investigated in carbonate buffer at pH 9.9 with varied borax concentrations at the same pH (Fig. 3). The ECL intensity of luminol–quercetin in carbonate buffer presented the greatest enhancement. As the content of borax increased, the enhancement was compromised. It was also observed that the addition of borax reduced the speed for ECL to reach a stable value as repetitive flow injections were made. When borate was 30%, the ECL intensity did not reach maximum within 1400 s.
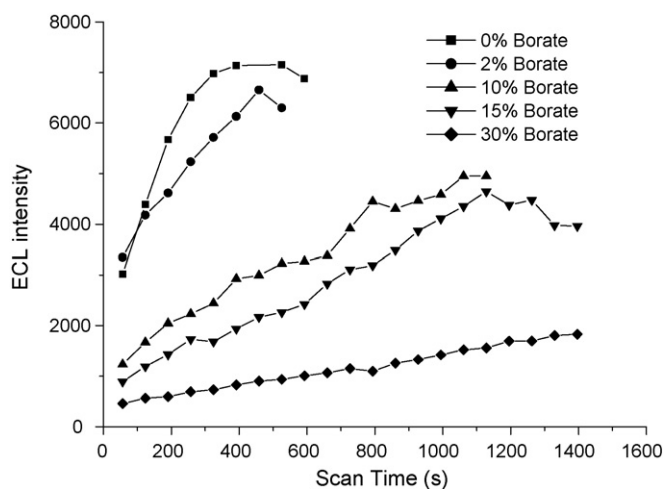

Fig. 3. Effect of borate content on 0.1 mmol L^{-1} luminol–0.02 mmol L^{-1} quercetin ECL signal in 0.12 mol L^{-1} pH 9.9 carbonate buffer as a function of time. Carrier solution, 0.12 mol L^{-1} KCl; flow rate, 1.1 ml min^{-1}; applied voltage, 0.8 V (vs. Ag/AgCl). Each point represents one injection.

Table 1
Calibration curves of quercetin[a]

Luminol	Linear range ($\mu mol\,L^{-1}$)	Regression equation	R
0.01 ($mmol\,L^{-1}$)			
$I = Ac + B$	1–12	$y = 50.1(5.43) + 8.9(0.9)x$	0.985
$Log(I_{ECL}) = E log(c) + F$	1–16	$y = 1.30(0.05) + 0.69(0.06)x$	0.997
0.05 ($mmol\,L^{-1}$)			
$I = Ac + B$	1–12	$y = 297.4(29.7) + 60.3(7.1)x$	0.980
$Log(I_{ECL}) = E log(c) + F$	1–20	$y = 2.08(0.04) + 0.69(0.05)x$	0.993
0.1 ($mmol\,L^{-1}$)			
$I = Ac + B$	1–20	$y = 573.4(20.3) + 142.9(5.0)x$	0.998
$Log(I_{ECL}) = E log(c) + F$	1–30	$y = 2.29(0.06) + 0.91(0.06)x$	0.995
0.2 ($mmol\,L^{-1}$)			
$I = Ac + B$	1–50	$y = 1183.9(33.3) + 234.1(2.1)x$	1.000
$Log(I_{ECL}) = E log(c) + F$	1–50	$y = 2.56(0.02) + 0.86(0.02)x$	0.996

[a] Experimental conditions: carrier solution, $0.12\,mol\,L^{-1}$ KCl; flow rate, $1.1\,ml\,min^{-1}$; applied voltage, 0.8 V (vs. Ag/AgCl).

Under the test buffer system and applied voltage, acetonitrile showed enhanced effect on the luminol ECL background signal by about 10%. In our experiments, enhanced ECL by quercetin was obtained by subtracting luminol ECL background in the presence of equivalent amount of acetonitrile introduced together with quercetin test solution. Therefore, enhancement by acetonitrile shall not be a problem for quantification of quercetin.

3.3. Analytical application

With luminol as the luminophor, ECL intensity was proportional to luminol concentration ($y = 48.8 + 6.44x$, $R = 0.999$, $n = 7$). The addition of quercetin enhanced the luminol ECL emission at every level with ECL intensity still proportional to luminol concentration ($y = -147.8 + 57.8x$, $R = 0.999$, $n = 7$). Based on the slopes of calibration curves, the sensitivity for luminol was higher in the presence of quercetin than its absence. Higher luminol concentrations provided a more extended linear range for quercetin calibration. At each tested luminol concentration, enhanced ECL intensity was proportional to quercetin concentration. The linear correlation also applied to logarithm function of both ECL intensity and concentration (Table 1). For $0.1\,mol\,L^{-1}$ luminol, the detection limit (S/N = 3) was $2.0 \times 10^{-8}\,mol\,L^{-1}$.

3.4. Autoxidation analysis of quercetin using UV spectrophotometry

Autoxidation of quercetin in alkaline solution was observed visually as the solution color became darker with time. Autoxidation was verified by UV absorption spectral change in our study as well as was reported by Dangles et al. [9]: the apparent descending of the absorption band I ($\lambda_{max} = 399$–428 nm depending on pH) and the simultaneous rising of absorption bands at about 320 nm. The absorption spectrum after 24 h oxidation was different from initial and 1 h autoxidation, indicating that solvent adduct underwent further oxidation.

For the initial autoxidation within 24 h, it was assumed that quercetin went through a series of fast oxidation reaction to a quasi-stationary intermediate. Apparent first-order kinetic model (Eq. (1)) was used to describe the quercetin autoxidation behavior in alkaline aqueous.

$$\ln c_Q = \ln(c_0 - c_{Q*}) = -kt + c \tag{1}$$

where k is the apparent reaction rate; c is a constant; c_0 is the initial quercetin concentration; c_Q and c_{Q*} are concentrations of quercetin and its intermediate at reaction time, t.

Eq. (1) was rewritten as

$$c_Q = c_0 - c_{Q*} = Be^{-kt} \tag{2}$$

According to Lambert–Beer's law,

$$\varepsilon_Q c_Q + \varepsilon_{Q*} c_{Q*} = \frac{A}{l} \tag{3}$$

where ε_Q and ε_{Q*} are the molar absorptivities of quercetin and its intermediate, respectively; A is collective absorbance of quercetin in both forms at reaction time, t; l is the light path.

Introducing Eq. (2) to Eq. (3), Eq. (4) was obtained

$$\varepsilon_{Q*}(c_0 - Be^{-kt}) + \varepsilon_Q Be^{-kt} = \frac{A}{l} \tag{4}$$

Table 2
Autoxidation reaction rate of quercetin[a] in different pH and buffer systems

Buffer	pH	k ($\times 10^{-4}\,s^{-1}$)	r^2
	7.24	0.123 ± 0.013	0.952
	7.54	0.130 ± 0.009	0.984
	8.36	0.374 ± 0.010	0.997
	8.69	0.563 ± 0.008	0.999
Britton–Robinson	8.95	1.11 ± 0.03	0.996
	9.37	1.77 ± 0.04	0.998
	9.62	3.17 ± 0.08	0.997
	10.38	3.69 ± 0.06	0.998
	11.20	2.56 ± 0.03	0.999
Phosphate	7.36	0.249 ± 0.012	0.991
Borate	8.68	0.198 ± 0.012	0.983
	9.68	0.612 ± 0.010	0.999

[a] Initial quercetin concentration: $0.025\,mmol\,L^{-1}$.
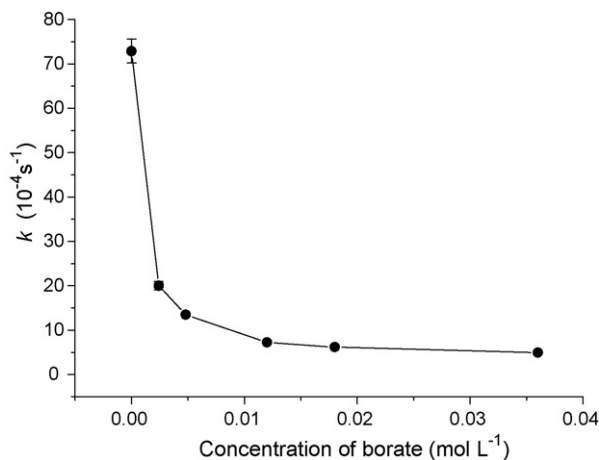
Fig. 4. Quercetin autoxidation rate as a function of borate content in $0.12 \, mol \, L^{-1}$ pH 9.9 carbonate buffer. Initial quercetin concentration was $0.02 \, mmol \, L^{-1}$.

i.e.

$$\varepsilon_{Q*}c_0 + (\varepsilon_Q - \varepsilon_{Q*})Be^{-kt} = \frac{A}{l} \qquad (5)$$

Because ε_{Q*} of intermediate was small enough that the item $\varepsilon_{Q*}c_Q$ in Eq. (6) was negligible. Thus, Eq. (6) was obtained.

$$(\varepsilon_Q - \varepsilon_{Q*})Be^{-kt} = \frac{A}{l} \qquad (6)$$

The wavelength of 420 nm was chosen for calculation of oxidation rate in Britton–Robinson buffer and borate buffer, 440 nm was chosen for calculation in carbonate buffer, 410 nm was chosen for calculation in phosphate buffer. The autoxidation rate of quercetin was higher with increase of pH (Table 2). When borate (adjusted to pH 9.9) was introduced into the carbonate buffer media with pH 9.9, autoxidation rate became lower as borate content increased (Fig. 4). This observation indicated that borate not only reduced the quercetin enhancement effect on luminol ECL, but also inhibited the autoxidation of quercetin because the (catecholato)borate complexes formed between the borate and catecholic hydroxyl groups in ring B of quercetin structure [41,42]. In the 1-h test period, autoxidation did not occur to rutin, morin and 3-hydroxyl flavonol in alkaline aqueous media because UV–vis absorption spectra did not change.

3.5. Autoxidation analysis of quercetin using HPLC–MS

Autoxidation of quercetin stock solution (0.1 mL, $2 \, mmol \, L^{-1}$) was initiated by diluting quercetin stock solution with carbonate buffer (0.9 mL, $0.12 \, mol \, L^{-1}$, pH 9.9)

and stopped by adding acetic acid (0.05 mL, $1.68 \, mol \, L^{-1}$) at 1, 2 and 5 min. The resulted solution was injected into HPLC–MS. Two major degradation products were observed from LC chromatogram with the peak height increasing during autoxidation while that of quercetin decreased. Compound **1** at 6.1 min retention time had the characteristic absorption of quercetin at 255, 373 and 310 nm (shoulder). This compound **1** was identified as quercetin by mass spectroscopy ($[M − H]^-$ of m/z 301 in negative mode, and daughter ions with m/z at 151 and 179). The compound **2** at 2.97 min exhibited a UV spectrum with three peaks at 225, 260 and 295 nm. In MS, one high intensity of m/z 153 and a low intensity of m/z 109 (loss of 44 from 153) were found for this compound in the negative mode identified as 3,4-dihydroxybenzoic acid [8].

The degradation products at 3.18 min in chromatogram had a small peak at 260 nm and a large absorption maximum at 295 nm at 1 min autoxidation with 260 nm peak disappearing at 2 and 5 min autoxidation. This observation was coincident with results of total ion chromatogram (TIC) which showed that there were two peaks at 3.18 min. In MS, one of the compounds with m/z at 317 and 169 in negative mode was identified as compound **3**, while another with m/z at 355, 217, 197, 179, 169 and 153 and height one order of magnitude lower than compound **3** remained to be identified. There were two possible pathways to form compound **3**. According to Dangles et al. [9], in aqueous solution, a fast addition of water on the quinone formed water adduct, thus compound **3** may be formed by the loss of H_2O from water adduct. However, superoxide and hydrogen peroxide were involved in the oxidation of quercetin [8], thus quercetin may react with $^{\bullet}OH$ [43]. It is hard to identify the pathways for formation of compound **2**. Its generation may be associated with compound **4** which could be identified in MS with m/z 305 [8] (Scheme 1).

3.6. Mechanism for enhancement of ECL by quercetin

In alkaline medium, luminol formed an anion that was electrochemically oxidized [35,44,45]. Further oxidation of the resulted diazo compound produced 3-aminophthalate (AP) in the excited state, which emitted light to return to the ground state. To elucidate the quercetin–luminol ECL reaction mechanism, the ECL emission spectrum was recorded with a F-4500 fluorescence spectrophotometer combined with a potentiostat and a cell assembled with a three-electrode system (Fig. 5). The luminol–quercetin showed a maximum emission at 425 nm, which demonstrated that excited state 3-aminophtalate was the ECL emitter [46].
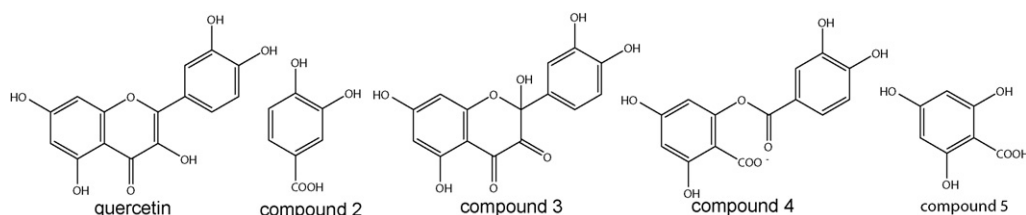
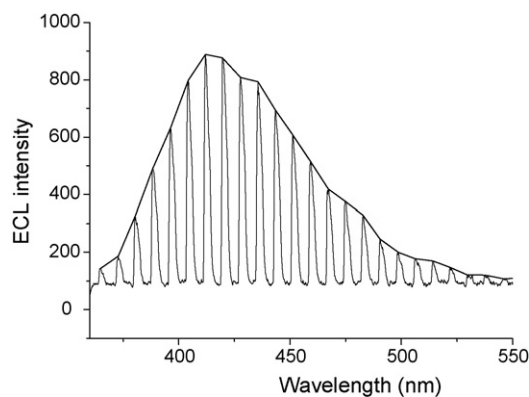Scheme 1. Proposed chemical structures of quercetin, compounds 2, 3, 4, and 5.

Fig. 5. ECL spectrum of $0.2 \, \text{mmol L}^{-1}$ luminol–$0.02 \, \text{mmol L}^{-1}$ quercetin system in $0.12 \, \text{mol L}^{-1}$ pH 9.9 carbonate buffer. Spectral scan rate, $6 \, \text{nm s}^{-1}$; cyclic voltammetric scan rate, $0.2 \, \text{V s}^{-1}$; scan range, from -0.125 to $0.650 \, \text{V}$ (*vs.* Ag/AgCl).
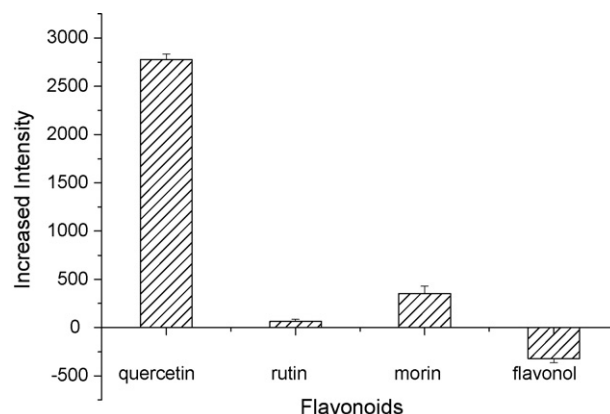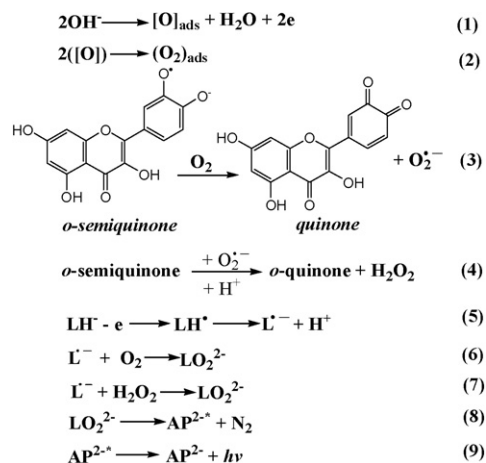

Fig. 7. Enhanced ECL intensity of $0.1 \, \text{mmol L}^{-1}$ luminol by $10 \, \mu\text{mol L}^{-1}$ flavonoids in $0.12 \, \text{mol L}^{-1}$ pH 9.9 carbonate buffer. Carrier solution, $0.12 \, \text{mol L}^{-1}$ KCl; flow rate, $1.1 \, \text{ml min}^{-1}$; applied voltage, $0.8 \, \text{V}$ (*vs.* Ag/AgCl).

Autoxidation of quercetin in aqueous alkaline solution has generated ROS such as superoxide and hydrogen peroxide [6–8]. Both the ECL intensity and autoxidation rate of quercetin were affected by pH and borate content, thus ECL emission of luminol–quercetin was related to the ROS involved in the autoxidation of quercetin in alkaline aqueous solution. The quercetin autoxidation products, 3,4-dihydroxybenzoic acid and compound **3**, in the carbonate buffer ($0.12 \, \text{mol L}^{-1}$, pH 9.9), were detected by LC–DAD–MS analysis. *o*-Semiquinone, which can react with O_2 to form superoxide [4], was the necessary intermediate to generate compound **3**.

Superoxide radical and hydrogen peroxide involved in the autoxidation of quercetin took part in the luminol ECL emission in a direct or indirect way. The existence of free radicals in the process of luminol ECL was proven by introducing PBN, a spin trap agent for hydroxyl and peroxide radicals. In the presence of PBN, luminol ECL emission was markedly quenched regardless of the presence of quercetin (Fig. 6), which demonstrated that radicals have been partially consumed by PBN and thus free radicals were critical for luminol ECL system.

Autoxidation of other flavonoids such as rutin, morin and 3-hydroxylfavonol was slow in carbonate buffer because UV–vis spectroscopy was found to be very stable in the same condition as that of quercetin. Coincidently these compounds did not show the enhancement effect on luminol ECL emissions as quercetin did (Fig. 7). Therefore autoxidation was crucial to the enhancement of luminol ECL in the present conditions. In our experiment, removal of dissolved oxygen by purging solution with nitrogen did not show reduced luminol ECL emission at 0.8 V because the active oxygen could be generated from the electro-oxidation of OH^- at 0.8 V [28]. The enhancement mechanism of luminol by quercetin was proposed as Scheme 2. In Scheme 2, Eqs. (1) and (2) were reported in Ref. [28] and Eqs. (3) and (4) were from Ref. [4]. OH^- plays a very important role in the formation of luminol anion, adsorptive oxygen on the surface of electrode by electrolysis and *o*-semiquinone in the process of autoxidation. The generated superoxide radical ($O_2^{\bullet-}$) (Eq. (3)) or H_2O_2 (Eq. (4)) by autoxidation reacted with luminol radical ($L^{\bullet-}$) to produce 3-aminophtalate excited state (AP^{2-*}), which generates light emission.

Fig. 6. PBN effect on the ECL signal of $0.1 \, \text{mmol L}^{-1}$ luminol and quercetin in $0.12 \, \text{mol L}^{-1}$ pH 9.9 carbonate buffer. b, b′: luminol and $0.01 \, \text{mmol L}^{-1}$ quercetin in the absence (a) or presence of $60 \, \text{mmol L}^{-1}$ PBN (b′); a, a′: luminol in the absence (a) or presence of $60 \, \text{mmol L}^{-1}$ PBN (a′); scan rate, $0.1 \, \text{V s}^{-1}$; scan range, from 0 to 1.0 V (*vs.* Ag/AgCl).

$$2OH^- \longrightarrow [O]_{ads} + H_2O + 2e \quad (1)$$

$$2([O]) \longrightarrow (O_2)_{ads} \quad (2)$$

$$\text{o-semiquinone} \xrightarrow{O_2} \text{quinone} + O_2^{\bullet-} \quad (3)$$

$$\text{o-semiquinone} \xrightarrow[+ H^+]{+ O_2^{\bullet-}} \text{o-quinone} + H_2O_2 \quad (4)$$

$$LH^- - e \longrightarrow LH^{\bullet} \longrightarrow L^{\bullet-} + H^+ \quad (5)$$

$$L^{\bullet-} + O_2 \longrightarrow LO_2^{2-} \quad (6)$$

$$L^{\bullet-} + H_2O_2 \longrightarrow LO_2^{2-} \quad (7)$$

$$LO_2^{2-} \longrightarrow AP^{2-*} + N_2 \quad (8)$$

$$AP^{2-*} \longrightarrow AP^{2-} + h\nu \quad (9)$$

Scheme 2. Enhancement mechanism of luminol ECL by quercetin. *Note*: Eqs. (1) and (2) from Ref. [28]. Eqs. (3) and (4) from Ref. [4]. AP^{2-*}: 3-aminophtalate excited state.

4. Conclusions

The present studies show that quercetin enhanced luminol ECL in alkaline solution. The quercetin enhancement effect was a sensitive method for the determination of quercetin as was established in this work. This method may be promising in coupling with capillary electrophoresis (CE) because the limit of detection was low. The enhancement mechanism is related to ROS generated by autoxidation. The catechol group on ring B of quercetin was sensitive to autoxidation and gave rise to stable semiquinone free radicals, thus quercetin can markedly enhanced luminol ECL emission, while other flavonoids without catechol or pyrogallol function group on ring B and 3-hydroxly group on ring C slightly enhanced or inhibited the luminol ECL emission. Therefore, this method would be feasible in selective determination of flavonoid mixtures. Furthermore, the association of autoxidation to ECL intensity provides the basis of methods for the assessment and interpretation of flavonoid antioxidant activity.

Acknowledgements

References

[1] C. Rice-Evans, Curr. Med. Chem. 8 (2001) 797.
[2] S.B. Lotito, B. Frei, Free Radic. Biol. Med. 41 (2006) 1727.
[3] S. Lesser, S. Wolffram, Curr. Top. Nutraceutical Res. 4 (2006) 239.
[4] D. Metodiewa, A.K. Jaiswal, N. Cenas, E. Dickancait'e, J. Segura-aguilar, Free Radic. Biol. Med. 26 (1999) 107.
[5] O. Dangles, C. Dufour, G. Fargeix, J. Chem. Soc. Perk. Trans. 2 6 (2000) 1215.
[6] W.F. Hodnick, F.S. Kung, W.J. Roettger, C.W. Bohmont, R.S. Pardini, Biochem. Pharmacol. 35 (1986) 2345.
[7] M. Ochiai, M. Nagao, K. Wakabayaski, T. Sigimura, Mutat. Res.-Environ. Mutat. 129 (1984) 19.
[8] C. Tournaire, M. Hocquaux, I. Beck, E. Oliveros, M.T. Maurette, Tetrahedron 50 (1994) 9303.
[9] O. Dangles, G. Fargeix, C. Dufour, J. Chem. Soc. Perk. Trans. 2 (1999) 1387.
[10] Y.T. Lin, S.L. Hsiu, Y.C. Hou, H.Y. Chen, P.D.L. Chao, Biol. Pharm. Bull. 26 (2003) 747.
[11] F.M. Wang, T.W. Yao, S. Zeng, J. Pharma. Biomed. 33 (2003) 317.
[12] P.C.H. Hollman, J.H.M. Devries, S.D. Vanleeuwen, M.J.B. Mengelers, M.B. Katan, Am. J. Clin. Nutr. 62 (1995) 1276.
[13] E.U. Graefe, M. Veit, Phytomedicine 6 (1999) 239.
[14] J.R. Rao, J.E. Cooper, J. Bacteriol. 176 (1994) 5409.
[15] A. Braune, M. Gutschow, W. Engst, M. Blaut, Appl. Environ. Microbiol. 67 (2001) 5558.
[16] U. Justesen, E. Arrigoni, Rapid Commun. Mass Spectrom. 15 (2001) 477.
[17] M. Blaut, L. Schoefer, A. Braune, Int. J. Vitam. Nutr. Res. 73 (2003) 79.
[18] A. Marfak, P. Trouillas, D.P. Allais, C.A. Calliste, J.L. Duroux, Radiat. Res. 159 (2003) 218.
[19] S. Labib, A. Erb, M. Kraus, T. Wickert, E. Richling, Mol. Nutr. Food Res. 48 (2004) 326.
[20] J. Labuda, M. Buckova, L. Heilerova, S. Silhar, I. Stepanek, Anal. Bioanal. Chem. 376 (2003) 168.
[21] H.Y. Choi, E.J. Jhun, B.O. Lim, I.M. Chung, S.H. Kyung, D.K. Park, Phytother. Res. 14 (2000) 250.
[22] X. Yang, H.H. Chu, Y.Y. Qi, J.W. Di, Y.F. Tu, Spectrosc. Spect. Anal. 25 (2005) 192.
[23] T. Toyo'oka, T. Kashiwazaki, M. Kato, Talanta 60 (2003) 467.
[24] E.E. Robinson, S.R.J. Maxwell, G.H.G. Thorpe, Free Radic. Res. 26 (1997) 291.
[25] R. Lei, H.W. Liu, N. Li, K. Li, Chin. Chem. Lett. 17 (2006) 1499.
[26] C. Lu, G. Song, J.M. Lin, TRAC-Trend Anal. Chem. 25 (2006) 985.
[27] A.W. Knight, TRAC-Trend Anal. Chem. 18 (1999) 47.
[28] Y.G. Sun, H. Cui, X.Q. Lin, Y.H. Li, H.Z. Zhao, Anal. Chim. Acta 423 (2000) 247.
[29] Y.G. Sun, H. Cui, Y.H. Li, X.Q. Lin, Talanta 53 (2000) 661.
[30] Y.G. Sun, H. Cui, Y.H. Li, H.Z. Zhao, X.Q. Lin, Anal. Lett. 33 (2000) 2281.
[31] L.D. Zhu, Y.X. Li, G.Y. Zhu, Anal. Lett. 35 (2002) 2527.
[32] E. Nalewajko, R.B. Ramirez, A. Kojlo, J. Pharm. Biomed. Anal. 36 (2004) 219.
[33] H.Y. Wang, G.B. Xu, S.J. Dong, Analyst 126 (2001) 1095.
[34] G.B. Xu, S.J. Dong, Analyst 124 (1999) 1085.
[35] X.Q. Lin, Y.G. Sun, H. Cui, Chin. J. Anal. Chem. 27 (1999) 497.
[36] H.R. Zare, M. Namazian, N. Nasirizadeh, J. Electroanal. Chem. 584 (2005) 77.
[37] A.J. Bard, L.R. Faulkner, Electrochemical Methods, Fundamentals and Applications, Wiley, New York, 2001.
[38] X.W. Zheng, Z.H. Guo, Z.J. Zhang, Anal. Chim. Acta 441 (2001) 81.
[39] P. Schmitt-Kopplin, N. Hertkorn, A.W. Garrison, D. Freitag, A. Kettrup, Anal. Chem. 70 (1998) 3798.
[40] P. Morin, F. Villard, M. Dreux, J. Chromatogr. 628 (1993) 153.
[41] J.H. Waite, Anal. Chem. 56 (1984) 1935.
[42] W.F. Hodnick, D.L. Duval, R.S. Pardini, Biochem. Pharmacol. 47 (1994) 573.
[43] A. Marfak, P. Trouillas, D.P. Allais, Y. Champavier, C.A. Calliste, J.L. Duroux, J. Agric. Food Chem. 50 (2002) 4827.
[44] K.A. Fahnrich, M. Pravda, G.G. Guilbault, Talanta 54 (2001) 531.
[45] K.E. Haapakka, J. Kankare, Anal. Chim. Acta 138 (1982) 263.
[46] White, Roswell, Chemi- and Bio-luminescence, Marcel Dekker, New York, 1985.

A coupled reagent of *o*-phthalaldehyde and sulfanilic acid for protein detection based on the measurements of light scattering signals with a common spectrofluorometer

Yuan Fang Li[*], Xiao Wei Shen, Cheng Zhi Huang

College of Chemistry and Chemical Engineering, CQKL-RATA, Southwest University, Chongqing 400715, China

Abstract

A rapid and sensitive method for the determination of proteins is proposed with a coupled reagent of *o*-phthalaldehyde and sulfanilic acid by measuring the light scattering (LS) signals with a common spectrofluorometer. Mechanism investigations showed that *o*-phthalaldehyde couples at first with sulfanilic acid with fast speed and forms a new synthesized Schiff base dye, which then interacts with protein rapidly on acidic condition, resulting in greatly enhanced LS signals with the maximum peak located at 344 nm. Based on the linear relationship between enhanced LS intensities and concentrations of proteins, a novel assay of HSA and BSA is established in the linear range of 0.1–25.0 μg ml^{-1} with the limits of detection (3σ) being 13 ng ml^{-1} depending on the concentration of the reagent. Results for sample detections of our method were consistent with the documented spectrophotometric method with CBB G250 assay.
© 2008 Elsevier B.V. All rights reserved.

Keywords: *o*-Phthalaldehyde (OPA); Sulfanilic acid; Human serum albumin (HSA); Bovine serum albumin (BSA); Light scattering (LS)

1. Introduction

Since organic dyes can serve as effective probes to detect the structures and functions in biological macromolecules, great interest has been raised in the study of the interaction between dyes and proteins or nucleic acids in recent decades, and various new dye binding methods have been put forward for protein analysis by spectrophotometric and fluorometric methods [1,2]. For distinct advantages of speed, convenience and sensitivity as an analytical method, light scattering signals have been extensively made use of and applied for both small and large molecules in various states [3,4]. Since the breakthrough of Pasternack to construct the resonance light scattering (RLS) technique with a common fluorescence spectrometer and to study biological macromolecules [3,5], light scattering signals have been increas-

ingly applied to the study and detection of nucleic acids [6–10], proteins [11–14], amino acid [15], saccharide [16,17], medicines [18,19] and metal ions [20,21] with high sensitivity and easy operations. These applications, however, are generally based on the interaction of organic dyes with the analytes such as proteins and nucleic acids. The detection methods of proteins, for example, are generally based on the electrostatic attraction between protein and negative dyes in the medium of pH lower than the isoelectric point (pI_0) values [22–25], and it is obviously necessary to develop new reagent for further investigation of macromolecules in order to discuss structural information of organic dyes or proteins, and of course, to develop simple detection methods of macromolecules.

The synthesis of Schiff base has been a hotspot for its advantages in the field of chemistry and biomedicine research in recent years [26,27]. *o*-Phthalaldehyde (OPA), as an important raw material, has found wide applications in the synthesis and research of Schiff base [28], while sulfanilic acid, which has a number of applications in the syntheses of organic dyes

[29], is widely used for the determination of macromolecule and metal ions [30,31]. In this contribution, we employed OPA as a coupled reagent with sulfanilic acid for the detection of proteins.

2. Materials and methods

2.1. Apparatus

The LS spectra were obtained with a Hitachi F-4500 spectrofluorometer (Tokyo, Japan) by simultaneously scanning the excitation and emission monochromators with $\Delta\lambda = 0$ nm, while the absorption spectra were measured with a Hitachi 3010 spectrophotometer (Tokyo, Japan). A pHS-3C digital pH meter (Shanghai Dazhong Analytical Instruments Plant, Shanghai, China) was used to measure the pH values of the aqueous solutions, and a QL-901 vortex mixer (Haimen Qilinbei'er Instrumental Ltd., Haimen, PRC) was employed to blend the solutions in volumetric flasks.

2.2. Reagents

Proteins in this study involve BSA and HSA (Sinopharm Chemical Reagent Co., Shanghai, China). Their stock solutions of 0.2 mg ml^{-1} were prepared by dissolving the commercial products in doubly distilled water and stored at $4\,^\circ$C. 2.0×10^{-2} mol l^{-1} stock solutions of OPA and sulfanilic acid (Yijing Chemical Reagent Co., Beijing) were prepared by dissolving the commercial crystals in doubly distilled water, respectively. Acetic acid–sodium acetate (HAc–NaAc) buffer solution was used to control the pH values of the interacting system, and 1.0 mol l^{-1} NaCl solution was employed to adjust the ionic strength. All working solutions were prepared by diluting the stock solution with distilled water.

2.3. Procedure

1.0 ml HAc–NaAc buffer, 0.5 ml 2.0×10^{-3} mol l^{-1} OPA, and 0.5 ml 2.0×10^{-3} mol l^{-1} sulfanilic acid were added into a 10.0 ml volumetric flask and mixed completely. Five minutes later, an appropriate volume of BSA or sample solution was also added. The mixture was vortexed after each addition, and finally diluted to 10.0 ml with doubly distilled water. After having been mixed thoroughly, the mixture was transferred for absorption and LS measurements.

3. Results and discussion

3.1. Reaction between OPA and sulfanilic acid

Fig. 1 shows the absorption spectral of OPA (Curve 1), sulfanilic acid (Curve 2) and their mixture (Curve 3). It can be found that neither sulfanilic acid nor OPA has characteristic absorption peak in the visible region from 350 to 650 nm, but the absorption of sulfanilic acid–OPA mixture from 350 to 650 nm could be observed, and at about 425 nm a strong absorption peak could be clearly observed. Fig. 1 (Curve 4–10) also shows the absorp-
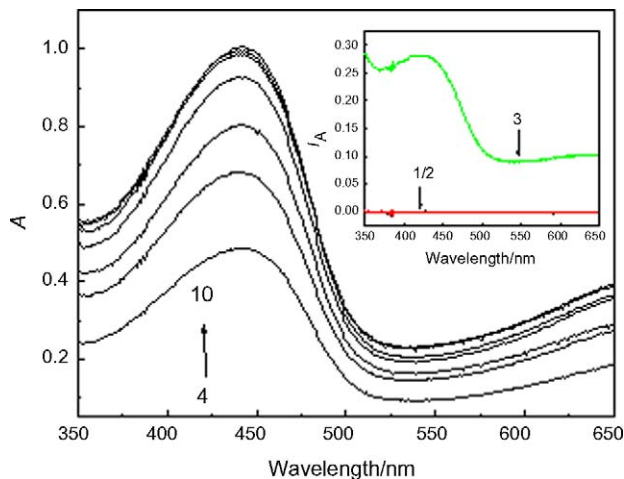

Fig. 1. The absorption spectra of reaction between OPA and sulfanilic acid. Concentrations: OPA (1, 3–10), 1.0×10^{-4} mol l^{-1}; sulfanilic acid (2–10 in order, $\times 10^{-4}$ mol l^{-1}), 1.0; 0.10; 0.25; 0.5; 0.75; 1.0; 1.25; 1.5; 1.75.

tion signals of OPA–sulfanilic acid when they were in different mole ratios. It can be found that the maximal absorption appears when the mole ratio of OPA with sulfanilic acid comes up to 1:1.

In order to identify the reaction mechanism with the coupled-reagent of OPA and sulfanilic acid, we separated the resulting products of the coupled reagents. By measuring the IR spectra of the products, we found that a Schiff base has formed from the reaction (Fig. 2 and Table 1) since the vibrations of OPA including the carbonyl group at 1766 cm^{-1} and benzene skeleton at 1693 and 1592 cm^{-1} have disappeared in the product, and the characteristic vibration of C=N bond at 1630 cm^{-1} appears (Table 1). From these spectra, we could draw the reaction mechanism displayed in Fig. 3. It should be noted that the reaction between OPA and sulfanilic acid yields one main product and we have found other side products are very small. Therefore, it is not necessary to separate and we can directly use OPA and sulfanilic acid for analytical applications.
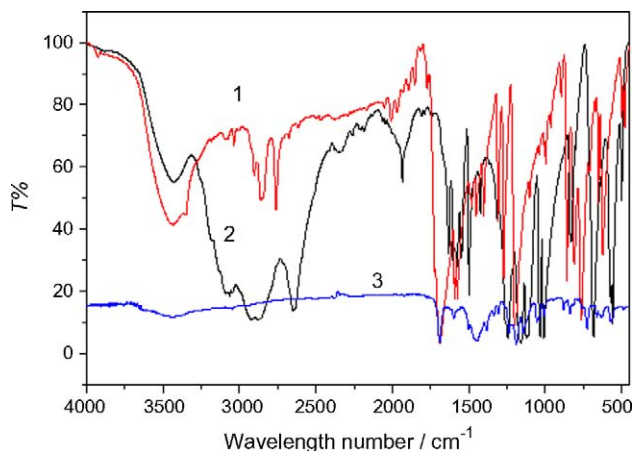

Fig. 2. Infrared spectrum of OPA (Curve 1), sulfanilic acid (Curve 2) and the synthesized Schiff base dye (Curve 3).

Table 1
Assignments of infrared spectrum

	ν_{N-H}	ν_{Ar-H}	$\nu_{HC=O}$	$\nu_{Benzene}$	ν_{C-N}	$\nu_{C=N}$	δ_{Ar-H}
OPA	–	3088	1766	1575, 1404	–	–	758
Sulfanilic acid	3433	3064	–	1602, 1578	1246	–	685
Schiff base	3425	3018	1691	1599, 1450	1190	1630	742

Unit, cm^{-1}.

Table 2
Tolerance of foreign substances

Substance	Concentration[a] (10^{-6} mol l^{-1})	Change of I_{LS} (%)	Substance	Concentration[a] (10^{-6} mol l^{-1})	Change of I_{LS} (%)
Ca^{2+}	500.0	+7.8	Tryptophan	2.5	−1.5
Ba^{2+}	100.0	−6.5	Lysine	15.0	−8.3
Mg^{2+}	100.0	−8.7	Leucine	10.0	−4.7
Zn^{2+}	25.0	+6.9	Alanine	15.0	−5.3
Cu^{2+}	1.0	+3.1	Glycine	25.0	−6.9
Al^{3+}	1.0	−4.6	Arginine	10.0	−7.2
Cd^{2+}	1.0	+6.6	Isoleucine	10.0	−5.6
Pb^{2+}	1.0	+8.1	Tyrosine	2.0	−2.6
Cu^{2+}	2.0	−3.5	Tritox-100	0.002[b]	+4.5
Cr^{3+}	2.0	+6.6	CTMAB	2.0	+3.2
Ni^{2+}	2.5	−7.6	Tween 60	0.002[b]	−3.1
Glucose	100	−6.4	SDBS	5.0	−2.8
Starch	10[c]	−4.5			

Concentration: OPA, 1.0×10^{-4} mol l^{-1}; sulfanilic acid, 1.0×10^{-4} mol l^{-1}. pH, 4.20. All the data were obtained at 344.0 nm.
[a] Represented in 10^{-6} mol l^{-1}.
[b] Represented in percentage (%).
[c] Represented in µg ml^{-1}.

Table 3
Analytical parameters for the detection of proteins

c_{OPA-SH} (10^{-4} mol l^{-1})	Protein	Linear range (µg ml^{-1})	Linear regression equation (c, µg ml^{-1})	LOD (3σ, ng ml^{-1})	Correlation coefficient (r)
0.5	BSA	0.12–15.0	$\Delta I = 84.4 + 145.8c$	12.4	0.9980 ($n=5$)
0.5	HSA	0.11–16.5	$\Delta I = 85.1 + 209.2c$	12.1	0.9976 ($n=7$)
1.0	BSA	0.10–18.0	$\Delta I = 73.1 + 160.1c$	12.0	0.9974 ($n=7$)
1.0	HSA	0.10–21.5	$\Delta I = 42.5 + 224.0c$	10.6	0.9991 ($n=10$)
2.0	BSA	0.08–20.0	$\Delta I = 75.7 + 175.0c$	10.2	0.9987 ($n=9$)
2.0	HSA	0.09–25.0	$\Delta I = 6.8 + 234.9c$	10.0	0.9989 ($n=15$)

pH, 4.20. All the data were obtained at 344.0 nm.

3.2. LS characteristics of the interaction between Schiff base dye and BSA

It can be found that all of the light scattering signals of sulfanilic acid, OPA or their mixtures with protein are very weak (Fig. 4A and B). If protein was added to the mixture of OPA and sulfanilic acid, in which Schiff base has formed, strong light scattering signals could be observed (Fig. 4A) characterized at 344.0 nm with two shoulder peaks at 470 and 520 nm, while the
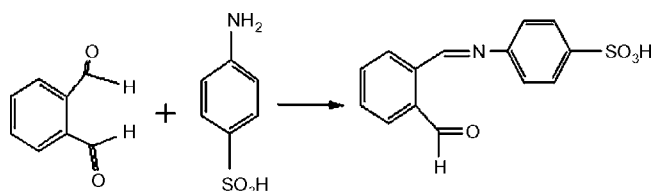
LS signals of both protein and Schiff base dye alone are very weak. Meanwhile, well-regulated enhanced LS signals could be observed with the increase of protein, indicating that the interaction of BSA with Schiff base dye has really been occurred. This light scattering enhancement is possibly due to the electrostatic attraction between the Schiff base and protein since they should have different charges as discussed in the next section concerning the effect of pH and ionic strength.

3.3. Optimal conditions of the assay

As the LS signals can reflect the binding properties between Schiff base dye and BSA. So, we could define the optimal conditions for the interaction between Schiff dye and BSA based on LS measurements. As Fig. 5 shows, the maximal enhancement of LS signals occurs at pH 4.2, which is below the pI_0 of BSA (p$I_0 = 4.9$) and HSA (p$I_0 = 4.7$–4.9). It is obvious that both BSA and HSA are positively charged in such acidic medium,

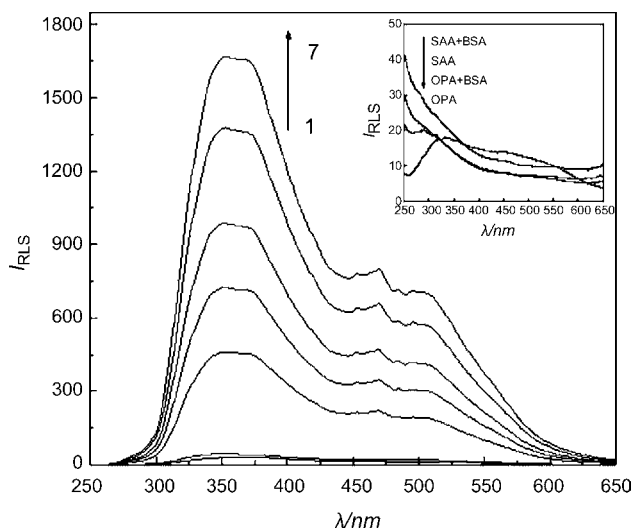Fig. 3. Reaction scheme of OPA with sulfanilic acid.

Fig. 4. The LS spectra of the Schiff dye and BSA (A), and those of the raw materials for the synthesis of Schiff base dye with protein (B). Concentrations: OPA, 1.0×10^{-4} mol l^{-1}; sulfanilic acid, 1.0×10^{-4} mol l^{-1}. BSA in A (1–7, mg l^{-1}), 0.0, 10.0 (without Schiff base dye), 2.0, 4.0, 6.0, 8.0, 10.0; BSA in B (mg l^{-1}), 10.0.

Table 4
Analytical results of human serum samples

Sample	Our method (mg ml^{-1}, $n = 5$)	CBB G250 assay (mg ml^{-1})	RSD of present method (%)
1	69.5	80.1	1.6
2	71.3	83.6	1.2
3	79.7	82.4	1.7

OPA, 1.0×10^{-4} mol l^{-1}; SA, 1.0×10^{-4} mol l^{-1}; pH, 4.20.

while the Schiff base dye is negative owing to sulfonic group. Thus, the enhanced LS signals may result from the electrostatic interaction between the Schiff base dye and proteins.

Test on the effect of ionic strength on the LS intensity showed that the LS intensity of Schiff base dye-BSA was almost
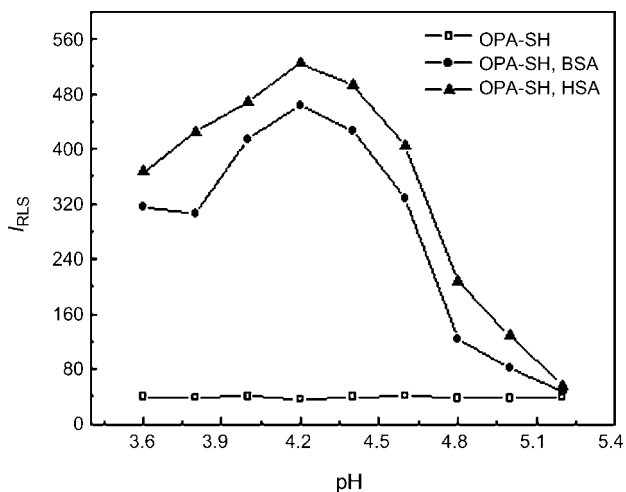
Fig. 5. pH dependence of the interaction between protein and Schiff base. Concentrations: OPA, 1.0×10^{-4} mol l^{-1}; sulfanilic acid, 1.0×10^{-4} mol l^{-1}; BSA, 2.0 mg l^{-1}; HSA, 2.0 mg l^{-1}.

unchangeable with the addition of increasing NaCl, indicating that electrostatic interaction may not be the only force for the combination of the interaction. As both of the Schiff base dye and the proteins contain hydrophobic phenyl, which would congregate with each other by the hydrophobic interaction in order to reduce the number of regulated H$_2$O molecules [32,33]. Thus, we suppose there might be hydrophobic interaction also between the interactions of Schiff base dye with BSA besides the electrostatic attraction.

3.4. Effect of foreign substance on the interaction

In order to test the specificity of the method, foreign substances including various ions, sugars, and surfactants have proved to exert effects on the interaction of Schiff base dye-BSA. As Table 2 shows, amino acids, Ca^{2+}, Ba^{2+}, Mg^{2+} and glucose can be present at high concentration levels. In contrast, those ions, such as Al^{3+}, Cu^{2+} and Cd^{2+}, which could have some combination with BSA or the Schiff base dye to form internal chelates, interstrand complexes or cross-links, can be allowed only at lower concentrates. Surfactants, such as Triton X-100, Tween 60, sodium dodecyl sulphonate (SDBS), cetyltrimethylammonium bromide (CTMAB), can be allowed at lower concentrations. The reason might be that the surfactants could compete with the interaction sites of Schiff base dye and BSA, and the non-ionic surfactant and anionic surfactant can be interacted with BSA by hydrophobic force.

3.5. Dynamic range of BSA and HSA detection

Under optimal conditions, the calibration graphs for BSA and HSA were constructed by increasing the BSA and HSA concentrations, respectively. It can be worked out that the LS intensity follows linear increase with the increasing protein concentration. Table 3 shows the dynamic range of the detection of BSA and HSA. To test the method, three samples of fresh human blood serum were used to interact with the Schiff base dye, and the results are identical to standard quantitative assay for the protein with CBB G250 assay. As Table 4 shows, our method is reliable.

4. Conclusion

In summary, we propose a method based on the formation of a new Schiff base dye, which could bind protein through electronic attraction and hydrophobic interaction with the results of enhanced light scattering signals at 344 nm. The new Schiff base dye plays an effective role as a protein probe in the determination of trace amount of proteins in the serum samples with LS signals. This method does not involve in the complicate operation procedure, and the easy preparation of a new Schiff base opens a window for synthesizing new light scattering reagent.

Acknowledgement

References

[1] X.W. Chen, J.H. Wang, Talanta 69 (2006) 681.
[2] G. Yao, K.A. Li, S.Y. Tong, Talanta 50 (1999) 585.
[3] R.F. Pasternack, C. Bustamante, P.J. Collings, A. Giannetto, E.J. Gibbs, J. Am. Chem. Soc. 115 (1993) 5393.
[4] R.F. Pasternack, P.J. Collings, Science 269 (1995) 935.
[5] R.F. Pasternack, K.F. Schaefer, P. Hambright, Inorg. Chem. 33 (1994) 2062.
[6] C.Z. Huang, K.A. Li, S.Y. Tong, Anal. Chem. 68 (1996) 2259.
[7] Z.P. Li, K.A. Li, S.Y. Tong, Talanta 55 (2001) 669.
[8] Z.G. Chen, W.F. Ding, F.L. Ren, J.B. Liu, Y.Z. Liang, Anal. Chim. Acta 550 (2005) 204.
[9] Z.G. Chen, W.F. Ding, F.L. Ren, Y.Z. Liang, J.B. Liu, Microchim. Acta 150 (2005) 34.
[10] Z.G. Chen, W.F. Ding, F.L. Ren, Y.L. Han, J.B. Liu, Anal. Lett. 38 (2005) 2301.
[11] R.P. Jia, L.J. Dong, Q.F. Li, X.G. Chen, Z.D. Hu, Talanta 57 (2002) 693.
[12] H. Zhong, J.J. Xu, H.Y. Chen, Talanta 67 (2005) 749.
[13] Z.G. Chen, T.Y. Zhang, F.L. Ren, W.F. Ding, Microchim. Acta 153 (2006) 65.
[14] Z.G. Chen, W.F. Ding, F.L. Ren, J.B. Liu, Y.L. Han, Can. J. Anal. Sci. Spect. 50 (2005) 54.
[15] Z.G. Chen, J.B. Liu, Y.L. Han, L. Zhu, Anal. Chim. Acta 570 (2006) 109.
[16] S.Z. Zhang, F.L. Zhao, K.A. Li, S.Y. Tong, Anal. Chim. Acta 431 (2001) 133.
[17] S.Z. Zhang, F.L. Zhao, K.A. Li, S.Y. Tong, Talanta 54 (2001) 333.
[18] C.Z. Huang, X.B. Pang, Y.F. Li, Y.J. Long, Talanta 69 (2006) 180.
[19] P. Feng, W.Q. Shu, C.Z. Huang, Y.F. Li, Anal. Chem. 73 (2001) 4307.
[20] S.P. Liu, Q. Liu, Z.F. Liu, M. Li, C.Z. Huang, Anal. Chim. Acta 379 (1999) 53.
[21] X.F. Long, S.P. Bi, H.Y. Ni, X.C. Tao, N. Gan, Anal. Chim. Acta 501 (2004) 89.
[22] A.H. Liang, N.N. Zhang, Acta Chim. Sin. 65 (2007) 1239.
[23] Z.G. Chen, J.B. Liu, Y.L. Han, Talanta 71 (2007) 1246.
[24] A.Y. Li, H.C. Zhao, L.P. Jin, Luminescence 22 (2007) 9.
[25] L.J. Dong, X.G. Chen, Z.D. Hu, Talanta 71 (2007) 555.
[26] F.X. Xie, Y.F. Liu, Chin. J. Med. Chem. 12 (2002) 229.
[27] Y.C. Guo, L.H. Guo, Y.L. Dang, Chem. Res. Appl. 16 (2004) 819.
[28] J. Zhang, Chem. Tech. Econ. 24 (2006) 46.
[29] R.Q. Brewster, W.E. Mcewen, Organic Chemistry, third ed., Prentice-Hall of India, New Delhi, 1971.
[30] S.A. Farokhi, S.T. Nandibewoor, Tetrahedron 59 (2003) 595.
[31] D.L. Ma, Y.R. Huang, J.P. Li, Y.L. Wang, W.T. Chen, H. Huang, W.R. Xing, W.M. Liu, Spectros. Spec. Anal. 20 (2000) 336.
[32] C. Tanford, The Hydrophobic Effect: Formation of Micelles and Biological Membranes, Wiley, New York, 1980.
[33] E. Creighton, Protein-Structures and Molecular Properties, Freeman, New York, 1993.

Development of a sensitive, rapid, biotin–streptavidin based chemiluminescent enzyme immunoassay for human thyroid stimulating hormone

Zhen Lin [a,b], Xu Wang [a,*], Zhen-Jia Li [c], Shi-Qi Ren [a,b], Guo-Nan Chen [b], Xi-Tang Ying [c], Jin-Ming Lin [a,*]

[a] *The Key Laboratory of Bioorganic Phosphorus Chemistry & Chemical Biology, Department of Chemistry, Tsinghua University, Beijing 100084, China*
[b] *Department of Chemistry, Fuzhou University, Fuzhou 350002, China*
[c] *Beijing Chemclin Biotech Co., Ltd., Beijing Academy of Science and Technology, Beijing 100094, China*

Abstract

A highly sensitive "two-site" chemiluminescent immunoassay specific for human thyroid stimulating hormone (TSH) was developed. The signal amplification was achieved via a biotin–streptavidin system (BSAS). The HRP–luminol–H_2O_2 chemiluminescent system with high sensitivity was chosen as the detection system. Biotinylated anti-TSH monoclonal antibody (MAb) and HRP-labeled streptavidin were first synthesized. Then the signal amplification was achieved through the interaction between the biotinylated anti-TSH MAb and the HRP–streptavidin conjugate. The light intensity developed was in proportion to the TSH present in the samples. The assay showed little cross-reactivity with three other glycoprotein hormones (human chorionic gonadotropin (HCG), luteinizing hormone (LH), follicle stimulating hormone (FSH)) due to the high specificity of the antibody. The working range for human thyroid stimulating hormone was 0.1–40 mU L^{-1}. Both the intra-assay and inter-assay coefficients of variation were less than 10% for the BSAS based chemiluminescent enzyme immunoassay (CLEIA). The proposed assay had a sensitivity of 0.01 mU L^{-1} which was 10-fold higher than the HRP–MAb conjugate based TSH immunoassay. Thus the higher sensitivity facilitated the clinical testing for thyroid states. The effects of several reaction parameters, such as incubation time, temperature, and reaction volume of the method, were also studied. This method has been successfully applied to the evaluation of TSH in human serum. Compared with the commercial enzyme chemiluminescent immunoassay, the correlation was satisfied.
© 2008 Elsevier B.V. All rights reserved.

Keywords: Human thyroid stimulating hormone; Biotin–streptavidin system; Signal amplification; Chemiluminescent immunoassay

1. Introduction

Thyroid gland function is regulated by the thyroid stimulating hormone (TSH), a hormone secreted by pituitary gland and with a molecular weight of approximately 28,000 Da. TSH secretion is in turn regulated by hypothalamic thyroliberin and by a feedback-inhibiting loop in which free hormones (triiodothyronine (T_3), thyroxine (T_4)) act at both pituitary and hypothalamic levels [1]. Sensitive TSH measurement for trace amount of TSH in human fluids is utilized as a "first line" thyroid test [2,3] and is in great need to distinguish hyperthyroid and primary hypothyroid states from euthyroidism, as well as to facilitate the clinical decision-making. Usually, elevated TSH levels indicate an inadequate thyroid hormone production, while suppressed levels suggest excessive unregulated production of hormone [4,5]. By virtue of its obvious importance for the clinical diagnosis, there has been an ongoing effort to develop analytical methods with high sensitivity for TSH in human body fluids.

The traditional analytical methods for TSH include radioimmunoassay (RIA), immunoradiometric assay (IRMA [3]), immunoenzymetric assay (IEMA) [6–9], immunochemiluminescent assay (ICMA) [10–14], time-resolved fluorescence immunoassay [15], bioluminescent immunoassay [16,17] as

well as some homogeneous particle based immunoassays [18]. RIA which used competitive mode required long incubation time and was relatively labor intensive. ^{125}I-labeled TSH was less stable than the ^{125}I-labeled immunoglobulin (IgG) [6,19]. The sensitivity of the method (0.5–1 mU L^{-1}) precluded accurate measurement of TSH in euthyroid subjects and in primary hyperthyroid. Although there was an improvement in the sensitivity of IRMA, there still needed a great effort to eliminate radioactive materials in the assay. ICMA, which used acridinium ester or luminol derivatives, has high sensitivity. However, a precise and automatic injection system is needed because of the flash-type chemiluminescent reaction. Expensive and complex instrumentations are necessary for time-resolved fluorescence immunoassay. Although some methods such as luminescent oxygen channeling assay (LOCT^{TM}) [20] and some immunoassays with novel chemiluminescent labels [21] have high sensitivity, it is still necessary to develop various methods with high sensitivity and simple operation, which are especially suitable for the daily clinical analysis.

In recent years, chemiluminescence enzyme immunoassay (CLEIA) has been widely used in the research of clinical diagnosis because of its advantages such as no radioactive pollution, acceptable sensitivity, rapid turnaround time, wide dynamic range, and glow-type chemiluminescent reaction. However, CLEIA reported for TSH were not so satisfied because of their limited sensitivity in the range of 0.04–4.5 mU L^{-1} [7–9]. Therefore, a methodology with sensitivity improvement for CLEIA to extend its clinical application was in urgent needed.

Avidin, a glycoprotein found in egg white with molecular weight of 67 kDa, contains four binding sites with an extraordinary affinity (dissociation constant: about 10^{-15} M) for the small molecule vitamin, biotin. Biotin could be easily covalently coupled to proteins, enabling a solid binding between the proteins and avidin. The biotin–streptavidin system (BSAS) has been widely used in immunohistochemistry [22,23] and immunoassay [24–28] because of its high specificity [29] and strong affinity [30]. Being attractive for researchers, excellent sensitivity could be achieved through signal amplification introduced by BSAS. In such a case, numbers of active biotins and enzymes could be conjugated to per antibody and per streptavidin, respectively, enabling more enzyme molecules catalyzing the substrate than the non-BSAS system [30,31]. Obviously, signal amplification could be implemented. Although the significance of BSAS in highly sensitive analysis, unfortunately, the combination of BSAS and CLEIA for the clinical determination of TSH was rarely reported.

In the present work, the combination of BSAS with the horseradish peroxidase (HRP)–luminol–H$_2$O$_2$ chemiluminescence system was performed to develop a highly sensitive CLEIA for TSH in human serum. Herein, biotinylated anti-TSH monoclonal antibody (MAb) and HRP-labeled streptavidin were first synthesized. Then a signal amplification system was achieved through the interaction between the biotinylated MAb and the HRP–streptavidin conjugate. The utility of BSAS increased the amount of enzyme linked to the immunocomplex. Thus the light intensity was amplified and the sensitivity was improved.

The BSAS based method showed a sensitivity of 0.01 mU L^{-1} versus 0.1 mU L^{-1} of the HRP–MAb conjugate based TSH immunoassay, meeting the demands of the clinical diagnosis. The assay for TSH was completed within 70 min (with 60-min immunoreaction and 5-min chemiluminescent incubation). The use of 96-well microplate also achieved the high throughput screening.

2. Experimental

2.1. Apparatus

Chemiluminescence microplate reader was purchased from Hamamatsu photons Technology Co. Ltd. (Beijing, China). Automatic plate washer was got from Beijing Tuopu Analytical Instruments Co. Ltd. (Type: DEM-β)(Beijing, China). 96-well microplates were from ShenZhen Jincanhua Industry Co. Ltd. (Shenzhen, China). Electronic balance (AUY-120) was purchased from Shimadzu Co. Ltd. (Japan). A model XW-80A vortex mixer (Jingke Industrial, Shanghai, China) was used for thorough mixing of substances. The incubation procedures were carried out using constant temperature incubator (HH.W21-Cr) (Chang'an scientific instrument factory, Beijing, China). Single-channel volume-adjustable micropipets were purchased from Dragon Medical & Instruments Co. Ltd. (Shanghai, China).

2.2. Chemicals and solutions

(+)-Biotin-N-hydroxysuccinimide ester (BNHSE), streptavidin and HRP were purchased from Sigma–Aldrich Co. (St. Louis, MO, USA). Anti-TSH MAbs were obtained from Fitzgerald Industries International, Inc. (Clone: M94205 and M94206, CA, USA). TSH antigen with standard grade was from Maine Biotechnology Services, Inc. (Portland, USA). Commercial chemiluminescence kit was purchased from Monobind, Inc. (CA, USA). Polyoxyethylenesorbitan monolaurate (Tween-20) was from Sigma Chemical Co. (MO, USA). Bovine serum albumin (BSA) and hydrolyzed gelatin were from Merck (Darmstadt, Germany). Luminol, chemiluminescent enhancer, and H$_2$O$_2$ were obtained from Monobind Inc. (CA, USA). EZ^{TM} biotin quantitation kit was purchased from Pierce (USA).

Highly purified distilled and deionized water was used throughout. The coating solution was 0.05 mol L^{-1} carbonate buffer (pH 9.5). The blocking solution was 0.01 mol L^{-1} phosphate buffer (pH 7.4) with 1% (w/v) BSA, 2.5% (w/v) sucrose, 0.5% (w/v) gelatin, and 0.1% (v/v) proclin-300. The washing solution was 0.01 mol L^{-1} phosphate buffer (pH 7.4) with 0.1% (v/v) Tween-20. The dilution solution for the biotinylated anti-TSH MAb and the HRP–streptavidin conjugate was 0.01 mol L^{-1} phosphate buffer (pH 7.4) with 0.1‰ (v/v) Tween-20, 1‰ (w/v) BSA, and 0.5% (v/v) mouse serum.

2.3. Procedure

2.3.1. Biotinylation of anti-TSH MAb

Anti-TSH MAb was first dialyzed against 0.05 mol L^{-1} carbonate buffer for 4 h. BNHSE was dissolved in dimethyl sul-

foxide, and then was added 20-, 40-, 50-, 100- and 150-fold molar excess against anti-TSH MAb in the dialysis solution. The solution was put still at room temperature for 2 h. After that, it was dialyzed against $0.01 \, mol \, L^{-1}$ phosphate buffer to remove unreacted materials. Finally, the conjugate was preserved in glycerol and stored at $4 \, °C$ for further use.

2.3.2. Calibrator preparation

The calibrators were prepared by spiking different amounts of TSH into TSH-free serum, and then were stored at $4 \, °C$. Then their concentrations were calibrated against national standards. TSH national standards (600 mU/ampoule) were bought from National Institute for The Control of Pharmaceutical and Biological Product (NICPBP). 600 mU of lyophilized TSH was dissolved in TSH-free serum and was diluted to serial concentrations. The concentrations of the calibrators were determined as the unknown samples by the use of national standards for five times. The average values were considered as the calibrators' true concentrations. The final concentrations of these calibrators were 0.1, 0.5, 2.5, 10, and $40 \, mU \, L^{-1}$, respectively. Meanwhile, the prepared calibrators were store at $37 \, °C$ to investigate the stability.

2.3.3. Immobilization of anti-TSH MAb on the microplate

Anti-TSH MAb was first diluted by the coating buffer. Then MAb solution of $110 \, \mu L$ was pipetted into each well on the plate. The plate was placed still for overnight at $4 \, °C$ to accomplish the immobilization. After that, $300 \, \mu L$ of the blocking buffer was added into each well and the plate was left at room temperature for 3 h in order to block the free sites on the plate. Subsequently, the solution in the well was aspirated and the plate was desiccated. Finally, the plate was vacuumized and stored for further use.

2.3.4. Synthesis of HRP–MAb conjugate and HRP–streptavidin conjugate

0.5 mg of HRP was dissolved in $500 \, \mu L$ of deionized water. Then freshly prepared $0.1 \, mol \, L^{-1}$ sodium periodate was added and the solution was stirred at room temperature for 30 min. After that, glycol $(0.16 \, mol \, L^{-1})$ solution was added to cease the oxidation reaction. Meanwhile, 0.5 mg of anti-TSH MAb was first dialyzed against $0.01 \, mol \, L^{-1}$ carbonate buffer (pH 9.5) for 4 h, and then was added into HRP solution mentioned above. The mixture was stirred for 2 h at room temperature. After that, $50 \, \mu L$ of freshly prepared sodium borohydride solution $(4 \, mg \, mL^{-1})$ was added and the mixture obtained was placed at $4 \, °C$ over a period of 2 h. The solution was then dialysed against phosphate buffer (pH 7.4) for 24 h to remove the unreacted materials. Finally, the conjugate was preserved in glycerol and stored at $4 \, °C$. The procedure for the synthesis of HRP–streptavidin conjugate was the same except substituting anti-TSH MAb with streptavidin.

2.3.5. Immunoassay procedures

The schematic illustration of the proposed BSAS CLEIA is presented in Fig. 1. Calibrators or samples with a volume
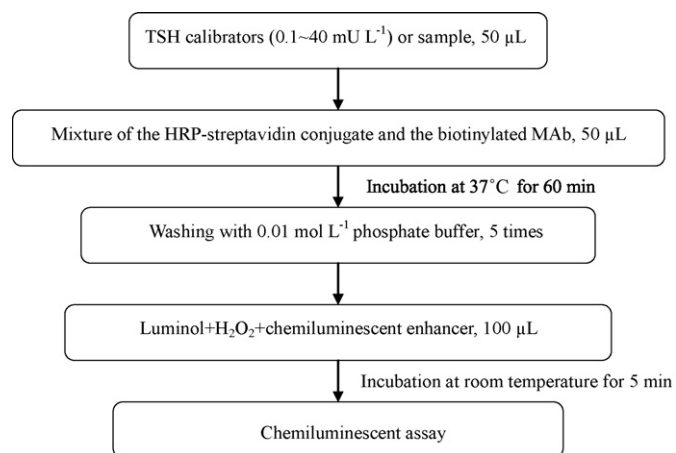

Fig. 1. Schematic illustration of the proposed BSAS CLEIA.

of $50 \, \mu L$ were added together with $50 \, \mu L$ of the mixture of the HRP–streptavidin conjugate and biotinylated MAb. The HRP–streptavidin conjugate and the biotinylated MAb were first mixed with the same volume. After incubation at $37 \, °C$ for 60 min, the microplate was washed by washing solution to separate the free compounds from the bound immunocomplex. $100 \, \mu L$ chemiluminescent substrate was pipetted into each well. After 5 min incubation at room temperature, the light intensity was measured. The working scheme of the HRP–MAb conjugate based CLEIA was the same except that HRP-labeled anti-TSH MAb was used instead of mixture of the HRP–streptavidin conjugate and the biotinylated MAb.

2.3.6. Procedure for quantitation of labeling ratio of moles of biotinylated MAb

The procedure was performed according to the kit introduction. The reagent was first equilibrated to room temperature. Solution containing the biotinylated MAb was added into the mixture of 4-hydroxyazobenzene-2-carboxylic acid (HABA) and avidin. Both the absorbance of the mixture of HABA/avidin and the mixture added with biotinylated MAb was measured at 500 nm. Then calculation was performed based on the kit introduction.

2.4. Data analysis

The chemiluminescence intensity was expressed by the RLU (relative light unit). Standard curves were got by plotting the logarithm of chemiluminescence intensity against the logarithm of corresponding sample concentration.

3. Results and discussion

3.1. Principle of the BSAS based CLEIA

The proposed method was a noncompetitive assay that used an excess of anti-TSH MAb coated on the solid phase. The principle of the BSAS based CLEIA is presented in Fig. 2. Biotin was first covalently coupled to the anti-TSH MAb. HRP-labeled streptavidin was synthesized too. After a sandwiched
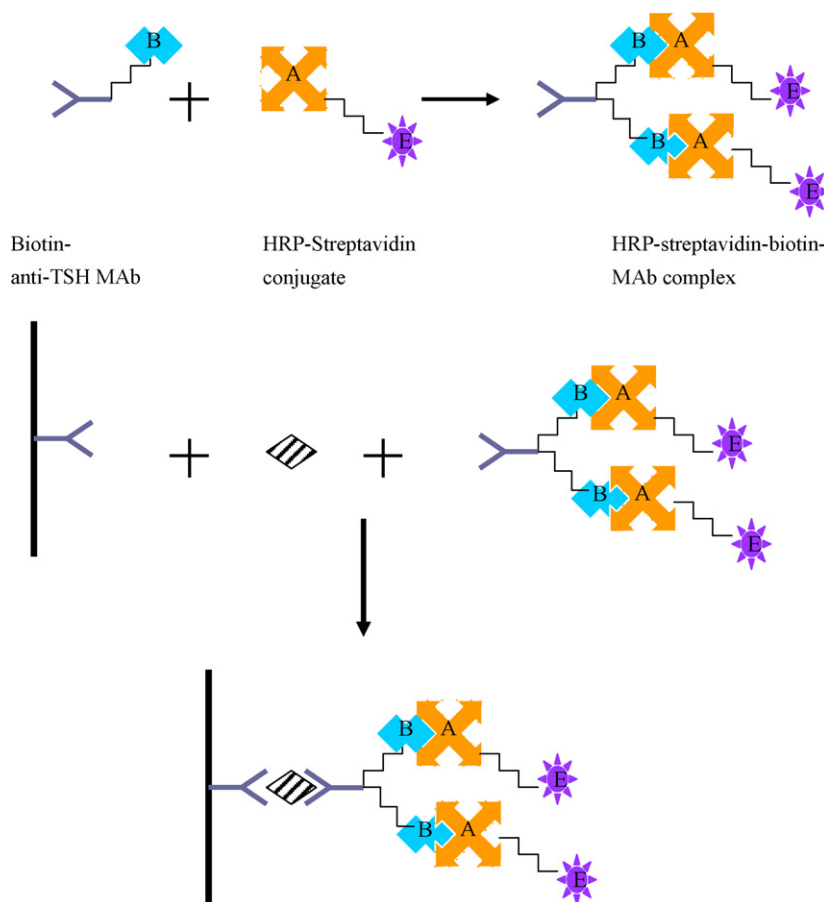
Fig. 2. The principle of the noncompetitive BSAS based CLEIA for TSH.

immunocomplex was formed among the capture anti-TSH MAb, TSH antigen, the biotinylated anti-TSH MAb, and the HRP–streptavidin conjugate, numbers of active biotins and enzymes were conjugated to per antibody and per streptavidin, respectively, enabling more enzyme molecules catalyzing the substrate to emit photons [30,31]. Thus sensitivity improvement was obtained through signal amplification. Then the unbound reagents were removed by a washing step. Subsequently, substrate was added and the light intensity was measured. It was found that the light intensity was in proportional to the TSH concentrations. The principle of the HRP–MAb conjugate based CLEIA was the same as the described BSAS based CLEIA except that the sandwiched immunocomplex was formed among the capture anti-TSH MAb, TSH antigen and HRP-labeled anti-TSH MAb.

3.2. Parameters affecting the sensitivity of the proposed BSAS CLEIA

The sensitivity of an immunoassay depends on both method itself and a series of experimental parameters, which include the kinetics of the immunoreaction and chemiluminescent reaction, the preparation and the concentration of immunoreagents, the condition of solid phase as well as some experimental procedures. These parameters were discussed as following.

3.2.1. The kinetics of immunoreaction and chemiluminescent reaction

The Effect of immunoreaction and chemiluminescent reaction time were studied to improve the immunoassay sensitivity. Taking both CL intensity and signal to noise ratio into consideration, the immunoreaction reached an equilibrium when the incubation time was longer than 60 min. RLU leveled off thereafter. Hence 60 min was chosen.

HRP has been widely used as the labeled enzyme in CLEIA with the development of substrates (luminol, iso-luminol) and series of chemiluminescent enhancers [32,33]. The overall kinetic of light emission was studied in the experiment. RLU reached maximum when the incubation time was 5 min. Therefore, incubation time of 5 min was selected.

3.2.2. Effect of ratio of biotin to anti-TSH MAb on the antibody biotinylation process

It is known that excess biotinylation may inactivate a biological molecule and meanwhile, insufficient biotinylation may lead to weak interaction and therefore, low amplification effect. Hence, the effect of various biotinylation on the conjugate activity was studied. The results showed that using the biotin with an amount of 150- or 100-fold molar excess against MAb inactivated the biological activity of the antibody obviously. Thus biotin with an amount of 40-fold molar excess against MAb

Table 1
Effect of different blocking conditions[a]

| | Blocking reagent | | | |
| | Phosphate buffer spiked with BSA and gelatin | | | Phosphate buffer spiked with BSA |
Blocking condition	4 °C (overnight)	37 °C (1 h)	Room temperature (3 h)	Room temperature (3 h)
$RLU_{(S0)}$	836	1501	723	2700
$RLU_{(S5)}/RLU_{(S0)}$	677	320	768	232

[a] All the calibrators were analyzed using 2-well replicated during three runs.

concentration was selected, and was used in the subsequent condition optimization testing.

3.2.3. Effect of solid immobilization conditions

The sensitivity of an assay depends on the solid phase condition to a great extent. Ideal solid phase should be consistent, stable and has low background signal.

The buffers frequently used for coating are $0.05 \, mol \, L^{-1}$ carbonate buffer (pH 9.6), $0.01 \, mol \, L^{-1}$ phosphate (pH 7.4), and $0.01 \, mol \, L^{-1}$ citric buffer (pH 4.8) [34]. MAb was diluted with these buffers for immobilization to investigate the effect of coating buffer. When $0.05 \, mol \, L^{-1}$ carbonate buffer was used, RLU was the highest among the three aforementioned coating buffers with the same MAb concentration, exhibiting maximum amount of MAb immobilization.

BSA and hydrolyzed gelatin were commonly used as blocking reagents to block the free sites on a solid phase. Two kinds of blocking reagents (one was mixture of BSA and gelatin, the other was BSA only) were used as the blocking buffer. The blocking buffer without gelatin had a higher background signal with RLU of 2700, resulting in worse sensitivity for the assay. Hence, phosphate buffer spiked with BSA and gelatin was chosen as the suitable blocking solution. The effect of coating and blocking time and temperature on the immunoassay was also studied. Finally, microplate was coated at 4 °C overnight, blocked at 4 °C overnight or 3 h at room temperature with phosphate buffer spiked with BSA and gelatin (Table 1).

3.2.4. Effect of biotinylated MAb concentration and dilution level of HRP–streptavidin conjugate

The binding of HRP to MAb is through the interaction between streptavidin and biotin. Streptavidin possesses four binding sites per molecular for biotin. So the relative molar ratio of the HRP–streptavidin conjugate to biotinylated anti-TSH MAb is of great importance. Excessive HRP–streptavidin conjugate or biotinylated anti-TSH MAb may lead to non-specific absorption, deteriorating the assay sensitivity.

Concentrations of biotinylated MAb and dilution levels of HRP–streptavidin conjugate were determined using the calibrators. The signal to background ratio was a function of both biotinylated MAb concentration and dilution levels of HRP–streptavidin conjugate. As shown in Fig. 3A, RLU increased with the concentration of biotinylated MAb. When the concentration of biotinylated MAb was $1.25 \, \mu g \, mL^{-1}$, RLU reached its peak value and the signal to background ratio also stayed a plateau. Therefore, the following experiment was executed with concentration of $1.25 \, \mu g \, mL^{-1}$ for biotinylated MAb.

As can be seen from Fig. 3B, the dilution level of 1:3000 for HRP–streptavidin conjugate was chosen as taking both the signal to background ratio and RLU into consideration.

3.2.5. Effect of heterophile antibodies

The human anti-mouse antibodies, which belong to heterophile antibody, may frequently bind to Fc fragments of murine IgGs, resulting in abnormal TSH concentration [35]. Herein, mouse serum was added into the antibody dilution solution and enzyme solution to "neutralize" anti-mouse antibodies. The effect of the mouse sera with concentrations from 0.1 to 0.5% (V/V) was investigated. In the whole tested range, the linear coefficient showed little changes and all were higher than 0.9985. When the mouse serum concentration was higher than
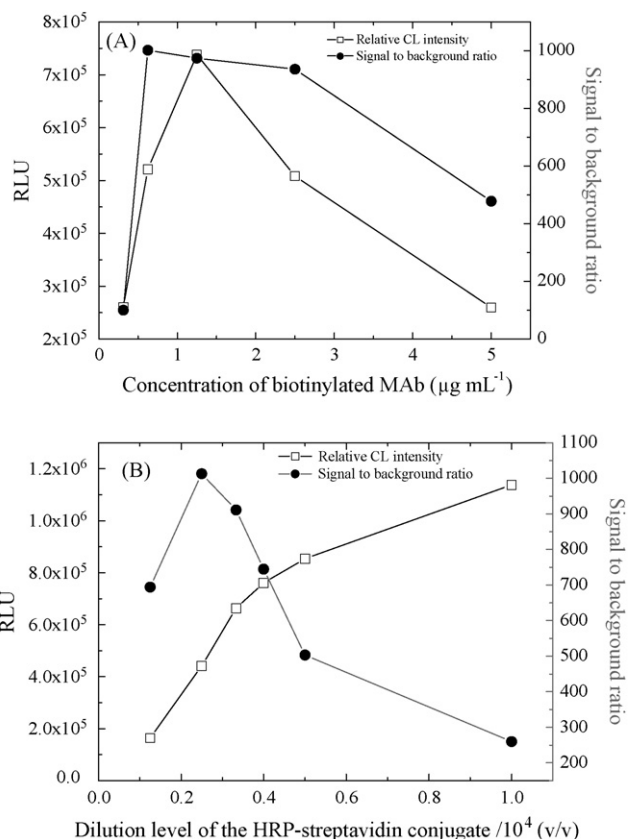

Fig. 3. Optimization of the dilution level of the biotinylated MAb and the HRP–streptavidin conjugate. The signal to background ratio is the chemiluminescent intensity ratio obtained between the two calibrators with the TSH concentration of 40 and $0 \, mU \, L^{-1}$. (A) Optimization of the biotinylated MAb concentration; (B) Optimization of the dilution level of the HRP–streptavidin conjugate. The immunoreaction time was 1 h.
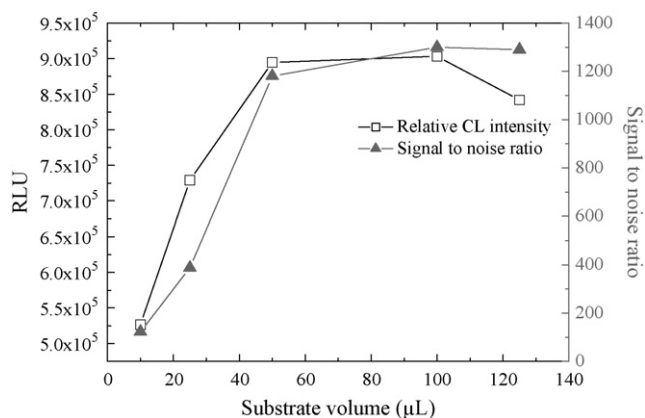
Fig. 4. Effect of the substrate volume on the chemiluminescent immunoassay.

Fig. 5. Linear dilution profiles.

0.5%, RLU decreased. Hence, the subsequent experiment was performed with 0.5% mouse serum.

3.2.6. Effect of substrate volume

It was reported that the substrate sensitivity referred to the signal intensity produced by a unit of enzyme activity [36]. The substrate volume was directly related to the light intensity as well as the sensitivity of an assay. Therefore, the volumes of substrate were studied from 10 to 150 μL. As can be seen from Fig. 4, RLU increased with increasing substrate volume up to 50 μL and leveled off thereafter. The value of the signal to background ratio presented the highest at the substrate volume of 100 μL. Therefore, substrate volume of 100 μL was selected.

3.3. Method evaluation

3.3.1. Standard curve and stability of the calibrators

Standard curve obtained was $y = 3.68 + 1.42x$, with linear range of 0.1–40 mU L^{-1} and correlation coefficient of 0.9984. The calibrators were stored at 37 °C for 3 and 6 days and the light intensity was measured. The light intensity of these calibrators after the investigation showed little change after 3 or 6 days, indicating enough stability of the calibrators.

3.3.2. Sample dilution

Serial dilution of high TSH sample with human serum yielded linear dilution profiles. It was an important evidence to check the major interference factors and the matrix differences between the standard matrix and human samples. The measured and expected values were subjected to linear functional analysis (Fig. 5). The correlation coefficient was 0.9992, proving that the dilution characteristic was satisfactory down to the assay's detection limit.

3.3.3. Specificity

Cross-reactivity is of special importance with respect to postmenopausal women and some outpatients who receive chemical treatment and have an abnormal concentration of pituitary glycoprotein hormones. 500 U L^{-1} of human chorionic gonadotropin (HCG) gave TSH reading of 0 mU L^{-1}. Furthermore, pregnant women have TSH value in the normal range with the proposed
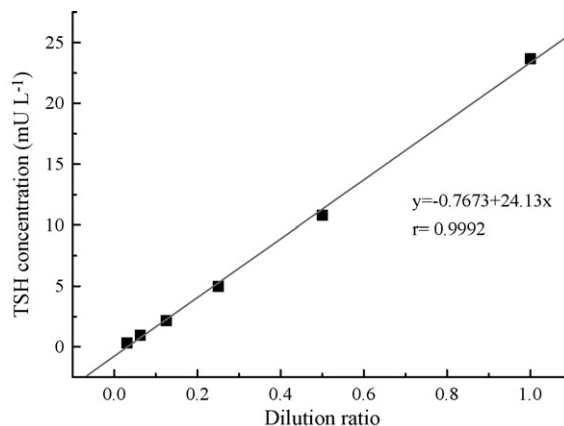
method. 100 U L^{-1} of follicle stimulating hormone (FSH) and 200 mU L^{-1} of luteinizing hormone (LH) gave TSH reading of 0.05 and 0.0 mU L^{-1}, respectively. These showed the satisfactory specificity of the developed method due to the use of paired monoclonal antibodies [37].

3.4. Comparison between BSAS based CLEIA and HRP–MAb based CLEIA

3.4.1. RLU comparison

Avidin has an extraordinary affinity for biotin. The interaction was rapid and was unaffected by most extreme pH and some organic solvent. Hence, HRP–streptavidin can bind tightly with biotin-labeled antibody. The EZ^{TM} biotin quantitation kit was used to quantitate biotinylation degree. The result showed that the average biotinylation degree was 3.12, meaning that biotinylated antibody bound with several number of HRP–streptavidin. The more the HRP linked to per antibody, the higher the CL intensity was.

RLU of the BSAS based CLEIA and HRP–MAb based CLEIA was compared using the calibrators (0.5, 2.5, 10, and 40 mU L^{-1}) and signal amplification was observed by BSAS based CLEIA for all these tested calibrators (Fig. 6).

3.4.2. Sensitivity

Sensitivity is diagnostically useful in hyperthyroidism and hypothalamic or pituitary hypothyroidism. Sensitivity is also an important factor that affects the reproducibility of an assay, especially for the samples with low TSH levels. Sensitivity was constructed with multiple measurements of zero point of the standard curve and was defined as RLU signals for zero point adding twice the standard deviation of the point [38] (LOD = S_0 + 2S.D.). Sensitivity calculated from the experimental result was 0.01 mU L^{-1} which was 10-fold higher than the HRP-labeled MAb based TSH measurement system (0.1 mU L^{-1}).

The sensitivity of the method was also compared with other reported CLEIA using HRP or alkaline phosphatase (ALP), which was listed in Table 2. Higher sensitivity was achieved by the proposed method, suggesting the advantages of BSAS amplification effect.
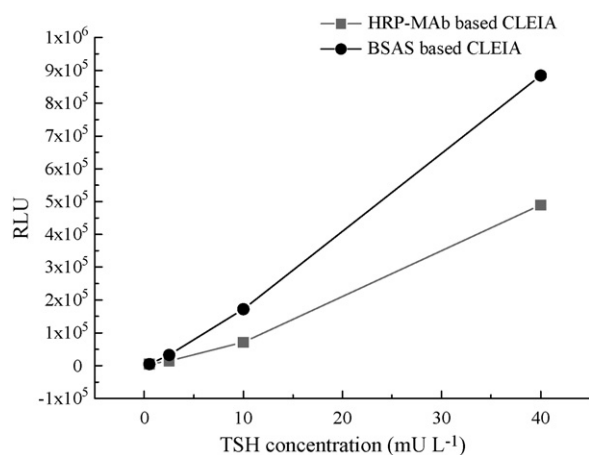
Fig. 6. Light comparison between the BSAS based CLEIA and the HRP–MAb based CLEIA. The dilution levels of the MAb immobilized on the solid phase for the two methods were 1:1000.

Table 2
Sensitivity comparison

Label	Sensitivity (mU L^{-1})	References
ALP	4.50	[7]
HRP	0.06	[8]
HRP	0.04	[9]
HRP	0.01	The proposed method

ficients of variation for HRP–MAb based CLEIA were also below 10%.

3.4.4. Recovery

Recovery test is a useful approach to check the accuracy of a method. Human serum pools were spiked with different amounts of TSH and the recoveries were measured (Table 4). The recoveries were in the range of 98.3–102 and 101–114% for the BSAS based CLEIA and the HRP–MAb based CLEIA, respectively.

3.5. Serum sample analysis

The concentration of TSH in 40 serum samples was determined with the developed BSAS based CLEIA and compared with that obtained by a commercial chemiluminescent kit. Good correlation was obtained with a coefficient of 0.9842 (Fig. 7). Several patients samples with very low TSH concentrations that could not be detected by the HRP–MAb based CLEIA showed detectable values by the proposed method, proving that the

3.4.3. Precision

Samples with various TSH concentrations were prepared by spiking different amounts of TSH to normal human serum pools. A series of samples were measured eight times within one run to obtain the intra-assay precision. Inter-assay precision was calculated by comparing value for a series of samples included in three assay runs. The results were presented in Table 3. The intra-assay coefficients of variation for the BSAS based CLEIA were in all cases lower than 4.3% and that of inter-assay were below 10%. Meanwhile, the intra-assay and inter-assay coef-

Table 3
Intra-assay and inter-assay precision

	Sample	Mean (mU L^{-1})	Standard deviation	C.V. (%)
Intra-assay ($n = 8$)				
BSAS based CLEIA	1	0.47	0.02	4.3
	2	2.57	0.05	2.0
	3	9.94	0.14	1.4
HRP–MAb based CLEIA	1	0.54	0.03	5.6
	2	2.24	0.13	5.8
	3	9.23	0.21	2.2
Inter-assay ($n = 24$)				
BSAS based CLEIA	1	0.45	0.04	8.9
	2	2.70	0.17	6.3
	3	10.1	0.23	2.3
HRP–MAb based CLEIA	1	0.51	0.05	9.8
	2	2.24	0.14	6.3
	3	9.46	0.32	3.4

Table 4
Recovery of the BSAS based CLEIA and the HRP–MAb based CLEIA

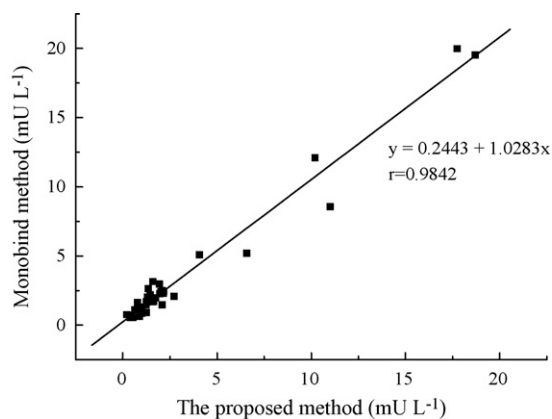|	Spiked TSH amount (mU L^{-1})	Recovery (%)			Average recovery (%)
BSAS based CLEIA	10.7	111	93.4	98.1	101
	5.40	105	104	96.2	102
	1.10	95.0	110	90.0	98.3
HRP–MAb based CLEIA	20.1	103	102	99.1	101
	13.1	104	102	113	106
	2.10	115	110	116	114

Fig. 7. Correlation between the proposed method and Monobind commercial kit.

developed method was able to distinguish the hyperthyroidism from euthyroid samples, which were suitable for the daily clinical practice.

4. Conclusions

The objective of the present work is to develop a highly sensitive CLEIA based on biotin–streptavidin system for TSH. The proposed method comprises MAb immobilized solid phase, the biotinylated MAb, the HRP–streptavidin conjugate and a CL detection system. Signal amplification was accomplished by introducing the interaction between biotinylated MAb and HRP–streptavidin conjugate. Features make this assay be suitable for clinical practice, including high sensitivity, rapid turnaround time, simple operation protocol, and high throughput screening. The sensitivity of the proposed method was 10-fold higher than the HRP–MAb based CLEIA. The intra-assay and inter-assay coefficients of variation were below 4.3 and 10%, respectively. The accuracy examination gave recoveries ranged from 98.3 to 102%. The correlation study between the proposed method and commercial kit was satisfied. The proposed method has exhibited great potentiality in the daily clinical practice and could act as a good tool for TSH analysis.

References

 [1] D.A. Fisher, Clin. Chem. 42 (1996) 135.
 [2] A.E. Pekary, J.M. Hershman, Clin. Chem. 32 (1986) 1009.
 [3] M.R. Hopton, J.S. Harrop, Clin. Chem. 32 (1986) 691.
 [4] C.M. Dayan, Lancet 357 (2001) 619.
 [5] L.E. Braverman, Clin. Chem. 42 (1996) 174.
 [6] Y.C. Tseng, K.D. Burman, J.R. Baker Jr., L. Wartofsky, Clin. Chem. 31 (1985) 1131.
 [7] I. Bronstein, J.C. Voyta, G.H. Thorpe, L.J. Kricka, G. Armstrong, Clin. Chem. 37 (1989) 1441.
 [8] M.C. Sheppard, E.G. Blac, Clin. Chem. 33 (1987) 179.
 [9] A.J. Pamham, I.F. Tarbit, Clin. Chem. 33 (1987) 1421.
[10] M. Roden, P. Nowotny, U. Hollenstein, B. Schneider, H. Vierhapper, W. Waldhäusl, Clin. Chem. 39 (1993) 544.
[11] D.J. Berty, P.M.S. Clark, C.P. Price, Clin. Chem. 34 (1988) 2087.
[12] M.P. Bounaud, J.Y. Bounaud, M.H. Bouln-Plneau, L. Orget, F. Begon, Clin. Chem. 33 (1987) 2096.
[13] D.S. Ross, G.H. Daniels, D. Gouveia, J. Clin. Endocrinol. Metab. 71 (1990) 764.
[14] C.A. Spencer, J.S. LoPresti, A. Patel, R.B. Guttler, A. Eigen, D. Shen, D. Gray, J.T. Nicoloff, J. Clin. Endocrinol. Metab. 70 (1990) 453.
[15] A. Papanastasion-Diamandi, T.K. Christopoulos, E.P. Diamandis, Clin. Chem. 38 (1992) 545.
[16] L.A. Frank, A.I. Petunin, E.S. Vysotski, Anal. Biochem. 325 (2004) 240.
[17] D.S. Sgoutas, T.E. Tuten, A.A. Verras, A. Love, E.G. Barton, Clin. Chem. 41 (1995) 1637.
[18] T.A. Wilkins, G. Brouwers, J.C. Mareschal, C.L. Cambiaso, Clin. Chem. 34 (1988) 1749.
[19] A.E. Pekary, J.M. Hershman, Clin. Chem. 30 (1984) 1213.
[20] E.F. Ullman, H. Kirakossian, A.C. Switchenko, J. Ishkanian, M. Ericson, C.A. Wartchow, M. Pirio, J. Pease, B.R. Irvin, S. Singh, R. Singh, R. Patel, A. Dafforn, D. Davalian, C. Skold, N. Kurn, D.B. Wanger, Clin. Chem. 42 (1996) 1518.
[21] I. Weeks, M. Sturgess, K. Siddle, M.K. Jones, J.S. Woodhead, Clin. Endocrinol. 20 (1984) 489.
[22] J.L. Guesdon, T. Ternynck, S. Avrames, J. Histochem. Cytochem. 27 (1979) 1131.
[23] G.C. Moriarty, G. Unabia, J. Histochem. Cytochem. 30 (1982) 713.
[24] R.B. Zhang, Y. Huang, C.P. Li, Y.B. Cui, World J. Gastroenterol. 10 (2004) 1369.
[25] A. Yu, T.T. Geng, Q. Fu, C. Chen, Y. Cui, J. Magn. Magn. Mater. 311 (2007) 421.
[26] L.V. Ding, Z.E. Selvanayagam, P. Gopalakrishnakone, K.H. Eng, J. Immunol. Methods 260 (2002) 125.
[27] J.T. He, Z.H. Shi, J. Yan, M.P. Zhao, Z.Q. Guo, W.B. Chang, Talanta 65 (2005) 621.
[28] Y. Matsumoto, H. Kuramitz, S. Itoh, S. Tanaka, Anal. Sci. 21 (2005) 319.
[29] X.C. Zhang, Y.R. Lu, Mod. Prev. Med. 28 (2001) 485.
[30] E.P. Diamandis, T.K. Christopoulos, Clin. Chem. 37 (1991) 625.
[31] E.P. Diamandis, Clin. Chem. 35 (1989) 491.
[32] G.H.G. Thorpe, L.J. Kricka, S.B. Moseley, T.P. Whitehead, Clin. Chem. 31 (1985) 1335.
[33] Y. Dotsikas, Y.L. Loukas, Talanta 71 (2007) 906.
[34] L.X. Zhao, J.-M. Lin, Z.J. Li, Anal. Chim. Acta 118 (2005) 177.
[35] N. Despres, A.M. Grant, Clin. Chem. 44 (1998) 440.
[36] W. Dungchai, W. Siangproh, J.-M. Lin, O. Chailapakul, S. Lin, X.T. Ying, Anal. Bioanal. Chem. 387 (2007) 1965.
[37] Y. Iijima, Y. Endo, N. Hata, H. Fujita, M. Unoki, K. Miyal, Clin. Chem. 34 (1988) 98.
[38] K.V. Waite, G.F. Maberly, G. Ma, C.J. Eastman, Clin. Chem. 32 (1986) 1966.

ELSEVIER

Talanta

Classification of extra virgin olive oils according to the protected designation of origin, olive variety and geographical origin

Silvia López-Feria [a], Soledad Cárdenas [a], José Antonio García-Mesa [b], Miguel Valcárcel [a],*

[a] *Department of Analytical Chemistry, Marie Curie Building (Annex), Campus de Rabanales, University of Córdoba, E-14071, Spain*
[b] *CIFA Venta del Llano, IFAPA, Ctra. Bailén-Motril km 18.5 Mengíbar, E-23620 Jaén, Spain*

Abstract

A headspace-mass spectrometry (HS-MS) coupling designed for the sensory characterization and classification of extra virgin olive oil on the basis of its protected designation of origin, olive variety and geographical origin is reported. The procedure involves the headspace generation and the direct injection of the homogenized gaseous phase into a mass spectrometer through a transfer line. The results obtained were chemometrically treated to achieve the best model capable of discriminating between the different olive oil categories. For this purpose, several procedures for variables selection, data pretreatments and unsupervised techniques were evaluated. In addition, K-nearest neighbor and soft independent modeling of class analogy algorithms were employed to the classification models building. Taking into account the prediction results obtained (ca. 87% of samples correctly classified and a specificity of ca. 97%), it can be concluded than the HS-MS coupling is, with an adequate chemometric treatment, an appropriate technique for routine control.
© 2007 Elsevier B.V. All rights reserved.

Keywords: Headspace-mass spectrometry (HS-MS); Extra virgin olive oil; Protected designation of origin (PDO); Geographic origin; Olive variety; Classification; Chemometrics

1. Introduction

Virgin olive oil is a foodstuff extracted from the fruit of *Olea europea* L. and, therefore, a valuable product from the Mediterranean basin. The countries of this geographic area generate 98% of the world production of olive oil. Within the European Union (EU), Spain, Italy and Greece supply more than 97% of the EU production [1]. The olive oil extraction system includes only mechanical methods directed to preserve its characteristic properties responsible for its nutritional, health benefits and pleasant flavour. Regarding the wholesome advantages of olive oil consumption, it owns a high antioxidant capability and reduces the risk of suffering from cardiovascular diseases and contracting breast or colon cancers, among others [2,3]. Concerning sensorial properties, the odour, taste and colour are the principal parameters, together with physical–chemical ones, for the evaluation of the sensory quality of this product. It permits the classification of the olive oils in two principal types, extra virgin

olive oil (EVOO) and lampante virgin olive oil (LVOO). The origin of these characteristics is, especially in the case of smell and taste, the presence of volatile chemical compounds in the olive oil, which differs according to the fruit variety, grown region, the influence of environmental, agronomic and technological factors, etc. These differences are the "added-value" offered by the protected designation of origin (PDO). Under this labelling, it is designated a product whose properties are due to the origin region and its characteristics and they are regulated by the EU [4–6]. This peculiarity not shared by other products of the same area ends in a higher price in the market. As a consequence, there is an obvious temptation of adulteration with cheaper oil to obtain a greater production. Therefore, a perfect knowledge of the physical and chemical characteristics of the oil as well as a proper definition of cultivar names is required, which acquires a particular relevance for products awarded the PDO status.

Several researches have tried to correlate the chemical composition of olive oil to fruit variety, geographic origin, denomination of origin, year of harvest or different qualities. Countless techniques of different complexity with numerous chemometric treatments have been employed for this purpose with promising results. The NMR profile of olive oil has been

---

* Corresponding author. Tel.: +34 957 218 616; fax: +34 957 218 616.
  E-mail address: qa1meobj@uco.es (M. Valcárcel).

used for differentiating Italian cultivars according to their geographic origin and for discriminating those from other olive oils of Mediterranean areas [7,8]. On the other hand, numerous physical and chemical parameters have been used for classifying diverse olive oil varieties corresponding to different geographic locations, viz. the fatty acid and triacyglycerol composition, acidity, UV absorption characteristics, sterols, oxidative stability, etc., some of which include the evaluation of sensory parameters by means of the panel test. Several PDOs have been included in these studies [9–16]. Other strategies try to find the way for the authentication of olive oils by studying the volatile organic components of the samples. In this sense, a great number of researches use the GC-MS coupling, mainly with a previous step of pre-concentration/extraction of the target analytes with SPME technique [17–20] for identifying the differences among the volatile composition of olive oils from several geographic origins, varieties, grown under different environmental conditions and PDOs. Finally, electronic noses based on conducting polymers have been employed with the object of reducing the analysis cost and time [21], even thought this device presents as disadvantage the instability of the electronic sensors [22,23]. To solve the previous shortcoming, the direct coupling headspace (HS) autosampler-mass spectrometric detector can be employed for differentiating fruit sources and geographic origin of olive oil [24,25]. In this way, our research group recently reported the applicability of HS-MS technique for rapid classification of virgin olive oils based on their quality [26,27] and detection of adulteration with other plant oils [28]. The present work is focused on the development of a reliable analytical method that ensures the genuineness of the product in compliance with the label. For this purpose, the headspace-mass spectrometry methodology was used for simple differentiation among virgin olive oils coming from several Spanish Protected Designations of Origin, at the same time that their fruit varieties and geographic area.

2. Experimental

2.1. Apparatus

The instrumental setup consists of a MPS2 headspace autosampler (Gerstel, Mülhein an der Ruhr, Germany) and a Hewlett-Packard HP5973 (Agilent, Palo Alto, CA) mass spectrometer. The autosampler is composed of a 32-space tray for headspace vials, an oven for sample heating/headspace generation and a robotic arm fitted with an automated injection system, which contains a 2.5 mL gastight HS-syringe whose temperature is controlled by the autosampler.

In this study, the syringe introduced a volume of 2.5 mL of the homogenized headspace from the vial into the injector (200 °C) of a chromatographic oven where the transfer line (5 m × 0.25 mm i.d. fused silica capillary) was placed. Helium (5.0 grade purity, Air Liquide, Seville, Spain), regulated by a digital pressure and flow controller, was used as carrier gas (1.4 mL/min). The quadrupole mass spectrometer detector operated in full scan mode and an electron impact ionization of 70 eV was used for analytes fragmentation. The transfer line, MS

source and quadrupole temperatures were maintained at 170, 230 and 150 °C, respectively. Total ion current chromatograms were acquired and processed using G1701BA Standalone Data Analysis software (Agilent Technologies) on a Pentium 4 computer that also controlled the whole system.

10-mL clear glass bottom round vials for headspace analysis with 20-mm polytetrafluoroethylene/silicone septa caps and a magnetic crimp cap (Supelco, Madrid, Spain) were also employed.

2.2. Extra virgin olive oil samples

A total of 102 extra virgin olive oil samples from six different geographical areas, three protected designations of origin and eight fruit varieties were analyzed. In particular, 26 samples corresponded to the PDO Baena (Córdoba, Spain) containing Picuda, Hojiblanca, Picual and Lechín varieties; 21 samples made up the PDO Priego de Córdoba (Córdoba, Spain) including Picuda, Hojiblanca and Picual varieties; 8 samples made up the PDO Montes de Granada (Granada, Spain) containing Picual, Lucio and Loaime varieties; and 47 samples corresponded to monovarietal olive oils; Arbequina (from two Spanish geographic origins, Málaga and Lleida), Picual and Frantoio. All samples come from the present harvest and they were obtained from specialized retailers. Once received in the laboratory, they were stored in amber bottles without headspace at room temperature until analysis. All categories are shown in Table 1. Regarding the PDOs varieties, the principal ones are listed in the third column and the presence of secondary varieties depends on the specific origin, mark, harvest, etc. As can be seen in the table, the virgin olive oil profiles resulting of the analysis process were divided into three subgroup; training, external validation and prediction sets, composed of five, three and five replicates, respectively. In the case of the prediction set, the samples analyzed were selected on the basis of the better accessibility.

2.3. Analytical method

The instrumental conditions used for the characterization of virgin olive oil samples were selected on the basis of the optimum values for headspace generation and the procedure was as follows. Aliquots of 5.0 g of extra virgin olive oil were placed into 10 mL vials hermetically sealed with a silicone septum/magnetic cap. The robotic arm placed them in the oven under controlled stirring for 30 min at 70 °C for headspace generation. On a subsequent step, the coupled HS-syringe took 2.5 mL of the volatile fraction which was transferred to the injector, maintained at 200 °C. After that, an helium stream carried the volatiles through the transfer line, heated at 170 °C, to the mass spectrometer without chromatographic separation and the whole of the components of the volatile fraction arrived the detector at the same time. This global signal was obtained in ca. 3 min and it can be considered as the spectral fingerprint of the sample and, therefore, used for classification purposes. The scan range chosen for this task was from m/z 41 to 180 (m/z 44 was not selected as its main contribution comes from atmospheric CO_2), which provided the complete volatile profile of the sample. Despite the

Table 1
Characteristics of the extra virgin olive oils used in this work

Sample	PDO	Variety	Geographic origin	Data set 1		Data set 2[a] (prediction set)
				Training set	EV set	
1	Baena1	Picuda	Córdoba (Baena, Doña Mencía, Nueva Carteya, Zuheros, Albendín, Castro del Río, Cabra)	5	3	5
2	Baena2	Picuda, Hojiblanca, Picual, Lechín	Córdoba (Baena, Doña Mencía, Nueva Carteya, Zuheros, Albendín, Castro del Río, Cabra)	5	3	5
3	Montes de Granada	Picual, Lucio, Loaime	Granada (Iznalloz)	5	3	–[b]
4	Priego de Córdoba1	Picuda, Hojiblanca, Picual	Córdoba (Priego, Carcabuey, Fuente Tójar, Almedinilla)	5	3	5
5	Priego de Córdoba2	Picuda, Hojiblanca, Picual	Córdoba (Priego, Carcabuey, Fuente Tójar, Almedinilla)	5	3	–[b]
6	None	Arbequina	Málaga (Antequera)	5	3	5
7	None	Arbequina	Lleida	5	3	5
8	None	Picual	Jaén (Úbeda)	5	3	5
9	None	Frantoio	Italy	5	3	–[b]

[a] The samples corresponding to the data set 2 were acquired and analyzed 1 month later than those corresponding to the data set 1.

[b] Class not selected to the prediction set. PDO, protected designation of origin. EV, external validation.

volatile generation time was 30 min, the instrumental configuration employed had an oven with 6 positions for simultaneously heating the samples which allows a significant increase in the sample throughput.

2.4. Multivariate analysis

Each data matrix employed to characterization of extra virgin olive oils (training, external validation and prediction) is composed by as many rows as samples analyzed and as many columns as m/z recorded during the data acquisition time. All chemometric treatments were performed by using the Pirouette v3.11 software from Infometrix Inc. (Woodinville, WA, USA).

Concerning the selection of the classification technique, K-nearest neighbor (KNN) and soft independent modeling of class analogy (SIMCA) were evaluated. Both algorithms construct models using samples preassigned to a category, so a model is built and refined based on a training set; later, it is used to predict classes of new samples (prediction set). But the KNN prediction consists of assigning each unknown to one and only one category defined in the training set, whereas SIMCA can assign it to more than one category and, the most important, the unknown sample may be deemed to belong to none of the categories included in the training set.

Prior to the building of the classification model, two unsupervised techniques, cluster analysis (CA) and principal components analysis (PCA) were applied to the data in order to find out a natural grouping tend as well as to detect the possible presence of outliers between the samples that are going to made up the training set.

3. Results and discussion

The optimized instrumental conditions described in Section 2 were employed to analyze the samples corresponding to the data set 1. The objective was the building of a classification model capable to discriminate between the different PDOs, varieties and geographic origins that constitute the EVOOs variability under study. For this purpose, the data matrix obtained after analysis of the data set 1 was divided, by means of a randomize complete block design, in two subgroup (see Table 1); the training set, used for model construction and composed by 5 replicates of each EVOO class, and the external validation (EV) set constituted by 3 replicates of each one and employed for evaluating the goodness of the model.

In a second step, once the classification model was built, a new array of EVOOs was acquired and analyzed 15 days later and the data matrix generated (data set 2) composed by 5 replicates of each type was utilized as prediction set to corroborate the capability of the model for distinguishing between unknown samples from different PDOs, varieties and origins.

3.1. Visualization tools

Firstly, a cluster analysis algorithm was run to generate a dendrogram which permits the easy recognition of the sample grouping in base of the Euclidean distance. The best clustering between replicates of the same category was obtained when mean-centre was applied as pretreatment of the raw data. As can be seen in Fig. 1, the similarity among samples of the same EVOO class is extremely high without risk of a replicate falls in the group corresponding to other oil category. On the other hand, it is clear the difference between classes showed in the figure by the association of each group to the rest of them with a lower value of the similarity index.

In addition, a principal component analysis tool was performed in order to represent graphically (as the previous technique) the intersample and interclass relationship. As in the above described approach, the pretreatment chosen for the data matrix was mean-centre. Regarding the number of principal components (PCs) selected, it was chosen according to the predicted residual error sum of squares (PRESS) arises during

Table 2
Influence of the number of *m/z* variables employed to create the classification model

	Variables selected (*m/z*)	No. of variables	Classification non-error-rate (%)	EV[a] non-error-rate (%)	Prediction non-error-rate (%)
Group 1	41–180	140	100	100.0	80.0
Group 2	41–43, 45–180	139	100	100.0	86.7
Group 3	41–43, 45, 48, 55, 77, 79, 137, 139	10	100	96.2	23.5

[a] EV, external validation.

cross-validation process. The number of PCs giving the minimal PRESS (or it does not differ significantly from the following) is selected as the optimum value [29]. In this study, six factors were used to obtain the best representation of the objects under consideration and this number of PCs was enough to explain the 99.96% of the data variance. In this way, a method of cross-validation leaving out ten samples a time was employed for selecting the number of PCs as well as the internal validation technique (other cross-validation methods were assayed with poorer/similar results). Fig. 2 shows the 3D scores plot where the different groups of samples that make up the training set can be seen. It is clear the difference between classes even when they correspond to the same PDO or the same variety (viz. groups 1–2 or 4–5 and 6–7, respectively), being the PDO Baena the least similar regarding the other classes. This fact suggests that a good classification model has been constructed. No potential outlier is found in the outlier diagnostic plot which is also reported by the PCA algorithm.

3.2. Model building

When large amounts of data are treated into a statistic package, some variables in the data matrix will be found to be of greater value than others which contain only noise. On the other hand, reducing the number of variables before creating a multivariate model could be an unnecessary reduction of the amount of useful data that can be used in the model building. For these reasons, a previous study for the selection of the most significant variables was carried out. Three groups of variables were selected in order to evaluate which of them modulate and discriminate better between the categories; the first one was composed by the complete range of the *m/z* ions established (from 41 to 180), the second one excludes the mass 44 because its higher abundance could mask the influence of the rest of ions and finally, the third group is reduced to the ten variables with higher values of discriminating power excluding the mass 44 (*m/z* 41–43, 45, 48, 55, 77, 79, 137 and 139). Table 2 lists the results concerning the study of the influence of the *m/z* variables employed to the building of the classification model. The term "non-error-rate" refers to the percentage of objects (samples) correctly classified. From these data, it can be concluded that the group 2 of variables is the most suitable to build the classification model, since it provided the best prediction results of both EV and unknown samples sets.
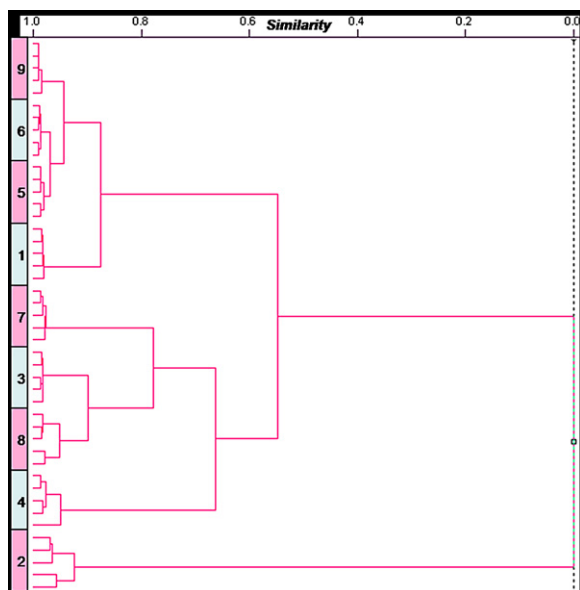
Once the data matrix has been defined, two supervised pattern recognition approaches, *K*-nearest neighbor and soft independent modeling of class analogy, were evaluated in order to obtain the best classification algorithm capable to discriminate between olive varieties, different PDOs and geographical origins of the olive trees. In both cases, several pretreatments were assessed

Fig. 1. Dendrogram generated by the application of the cluster analysis algorithm to nine EVOO categories. In the *x*-axis, the similarity index. 1, PDO Baena1; 2, PDO Baena2; 3, PDO Montes de Granada; 4, PDO Priego de Córdoba1; 5, PDO Priego de Córdoba2; 6, Arbequina variety (Málaga); 7, Arbequina variety (Lleida); 8, Picual variety; 9, Frantoio variety.
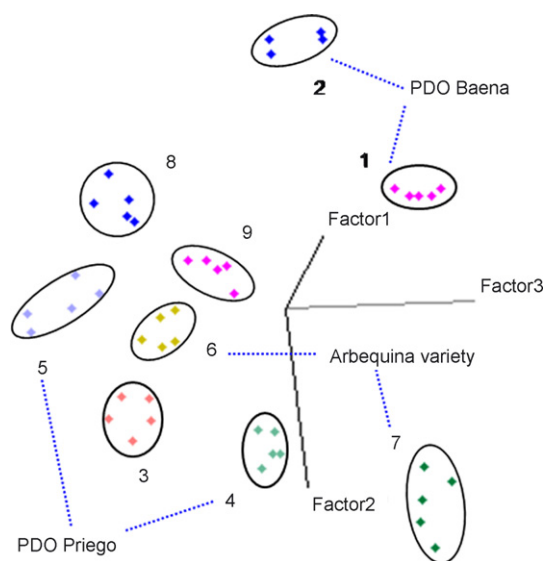

Fig. 2. The 3D scores plot of PCA algorithm for the EVOO. 1, PDO Baena1; 2, PDO Baena2; 3, PDO Montes de Granada; 4, PDO Priego de Córdoba1; 5, PDO Priego de Córdoba2; 6, Arbequina variety (Málaga); 7, Arbequina variety (Lleida); 8, Picual variety; 9, Frantoio variety. For details, see text.

Table 3
Results obtained after the application of SIMCA and KNN techniques to the training and prediction sets

	Class	SIMCA										KNN										Sensitivity		Specificity	
		1	2	3	4	5	6	7	8	9	No match	1	2	3	4	5	6	7	8	9	No match	SIMCA	KNN	SIMCA	KNN
Training set																									
1	Baena	5	0	0	0	0	0	0	0	0	0	5	0	0	0	0	0	0	0	0	0	100	100	100	100
2	Baena	0	5	0	0	0	0	0	0	0	0	0	5	0	0	0	0	0	0	0	0	100	100	100	100
3	M. Granada	0	0	5	0	0	0	0	0	0	0	0	0	5	0	0	0	0	0	0	0	100	100	100	100
4	Priego	0	0	0	5	0	0	0	0	0	0	0	0	0	5	0	0	0	0	0	0	100	100	100	100
5	Priego	0	0	0	0	5	0	0	0	0	0	0	0	0	0	5	0	0	0	0	0	100	100	100	100
6	Arbequina	0	0	0	0	0	5	0	0	0	0	0	0	0	0	0	5	0	0	0	0	100	100	100	100
7	Arbequina	0	0	0	0	0	0	5	0	0	0	0	0	0	0	0	0	5	0	0	0	100	100	100	100
8	Picual	0	0	0	0	0	0	0	5	0	0	0	0	0	0	0	0	0	5	0	0	100	100	100	100
9	Frantoio	0	0	0	0	0	0	0	0	5	0	0	0	0	0	0	0	0	0	5	0	100	100	100	100
Prediction set																									
1	Baena	4	0	0	0	0	1	0	0	0	0	5	0	0	0	0	0	0	0	0	0	80	100	80	100
2	Baena	0	5	0	0	0	0	0	0	0	0	0	5	0	0	0	0	0	0	0	0	100	100	100	80
3	M. Granada	–	–	–	–	–	–	–	–	–	–	–	–	–	–	–	–	–	–	–	–	–	–	100	100
4	Priego	0	0	0	4	0	0	0	0	0	1	0	0	0	0	0	0	0	5	0	0	80	0	100	100
5	Priego	–	–	–	–	–	–	–	–	–	–	–	–	–	–	–	–	–	–	–	–	–	–	100	100
6	Arbequina	0	0	0	0	0	4	0	0	0	1	0	0	0	0	0	0	0	5	0	0	80	0	100	100
7	Arbequina	0	0	0	0	0	0	4	0	0	1	0	0	0	0	0	0	5	0	0	0	80	100	100	100
8	Picual	0	0	0	0	0	0	0	5	0	0	0	5	0	0	0	0	0	0	0	0	100	0	100	67
9	Frantoio	–	–	–	–	–	–	–	–	–	–	–	–	–	–	–	–	–	–	–	–	–	–	100	100

(non-pretreatment, mean-centre, autoscale, range scale and variance scale) concluding that mean-centre with a data normalized were which provided the best results. Regarding KNN technique, the value of K was selected by optimization between 1 and 5 values, as this last is the maximum number of replicates for each EVOO category. Determining the classification capability and misclassifications, $K = 1$ was the value selected since it achieved the best results and moreover, it was chosen as the optimal neigh-

bor by the software. The correctly predicted and misclassified results are shown in Table 3. On the other hand, when SIMCA algorithm is employed, an independent model for each class by PCA is constructed. In this sense, the number of principal components was selected in order to reduce the model complexity with the minimum loss of useful information. A maximum of three factors (PCs) for each category was chosen providing a cumulative variance between 60 and 95%.
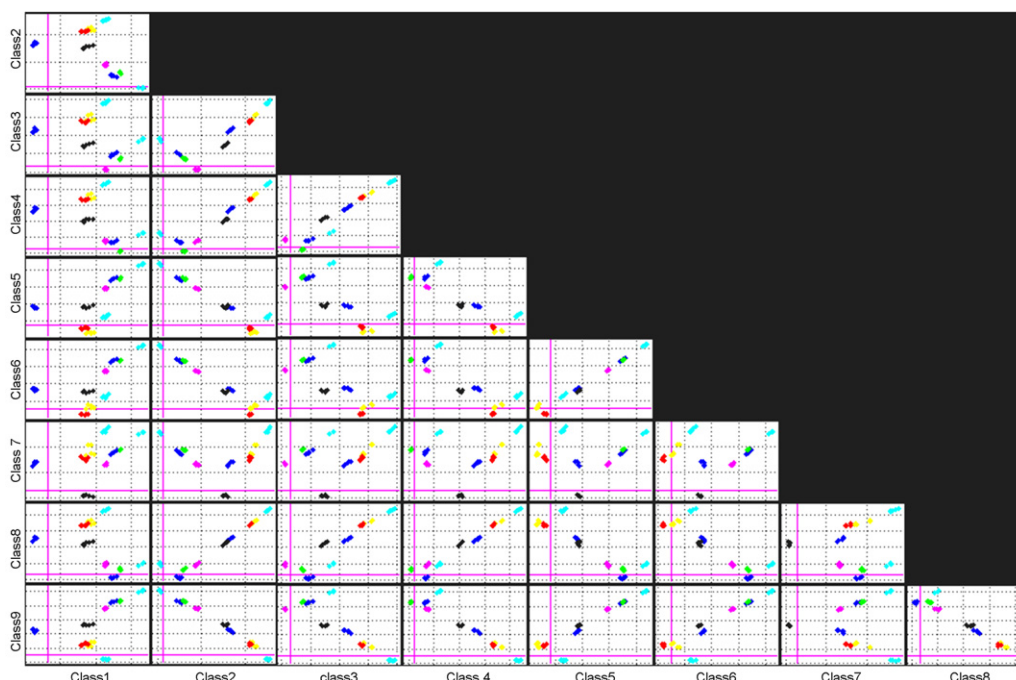
Fig. 3. Multiplot of class distances obtained by SIMCA model application to the training set. The axes of each plot represent the threshold distances for the studied categories.

As can be seen in the table, both KNN and SIMCA techniques distinguished correctly the whole of the samples analyzed concerning the training set. But when the algorithms were applied to a new set of samples (prediction set), a clear difference between both was reported: in the case of employing the SIMCA model, the outliers found in several groups of samples of the prediction set were classified into a new category named "no match". However, the KNN model classifies these samples into other group corresponding to other EVOO category. For this reason, the reliability of the results is higher when SIMCA is selected as classification model.

3.3. Application of the method

As it has been concluded in the previous section, SIMCA model was selected for applying it to a new set of unknown samples. Its characteristics are summarized as following: the data matrix has been made up by forty five objects corresponding to nine EVOO categories (in quintuplicate) and one hundred thirty nine variables established by the complete scan range (m/z 41–180) excluding the ion 44. This matrix was treated previously to the model building by means of mean-centre pretreatment and data normalized. The factors selected to each class were 3, 1, 1, 3, 1, 3, 1, 1, and 1, respectively. A multiplot of class distances, also named Coomans plot [30], was reported when the SIMCA model is built and it is shown in Fig. 3. As can be seen, the most of samples of the training set were correctly plotted in their correspondent class space. Only a slight overlapping was observed between the 5 and 6 classes; however, a negligible influence on the model building was observed. Finally, the ultimate goal of SIMCA algorithm is the correct discrimination of unknown samples and classification into the correspondent EVOO category, either into a PDO, olive variety or geographical area. In this way, a second data set was acquired and analyzed 2 weeks later for prediction purpose and was composed by six of the nine EVOO classes (see Table 1). Table 3 shows the results of SIMCA prediction. The goodness of the model was measured by means of two variables: sensitivity and specificity. The first one refers to the percentage of samples of the modeled class which are accepted by the class model. The second criterion indicates the percentage of other classes which are rejected by the class model. As can be seen in the table, all samples categories predicted offered a percentage of correct classification over the 80% and only one of the cases did not achieve the 100% of specificity (worse results were obtained in all classes when KNN model was applied).

4. Conclusions

The use of the methodology based on the headspace-mass spectrometry coupling for the discrimination of extra virgin olive oils belonging to diverse PDOs, olive varieties and geographical origins is presented as an adequate alternative to the traditional techniques for routine control because it does not require the obtaining of individual information about the volatile organic compounds, reducing the time-analysis and the treatment of the samples.

Regarding multivariate statistical treatment, the SIMCA model obtained after a performing process by means of the variable selection, the pretreatment of data matrix and the exploratory analysis carried out was capable of providing a percentage of correct classification of the 100% of the samples employed in the training set building.

Finally, taking into account the prediction results when a new set of samples is analyzed (an average of ca. 87% of samples correctly classified and a specificity of ca. 97%), it can be concluded than the HS-MS coupling is, with an adequate chemometric treatment, an appropriate technique for routine control laboratory and only in doubtful cases, it would be necessary the application of the conventional methods, which are more expensive and time-consuming.

References

[1] R. Aparicio, J. Harwood, A. Madrid Vicente. Manual del Aceite de Oliva, 2003.
[2] M.D. Medeiros, in: R.E.C. Wildman (Ed.), The Handbook of Nutraceuticals and Functional Foods, Boca Raton, 2001.
[3] E. Gimeno, M. Fito, R.M. Lamuela-Raventós, A.I. Castellote, M. Covas, M. Farré, Eur. J. Clin. Nutr. 56 (2002) 114.
[4] Regulation (EC) 2081/92, Eur. Commun. Off. J. L208 (1992) 1.
[5] Regulation (EC) 2082/92, Eur. Commun. Off. J. L208 (1992) 9.
[6] Regulation (EC) 2037/93, Eur. Commun. Off. J. L185 (1992) 5.
[7] A.D. Shaw, A. Di Camillo, G. Vlahov, A. Jones, G. Bianchi, J. Rowlan, D.B. Kell, Anal. Chim. Acta 348 (1997) 357.
[8] S. Rezzi, D.E. Axelson, K. Héberger, F. Reniero, C. Mariani, C. Guillou, Anal. Chim. Acta 552 (2005) 13.
[9] S. Lanteri, C. Armanino, E. Perri, A. Palopoli, Food Chem. 76 (2002) 501.
[10] A. Cichelli, G.P. Pertesana, J. Chromatogr. A 1046 (2004) 141.
[11] F. Marini, A.L. Magrì, R. Bucci, F. Balestrieri, D. Marini, Chemom. Intell. Lab. Syst. 80 (2006) 140.
[12] M.P. Aguilera, G. Beltrán, D. Ortega, A. Fernández, A. Jiménez, M. Uceda, Food Chem. 89 (2005) 387.
[13] D. Ollivier, J. Artaud, C. Pinatel, J.P. Durbec, M. Guérère, Food Chem. 97 (2006) 382.
[14] J.E. Pardo, M.A. Cuesta, A. Alvarruiz, Food Chem. 100 (2007) 977.
[15] L.C. Matos, S.C. Cunha, J.S. Amaral, J.A. Pereira, P.B. Andrade, R.M. Seabra, B.P.P. Oliveira, Food Chem. 102 (2007) 406.
[16] F. Aranda, S. Gómez-Alonso, R.M. Rivera del Álamo, M.D. Salvador, G. Fregapane, Food Chem. 86 (2004) 485.
[17] S. Vichi, L. Pizzale, L.S. Conte, S. Buxaderas, E. López-Tamames, J. Agric. Food Chem. 51 (2003) 6572.
[18] S. Ben Temime, E. Campeol, P.L. Cioni, D. Daoud, M. Zarrouk, Food Chem. 99 (2006) 315.
[19] F. Mahjoub Haddada, H. Manai, D. Daoud, X. Fernandez, L. Lizzani-Cuvelier, M. Zarrouk, Food Chem. 103 (2007) 467.
[20] B. Baccouri, S. Ben Temime, E. Campeol, P.L. Cioni, D. Daoud, M. Zarrouk, Food Chem. 102 (2007) 850.
[21] A. Guadarrama, M.L. Rodríguez-Méndez, C. Sanz, J.L. Ríos, J.A. de Saja, Anal. Chim. Acta 432 (2001) 283.
[22] Y. González Martín, J.L. Pérez-Pavón, B. Moreno Cordero, C. García Pinto, Anal. Chim. Acta 384 (1999) 83.

[23] Y. González Martín, C. Cerrato Oliveros, J.L. Pérez-Pavón, C. García Pinto, B. Moreno Cordero, Anal. Chim. Acta 449 (2001) 69.

[24] I. Marcos-Lorenzo, J.L. Pérez-Pavón, M.E. Fernández-Laespada, C. García-Pinto, B. Moreno-Cordero, L.H. Henriques, M.F. Peres, M.P. Simões, P.S. Lopes, Anal. Bioanal. Chem. 374 (2002) 1205.

[25] C. Cerrato-Oliveros, R. Boggia, M. Casale, C. Armanino, M. Forina, J. Chromatogr. A 1076 (2005) 7.

[26] F. Peña, S. Cárdenas, M. Gallego, M. Valcárcel, J. Am. Oil Chem. Soc. 79 (2002) 1103.

[27] S. López-Feria, S. Cárdenas, J.A. García-Mesa, M. Valcárcel, Anal. Chim. Acta 583 (2007) 411.

[28] F. Peña, S. Cárdenas, M. Gallego, M. Valcárcel, J. Chromatogr. A 1074 (2005) 215.

[29] Pirouette®: Multivariate Data Analysis, ver. 3.11, Infometrix, Inc., Woodinville, WA, USA, 2003.

[30] D. Coomans, I. Broeckaert, Potential Pattern Recognition in Chemical and Medical Decision Making, Research Studies Press LTD., John Wiley, Letchworth, England, 1986.

Erratum

Erratum to "A simple spectrophotometric technique for the determination of carbaryl pesticides in various environments" [Talanta 59(5) (2003) 1015–1019]

A.B. Manjubhashini [a], G.K. Raman [b], A. Suresh Kumar [c],[*], P. Chiranjeevi [b]

[a] *Department of Chemistry, Pondicherry Engineering College, Pondicherry 605104, India*
[b] *Department of Chemistry, S.V. University, Tirupati 517502, India*
[c] *USIC, S.V. University, Tirupati 517502, India*

This article has been retractedat the request of the Editors-in-Chief.

Considerable concern was raised about the research purportedly conducted at Sri Venkateswara University, India with the alleged involvement of Prof. P. Chiranjeevi. Questions were raised as to the volume of publications, the actual capacity (equipment, orientation and chemicals) of the laboratory in which Prof. Chiranjeevi worked, the validity of certain of the research data identified in the articles, the fact that a number of papers appear to have been plagiarized from other previously published papers, and some aspects of authorship.

Professor Chiranjeevi was given the opportunity to respond to these allegations. Thereafter, a committee was constituted by the University to look into these allegations. Based on the enquiry committee report, we have been informed by the head of the Department of Chemistry at Sri Venkateswara University that the university authorities have taken disciplinary action against Prof. Chiranjeevi, as the university considers that there are grounds for such action.

Therefore, based on the results of this investigation, the Editor is retracting this article.

Micro-Raman and X-ray fluorescence spectroscopy data fusion for the classification of ochre pigments

Pablo Manuel Ramos [a], Itziar Ruisánchez [a,*], Konstantinos S. Andrikopoulos [b,c]

[a] *Department of Analytical Chemistry and Organic Chemistry, Rovira i Virgili University, Campus Sescelades,*
C/. Marcel·lí Domingo, s/n 43007 Tarragona, Spain
[b] *"Ormylia" Art Diagnosis Center, Sacred Convent of the Annunciation IMSP Ormylia-Chalkidiki, EL-63071 Ormylia, Greece*
[c] *Physics Division, School of Technology, Aristotle University of Thessaloniki, 54124 Thessaloniki, Greece*

Abstract

Two different data-fusion strategies are evaluated for the combination of the outputs of combined Raman/X-Ray fluorescence instrument. The studied application deals with the classification of ochre pigments investigated in the field of cultural heritage. The two fusion strategies are: (1) first level fusion: combines raw signals obtained from each technique and (2) second level fusion: combines extracted features provided individually by each technique. Classification tool is partial least squares-discriminant analysis (PLS-DA). Classification results obtained performing different data-fusion strategies are compared with those results obtained performing a single classification model for each data source. The results show that the combination of signal features is the most suitable for a rapid and unique processing of both types of spectra. Benefits and drawbacks of each strategy are also discussed.
© 2007 Elsevier B.V. All rights reserved.

Keywords: Data fusion; Multivariate classification; Micro-Raman spectroscopy; Micro X-ray spectrometry; Ancient pigments

1. Introduction

It is well known that micro-Raman (Raman) and micro X-ray fluorescence (XRF) spectroscopy are particularly amenable to cultural heritage field [1–3]. Raman spectroscopy provides information regarding the molecular structure of the material under investigation. It provides a measure of molecular and crystal lattice vibrations and hence is sensitive to the composition, chemical environment and crystalline structure of the art material analysed [4]. By contrast, XRF is a technique that enables qualitative and quantitative elemental analysis [5–7].

Their increasing contribution to the study of art-works is partly due to the recent major improvements in instrument configuration [1,5,8], where the development of portable instruments that are capable for undertaking *in situ* measurements and collecting suitable information in a non-destructive way has played a significant role. Indeed, since the turn of the century,

a new generation of analytical instruments has been developed in the art diagnosis field. Among which, a rather promising is a prototype instrument (PRAXIS prototype) that combines both Raman and XRF techniques, with all the respective attributes. This instrument has been already tested [1] and is currently being applied in art and archaeological studies.

Thanks to this analytical instrumentation, we can now obtain micro-Raman and micro-XRF spectra from the same spot on a given sample. A novel perspective of data processing is therefore needed in order to find tools for processing large amounts of data from several sources (complementary techniques) rapidly and effortlessly and, by means of data fusion, obtain a distinct and reliable result. Data fusion is a formal framework in which the means and tools for combining data from several sources are expressed. It has been widely applied to robotics, remote sensing, image analysis and analytical chemistry [9,11–13].

The aim of this paper is to introduce an improved method for classification of pigments belonging to the cultural heritage field. The method is based on the evaluation of the spectroscopic data (Raman and XRF) both collected by the PRAXIS prototype from the same spot using different data-fusion strategies. The data-

fusion strategies are tested on experimental data obtained from reference and test samples of ochre pigments. More specifically, an evaluation of their predictions related to the classification of these pigments is considered.

This specific classification is selected as ochre differentiation is a rather complicated problem. All ochre pigments are natural and contain iron oxide(III) (Fe_2O_3) as their main component. They are therefore distinguished by investigating the presence of minor components. Natural ochre pigments present a wide range of colours, from yellow to orange, red and violet. In some cases, it is not possible to distinguish them just by visual inspection. And it is really difficult when we are dealing with trace analysis, for instance, in restoration studies, identification of ancient works, etc. Their colour is given away by the ferric oxide (Fe_2O_3) or ferric oxide monohydrate ($Fe_2O_3 \cdot H_2O$). The various shades are determined by several factors: the average size of crystallites and the corresponding dispersion; their proportion with respect to the presence of other chemical components such as aluminosilicate materials (kaolinite, quartz, manganese oxide, etc.) and other minor components (calcite, gypsum, etc.). Also, the presence of magnetite (Fe_3O_4) may also contribute to the material's shade.

The identification of ochre pigments is rather complicated and implies the characterization of the specific iron oxide or hydroxide material, as well as the designation of the minor components existing in the natural material. Data from different techniques is usually required and combination of the results leads to the final identification of the ochre pigment [10–13]. One of the works that clearly demonstrated this issue is the one of Bikiaris et al. [10] in which Raman spectroscopy (that enables one to differentiate between the various iron oxides and hydroxides) is combined with energy dispersive spectroscopy analysis from scanning electron microscopy (that enables elemental composition of the minor components) or Fourier transform infrared spectroscopy (that enables the identification of kaolinite and quartz).

In the current work we try to observe whether data obtained from Raman and X-ray fluorescence from the same spot on ochre pigments (which are related to structure and elemental composition respectively) can be properly handled using data-fusion strategies and classification can thus be accomplished.

2. Theory

2.1. Signal processing

An initial signal process, previous to the fusion strategy, is necessary to focus on the deterministic information present in the data. Dealing with spectroscopic data, allocate the spectra properly implies smoothing and de-noising procedures, background correction and normalization. In Raman and XRF data-fusion, this stage is highly required due to the presence of noise and background signal components in the raw spectra. In this work the wavelet transform was applied for noise suppression and multipoint baseline correction for background suppression in spectra.

Data alignment is also necessary to achieve a common spatial reference. When data to be fused come from different techniques, they might be in different scales, so before applying the fusion process they have to be formatted into a common form and aligned in the time domain. In this work, normalization was applied to achieve this. It is also an attempt to correct the systematic bias in data and permits to balance data before it enters the data-fusion system.

2.2. Data fusion

Data fusion combines information from several sources to produce a single model or decision. Hall and Llinas [14] propose different techniques for multisensor data fusion and define a group of strategies. Two of them are suitable to be used with spectral data: (1) data level fusion or low-level fusion and (2) feature level fusion or mid-level fusion. Fig. 1 shows both strategies in which the spectra coming from Raman and XRF measurements are fused.

In low-level fusion, the raw data is fused. In our particular case the raw Raman and XRF spectra are just fused. For the raw data fusion it has to be considered that data must be commensurate and must be properly associated. Thus, for example, if the same spectroscopic technique is used, the spectra must be able to be co-aligned on the same scale. If different spectroscopic techniques are used, the spectra need to be balanced in order to perform a correct data sensor association. Once the raw data is
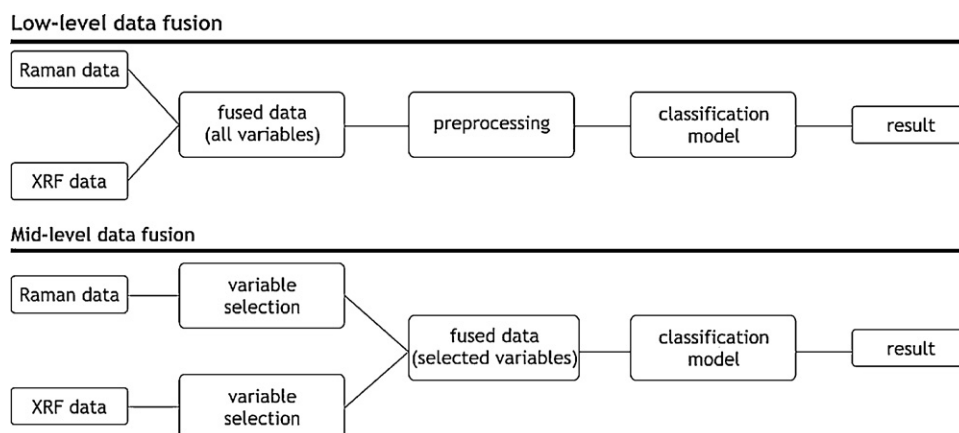

Fig. 1. Two data-fusion architectures: low-level and mid-level.

fused, a unique and final result is obtained as a result of the classification performed. Depending on the problem ahead, there are several methods that could be applied for this; in our case study we use multivariate classification methods as PLS-DA.

In mid-level fusion, the fusion is done ideally over the most relevant features, so a previous variable selection step is performed. Among all possibilities of selecting variables, in the present work we have chose the one based on the Indahl and Naes method [13]. This method identifies the local positive maxima and negative minima of the loading weights which define the directions in the variable space with good classification power [15,16]. In our application, we use the loading weights obtained from the standard PLS-DA algorithm and select a small set of wavelengths around each selected point to provide more stable models. The selected features are concatenated together into a single feature vector which is the input to the classification or cluster algorithm. Similarly as in the low-level fusion, the output of the classification is a unique result based on the information coming from both sensors (Raman and XRF). For the mid-level fusion, also data alignment and association/correlation must be performed prior to linking the feature vectors from individual sensors into a single large feature vector.

2.3. PLS-DA

As its name implies, in PLS-DA (partial least squares-discriminant analysis) a PLS model is developed to predict the class assignment of each sample. We will not go into details on the theory of PLS and PLS-DA here since it has largely been described elsewhere [17,18]. PLS-DA is carried out using an exclusive binary coding scheme with one bit per class. For example, if we want to discriminate between four classes, a response encoded {0, 0, 1, 0} means that the sample belongs to class 3. During the calibration process the PLS-DA method is trained to compute the four "membership values" one for each class. The sample is then assigned to the class that shows the highest membership value. The resulting class assignment is expressed in terms of a value from 0 to 1, but these values are the projected results in the multidimensional space defined by the factors selected. The fact is that these values are normally distributed around 0 when the prediction is "not being in a class" and around 1 when the prediction is "to be in a class". For that reason it is possible to obtain prediction values below 0 (negative values) and also above 1.

In addition to the PLS-DA class assignment, we have implemented the Bayes theorem to obtain a threshold value for each class. The purpose is to obtain a discrete class assignment for the continuous values obtained from the PLS-DA. More specifically, Bayes theorem is used to calculated a threshold value to assume that a sample belongs or not to a determinate class of pigments. For instance, a sample is classified in the class for which the PLS-DA class assignment value is greater than the threshold value. The Bayesian threshold calculation assumes that the predicted values follow a distribution similar to the one of future samples. Using these estimated distributions, a threshold is selected at the point where the two estimated distributions cross. This is the value at which the number of false positives and false negatives should be minimized for future predictions.

To study the robustness of the models, prediction probability is obtained with the references samples used to build the PLS-DA model. The purpose of the implemented algorithm is to discriminate probabilities of discrete classes for continuous predicted values. The actual PLS-DA class assignments for the references are used to obtain a probability that the given value belongs to each of the original classes.

The residual Q and the Hotelling T^2 values are calculated to obtain the lack of fit for the PLS-DA model. The Q statistics indicates how well each sample conforms to the PLS-DA model. It is a measure of the difference or residual between a sample and its projection into those latent variables retained in the model. The T^2 statistics is a measure of the variation in each sample within the PLS-DA model. Tables 1–3 contain the reduced Q and T^2 values which are the original Q and T^2 values divided by the respective Q and T^2 values at the 95% confidence interval. Inspection of the reduced Q and T^2 reveals how many samples are not within the 95% limits of the classes.

An important aspect of this general PLS-DA approach is that we get access to very useful score-plots of the X-space (samples space), showing disposition of all objects and classes reflecting the PLS-DA derived discrimination.

3. Experimental

3.1. Samples and instruments

The pigments studied are commercially manufactured and used by conservationists in restoration works. They consist of a set of ochre pigments, with iron oxide(III) (Fe_2O_3) as the main component. The pigments included in this set were: hematite,

Table 1
Raman PLS-DA prediction values of unknown samples

Sample	PLS-DA class assignment						Threshold	Q (red)	T^2 (red)	Predicted probability					
	$C(1)$	$C(2)$	$C(3)$	$C(4)$	$C(5)$	$C(6)$				$P(1)$	$P(2)$	$P(3)$	$P(4)$	$P(5)$	$P(6)$
Hematite	0.21	0.17	0.00	−0.20	−0.04	−0.14	0.13	0.27	0.04	1.00	0.00	0.00	0.00	0.00	0.00
Caput mortum	0.39	0.42	0.19	−0.26	−0.43	−0.32	0.35	0.75	0.21	1.00	1.00	0.00	0.00	0.00	0.00
Caput mortum violet	−0.07	−0.19	0.70	−0.19	−0.09	−0.16	0.49	0.12	0.19	0.02	0.00	1.00	0.00	0.00	0.00
Red ochre	−0.11	−0.16	−0.17	0.70	0.15	−0.40	0.22	1.47	0.21	0.01	0.00	0.00	1.00	0.90	0.00
Yellow ochre	−0.30	−0.15	0.05	−0.19	0.63	−0.04	0.11	0.49	0.17	0.02	0.00	0.00	0.00	1.00	0.00
Burnt Sienna	−0.20	−0.11	0.04	−0.16	0.02	3.42	0.10	1.20	0.08	0.01	0.00	0.00	0.00	0.01	1.00

Table 2
XRF prediction for samples not included in the PLS-DA model

Sample	PLS-DA class assignment						Threshold	Q (red)	T^2 (red)	Predicted probability					
	$C(1)$	$C(2)$	$C(3)$	$C(4)$	$C(5)$	$C(6)$				$P(1)$	$P(2)$	$P(3)$	$P(4)$	$P(5)$	$P(6)$
Hematite	0.43	−0.06	0.06	−0.22	−0.05	−0.15	0.19	0.91	0.13	1.00	0.00	0.00	0.00	0.00	0.00
Caput morturn	−0.01	0.14	0.16	−0.11	0.02	−0.20	0.43	0.76	0.11	0.00	0.00	0.00	0.00	0.00	0.00
Caput mortum violet	0.06	−0.04	0.47	−0.11	−0.29	−0.09	0.45	1.03	0.11	0.00	0.01	1.00	0.00	0.00	0.00
Red ochre	0.00	−0.15	−0.06	0.35	0.00	−0.14	0.14	0.95	0.05	0.00	0.00	0.00	0.97	0.17	0.00
Yellow ochre	−0.20	−0.06	−0.20	0.17	0.58	0.04	0.26	0.67	0.14	0.00	0.00	0.00	0.00	1.00	0.00
Burnt Sienna	−0.02	−0.28	−0.23	o IS	−0.07	0.77	0.27	0.82	0.11	0.00	0.00	0.00	0.00	0.00	1.00

Table 3
Raman–XRF prediction obtained from a low-level data-fusion system

Sample	PLS-DA class assignment						Threshold	Q (red)	T2 (red)	Predicted probability					
	$C(1)$	$C(2)$	$C(3)$	$C(4)$	$C(5)$	$C(6)$				$P(1)$	$P(2)$	$P(3)$	$P(4)$	$P(5)$	$P(6)$
Hematite	0.35	0.08	0.01	−0.20	−0.07	−0.16	0.18	0.61	0.08	1.00	0.00	0.00	0.00	0.00	0.00
Caput mortum	0.16	0.54	0.02	−0.26	−0.23	−0.20	0.23	0.94	0.22	0.00	1.00	0.00	0.00	0.00	0.00
Caput mortum violet	0.01	−0.21	0.80	−0.19	−0.10	−0.12	0.41	0.64	0.18	0.00	0.00	1.00	0.00	0.00	0.00
Red ochre	−0.03	−0.23	−0.06	0.69	0.01	−0.36	0.20	1.26	0.17	0.00	0.00	0.00	1.00	0.00	0.00
Yellow ochre	−0.23	−0.18	−0.09	−0.13	Q75	0.07	0.13	0.71	0.17	0.00	0.00	0.00	0.00	1.00	0.00
Burnt Sienna	−0.08	−0.17	−0.19	−0.12	0.08	0.63	0.24	1.23	0.15	0.00	0.00	0.00	0.00	0.00	1.00

caput mortum, caput mortum violet, yellow ochre, red ochre and burnt sienna. Fig. 2 shows the Raman (Fig. 2a) and XRF (Fig. 2b) spectra of the studied pigments. For each pigment, simultaneous Raman and XRF spectra were obtained at different spots on the pigment. A data set of 24 samples (48 spectra) were measured, where three samples were used to build the PLS-DA model and one sample, not included in the model, was used for prediction. The samples designated to be references or "unknown-sample" were selected at random.

The instrument used was a prototype of a micro-Raman and micro-XRF instrument. It combines the excitation radiation from both techniques applied to a small sample area that allows a position sensitive analysis with a spatial resolution of 5–50 μm. It consists of an energy dispersive micro-beam X-Ray fluorescence spectrometer with a fine focus X-Ray tube (max. 50 kV, 30 W), a polycapillary optic with a spot size of approximately 30 μm (MoK) and a drift chamber detector with a sensitive area of 5 mm^2 and energy resolution of <140 eV (MnK). The Raman spectrometer component (Jobin Yvon) has two wavelength laser excitation (633 and 785 nm), a fibre optic connection of the measuring head to the spectrometer and a compact axial optical spectrometer for these two wavelengths. The Raman-XRF microprobe has a camera to select different grains and measures in the middle of each one [1].

3.2. Software

The algorithms were programmed with the Matlab software version 6.5. The wavelet transform applications belonged to the Wavelet toolbox 2.0 from Matlab software, PLS applications belonged to the PLS toolbox 3.5 from Eigenvector Research Incorporated.
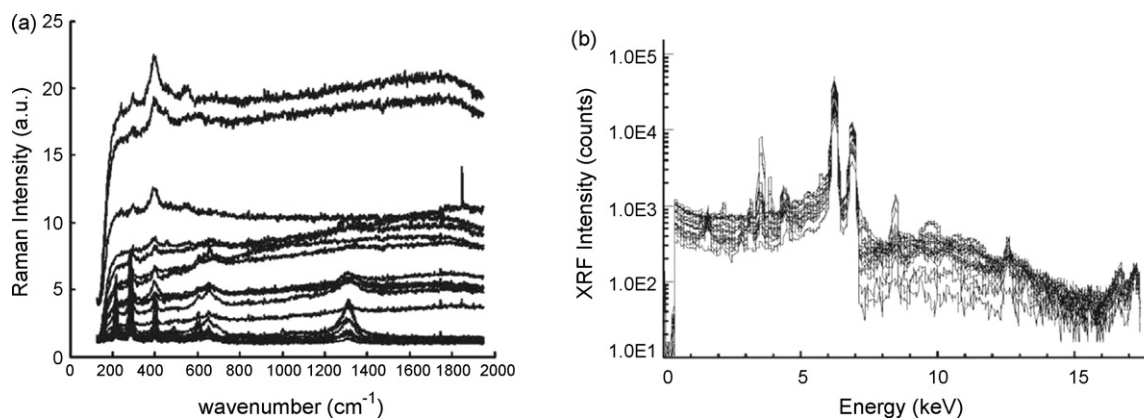
Fig. 2. (a) Raman spectra and (b) XRF spectra from ochre pigments.

4. Results and discussion

We have divided the results presentation in two parts. First the classification of ochre pigments is discussed by means of each individual technique (first Raman spectroscopy and then X-ray fluorescence). In both studies principal component analysis is performed for a pre-visualization of the patterns present in each data set. After that, partial least squares discriminant analysis is used for the classification and prediction of different groups of ochre pigments. Secondly, the two described data-fusion strategies are implemented in order to improve the ochre classification results. Finally, results obtained with both strategies are compared and the benefits and drawbacks of these methodologies applied to these types of data are discussed.

Samples from known classes are denoted with labels beginning with HM (hematite), CM (caput mortum), CMv (caput mortum violet), YO (yellow ochre), RO (red ochre) and BS (burnt sienna). Unknown samples are labeled with the term "samples 1–6" and are shown as filled dark grey circles.

4.1. Raman classification

Principal components analysis (Fig. 3) shows that the plot of PC1 versus PC2 is not enough for grouping all samples in their corresponding classes. Classes CMv and BS cannot be differentiated but their separation can be achieved by projecting the data in the PC1 versus PC3 plot.

Classification and prediction of new samples was performed by means of PLS-DA. The model was performed using five latent variables which were determined by the leave-one-out cross-validation method. The score plots of the latent variables (Fig. 4a and b) represent a similar separation of data obtained by PCA. The loading weights of the PLS-DA model were inspected in order to determine the variables responsible for the discrimination between classes (Fig. 4c). The highest (positive and negative) values are marked and associated with their corresponding variable in the original Raman spectra. It can be seen that the PLS-DA model discriminates the pigment samples using the information about differences in relative intensities and

shapes of the Raman bands. Especially those bands positioned in 223, 242, 291, 409, 609, 657 and 1311 cm^{-1} which are used to characterize iron oxide(III) pigments.

In the prediction of unknown samples (Table 1) it can be seen that the model cannot predict the hematite and caput mortum samples correctly as both classes are misclassified. Hematite is also assigned as capum mortun (0.17) and capum mortum is also assigned as hematite (0.39). This limitation of the model is also denoted by the predicted probability results obtained in the analysis of caput mortum samples, where hematite (P1) and caput mortum (P2) classes have predicted probability values equal to 1. The model has also problems with the prediction of future samples of red ochre pigments as might be misclassified since red and yellow ochre (P4 and P5) classes have predicted probability values close to 1. Finally, it has to be remarked that the reduced values of Q_{red} and T_{red}^2 show that the values corresponding to red ochre (1.47) and burnt sienna (1.20) are higher than 1 and therefore they are out of the interval confidence given for the PLS-DA model.

This table reflects the slight Raman spectra differences mainly associated with the relative intensities of some Raman bands. A deep spectroscopic study explaining these differences was performed by de Oliveira et al. [19].

4.2. XRF classification

Following the same structure of analysis performed on Raman data, the set of pigments was studied by means of micro-XRF spectrometry so classification of ochre pigments was also conducted using the qualitative information extracted from spectra.

The PCA plot of data projected on PC1–PC2 axes (Fig. 5a), presents three groups which are easily identified: YO, RO and BS samples. And the PC1–PC3 score plot (Fig. 5b), allows to visually discriminate the other three classes (HM, CM and CMv). So, as with the Raman analysis, it is possible to observe a satisfactory separation for the six classes of ochre pigments and also for the unknown samples. But when the unknown samples are classified by means of the PLS-DA model, some problems arise.
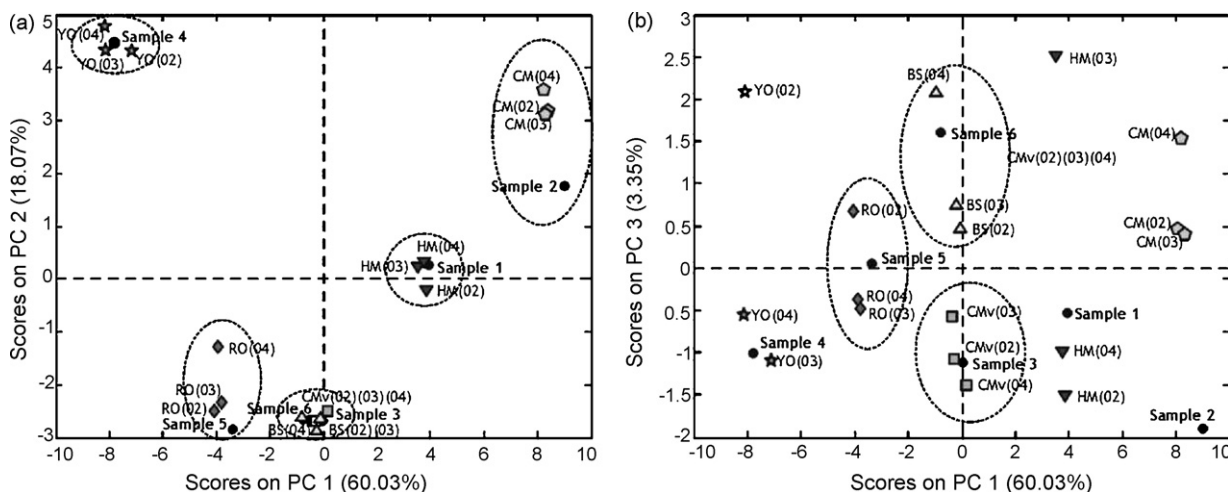
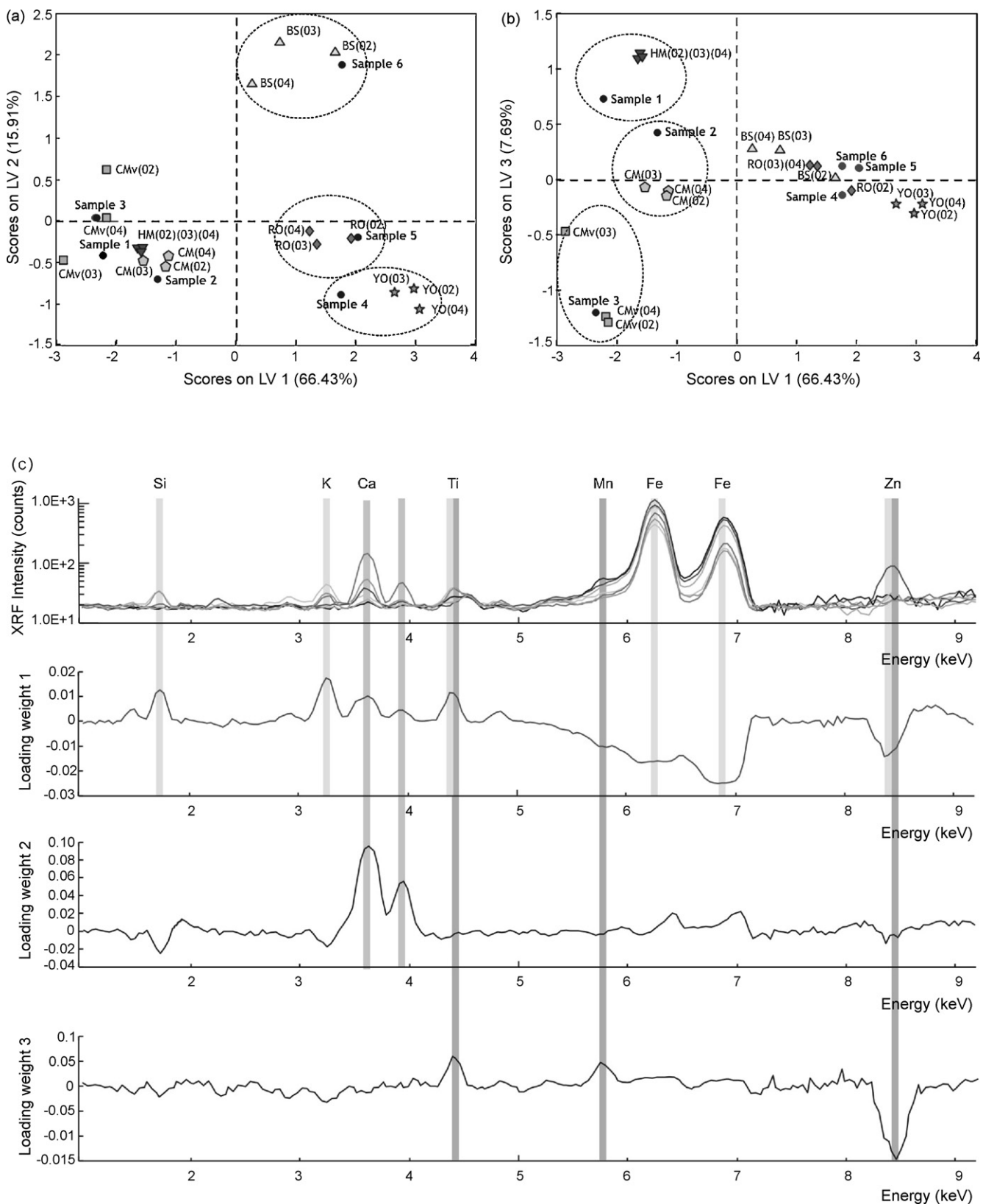Fig. 3. PCA on Raman spectra: (a) PC1–PC2 score plot and (b) PC1–PC3 score plot.
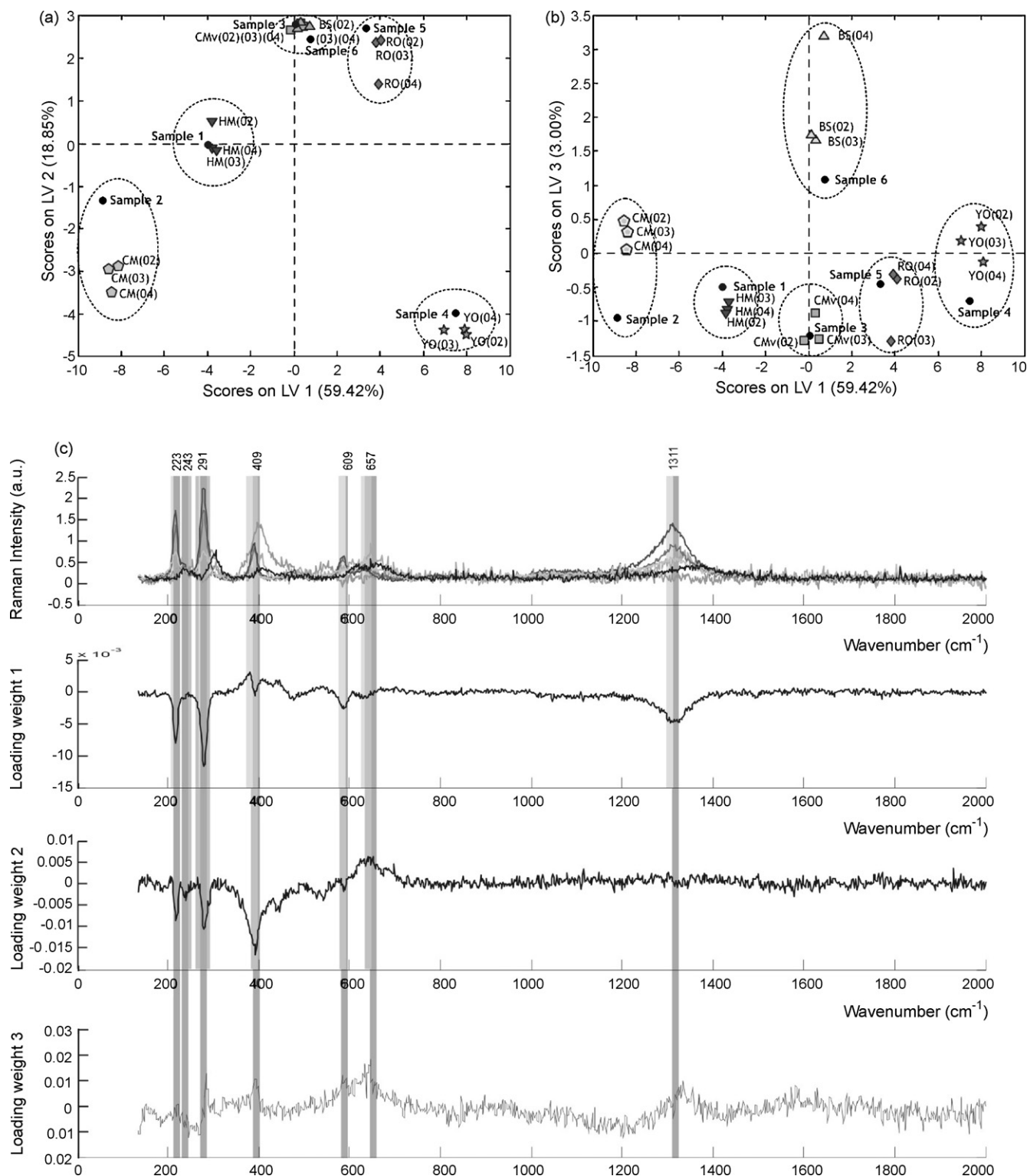
Fig. 4. PLS-DA on Raman spectra: (a) LV1–LV2 score plot, (b) LV1–LV3 score plot and (c) projection of maximum (positive and negative) values from loading weights 1, 2 and 3 on original variables from Raman spectra.
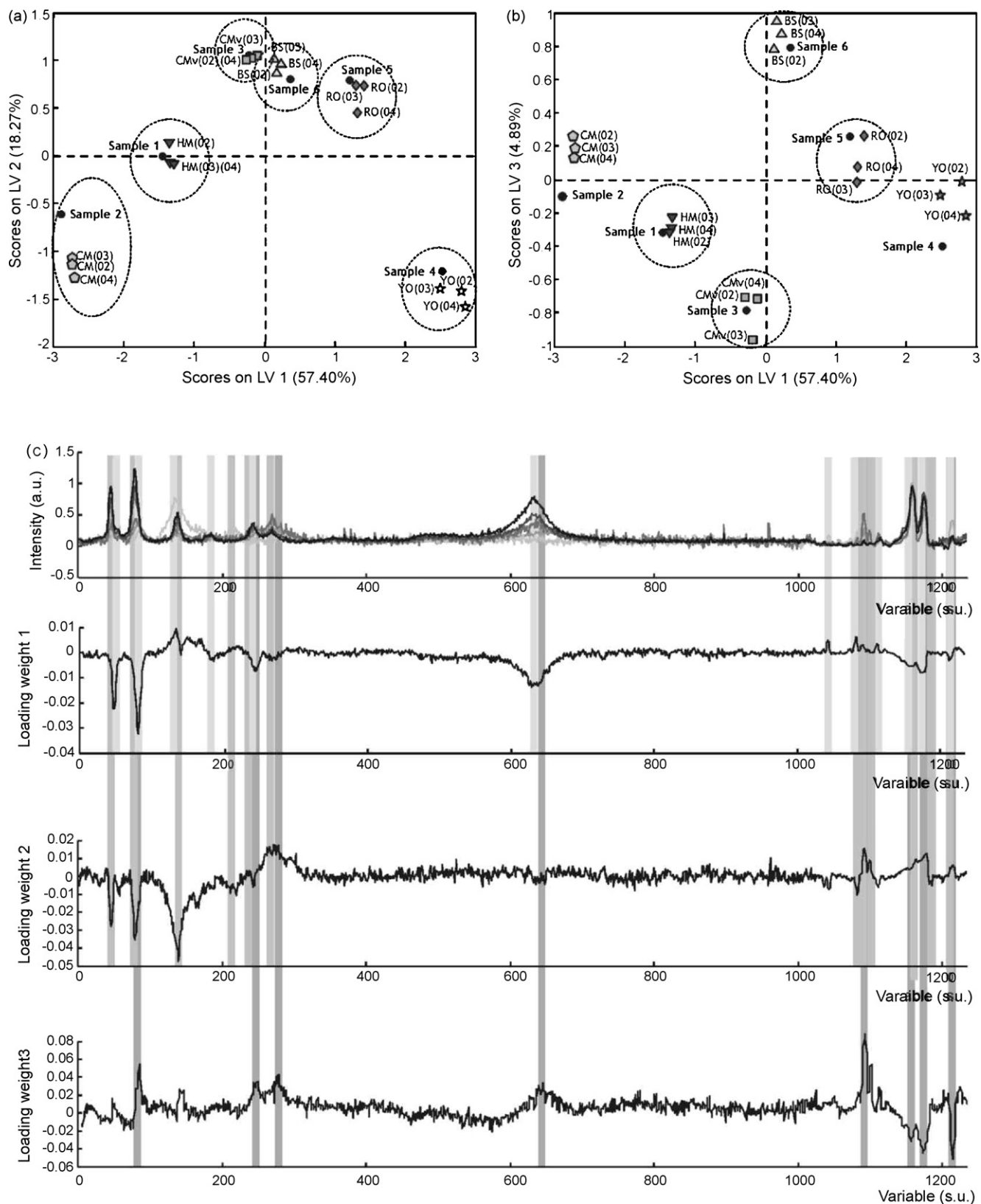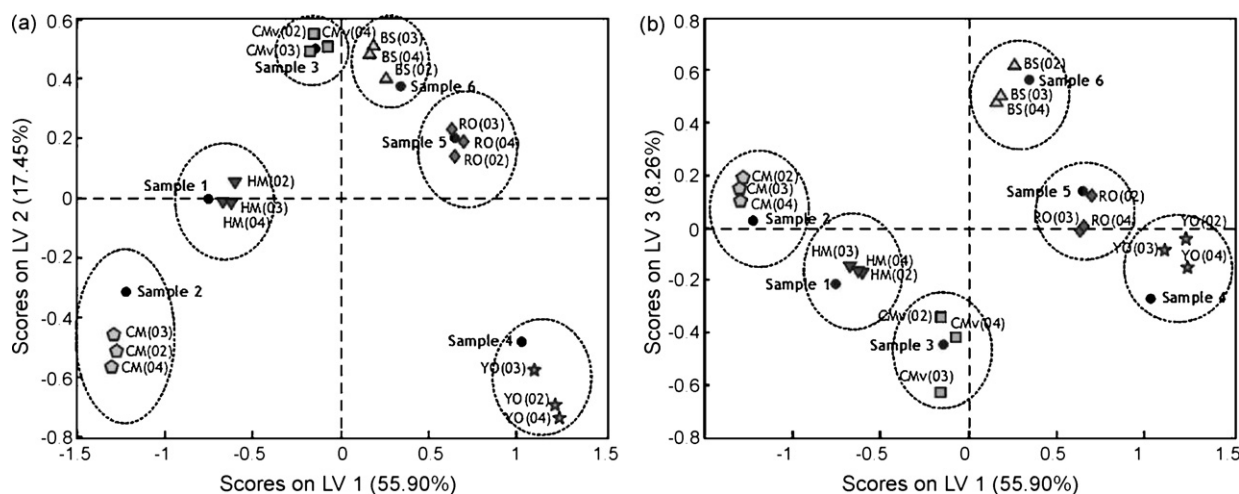
The score plots (Fig. 6a and b) show similar group distribution as the previously visualized by the PCA processing only with Raman spectra. The loading weights of the PLS-DA model (Fig. 6c) show that classification of ochre samples is done principally by the minor peaks present in the spectra with energies below 6 eV that correspond to Si, K, Ca, Ti, Mn and Zn and

also by the differences in intensity observed in the major peaks located between 6 and 7 keV, which correspond to the amount of iron.

The unknown samples predicted by the model are listed in Table 2 along with their corresponding result. In this case only the caput mortum sample could not be predicted by the model,

Fig. 5. PCA on XRF spectra: (a) PC1–PC2 score plot and (b) PC1–PC3 score plot.

and also the predicted probability $P(2)$ is 0, showing that future samples of this class cannot be predicted. The rest of the samples were correctly classified and predicted, although the class assignments values are lower and closer to the threshold values than the ones obtained only by Raman. It has to be remarked that the reduced values of Q_{red} and T^2_{red} show that all the samples are within the 95% limits of the classes (Table 2) as the values are lower or close to 1.

4.3. Low-level Raman and XRF data fusion

The Raman and XRF spectra were concatenated according to the methodology described in the theory section, and the Raman-XRF meta-spectra obtained was processed by the PLS-DA. The model was performed using five latent variables and they were determined by the leave-one-out cross-validation method. Fused data projected on the first latent variables of the PLS-DA model (Fig. 7a and b) show better distribution of classes compared with the individual models. As it was expected, the inspection of loading weights of the PLS-DA model (Fig. 7c) reveals that the variables responsible for the discrimination between classes are mostly those which were used in the individual Raman and XRF models.

With the low-level fusion, all future samples from each class can be correctly identified as the predicted probabilities are 1 for each corresponding class and 0 for the rest of the classes (Table 3). The assignation of capum mortum is clearly

improved as is not assigned to other class (0.54 for CP). With that model, two samples are out of the 95% limits of the classes since the limit values are 1.26 for red ochre and 1.23 for burnt sienna.

4.4. Mid-level Raman and XRF data fusion

Raman and XRF extracted features are used to set up the Raman-XRF meta-spectra. These features are those variables which denote the maximum discrimination power between classes as it was explained in the theory section.

Following the same scheme of methodologies as in the low-level sensor fusion study, classification and prediction of new samples (Raman-XRF) was performed by a PLS-DA model. The model was performed using five latent variables and it was determined by the leave-one-out cross-validation analysis.

As in the low-level fusion, the visual inspection of the score plots (Fig. 8) showed that all the classes are properly discriminate, also known and unknown samples are better clustered in their corresponding classes. The distribution of classes is better than those obtained with the low-level Raman-XRF fusion and the Raman and XRF individual models.

The prediction of unknown samples (Table 4) shows that the model is able to discriminate between hematite (HM) and capum mortum (CP) samples. With that model, and for all classes, the class assignment values are higher and far away

Table 4
Raman–XRF prediction obtained from a mid-level data-fusion system

Sample	PLS-DA class assignment						Threshold	Q (red)	T2 (red)	Predicted probability					
	$C(1)$	$C(2)$	$C(3)$	$C(4)$	$C(5)$	$C(6)$				$P(1)$	$P(2)$	$P(3)$	$P(4)$	$P(5)$	$P(6)$
Hematite	0.47	0.15	0.05	−0.20	−0.03	−0.25	0.34	0.66	0.08	1.00	0.00	0.00	0.00	0.00	0.00
Caput mortum	0.03	0.55	−0.02	−0.22	−0.16	−0.23	0.30	0.91	0.12	0.00	1.00	0.00	0.00	0.00	0.00
Caput mortum violet	0.09	−0.12	0.82	−0.17	−0.18	−0.18	0.41	0.33	0.12	0.00	0.00	1.00	0.00	0.00	0.00
Red ochre	0.03	−0.22	−0.03	0.62	0.05	−0.35	0.20	1.16	0.15	0.00	0.00	0.00	1.00	0.00	0.00
Yellow ochre	−0.19	−0.12	−0.08	−0.07	0.81	−0.06	0.20	0.84	0.08	0.00	0.00	0.00	0.00	1.00	0.00
Burnt Sienna	−0.04	−0.13	−0.19	−0.16	0.06	0.72	0.31	1.06	0.10	0.00	0.00	0.00	0.00	0.00	1.00

Fig. 6. PLS-DA on XRF spectra: (a) LV1–LV2 plot, (b) LV1–LV3 plot and (c) projection of maximum (positive and negative) values from loading weights 1, 2 and 3 on original variables from Raman spectra.

Fig. 7. PLS-DA on Raman–XRF meta-spectra from a low-level data-fusion model: (a) LV1–LV2 score plot, (b) LV1–LV3 score plot and (c) projection of maximum (positive and negative) values from loading weights on variables from Raman–XRF meta-spectra.

Fig. 8. PLS-DA on Raman–XRF meta-spectra from a mid-level data-fusion model: (a) LV1–LV2 score plot and (b) LV1–LV3 score plot.

of their threshold value. The predicted probabilities for each corresponding class are 1 and 0 for the rest of the classes, asserting that all classes can be correctly identified. Finally, the reduced values of Q_{red} and T^2_{red} show that, all the samples are mostly within the 95% limits of the classes. Therefore, we can conclude that with this model we do not have problems to differentiate samples belonging to one of the studied classes.

5. Conclusions

The combination of micro-Raman and micro-X-ray fluorescence spectroscopy offers a powerful tool for the characterization of pigments in works of art. The combination of signals coming from several instrumental techniques requires to be complemented with robust methodologies for data processing. Two strategies to perform data-fusion followed by classification analysis were presented and successful results were obtained for the classification of ochre pigments. Their benefits and drawbacks are discussed below.

Low-level fusion is the simplest way to perform data fusion. However, signal processing must be performed after concatenation of raw spectra, especially to remove background signal components from both types of spectral data in order to apply chemometric tools on the fused data. Redundancies in data and different types of noise could convey a poor performance of the classification method. In spite of this, classification of ochre pigments was improved using low-level fusion. PCA and PLS-DA models performed with the fused data are more robust for prediction of new samples and visual discrimination from class distributions is better with respect to those results obtained by individual classification.

Mid-level fusion implements another step in which features from each type of signals are extracted and fused. The main advantage of this methodology is the possibility of discarding irrelevant data. The extra computation needed for variable selection is compensated with the rapid processing of only a few

sets of variables fused instead of the full spectra concatenated. The benefit of this approach is demonstrated by the reduction of the reduced values of Q_{red} and T^2_{red} to values closer or smaller than one. Also, a better distribution of classes in the multivariate space given by PCA and PLS-DA is obtained. In that way, each group could be easily identified in PCs plots.

In a further study, quantification results obtained by XRF analysis may also be incorporated to the Raman–XRF data-fusion model in order to improve classification results.

Acknowledgment

References

[1] K.S. Andrikopoulos, S. Daniilia, B. Roussel, K. Janssens, J Raman Spectrosc 37 (2006) 1026–1034.
[2] N. Civici, O. Demko, R.J.H. Clark, J Cult Heritage 6 (2005) 157–164.
[3] G. Paternoster, R. Rinzivillo, F. Nunziata, E.M. Castellucci, C. Lofrumento, A. Zoppi, A.C. Felici, G. Fronterotta, C. Nicolais, M. Piacentini, J Cult Heritage 6 (2005) 21–28.
[4] R.J.H. Clark, Comptes Rendus Chimie 5 (2002) 7–20.
[5] P. Moioli, C. Seccaroni, X-Ray Spectrom 29 (2000) 48–52.
[6] K.H.A. Janssens, F.C.V. Adams, A. Rindby, Microscopic X-ray fluorescence analysis, John Wiley & Sons Ltd., 2000.
[7] K. Janssens, R. Van Grieken, Non-destructive micro analysis of cultural heritage materials, Elsevier, 2004.
[8] P. Vandenabeele, T.L. Weis, E.R. Grant, L.J. Moens, Anal Bioanal Chem 379 (2004) 137–142.
[9] J. Esteban, A. Starr, R. Willetts, P. Hannah, P. Bryanston-Cross, Neural Comput Appl 14 (2005) 273–281.
[10] D. Bikiaris, S.X. Daniilia, S. Sotiropoulou, O. Katsimbiri, E. Pavlidou, A.P. Moutsatsou, Y. Chryssoulakis, Spectrochim Acta A 56 (2000) 3–18.
[11] V. Steinmetz, F. Sevila, V. Bellon-Maurel, J Agri Eng Res 74 (1999) 21–31.
[12] P. Boilot, E.L. Hines, M.A. Gongora, R.S. Folland, Sens Actuat B Chem 88 (2003) 80–88.

[13] S. Roussel, W. Bellon-Maurel, J.M. Roger, P. Grenier, J Food Eng 60 (2003) 407–419.

[14] J. Llinas, D.L. Hall, An introduction to multi-sensor data fusion, in: Proceedings of the 1998 IEEE International Symposium on Circuits and Systems 1998, ISCAS '98, vol. 536, 1998, pp. 537–540.

[15] U. Indahl, T. Naes, J Chemometr 18 (2004) 53–61.

[16] H. Nocairi, E. Mostafa Qannari, E. Vigneau, D. Bertrand, Computation Stat Data Anal 48 (2005) 139–147.

[17] P. Geladi, B.R. Kowalski, Anal Chim Acta 185 (1986) 1–17.

[18] M. Barker, W. Rayens, J Chemometr 17 (2003) 166–173.

[19] L.F.C. de Oliveira, H.G.M. Edwards, R.L. Frost, J.T. Kloprogge, P.S. Middleton, Analyst 127 (2002) 536–541.

Assessment of total arsenic and arsenic species stability in alga samples and their aqueous extracts

S. García Salgado, M.A. Quijano Nieto, M.M. Bonilla Simón *

Departamento de Ingeniería Civil: Tecnología Hidráulica y Energética, Escuela Universitaria de Ingenieros Técnicos de Obras Públicas, Universidad Politécnica de Madrid, Alfonso XII 3 y 5, 28014 Madrid, Spain

Abstract

In order to achieve reliable information on speciation analysis, it is necessary to assess previously the species stability in the sample to analyse. Furthermore, in those cases where the sample treatment for species extraction is time-consuming, an assessment of the species integrity in the extracts is of paramount importance. Thus, the present paper reports total arsenic and arsenic species stability in alga samples (*Sargassum fulvellum* and *Hizikia fusiformis*), as well as in their aqueous extracts, which were stored in amber glass and polystyrene containers at different temperatures. Total arsenic determination was carried out by inductively coupled plasma atomic emission spectroscopy (ICP-AES), after sample acid digestion in a microwave oven, while arsenic speciation was conducted by anion exchange high performance liquid chromatography on-line coupled to ICP-AES, with and without sample introduction by hydride generation (HPLC-ICP-AES and HPLC-HG-ICP-AES), after aqueous microwave-assisted extraction.

The results obtained for solid alga samples showed that total arsenic (for Hijiki alga) and arsenic species present (As(V) for Hijiki and NIES No. 9 Sargasso) are stable for at least 12 months when samples are stored in polystyrene containers at $+20\,^\circ$C. On the other hand, a different behaviour was observed in the stability of total arsenic and As(V) species in aqueous extracts for both samples, being the best storage conditions for Sargasso extracts a temperature of $-18\,^\circ$C and polystyrene containers, under which they are stable for at least 15 days, while Hijiki extracts must be stored in polystyrene containers at $+4\,^\circ$C in order to ensure the stability for 10 days.
© 2007 Elsevier B.V. All rights reserved.

Keywords: Alga; Arsenic stability; High performance liquid chromatography; Hydride generation; Inductively coupled plasma atomic emission spectroscopy

1. Introduction

Arsenic is a toxic element widely distributed in the environment, due to both natural sources and anthropogenic applications, and its speciation has received significant attention over the last years due to its species-dependent toxicity [1]. Detailed information concerning analytical methods for arsenic species determination can be found in several reviews [2–4]. The analytical speciation of arsenic has been generally achieved with the use of hyphenated techniques, i.e. a chromatographic system coupled to an arsenic-selective detector. Alga are considered to accumulate high percentages of arsenic, so several authors have been focused on arsenic speciation analysis in this kind of samples during the last years [5–11].

The achievement of reliable results in speciation analysis requires not only sensitive techniques but also sureness of species stability. Hence, stability studies are necessary in that it is important to know with absolute certainty that there is not any species transformation during sample treatment and storage.

A number of sources can be cited as possible causes of arsenic species instability, such as chemical reactions between species, interactions with the container material, microbial activity, temperature, pH, concentration level or light action. Therefore, it is essential to take into account the influence of these factors on species stability in order to get both a representative speciation analysis of the sample studied and an accurate assessment of the environmental problem [12–14].

For arsenic analysis, contamination only occurs rarely, and events such as changes in oxidation state, changes induced by microbial activity or losses by volatilization or adsorption, have to be avoided. Several procedures are recommended for preservation of species integrity, such as freezing, cooling, acid-

* Corresponding author. Tel.: +34 913364214; fax: +34 913367958.
E-mail address: milagros.bonilla@upm.es (M.M.B. Simón).

ification, sterilization, deaeration, and/or storage in the darkness. Nevertheless, there is no general agreement on these procedures. For samples where bacteria exist naturally, storage at low temperatures, or even freeze-drying, is required to prevent biological activity from modifying the sample nature [13].

Previous studies on arsenic compounds stability has been focused mainly on water samples and inorganic arsenic forms [15]. Several acids (sulphuric, hydrochloric, nitric, phosphoric or ascorbic acid) have been proposed for arsenic stabilisation in water samples to reduce sample pH below 2, since acidification is necessary to keep the iron in solution, which avoided co-precipitation of arsenic or adsorption onto the iron oxy-hydroxide. Furthermore, acidification allows the storage of water samples at room temperature, where inorganic arsenic species remain stable for two months, both in Pyrex and polyethylene containers. Methylarsenicals are more stable than inorganic arsenicals both in water and in urine samples [2]. In water samples, MMA and DMA have shown stability during several months, when hydrochloric acid was added [12,13]. However, other authors have reported that acidification of treated wastewater samples leads to the transformation of As(III) into As(V), as well as the kinetics rise with the storage temperature [16]. The phosphoric acid addition to preserve inorganic arsenicals has been recommended in the case of water samples with high concentration levels of iron and manganese [17]. Freezing has been reported to induce chemical changes such as precipitation of arsenic species, which were not reversed on melting. Better results were obtained when samples were stored at +4 °C. Under these conditions, As(III) and As(V) at higher concentrations (20 μg L^{-1}) were stable for about 30 days, when samples were previously filtered (45 μm). Storage at higher temperatures (+20 and +40 °C) in the presence of light leads to oxidation processes from As(III) to As(V) and production of MMA from DMA. Flocculation, probably owing to the presence of phosphates, was also observed [12].

The use of additives has not improved arsenic species stability in urine samples, which can be stored at low temperatures (+4 and −20 °C) for two months. On the other hand, the addition of 0.1 M HCl to urine samples has shown to cause relative changes in inorganic arsenic species [18]. Palacios et al. [19] reported transformations of As(III) and AsC species in untreated urine samples by oxidation to As(V) and AsB species, respectively. Arsenic species stability in urine samples improved, for at least 67 days at ambient temperature or +4 °C, when samples are treated to obtain a clean-up dry residue.

Regarding solid samples, stability studies have been performed mainly on aqueous extracts. Pizarro et al. [20] reported that arsenic species in (1:1) methanol water extracts from rice remained stable for at least three months, whereas in fish and chicken tissue extracts, AsB was transformed into DMA over time. On the other hand, methylarsenicals compounds were stable in phosphoric acid extracts from soils, whereas As(III) oxidised to As(V). Furthermore, arsenite in phosphoric–ascorbic acid extracts from contaminated soil samples was also observed to be unstable [21].

Recovery studies should be also considered in order to assess the arsenic species stability during extraction and chromatogra-phy steps [11,22]. Since arsenic species stability is dependent on the matrix, concentration level and the treatment followed for sample analysis, it is necessary to perform stability studies for each case.

This work focuses on total arsenic and arsenic species stability in alga samples and their aqueous extracts. Storage temperature and container material were assessed. Losses, species transformations and matrix influence were studied. Stability tests on aqueous extracts obtained from alga samples allowed us to know the period of time during which extracts integrity can be maintained, in order to avoid the immediate analysis.

2. Experimental

2.1. Instrumentation

A MARS 5 Microwave oven (CEM, Matthews, NC, USA) was used for digestion and extraction of the samples. The temperature was monitored in a control vessel by an armoured fibre-optic temperature control probe. The reaction vessels used were made of Teflon for digestion and Pyrex for extraction procedures, respectively.

An Eppendorf centrifuge 5804 R (Hamburg, Germany) was used for the centrifugation of the alga extracts.

0.45 μm Millipore nylon filters were used to filter all the HPLC solutions, as well as 0.20 μm Millex syringe filters to filter the alga extracts before their injection in the HPLC system.

The inductively coupled plasma atomic emission spectrometry instrument used was a Liberty Series II Axial Sequential ICP-AES (Varian Australia, Mulgrave, Australia). The hydride generation system used was a VGA-77 unit (Varian). Before coupling the chromatographic system, the ICP-AES working conditions were optimised using a standard solution containing 1.0 mg L^{-1} of manganese. The arsenic signal was then optimised using a 1.0 mg L^{-1} arsenate standard solution for subsequent HPLC-ICP-AES experiments and a 0.1 mg L^{-1} arsenite standard solution when the hydride generation system was coupled.

The chromatographic system consisted of a Jasco PU-980 HPLC pump (Jasco, Tokyo, Japan) with a Rheodyne 7725 six-port sample injection valve fitted with a 100 μL sample loop (Rheodyne, CA, USA). Separations were carried out in a Hamilton PRP-X100 (250 mm × 4.1 mm, 10 μm) (Phenomenex, Torrance, CA, USA) anion exchange column. A guard column Hamilton PRP-X100 (25 mm × 2.3 mm, 12–20 μm) (Phenomenex) was used in order to preserve the analytical column.

The chromatographic system was then coupled to the ICP-AES instrument by a polytetrafluoroethylene capillary tube (20 cm, 0.5 mm I.D.), which connected the column outlet to the Meinhard nebuliser inlet. When the hydride generation unit was used, the chromatographic system was coupled to the hydride generation unit by the same capillary tube, running from the column outlet to the hydride generation unit inlet.

Chromatographic signals were registered using a Star 800 module interface box and processed using the Star software (Varian). Signal quantification was carried out in the peak area mode.

2.2. Reagents and standard solutions

Stock solutions of $1000 \, mg \, L^{-1}$ arsenic were prepared by dissolving the respective amount of the pure compound in deionised water (Milli-Q system, Millipore, USA). As(III) and As(V) standards solutions were prepared from $NaAsO_2$ and Na_2HAsO_4, respectively (Panreac, Barcelona, Spain), MMA from $CH_3AsO_3Na_2$ (Supelco, Bellefonte, PA, USA) and DMA from $(CH_3)_2AsNaO_2 \cdot 3H_2O$ (Fluka, Neu Ulm, Germany). The stock solutions were kept at $+4 \, °C$ in the darkness. Working solutions were prepared daily and then diluted with deionised water to the final concentration.

The eluent used for the chromatographic separations was phosphate buffer (pH 5.5) at a concentration of 17 mM. It was prepared by mixing independent solutions of $(NH_4)_2HPO_4$ and $(NH_4)H_2PO_4$ (Fluka, Neu Ulm, Germany) until the desired pH was reached.

All HPLC solutions were filtered and degassed before use.

Nitric acid 69.5% (Scharlau, Barcelona, Spain) was used to digest the samples.

Sodium borohydride solution 0.5% (w/v) was prepared by dissolving $NaBH_4$ powder (Aldrich, Milwaukee, WI, USA) of 98% purity in deionised water and stabilising it with 0.5% (w/v) sodium hydroxide (Fluka, Neu Ulm, Germany). The resulting solution was filtered and kept at $+4 \, °C$ in the darkness. Hydrochloric acid solution (4.0 M) was prepared by dilution of HCl 37% (Scharlau, Barcelona, Spain).

2.3. Alga samples

The reference material NIES No. 9, certified for total arsenic ($115 \pm 9 \, \mu g \, g^{-1}$), was a lyophilised Sargasso material (*Sargassum fulvellum*), purchased from National Institute for Environmental Studies (Tsukuba, Ibaraki, Japan). The alga sample Hijiki (*Hizikia fusiformis*) was acquired in food Spanish markets as dry material, grinded in a mill to a particle size of $125 \, \mu m$, and stored in a polystyrene container at $+20 \, °C$.

The alga samples selected for the stability study have been thoroughly studied [10,11]. Hijiki alga was selected due to its similarity to the certified reference material (Sargasso), in terms of total arsenic content and arsenic species present (As(V)) in both samples.

2.4. Procedures

2.4.1. Sample treatment

Total arsenic content in alga samples was determined by ICP-AES following the microwave digestion method described in a previous work [10]. The results obtained for five replicates were 106 ± 6 and $88 \pm 6 \, \mu g \, g^{-1}$ of arsenic for NIES No. 9 and Hijiki samples, respectively.

For arsenic species extraction, approximately 200 mg of alga sample were accurately weighed into a Pyrex vessel and 8 ml of deionised water were added. The vessel was introduced in the microwave-assisted extraction system and a temperature of $90 \, °C$ was applied for 5 min. Then, the extract obtained was centrifuged for 10 min at 14000 g. This extraction process was

Table 1
ICP-AES, hydride generation and chromatographic operating conditions

ICP-AES	
Forward power	1200 W
Photomultiplier tube voltage	650 V
Nebulisation argon pressure	180 kPa
Auxiliary argon flow rate	$1.50 \, L \, min^{-1}$
Coolant argon flow rate	$15.0 \, L \, min^{-1}$
Nebuliser type	Meinhard concentric glass
Hydride generation system	
Acid solution	4 M HCl
Reductant solution	0.5% (w/v) $NaBH_4$ (stabilised with 0.5% (w/v) NaOH)
Carrier argon pressure	350 kPa
Chromatographic system	
Guard column	Hamilton PRP-X100 (25 mm × 2.3 mm, 12–20 μm)
Analytical column	Hamilton PRP-X100 (250 mm × 4.1 mm, 10 μm)
Mobile phase	Phosphate buffer 17 mM at pH 5.5
Flow rate	$1.0 \, mL \, min^{-1}$
Injection volume	100 μl

repeated three times. The supernatants were mixed and diluted up to 25 mL with deionised water. The concentration of total arsenic extracted was determined by ICP-AES.

Prior to the chromatographic analysis, final extracts were filtrated with $0.20 \, \mu m$ Millex syringe filters. The arsenic species studied (As(III), As(V), MMA and DMA) were separated and detected by HPLC-HG-ICP-AES, using the operation conditions given in Table 1. All the extracts were also analysed by HPLC-ICP-AES, in order to check the absence of other arsenic species, different to those studied, in the samples. The analytical peaks obtained were evaluated in terms of peak area by external calibration at 193.696 nm line. The instrument drift was checked by injection of a standard solution every two samples injections.

The chromatographic profiles obtained by HPLC-ICP-AES and HPLC-HG-ICP-AES for standard solutions and the aqueous extracts from Sargasso and Hijiki alga, are shown in previous papers with references [10] and [11], respectively, as well as the analytical characteristics of both methods.

The arsenic species stability during the extraction method was confirmed by further experiments on spiked alga samples, due to the absence of reference materials certified for arsenic species, in a previous work [11].

2.4.2. Design of the stability study

The storage containers used for stability tests on aqueous extracts and dry samples were 12 mL vials of amber glass and polystyrene and 60 mL polystyrene containers, respectively. Containers were previously washed with deionised water, immersed in a 5% HNO_3 bath for 24 h, and finally rinsed with deionised water before use.

2.4.2.1. Stability test on dry alga samples.
For the stability test performed on dry alga samples, different portions of the solid were placed, previous homogenisation by manual shaking for 10 min, in 60 mL polystyrene containers, which were sealed

with parafilm and maintained in the darkness at +20 °C. The reference concentration values (C_{ref}) of total arsenic and arsenic species identified in the sample were evaluated by ten independent analyses prior to the beginning of the stability test. The stability study measurements were performed after 1, 7, 15, 30, 90, 180 and 365 days, preparing the sample for total arsenic determination and arsenic speciation immediately before the measurement. Only arsenic species stability test was carried out on the lyophilised Sargasso NIES No. 9, since this reference material is certified for total arsenic even though no information on species concentration and stability is available.

2.4.2.2. Stability test on alga aqueous extracts. The stability test on aqueous extracts was performed as follows: 24 alga sample portions of approximately 200 mg were processed following the extraction method specified in Section 2.4.1 (Sample treatment), from Section 2.4 (Procedure). The aqueous extracts obtained were mixed and placed into 30 polystyrene and 30 amber glass vials, which were sealed with parafilm until analysis. 15 vials of each container material were maintained in the darkness at −18 and +4 °C. A total of 60 vials were prepared to be stored under each experimental condition, and each vial was used only once. Once the samples were prepared and stored under the different conditions, three vials of each type were analysed after 1, 4, 7, 10 and 15 days, respectively. The reference concentration values (C_{ref}) were obtained from ten measurements of three different vials after sample preparation.

3. Results and discussion

The stability R_x, expressed as a percentage, was evaluated as the ratio of the average of three concentration measurements made under each storage condition (C_x) to the mean value (C_{ref}) of ten different measurements made at reference time ($t = 0$), as follows [23,24]:

$$R_X = \frac{C_X}{C_{ref}} \times 100$$

The uncertainty U_x in the ratio R_x was obtained from the coefficient of variation of each set of measurements according to the following expression [23,24]:

$$U_X = \sqrt{(CV_X^2 + CV_{ref}^2)} \times R_X$$

where CV_x is the coefficient of variation of three independent measurements under each storage condition and CV_{ref} is the coefficient of variation obtained for the reference conditions.

In the case of ideal stability, R_x should be 100%, but in practice there are random variations due to the uncertainty in the measurements because of the standard deviation observed. Therefore, the value R_x should be between the limits [$100 - U_x$] and [$100 + U_x$] to conclude the species stability [23,24].

3.1. Stability tests on dry alga samples

Total arsenic and arsenic species stability was determined in Hijiki alga sample. In the reference material of lyophilised
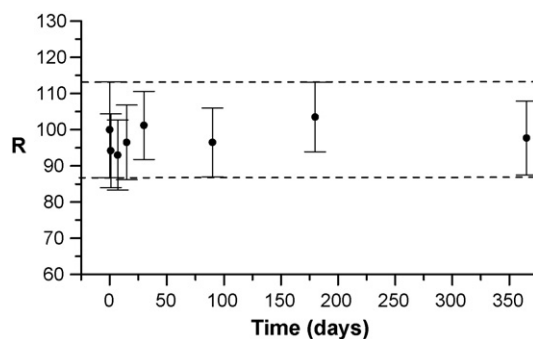
Fig. 1. Total As stability in Hijiki dry alga stored at +20 °C in polystyrene containers; dots: stability R_x; I uncertainty for each point U_x; dashes: uncertainty associated with $t = 0$ days.

Sargasso, only the arsenic species stability test was performed. Both samples were analysed immediately after reception. The reference concentration value, C_{ref} ($t = 0$ days, $n = 10$) used in the stability test, of total arsenic for Hijiki sample was 86 ± 8 μg g^{-1}, while the reference concentration values of As(V) species for Sargasso and Hijiki samples were 73 ± 4 and 62 ± 3 μg g^{-1}, respectively.

The results obtained for total arsenic in Hijiki alga after 1, 7, 15, 30, 90, 180 and 365 days are given in Fig. 1, and show that total arsenic in the dry material is stable when the sample is stored in polystyrene containers at +20 °C, for at least one year.

Fig. 2 shows the results obtained for the arsenic species found, which is As(V), in Sargasso (Fig. 2a) and Hijiki (Fig. 2b) samples. This study was performed during the same time period and under the same storage conditions as in the total arsenic study. The results allow us to conclude that the identified arsenic
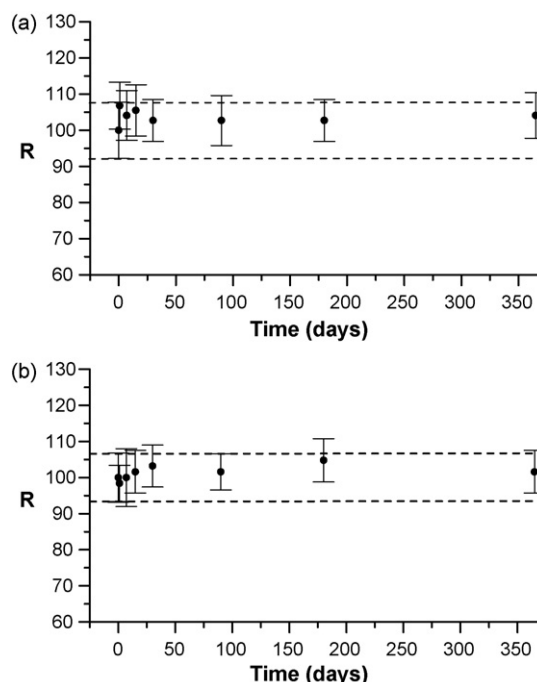
Fig. 2. As(V) species stability in (a) lyophilised Sargasso and (b) dry Hijiki stored at +20 °C in polystyrene containers.

species is stable when samples are stored in polystyrene containers at +20 °C, for at least one year.

Therefore, the storage of the dry material could be carried out without any special consideration, in polystyrene containers at +20 °C.

3.2. Stability tests on aqueous extracts

The total arsenic stability test on the aqueous extracts from Sargasso and Hijiki algae were carried out under the conditions indicated in the above section. The temperature of +20 °C was excluded in order to avoid the microbiological activity,

which may cause sample decomposition. The stability study was limited to 15 days in that the decomposition of the aqueous extracts was observed. The reference concentration values, C_{ref}, ($t = 0$ days, $n = 10$) of total arsenic and As(V) species found in the aqueous extracts from Sargasso sample were 94 ± 5 and $72 \pm 4 \ \mu g \ g^{-1}$, respectively, while those found in Hijiki aqueous extracts were 72 ± 4 and $62 \pm 7 \ \mu g \ g^{-1}$, respectively.

The results obtained (Fig. 3) show that total arsenic in the aqueous extracts from Sargasso (Fig. 3a) and Hijiki (Fig. 3b) samples stored at -18 °C in polystyrene containers, as well as at $+4$ °C in both kind of containers, is stable for at least 15 days, in spite of the decomposition of the extracts observed at $+4$ °C
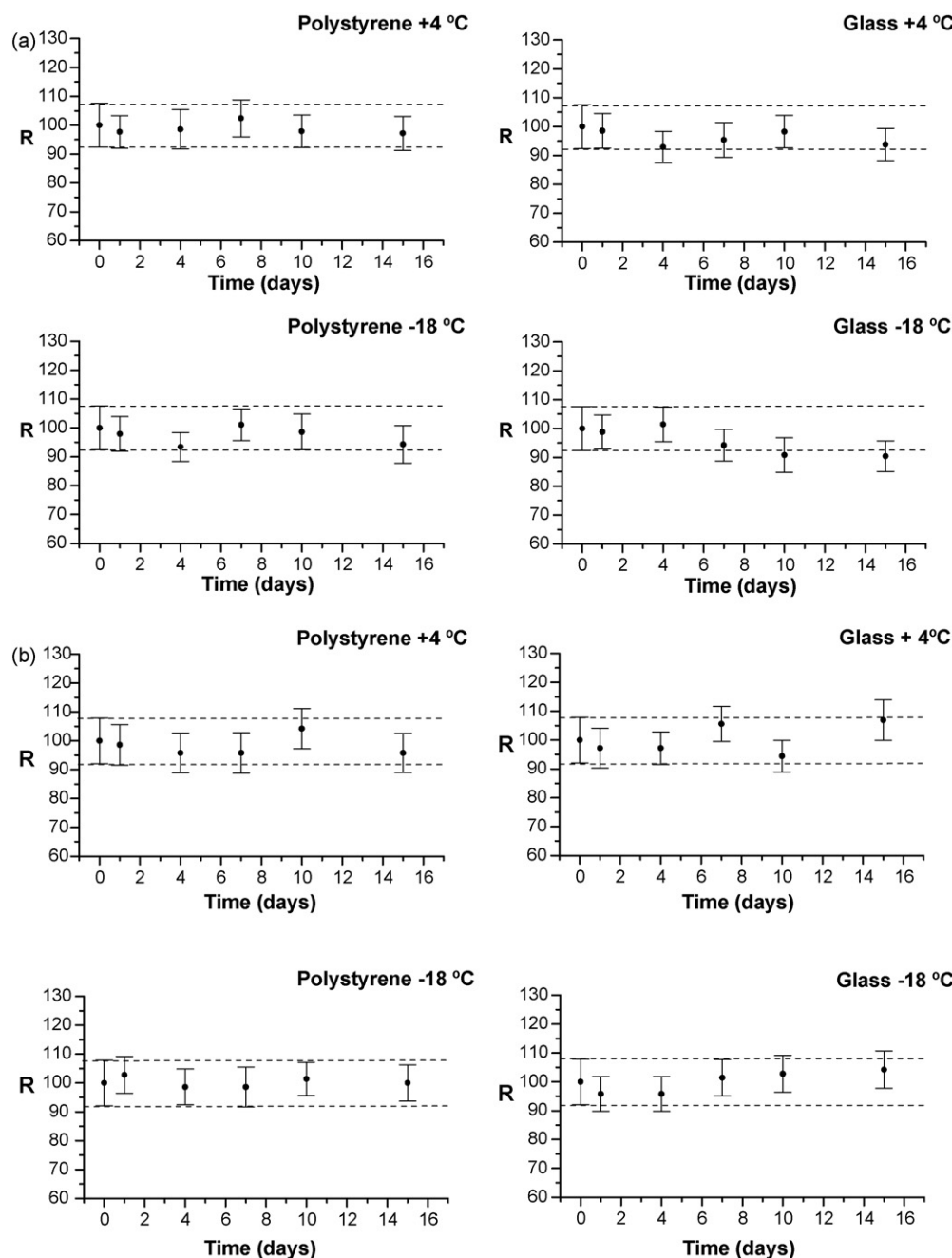
Fig. 3. Total As stability in the aqueous extracts from (a) Sargasso and (b) Hijiki stored at +4 and −18 °C in polystyrene and amber glass containers.

since the 10th day of storage. However, a different behaviour was observed in glass containers at −18 °C for both samples studied. Thus, total arsenic remains stable in the aqueous extracts from Hijiki alga, while significant losses were observed in Sargasso extracts, so the stability can only be ensured for 7 days in the extracts stored under these conditions.

Fig. 4 shows the results of the stability test obtained for the species As(V) in the aqueous extracts of Sargasso (Fig. 4a) and Hijiki (Fig. 4b) samples.

The results obtained for Sargasso extracts (Fig. 4a) show that As(V) species remains stable for at least 15 days when extracts are stored in polystyrene at both temperatures tested. However, in amber glass containers As(V) remains stable at −18 °C, while significant losses are observed at +4 °C after 10 days of storage.

Therefore, a relation between the stability of total arsenic and As(V) species present in Sargasso extracts stored in glass containers was not found. Total arsenic losses observed at −18 °C and As(V) species stability at this same temperature may be associated with precipitation or adsorption processes of different arsenic species, which were not reversed on melting [12]. On the other hand, As(V) species instability observed at +4 °C can not be related to similar processes, due to total arsenic stability observed under these conditions. Furthermore, since any new peak was not detected in the chromatograms by HPLC-ICP-AES and HPLC-HG-ICP-AES, a species transformation cannot be confirmed. However, As(V) species instability is coincident with the extract decomposition, which leads us to think that a fraction of this species may be transformed or captured
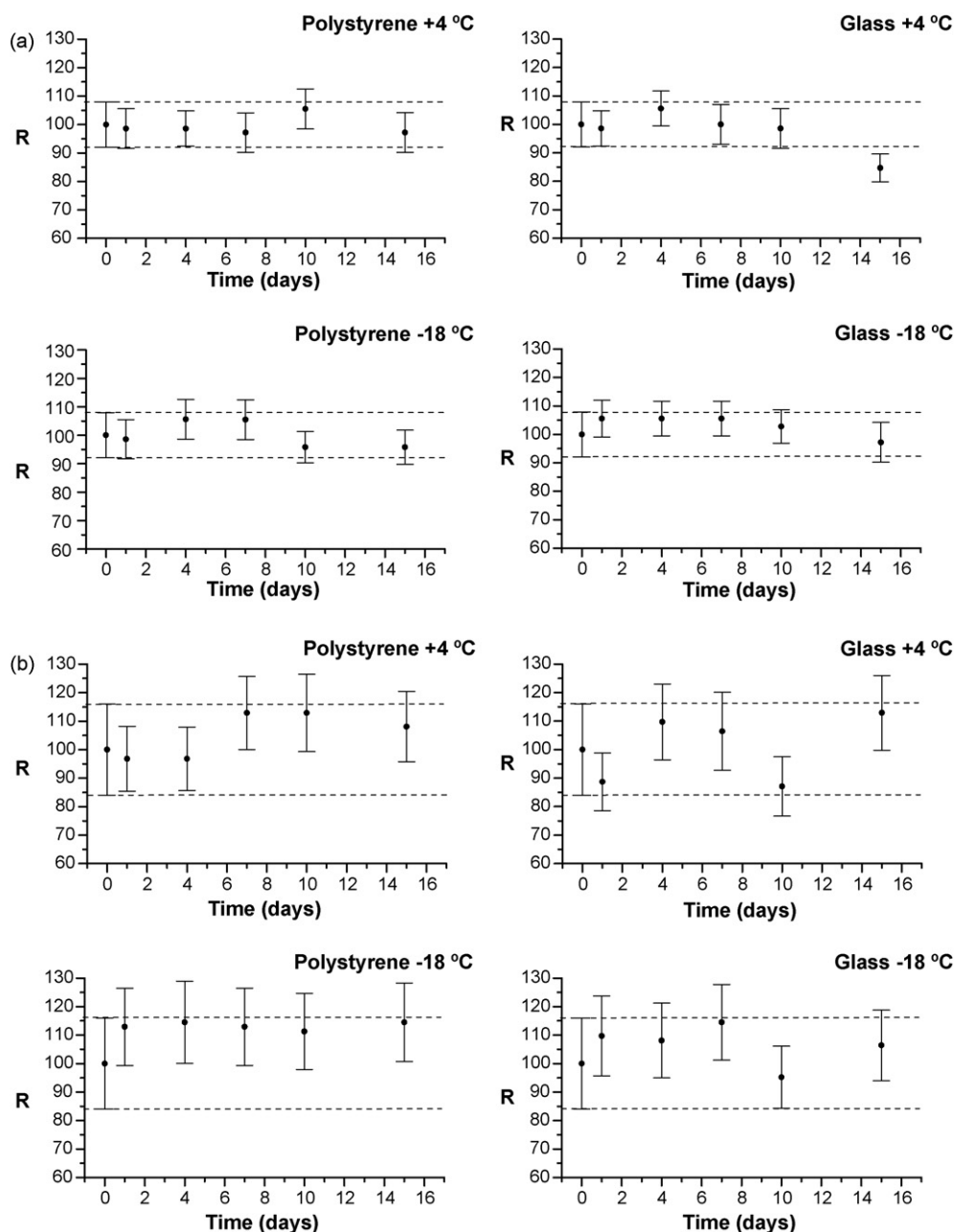
Fig. 4. As(V) stability in the aqueous extracts from (a) Sargasso and (b) Hijiki stored at +4 and −18 °C in polystyrene and amber glass containers.
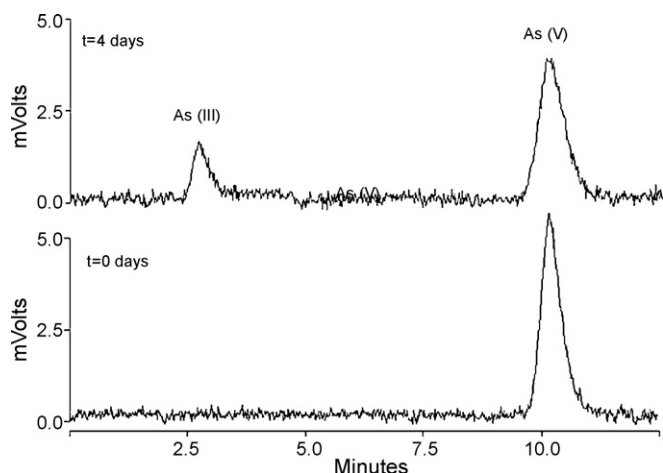
Fig. 5. HPLC-HG-ICP-AES chromatogram obtained for aqueous extracts from Hijiki stored at −18 °C in polystyrene containers at the 4th day of storage, compared to the reference chromatogram (t = 0 days).

as a complex form, which can be retained in any step of the chromatographic method.

The results obtained for Hijiki extracts (Fig. 4b) show that As(V) species remains stable for at least 15 days at both temperatures tested and in both types of containers. However, in Hijiki extracts stored at −18 °C and in both types of containers tested, the appearance of As(III) species was observed since the 4th day of storage (Fig. 5). The concentration of As(III) found in the extracts stored in both amber glass and polystyrene containers was about $(3.4 \pm 1.5)\,\mu g\,g^{-1}$, and remained stable for the remaining time of the study. The species As(III) appearance is not the result of the transformation of As(V), since losses of this species were not observed. Furthermore, reduction reactions are not liable to occur in aqueous solutions without deaeration. It is more likely that As(III) species comes from the transformation or release from non-detectable arsenic species present in the extract by the chromatographic method used.

4. Conclusions

The results obtained for the stability tests on solid alga samples (lyophilised Sargasso and dry Hijiki) show that transport and storage of these materials can be carried out at room temperature using polystyrene containers. Furthermore, they show that it is not necessary to carry out the lyophilisation of the sample in order to enhance its stability.

Regarding the aqueous extracts, different results were found for both samples. The optimum storage conditions for Sargasso extracts consist of using polystyrene containers and a temperature of −18 °C, under which both total arsenic and As(V) species remain stable for at least 15 days. However, Hijiki extracts can be stored in the same type of containers at +4 °C for a maximum of 10 days.

The differences observed in both samples studied show the influence of sample matrix on the stability of total arsenic and arsenic species. This fact emphasizes the necessity of conducting stability studies on each kind of sample studied.

Acknowledgement

References

[1] S. Karthikeyan, S. Hirata, Appl. Organomet. Chem. 18 (2004) 323.
[2] Z. Gong, X. Lu, M. Ma, C. Watt, X.C. Le, Talanta 58 (2002) 77.
[3] S. McSheehy, J. Szpunar, R. Morabito, Ph. Quevauviller, Trends Anal. Chem. 22 (2003) 191.
[4] J. Szpunar, Analyst 125 (2000) 963.
[5] G. Raber, K.A. Francesconi, K.J. Irgolic, W. Goessler, Fresenius J. Anal. Chem. 367 (2000) 181.
[6] R. Tukai, W.A. Maher, I.J. McNaught, M.J. Ellwood, Anal. Chim. Acta 457 (2002) 173.
[7] W. Li, C. Wei, C. Zhang, M. Van Hulle, R. Cornelis, X. Zhang, Food Chem. Toxicol. 41 (2003) 1103.
[8] E. Schmeisser, W. Goessler, N. Kienzl, K.A. Francesconi, Anal. Chem. 76 (2004) 418.
[9] O. Muniz-Naviero, A. Moreda-Pineiro, A. Bermejo-Barrera, P. Bermejo-Barrera, At. Spectrosc. 25 (2004) 79.
[10] S. García Salgado, M.A. Quijano Nieto, M.M. Bonilla Simón, Talanta 68 (2006) 1522.
[11] S. García Salgado, M.A. Quijano Nieto, M.M. Bonilla Simón, J. Chromatogr. A 1129 (2006) 54.
[12] J.L. Gómez Ariza, E. Morales, D. Sánchez-Rodas, I. Giráldez, Trends. Anal. Chem. 19 (2000) 200.
[13] M. Leermakers, W. Baeyens, M. De Gieter, B. Smedts, C. Meert, H.C. De Bisschop, R. Morabito, P. Quevauviller, Trends. Anal. Chem. 25 (2006) 1.
[14] G.E.M. Hall, J.C. Pelchat, G. Gauthier, J. Anal. At. Spectrom. 14 (1999) 205.
[15] L.F. Braña, F. Sánchez, M.A. Palacios, M.M. Bonilla, R. Torralba, Química Analítica 20 (2002) 181.
[16] M. Segura, J. Muñoz, Y. Madrid, C. Cámara, Anal. Bioanal. Chem. 374 (2002) 513.
[17] B. Daus, H. Weiss, J. Mattusch, R. Wennrich, Talanta 69 (2006) 430.
[18] J. Feldmann, V.W.-M. Lai, W.R. Cullen, M. Ma, X. Lu, X.C. Le, Clin. Chem. 45 (1999) 1988.
[19] M.A. Palacios, M. Gómez, C. Cámara, M.A. López, Anal. Chim. Acta 340 (1997) 209.
[20] I. Pizarro, M. Gómez, C. Cámara, M.A. Palacios, Anal. Chim. Acta 495 (2003) 85.
[21] M.J. Ruiz-Chancho, J.F. López-Sánchez, R. Rubio, Anal. Bioanal. Chem. 387 (2007) 627.
[22] K.A. Francesconi, D. Kuehnelt, Analyst 129 (2004) 373.
[23] M. Segura, Y. Madrid, C. Cámara, C. Rebollo, J. Azcárate, G. Kramer, Ph. Quevaullier, J. Environ. Monit. 2 (2000) 576.
[24] P. Moreno, M.A. Quijano, A.M. Gutiérrez, M.C. Pérez-Conde, C. Cámara, Anal. Bioanal. Chem. 374 (2002) 466.

Determination of iron in water samples by adsorptive stripping voltammetry with a bismuth film electrode in the presence of 1-(2-piridylazo)-2-naphthol

Rodrigo Segura [a],*, María Inés Toral [a], Verónica Arancibia [b]

[a] *Departamento de Química Analítica, Facultad de Química, Universidad de Chile,*
Las Palmeras 3425, Casilla 653, Santiago, Chile
[b] *Departamento de Química Inorgánica, Facultad de Química, Pontificia Universidad Católica de Chile,*
Vicuña Mackenna 4860, Santiago 22, Chile

Abstract

An adsorptive stripping voltammetry method for the determination of iron has been developed. The procedure is based on the adsorptive collection of a complex of iron with 1-(2-piridylazo)-2-naphthol (PAN) on a bismuth-coated glassy carbon electrode (BiFE). Factors affecting the stripping performance, such as pH, PAN concentration (C_{PAN}), potential, accumulation time (E_{ads}, t_{ads}), and interference by other ions were also studied. The optimum conditions were obtained in a $0.1 \, mol \, L^{-1}$ acetate buffer at pH 4.0, C_{PAN} $5.0 \, \mu mol \, L^{-1}$, t_{ads} 60 s, E_{ads} $-400 \, mV$, pulse height 4.0 mV, pulse amplitude 25 mV, and frequency 15 Hz. The detection limit was found to be $0.1 \, \mu g \, L^{-1}$ when a t_{ads} of 60 s was used, and the linear range was from 0.4 to $60.0 \, \mu g \, L^{-1}$. The proposed procedure was validated by determining of Fe(III) in CRM-MFD, QCS-19 and CRM-SW certified reference materials and applied in seawater samples with satisfactory results.
© 2008 Elsevier B.V. All rights reserved.

Keywords: Adsorptive stripping voltammetry; Iron; 1-(2-Piridylazo)-2-naphthol (PAN); Seawater samples; Bismuth film electrode

1. Introduction

Total dissolved iron in surface waters of oceanic regimes can range from less than 0.05 to greater than $10 \, nmol \, L^{-1}$ [1–3]. However, in some beaches near populated or industrial areas iron concentration can be higher. The analysis of iron in seawater is difficult due to both the low concentrations and the seawater matrix. Therefore, shipboard determination of iron in seawater requires a sensitive analytical technique and trace-metal clean sample handling to obtain meaningful, oceanographically consistent results. The presence of iron in research vessels, laboratories and many manufactured materials poses a risk of contamination during sampling, filtration, storage and analysis. The first large-scale international intercomparison of analytical methods for the determination of dissolved iron in seawater was carried out between October

2000 and December 2002. The exercise was conducted as a rigorously "blind" comparison of seven analytical techniques by 24 international laboratories. For the complete dataset of 45 results (after excluding three outliers not passing the screening criteria), the mean concentration of dissolved iron in the ironages samples was $0.59 \pm 0.21 \, nmol \, L^{-1}$, with a coefficient of variation of 36% [4]. Higher values were found in acidified samples from Monterey Bay by a flow injection method combined with inductively coupled plasma sector field mass spectrometry (ICP-SFMS) using the NTA superflow resin in the preconcentration step (average $2.89 \, nmol \, L^{-1}$) [5]. Iron can be determined by several methods such as inductively coupled plasma mass spectrometry (ICP-MS) [6], electrothermal atomization atomic absorption spectrometry (ETAAS) [7], cathodic stripping voltammetry (CSV) [8–10], luminescence [11], and spectrophotometry [12], preceded sometimes by column preconcentration. However, most of the sensitive and selective methods available are expensive to be used in routine analysis (ICP-MS and ETAAS). Electroanalytical techniques like anodic stripping voltammetry (ASV), cathodic stripping voltammetry (CSV),

and adsorptive stripping voltammetry (AdSV) have important advantages including high sensitivity, accuracy and precision, as well as the low cost of instrumentation. AdSV is based on prior accumulation of the analyte on a suitable working electrode by potential controlled adsorption and subsequent electrochemical oxidation or reduction of the preconcentrated species. For decades, due to several electrochemical advantages, mercury electrodes have been widely used in stripping analysis. However, the well-known toxicity and handling inconveniences of mercury have recently declined considerably the popularity of mercury electrodes. The bismuth film electrode (BiFE) was introduced as an extremely promising alternative, based in that no present toxic character in relation to with those mercury electrodes [13–22]. BiFE has been used principally in anodic stripping voltammetry (Fe(III) [23]; Sn [24]; U [25]; Co [26–28]; Ni [29]; Mo [30]; Cr [31,32]; V [33]) and over the last years (2003–2007), a few selected application of AdSV on the BiFE have also been reported with promising results (Cr with DTPA [34]; Co-DMG [35–37]; Ni-DMG [38]; Co and Ni with DMG [39–41]; U-Cupferron [42]; Al-Cupferron [43]).

The aim of this study was to optimize the determination of iron using the bismuth film electrode. The metal was accumulated as the Fe(III)-1-(2-piridylazo)-2-naphthol (PAN) complex. This ligand has been widely used as chomophore reagent in spectroscopic techniques for the determination of several metal ions at trace level, but there are no reports on adsorptive stripping voltammetry with BiFE. The method was validated using certified reference material (CRM-MFD mixed food diet and QCS-19 standard solution) and was applied to the analysis of seawater samples obtained from five beaches in highly populated zones.

2. Experimental

2.1. Instruments

Square wave adsorptive stripping voltammograms (SWAdSV) were obtained with a CV50W Voltammetric analyzer (Bioanalytical Systems, Inc., BAS, USA). A 10 mL capacity cell was equipped with Ag/AgCl/KCl 3 mol L^{-1} reference electrode, a glassy carbon working electrode (3-mm diameter, BAS, USA) and auxiliary platinum electrode. A mechanical mini-stirrer, and a capillary to supply an inert gas were also used. An Orion pH meter was used to determine the pH of the solutions.

2.2. Reagents

All solutions were prepared with ultra pure water from a Millipore Milli-Q system (Milford, MA, USA). Bismuth and iron standard solutions (1000 mg L^{-1}) were obtained from Merck (Darmstadt, Germany). Acetic acid buffers (pH 3.0–6.0) were prepared by mixing 5.7 mL of acid and diluting to 1 L with water. The pH was adjusted with sodium hydroxide solution. A 1 mmol L^{-1} solution of PAN (Sigma) was prepared by dissolving 0.2493 g of solid compound in 100 mL of ethanol. ASTM D 665 synthetic seawater was obtained from Aldrich.

Certified reference material of seawater (CRM-SW), trace metals in mixed food diet (CRM-MFD) reference materials, and quality control standards (QCS-19) obtained from high-purity standards (Charleston, SC, USA) were used for validation measurements.

2.3. Preparation of BiFE electrode

The glassy carbon electrode (GCE) was polished with 0.3-μm alumina powder, then, washed with deionized water in an ultrasonic bath. Bismuth was deposited on the GCE from 10.0 mL of a 100 mg L^{-1} Bi(III) solution containing 0.1 mol L^{-1} of acetate buffer (pH 5.0) at an applied potential of −1000 mV vs. Ag/AgCl for 5 min with stirring. The modified electrode was rinsed with water and was ready for use.

2.4. Procedure

All bottles and containers used for standards and samples were thoroughly cleaned with 5% nitric acid before use. Filtration was done through 0.45-μm membrane filters. Seawater samples were obtained from five different beaches of Viña del Mar (Chile) in a highly populated zone and near copper and oil industries.

All voltammetric measurements were carried out in 0.10 mol L^{-1} acetate buffer solution (pH 4.0) at room temperature (23 ± 2 °C) containing 5.0 μmol L^{-1} PAN as complexing agent. The solution was purged with nitrogen for at least 5 min. A deposition potential of −400 mV vs. Ag/AgCl was applied to the working electrode. During the deposition step, the solution was stirred, and after an equilibration period of 10 s the voltammogram was recorded by applying a negative-going potential scan between −300 and −1100 mV. Square wave voltammograms were obtained with an amplitude of 25 mV, a frequency of 15 Hz, and a potential step of 4 mV.

3. Results and discussion

3.1. Cyclic voltammetry

Two successive cyclic voltammograms of a solution containing PAN in the presence and absence of Fe(III) are shown in Fig. 1 (scan between −300 and −1250 mV). In the absence of Fe(III) a cathodic peak was obtained at −470 mV (solid line in Fig. 1), attributed to the reduction of free PAN. In the presence of Fe(III) the voltammograms show two peaks at −470 and −670 mV (dotted line in Fig. 1). The second peak is attributed to the reduction of the Fe(III)–PAN complex. In the back scan no peaks were observed, suggesting that the reduction of the free PAN and the reduction of the complex are irreversible processes.

3.2. Effect of pH

The formation of the complexes and their stability are strongly dependent on the pH of the solution. The influence of pH on the peak current of the Fe(III)–PAN complex was
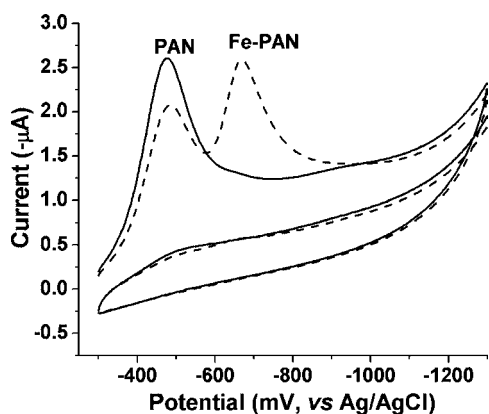
Fig. 1. Cyclic voltammograms of a solution containing $10.0\,\mu mol\,L^{-1}$ PAN (solid line) plus $20.0\,\mu g\,L^{-1}$ Fe(III) (dotted line) in $0.1\,mol\,L^{-1}$ acetate buffer, pH 4.0, with E_{ads} $-400\,mV$, t_{ads} 60 s, and a scan rate of $100\,mV\,s^{-1}$.

studied in the range of pH 3.0–6.0 in acetate buffer media (Fig. 2). It was found that at pH 4.0 the peak current of the Fe(III)–PAN complex was maximum. At higher pH values the peak current decreases and then remains constant. This profile indicates that about pH 4.0 offers the most favorable performance, and this value was used in all succeeding measurements.

3.3. Effect of adsorptive potential

The adsorption of a complex on BiFE depends strongly not only on the potential at which the accumulation process is carried out, but also on both the complex and the electrode charge. Complexes with positive charge will be adsorbed strongly on surfaces with a negative charge. The effect of adsorptive potential on the peak current of the Fe(III)–PAN complex was studied in the range between -300 and $-1100\,mV$ (Fig. 3). The peak current due to the Fe–PAN complex increased from -300 to $-400\,mV$ and then decreased to zero. The peak current was obtained at about $-400\,mV$, and this value was used in all later measurements.

Fig. 3. Effect of accumulation potential on the peak current of the Fe–PAN complex. Conditions: Fe(III) $10.0\,\mu g\,L^{-1}$; PAN $5.0\,\mu mol\,L^{-1}$; supporting electrolyte $0.1\,mol\,L^{-1}$ acetate buffer, pH 4.0; t_{ads} 60 s; amplitude 25 mV; frequency 15 Hz; step potential 4 mV, and stirring speed in the accumulation step 700 rpm.

3.4. Effect of accumulation time

The effect of accumulation time on the Fe(III)–PAN complex peak current was studied in the 0–400 s range in solutions containing 0.5, 0.9 and $10.0\,\mu g\,L^{-1}$ of Fe, as illustrated in Fig. 4. It is seen that the peak current of the Fe(III)–PAN complex increases linearly as accumulation time increases, up to 80 s ($10.0\,\mu g\,L^{-1}$), 120 s ($0.9\,\mu g\,L^{-1}$), and 200 s ($0.5\,\mu g\,L^{-1}$). At longer times the peak current for higher concentration ($10.0\,\mu g\,L^{-1}$) decreased notoriously and for 0.5 and $0.9\,\mu g\,L^{-1}$ concentration became almost constant, probably due to saturation of the film electrode. For succeeding studies an accumulation time of 60 s was chosen.

3.5. Effect of PAN concentration

PAN concentration affects greatly the voltammetric peak height. Fig. 5 shows the effect when PAN concentration was varied from 1.0 to $17.0\,\mu mol\,L^{-1}$. The peak current of the complex was maximum between 3.8 and $5.0\,\mu mol\,L^{-1}$ of ligand concentration; for higher values a significant decrease was seen due to

Fig. 2. Effect of pH on the peak current of the Fe–PAN complex. Conditions: Fe(III), $10.0\,\mu g\,L^{-1}$; PAN, $5.0\,\mu mol\,L^{-1}$; supporting electrolyte, $0.1\,mol\,L^{-1}$ acetate buffer; E_{ads} $-400\,mV$; t_{ads} 60 s; amplitude 25 mV; frequency 15 Hz; step potential 4 mV, and stirring speed in the accumulation step 700 rpm.
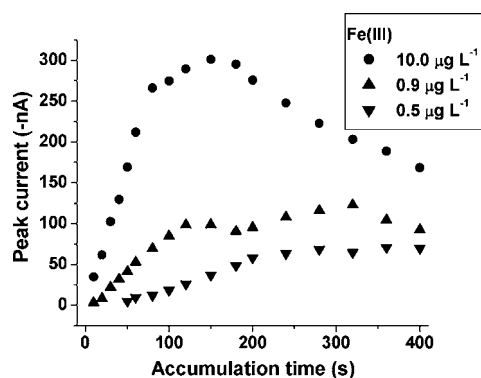
Fig. 4. Effect of accumulation time on the peak current of the Fe–PAN complex. Conditions: Fe(III) 0.5, 0.9, and $10.0\,\mu g\,L^{-1}$; PAN $5.0\,\mu mol\,L^{-1}$; supporting electrolyte $0.1\,mol\,L^{-1}$ acetate buffer, pH 4.0; E_{ads} $-400\,mV$; amplitude 25 mV; frequency 15 Hz; step potential 4 mV, and stirring speed in accumulation step 700 rpm.
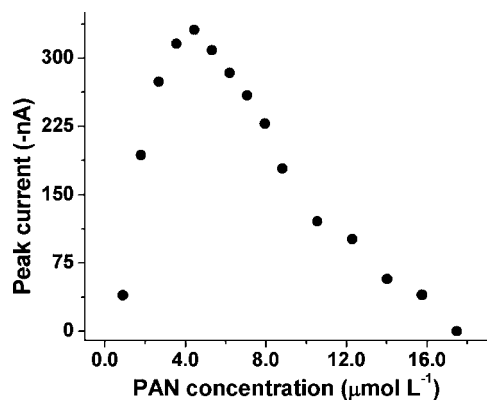
Fig. 5. Effect of PAN concentration on the peak current of $10.0 \mu g L^{-1}$ Fe(III). Conditions: supporting electrolyte $0.1 mol L^{-1}$ acetate buffer, pH 4.0; E_{ads} $-400 mV$; t_{ads} 60 s; amplitude 25 mV; frequency 15 Hz; step potential 4 mV and stirring rate in accumulation step 700 rpm.

competitive adsorption between free PAN and the Fe(III)–PAN complex on the electrode. A PAN concentration of $5.0 \mu mol L^{-1}$ was used in all succeeding measurements.

3.6. Construction of calibration curves and determination of detection limits and linear range

For the evaluation of the analytical parameters, a study of the influence of the concentration of the Fe(III)–PAN complex was made in aqueous solution under the optimal conditions mentioned above. Measurements were made with successive additions of aliquots of Fe(III) solution, with increments of about $0.9 \mu g L^{-1}$. An accumulation time of 60 s and an accumulation potential of $-400 mV$ were applied. Fig. 6(A) shows the voltammograms and Fig. 6(B) calibrate curve obtained. The peak current increased linearly with metal concentration in the range of 0.9–$60.0 \mu g L^{-1}$ ($Y = 3.591x + 11.138; R^2 = 0.998$). The detection limit was $0.10 \mu g L^{-1}$ as Fe(III) [44]. A series of repetitive measurements with $20.0 \mu g L^{-1}$ of Fe(III) solution produced a very stable response with a relative standard devi-
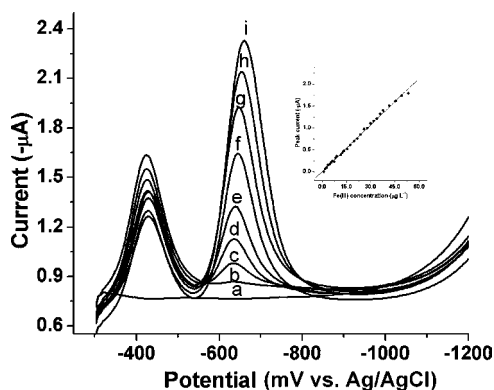
Fig. 6. (A) Adsorptive voltammograms of PAN solution in the presence of increasing amounts of Fe(III). Conditions: E_{ads} $-400 mV$; t_{ads} 60 s; amplitude 25 mV; frequency 15 Hz; step potential 4 mV, and stirring speed in accumulation step 700 rpm (a) supporting electrolyte $0.1 mol L^{-1}$ acetate buffer, pH 4.0; (b) PAN $5 \mu mol L^{-1}$; (c–i) Fe(III) 10.0, 20.0, 29.9, 39.8, 49.8, 59.6 and $69.5 \mu g L^{-1}$. (B) Dependence of peak current of Fe(III)–PAN complex on Fe(III) concentration.

Table 1
Analytical results of Fe determination in synthetic seawater, in certified reference material and in seawater samples

Sample	Fe found ($\mu g L^{-1}$)	Fe certified ($\mu g L^{-1}$)
Synthetic seawater[a]	11.0 ± 1.0	10.0 spiked
Synthetic seawater[a]	41.0 ± 2.5	40.0 spiked
CRM-MFD mixed food dietary[a]	823.0 ± 0.3	800.0
QCS-19 quality control[a]	$109.3 \pm 4.0 mg L^{-1}$	$100.0 mg L^{-1}$
CRM-SW[a]	23.0 ± 1.2	20.0
1[b]	58.0 ± 1.9	60.0 ± 0.2[c]
2[b]	41.0 ± 1.3	40.0 ± 0.2[c]
3[b]	6.0 ± 0.8	5.0 ± 0.2[c]
4[b]	42.0 ± 1.5	40.0 ± 0.2[c]
5[b]	ND	ND[c]

[a] $n = 8$.
[b] $n = 3$.
[c] Values obtained with ICP-MS.

ation of 3.8% (t_{ads} 60 s). These results were obtained without an electrochemical cleaning period, using the same bismuth electrode surface, indicative of total desorption of the complex.

3.7. Interferences

High sensitivity and reproducibility are coupled with high selectivity. The possible interference of various trace metals was investigated to test for selectivity. When a solution containing Ag(I), Al(III), As(III), Bi(III), Cu(II), Cd(II), Cr(III), Mo(VI), Ni(II) and Zn(II) at $100 \mu g L^{-1}$ concentration contains $20.0 \mu g L^{-1}$ of Fe(III) in the presence of $5.0 \mu mol L^{-1}$ of PAN (pH 4.0), the peak current of the Fe(III)–PAN complex was not affected. This agrees with literature reports, because these metals form complexes with PAN at pH higher than 4.0, and their reduction peaks were not observed in this potential zone.

3.8. Validation of the methodology

The usefulness of the present method was evaluated by examining the analysis of Fe(III) in CRM-MFD mixed food diet, seawater CRM-SW certified reference material, and QCS-19 quality control standards using an ex situ plated bismuth film electrode. A standard addition method was used for Fe(III) quantitation. Three replicate analyses were carried out for each sample. The results are given in Table 1, indicating that the proposed method is applicable to the analysis of seawater samples containing more than $0.1 \mu g L^{-1}$ of Fe(III). The proposed method was successfully applied to the determination of iron in synthetic seawater (ASTM D665) spiked with 10.0 and $40.0 \mu g L^{-1}$ of Fe(III).

3.9. Application of the proposed method

Direct measurements of the samples were not possible due to lack of reproducibility. For that reason, 10.0 mL aliquots of the samples were previously digested with concentrated nitric acid and warmed on a hot plate almost to dryness. The pH was then adjusted to 4.0, the volume was made up to 10.0 mL with
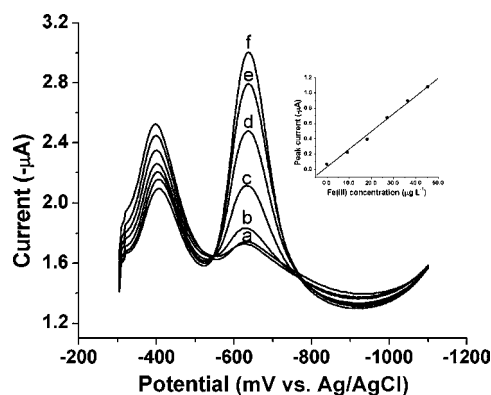
Fig. 7. (A) Typical voltammograms for the determination of Fe(III) contents in a seawater sample by the standard addition method. Conditions: E_{ads} −400 mV; t_{ads} 120 s; amplitude 25 mV; frequency 15 Hz; step potential 4 mV, and stirring speed in accumulation step 700 rpm (a) sample in 0.1 mol L^{-1} acetate buffer, pH 4.0; (b) (a) plus 9.1; (c) (a) plus 18.1; (d) (a) plus 27.2; (e) (a) plus 36.2 and (f) (a) plus 45.2 μg L^{-1} of Fe(III), respectively. (B) Dependence of peak current of the Fe(III)–PAN complex in a seawater sample in the presence of increasing amounts of Fe(III).

deionized water, and Fe(III) was determined. Iron concentration was obtained using the standard addition method. Adsorptive voltammograms of a digested seawater sample are shown in Fig. 7(A) and calibrate curve in Fig. 7(B). The data obtained with spiked and real samples were compared with those obtained by inductively coupled plasma spectrometry (ICP) in a service laboratory. The results obtained by both methods were compared (Table 1), showing that there are no significant differences between them.

4. Conclusion

The optimized method has been successfully applied to the determination of Fe(III) in seawater samples with good accuracy and precision. The proposed method is inexpensive and fast. The detection limit of 0.10 μg L^{-1} can be lowered further by increasing accumulation time. Acceptable agreement was found between the results obtained and the values of certified reference material.

Acknowledgement

References

[1] R.M. Gordon, J.H. Martin, G.A. Knauer, Nature 299 (1982) 611.
[2] D.A. Weeks, K.W. Bruland, Anal. Chim. Acta 453 (2002) 21.
[3] L. Vong, A. Laës, S. Blain, Anal. Chim. Acta 588 (2007) 237.
[4] A.R. Bowie, E.P. Achterberg, P.L. Croot, H.J.W. de Baar, P. Laan, J.W. Moffett, S. Ussher, P.J. WorsfoldL, Mar. Chem. 98 (2006) 81.
[5] M.C. Lohan, A.M. Aguilar-Islas, R.P. Franks, K.W. Bruland, Anal. Chim. Acta 530 (2005) 121.
[6] J. Wu, E.A. Boyle, Anal. Chim. Acta 367 (1998) 183.
[7] M. Grotti, M.L. Abelmoschi, F. Soggia, R. Frache, Anal. Bioanal. Chem. 375 (2003) 242.
[8] J. Gun, P. Salaün, C.M.G. van den Berg, Anal. Chim. Acta 571 (2006) 86.
[9] K. Yokoi, C.M.G. van den Berg, Electroanalysis 4 (1992) 65.
[10] H. Obata, C.M.G. van den Berg, Anal. Chem. 73 (2001) 2522.
[11] H. Obata, H. Karatani, E. Nakayama, Anal. Chem. 65 (1993) 1524.
[12] C.I. Measures, J. Yuan, J.A. Resing, Mar. Chem. 50 (1995) 3.
[13] J. Wang, J. Lu, S.M. Hocevar, P.A.M. Farias, B. Ogorevc, Anal. Chem. 72 (2000) 3218.
[14] E.A. Hutton, B. Ogorevc, S.B. Hocevar, F. Weldon, M.R. Smyth, J. Wang, Electrochem. Commun. 3 (2001) 707.
[15] J. Wang, R.P. Deo, S. Thongngamdee, B. Ogorevc, Electroanalysis 13 (2001) 1153.
[16] S.B. Hocevar, J. Wang, R.P. Deo, B. Ogorevc, Electroanalysis 14 (2002) 112.
[17] S.B. Hocevar, B. Ogorevc, J. Wang, B. Pihlar, Electroanalysis 14 (2002) 1707.
[18] J. Wang, US Patent 6,682,647 (2004).
[19] R. Pauliukaite, S.B. Hocevar, B. Ogorevc, J. Wang, Electroanalysis 16 (2004) 719.
[20] J. Wang, Electroanalysis 17 (2005) 1341.
[21] I. Svancara, K. Vytras, Chem. Listy 100 (2006) 90.
[22] S. Legeai, O. Vittori, Anal. Chim. Acta 560 (2006) 184.
[23] A. Bobrowski, K. Nowak, J. Zareogonbski, Anal. Bioanal. Chem. 382 (2005) 1691.
[24] E.A. Hutton, S.B. Hocevar, L. Mauko, B. Ogorevc, Anal. Chim. Acta 580 (2006) 244.
[25] L. Lin, S. Thongngamdee, J. Wang, Y. Lin, O.A. Sadik, S.-Y. Ly, Anal. Chim. Acta 535 (2005) 9.
[26] M. Korolczuk, A. Moroziewicz, M. Grabarczyk, Anal. Bioanal. Chem. 382 (2005) 1678.
[27] M. Morfobos, A. Economou, A. Voulgaropoulos, Anal. Chim. Acta 519 (2004) 57.
[28] E.A. Hutton, B. Ogorevc, S.B. Hocevar, M.R. Smyth, Anal. Chim. Acta 557 (2006) 57.
[29] J. Wang, J. Lu, Electrochem. Commun. 2 (2000) 390.
[30] J. Wang, S. Thongngamdee, D. Lu, Electroanalysis 18 (2006) 59.
[31] E. Chatzitheodorou, A. Economou, A. Voulgaropoulos, Electroanalysis 16 (2004) 1745.
[32] L. Lin, N.S. Lawrence, S. Thongngamdee, J. Wang, Y. Lin, Talanta 65 (2005) 144.
[33] J. Wang, D. Lu, S. Thongngamdee, Y. Lin, O.A. Sadik, Talanta 69 (2006) 914.
[34] L. Yong, K.C. Armstrong, R.N. Dansby-Sparks, N.A. Carrington, J.Q. Chambers, Z.-L. Xue, Anal. Chem. 78 (2006) 7582.
[35] A. Królicka, A. Bobrowski, Electrochem. Commun. 6 (2004) 99.
[36] K. Nowak, A. Bobrowski, Anal. Lett. 38 (2005) 1887.
[37] A. Krolicka, A. Bobrowski, K. Kalcher, J. Mocak, I. Svancara, K. Vytras, Electroanalysis 15 (2003) 1859.
[38] S. Legeai, S. Bois, O. Vittori, J. Electroanal. Chem. 591 (2006) 93.
[39] E.A. Hutton, S.B. Hocevar, B. Ogorevc, M.R. Smyth, Electrochem. Commun. 5 (2003) 765.
[40] A. Economou, A. Voulgaropoulos, Talanta 71 (2007) 758.
[41] D. Ruhlig, A. Schulte, W. Schuhmann, Electroanalysis 18 (2006) 53.
[42] G. Kefala, A. Economou, A. Voulgaropoulos, Electroanalysis 18 (2006) 223.
[43] G. Kefala, A. Economou, M. Sofoniou, Talanta 68 (2006) 1013.
[44] J.C. Miller, J.N. Miller, Statistics for Analytical Chemistry, third ed., Ellis Horwood, New York, 1993.

A rapid method for detection of catalase-positive and catalase-negative bacteria based on monitoring of hydrogen peroxide evolution at a composite peroxidase biosensor

B. Serra [a], J. Zhang [a,b], M.D. Morales [a], A. Guzmán-Vázquez de Prada [a],
A.J. Reviejo [a], J.M. Pingarrón [a,*]

[a] *Departamento de Química Analítica, Facultad de CC. Químicas, Universidad Complutense de Madrid,*
28040 Madrid, Spain
[b] *Test Center, Fujian Agriculture and Forestry University,*
35002 Fuzhou, China

Abstract

The rapid detection of catalase-positive and catalase-negative bacteria in complex culture media has been accomplished by monitoring of hydrogen peroxide consumption or generation with a graphite–Teflon–peroxidase–ferrocene composite electrode. *Escherichia coli* and *Streptococcus pneumoniae* have been used as model catalase-positive and catalase-negative bacteria, respectively. Hydrogen peroxide evolution was amperometrically measured at 0.00 V. Experimental conditions, including the working solution composition, the incubation time and the hydrogen peroxide concentration, were optimized. The reusability of the biosensor was improved by placing a nylon membrane on the bioelectrode surface to prevent fouling caused by the bacterial medium. The developed methodology allowed the detection of *E. coli* and *S. pneumoniae* at concentration levels of approximately 2×10^6 and 2×10^5 cfu/mL, in assays taking 10 and 15 min, respectively, without any pre-concentration step or pre-enrichment procedure.
© 2008 Elsevier B.V. All rights reserved.

Keywords: Catalase activity; Hydrogen peroxide; Bacteria detection; Peroxidase biosensor

1. Introduction

Bacterial pathogens detection is particularly relevant in fields like medicine, where the correct treatment is determined by the bacterial species causing an infection, water quality control, food safety, where a close control of the food chain is essential for public health but very difficult to ensure due to its complexity, and biological warfare security. Unfortunately, pathogen detection and identification is an intricate area, as only a few portion of the ubiquitous incredible diversity of bacteria are pathogenic, and the traditional methods for their detection based on specific microbiological and biochemical identifications [1–3] have the mayor limitation of long incubation times (days to weeks

depending on the organism) [4] which are inadequate for crucial short time remediation responses.

Therefore, early detection techniques are desperately needed. In this sense, biosensors offer an exciting alternative, allowing rapid "real-time" and multiple analyses [5]. Accordingly, different types of biosensors for bacterial pathogen have been developed [6–16]. Most of the applications are based on the monitoring of pathogen–antibody binding or pathogenic DNA-probe DNA hybridization events. These methods provide great selectivity and very often suitable sensitivity, but they are complex, and therefore difficult to apply to real samples. Moreover, they are targeted to a particular pathogen, which is not very useful when the source of contamination is unknown. Recent developments in the field of pathogen bacteria biosensors, including electrochemical biosensors, have been recently reviewed [17].

The measurement of a metabolic product for bacterial determination is an interesting approach, which provides several

---

* Corresponding author. Tel.: +34 91 3944315; fax: +34 91 3944331.
E-mail address: pingarro@quim.ucm.es (J.M. Pingarrón).

advantages: simplicity, low cost, possibility to distinguish viable and non-viable cells, amplification is usually achieved, and detection with no need for the use of a label. For example, bacterial catalase is a sensitive marker of aerobic and facultative anaerobic micro-organism's numbers. The measurement of its activity has been suggested as a method to quantify catalase-positive bacterial content [18], for example in milk [19], sewage treatment plants [20] and soil samples [21]. Catalase can catalyze the dismutation of hydrogen peroxide into water and oxygen. Hydrogen peroxide is a harmful by-product of many metabolic processes and if it is accumulated it can be lethal for bacterial cells. Therefore, catalase is frequently used by cells to rapidly catalyse the decomposition of hydrogen peroxide. Accordingly, monitoring the hydrogen peroxide consumption by bacterial catalase can be used for micro-organisms detection.

On the other hand, many catalase-negative bacteria can generate hydrogen peroxide during their metabolic activity in concentrations up to the millimolar range [22]. Therefore, monitoring its formation seems to be a potential way for catalase-negative bacteria detection.

Based on these premises, we have developed a simple amperometric method to detect bacterial pathogens by monitoring the consumption or generation of hydrogen peroxide by different types of bacteria. A graphite–Teflon–peroxidase–ferrocene composite electrode has been employed for the H_2O_2 determination, due to the advantageous analytical characteristics in terms of renewability, sensitivity and robustness exhibited by this amperometric biosensor [23]. To the best of our knowledge, no similar approaches have been described in the literature. However, electrochemical detection and identification of catalase-positive micro-organisms has been reported by combining lateral flow immunoassay with amperometry using a Clark cell at 0.7 V for the detection of hydrogen peroxide [24].

The proposed methodology has been evaluated using *Escherichia coli* and *Streptococcus pneumoniae* as model catalase-positive and catalase-negative bacteria, respectively. In fact, one of the objectives is to check the method usefulness to differentiate catalase-positive from catalase-negative bacteria by hydrogen peroxide evolution in selective culture media.

2. Experimental

2.1. Apparatus and reagents

Amperometric measurements were carried out on a Palm-Sense Electrochemical Sensor Interface controlled by Hewlet Packard pocket PC software. The electrochemical cell was a BAS VC-2 cell with a BAS RE-5 Ag/AgCl/KCl (3 M) reference electrode, and a Pt wire auxiliary electrode. Graphite–Teflon–peroxidase–ferrocene composite electrodes were used as the working electrode. A Raypa AES-75 steam sterilizer, a P-Selecta Agimatic-N magnetic shaker, a Griffin flask shaker and a P-Selecta Tectron 200 thermostatic bath were also used.

2.2. Reagents and solutions

Wild type *E. coli* were obtained from the Spanish Collection of Type Cultures and *S. pneumoniae R6* were generously provided by Centro de Investigaciones Biológicas, CSIC, in Madrid. Horseradish peroxidase (HRP) (EC 1.11.1.7, type II, activity 180 U mg^{-1} of solid, Sigma), graphite (ultra F purity; Carbon of America, Bay City, USA), Teflon powder (Aldrich) and ferrocene (Fluka, Buchs, Switzerland) were used for the fabrication of the biosensor. Hydrogen peroxide (30% w/w) was supplied by Sigma.

0.1 M hydrogen peroxide stock solutions were prepared daily in 0.05 M phosphate buffer solution of pH 6.5. More dilute standards were prepared by suitable dilution with the same buffer solution. Culture media consisted on Luria broth (LB) for *E. coli* (Scharlau) and brain heart infusion broth (Oxoid) for *S. pneumoniae*, and LB agar (Scharlau) and blood agar plates (Oxoid) were used for plate colony counting for *E. coli* and *S. pneumoniae*, respectively. Culture media and flasks were sterilized by autoclaving at 121 °C during 15 min. All chemicals were of analytical-reagent grade, and the water used was obtained from a Milli-Q purification system (Millipore).

2.3. Fabrication of graphite–Teflon–HRP–ferrocene (GTHF) composite electrode

Composite electrodes were fabricated in the form of cylindrical pellets as described elsewhere [23]. A portion of a 47 mm-diameter, 0.45 μm-pore size nylon membrane (Osmonics) was used for preventing the direct contact between electrode surface and bacterial medium by placing it on the electrode surface by means of a rubber o-ring.

2.4. Bacteria culture and plating method

S. pneumoniae R6 belongs to the micro-organism biosafety level 1 and wild-type *E. coli* to the level 2 group and, consequently, all safety considerations concerning these groups [25] were accomplished in the manipulation of these bacteria. *E. coli* cultures were grown overnight in Luria broth medium at 37 °C with aeration by shaking, which allowed the growing stationary phase to be reached. Then, bacterial cultures were serially diluted (10-fold steps) and 10 μL of samples were applied to LB agar plates and incubated for 24 h at 37 °C for enumeration of colonies. The stationary-phase cultures were properly diluted with 0.05 M phosphate buffer of pH 6.5 in order to obtain 10–10^8 cfu/mL.

S. pneumoniae was grown until mid-log-phase by culture in brain heart infusion (BHI) broth at 30 °C for 6 h under microaerophilic conditions. Bacteria were then centrifuged at 5000 × g for 20 min and washed with BHI in order to eliminate hydrogen peroxide from the medium. Then, bacterial cultures were serially diluted (10-fold steps) and 10 μL of samples were applied to blood agar plates and incubated for 24 h at 30 °C for enumeration of colonies. At the same time, the mid-log-phase cultures were diluted to 10–10^8 cfu/mL in BHI.

2.5. Amperometric measurements of hydrogen peroxide with the composite biosensor

The graphite–Teflon–HRP–ferrocene composite electrode was used to detect hydrogen peroxide. Amperograms were monitored at room temperature, in the electrochemical cell containing 5.0 mL of 0.05 M phosphate buffer which was mechanically stirred at a constant rate. A potential of 0.00 V was applied and the background current was allowed to stabilize. Then the solution containing the appropriate amount of hydrogen peroxide was added and the current was monitored until the steady state was reached.

2.6. Direct detection of E. coli

After the addition of the appropriate amount of H_2O_2 to the electrochemical cell and later current stabilization, different concentrations of E. coli were also pipetted into the cell, and the current deflection was monitored.

2.7. Indirect detection of E. coli after a separated consumption step

Indirect detection of E. coli consisted of a two separated steps procedure. Firstly, an appropriate amount of hydrogen peroxide was added to an E. coli suspension in phosphate buffer, allowing the catalase action on H_2O_2 to take place for a fixed period of time. Secondly, an aliquot of this suspension was added to the electrochemical cell containing 5 mL of 0.05 M phosphate buffer at the appropriate pH and the remaining hydrogen peroxide was measured at 0.00 V. Subsequently, an aliquot from a negative control sample (without E. coli) was also added to the cell, and the obtained current was compared to the first one in order to compare hydrogen peroxide consumption by bacteria.

2.8. Indirect detection of S. pneumoniae

Indirect detection of S. pneumoniae was carried out by allowing bacterial BHI solution to grow, and, at appropriate periods of time, aliquots of 1 mL of these suspensions were added to the electrochemical cell containing 4 mL of 0.05 M phosphate buffer at the appropriate pH, the generated hydrogen peroxide being measured at 0.00 V.

3. Results and discussion

The determination of hydrogen peroxide, related to bacterial growth, is accomplished in this work by using a composite graphite–Teflon–HRP–ferrocene biosensor developed previously by our research group [23]. This biosensor was selected because of its excellent analytical performance for the determination of hydrogen peroxide. Thus, the amperometric measurements can be carried out at a low potential such as 0.0 V, which minimises possible interferences. Moreover, the biosensor exhibits a fairly good renewability of the electrode surface by polishing as well as a long-term operation and stability.
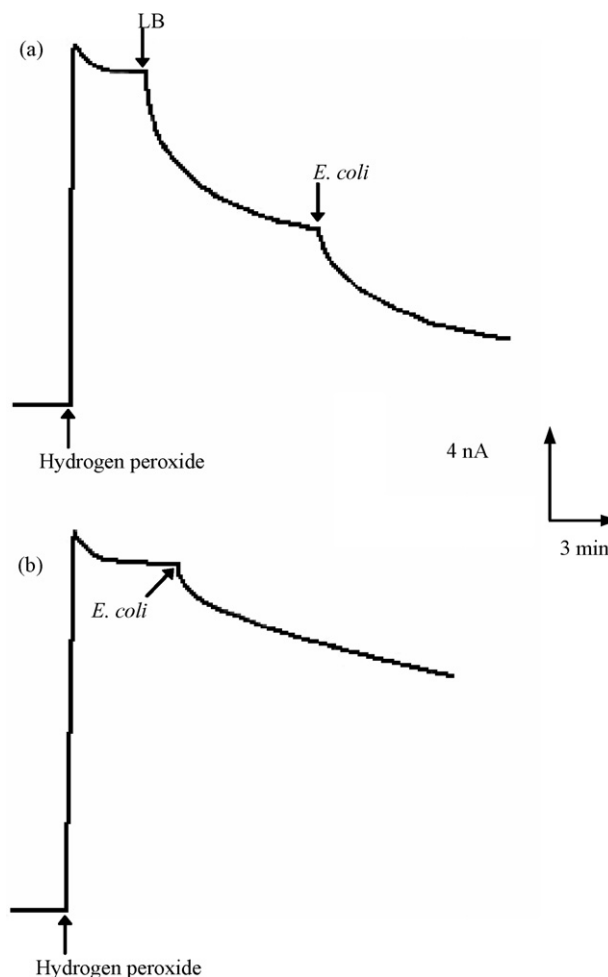
Fig. 1. Current–time curves obtained at a working gold electrode in an electrochemical cell containing 5.0 mL of 0.05 M phosphate buffer (pH 6.5) after the addition of 2.5 mM H_2O_2 and subsequent addition of (a) 100 μL of Luria broth and 100 μL of 10^8 cfu/mL Escherichia coli suspension in Luria broth, respectively; (b) 100 μL of 10^8 cfu/mL E. coli suspension filtered from Luria broth medium and resuspended in 0.05 M phosphate buffer (pH 6.5). $E_{app} = 0.00$ V.

3.1. Monitoring of hydrogen peroxide consumption by catalase-positive bacteria using graphite–Teflon–HRP–ferrocene electrode

Although hydrogen peroxide can be amperometrically detected at many electrode surfaces, its direct amperometric detection in a complex medium such as bacteria suspensions can be affected by many interferences. For example, Fig. 1 shows the influence on the amperometric response for H_2O_2 obtained on a gold electrode at 0.00 V when an aliquot of LB medium containing no bacteria (typically used for E. coli growing) is added to the amperometric cell and when E. coli suspensions in phosphate buffer solution are also added.

It is observed that it was not possible to distinguish between the signal due to bacteria catalase hydrogen peroxide consumption and the current decrease that appeared when an aliquot of the LB medium was injected. On the contrary, if a graphite–Teflon–HRP–ferrocene electrode is used, no influence from the culture medium was observed thus being possible to
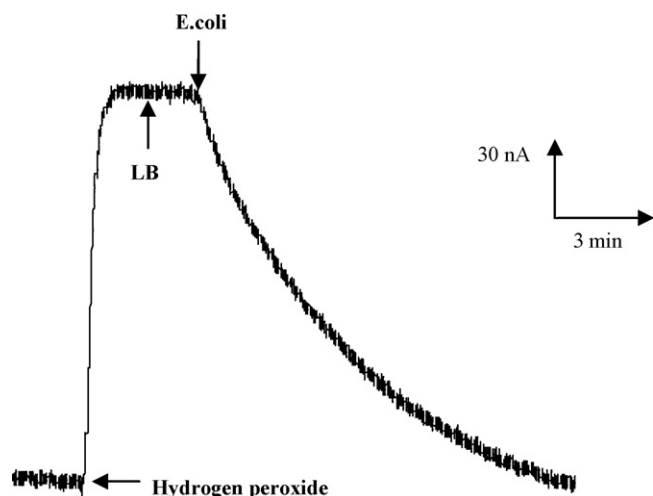
Fig. 2. A current/time response curve for 10^8 cfu/mL *E. coli* LB suspension in 5 mL of 0.05 M phosphate buffer solution (pH 6.5) on a graphite–Teflon–HRP–ferrocene composite electrode. $E_{app} = 0.00$ V; initial H_2O_2 cell concentration, 25 μM. The addition of 100 μL of LB did not affect the response.

distinguish the response due to catalase action (Fig. 2). From the figure, it is also observed that the initial amperometric baseline is recovered after 15 min of *E. coli* suspension addition, demonstrating that bacteria consumption of hydrogen peroxide is fast. Therefore, its monitoring can provide a rapid method for the detection of *E. coli*.

3.1.1. Reproducibility of the measurements

Prior to the evaluation of the analytical characteristics of the biosensor for *E. coli* determination, the reproducibility and stability of the device must be studied. It should be remarked that although the composite biosensor exhibited a good analytical performance for hydrogen peroxide determination [23], it is now used in a more complex system, making it necessary to evaluate these aspects again. Therefore, five different measurements were performed in the same conditions as in Fig. 2. The relative standard deviation (R.S.D.) obtained (29.3% for 10^8 cfu/mL *E. coli*) showed a high dispersion of the analytical responses. Therefore, the micro-organisms environment seems to affect the stability of the biosensor, most likely due to surface fouling. Consequently, in order to avoid this surface contamination, the composite electrode was covered with a nylon membrane with a pore size of 0.45 μm to prevent bacteria adhesion on the electrode surface. Five measurements carried out under these conditions yielded an R.S.D. value for *E. coli* responses of 3.1%. These results demonstrate the effective prevention of surface fouling using the nylon membrane. Calibration plots obtained for hydrogen peroxide using a graphite–Teflon–HRP–ferrocene composite electrode non-covered and covered with a nylon membrane are compared. The uncovered electrode showed a range of linearity ($r = 0.998$) between 1.2 and 11.2 μM H_2O_2 with a slope value of 3.52 nA μM^{-1}. In the case of the nylon membrane covered-electrode, the linear range ($r = 0.9990$) was 2.4–22.4 μM H_2O_2 with a slope value of 3.37 nA μM^{-1}. As expected, the response was slightly smaller and the linear range extended as the mem-
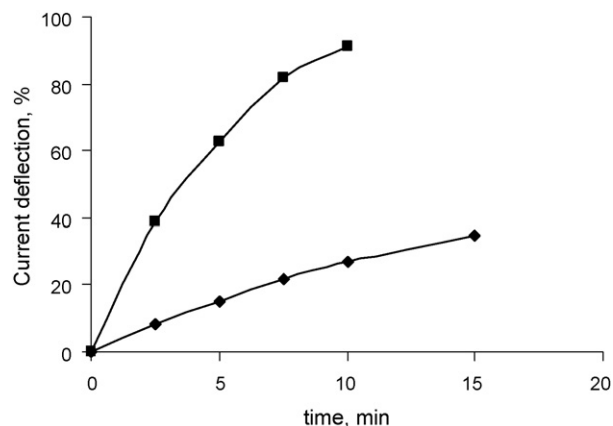
Fig. 3. Effect of assay time on the response of a 0.45-μm nylon membrane–graphite–Teflon–HRP–ferrocene composite electrode to: 1×10^7 cfu/mL *E. coli* (♦) and 1×10^8 cfu/mL *E. coli* (■). Conditions as in Fig. 2.

brane reduces the diffusion rate of hydrogen peroxide from the solution to the electrode surface.

3.1.2. Optimization of working conditions

3.1.2.1. Effect of pH on the biosensor response to E. coli.
In this assay protocol for *E. coli* determination based on the detection of their catalase activity, there are two enzymatic reactions involved: the reduction of hydrogen peroxide catalysed by HRP at the electrode surface and the consumption of H_2O_2 in the bulk of the solution by catalase. With the purpose of studying the effects of pH on both enzyme reactions separately, detection of *E. coli* is carried out using the indirect method described in Section 2.7. Therefore, *E. coli* suspensions at different pH values were allowed to react with hydrogen peroxide for 5 min. Then, an aliquot of these suspensions was added to the electrochemical cell containing phosphate buffer at a pH value of 6.5. In this way, it was possible to observe the optimum pH value for catalase activity in *E. coli*. On the other hand, the response of graphite–Teflon–HRP–ferrocene electrode to H_2O_2 in the electrochemical cell containing working solutions of different pH values was also evaluated in order to determine the optimum value for HRP reaction. No significant changes in current signal for H_2O_2 were observed in the 5.0–7.5 range of pH values in the electrochemical cell. However, a maximum response was observed for the *E. coli* suspensions incubated with H_2O_2 at pH between 5.5 and 6.5. Furthermore, it was found that it took longer to obtain a stable amperometric baseline for lower buffer pHs. Therefore, a pH value of 6.5 was selected for *E. coli* determination with our biosensor system.

3.1.2.2. Optimization of assay time.
Fig. 3 shows the relationship between the current deflection and the assay time after *E. coli* addition to the electrochemical cell. Obviously, the longer the assay time the more sensitive the response. Using an *E. coli* concentration of 10^8 cfu/mL, the response increased quickly, and reached 90% of cell hydrogen peroxide consumption after 10 min of assay. For lower *E. coli* concentrations, the response increased slower, but after 10 min the consumption rate also

decreased. Therefore, these results suggested that 10 min of assay could be a good compromise between sensitivity and speed of assay.

3.1.2.3. Optimization of H_2O_2 concentration in the electrochemical cell.

Hydrogen peroxide concentration in the electrochemical cell will influence the sensitivity of the response to *E. coli*. In order to study this effect, assays were performed using 5, 10 and 25 μM H_2O_2 in the measuring cell. These concentrations lay in the linear range of the calibration plot for H_2O_2 with the graphite–Teflon–HRP–ferrocene biosensor and, therefore, the decrease in current due to bacteria presence could be directly correlated with hydrogen peroxide consumption by bacteria, being possible to assess the speed of bacteria respiration. The results indicated that the lower the concentration of hydrogen peroxide the greater current deflection was observed. So, for 5 μM H_2O_2 a current deflection of $68 \pm 4\%$ was obtained whereas $39 \pm 1\%$ and $26 \pm 4\%$ were obtained for 10 and 25 μM H_2O_2, respectively. Despite this fact, 10 μM hydrogen peroxide was chosen for further studies, considering that the low current obtained for 5 μM gave rise to a lower signal-to-noise ratio than for 10 μM.

3.1.3. Calibration curves for direct E. coli determination

Different *E. coli* concentrations were added to the electrochemical cell containing 10 μM of hydrogen peroxide. The decrease in current was measured after 5 and 10 min of bacteria addition, respectively. Plotting the percentage of hydrogen peroxide consumption versus the logarithm of *E. coli* concentration allowed to obtain the calibration graphs with a non-linear shape. The experimental points can be adjusted to polynomial equations ($y = 7.60x^2 - 78.82x + 210.5$, $r^2 = 0.98$ after 5 min, and $y = 7.70x^2 - 74.88x + 194.0$, $r^2 = 0.94$ after 10 min) which would allow the calculation of bacteria concentration in an unknown sample by interpolating the percentage of hydrogen peroxide consumed into the equation. Therefore, this method allowed the quantification of *E. coli* in water samples with a detection limit of 5.7×10^7 and 3.6×10^6 cfu/mL, for 5 and 10 min assay time, respectively, taking into account the sample dilution after addition to the electrochemical cell. The detection limits were calculated as the bacterial concentration producing a decrease in the hydrogen peroxide signal of 3-fold the background noise.

3.1.4. Indirect E. coli determination

In order to avoid bacteria sample dilution due to the addition of a sample aliquot to the electrochemical cell, methodology described in Section 2.7, where hydrogen peroxide was added to the bacteria sample and was allowed to react for a fixed period of time, was implemented. Then, the remaining H_2O_2 in the *E. coli* sample is measured in the electrochemical cell with the graphite–Teflon–HRP–ferrocene composite biosensor. Prior to establish the analytical characteristics of this method, some experimental variable were optimised.

3.1.4.1. Influence of hydrogen peroxide concentration in consumption step.

The hydrogen peroxide concentration in bacteria samples needs to be high enough to allow the measurement of
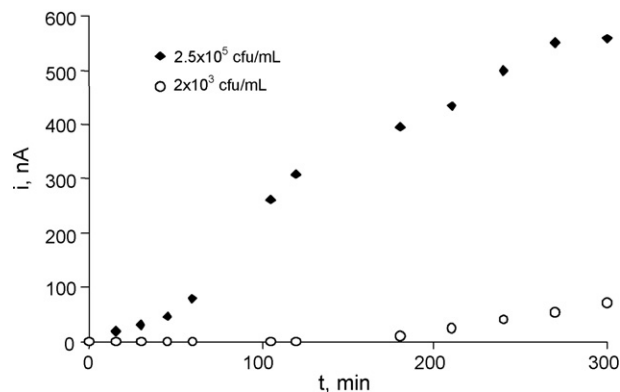
Fig. 4. Amperometric responses obtained with a 0.45-μm-pore size nylon membrane–graphite–Teflon–HRP–ferrocene composite electrode at an applied potential of 0.00 V, when 1 mL of *Streptococcus. pneumoniae* suspension was added to the cell after different incubation times in BHI broth at 30 °C.

the remaining current in the electrochemical cell. Nevertheless, if cannot be so high that the concentration in the cell is out of the linear range. Furthermore, very high hydrogen peroxide concentrations can be toxic for bacteria, despite the action of catalase. Pericone et al. [22] estimated that the minimum bactericidal H_2O_2 concentration for *E. coli* was of 15 mM. There were no significant differences between the percentages of hydrogen peroxide consumed by *E. coli* for H_2O_2 concentrations between 0.5 and 1.25 mM. Lower or higher concentrations produced smaller responses, and, accordingly, 1.25 mM hydrogen peroxide was selected for further work.

3.1.4.2. Optimisation of reaction time in H₂O₂ consumption step.

The influence of the reaction time on the amount of hydrogen peroxide consumed by *E. coli* in the indirect detection method was evaluated by allowing a 2.5×10^7 cfu/mL *E. coli* suspension to react with 1.25 mM hydrogen peroxide for different periods of time comprised between 2.5 and 15 min. Then, a 40 μL aliquot of this suspension was added to the electrochemical cell containing 5 mL of 0.05 M phosphate buffer solution of pH 6.5, and the current at 0.00 V was compared with that measured after the addition of a negative control solution without *E. coli*. The response increased with reaction time, but the increase was remarkably smaller from 10 to 15 min. A reaction time of 10 min was chosen in order to maintain assay time as short as possible.

3.1.4.3. Calibration curve for E. coli detection with the indirect method.

Under the optimised conditions mentioned above, the peroxide consumed was determined by comparison of the measured current with that of a negative control solution. The calibration plot obtained obeyed the equation: hydrogen peroxide consumed %, $y = 20.35x^2 - 247.03x + 760.3$, $r^2 = 0.9455$. The limit of detection obtained in this case, according to the same criterion mentioned above, was 1.8×10^6 cfu/mL of *E. coli*.

3.2. Monitoring of hydrogen peroxide generation by catalase-negative bacteria using the graphite–Teflon–HRP–ferrocene electrode

It has been established that different *S. pneumonia* strains can generate up to 0.7 mM of hydrogen peroxide in their culture media [22]. Monitoring formation of a product instead of its consumption is a much simpler and sensitive approach. Therefore, a sensitive detection of *S. pneumoniae* through its peroxide formation is expected.

In this case, again both direct and indirect detection were considered. Direct detection consisted of the immersion of the electrodes in the bacterial culture from $t = 0$. When initial concentrations were lower than 10^7 cfu/mL, it was not possible to distinguish between the background drift and peroxide signal.

Consequently, in order to achieve an improved sensitivity in short times, indirect measurements were preferred, where aliquots of the culture media were added to the electrochemical cell after certain periods of culture time. Fig. 4 shows the amperometric signal due to hydrogen peroxide presence in the aliquots added to the cell for two different starting *Streptococcus* concentrations. It is observed that it was possible to detect H_2O_2 formation after 15 min of incubation at 30 °C of cultures containing 2.5×10^5 cfu/mL. Moreover, smaller bacteria concentrations, as low as 2×10^3 cfu/mL can be detected after 3 h of growing. Therefore, depending on the initial concentration of bacteria, different incubation times are required, but, in any case, a very sensitive detection is achieved in short periods of time, comparing to other methods.

3.3. Discussion

From the results shown above, it is demonstrated the feasibility to detect both catalase-positive and -negative bacteria in very short time. A standard assay would consist of adding the real sample in the appropriate generic media and allow its growing under aerobic and microaerophilic conditions, and monitor hydrogen peroxide formation or consumption. In this way, it would be possible to distinguish between both types of bacteria in a simple manner, and even more, to detect both of them when they are coexisting, as, under each of the mentioned growing conditions, only one type would grow. Moreover, if more selective information is required, it would be possible to establish a battery of culture in different selective media, or media containing different types of antibiotics, and monitor hydrogen peroxide evolution in all of them sequentially or simultaneously, in order to obtain information that allowed the identification of one species. On the other hand, the developed methodology can also be coupled to a previous selective capture step, such as immunofiltration, for example, in order to achieve specific detection. Future work will involve evaluation of such possibilities.

4. Conclusions

The use of a composite peroxidase biosensor for hydrogen peroxide measurement allowed direct monitoring of catalase-positive and catalase-negative bacteria in complex culture media, as interference effects are minimized at the applied potential value of 0.00 V for the amperometric measurements, in a simple, rapid, sensitive and reproducible way. The proposed methodology under the optimised conditions yielded reproducible measurements and a limit of detection of $\approx 2 \times 10^6$ cfu/mL *E. coli* in 10 min of assay, and of $\approx 2 \times 10^5$ cfu/mL *S. pneumoniae* in 15 min of assay, with no need of any pre-concentration, pre-enrichment or bacteria permeabilization step. Therefore, much lower limits of detection can be achieved easily, for example by sample filtration. The fast and simple detection method can be combined with a selective capture step to obtain rapid and selective analytical procedures for a large number of different bacteria, and can be easily automated for routine application.

Acknowledgement

References

[1] E. De Boer, R.R. Beumer, Int. J. Food Microbiol. 50 (1999) 119.
[2] K. Helrich, Official Methods of Analysis of the Association of Official Analytical Chemists, Microbiological Methods, vol. 2, 15th ed., AOAC, Arlington, VA, 1990, pp. 425–497, (Chapter 17).
[3] N.S. Hobson, I. Tothill, A.P.F. Turner, Biosens. Bioelectron. 11 (1996) 455.
[4] A. Rompré, P. Servais, J. Baudar, M.R. De-Roubin, P. Laurent, J. Microbiol. Methods 49 (2002) 31.
[5] P. Leonard, S. Hearty, J. Brennan, L. Dunne, J. Quinn, T. Chakraborty, R. Kennedy, Enzyme Microb. Technol. 32 (2003) 3.
[6] P.M. Fratamico, Biotechnol. Tech. 12 (7) (1998) 571.
[7] E.A. Perkins, D.J. Squirrell, Biosens. Bioelectron. 14 (2000) 853.
[8] S.T. Pathirana, J. Barbaree, B.A. Chin, M.G. Hartell, W.C. Neely, V. Vodyanoy, Biosens. Bioelectron. 15 (2000) 135.
[9] X. Su, S. Low, J. Kwang, V.H.T. Chew, S.F.Y. Li, Sens. Actuator B 75 (2001) 29.
[10] S. Tombelli, M. Mascini, C. Sacco, A.P.F. Turner, Anal. Chim. Acta 418 (2001) 1.
[11] E. Howe, G. Harding, Biosens. Bioelectron. 15 (2000) 641.
[12] Y. Hasebe, K. Yokobari, K. Fukasawa, T. Kogure, S. Uchiyama, Anal. Chim. Acta 357 (1997) 51.
[13] J. Rishpon, D. Ivnitski, Biosens. Bioelectron. 12 (1997) 195.
[14] K. Dill, L.H. Stanker, C.R. Young, J. Biochem. Biophys. Methods 41 (1999) 61.
[15] A.G. Gehring, D.L. Patterson, S. Tu, Anal. Biochem. 258 (1998) 293.
[16] K.A. Uithoven, J.C. Schmidt, M.E. Ballman, Biosens. Bioelectron. 14 (2000) 761.
[17] O. Lazcka, F. Javier Del Campo, F. Xavier Muñoz, Biosens. Bioelectron. 22 (2007) 1205.
[18] R. Charbonneau, J. Therrien, M. Gagon, Can. J. Microbiol. 21 (1975) 580.
[19] J.D. Phillips, M.W. Griffiths, J. Appl. Bacteriol. 62 (1987) 223.
[20] B.B. Hosetti, H.S. Patil, Int. Rev. Ges. Hydrobiol. 73 (1988) 641.
[21] A.J. Guwya, S.R. Martina, F.R. Hawkesb, D.L. Hawkesa, Enzyme Microb. Technol. 19 (1999) 669.
[22] C.D. Pericone, K. Overweg, P.W.M. Hermans, J.N. Weiser, Infect. Immun. 68 (7) (2000) 3990.
[23] M.A. Del Cerro, G. Cayuela, A.J. Reviejo, J.M. Pingarrón, J. Wang, Electroanalysis 9 (1997) 1113.
[24] N. Sippy, R. Luxton, R.J. Lewis, D. Cowell, Biosens. Bioelectron. 18 (2003) 741.
[25] Protection of workers from risks related to exposure to biological agents at work Directive 2000/54/EC.

NHS-mediated QDs-peptide/protein conjugation and its application for cell labeling[☆]

Yaming Shan[a], Liping Wang[a,*], Yuhua Shi[a], Hao Zhang[b], Hongmei Li[a], Hanzhi Liu[a], Bai Yang[b], Tianyu Li[a], Xuexun Fang[a], Wei Li[a,*]

[a] *College of Life Science, Jilin University, Jiefang Road 115, Changchun 130023, PR China*
[b] *College of Chemistry, Jilin University, Changchun 130023, PR China*

Abstract

3-Mercaptopropyl acid-stabilized CdTe nanoparticles synthesized in aqueous solution are found to be able to conjugate with peptides or proteins mediated by *N*-hydroxysulfo-succinimide (NHS) but 1-ethyl-3(3-dimethylaminopropyl) carbodiimides hydrochloride (EDC). The reaction time and pH have been optimized. Gel-permeation HPLC was applied following the conjugation, which could quickly and simultaneously detect and purify the quantum dots (QDs) conjugates. The biological activities of QDs conjugates are maintained and give superior results in cell labeling. These results are encouraging regarding the application of QDs molecules for use in living cells, diagnostics and drug delivery.
© 2008 Elsevier B.V. All rights reserved.

Keywords: Quantum dot; NHS-mediated conjugation; Cell labeling; Nuclear targeting signal

1. Introduction

Fluorescent labeling of biological materials using small organic dyes has been widely employed in the life science including diagnostics and biological imaging [1]. Problems arise mainly from poor photostability and brightness, especially for samples with high background fluorescence [2]. Therefore, it is highly desirable to develop new fluorescent probes for biochemical assays.

Semiconductor quantum dots (QDs) are nanoparticles that have superior fluorescent properties [3]. In recent years, QDs have emerged as a class of fluorescent probes for many biological and biomedical applications, especially for cellular imaging [4–7]. QDs have several advantages over conventional organic dye fluorophores as fluorescent probes [8,9]. The emission spectra of QDs are narrow, symmetrical, and tunable according to their size and material composition. They have broad absorption spectra and exhibit excellent photostability, which makes it possible to excite all colors of QDs simultaneously with a single excitation light source and to minimize sample autofluorescence by choosing an appropriate excitation wavelength.

The QDs used in the above-mentioned studies, however, were generally produced with a capping layer composed of one or more organic ligands such as trioctylphosphine or trioctylphosphine oxide. These ligands are hydrophobic and thus nanoparticles capped with these coatings are not compatible with aqueous bioassay conditions. Consequently, it is necessary to substitute these organic ligands with hydrophilic capping agents for biological application. Such processes are not only complicated, but also necessary to use hazardous organic ligands.

Therefore, some simpler and more feasible methods applying to synthesize water-soluble QDs directly have been reported [10–13]. The application of water-soluble QDs in conjugating with biomolecules has been studied recently [14–16]. Recently, thioglycolic acid-stabilized green- and red-emitting CdTe nanoparticles were attached to antibody and antigen via the *N*-hydroxysulfo-succinimide (NHS) and 1-ethyl-3(3-dimethylaminopropyl) carbodiimide hydrochloride (EDC) reaction [14]. In these cases, biomolecules were immobilized onto the surface of the quantum dots by covalent interactions or via electrostatic interaction [15]. These bioconjugates provide

powerful new means to study genes and proteins in cells, tissues, and even living animals.

Our research group found that, however, 3-mercaptopropyl acid-stabilized water-soluble CdTe nanoparticles synthesized in aqueous solution were found to be able to conjugate with peptides or proteins mediated by NHS but EDC. The stable QDs-peptides/protein conjugates can provide great potential power in cell labeling application.

2. Materials and methods

2.1. Preparation of water-soluble CdTe QDs

QDs used in this paper are 3-mercaptopropyl acid (MPA) modified water-soluble CdTe nanoparticles. MPA (99%), tellurium powder (200 mesh, 99.8%), CdCl$_2$ (99%), and NaBH$_4$ (99%) were purchased from Aldrich Chemical Company. All other reagents were of analytical reagent grade and used without further purification [15].

QDs were synthesized in an aqueous solution using a previously described synthesis method [17,18]. In brief, freshly prepared oxygen-free NaHTe solution was added to a nitrogen-saturated 1.25×10^{-3}M CdCl$_2$ aqueous solution at pH 11.4 in the presence of MPA as a stabilizing agent. NaHTe was produced by the reaction of NaBH$_4$ with tellurium powder (2:1 molar ratio). The molar ratio of Cd^{2+}:MPA:Te$^-$ was 1:2.4:0.5. The solution was refluxed for different times to control the size of the QDs. The fluorescence quantum yield of QDs at room temperature was ~25% (determined by comparing the integrated emission of the QDs in solution to that of a solution of rhodamine 6 G of identical optical density at the excitation wavelength).

Extract-Clean^{TM} cartridges (Alltech Associates Inc.) were applied for isolation of QDs from the solution. The columns were conditioned and equilibrated with methanol followed by deionized water before use. The solutions with different size QDs were transferred into a SPE column cartridge. After washing the cartridge with deionized water, QDs were eluted using 60% methanol. The elution was evaporated to dryness at 30 °C in vacuum and dissolved in phosphate-buffered saline (PBS), pH 7.

2.2. Proteins and peptides

Rh-interferon-α (IFN) (purity ≥95%, cell culture tested, buffered aqueous solution, recombinant, expressed in *Escherichia coli*, MW: 80,000) and insulin (INS) (purity ≥95% (HPLC), powder, ~24 IU/mg protein, MW: 5734) were purchased from Sigma–Aldrich.

Bovine serum albumin (BSA) (MW: 67,000) and streptavidin (SA) (MW: 66,000) were purchased from Amresco Inc.

In this study, one class of cell-penetrating peptide (CPP) (Langel, 2002) resembling the archetypal nuclear locating signal of the Simian Virus SV40 large tumor antigen (T-ag), which comprises a single short stretch of basic amino acids (PKKKRK[132]), was selected as basic sequence for cell labeling and named nuclear targeting signal (NTS) [19,20]. The peptide, named biotin-NTS, was prepared with a terminal biotin to permit conjugation to the SA which was coated with QDs.

The IVRLQA sequence in insulin-mimic peptide (INS-mimic) was obtained by screening phage display random hexapeptide library against CHO-IR cell line. The INS-mimic exhibited excellent binding activity to insulin receptor [21].

Both peptides were synthesized on a PS3 peptide synthesizer using F-moc amino acids. Mass spectrometry confirmed the predicted mass. Peptides were further purified on Prep LC^{TM} 25 mm Module (Waters) by BioCAD 700E Perfusion Chromatography Workstation (PerSeptive Biosystems Inc.), lyophilized (in the dark), resuspended in PBS, and filter sterilized.

2.3. NHS-mediated QDs conjugation

N-hydroxysulfo-succinimide (NHS) was purchased from Sigma–Aldrich, CAS Number 106627-54-7. 1:10 molar ratio of NHS:QDs was mixed for 5 min. Then equal molar ratio of protein/peptide to NHS was added and the solutions were gently mixed at room temperature for 0–8 h. Excess QDs were added to ensure that all peptide/protein molecules could be labeled. 1-Ethyl-3(3-dimethylaminopropyl) carbodiimides hydrochloride (EDC, purchased from Sigma–Aldrich, CAS Number 25952-53-8) which was equal molar ratio to NHS, was added to the mixture as control. 1 M glycine was added to block the activated carboxol and terminate the reaction. The final molar ratio of glycine to QDs was about 10:1. The reaction mixtures were detected by gel-permeation HPLC and then dialysed at 4 °C overnight.

QD574-SA–biotin-NTS were assembled by conjugating QD574 to SA and then attaching QD574-SA conjugates to biotin-NTS.

2.4. Spectral measurement

Ultraviolet–visible absorption spectra (UV–vis) were obtained using a Shimadzu 3100 UV–vis-near-IR recording spectrophotometer. Fluorescence spectra (FS) were recorded by a Shimadzu RF-5301 PC spectrofluorophotometer. In both experiments 10 mm optical-path cells were used to collect the absorption and fluorescence spectra. All measurements were carried out under ambient conditions.

2.5. Gel-permeation HPLC method

To detect and separate the QDs conjugates, the reaction mixtures were monitored by gel-permeation HPLC on Shodex Protein KW802.5 column equipped with a Waters 2487 UV detector 214 nm and a Waters 2475 Multi λ Fluorescence Detector. The molecular weight and distribution were determined according to the instruction manual of Shodex KW802.5 (Showadenko, Tokyo). Before the analysis, the column was pre-equilibrated with PBS at pH 7 for 20 min. A 20 μL aliquot of sample solution was injected to the chromatograph. Separation was performed at a flow rate of 0.8 mL min^{-1}.

2.6. Cell culture and QDs conjugates delivery

HEp-2, CHO-IR and L929 cell lines were maintained in Minimum Essential Medium Eagle (EMEM) or Dulbecco's
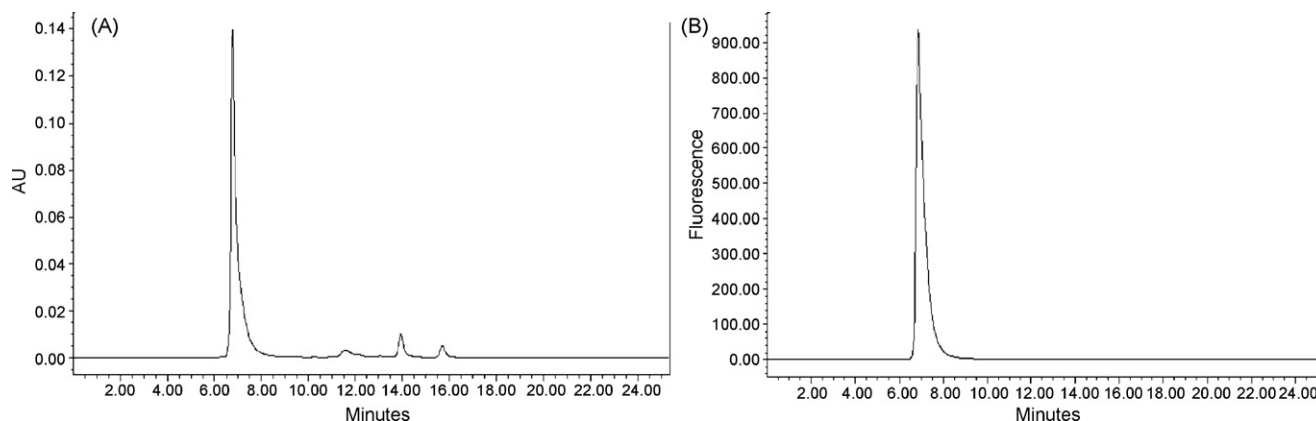
Fig. 1. Detection and purification of the QD527-IFN on gel-permeation HPLC. (A) UV absorption at 280 nm. (B) Fluorescence emission at 527 nm of QD527-IFN. The prominent individual elution peak appeared at 7.1 min was monitored by both fluorescence and UV monitoring system at the same time. The retention times of free IFN and QD527 were about 14.0 min and 15.8 min, respectively. QD527 showed weak UV absorption and indistinguishable fluorescent intensity.

Modified Eagles Medium (DMEM) growth media (Gibco product) without addition of antibiotics at 37 °C in controlled CO_2 atmosphere. For investigating the cellular localization of peptides, cells were plated on glass coverslips and grown to 75% confluency in 12-well plates and then incubated with QDs conjugates (150 pM) for various times. It has been shown that the presence of serum in the culture medium inhibits cellular binding/uptake of cationic lipids and reduces their efficiency as nucleic acid carriers [22]; therefore, most cellular delivery agents available today require serum-free media during delivery. The presence of BSA contributed greatly to the stability of nanoparticle conjugates in serum-containing media. All studies shown herein were conducted using media which contain 10% FBS. At indicated time points the coverslips were rinsed extensively with PBS, and the cells were fixed with 4% paraformaldehyde in PBS for 15 min at room temperature and then rehydrated in PBS. Following fixation, the cover slip with cells were mounted onto glass slides and allowed to dry overnight prior to microscopy analysis.

2.7. Microscopy

Microscopy was performed on an inverted Olympus fluorescent microscope IX71 (Japan). The video system comprises an Olympus DP70 digital camera, with software-based manual control of color balance and contrast enhancement on live and captured images. Acquisition times ranged from 30 to 4 s.

3. Results and discussion

3.1. Preparation of QDs

Nanoparticles were prepared as described above and characterized by transmission electron micrograph (TEM), UV–vis and FS. QDs with three diameters, 2.8, 3.0, and 3.3 nm, whose emission wavelength are 527, 542 and 574 nm, respectively, were employed in the study.

Capped with 3-mercaptopropyl acid is compatible with aqueous bioassay conditions. This method is not only feasible and

easy, but also avoids the use of hazardous organic ligands that would be harmful to biomolecules and cells. As a novel fluorescence material, the nanoparticles have the advantages in small and uniform size, high hydrophilic, strong fluorescence, high stability and significantly reduced dye leaching in solution [15].

3.2. Detection and separation of the QDs-peptide/protein conjugates by gel-permeation HPLC

Sensitive detection and efficient separation of the conjugated molecules can minimize the interference from the unconjugated peptide/protein, free QDs and other molecules in subsequent applications. Due to the fluorescent properties and molecular weights of the QDs conjugates, gel-permeation HPLC equipped with fluorescence/UV monitoring system was employed for detection, purification and quantification.

Using water-soluble carbodiimides EDC and NHS to form the QDs-protein covalent conjugates is one of the most frequent coupling methods [14]. In the presence of EDC, however, 3-mercaptopropyl acid-stabilized CdTe nanoparticles used in this paper are unstable and the fluorescence is always quenched. We could not achieve the QDs-protein/peptide conjugates by inducing covalent amide formation with EDC in combination with NHS. The main reason is likely that the solution pH being directly related to the stability of CdTe nanoparticles at pH 4.8–8.8 [23].

Addition of neither EDC nor NHS to the mixture of QDs and peptide/protein could produce any stable fluorescent product. The result implies that QDs could not coat the peptide/protein by means of electrical charge. After addition of NHS to such mixture, the individual peaks of QDs-protein conjugates were identified based on their molecular weights by gel-permeation HPLC (Fig. 1) and further separated by polyacrylamide gel electrophoresis (data not shown). The molecular weight analysis and the simultaneous detection guarantee the presence of only QD527-IFN conjugate formed by QD527 and IFN. It's obvious that NHS could mediate QDs conjugating with the proteins/peptides. This method is simple but effective for preparing
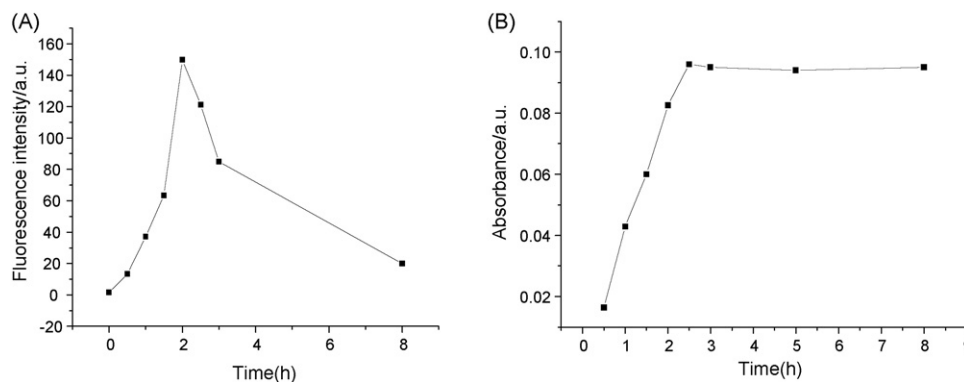
Fig. 2. The fluorescent intensities of QD542 conjugated with BSA for 0–8 h detected by gel-permeation HPLC (A), and UV absorption of the QD542-BSA is shown in (B).

QDs-protein/peptide conjugates, although further study is warranted to fully understand the reaction mechanism.

Remarkably, upon conjugation to IFN, the fluorescent intensity of the QDs was enhanced dramatically (Fig. 1B). The result could be explained by the fluorescent resonant energy transfer between the IFN and QDs [24]. Similar data was also obtained by the conjugation of BSA and QDs.

The operation parameters were investigated subsequently so as to achieve higher yield of the conjugates.

3.3. The determination of optimal time for the conjugation

The reactions were performed at pH 9–10 and sampled per hour from 0 to 8 h. Although QD542-BSA had similar elution time to BSA by gel-permeation HPLC, the strongest fluorescent intensities of the reaction mixture were detected at 2 h (Fig. 2A), after which they were gradually decreased. As the stable area of the QD542-BSA in UV absorption detected by HPLC after 2 h (Fig. 2B), it is not due to the lower reaction efficiency. Since the reaction time has a significant effect on the yield of QDs conjugates, the optimal time for conjugating is set for 2 h.

3.4. The determination of optimal pH for the conjugation

The conjugating reaction of QDs and BSA mediated by NHS was investigated at different pH value ranging from 5 to 11. We found that the higher pH of the reaction mixture, the stronger intensity of the fluorescence was obtained, which representing
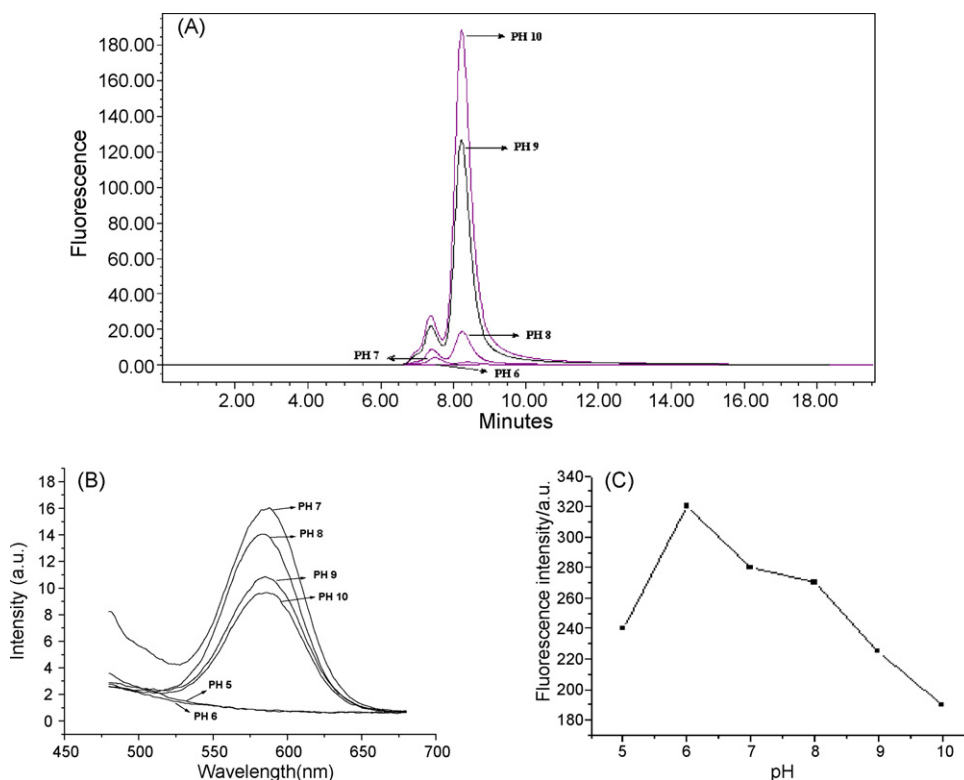
Fig. 3. (A) At different reaction pH value changing from 6 to 10 for 2 h, the fluorescent intensities of QD574-BSA were detected by gel-permeation HPLC. (B) and (C) are the fluorescent intensities of QD574 and QD574-BSA detected by fluorospectrophotometer at different pH, respectively.
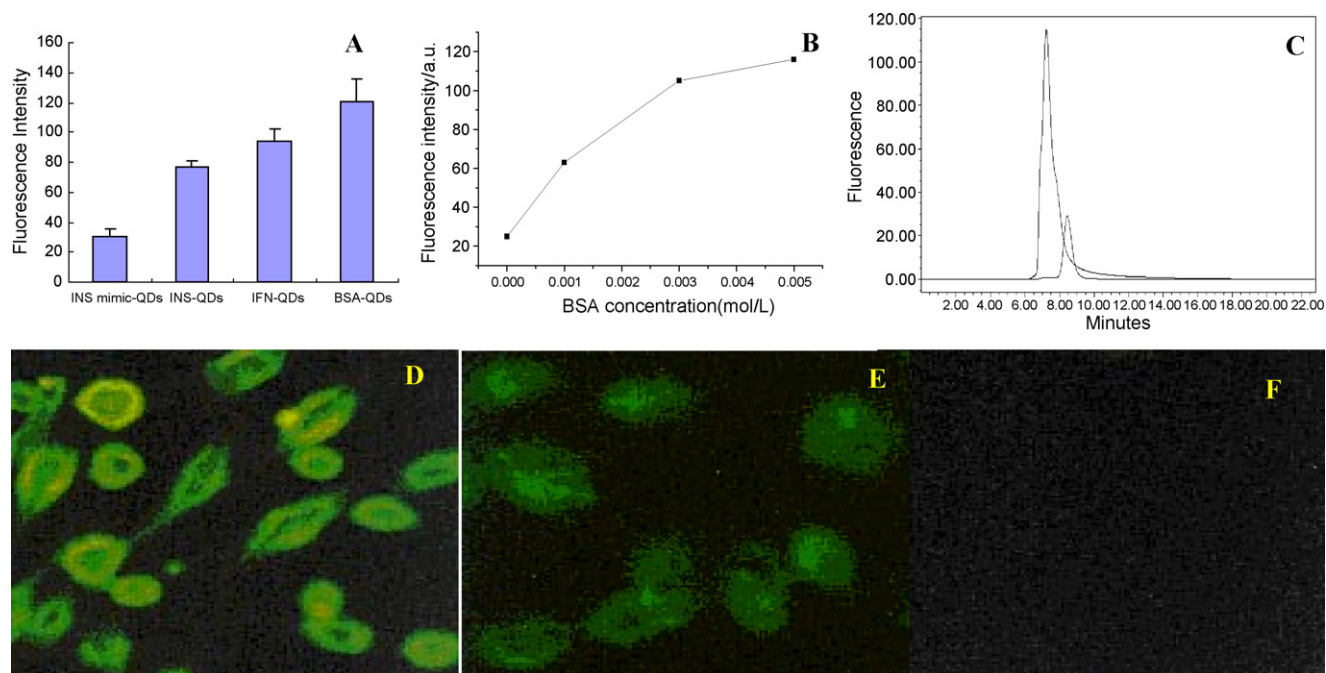
Fig. 4. (A) Fluorescent intensities of QD542-peptide/protein with different sizes and molecular weights; (B) Fluorescent intensities of QD542-INS mimic/BSA in the presence of increasing concentrations of BSA in the conjugation reaction; (C) the major elution peak at 7.1 min elution time is QD542-INS mimic/BSA in the presence of 0.003 mol/L BSA, the weak peak is QD542-INS mimic without adding BSA. CHO-IR cells were incubated with QD542-INS mimic/BSA (D), QD542-INS mimic (E) and QD542-BSA (F) for 1 h.

the presence of more product (Fig. 3A). In order to maintain the native conformation and the activity of the proteins and also keep the highest efficiency of the conjugation reaction at the same time, the reactions were preferred at the mildly basic pH 9–10.

3.5. The effect of pH on fluorescent property

To investigate the effect of surrounding environment on QDs, fluorescence of QD574-BSA were determined in PBS at different pH (Fig. 3C). The result was compared with QDs (Fig. 3B). The strongest fluorescence intensity of QD574-BSA was obtained at pH 6, while that of QD574 was obtained at pH 7. The maxim emission intensity of QDs was drifted to acidic at pH 6 after conjugated with BSA, while that of the sole QDs was weak at pH 7 and almost quenched at pH 6. Similar results were also found in conjugating with other proteins, which indicate that protein would stable the structure of the QDs and enhance the fluorescent intensity. The result also indicates that the conjugates will be fit for cell labeling and maintaining the native activities of biomolecules after conjugation, especially for enzymes.

3.6. The effects of molecular weight on the conjugation

Peptides/proteins with different sizes and MWs were conjugated with QDs at pH 9 for 2 h, and then the mixtures were analyzed by gel-permeation HPLC. Although the molar ratio and the conjugating conditions remained the same, the fluorescent intensities were depressed with the decreased MWs of the protein/peptide (Fig. 4A). Partial QDs were always destroyed

and the precipitations were visible when conjugating with short peptides. We hypothesize that the structure of the QDs can be better stabilized and their fluorescent properties can be better enhanced after conjugating with higher MWs molecules.

As QDs-peptides conjugates indicated weak fluorescent intensities, it is undesirable to apply them in subsequent applications in biological systems. Molecules with higher MWs were able to enhance the fluorescent intensities; different concentration of BSA (0.001, 0.003, and 0.005 mol L^{-1}) was added to the reaction mixture when QDs were conjugated with short peptides (Fig. 4B). The fluorescent intensities of QD542-INS mimic/BSA increased dramatically with the augmented amount of BSA added in the labeling reaction (Fig. 4C). This could likely be that static passivation of the surface defects by molecules in the environment plays an important role in the surfacerelated emission and stability of the photophysical properties of the QDs [25].

3.7. Bioactivities of QDs-peptide/protein in cell labeling

Biomolecules such as peptide/protein with labels allows us to study cellular localization and interaction with other molecular and cellular components. Stable water-soluble CdTe nanoparticles with various wavelengths conjugated with a number of peptides and proteins have been prepared and separated as described. The bioactivities of QDs-peptide/protein were studied in cell labeling.

After incubation with CHO-IR for 1 h, which can overexpress insulin receptors on its membrane, the optimized QD542-INS mimic/BSA was found clustered on the membrane
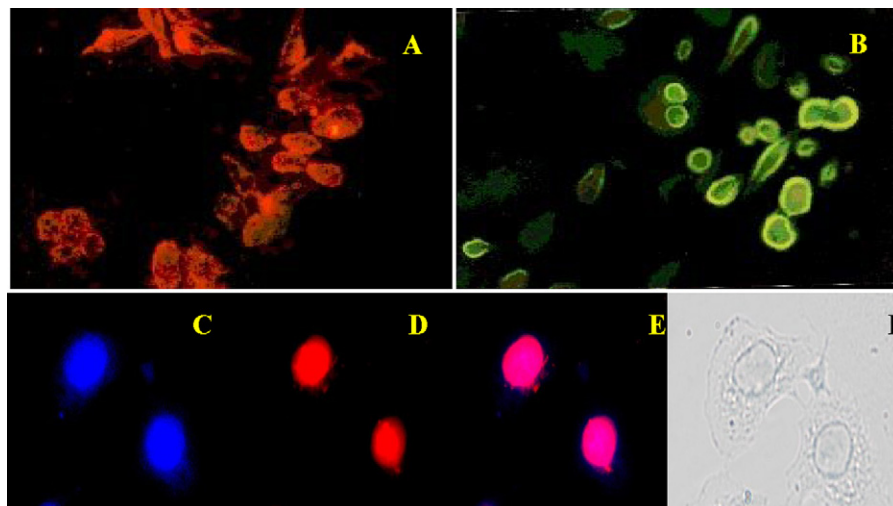
Fig. 5. (A) L929 cells were incubated with QD574-IFN; (B) CHO-IR cells were incubated with QD527-INS. (C–F) are internalization and localization of fluorescent micelles in the cytoplasmic compartment of HEp-2 cells using a 40X objective. (C) Nuclear staining with Hoechst 33342; (D) nuclear staining with QD574-SA–biotin-NTS; (E) an overlay of (C) and (D), pink areas indicate colocalization of micelles (red) with the nucleus (blue); (F) visible light (For interpretation of the references to color in this figure legend, the reader is referred to the web version of the article.).

(Fig. 4D), while QD542-INS mimic resulted in weak fluorescent labeling (Fig. 4E). QD542-BSA did not bind to the cell surface nor give any positive labeling (Fig. 4F). Unconjugated QDs showed no association with cells and no fluorescence of washed samples (data not shown). The addition of moderate BSA in conjugating reaction can both enhance the fluorescent intensity and maintain the bioactivities of biomolecules. Both QD574-IFN (Fig. 5A) and QD527-INS (Fig. 5B) gave strong and specific fluorescent labeling.

Molecular probes for biomolecular recognition are of great importance in the fields of chemistry, biology and medical science as well as in biotechnology. The QDs conjugates were evaluated for their subcellular distribution in cells. QD574-SA–biotin-NTS was internalized by the HEp-2 cells and localized in the nucleus (Fig. 5D), while the QD574-SA conjugate gave no fluorescent signal. Similar results were also obtained in the mitochondria of neonatal rat cardiomyocytes (NRCMs) incubated with QDs-mitochondria signal peptide (data not shown).

Cell behavior and MTT studies showed that labeling with QDs or QDs conjugates caused no obvious toxicity. Strong fluorescent intensities of the labeled cells could be observed without obviously depressed even after storage at $-20\,^\circ$C for 5 months [26].

Recently, we are studying about labeling cells with multiple fluorescent QDs conjugated to several functional proteins simultaneously. This approach might provide great help to the functional genome or protein research.

4. Conclusions

We provide a novel method mediated by NHS for conjugating 3-mercaptopropyl acid-stabilized CdTe nanoparticles synthesized in aqueous solution to peptide/protein. The optimum reaction pH and time were successfully confirmed. The method presented in this paper is simple, but effective and feasible. And most important, the fact that the reaction performed by these proteins and peptides does not change the nature of their interaction with living cells, gives further support to the promise offered by this new technology.

Although the mechanism of the conjugation reaction between the QDs and the protein/peptide molecules has yet to be dissected, the current work demonstrates that this does not affect the functional study of these conjugates. These new types of nanoparticles–biomolecules conjugates could find their own potential application in cell surface labeling, intracellular tracking studies, and other imaging applications.

Acknowledgment

References

[1] Q. Ma, X. Wang, Y. Li, Y. Shi, X. Su, Talanta 72 (2007) 1446.
[2] D. Trau, W. Yang, M. Seydack, F. Caruso, N.T. Yu, R. Renneberg, Anal. Chem. 74 (2002) 5480.
[3] A.P. Alivisatos, Science 289 (2000) 736.
[4] Y. Kim, A.M. Lillo, S.C. Steiniger, Y. Liu, C. Ballatore, A. Anichini, R. Mortarini, G.F. Kaufmann, B. Zhou, B. Felding-Habermann, K.D. Janda, Biochemistry 45 (2006) 9434.
[5] X. Yu, L. Chen, K. Li, Y. Li, S. Xiao, X. Luo, J. Liu, L. Zhou, Y. Deng, D. Pang, Q.J. Wang, J. Biomed. Opt. 12 (2007) 014008.
[6] H. Duan, S. Nie, J. Am. Chem. Soc. 129 (2007) 3333.
[7] J. Peng, K. Wang, W. Tan, X. He, C. He, P. Wu, F. Liu, Talanta 71 (2007) 833.
[8] C.M. Niemeyer, Angew. Chem. Int. Ed. 42 (2003) 5796.
[9] J. Weng, X. Song, L. Li, H. Qian, K. Chen, X. Xu, C. Cao, J. Ren, Talanta 70 (2006) 397.
[10] A.L. Rogach, L. Katsikas, A. Kornowski, D. Su, A. Eychmüller, H. Weller, Ber. Bunsenges. Phys. Chem. 100 (1996) 1772.

[11] A.L. Rogach, L. Kattsikas, A. Kornowski, D. Su, A. Eychmüller, H. Weller, Ber. Bunsenges. Phys. Chem. 101 (1997) 1668.

[12] M.Y. Gao, S. Kirstein, H. Möhwald, A.L. Rogach, A. Kornowski, A. Eychmüller, H. Weller, J. Phys. Chem. B. 102 (1998) 8360.

[13] A.L. Rogach, D. Nagesha, J.W. Ostrander, M. Giersig, N.A. Kotov, Chem. Mater. 12 (2000) 2676.

[14] S. Wang, N. Mamedova, N.A. Kotov, W. Chen, J. Studer, Nano Lett. 2 (2002) 817.

[15] Z. Lin, S. Cui, H. Zhang, Q. Chen, B. Yang, X. Su, J. Zhang, Q. Jin, Anal. Biochem. 319 (2003) 239.

[16] A.R. Clapp, E.R. Goldman, H. Mattoussi, Nat. Protoc. 1 (2006) 1258.

[17] M. Gao, A.L. Rogach, A. Kornowski, S. Kirstein, A. Eychmuller, H. Mohwald, H.J. Weller, Phys. Chem. B. 102 (1998) 8360.

[18] H. Zhang, B. Yang, Thin Solid Films 418 (2002) 169.

[19] C.K. Chan, D.A. Jans, Immunol. Cell Biol. 80 (2002) 119.

[20] S.M. Fujihara, J.S. Cleaveland, L.S. Grosmaire, K.K. Berry, K.A. Kennedy, J.J. Blake, J. Loy, B.M. Rankin, J.A. Ledbetter, S.G. Nadler, J. Immunol. 165 (2000) 1004.

[21] J. Piao, H. Li, L. Wang, L. Gao, Y. Shi, W. Li, J. Jilin Univ. (Sci. Ed.) 3 (2003) 384.

[22] S. Kang, E. Zirbes, R. Kole, Antisense Nucleic Acid Drug Dev. 9 (1999) 497.

[23] H. Zhang, G. Lu, X. Ji, Z. Li, B. Yang, Chem. J. Chin. Univ. 24 (2003) 178.

[24] Q. Chen, Q. Ma, Y. Wan, X. Su, Z. Lin, Q. Jin, Luminescence 20 (2005) 251.

[25] V. Biju, R. Kanemoto, Y. Matsumoto, S. Ishii, S. Nakanishi, T. Itoh, Y. Baba, M. Ishikawa, J. Phys. Chem. C 111 (2007) 7924.

[26] H. Li, H. Liu, H. Zhang, G. Zhu, L. Wang, B. Yang, W. Li, Chem. Res. Chin. Univ. 5 (2004) 982.

A simple and efficient colorimetric anion sensor based on a thiourea group in DMSO and DMSO–water and its real-life application

Jie Shao [a], Hai Lin [b], Hua-Kuan Lin [a],*

[a] *Department of Chemistry, Nankai University, Tianjin 300071, People's Republic of China*
[b] *Key Laboratory of Functional Polymer Materials of Ministry of Education, Nankai University, Tianjin 300071, People's Republic of China*

Abstract

An efficient colorimetric sensor with a thiourea moiety as binding sites and *p*-nitrophenylhydrazine as a signaling unit has been synthesized by only one single-step procedure. Selectivity for anions with the distinct geometry (tetrahedral, trigonal planar and spherical) has been investigated in dry DMSO and even in DMSO/H$_2$O (95:5, v/v) solutions through the naked-eye experiment, UV–vis titration and ^{1}H NMR titration techniques. In particular, the fluoride of toothpaste can be detected qualitatively by the sensor 1.
© 2008 Elsevier B.V. All rights reserved.

Keywords: Anion recognition; Colorimetric sensor; Thiourea; Aqueous; Toothpaste

1. Introduction

In the recent years, considerable interest has been attracted in selective recognition and sensing of anions species via artificial receptors [1,2], because anions play important roles in the environment (pollutant anions from over use of agricultural fertilizers cause eutrophication of lakes and inland waterways) [3], in biological systems (misregulation of anion transport is responsible for a number of medical conditions including cystic fibrosis) [4], and in the clinic (the maintenance of sulfate anion concentration in dialysis patients continues to be problematic) [5]. In particular, more and more importance is attached to colorimetric anion sensors [6,7] since the colorimetric anion sensing system would allow the so-called 'naked-eye' detection of anions without resorting to any spectroscopic instrumentation, being simple and convenient for detection. One successful approach for preparing chromogenic sensors involves the formation of molecular architectures, which contain one or more optical-signaling chromophoric groups that are covalently or noncovalently linked to the receptor moiety, and thus colorimetric sensing of anions with both temporal and spatial resolution would be achieved. Hydrogen-bonding sites typically used in chromogenic or fluorogenic chemosensors are urea [8], thiourea [9], amide [10], phenol [11], or pyrrole subunits [12]. Among them, the thiourea group often chosen as anion binding sites as a functional group is a good hydrogen-bond donor and therefore results in quite stable strongly hydrogen-bonded complexes with different anions such as acetate, phosphate or fluoride. Therefore, large numbers of anion receptors containing the thiourea subunits have been designed, synthesized and tested for anion recognition and sensing during the past decades. For example, Kim et al. [7] have synthesized some receptors by integrating two *p*-nitrophenylthiourea groups into 4, 5-dimethyl-1,2-diaminobenzene, which have been proven to be efficient and colorimetric chemosensors for fluoride and acetate. However, the colorimetric change is observed upon addition of excessive equivalents of anions (65 eq. for fluoride and acetate) only in noncompetitive organic solvents. Up to now, few receptors, which can bind anions in competitive solvents such as H$_2$O and CH$_3$CH$_2$OH, are reported. So the challenges faced for the development of colorimetric sensors capable of anion binding within competitive media still remain.

* Corresponding author. Tel.: +86 22 23502624; fax: +86 22 23502458.
E-mail address: hklin@nankai.edu.cn (H.-K. Lin).

Recently, 4-nitro (and 2,4-dinitro) phenylhydrazine [13,14] is proven to be an optical-signaling group for anion recognition site. All these prompted us to develop a novel, sensitive and colorimetric sensor with thiourea unit as anion recognition sites and *p*-nitrophenylhydrazine unit a chromophore for color change. Sensor 1 was obtained (Fig. 1) by reacting *p*-nitrophenylhydrazine with phenylisothiocyanate as a slight red solid in 80% yield. As expected, it was sensitive to anions and showed a unique color change in the presence of F^-, CH_3COO^- and $H_2PO_4^-$. And it was more interesting that the recognition of the biologically important F^-, CH_3COO^- and $H_2PO_4^-$ anions was achieved in DMSO–water solution via hydrogen-bonding at charge-neutral sites. These results imply that the host 1 has a higher capability of competing with H_2O for anion binding, a character significant for anion receptors for practical detection of analyte of interest.

2. Experimental

2.1. Materials

All reagents for synthesis were obtained commercially and were used without further purification. In the titration experiments, all the anions were added in the form of tetrabutylammonium (TBA) salts, which were purchased from Sigma–Aldrich Chemical, stored in a vacuum desiccator containing self-indicating silica and dried fully before using. DMSO was dried with CaH_2 and then distilled in reduced pressure. And CH_3CN was dried with P_2O_5 (0.5–1:100, v/v) stirring at room temperature overnight and then distilled.

2.2. Apparatus

^{1}H NMR spectra were obtained on a Varian UNITY Plus-400 MHz Spectrometer using tetramethylsilane (TMS) as an internal standard. ESI-MS was performed with a MARINER apparatus. C, H, N elemental analyses were made on an elementar vario EL. UV–vis spectra were recorded on a Shimadzu UV2450 Spectrophotometer with a quartz cuvette (path length = 1 cm) at 298.2 ± 0.1 K.

2.3. General method

All experiments were carried out at 298.2 ± 0.1 K, unless otherwise mentioned. UV–vis spectra were measured using an ultraviolet–visible spectrophotometer, UV-2450 (Shimadzu

Corp., Kyoto, Japan). A 4.0×10^{-4} M solution of the compound 1 in DMSO was prepared and stored in the dry atmosphere. This solution was used for all spectroscopic studies after appropriate dilution. Solutions of 1.0×10^{-2} M tetrabutyl ammonium salts of the respective anions were prepared in dried and distilled DMSO and were stored under a dry atmosphere. Then, the mixture of 0.5 ml solution of the receptor 1, given amount of anions and 0.25 ml H_2O (H_2O would not be added when titrations were carried out in dry DMSO) was diluted with DMSO to 5 ml, whose absorbance was tested immediately.

^{1}H NMR titration experiments were carried out in the DMSO-d_6 solution (TMS as an internal standard). A 1.0×10^{-2} M solution of the compound 1 in DMSO-d_6 was prepared. Then, the increased amount of acetate anion (1.0 M in DMSO-d_6) was added to the solution above-mentioned and ^{1}H NMR of the host–guest system was tested.

Sample containing toothpaste was prepared as following [15,16]: 1 mg commercially available toothpaste (Crest brand) was added to 1 ml H_2O. After toothpaste was dissolved fully in water, the foam was filtered and 0.25 ml filtrate was added to the solution containing 2×10^{-7} mol sensor 1 and 2×10^{-6} mol tetrabutylammonium fluoride. Then the resulting solution was diluted with DMSO to 5 ml, whose absorbance was tested immediately.

2.4. Synthesis of β-N-(p-nitroanilinyl)-phenylthiourea

The synthesis route of receptor 1 is shown in Fig. 1. *p*-Nitrophenylhydrazine (0.153 g, 1 mmol) was dissolved in dry 20 ml CH_3CN. To this solution was added phenylisothiocyanate (0.135 g, 1 mmol) dropwise slowly and stirred under inert atmosphere refluxing for 5 h. Then the reaction mixture was cooled to room temperature. Precipitate formed was filtered and washed with CH_3CN and gained 0.22 g. Yield = 80%. ^{1}H NMR (DMSO-d_6) δ H 9.962 (s 1H), 9.922 (s 1H), 9.20 (s 1H), 8.16 (d 2H $J = 8$ Hz), 7.46 (d 2H $J = 8$ Hz), 7.33 (t 2H $J = 13.2$ Hz), 7.17 (t 1H $J = 15.2$ Hz), 6.84 (d 2H $J = 8$ Hz). Elemental analysis calcd for $C_{13}H_{12}N_4O_2S$ ($M = 288.068$): C, 54.15 H, 4.20 N, 19.43; found: C, 54.15; H, 4.17; N, 19.47.

3. Results and discussion

3.1. UV–vis spectral responses of 1

Compound 1 exhibited two main bands at about 372 nm and 532 nm in the UV–vis spectrum in DMSO solution. The weak
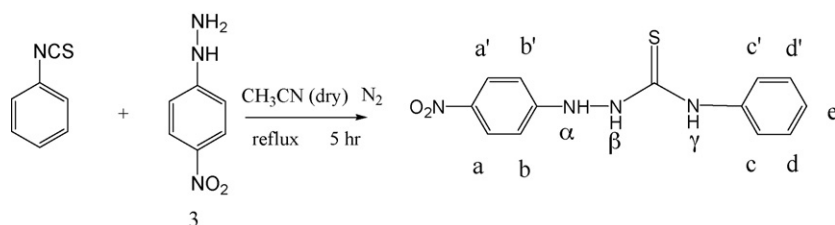
Fig. 1. Synthesis of the sensor 1.
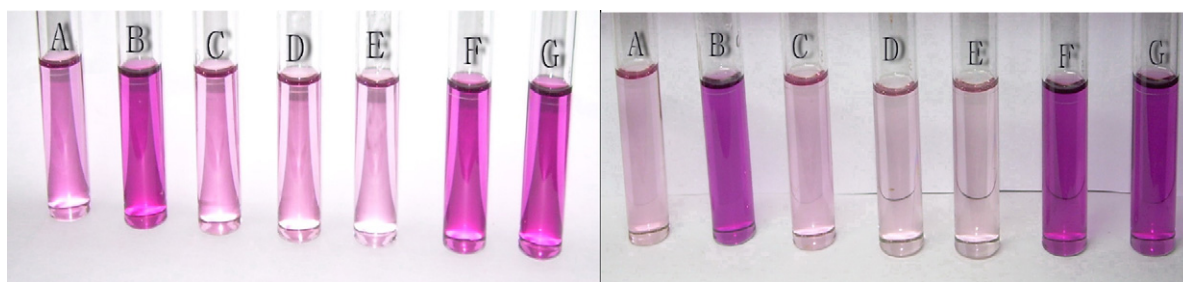
Fig. 2. Color changes of sensor 1 in 95:5 DMSO/H$_2$O (left) and DMSO (right) (4 × 10^{-5} mol L^{-1}) after addition of 10 eq. anions. A: 1 only; B: 1 + F$^-$; C: 1 + Cl$^-$; D: 1 + Br$^-$; E: 1 + I$^-$; F: 1 + H$_2$PO$_4$$^-$; G: 1 + AcO$^-$.

absorbance band at 532 nm was ascribed to π–π* transition of *p*-nitrophenylhydrazine. The presence of fluoride resulted in the intensity of the absorbance band at 372 nm decreasing gradually and the absorbance band at 532 nm increasing gradually, simultaneously accompanied with significant color changes from light purple to deep purple (see Fig. 2 right). On the contrary, addition of an excess amount of chloride, bromide and iodide did not induce any notable spectrum changes (see Fig. 1 in supplementary data). As observed in Fig. 3, the presence of two well-defined isosbestic points indicated that only two species were present at equilibrium: 1 and 1·F$^-$ adduct with an association constant K_{ass} = 7.90 (±0.16) × 10^4 mol^{-1} L (see Table 1). In addition, a Job plot using mixtures of 1 and F$^-$ in DMSO solution also showed the 1:1 stoichiometry of the adduct. On the other hand, the addition of CH$_3$COO$^-$ and H$_2$PO$_4$$^-$, whose association constants for the 1:1 stoichiometry host–guest complex were calculated as 1.58 (±0.30) × 10^5 mol^{-1} L and 3.18 (±0.60) × 10^4 mol^{-1} L, respectively, led to the similar changes of the absorption spectrum with that of fluoride (see supplementary data).

Generally speaking, most spectrum changes and color changes would disappear quickly upon the addition of competitive hydrogen-bonding solvents such as ethanol or water [17]. To our surprise, the distinctive color changes, which were shown in Fig. 2 (left), were observed upon addition of F$^-$, H$_2$PO$_4$$^-$ and AcO$^-$ in DMSO–water solution. To explore potential and analytical application of the sensor 1 for anions tested, the UV–vis titrations were carried out in 95:5 DMSO/H$_2$O mixtures. The anion binding ability of the host 1 was further evaluated through UV–vis titration and the identical titrations of 1, which were similar with those obtained in DMSO solution, were obtained in 95:5 DMSO/H$_2$O solutions (see Fig. 4). The results revealed that the spectra changed similarly as that of dry DMSO solution (see Fig. 4). Likewise, there was significant increase in the intensity of the band at 532 nm upon addition of F$^-$, H$_2$PO$_4$$^-$ ions (see supplementary data), which corresponded to light-deep color changes. Accordingly, not only color changes but also association constants indicated that the addition of small amounts of competitive solvents such as water was of little effect on anion sensing property of 1. The fact that the addition of water to DMSO up to 5% did not interfere in the anion sensing and in the binding affinity of the anions for 1 could be rationalized as follows. Firstly, the compound 1 bearing thiourea group which has been proven to be a good hydrogen-bonding acceptor could make strong hydrogen-bonds with the anions, which water molecules could not break [18]. Secondly, DMSO is a very good hydrogen-bond accepting solvent and in this situation it can interact strongly with the water molecules in the concentration utilized. Consequently, the possibility of
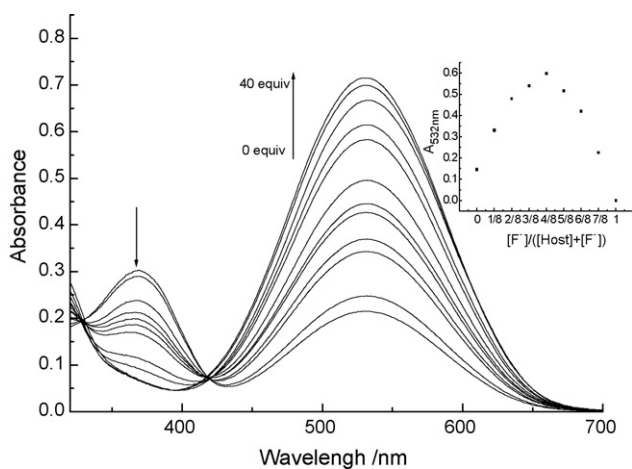
Fig. 3. Titration of 4 × 10^{-5} mol L^{-1} solution of 1 in DMSO with a standard solution of tetrabutylammonium fluoride in DMSO. Inset: the stoichiometry analysis of fluoride complex 1·F$^-$ by Job plot analysis; [1] + [F$^-$] = 8 × 10^{-5} mol L^{-1}, at 298 ± 0.1 K.
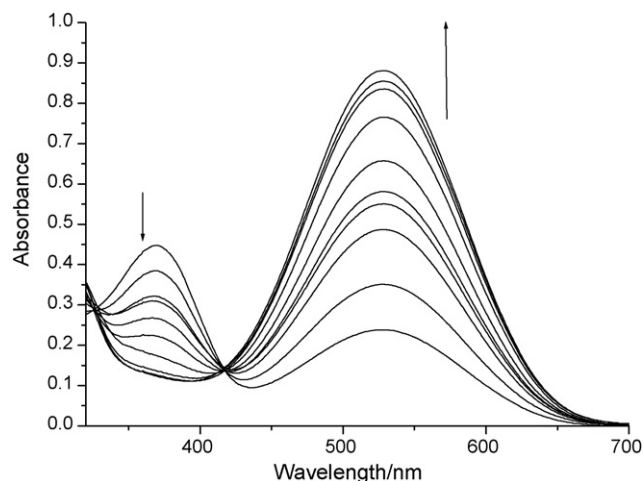
Fig. 4. Changes in the absorption spectra of 1 (4 × 10^{-5} mol L^{-1}) on addition of Ac$^-$ in 95:5 DMSO/H$_2$O (v/v).

Table 1
Association constants (K_{ass}, M^{-1}) of the sensor 1 with anions in DMSO and DMSO:H$_2$O (95:5, v/v) at 298.2 ± 0.1 K

Anion[a]	F$^-$	CH$_3$COO$^-$	H$_2$PO$_4$$^-$	Cl$^-$ Br$^-$ I$^-$
K_{ass} [b]	7.90(±0.16) × 10^4	1.58(±0.30) × 10^5	3.18(±0.60) × 10^4	_[d]
K_{ass} [c]	1.07(±0.18) × 10^4	8.31(±0.45) × 10^4	1.98(±0.17) × 10^4	–

[a] All the anions were added in the form of tetra-*n*-butylammonium (TBA) salts.
[b] The association constant was determined in DMSO.
[c] The association constant was determined in 95:5 DMSO/H$_2$O.
[d] The association constant could not be determined.

the interaction of the anions with the sensor was improved greatly.

3.2. Association constants

The association constants were determined by nonlinear fitting analyses of the titration curves according to the Eq. (1), 1:1 host–guest complexation [19].

$$A = \frac{A_0 + (A_{lim} - A_0)\{c_H + c_G + 1/K_s - [(c_H + c_G + 1/K_{ass})^2 - 4c_H c_G]^{1/2}\}}{2c_H} \tag{1}$$

where c_G and c_H are the concentration of guest and host, respectively and A is the intensity of absorbance at certain concentration of host and guest. A_0 is the intensity of absorbance of host only and A_{lim} is the maximum intensity of absorbance of host when guest is added. K_{ass} is the affinity constant of host–guest complexation. As clearly observed in Table 1, the selectivity trends of binding affinities of anions for 1 (in DMSO–water solution or dry DMSO) were determined to be AcO$^-$ > F$^-$ ~ H$_2$PO$_4$$^-$ ≫ Cl$^-$ ~ Br$^-$ ~ I$^-$. The selectivity for special analyte of the host molecule could be rationalized on the basis of not only the guest basicity but also shape complementarity between the host and the anionic guests. So, the selectivity for AcO$^-$ could be rationalized on the basis of the guest basicity and structure of the complex. Fabbrizzi and other research group's [20,21] studies showed that thiourea is a good H-bonds donor and excellent receptor for tetrahedral anions and Y-shaped anions through the formation of multitopic H-bonds. And therefore the acetate anion, which is trigonal planar, might be the fittest for binding sites of the receptor among the anions tested and form multitopic hydrogen-bonding interactions with 1 (see Fig. 5), which would be further verified from the ^{1}H NMR titrations. This clearly accounted for that anions were capable of

being sensed in highly competitive media by the host 1, where the recognition was through hydrogen-bonding.

3.3. ^{1}H NMR titration

To identify the possible anion binding mode, ^{1}H NMR titrations, which were shown in Fig. 6, were carried out in DMSO-d_6.

It was found that the amide NH (H$_\beta$ and H$_\gamma$) proton signals were broaden and underwent a continuous downfield shift [9,13], with increasing F$^-$ concentration from 0 eq. to 4.5 eq. indicating the formation of a host–guest hydrogen-bonding complex and an overall change of the electron distribution [7]. However; the proton signal of H$_\alpha$ did not shift at all proving that H$_\alpha$ did not participate in the formation of hydrogen-bonding. In addition, the proton signals such as H$_b$ and H$_c$ in the benzene ring exhibited a downfield shift, suggesting the formation of C–H···F$^-$ hydrogen-bonding [13]. As mentioned above, the proposed binding mode in solution was shown in Fig. 5, and the strong interaction of the amide NH with fluoride might cause internal charge transfer (ICT), which accounted for increase in

Fig. 5. The proposed host–guest binding mode in solution.

Fig. 6. ^{1}H NMR titrations of 1 in DMSO-d_6 (0.01 mol L^{-1}) with F$^-$ (as tetra-butylammonium salt). (a) 0 eq. (b) 0.5 eq. (c) 2 eq. (d) 4.5 eq.
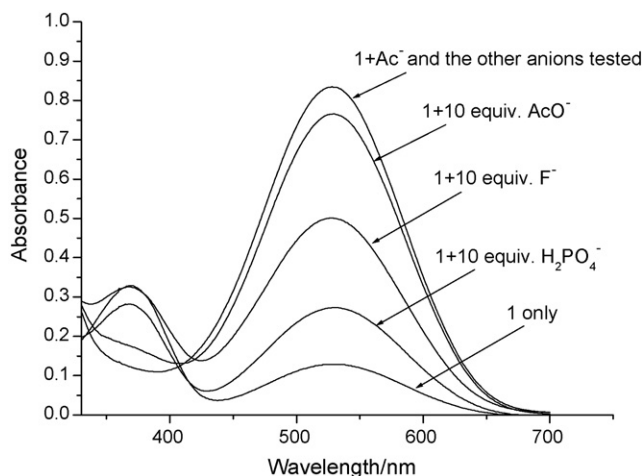
Fig. 7. UV–vis spectra of 1 (4×10^{-5} mol L^{-1}) in 95:5 DMSO/H$_2$O (v/v) in the presence of 10 eq. of AcO$^-$ ion and miscellaneous anions including F$^-$, H$_2$PO$_4^-$, Cl$^-$, Br$^-$ and I$^-$.

the intensity of the absorbance band and the generation of a deep purple color.

4. Analytical application

As an excellent anion sensor, the high selectivity for the analyte of interest over a complex background of potentially competing species would be achieved. Consequently, the competition experiments were carried out in the presence of 10 eq. of one of the above anions or the mixture of them, respectively. Obviously, the increase of absorbance resulting from the addition of the AcO$^-$ ion was influenced slightly by the subsequent addition of miscellaneous anions (see Fig. 7). Recently, we were inspired by Koide and coworkers [15,16], who reported qualitative detection of palladium and fluoride in real-life application, respectively. Therefore, to further determine whether this colorimetric sensor could be applied to F$^-$ analyses in real-life, a sample that contained commercially available toothpaste and F$^-$ (as tetrabutylammonium salts) was prepared in H$_2$O solution. The proper amount of the sample was added to the solution of the sensor 1 in DMSO and the resulting solution, which con-

sisted of 0.05 mg mL^{-1} toothpaste, 4×10^{-4} mol L^{-1} F$^-$ ions and 4×10^{-5} mol L^{-1} sensor 1 in DMSO:H$_2$O (95:5, v/v), was obtained. Then the UV–vis absorbance of the resulting solution was measured and compared to a control (toothpaste-free F$^-$ solution). Just as shown in Fig. 8, the signal from the F-contaminated toothpaste solution was different from that of the control, which was ascribed to fluoride of toothpaste, demonstrating that the sensor 1 could be applied in qualitative detection of fluoride in toothpaste.
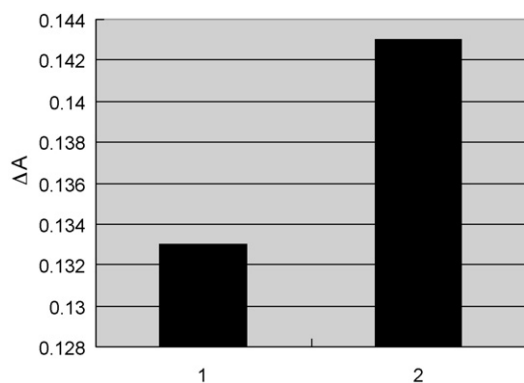
5. Conclusion

To sum up, we have presented a simple and colorimetric charge-neutral receptor, which allows so-called "naked-eye" detection in a straightforward and inexpensive manner in aqueous solution, offering qualitative and quantitative information without using expensive equipments. In addition, the sensor has detected successfully fluoride of toothpaste and is expected to have many opportunities in detection of anions in real-life owing to the simplicity and sensitivity of the analysis.

Appendix A. Supplementary data

Supplementary data associated with this article can be found, in the online version, at doi:10.1016/j.talanta.2007.12.041.

References

[1] V. Amendola, M. Bonizzoni, D. Esteban-Gómez, L. Fabbrizzi, M. Licchelli, F. Sancenón, A. Taglietti, Coord. Chem. Rev. 250 (2006) 1451.
[2] T. Gunnlaugsson, M. Glynn, G.M. Tocci(née Hussey), P.E. Kruger, F.M. Pfeffer, Coord. Chem. Rev. 250 (2006) 3094.
[3] R. Martinez-Manez, F. Sancenon, Chem. Rev. 103 (2003) 4419.
[4] M. Yu, H. Lin, G.H. Zhao, H.K. Lin, J. Mol. Recognit. 20 (2007) 69.
[5] M. Brunetti, L. Timio, P. Saronio, E. Capodicasa, J. Nephephrol. 14 (2001) 27.
[6] X. He, S. Hu, K. Liu, Y. Guo, J. Xu, S. Shao, Org. Lett. 8 (2006) 333.
[7] Y.J. Kim, H. Kwak, S.J. Lee, J.S. Lee, H.J. Kwon, S.H. Nam, K. Lee, C. Kim, Tetrahedron 62 (2006) 9635.
[8] E.J. Cho, B.J. Ryu, Y.J. Lee, K.C. Nam, Org. Lett. 7 (2005) 2607.
[9] M. Vázquez, L. Fabbrizzi, A. Taglietti, R.M. Pedrido, A.M. González-Noya, M.R. Bermejo, Angew. Chem. Int. Ed. 43 (2004) 1962.
[10] S.O. Kang, R.A. Begum, K. Bowman-James, Angew. Chem. Int. Ed. 45 (2006) 7882.
[11] E.R. Libra, M.J. Scott, Chem. Commun. (2006) 1485.
[12] T. Mizuno, W.H. Wei, L.R. Eller, J.L. Sessler, J. Am. Chem. Soc. 124 (2002) 1134.
[13] X.D. Yu, H. Lin, Z.Sh. Cai, H.K. Lin, Tetrahedron Lett. 48 (2007) 8615.
[14] J. Shao, H. Lin, M. Yu, Z.Sh. Cai, H.K. Lin, Talanta 75 (2008) 551.
[15] M.A. Palacios, R. Nishiyabu, M. Marquez, P. Anzenbacher Jr., J. Am. Chem. Soc. 129 (2007) 7538.
[16] F. Song, A.L. Garner, K. Koide, J. Am. Chem. Soc. 129 (2007) 12354.

Fig. 8. The proof of concept for fluoride detection in toothpaste (1) sensor + tetrabutylammonium fluoride; (2) sensor + tetrabutylammonium fluoride + toothpaste ($\Delta A = A_{\text{host+guest}} - A_{\text{host only}}$).

[17] V. Thiagarajan, P. Ramamurthy, D. Thirumalai, V.T. Ramakrishnan, Org. Lett. 7 (2005) 657.

[18] T. Gunnlaugsson, P.E. Kruger, P. Jensen, J. Tierney, H.D.P. Ali, G.M. Hussey, J. Org. Chem. 70 (2005) 10875.

[19] J. Bourson, J. Pouget, B. Valeur, J. Phys. Chem. 97 (1993) 4552.

[20] M. Boiocchi, L. Del Boca, D.E. Gomez, L. Fabbrizzi, M. Licchelli, E. Monzani, J. Am. Chem. Soc. 126 (2004) 16507.

[21] D.H. Lee, K.H. Lee, J.I. Hong, Org. Lett. 3 (2001) 5.

Blends of TiO$_2$ nanoparticles and poly (*N*-isopropylacrylamide)-*co*-polystyrene nanofibers as a means to promote the biorecognition of an anticancer drug

Min Song [a], Chao Pan [b], Jingyuan Li [a], Renyun Zhang [a], Xuemei Wang [a,*], Zhongze Gu [a]

[a] *State Key Lab of Bioelectronics, Chien-Shiung Wu Laboratory, Southeast University, Nanjing 210096, China*
[b] *College of Science, Dalian Fisheries University, Dalian, Liaoning 116023, China*

Abstract

The poly (*N*-isopropylacrylamide)-*co*-polystyrene (PNIPAM-*co*-PS) nanofibers have been fabricated by electrospinning, and the blends of PNIPAM-*co*-PS nanofibers with titanium dioxide (TiO$_2$) nanoparticles have been characterized and utilized as the new nanocomposites to enhance the relevant detection sensitivity of biomolecular recognition of an anticancer drug daunorubicin. Our observations demonstrate that upon application of the nanoTiO$_2$–PNIPAM-*co*-PS polymer nanocomposites, the drug molecules could be readily deposited on the surface of the relevant blends so that the remarkable enhancement effect of the new nanocomposites on the respective biorecognition of daunorubicin could be observed, suggesting the potential valuable application of the blending of the nanoTiO$_2$ and PNIPAM-*co*-PS polymer nanocomposites in high sensitive bioanalysis.
© 2008 Elsevier B.V. All rights reserved.

Keywords: Biomaterials; Thin films; Electrochemistry; Self-organization; Polymer; Anticancer drug

1. Introduction

Study on the biorecognition of anticancer drugs by combination with nanotechnology may lead to the revealing of the important mechanisms of the relevant antitumor or antiviral components. Recently, the emergence of nanomaterials such as polymeric micelles, polymer conjugates, metal or semiconductor nanoparticles and nanotubes has attracted continuing interest in biomedical and bioengineering, which may afford new strategies to facilitate the respective biomolecular recognition and enhance the specific binding ability of target system to biomacromolecules like DNA and proteins [1–6]. It has been reported that nanotitanium dioxide (TiO$_2$) is one of the most promising biocompatible nanomaterials capable of a wide variety of biomedical applications, which possess the high reactivity and the specific ability to advance photochemical applications and can efficiently separate photogenerated charges that could facilitate some redox chemical reactions with attached biomolecules [7,8]. Besides, polymer micelle (PM) has been developed as a valuable alternative to "classical" low-molecular weight surfactants owing to their relatively low toxicity and high drug loading capacity. The core-shell assemblies obtained via the hydrophobic association of amphiphilic polymers generally exhibit low critical association concentrations (CAC), resulting in remarkable stability in solution [9]. Since Pelton and co-workers first reported the colloidal particles based on poly (*N*-isopropylacrylamide) (PNIPAM) [10], PNIPAM-based polymer colloids have attracted subsequently intensive interest. Now it is well known that aqueous solutions of PNIPAM have a rather low critical solution temperature (LCST). At the LCST, PNIPAM exhibits a coil–globule transition and a rapid change in interfacial properties. By utilizing this unique property, PNIPAM has been extensively investigated in the field of drug delivery systems, tissue engineering, biomedical, and other pharmaceutical applications [11–14]. Moreover, PNIPAM microgel was found to exhibit outstanding capabilities as potential carriers or pro-

tective containers for biologically active molecules [9,13]. If immobilized onto a flat substrate, the LCST behavior of PNI-PAM could lead to a temperature-controlled wettability and mechanical change on the surface [15], which could be used for the control of protein adsorption [16,17] and cell adhesion [18,19].

Since electrospinning is a convenient approach for generating nanofibers, a variety of materials such as polymers, ceramics with well-controlled sizes, compositions, and morphologies can be fabricated by this method [20–23]. In our study, we firstly used the electrospinning method to fabricate poly (N-isopropylacrylamide)-co-polystyrene (PNIPAM-co-PS) nanofibers. Then, by combining with other nanoparticles such as nanoTiO$_2$, we have explored the possibility to blend the bare TiO$_2$ nanoparticles with PNIPAM-co-PS nanofiber suspension to prepare the new TiO$_2$–PNIPAM-co-PS nanocomposites, which were also characterized by TEM study. Furthermore, the prepared TiO$_2$–PNIPAM-co-PS nanocomposites have been utilized as the new functional nanocomposites to promote the respective biorecognition of anticancer drug daunorubicin. The results of our studies demonstrate that these new nanocomposites can remarkably enhance the relevant detection sensitivity of biomolecular recognition and efficiently facilitate the DNA binding affinity of anticancer drug daunorubicin.

2. Experimental

2.1. Materials

Calf thymus DNA (CT-DNA) was purchased from Sigma, while daunorubicin was obtained from Nanjing pharmacy factory (analytical grade). Bare TiO$_2$ nanoparticles (P25) with a diameter of about 30 nm were purchased from Degussa. TiO$_2$ nanoparticles were dispersed in double-distilled water to prepare the suspension. All other reagents were analytical grade. Daunorubicin stock solutions were freshly prepared and stored in the dark at 4 °C. Phosphate buffer solutions (0.1 M, pH 7.2) were prepared by using double-distilled water.

N-isopropylacrylamide (NIPAM Acros; KOH JIN, Japan, 1% inhibitor) was recrystallized from hexane/toluene (v/v = 1/1). Potassium persulfate (KPS; 99% Aldrich Chemicals, Milwaukee) were recrystallized from water. Styrene (Sigma) was purified by pressure reducing distillation.

2.2. Synthesis of PNIPAM-co-PS co-polymer

A free-radical emulsion polymerization method was used to prepare poly (N-isopropylacrylamide)-co-polystyrene (PNIPAM-co-PS). In a typical experiment, certain amounts of styrene and NIPAM were dissolved in an appropriate amount of de-ionized water in a two-necked, round-bottom flask with N$_2$ bubbling for 30 min for the removal of any dissolved oxygen. The monomer mixture was then heated to 70 °C in an aqueous temperature bath. Certain amount of KPS was added to the system to act as a thermal initiator, and the polymerization process was allowed to continue for 12 h. The product was then precipitated out by the elevation of the solution temperature to 70 °C.
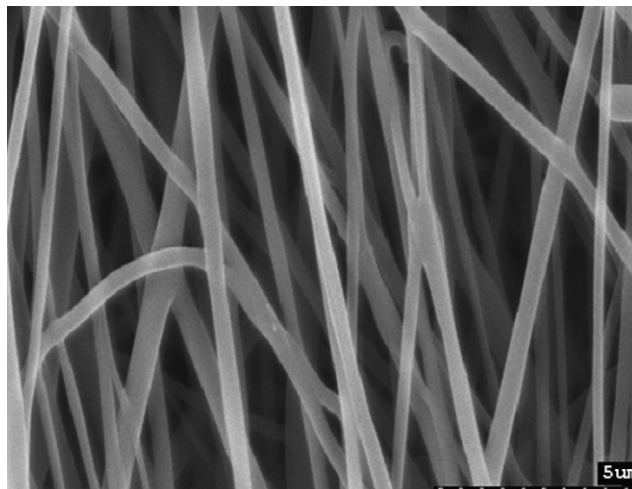
Fig. 1. Scanning electron micrograph (SEM) of poly (N-isopropylacrylamide)-co-polystyrene (PNIPAM-co-PS) nanofibers.

Excess reagents were removed with a water rinse in a cyclic fashion between the ambient temperature and 70 °C for three times; the water was refreshed for each cycle. The final product was dried at 70 °C for 24 h.

2.3. Preparation of PNIPAM-co-PS nanofibers

PNIPAM-co-PS nanofibers were fabricated by electrospinning. As a typical procedure, the PNIPAM-co-PS (Mn = 340 000) was dissolved in N, N'-dimethylformamide (DMF) (10 wt%), which was stirred for 2 h. Then, the mixture was loaded into a syringe with a stainless needle with the diameter of 500 μm and connected to a high-voltage supply capable of generating voltage up to 30 kv. An aluminum foil is used as the collector, while the distance from the tip of the needle to the aluminum foil is 15 cm and the feeding is 1 mL/h. The scanning electron microscope (SEM) was utilized to characterize the PNIPAM-co-PS nanofibers. The typical SEM image of the PNIPAM-co-PS nanofibers was illustrated in Fig. 1 (magnification: 10 000×; accelerating voltage: 20 kV).

2.4. Preparation of TiO$_2$–PNIPAM-co-PS nanocomposites

Initially, the aqueous suspension of nanoTiO$_2$ (4.0×10^{-3} g/L) and PNIPAM-co-PS (4.0×10^{-3} g/L) nanofibers was prepared respectively in double-distilled water by ultrasonic for about 20 min. Then, the TiO$_2$ (4.0×10^{-3} g/L) and PNIPAM-co-PS (4.0×10^{-3} g/L) suspension was blended together with the equivalent volume for at least 12 h to prepare the new TiO$_2$–PNIPAM-co-PS nanocomposites. Afterwards, the relevant PNIPAM-co-PS nanofibers and TiO$_2$–PNIPAM-co-PS nanocomposites were characterized by TEM, respectively.

2.5. Apparatus and procedures

Differential pulse voltammetry (DPV) and cyclic voltammetry (CV) studies were performed on CHI660b (USA) electrochemical workstation to detect the respective electro-

chemical behavior of daunorubicin at different pH values and in the absence/presence of nanoTiO$_2$–PNIPAM-*co*-PS polymer nanocomposites or DNA. The relevant measurements were carried out at ambient temperature (20 ± 2 °C) in a three electrodes electrochemical cell consisting of a glassy carbon electrode (GCE) as the working electrode, a Pt wire as the counter electrode and an Ag wire as the quasi-reference electrode. We found that the reference potential of a SCE and the Ag wire in 0.1 M pH 7.2 phosphate buffer, has the relationship of $V_{SCE} = V_{Ag\ wire} + 0.07\ V$. All solutions for the study of the biorecognition of daunorubicin were prepared in PBS (pH 7.2, 0.1 M). All experiments were repeated at least three times.

Daunorubicin (3.3×10^{-4} M) and DNA (1.5×10^{-3} M) were dissolved in PBS (pH 7.2, 0.1 M). During electrochemical measurements, the TiO$_2$–PNIPAM-*co*-PS nanocomposites (8.8×10^{-4} g/L) were added to the relative solutions including daunorubicin or/and DNA. In control experiments, only nanoTiO$_2$ (8.8×10^{-4} g/L) or PNIPAM-*co*-PS nanofibers (8.8×10^{-4} g/L) were injected into the solutions of daunorubicin or/and DNA.

2.6. SEM and TEM characterization

Scanning electron micrographs (SEM) were obtained with a scanning electron microscope (Hitachi, S-3000N), using an accelerating voltage of 20 kV. TEM images of PNIPAM-*co*-PS nanofibers and TiO$_2$–PNIPAM-*co*-PS nanocomposites were obtained by using JEM2000EX (JEOL) at room temperature (20 ± 2 °C).

3. Results and discussion

3.1. Optimization of electrospinning process parameters

A number of parameters are known to influence the size and the morphology of the fibrous mat obtained by electrospinning process [24]. In the present study, some of the process parameters were optimized so as to obtain membranes that consist of free fibers with uniform size and well-defined morphology. Based on a few preliminary experiments, the following process parameters have been optimized initially including the gap between spinneret and collector, 15 cm; spinneret needle size, 0.5 mm; solution feed rate, 1 mL min^{-1}; applied electric voltage, 15 kV.
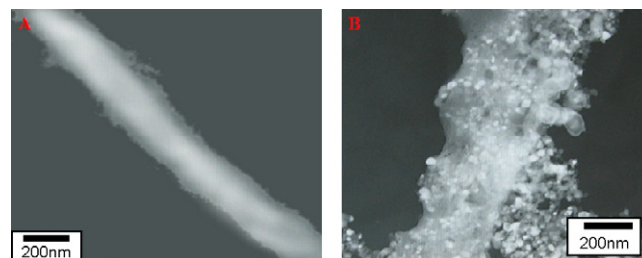
Fig. 2. Typical TEM images of the PNIPAM-*co*-PS nanofibers (A) and nanoTiO$_2$–PNIPAM-*co*-PS polymer nanocomposites (B).

Fig. 1 shows typical SEM image of electrospun fibers. The morphologies were obtained for the PNIPAM-*co*-PS membranes with 10 wt% solution in DMF, which indicates the uniform PNIPAM-*co*-PS polymer fibers. The nanofibers diameter varies in the range of 400–500 nm. The electrospun fibers are circular in cross-section with a smooth surface finish and the interlaying of the fibers generates the microporous structure with fully interconnected pores.

3.2. The electrochemical behavior of daunorubicin in the presence of nanoTiO$_2$–PNIPAM-co-PS polymer nanocomposites

To prepare the nanoTiO$_2$–PNIPAM-*co*-PS polymer nanocomposites, the PNIPAM-*co*-PS nanofibers were initially fabricated in this study by electrospinning method. Afterwards, PNIPAM-*co*-PS nanofibers were added into double-distilled water. And then the relevant nanoTiO$_2$ (4.0×10^{-3} g/L) and PNIPAM-*co*-PS (4.0×10^{-3} g/L) suspension was blended together with the equivalent volume to prepare the new TiO$_2$–PNIPAM-*co*-PS nanocomposites. The typical TEM images of PNIPAM-*co*-PS nanofibers and TiO$_2$–PNIPAM-*co*-PS polymer nanocomposites were illustrated in Fig. 2A and B, respectively. It is evident from Fig. 2B that nanoTiO$_2$ has been readily self-assembled on the surface of PNIPAM-*co*-PS nanofibers as the new TiO$_2$–PNIPAM-*co*-PS nanocomposites.

On the basis of these observations, we have further explored the potential effect of the new TiO$_2$–PNIPAM-*co*-PS nanocomposites to the respective biorecognition of anticancer drugs. The apparent enhancement effect of the relevant nanomaterials on the electrochemical behavior of anticancer drug daunorubicin
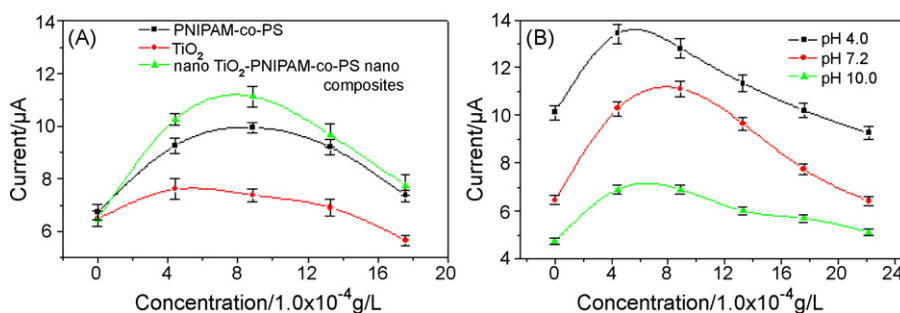
Fig. 3. Plots of differential pulse voltammetry (DPV) peak current of daunorubicin (3.3×10^{-4} M) vs. different materials concentrations, A: peak current of daunorubicin in PBS (pH 7.2, 0.1 M) in the presence of different material concentrations, B: peak current of daunorubicin in the presence of different concentrations of the nanoTiO$_2$–PNIPAM-*co*-PS polymer nanocomposites at different pH values. Pulse amplitude: 50 mV, pulse width: 50 ms, pulse period: 0.2 s.

has been observed by using cyclic voltammetry and differential pulse voltammetry studies, which is found to be pertaining to the concentrations of the related nanomaterials. Fig. 3A shows the plot of the electrochemical response of daunorubicin at different concentrations of the respective nanomaterials, indicative of the stronger enhancement effect of the new TiO$_2$–PNIPAM-*co*-PS nanocomposites than that of nanoTiO$_2$/or PNIPAM-*co*-PS nanofibers alone. The results demonstrate that the addition of TiO$_2$ nanoparticles into the nanofibers could increase the electron transfer, thus leading to the stronger enhancement of the electrochemical response of daunorubicin. This observation is similar to the previous report that the incorporation of nanoparticles to polymers could decrease the resistance of the polymer interface and thus increases the electron transfer for the redox of molecules [25].

Besides, it is noted that the pH of the electrolyte could affect the charge of the daunorubicin and the new nanocomposites, and thus it will affect the number of the assembled daunorubicin molecules on the surface of the blends. As shown in Fig. 3B, the electrochemical behavior of daunorubicin in the presence of the nanoTiO$_2$–PNIPAM-*co*-PS polymer nanocomposites at different pH values illustrate that the different electrochemical transfer rate of daunorubicin could be detected at different pH values, and the strongest peak current of daunorubicin is observed at pH 4.0, while the lowest peak current is observed at pH 10.0. Since biological conditions are usually at neutral pH, the following experiments have been performed at pH 7.2.

3.3. Promotion of the new TiO$_2$–PNIPAM-co-PS polymer nanocomposites to the DNA binding behavior of daunorubicin

To further investigate the respective effect of the new nanocomposites on biomolecules and the new strategy to facilitate the relevant biorecognion, differential pulse voltammetry study (see Fig. 4) and the cyclic voltammetry study (see Fig. 5) was adopted to explore the binding behavior of anticancer drug daunorubicin to DNA in the absence and presence of the new TiO$_2$–PNIPAM-*co*-PS polymer nanocomposites. Since daunorubicin could bind to DNA with intercalation mode, the relative intercalating interaction would lead to the considerable decrease of the peak current and the remarkable change of the peak position of the daunorubicin [26]. The results of our studies demonstrate the specific enhancement effect of these new nanocomposites on the electrochemical response of daunorubicin and its DNA binding behavior. As shown in Fig. 4A, it is apparent that daunorubicin itself could strongly bind to DNA, which leads to the decrease of the peak current of daunorubicin as well as the negative shift of its peak potential. It is observed that in the absence of the nanocomposites, the peak current of daunorubicin (3.3×10^{-4} M) alone is 1.4×10^{-5} A, while the relevant peak current decreased to 9.7×10^{-6} A upon addition of DNA (1.5×10^{-3} M). Thus, the peak current decrease of daunorubicin is about 32% when binding to DNA in the absence of the nanocomposites. In comparison, in the pres-
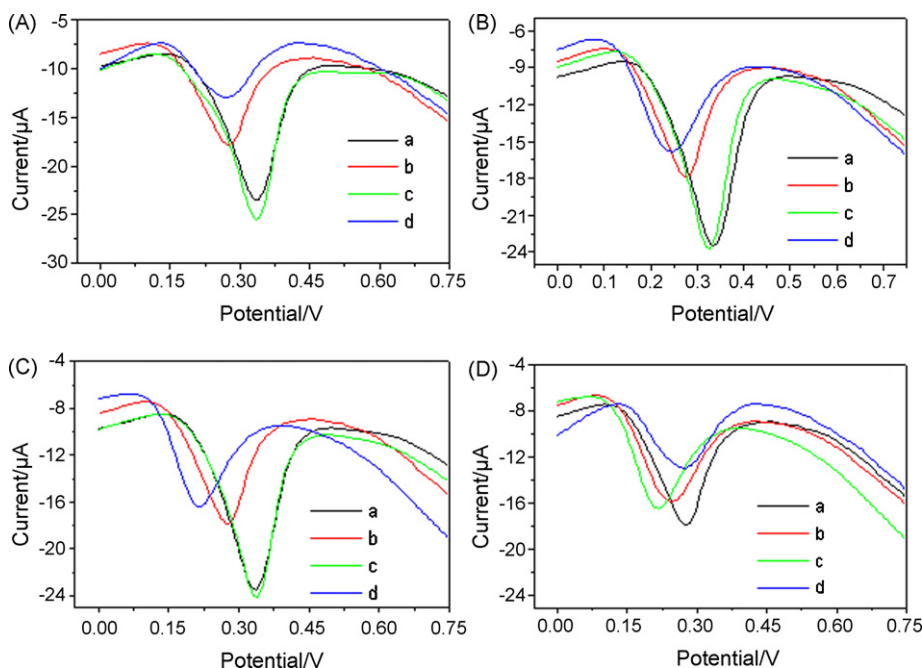
Fig. 4. A–C represents the differential pulse voltammetry (DPV) study of daunorubincin (3.3×10^{-4} M) binding to DNA (1.5×10^{-3} M) in the absence (a, b) and presence (c, d) of (A) nanoTiO$_2$–PNIPAM-*co*-PS polymer nanocomposites (8.8×10^{-4} g/L); (B) PNIPAM-*co*-PS nanofibers (8.8×10^{-4} g/L); (C) TiO$_2$ nanoparticles (8.8×10^{-4} g/L). (a) DPV study of daunorubicin (3.3×10^{-4} M) alone; (b) DPV study of daunorubicin (3.3×10^{-4} M) after binding to DNA (1.5×10^{-3} M); (c) DPV study of daunorubicin (3.3×10^{-4} M) in the presence of (A) nanoTiO$_2$–PNIPAM-*co*-PS polymer nanocomposites (8.8×10^{-4} g/L); (B) PNIPAM-*co*-PS nanofibers (8.8×10^{-4} g/L); (C) TiO$_2$ nanoparticles (8.8×10^{-4} g/L); (d) DPV study of daunorubicin (3.3×10^{-4} M) after binding to DNA (1.5×10^{-3} M) in the presence of (A) nanoTiO$_2$–PNIPAM-*co*-PS polymer nanocomposites (8.8×10^{-4} g/L); (B) PNIPAM-*co*-PS nanofibers (8.8×10^{-4} g/L); (C) TiO$_2$ nanoparticles (8.8×10^{-4} g/L). (D) represents the DPV study of the interaction of daunorubincin (3.3×10^{-4} M) with DNA (1.5×10^{-3} M) in the absence (a) and presence of PNIPAM-*co*-PS nanofibers (8.8×10^{-4} g/L) (b), TiO$_2$ nanoparticles (8.8×10^{-4} g/L) (c) and nanoTiO$_2$–PNIPAM-*co*-PS polymer nanocomposites (8.8×10^{-4} g/L) (d). Pulse amplitude: 50 mV, pulse width: 50 ms, pulse period: 0.2 s.
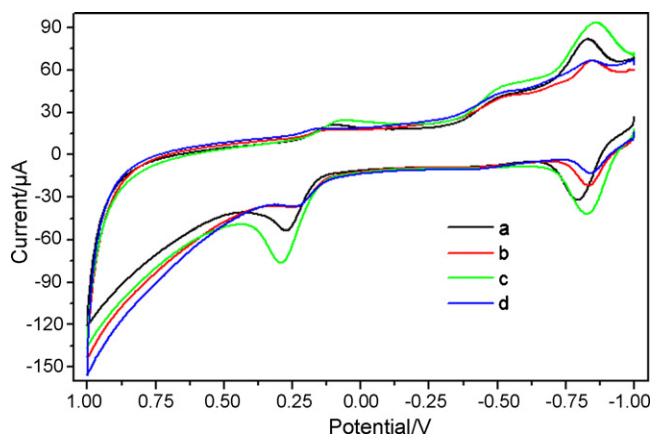
Fig. 5. Cyclic voltammetry (CV) study of daunorubincin (3.3×10^{-4} M) binding to DNA (1.5×10^{-3} M) in the absence (a, b) and presence (c, d) of nanoTiO$_2$–PNIPAM-*co*-PS polymer nanocomposites (8.8×10^{-4} g/L). (a) CV study of daunorubicin (3.3×10^{-4} M) alone; (b) CV study of daunorubicin (3.3×10^{-4} M) after binding to DNA (1.5×10^{-3} M); (c) CV study of daunorubicin (3.3×10^{-4} M) in the presence of nanoTiO$_2$–PNIPAM-*co*-PS polymer nanocomposites (8.8×10^{-4} g/L); (d) CV study of daunorubicin (3.3×10^{-4} M) after binding to DNA (1.5×10^{-3} M) in the presence of nanoTiO$_2$–PNIPAM-*co*-PS polymer nanocomposites (8.8×10^{-4} g/L). Scan rate: 100 mV s^{-1}.

Scheme 1. Scheme for the enhancement effect of the self-assembled TiO$_2$–PNIPAM-*co*-PS polymer nanocomposites on the electrochemical response of daunorubicin.

ence of the new TiO$_2$–PNIPAM-*co*-PS polymer nanocomposites (8.8×10^{-4} g/L), the respective peak current of daunorubicin (3.3×10^{-4} M) alone increased to 1.6×10^{-5} A, while the peak current of daunorubicin decreased to 5.2×10^{-6} A upon addition of DNA (1.5×10^{-3} M). Based on the above studies, it appears that the relevant peak current is decreased about 67% in the presence of nanocomposites under identical experimental conditions. These observations indicate that the presence of the TiO$_2$–PNIPAM-*co*-PS nanocomposites could efficiently facilitate the binding behavior of daunorubicin to DNA and remarkably enhance the detection sensitivity of the respective biomolecular recognition.

It is already known that the surface of nanoTiO$_2$ could be negatively charged when the pH of the aqueous solution is at 7.2 [8]. Furthermore, Chadwick et al. has reported that at most values of pH it is favorable for the hydroxyl groups of nanoTiO$_2$ to donate protons, as was observed by the negative charge pertaining for dispersion in water [14]. Since nanoTiO$_2$ could be self-assembled on the surface of the PNIPAM-*co*-PS nanofibers, the new TiO$_2$–PNIPAM-*co*-PS nanocomposites may be negatively charged. Meanwhile, oxidized daunorubicin is positively charged. As such daunorubicin could be readily self-assembled onto the new nanoTiO$_2$–PNIPAM-*co*-PS nanocomposites surface by electrostatic interactions under certain pH conditions. Scheme 1 illustrates the possible biorecognition process of daunorubicin in the presence of the relevant nanocomposites. In view of the large surface area of the new polymer nanocomposites, the presence of TiO$_2$–PNIPAM-*co*-PS nanocomposites could efficiently facilitate the self-assembled accumulation of daunorubicin on the surface of TiO$_2$–PNIPAM-*co*-PS nanocomposites, which could enable much more daunorubicin molecules to come close to the surface of the glassy carbon electrode together with the new nanocomposites upon application of the external redox potentials, and thus lead to the significant
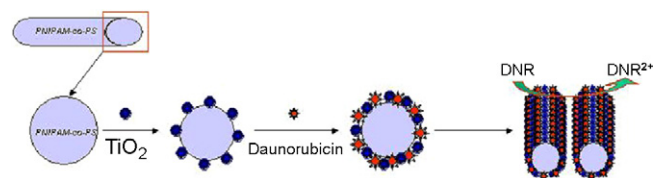
enhancement of the respective detection sensitivity for the target biomolecular recognition process. Additionally, it is noted that the addition of TiO$_2$ nanoparticles into the nanofibers could form some porous structure on the nanofiber surface [27], which will readily enable much more daunorubicin molecules and their target biomolecules adsorbed on the relevant nanocomposite surface.

Meanwhile, the respective effect of PNIPAM-*co*-PS nanofibers and nanoTiO$_2$ on the DNA binding behavior of daunorubicin has also been explored by means of the control experiments. Fig. 4B illustrates the DPV study of daunorubicin binding to DNA in the absence and presence of PNIPAM-*co*-PS nanofibers. Since PNIPAM-*co*-PS nanofibers have no electrochemical properties, the relative electrochemical response was only generated by the anticancer drug daunorubicin [28]. It is observed that the presence of PNIPAM-*co*-PS nanofibers could facilitate the DNA binding affinity of daunorubicin and lead to the bigger change of the relevant peak current and negative shift of the peak potential than that of daunorubicin alone binding to DNA. Nevertheless, it is noted from the above studies that upon application of PNIPAM-*co*-PS nanofibers there is much less decrease of the peak current of daunorubicin than that in the presence of nanoTiO$_2$–PNIPAM-*co*-PS polymer nanocomposites under the identical experimental conditions. This observation indicates the much less effect of PNIPAM-*co*-PS nanofibers on the relevant biorecognition of daunorubicin than that in the presence of TiO$_2$–PNIPAM-*co*-PS polymer nanocomposites.

Fig. 4C illustrates the relative effect of nanoTiO$_2$ on the DNA binding behavior of daunorubicin, which demonstrates the apparent synergistic effect on the respective biomolecular recognition process upon application of TiO$_2$ nanoparticles. This phenomenon is consistent with our previous studies [8], indicating that the presence of TiO$_2$ nanoparticles could enhance the DNA binding affinity of anticancer drug daunorubicin, though there exists less effect of TiO$_2$ nanoparticles than that in the presence of TiO$_2$–PNIPAM-*co*-PS nanocomposites. Fig. 4D demonstrates the relevant DNA binding behavior of daunorubincin in the presence of PNIPAM-*co*-PS nanofibers, TiO$_2$ nanoparticles and nanoTiO$_2$–PNIPAM-*co*-PS polymer nanocomposites, respectively. It appears that the nanoTiO$_2$–PNIPAM-*co*-PS polymer nanocomposites have much more remarkable enhancement effect on the biorecognition of daunorubicin due to the relatively larger surface area of the new nanoTiO$_2$–PNIPAM-*co*-PS nanocomposites. These results are consistent with our observations of cyclic voltammetry (CV) study (as shown in Fig. 5), suggesting the apparently

synergetic enhancement effect of TiO_2–PNIPAM-*co*-PS polymer nanocomposite.

Thus, based on the above studies, it is evident that the addition of TiO_2 nanoparticles into PNIPAM-*co*-PS nanofibers could efficiently increase the surface area of the nanocomposites and enhance the electron transfer at the TiO_2–PNIPAM-*co*-PS nanocomposite interface. These observations demonstrate that the TiO_2–PNIPAM-*co*-PS nanocomposites show unique advantages through the blends of TiO_2 nanoparticles with PNIPAM-*co*-PS nanofibers, which could lead to the remarkable enhancement of detection sensitivity of relevant biomolecular recognition. This also raises the possible potential application of TiO_2–PNIPAM-*co*-PS nanocomposites in the development of high sensitive biosensors to detect some specific bioprocesses.

4. Conclusions

In this study, the poly (*N*-isopropylacrylamide)-*co*-polystyrene (PNIPAM-*co*-PS) nanofibers have been fabricated by electrospinning and then the blends of PNIPAM-*co*-PS nanofibers with titanium dioxide (TiO_2) nanoparticles have been characterized and utilized as the new functional nanocomposites to promote the respective biorecognition of an anticancer drug daunorubicin. The results of our studies demonstrate that the presence of the blends of TiO_2 nanoparticles with PNIPAM-*co*-PS nanofibers could efficiently facilitate the self-assembled accumulation of daunorubicin on the surface of TiO_2–PNIPAM-*co*-PS polymer nanocomposites, and thus the synergistic effect of nanoTiO_2 accompanying with PNIPAM-*co*-PS nanofibers could remarkably enhance the relevant detection sensitivity of biomolecular recognition of daunorubicin as well as its DNA binding affinity. These observations suggest that the new biocompatible TiO_2–PNIPAM-*co*-PS polymer nanocomposites may find some promising applications in high sensitive bio-analysis and as the novel efficient drug carrier for target disease treatment.

Acknowledgments

References

[1] H.L. Qi, X.X. Li, P. Chen, C.X. Zhang, Talanta 72 (2007) 1030.
[2] G. Wang, J. Zhang, R.W. Murray, Anal. Chem. 74 (2002) 4320.
[3] C.H. Fan, K.W. Plaxco, A.J. Heeger, J. Am. Chem. Soc. 124 (2002) 5642.
[4] X.Q. Lu, L. Wang, H.D. Liu, R. Wang, J. Chen, Talanta 73 (2007) 444.
[5] A. Erdem, Talanta 74 (2007) 318.
[6] M.J. Moghaddam, S. Taylor, M. Gao, S. Huang, L. Dai, M.J. McCall, Nano Lett. 4 (2004) 89.
[7] N.M. Dimitrijevic, Z.V. Saponjic, B.M. Rabatic, T. Rajh, J. Am. Chem. Soc. 127 (2005) 1344.
[8] M. Song, R.Y. Zhang, X.M. Wang, Mater. Lett. 60 (2006) 2143.
[9] M.H. Dufresne, D. Le Garrec, V. Sant, J.C. Leroux, M. Ranger, Int. J. Pharm. 277 (2004) 81.
[10] J. Liu, R. Pelton, A.N. Hrymak, J. Colloid Interface Sci. 227 (2000) 408.
[11] E.C. Cho, Y.D. Kim, K. Cho, J. Colloid Interface Sci. 286 (2005) 479.
[12] J.M. Song, A. Asthana, D.P. Kim, Talanta 68 (2006) 940.
[13] Y.P. Wang, K. Yuan, Q.L. Li, L.P. Wang, S.J. Gu, X.W. Pei, Mater. Lett. 59 (2005) 1736.
[14] H. Gao, W. Yang, K. Min, L. Zha, C. Wang, S. Fu, Polymer 46 (2005) 1087.
[15] X. Cheng, H.E. Canavan, M.J. Stein, J.R. Hull, S.J. Kweskin, M.S. Wagner, G.A. Somorjai, D.G. Castner, B.D. Ratner, Langmuir 21 (2005) 7833.
[16] D.L. Huber, R.P. Manginell, M.A. Samara, B.I. Kim, B.C. Bunker, Science 301 (2003) 352.
[17] V. Grabstain, H. Bianco-Peled, Biotechnol. Prog. 19 (2003) 1728.
[18] L.K. Ista, S. Mendez, V.H. Perez-Luna, G.P. Lopez, Langmuir 17 (2001) 2552.
[19] H.E. Canavan, X. Cheng, D.J. Graham, B.D. Ratner, D.G. Castner, Langmuir 21 (2005) 1949.
[20] D. Li, Y.N. Xia, Nano Lett. 3 (2003) 555.
[21] D. Li, Y.N. Xia, Adv. Mater. 16 (2004) 115.
[22] S. Xu, J. Zhang, C. Paquet, Y. Lin, E. Kumacheva, Adv. Funct. Mater. 13 (2003) 468.
[23] X. Zhao, X. Ding, Z. Deng, Z. Zheng, Y. Peng, X. Long, Macromol. Rapid Commun. 26 (2005) 1784.
[24] Z.M. Huang, Y.Z. Zhang, M. Kotaki, S. Ramakrishna, Compos. Sci. Technol. 63 (2003) 2223.
[25] L. Sheeney-Haj-Ichia, G. Sharabi, I. Willner, Adv. Funct. Mater. 12 (2002) 27.
[26] Y.H. Zhu, Z.L. Zhang, D.W. Pang, Anal. Lett. 38 (2005) 2579.
[27] T.H. Bae, T.M. Tak, J. Membr. Sci. 249 (2005) 1.
[28] C.R. Krishnamoorthy, S.F. Yen, J.C. Smith, J.W. Lawn, W.D. Wilson, Biochemistry 25 (1986) 5933.

Retraction notice

Retraction notice to "Spectrophotometric determination of Fenitrothion in formulations and environmental samples" [Talanta 72(1) (2007) 106–112]

P. Subrahmanyam [a,b], B. Krishnapriya [a,b], L. Ravindra Reddy [a,b], B. Jayaraj [a,b], P. Chiranjeevi [a,b,*]

[a] *Department of Mathematics, S.V. University, Tirupati 517502, Andhra Pradesh, India*
[b] *Environmental Monitoring Laboratories, Department of Chemistry, S.V. University, Tirupati 517502, Andhra Pradesh, India*

Available online 1 April 2008

This article has been retracted at the request of the Editors-in-Chief.

Considerable concern was raised about the research purportedly conducted at Sri Venkateswara University, India with the alleged involvement of Professor P. Chiranjeevi.

Questions were raised as to the volume of publications, the actual capacity (equipment, orientation and chemicals) of the laboratory in which Professor Chiranjeevi worked, the validity of certain of the research data identified in the articles, the fact that a number of papers appear to have been plagiarized from other previously published papers, and some aspects of authorship.

Professor Chiranjeevi was given the opportunity to respond to these allegations. Thereafter, a committee was constituted by the University to look into these allegations. Based on the enquiry committee report, we have been informed by the head of the Department of Chemistry at Sri Venkateswara University that the university authorities have taken disciplinary action against Professor Chiranjeevi, as the university considers that there are grounds for such action.

Therefore, based on the results of this investigation, the Editors-in-Chief are retracting this article.

Erratum

Erratum to "Simultaneous flow-through determination of nitrites, nitrates and their mixtures in environmental and biological samples using spectrophotometry" [Talanta 66 (2) (2005) 505–512]

K. Suvardhan [a], K. Suresh Kumar [a], S. Hari Babu [a], B. Jayaraj [b], P. Chiranjeevi [a],*

[a] Environmental Monitoring Laboratory, Department of Chemistry, S.V. University, Tirupati 517502, India
[b] Department of Mathematics, S.V. University, Tirupati 517502, India

This article has been retracted at the request of the Editors-in-Chief.

Considerable concern was raised about the research purportedly conducted at Sri Venkateswara University, India with the alleged involvement of Professor P. Chiranjeevi.

Questions were raised as to the volume of publications, the actual capacity (equipment, orientation and chemicals) of the laboratory in which Professor Chiranjeevi worked, the validity of certain of the research data identified in the articles, the fact that a number of papers appear to have been plagiarized from other previously published papers, and some aspects of authorship.

Professor Chiranjeevi was given the opportunity to respond to these allegations. Thereafter, a committee was constituted by the University to look into these allegations. Based on the enquiry committee report, we have been informed by the head of the Department of Chemistry at Sri Venkateswara University that the university authorities have taken disciplinary action against Professor Chiranjeevi, as the university considers that there are grounds for such action.

Therefore, based on the results of this investigation, the Editors-in-Chief are retracting this article.

Short communication

Identification of selenium-containing proteins in selenium-rich yeast aqueous extract by 2D gel electrophoresis, nanoHPLC–ICP MS and nanoHPLC–ESI MS/MS

Laure Tastet [a], Dirk Schaumlöffel [a,*], Brice Bouyssiere [a], Ryszard Lobinski [a,b]

[a] Laboratoire de Chimie Analytique Bio-Inorganique et Environnement, CNRS UMR 5254, Hélioparc, 2 av. Pr. Angot, F-64053 Pau, France
[b] Department of Chemistry, Warsaw University of Technology, Noakowskiego 3, 00-664 Warsaw, Poland

Abstract

An approach based on the consecutive use of nanoHPLC–ICP collision cell MS and nanoHPLC–electrospray MS was proposed for the analysis of water-soluble selenium-containing proteins in selenium-rich yeast after their separation by 2D gel electrophoresis (GE). An ultrasonic probe was employed for fast protein extraction avoiding sample heating and thus reducing the risk of protein degradation. The efficiency of different extraction steps were critically evaluated by total selenium analysis and size-exclusion chromatography (SEC)–ICP MS. Prior to electrophoresis proteins were purified by acetone precipitation. The protein-containing spots from 2D GE were excised and digested with trypsin. The digests obtained were analyzed by nanoHPLC–ICP MS in order to check for the presence of selenium-containing peptides; this allowed the detection of target proteins for further analyses (two out of five spots). The subsequent analyses of the selected digests by nanoHPLC–ES MS/MS allowed the attribution of amino acid sequences to peaks detected by ICP MS revealing the presence of two selenium-containing proteins: SIP 18 and HSP 12.
© 2008 Elsevier B.V. All rights reserved.

Keywords: 2D gel electrophoresis; NanoHPLC; ICP MS; Electrospray MS/MS; Selenium-containing proteins; Selenium-rich yeast

1. Introduction

Selenium is known to be either essential or toxic for living organisms depending on the concentration and the chemical form [1]. Its biological functions are primarily mediated by selenoproteins, such as, e.g. glutathione peroxidases and iodothyronine deiodinases [2]. A report on the putative role of selenium, administered as selenium-rich yeast, in the protection of cancer, still increased the interest in analytical methods able to identify and quantify selenium-containing chemical species [3–5].

2D electrophoresis in polyacrylamide gels, widely established in proteomics, is a potentially attractive tool for the characterization of Se-containing proteins. A first attempt of its use to the characterization of the selenoproteome in yeast was made by Chassaigne et al. who proposed the 2D GE–LA

ICP MS for mapping of Se-containing proteins in a yeast protein extract [6]. The authors published electrospray mass spectra of apparently intact proteins collected from selenium-rich spots (identified by LA ICP MS) but the resolution of ESI TOF MS spectra was insufficient to prove whether the spectra did reflect proteins containing selenium [6]. An alternative was the use of MALDI or ESI TOF MS for the mapping of selenopeptides in the enzymatic digests of selenoproteins excised, usually, from 1D gels [7,8]. The applications have been limited to concentrated and well-purified proteins. Often, the bands were not targeted for the selenium content.

A serious limitation to electrospray MS/MS is the critical dependence of the response of an analyte on the presence of concomitant readily ionized species. If a minor species arrives at the ionization source accompanied by an easily ionisable major one, the ionization of the former is likely to be suppressed leading to the absence of a relevant peak in the mass spectrum. Hence, there is a need for efficient purification protocols on the picomole mass scale and for analytical techniques allowing monitoring their optimization and efficiency. ICP MS is ideally suited for

this purpose, provided the analyte contains a heteroelement, such as, e.g. Se, because of is subpicogram detection limits regardless of the matrix [9].

In our former work [10], capillary HPLC–ICP MS was developed as a technique for the mapping of selenopeptides extracted with trypsin from 1D gel bands or 2D gel spots. However, the analysis of the same digests by capillary LC–ESI MS/MS did not allow the detection of any selenopeptide, apparently because of the insufficient concentration and the abundance of concomitant species preventing the efficient ionization of the target analytes.

The goal of this work was to improve the ESI MS signal-to-background ratio by the optimization of the protein extraction, purification, 2D electrophoretic separation and digestion and replacement of capillary HPLC by nanoHPLC with on-line pre-concentration. In contrast to another work [11] using ultrasonic probe extraction of Brazil nuts, one objective of this work was to apply and optimize this technique for selenium-rich yeast extraction. Therefore the efficiency of the different extraction and purification steps were critically evaluated by total selenium analysis and size-exclusion chromatography (SEC)–ICP MS. NanoHPLC–ICP MS was optimized in parallel in order to verify the extraction of selenium-containing peptides from the gel and to determine (with subpicogram detection limits regardless of the co-eluting interfering species) the number and the retention times of these peptides to be then identified by ESI MS/MS.

2. Experimental

2.1. Materials and reagents

A commercial preparation of selenium-rich yeast, Sel-Plex (Alltech, Lexington, KY) corresponding to yeast strain *Saccharomyces cerevisiae* CNCM I-3060 and containing 2.1 ± 0.1 mg g^{-1} Se [12] was used. Analytical reagent grade chemicals purchased from Sigma–Aldrich (Saint-Quentin Fallavier, France) were used throughout unless stated otherwise. Water (18.2 MΩ cm) was purified with a Milli-Q system (Millipore, Bedford, MA). Trypsin (mass spectrometry grade) was obtained from Promega (Charbonnières-les-Bains, France).

2.2. Instrumentation

2.2.1. Sample preparation

An ultrasonic probe (Branson Ultrasonics Corporation, Danbury, USA) was used to prepare the yeast water extract. Size-exclusion chromatography used for the fractionation of the yeast water extract was carried out with a HiLoad 26/60 Superdex 30 Prep (Pharmacia, Uppsala, Sweden) and an AKTA-Prime system (Pharmacia). A HiLoad Superdex peptide HR 10/30 (Pharmacia, Uppsala, Sweden) was coupled on-line to ICP MS (Elan 6000, PerkinElmer, Wellesley, MA) in order to control different sample preparation steps. The pooled fractions were lyophilized by a Model LP3 lyophilizer (Jouan, France). A Speed Vac vacuum dryer (model DNA120, Thermo Quest, NY) was used for solvent evaporation from the gels.

2.2.2. Gel electrophoresis (GE)

The first dimension separation was carried out using a IPG-phor isoelectric focusing (IEF) system (Amersham Biosciences, Piscataway, NJ), dedicated for immobilized pH gradient IEF with a gradient of pH 3–10. This IPG strips featured a non-linear (NL) pH gradient. Polyacrylamide gel electrophoresis (SDS-PAGE) was carried out with a Mini Protean 3 Electrophoresis System (Bio-Rad Laboratories, Hercules, CA) with 4% of polyacrylamide for the stacking gels, 15% of polyacrylamide for resolving gels (8 cm × 7 cm × 0.075 cm).

2.2.3. NanoHPLC–ICP MS

NanoHPLC separations with on-line preconcentration were performed using a nanoflow HPLC pump (Ultimate, Dionex, Sunnyvale, CA) on a 75-μm i.d. reversed-phase nanoHPLC column (C$_{18}$ PepMap100, 75 μm i.d. × 15 cm, 3 μm, LC Packings) with a flow rate of 300 nL min^{-1}. The chromatographic system described in detail elsewhere [13] was coupled on-line via a recently developed nanoflow nebulizer (nDS-200) [14] to an ICP MS fitted with a collision cell (Agilent Model 7500ce, Agilent Technologies, Tokyo, Japan).

2.2.4. NanoHPLC–ESI TOF MS

An ESI-q-TOF MS/MS (Applied Biosystems QSTAR XL, Foster City, CA) was used for parallel nanoHPLC–ESI TOF MS experiments. The nanoHPLC was coupled via a nanoelec-trospray source (Applied Biosystems) to the mass spectrometer as described elsewhere [13].

2.3. Procedures

2.3.1. Isolation of the water-soluble selenium-containing protein fraction

A former sample extraction protocol [15] was modified by employing an ultrasonic probe instead of an ultrasonic bath. A sample of 0.3 g selenium-rich yeast was extracted during 2 min with a probe in 10 mL water containing 0.1% (w/v) dithiothreitol (DTT, anti-oxidant) and 0.1 mmol L^{-1} phenylmethylsulfonyl fluoride (inhibitor of protease activity) in ice. In order to measure the total selenium extraction recovery, 300 μL of the super-natant were analyzed by ICP MS (five replicates). In addition, an aliquot of 200 μL was analyzed by on-line SEC–ICP MS to check for the presence of selenium-containing proteins at conditions optimized elsewhere (10-mM ammonium acetate, pH 9.5, at 2.5 mL min^{-1}) [16]. The rest of the supernatant was precipitated with 80% acetone during 20 min at -20 °C and centrifuged at $14,000 \times g$ for 20 min at 4 °C. The precipitate was dissolved in 1 mL of water. Again, a 300-μL aliquot was analyzed for total selenium (five replicates) and a 200-μL aliquot was used to determine the Se-containing species distribution by on-line SEC–ICP MS.

2.3.2. Gel electrophoresis

Isoelectric focusing and SDS-PAGE were performed under conditions described in our former work [10]. In brief, the precipitate prepared as described above was dissolved in a buffer solution containing 8 mol L^{-1} urea, 4% (w/v) CHAPS,

60 mmol L^{-1} DTT, 2% (v/v) Pharmalyte^{TM} (pH 3–10), and 0.002% (w/v) bromophenol blue at room temperature, homogenized and centrifuged at $15,000 \times g$ for 10 min.

2.3.3. In-gel tryptic digestion

The excised gel spots were digested as described in our former work. In brief, the tryptic peptides were extracted from the gel slice in two steps using an ultrasonic probe: firstly with 150 μL of water for 1 min, and then with 5% (v/v) TFA in 50% (v/v) acetonitrile, both steps for 1 min. The two extracts were pooled and dried in vacuum (Speed Vac) for 2 h. The digest was stored at −20 °C. In order to analyze the extraction efficiency of the selenium-containing peptides, the total selenium content in the extracts and the remaining gel slice was determined by ICP MS.

2.3.4. NanoHPLC–ICP MS and nanoHPLC–ESI MS after in-gel tryptic digestion

The mobile phases A and B were 0.05% TFA solutions in water and in acetonitrile, respectively. The solvents were degassed by purging with helium. Selenium-containing peptides were eluted using a gradient: 0–5 min 5–20% B linear, 5–10 min 20–50% B linear, 10–20 min 50–95% B linear, 20–35 min 95% B isocratic, 35–40 min 95–5% B linear, 40–50 min 5% B isocratic. The ^{80}Se isotope intensity was measured on-line by ICP MS in order to detect selenium-containing peptides. ^{40}Ar^{40}Ar interferences were removed by a hydrogen reaction cell (3.8 mL min^{-1} H$_2$). The octopole bias was set to −18 V, the quadrupole bias to −16 V. ICP MS measurements conditions (nebulizer gas flow, rf power, and lens voltage) were optimized daily for the highest intensity of the multielement solution containing Li, Y, and Tl (200 μg L^{-1}) added to the mobile phases A and B. The nebulization process was optimized by adjusting the position of the fused-silica needle tip in the nebulizer orifice while monitoring the ^{7}Li, ^{89}Y, and ^{205}Tl signals by ICP MS. Furthermore, the continuous signal of ^{89}Y served as an internal standard to monitor the stability of the nebulization process during a chromatographic run.

ESI-q-TOF mass spectra of selenium-containing peptides were acquired in the range m/z 300–2000. The needle voltage was 2000 V and the entrance potential 60 V.

3. Results and discussion

3.1. Optimization of the sample preparation procedure

Our former extraction procedure [10] was optimized with respect to duration, protein integrity and selenium recovery. For that reason an ultrasonic probe instead of an ultrasonic bath was employed followed by a protein precipitation step. Using an ultrasonic probe, the extraction time was distinctly decreased and a warm-up of the sample was avoided which reduced the risk of sample degradation. In contrast to another work [11] where this technique was simply used for the extraction of Brazil nuts without further optimization, the efficiency of the different extraction and purification steps were critically evaluated by the analysis of the selenium recovery and SEC–ICP
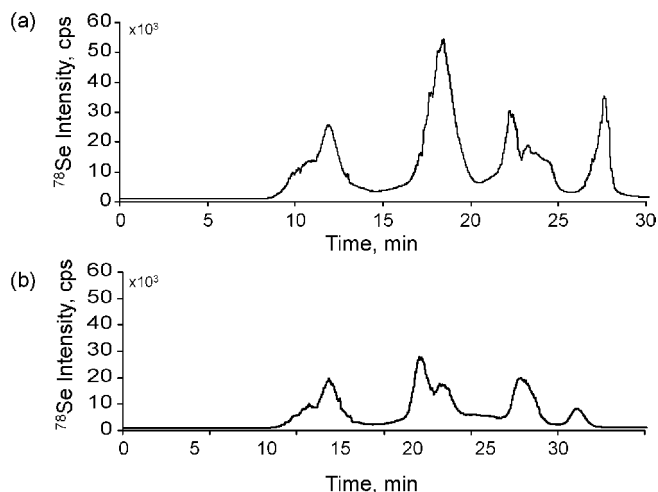

Fig. 1. On-line SEC–ICP MS analysis at different steps at the sample preparation procedure: (a) water extract preparation with ultrasonic probe and (b) redissolved precipitate after acetone precipitation.

MS. A SEC–ICP MS analysis of the water extract revealed a similar chromatographic profile (Fig. 1a) as reported elsewhere [10]. The selenium recovery of the extraction step was $17 \pm 1\%$. A simple protein precipitation step commonly used for protein purification in biochemistry replaced the former laborious and time-consuming procedure of SEC-fractionation followed by lyophilization for the recovery of the protein fraction from the sample. This faster procedure minimized the risk of protein oxidation and sample loss. Indeed, the selenium recovery of this step accounted for $13.7 \pm 0.4\%$ of the total selenium in the yeast. This means that the precipitation step recovers 80% of the selenium present in the aqueous extract. The SEC–ICP MS chromatogram of the precipitate (Fig. 1b) shows a similar peak profile and intensity for the protein fraction at 9–14 min as in the chromatogram of the water extract (Fig. 1a). Thus the protein fraction is not only desalted but also enriched in comparison with the low-molecular species which are, however, also precipitated. The chromatograms in Fig. 1 demonstrate that the 20% selenium loss during the protein precipitation is largely due to the loss of low-molecular weight selenium species eluting after 15 min.

3.2. NanoHPLC–ICP MS mapping of selenium-containing peptides in tryptic digests of spots after 2D gel electrophoresis

The 2D electropherogram (Fig. 2) produced five fairly intense spots. Three spots (1–3) appear at around 20.1 kDa; spot 2 is the most intense. Spots 4 and 5 correspond to proteins with the apparent masses of approximately 14.4 kDa. The spots were excised, digested and analyzed by nanoHPLC–ICP MS revealing the presence of peaks (^{80}Se channel), and thus of selenium-containing proteins in spots 2 and 4, but not in spots 1, 3 and 5. The extraction efficiency of selenium-containing peptides after tryptic digestion was determined for spots 2 and 4 to be $43 \pm 1\%$ and $39 \pm 1\%$, respectively. Note that a similar extraction rate was obtained elsewhere [10], but the use of an
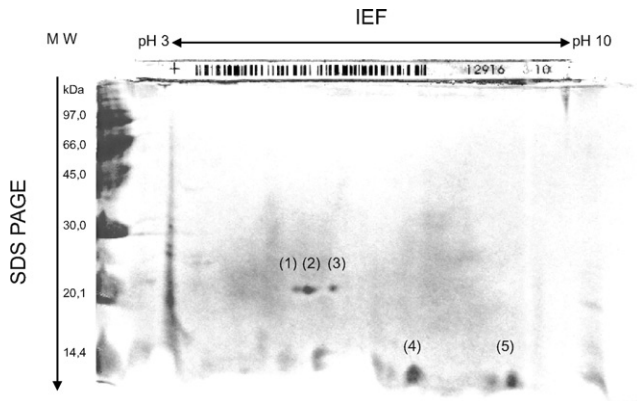
Fig. 2. Bidimensional gel electrophoresis of the purified water extract.

ultrasonic probe instead of a shaker reduced the extraction time from 60 min to 1 min. The digest of the spot 4 gave a chromatogram (Fig. 3a) with one major peak at 17 min similar to that of the digest of the 12 kDa protein band in 1D electrophoresis recently reported [10]. The chromatographic profile of the digest of spot 2 (Fig. 4a) was virtually similar to that of the 18 kDa protein digest after 1D gel electrophoresis [10]. In contrast to our former results [10] no protein carbamylation was

observed. This demonstrates that the optimized sample protocol used in this work was better adapted to protein extraction and preserved their integrity.

3.3. Identification of selenium-containing peptides in tryptic digests of spots after 2D gel electrophoresis by nanoHPLC–ESI-q-TOF MS/MS

The use of nanoHPLC–ESI-q-TOF MS/MS in parallel to nanoHPLC–ICP MS allowed the identification of selenium-containing peptides and the corresponding selenium-containing proteins in spots after 2D gel electrophoresis. Fig. 3b shows a nanoHPLC–ESI MS chromatogram of the digest of spot 4. One major peak can be seen, similarly as in the chromatogram with ICP MS detection at a similar retention time. In the corresponding mass spectrum (Fig. 3c) a typical selenium isotopic pattern was found centered on m/z 402 (Fig. 3c inset). The fragmentation of the most intense ion at m/z 402.1430 produced series of b and y ions in the MS/MS spectrum (Fig. 3d) allowing the sequencing of a selenium-containing peptide. This peptide, together with other peptides (Table 1) identified during this HPLC run, allows the identification of a selenium-containing HSP12 protein (11,693 Da).
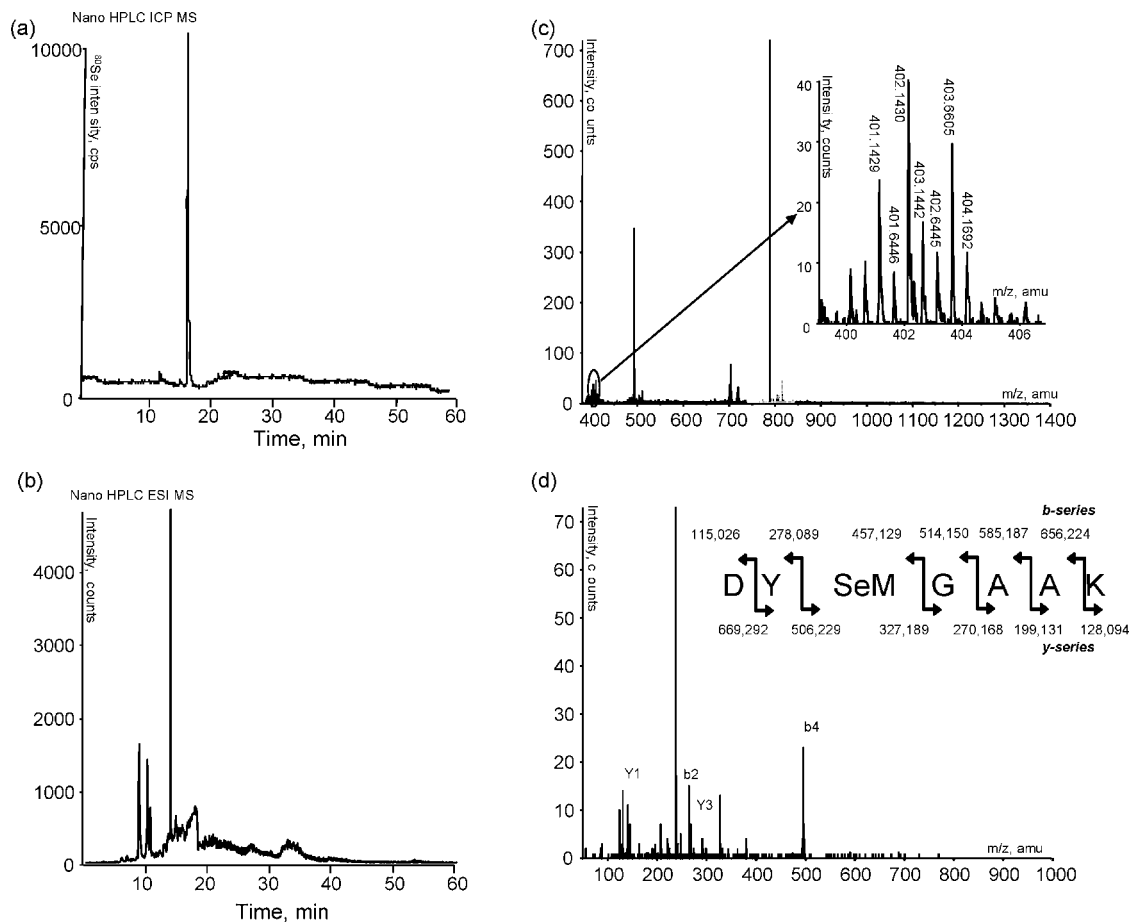
Fig. 3. Analysis of spot 4—(a) nanoHPLC–ICP MS chromatogram of the digest of spot 4; (b) NanoHPLC–ESI MS analysis: XIC (m/z 402.1430) of the digest of spot 4; (c) Mass spectrum at the peak at 14 min; inset: zoom of the mass spectrum, selenium-containing peptide detection by typical selenium isotopic pattern; (d) Fragmentation of the ion at m/z 402.143, inset: identified sequence and series of b and y ions.
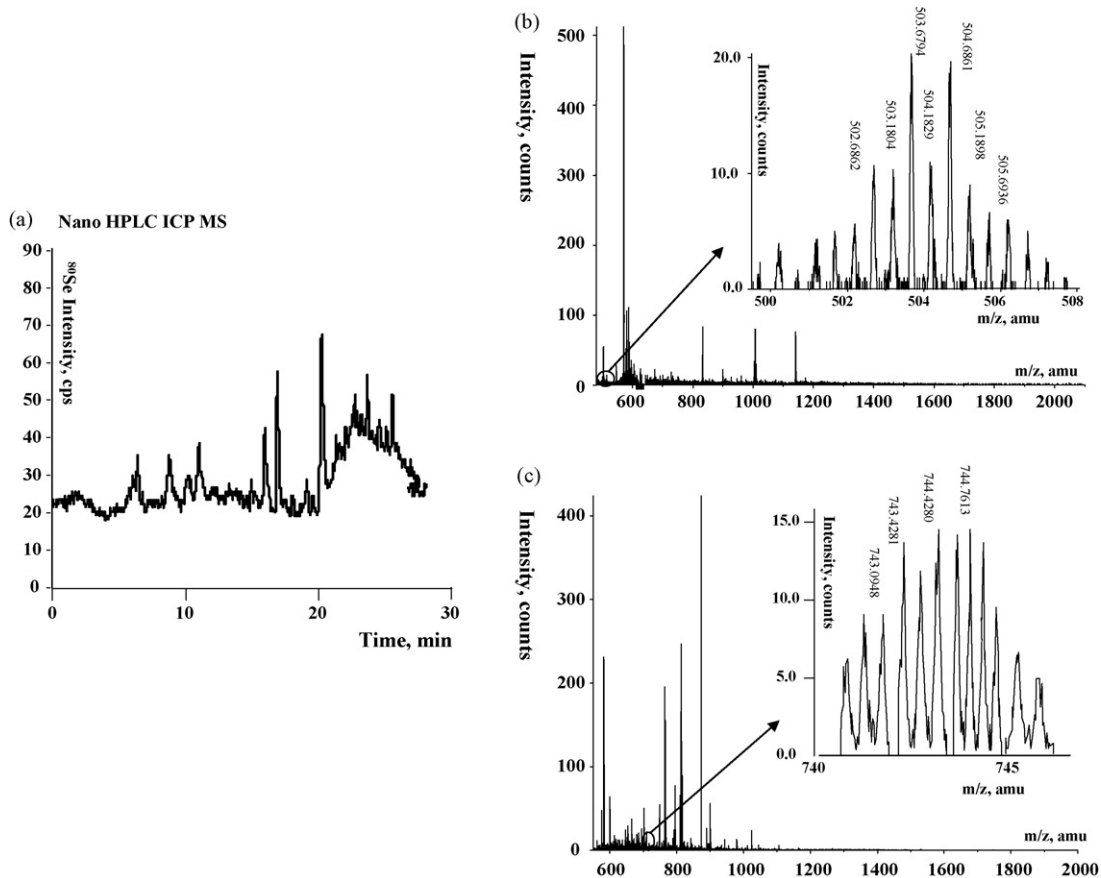
Fig. 4. Analysis of spot 2—(a) nanoHPLC–ICP MS chromatogram of the digest of spot 2; (b) NanoHPLC–ESI MS analysis: mass spectrum at the peak at 17 min; inset: zoom of the mass spectrum; (c) NanoHPLC–ESI MS analysis: mass spectrum at the peak at 21 min, inset: zoom of the mass spectrum.

The same approach was applied to the digest of spot 2. The mass spectra (Fig. 4) revealed the identity of two selenium-containing peptides together with their sulfur-containing analogs (Table 2) confirming the presence of selenium-containing SIP18 (17,748 Da). Note that even despite such an extensive purification procedure a number of compounds coelute. Although they suppress the ionization of the selenium-containing peptides of interest which occur as very minor compounds in the mass spectra (Figs. 3c and 4b and c), a clear identification of these peptides was possible.

Table 1
Peptides of HSP 12 identified by nanoHPLC–ESI MS

Resulting peptide sequence	Peptide mass (Da)
ASEALKPDSQK	1173.288
SYAEQGK	781.820
EYITDK	767.834
GVFQGVHDSAEK	1273.368
DNAEGQGESLADQAR	1560.554
DYXGAAK[a]	802.856
DYMGAAK	754.856
LNDAVEYVSGR	1222.320
VHGEEDPTK	1011.056

[a] X denotes SeMet.

Table 2
Peptides of SIP 18 identified by nanoHPLC–ESI MS

Resulting peptide sequence	Peptide mass (Da)
DDMNMDMGMGHDQSEGGMK	2086.284
DDXNXDXGMGHDQSEGGMK[a]	2230.284
XGHDQSGTK[a]	1008.029
MGHDQSGTK	960.029
MNAGR	547.630

[a] X denotes SeMet.

4. Conclusions

The optimization of the sample preparation protocol prior to 2D PAGE was important for protein purification under preservation of their integrity. The latter could be demonstrated by SEC–ICP MS after each extraction and purification step in the protocol. In addition, the replacement of capillary HPLC by nanoHPLC with on-line preconcentration allowed the identification of the selenium-containing peptides issued from the proteins excised from the gels and digested. NanoHPLC–ICP MS is a highly sensitive technique for selenium-containing peptide mapping in spot digests in order to mark targets for the ES MS/MS identification. The procedure developed opens the way to a systematic study of the Se-rich yeast proteome and

Se-proteomes of other samples after their separation by 2D gel electrophoresis.

References

[1] M.S. Alaejos, C.D. Romero, Food Chem. 52 (1995) 1.
[2] D.H. Holben, A.M. Smith, J. Am. Diet. Assoc. 99 (1999) 836.
[3] T.C. Stadtman, J. Biol. Chem. 266 (1991) 16257.
[4] L.C. Clark, G.F. Combs Jr., B.W. Turnbull, E.H. Slate, D.K. Chalker, J. Chow, L.S. Davis, R.A. Glover, G.F. Graham, E.G. Gross, A. Krongrad, J.L. Lesher Jr., H.K. Park, B.B. Sanders Jr., C.L. Smith, J.R. Taylor, J. Am. Med. Assoc. 276 (1996) 1957.
[5] M.P. Rayman, Lancet 356 (2000) 233.
[6] H. Chassaigne, C.C. Chéry, G. Bordin, F. Vanhaecke, A.R. Rodriguez, J. Anal. At. Spectrom. 19 (2004) 85.
[7] G. Ballihaut, L. Tastet, C. Pecheyran, B. Bouyssiere, O. Donard, R. Grimaud, R. Lobinski, J. Anal. At. Spectrom. 20 (2005) 493.
[8] G. Ballihaut, C. Pecheyran, S. Mounicou, H. Preud'homme, R. Grimaud, R. Lobinski, TrAC Trends Anal. Chem. 26 (2007) 183.
[9] R. Lobinski, D. Schaumlöffel, J. Szpunar, Mass Spectrom. Rev. 25 (2006) 255.
[10] L. Tastet, D. Schaumlöffel, B. Bouyssiere, R. Lobinski, Anal. Bioanal. Chem. 385 (2006) 948.
[11] M. Dernovics, P. Guisti, R. Lobinski, J. Anal. At. Spectrom. 22 (2007) 41.
[12] A. Polatajko, M. Sliwka-Kaszynska, M. Dernovics, R. Ruzik, J.R. Encinar, J. Szpunar, J. Anal. At. Spectrom. 19 (2004) 114.
[13] P. Giusti, R. Lobinski, J. Szpunar, D. Schaumlöffel, Anal. Chem. 78 (2006) 965.
[14] D. Schaumlöffel, J.R. Encinar, R. Łobinski, Anal. Chem. 75 (2003) 6837.
[15] J. Ruiz Encinar, L. Ouerdane, W. Buchmann, J. Tortajada, R. Lobinski, J. Szpunar, Anal. Chem. 75 (2003) 3765.
[16] J. Ruiz Encinar, R. Ruzik, W. Buchmann, J. Tortajada, R. Lobinski, J. Szpunar, Analyst 128 (2003) 220.

Direct determination of ephedrine intermediate in a biotransformation reaction using infrared spectroscopy and PLS

Marcello G. Trevisan [1], Ronei J. Poppi *

Instituto de Química, UNICAMP, P.O. Box 6154, Campinas 13084-971, SP, Brazil

Abstract

Fourier transform mid-infrared spectroscopy (FT-MIR) coupled with a homemade attenuated total reflectance (ATR) flow-cell was used for on-line monitoring of a biotransformation reaction. The reaction was also monitored off-line by gas chromatography–mass spectrometry (GC–MS) enabling to establish a multivariate model for the infrared data based on partial least squares (PLS) regression. The method developed allowed the simultaneous determination of the substrate, two intermediates and the final product involved in the reduction reaction of 1-phenyl 1,2-propanedione at an initial concentration of 0.5% (v/v). The reaction was accomplished with a whole-cell suspension of *Saccharomyces cerevisiae* in a phosphate buffer of pH 3.0 at $32 \pm 1\,^\circ$C. The ATR infrared monitoring was performed directly on the suspension cell without any separation process or extraction over 3 h, totaling 188 spectra. The data were split into two subsets, with 158 times for calibration and 30 times for validation. The results showed that the proposed method may be used for on-line monitoring of the biotransformation reactions when the initial concentration is very low.
© 2008 Elsevier B.V. All rights reserved.

Keywords: Biocatalysis; Reaction monitoring; Process analytical technology (PAT); Infrared spectroscopy

1. Introduction

Biotechnology has been used for millennia, especially in the production of fermented foods, however, since the manufacture of penicillin during the second world war, the attention of biotechnology has been directed to pharmaceutical production [1]. Although chirality is the most interesting characteristic of biotransformation reactions, with high stereoselectivity and enantiomeric excesses (e.e.), other advantages can be obtained, such as contributions to sustainable technology (green chemistry) [2,3]. Microbial or enzymatic syntheses are increasing, compared to pure chemical reactions [2,4], according to a report from UK trade and investment [5], Europe's biotechnology industries were responsible for US$ 19.1 billion of dollars of revenue in 2003, producing complex intermediates and products for pharmaceutical, agrochemical and flavoring industries.

Biotransformation is a well-established industrial process and one of the most economically significant processes for the manufacture of pharmaceutical products [6]. Process monitoring is an indispensable requisite in biotechnology and many on-line techniques have been used to achieve this procedure [7,8], especially after the process analytical technology (PAT) [9] initiative by FDA. Conventionally, the monitoring of bioprocesses is conducted off-line, using laboratory methods such as gas chromatography–mass spectrometry (GC–MS) and HPLC. However, in-line methods are especially useful when the removal of a sample from the reactor is problematic, for example, for reasons of operational toxicity and/or sterility or when remote location of equipment is a disadvantage [10], or when dealing with fast reactions or decomposable substrates.

As well exemplified by Gavrilescu and Chisti [11], many traditional chemical and pharmaceutical products are now being synthesized by biological routes. Biocatalysis in the preparation of pharmaceuticals is just one part in this field [12–14]. Ephedrine, for example, a much used drug for increasing overall alertness and reducing fatigue, was one of first drugs to have a biological synthesis route been developed [15].

Spectroscopic techniques have the advantage of speed, simultaneous multi-analyte determination and non-destructiveness of the sample [16,17]. The highest selectiveness of the spectroscopic techniques can be reached with fluorescence methods,
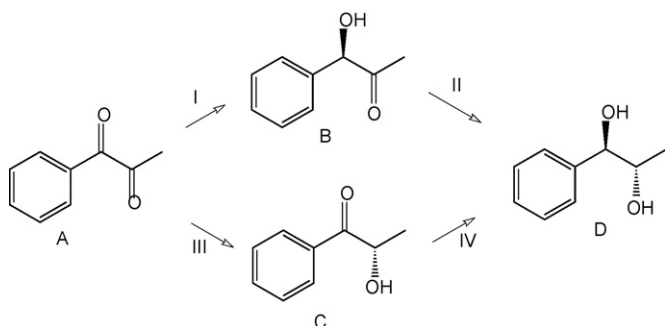
Fig. 1. Scheme of the proposed reaction: 1-phenyl-1,2-propanedione (A); (R)-1-hydroxy-1-phenyl-2-propanone (B); (S)-2-hydroxy-1-phenyl-1-propanone (C) and (1R,2S)-1-phenyl-1,2-propanodiol (D).

however, they are only indicated when the analyte has a fluorescent group [18,19]. Vibrational spectroscopic techniques have some attractive characteristics, such as speed, no-sampling requirements and no need for added reagents [20,8] with great advantages for process monitoring and control [21]. Although rich in chemical information, holistic infrared (IR) spectroscopy methods used for chemical quantification in bioprocesses are strongly influenced by the biological background [22]. However, when IR spectral data are analyzed by multivariate calibration techniques, such as partial least squares (PLS) [23], a known set of advantages is obtained, such as multi-simultaneous determinations [24,25]. Middle-infrared (MIR) not only presents highly selective chemical information but also shows intense absorption overlapping. The advantage of near infrared (NIR) over MIR methods is its low instrumentation cost, especially when using in-line probes, and its robust optics [26]. Separation methods are still being developed and are used to monitor bioprocesses [27–31] in academia and, especially, in industrial situations.

In this work, the reduction reaction of 1-phenyl-1,2-propanedione with a whole-cell suspension of *Saccharomyces cerevisiae* (Baker's yeast), producing a chiral intermediate used in the synthesis of ephedrine [15], was monitored by on-line attenuated total reflectance mid-infrared spectroscopy (ATR-MIR) and off-line by gas chromatography–mass spectrometry. The reaction studied, presented in Fig. 1, is a two-step reaction, where a substrate, 1-phenyl-1,2-propanedione (A), is biotransformed into two intermediates: (R)-1-hydroxy-1-phenyl-2-propanone (B) and (S)-2-hydroxy-1-phenyl-1-propanone (C). In the next step, the biotransformation gives only one product (1R,2S)-1-phenyl-1,2-propanodiol (D) [9]. Using the kinetic profile obtained by GC–MS (concentrations) and MIR (spectra), multivariate models based on PLS were reached to predict the concentration of the four species involved in the reaction, yielding a direct on-line alternative spectroscopy method.

2. Experimental

2.1. Reagents and samples

Commercially available baker's yeast (*S. cerevisiae*), lyophilized powder (DSM Bakery, Norway), 85% phosphoric acid (Synth, Brazil), monobasic potassium phosphate (Merck,

Germany), 1-phenyl-1,2-propanedione (Sigma, USA) and ethyl acetate (IQ/Unicamp pilot plant) were used in this work. Analytical grade reagents and deionized water obtained from a Milli-Q system (Millipore Corp.) were used to prepare all solutions.

2.2. Apparatus and software

A homemade flow-cell (Fig. 2) based on horizontal attenuated total reflectance (HATR) having a ZnSe crystal was constructed and used to obtain all on-line infrared data. The flow system consists of silicon tubing (inner diameter of 3 mm) connected to the reactor with a peristaltic pump (Ismatec IPC, Switzerland) model 78001-22 to produce a flow rate of $10 \, \text{mL min}^{-1}$. The reactor was connected to a controlled temperature water bath (Quimis, Brazil) model 215.M2.BS, to keep the temperature constant at $32 \pm 1 \, ^\circ\text{C}$.

Spectra were acquired using a Bomen MB-100 FT-IR spectrometer. Sequential scans of the reaction medium were obtained using 16 co-added scans and a resolution of $8 \, \text{cm}^{-1}$. The spectra range was from 2900 to $780 \, \text{cm}^{-1}$.

Gas chromatographic (GC) analysis with mass selective detection was performed on an Agilent 6890/HP 5973 equipped, with a HP-5MS column (0.25 mm ID, 30 m long). Helium at $1 \, \text{mL min}^{-1}$ was used as carrier gas. Data analyses were carried out using Matlab 6.5 (The MathWorks, Natick, USA) with PLS toolbox (Eigenvector Technologies, Manson, USA) [32] version 3.5 in a microcomputer AMD Athlon 1.3 GHz with 256 Mb of RAM, using a Fedora core 3 system.

2.3. Procedure

Phosphate buffer of pH 3.0 was prepared with 1.35 mL of phosphoric acid and 27.2 g of monobasic potassium phosphate, completing the volume with deionized water to 1 L. The biotransformation was carried out in a 250 mL homemade bioreactor equipped with a magnetic stirring bar and temperature control. A whole-cell suspension of baker's yeast was prepared by dissolution of 8.0 g of dry yeast in 100 mL of phosphate buffer and mixed for 5 min at $32 \, ^\circ\text{C}$. A solution of 600 mg of 1-phenyl-1,2-propanedione dissolved in 1 mL of ethanol was then added to the reactor.

2.4. Monitoring and data analysis

Concentrations of the four species involved in the reaction were obtained by an off-line monitoring using gas chromatography–mass spectrometry with total ion chro-
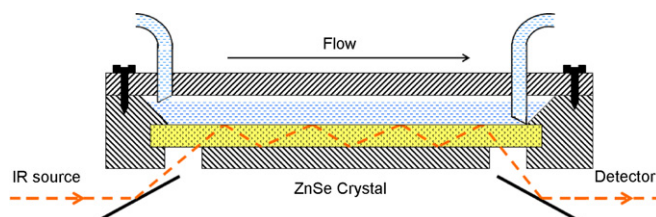

Fig. 2. The homemade flow-through ATR cell.

matogram (TIC) abundances. Direct monitoring was also established during in the same reaction by infrared spectroscopy using a homemade flow-through horizontal attenuated total reflectance cell with ZnSe crystal. In the off-line GC monitoring, samples (1 mL) were withdrawn from the reactor mixture at 0.0, 0.5, 1.0, 2.0 and 3.0 h and extracted with 6 mL of ethyl acetate for 30 s. Continuous concentration profiles around the time (kinetic profile) were estimated by fitting an equation to the individual points. Four different kinetic equations were obtained, describing the variation of the four species (A, B, C and D, Fig. 1) over the reaction time. The samples for infrared analysis were used directly from the reaction medium, without any separation or extraction step, for 3 h, in 1 min steps, without intervals, totalizing 188 spectra. Each spectrum was composed of 16 co-added scans taken during 1 min of acquisition. The first spectrum relates to the average of all reaction variations during the first minute and so on.

The kinetic equations obtained by GC–MS were used to estimate the four concentrations throughout 188 times. Thus, a parallel set of infrared spectra (X-block) and their related estimated concentrations (Y-block) were obtained. This data set was divided into two subsets: calibration and validation. For the calibration set, the concentrations obtained at 155 different times (samples) were used and for the validation set, the other 33 times. Each value of the validation set was obtained in equal intervals (between 5 points) of each point from the calibration set.

Before the development of the calibration models, as preprocessing, the baseline variation was corrected using the function baseline from the PLS toolbox. Isolated PLS-1 models, for each substance in the reaction, were developed, totaling four different models. The optimum number of latent variables was chosen by
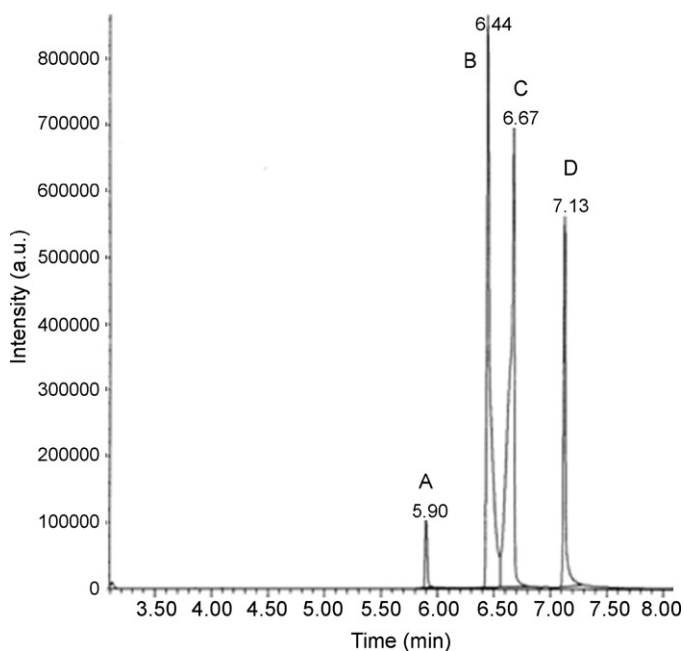
root mean square error of cross-validation (RMSECV) obtained from the calibration set by internal validation (leave-one-out) [33], expressed by Eq. (1):

$$RMSECV = \sqrt{\frac{\sum_{i=1}^{n}(\hat{y}_i - y_i)^2}{n}} \qquad (1)$$

where n is the number of samples and y_i and y_i are the predicted and the reference value for ith sample, respectively. The performance of the models was evaluated by a percentage of root mean square prediction difference (RMSPD), as follows [34]:

$$RMSPD = 100\sqrt{\frac{1}{n}\sum_{i=1}^{n}\left(\frac{\hat{y}_i - y_i}{y_i}\right)^2}. \qquad (2)$$

3. Results and discussion

3.1. Reaction monitoring

The proposed reaction results in the reduction of 1-phenyl-1,2-propanedione using a whole-cell suspension of Baker's yeast in phosphate buffer, and produces an intermediate that is then used in the ephedrine synthesis. Gas chromatography was used to model the reaction, obtaining the kinetic profiles. A gas chromatogram at the time 0.5 h (30 min) is shown in Fig. 3.

Infrared spectroscopic monitoring was carried out using the homemade flow-through cell with horizontal attenuated total reflectance. The background spectrum used was the first spectrum obtained one minute after of addition of the substrate to the reactor, having a homogeneous system. Fig. 4A presents the infrared spectra obtained during the three hrs. of reaction monitoring and Fig. 4B the principal absorbance variations.

3.2. Kinetic fitting

Five samples were withdrawn from the reaction batch and extracted at the times of 0.0, 0.5, 1.0, 2.0 and 3.0 h and then analyzed by GC–MS. The relative concentrations of the four species were obtained by TIC, and then the kinetic profiles were obtained by fitting non-linear equations into the experimental points by Origin® version 5.0. As show in Fig. 5, the concentrations of the intermediates (B and C) with the time are governed by two principal mechanisms (steps I and III, Fig. 1). Between the times 0–1.5 h, the concentrations of B and C are related principally to their production from the substrate (A). After the substrate has gone the concentrations of species B and C are described by their conversion to species D, the final product (steps II and IV, Fig. 1). Although this mechanism is a simplification from a much more complex enzymatic/whole-cell reaction, it summarizes the real mechanisms [35,36]. The kinetic equations obtained for the steps I/III and II/IV are described as follow.

For the species A (substrate), the kinetic behavior is described by the equation:

$$C_A = k_1 e^{(-t/k_2)} + a_0 \qquad (3)$$

Fig. 3. GC chromatogram using total ion chromatogram (TIC) for 1-phenyl-1,2-propanedione (A), (R)-1-hydroxy-1-phenyl-2-propanone (B), (S)-2-hydroxy-1-phenyl-1-propanone (C) and (1R,2S)-1-phenyl-1,2-propanodiol (D).
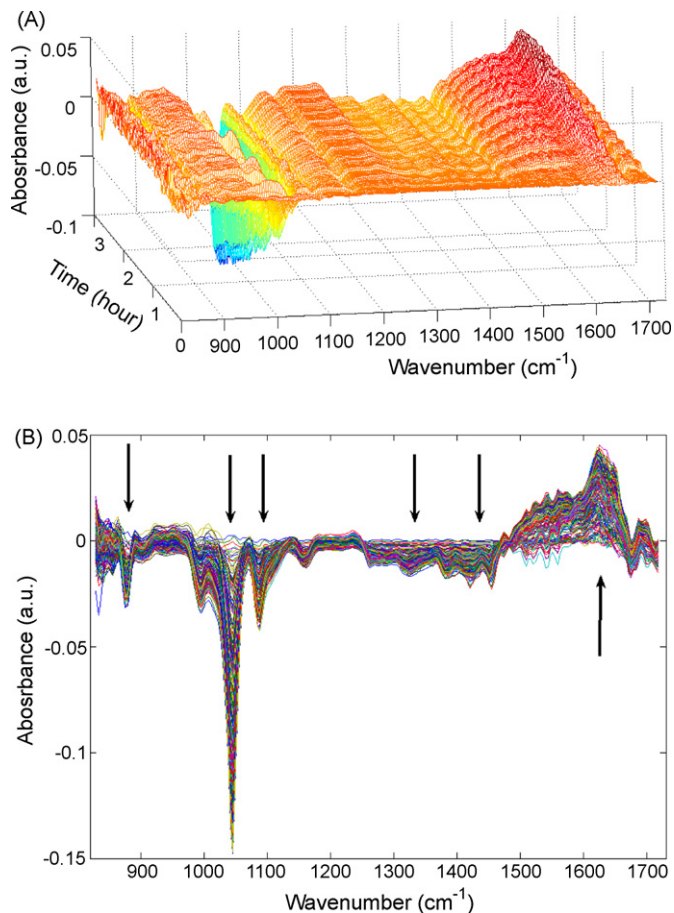
Fig. 4. Mid-infrared monitoring for the system (*S. cerevisiae* and buffer) with substrate, full landscape (A) and an absorbance variations plot (B).

where k_1, k_2 and a_0 are $6.86 \times 10^{-3} \pm 1.16 \times 10^{-2}$, $5.57 \times 10^{-1} \pm 2.84 \times 10^{-2}$ and $9.97 \times 10^{-1} \pm 2.09 \times 10^{-2}$, respectively, and t is the variable time. For the intermediate B, two kinetic behaviors are observed. Its growing is described
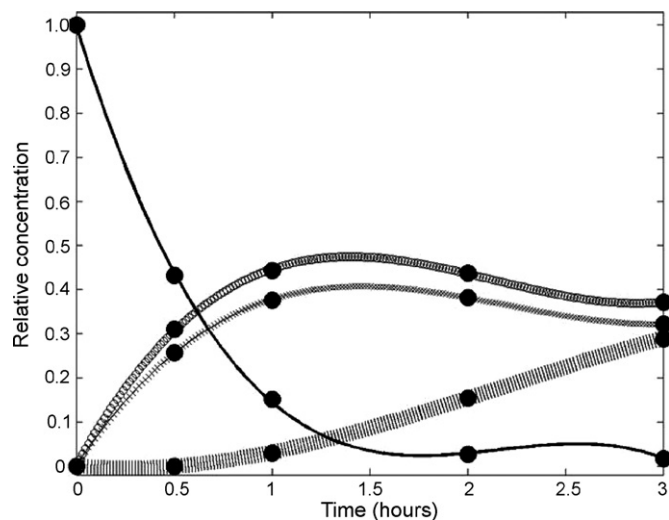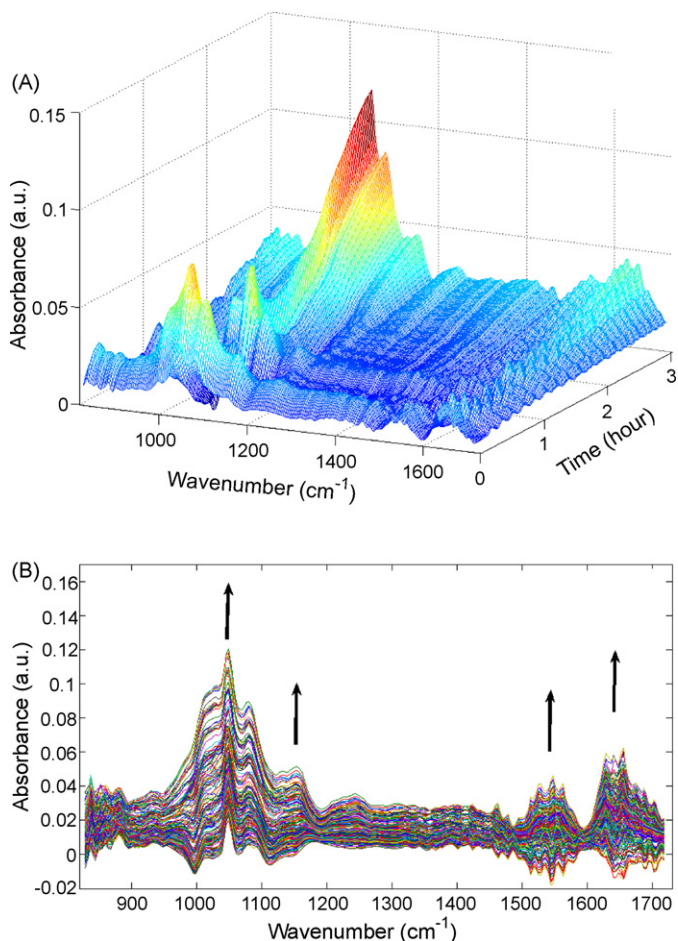
by two different kinetic processes happening sequentially. The first fast phase has the concentration increase up to 2 h, where a maximum is obtained. This phase can be described as follow:

$$C_{B_1} = k_1 t + k_2 t^2 \tag{4}$$

where the terms k_1 and k_2 are $5.74 \times 10^{-1} \pm 4.4 \times 10^{-2}$ and $-1.93 \times 10^{-1} \pm 2.0 \times 10^{-2}$, respectively.

The second slower phase shows a linear decrease:

$$C_{B_2} = k_1 + k_2 t \tag{5}$$

where k_1 and k_2 are $4.94 \times 10^{-1} \pm 7 \times 10^{-3}$ and $-5.6 \times 10^{-2} \pm 2 \times 10^{-3}$, respectively.

For the intermediate C, the same kinetic characteristics are seen, with two phases. For this component, Eqs. (6) and (7) were fitted for the faster phase:

$$C_{C_1} = k_1 t + k_2 t^2 \tag{6}$$

where k_1 and k_2 are $6.87 \times 10^{-1} \pm 6.0 \times 10^{-2}$ and $-2.36 \times 10^{-1} \pm 2.8 \times 10^{-2}$, respectively. And for the next step, the decrease is represented by:

$$C_{C_2} = k_1 + k_2 t \tag{7}$$

Fig. 5. Kinetic fitting for the substrate (−); (*R*)-1 intermediate (×); (*S*)-2 intermediate (○) and the final product (+). Off-line analysis is represented by single points (●).

Fig. 6. Mid-infrared monitoring for the system (*S. cerevisiae* and buffer) without substrate, full landscape (A) and an absorbance variations plot (B).
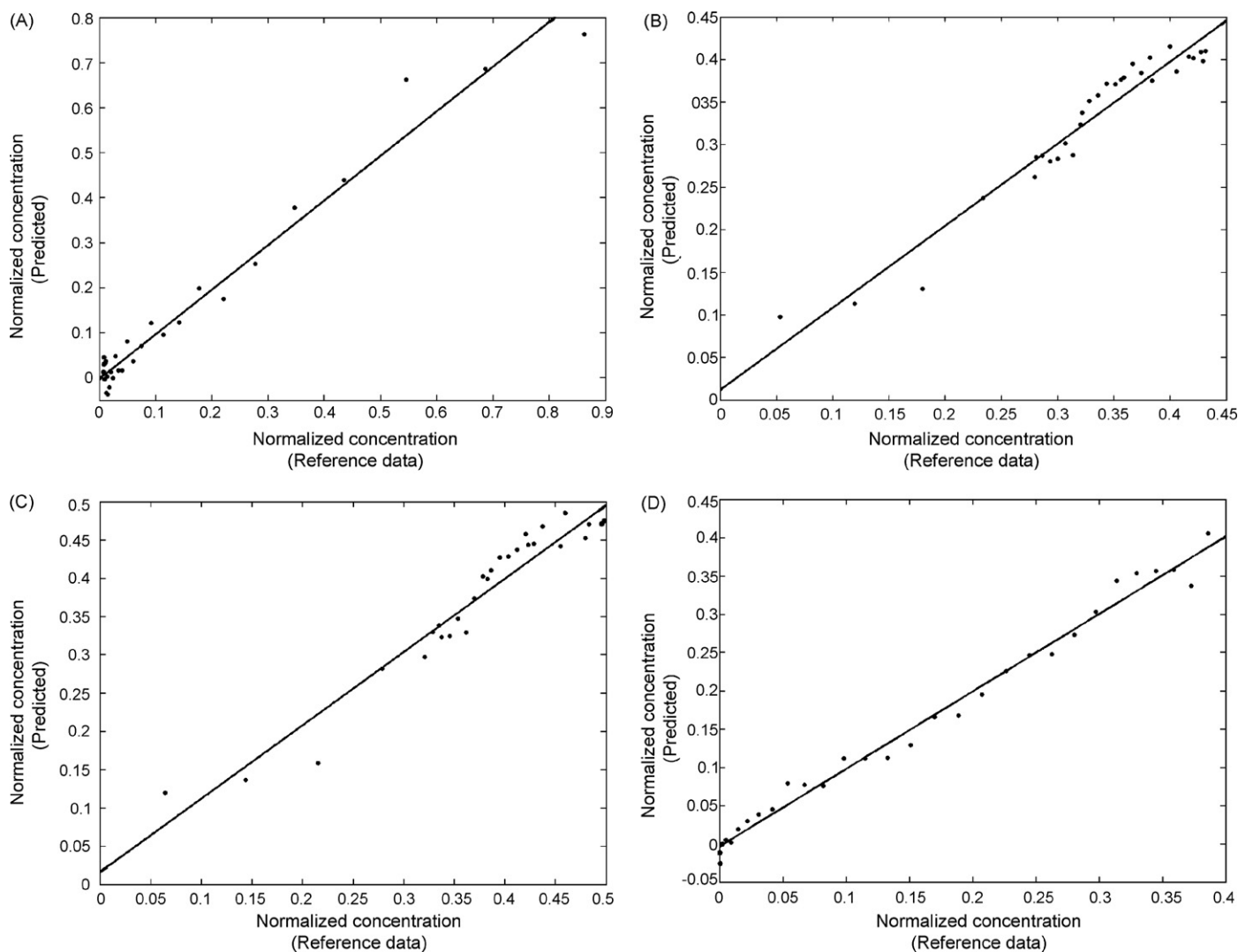
Fig. 7. Concentration correlation plots between the PLS model (predicted) and GC–MS (reference) results using the validation set for substrate (A), (R)-1 substrate (B), (S)-2 substrate (C) and the final product (D).

where k_1 and k_2 are $5.65 \times 10^{-1} \pm 2 \times 10^{-3}$ and $-6.4 \times 10^{-2} \pm 1 \times 10^{-3}$ respectively.

The final product slowly increases and its concentration as a function of time can be described as:

$$C_D = k_1 \frac{t^n}{k_2^n + t^n} \tag{8}$$

where k_1, k_2 and n are $6.28 \times 10^{-1} \pm 6.9 \times 10^{-2}$, $3.165 \pm 3.03 \times 10^{-1}$ and $2.531 \pm 2.23 \times 10^{-1}$, respectively.

These equations were used to obtain the estimated concentrations at the 188 times for the four species involved in the reaction. All the kinetic parameters showed good agreements with those previously reported for this biotransformation [15]. The estimated kinetic profile (188 points) and the experimental points are shown in Fig. 5.

3.3. IR spectra variations

Before attempting to construct a multivariate model for the IR data and the kinetic profiles, the background IR spectra vari-

ability was evaluated by monitoring a batch without the addition of the substrate 1-phenyl-1,2-propanedione (only *S. cerevisiae* suspension, buffer and ethanol). The monitoring was carried out using same conditions as used for that contain the substrate, producing 188 spectra, as shown Fig. 6A. In this series, the background (absorbance equal to zero) was the first spectrum after the homogenization of the medium reaction. The largest absorbance variations occur at specific wavenumbers (Fig. 6B): an increasing absorbance at 975–1100 cm^{-1} due to C–O bonding (alcohols); 1500–1600 cm^{-1} (–COO^{-}) and 1600–1700 cm^{-1} (–COOH, ester and ketone). Few variations are seen in the first minutes of monitoring but after 1.5–2 h, the spectral changes increase rapidly, especially the absorbance at 1050 cm^{-1}. These IR variations are related to the natural enzymatic reactions of the whole-cell suspension of baker's yeast in phosphate buffer and the strong increase of C–O absorbance band is related to the oxidation process inside of the cells. The monitoring was carried out for 8 h and, although these results are not shown in Fig. 6, no more absorbance changes can be observed after the fifth hour, probably due to inac-
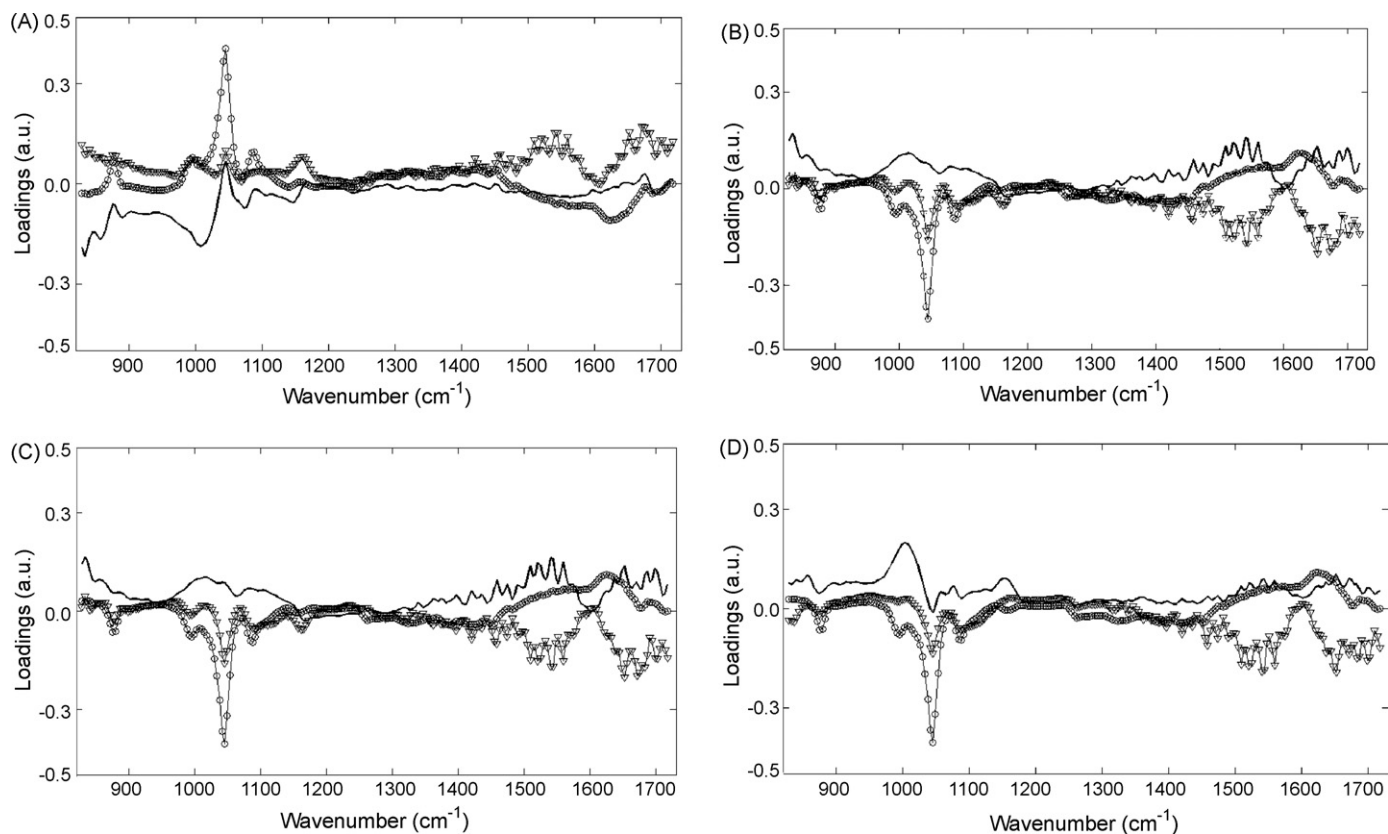
Fig. 8. The loadings for each PLS-1 model for the first three latent variables (LV). The first (○), second (−) and third (▽) LV are presented for the substrate (A), (R)-1 substrate (B), (S)-2 substrate (C) and the final product (D).

tivation of the enzymes inside of the cells (higher state of oxidation).

The monitoring obtained from the batch with the substrate, shown in Fig. 4B, presents some similarities with this background spectral monitoring (Fig. 6B). In the reaction monitoring, the background spectrum was obtained from the first spectrum, with the substrate. As a consequence, a strong negative absorbance variation is observed, while the substrate is consumed during the reaction, as can be seen in Fig. 4B. Three principal bands present a significant decrease, at wavenumbers 1000, 1050 and 1100 cm^{-1}, which can be attributed to C−O bonding. The observed absorbance in the region at 1300–1450 (−COOH and −COO^{-}) and an increase at 1550–1650 cm^{-1} (ester and CHO), reveal the general oxidation of the compounds. However, some absorbance changes can be observed in restricted wavenumbers and it is not possible to build a univariate model using these data to predict the concentrations of the compounds during the reaction. Due the complex background variation from the whole-cell suspension of *S. cerevisiae*, the concentration prediction needs a multivariate statistical analysis, such as PLS regression.

3.4. PLS-1 calibration and validation

The recorded FT-IR spectra (X-block) together with the estimated concentration for the four compounds obtained by

GC–MS (y-block) were divided into two sets: 158 points to build the multivariate models and 30 to validate the obtained models. Initially, the spectra were preprocessed, removing the floating baseline. Several models were studied and the best results were obtained using a selection of the wavenumbers in the region of 820–1730 cm^{-1}, totaling 231 wavenumber points. In this way, the calibration set is characterized by an X-matrix of 158 samples by 231 wavenumbers and a y-vector of 158 samples by one that describes the relative concentration of one of the four compounds around the time of reaction. A multivariate model was built for each compound (A, B, C and D). The individual models were developed using the lowest value of RMSECV (Eq. (1)) to choose the optimal number of latent variables. Each one of the four chosen models used five latent variables to predict the concentration variations during the reaction time.

The prediction capabilities of the obtained models were evaluated through the prediction of the validation set. The spectra of the validation set was preprocessed in the same way as the calibration data and then the estimated concentrations were plotted with the reference data (kinetic profile obtained by GC–MS). The real against the predicted values were plotted, as shown in Fig. 7. Many of the predicted values for the substrate concentration are close to zero (Fig. 7A) due the consumption of substrate during the reaction; the substrate falls asymptotically and, after 1.5 h until the end of the reaction, its concentration is close to zero. The predicted concentrations for the two inter-

mediates are shown in Fig. 7B and C and the predicted values are very similar. The concentrations estimated for the final product are shown in Fig. 7D. Probably the similarity between the kinetic profiles and/or between the chemical structures of the two intermediates makes their predicted values so close. As can be seen, all the estimated values for the four compounds are well distributed around the correction line, with negative and positive residuals. Using Eq. (2) (RMSPD), the global relative errors for these results were around 5% in relation to the estimated kinetic profile.

Analysis of the loadings of PLS regression is a known strategy to verify the similarities between the proposed models and to study the possible correlations of the several models constructed with the same X-data (spectra) and several calibration parameters, such as in multi-analyte or simultaneous determinations methodologies [23]. In this work, the profiles of the loadings of regression for each of the four developed PLS models were also evaluated. Although five latent variables (LV) were used in each model, the first three LV capture more than 95% of the cumulative variance for the X-block (spectra) and more than 87% of the y-block (concentration). As can see in Fig. 8, the region of $1000–1100\,cm^{-1}$ has significant importance for all the models. Fig. 8A shows the loadings for the substrate and the region of $820–1000\,cm^{-1}$ also has an importance to this model. The loadings in Fig. 8B and C are related to the intermediates. The high correlation of the loadings between the two models suggests the probable impossibility to distinguish the two intermediates. The IR spectrum of the two intermediates directly measured in a biotransformation medium in the presence of a higher concentration of baker's yeast can have a lower selectivity for primary or secondary ketones (intermediates B and C). Nevertheless, the predictions of the intermediates works well with lower than 5% of relative error of prediction. The final product (Fig. 8D) has a distinct positive broad band in the region of $1000\,cm^{-1}$ and some other smaller differences between the loadings for the other compounds. These results suggests that the obtained FT-IR spectra using the homemade flow-through ATR cell can determine the four compounds involved in the bioconversion reaction directly in the whole-cell medium using a continuous on-line systems.

4. Conclusions

The proposed method provides an on-line FT-IR determination of the four species involved in a biotransformation reaction, without steps of extraction or chromatographic separation. The determination was evaluated by direct on a whole-cell suspension of baker's yeast, being a rapid and low cost method. The methodology developed is a contribution to more reliable on-line methods that can be used for industrial applications or real-time system optimizations.

Acknowledgments

References

[1] D. Goodman, B. Sorj, J. Wilkinson, From Farming to Biotechnology: A Theory of Agro-Industrial Development, Blackwell, Oxford, 1987.
[2] H.E. Schoemaker, D. Mink, M.G. Wubbolts, Science 299 (2003) 1694.
[3] M.G. Trevisan, R.J. Poppi, Talanta 74 (2008) 971.
[4] R.N. Patel, Enzyme Microb. Technol. 31 (2002) 804.
[5] http://www.uktradeinvest.gov.uk/, accessed in October 2007.
[6] S. Macauley-Patrick, S.A. Arnold, B. McCarthy, L.M. Harvey, B. McNeil, Biotechnol. Lett. 25 (2003) 257.
[7] J.B. Callis, D.L. Illman, B.R. Kowalski, Anal. Chem. 59 (1987) A624.
[8] M.G. Trevisan, R.J. Poppi, Quim. Nova 29 (2006) 1065.
[9] FDA Draft Guide for Industry, PAT—A Framework for Innovative Pharmaceutical Manufacturing and Quality Assurance, September 2003.
[10] P.A. Bird, D.C.A. Sharp, J.M. Woodley, Org. Process Res. Dev. 6 (2002) 569.
[11] M. Gavrilescu, Y. Chisti, Biotechnol. Adv. 23 (2005) 471.
[12] V. Gotor, Org. Process Res. Dev. 6 (2002) 420.
[13] J.P. Rasor, E. Voss, Appl. Catal. A 221 (2001) 145.
[14] A. Zaks, D.R. Dodds, Drug Discov. Today 2 (1997) 513.
[15] E. Lourenco, J.A.R. Rodrigues, P.J.S. Moran, J. Mol. Catal. B: Enzyme 29 (2004) 37.
[16] R. Ulber, J.G. Frerichs, S. Beutel, Anal. Bioanal. Chem. 376 (2003) 342.
[17] S. Vaidyanathan, G. Macaloney, J. Vaughn, B. McNeil, L.M. Harvey, Crit. Rev. Anal. Chem. 19 (1999) 277.
[18] C. Gourlay, C. Miege, J. Garric, M.H. Tusseau-Vuillemin, J.M. Mouchel, Polycyclic Aromat. Compd. 22 (2002) 501.
[19] A. Hagedorn, W. Levadoux, D. Groleau, B. Tartakovsky, Biotechnol. Prog. 20 (2004) 361.
[20] D.C. Hassell, E.M. Bowman, Appl. Spectrosc. 52 (1998) 18A.
[21] S.P. Gurden, J.A. Westerhuis, A.K. Smilde, AIChE J. 48 (2002) 2283.
[22] R. Bro, Ph.D. Thesis, University of Amsterdam, Amsterdam, Netherlands, 1998.
[23] H. Martens, T. Naes, Multivariate Calibration, John Wiley, New York, 1989.
[24] S. Sivakesava, J. Irudayaraj, D. Ali, Process Biochem. 37 (2001) 371.
[25] M. Blanco, A.C. Peinado, J. Mas, Biotechnol. Bioeng. 88 (2004) 536.
[26] W.F. McClure, Anal. Chem. 66 (1994) A43.
[27] M. Kulp, I. Vassiljeva, R. Vilu, M. Kaljurand, J. Sep. Sci. 25 (2002) 1129.
[28] S. Ehala, I. Vassiljeva, R. Kuldvee, R. Vilu, M. Kaljurand, Fresenius J. Anal. Chem. 371 (2001) 168.
[29] K. Schugerl, J. Biotechnol. 85 (2001) 149.
[30] Y.C. Liu, F.S. Wang, W.C. Lee, Biochem. Eng. J. 7 (2001) 17.
[31] V.P. Hanko, J.S. Rohrer, Anal. Biochem. 283 (2000) 192.
[32] Eigenvector Research, Inc., http://www.eigenvector.com/, accessed in July 2007.
[33] R.G. Brereton, Analyst 125 (2000) 2125.
[34] N.J. Millerihli, T.C. Ohaver, J.M. Harnly, Spectrochim. Acta Part B 39 (1984) 1603.
[35] W.C. Gardiner, Rates and Mechanisms Chemical Reactions, Benjamin-Cummings Publishing Co., 1969.
[36] M.A.B. Levi, L.S. Scarminio, R.J. Poppi, M.G. Trevisan, Talanta 62 (2004) 299.

Talanta

Review

Ultrasonic-assisted enzymatic digestion (USAED) for total elemental determination and elemental speciation: A tutorial

G. Vale [a], R. Rial-Otero [a], A. Mota [b], L. Fonseca [c], J.L. Capelo [a],*

[a] REQUIMTE, Departamento de Química, Faculdade de Ciências e Tecnologia, Universidade Nova de Lisboa, 2829-516 Monte da Caparica, Portugal
[b] Centro de Química Estrutural, Instituto Superior Técnico de Lisboa, Torre Sul. Av. Rovisco Pais, 1049-001 Lisboa, Portugal
[c] IBB-Institute for Biotechnology and Bioengineering, Centre for Biological and Chemical Engineering, Instituto Superior Técnico, Av. Rovisco Pais, 1049-001 Lisboa, Portugal

Abstract

Due to its potential as sample treatment for Analytical Chemistry, the Ultrasonic-Assisted Enzymatic Digestion (USAED) for total elemental determination and elemental speciation is described under the most recent achievements published in literature, focusing on the variables that critically affect the performance of this relatively new sample treatment, such as the type of enzymes or the type of ultrasonic system used for the acceleration of the solid–liquid extraction process. Moreover, analytical chemists are aware of common errors produced in data interpretation concerning USAED. In addition, a guide for the rapid application of this methodology is also provided along with detailed explanations. Finally, future trends regarding USAED are also given and commented.
© 2007 Elsevier B.V. All rights reserved.

Keywords: Ultrasonication; Enzymes; Elemental speciation; Elemental determination; Tutorial

Contents

1. Introduction

The challenge for studies regarding metals and metalloids nowadays is focused on chemical speciation. As an example, Se is supplemented in many diets due to its recognized medical properties [1]. However, the same health benefit is not obtained if Se is added in the food as inorganic Se, e.g. Se(VI) or Se(IV), or as organic Se, e.g. Se-methionine.

Chemical speciation is a difficult issue that demands advanced analytical techniques and highly qualified personnel [2]. Therefore, the search for new methods for chemical speciation accomplishing simplicity, robustness and rapidity is an objective of main importance in analytical chemistry.

The use of ultrasounds to speed up enzymatic reactions for chemical speciation was first reported by Capelo et al. [3] for Se speciation in yeast. This method is named Ultrasonic-assisted enzymatic digestion (USAED) and it meets the requirements of simplicity, robustness and rapidity. Since it was reported for first time the USAED sample treatment has been further applied in different matrixes for chemical speciation of other metals as can be seen in Table 1 . In addition, some improvements on the methodology have been also done.

Despite its simplicity, USAED as sample treatment has been used scarcely since 2004 to date in the field of elemental speciation. In our opinion, the methodology is not known enough among the analytical community. Therefore, the main aim of the present work is to provide a tutorial to teach clearly how USAED must be applied in the analytical laboratory, focusing to highlight the variables affecting USAED performance, along with its drawbacks and how to overcome them.

2. Essentials about ultrasonics

When ultrasonic waves cross a liquid solution, different chemical and physical phenomena take place. It is out of the scope of this review to describe in detail such phenomena. For a complete understanding of the effects of ultrasonication for chemical processes, the books of Prof. T. J. Mason, especially the one entitled sonochemistry, are highly recommended [4]. In brief, the most important properties caused by ultrasonic waves crossing through a liquid medium come from a physical phenomenon called cavitation. Cavitation refers to a process by which numerous micro-gas bubbles are formed, as the ultrasonic waves compress and decompress the liquid media as they pass through it. These bubbles can grow, oscillate, split and implode,

causing the following effects:

(i) Temperatures of ca. 5000 °C.
(ii) Pressures of ca. 1000 atm.
(iii) Formation of highly reactive chemical radicals.
(iv) Mechanical erosion of solids (if present in solution) and particle disruption.

The former properties of ultrasonic energy make it a powerful tool in analytical chemistry, as demonstrated by the increasing number of analytical chemistry applications published during the last decade [5]. Some reviews on analytical uses of ultrasonication can be found in recent literature [5–11], focusing on the following items:

(i) Solid–liquid extraction of metals, metalloids and organics from solid samples.
(ii) Elemental speciation.
(iii) Shortening of sequential extraction schemes.
(iv) Acceleration of liquid–liquid extraction processes.
(v) Acceleration of solid–liquid extraction of organics.
(vi) Electroanalytical applications.

It must be pointed out that nowadays there are many types of ultrasonic devices [6]. For instance, ultrasonic probes, ultrasonic baths, sonoreactors, and cup horns are ultrasonic systems that can be used for sample treatment in analytical chemistry. Nevertheless, a minimum knowledge of their properties is required otherwise unexpected effects can be obtained. As an example, the intensity of sonication, which ultimately dictates the properties of cavitation, is considerably different among the above-mentioned systems. Additional examples are given below:

(i) Ultrasonic bath cannot boost enzymatic kinetics in the same way as the ultrasonic probe or sonoreactor does. The capabilities of the aforementioned apparatus to speed the enzymatic reactions follow the same order that their respective intensities of sonication: ultrasonic probe > sonoreactor > ultrasonic bath.
(ii) Considering the sample container as 1-ml eppendorf cups, the number of samples that can be treated at once is by large higher for the ultrasonic bath, the number of samples depending on its size: for a 3-l ultrasonic bath, this number is 120. The sonoreactor allows ultrasonication of at least six eppendorf cups at the same time whilst the ultrasonic probe allows only one at a time.

Table 1
Literature reporting USAED for total elemental determination and elemental speciation

	Analytical methodology
(a) [3]; (b) Yeast, CRM 710 Oyster tissue and CRM 278 mussel tissue; (c) Protease XIV, 10% (w/w); (d) Total Se and SeMet	HPLC–ICP-MS. Total Se determination and Se speciation. Cationic exchange column Hamilton PRP-X200 (250 mm × 4.1 mm; 10 μm). Mobile phase: 4 mM pyridine formate solution (pH 2.8) with 3% of methanol at 1 ml/min in the isocratic mode. Injection volume: 200 μl. USAED procedure: (a) for total metal determination: 10 mg of sample + 1 mg of protease XIV + 1 ml water + sonication during 5 s at 20 W. The mixture was centrifuged and 20 μl of the supernatant was diluted up to 10 ml with water; (b) for metal speciation: 10 mg of yeast + 1 mg of protease XIV + 1 ml of water + sonication during 30 s. The mixture was filtered through a 0.45 μm nylon filter. The total Se recoveries found for yeast, oyster and mussel tissue were 105%, 106% and 96%, respectively. In yeast it was found an 87% in SeMet from the total Se
(a) [14]; (b) Spanish rice and Indian basmati; (c) 0.33% (w/w) α-amylase and 1% (w/w) protease type XIV; (d) Total As, As(III), As(V), DMA, and MMA	HPLC–ICP-MS. Total As determination and As speciation. Anion exchange column Hamilton PRP-X100 (250 mm × 4.1 mm; 10 μm). Mobile phase: 10 mM $HPO_4^{2-}/H_2PO_4^-$ with 2% methanol (pH 6) at 1 ml/min in the isocratic mode. Injection volume: 100 μl. The analytes were extracted using and Ultrasonic Probe, UP with a 3-mm titanium microtip. USAED procedure—first step: 3 g of sample + 10 mg of α-amylase + 3 ml of water + sonication during 1 min. Second step: 30 mg of protease XIV + sonication during 2 min. After sonication, the extracts were centrifuged (4000 rpm, 10 min) and filtered (0.22 μm). For method validation the reference material rice SRM 1568a (NIST, USA) was used. The total As recovery was 99.7 ± 0.8%. LODs were 0.05 μg/kg for As(III) and 0.2 μg/kg for all the other As species
(a) [15]; (b) BCR-414 Plankton, ERM-CE 278 mussel tissue, oyster tissue; (c) Protease XIV, 100% (w/w); (d) Total Se	The analytes were extracted using an UP with a 1 mm microtip at 50% amplitude. USAED procedure: 10 mg of sample + 10 mg of protease XIV + 1 ml of water or Tris–HCl buffer (pH 7.5) + sonication during 2 min. Matrix modifier $Pd(NO_3)_2$ and H_2O_2. The total Se recoveries found for mussel tissue, plankton and oyster tissue were 93%, 106% and 111%, respectively. LOD was 0.6 ng/g and LOQ was 2 ng/g
(a) [16]; (b) Rice and chicken muscle samples. All of them candidate to reference material (European project SEAS-G6RD-CT2001-00473); (c) For rice samples: 1% (w/w) of α-amylase and 10% (w/w) protease XIV. For chicken samples: 10% (w/w) of protease XIV; (d) Total As, As(III), As(V), AsB, DMA, and MMA	HPLC–ICP-MS. Total As determination and As speciation. The analyte was extracted using an UP with a 3-mm titanium microtip at 30% amplitude. USAED procedure—(a) rice sample: first step: 0.3 g of rice + 3 mg of α-amylase + 3 ml water + sonication during 1 min; second step: 30 mg/ml of protease XIV + 2-min sonication time. (b) chicken samples: 0.15 g of sample + 15 mg of protease XIV + 3 ml of water + 4-min sonication time. All the extracts were centrifuged (5000 rpm, 10 min) and then filtered (0.22 μm). Anion Chromatography column Hamilton PRP-X100 (250 mm × 4.1 mm; 10 μm). Mobile phase: 10 mM $HPO_4^{2-}/H_2PO_4^{2+}$ with 2% methanol (pH 8.5) at 1.5 ml/min in the isocratic mode. Injection volume: 100 μl. For method validation the following reference materials were used: rice flour SRM 1568a (NIST, USA). Recoveries: 98–110% (±7). LOD: 13–20 ng/l
(a) [17]; (b) Human hair; (c) Protease XIV and lipase; (d) Total As, As(III), As(V), DMA, and MMA	HPLC–ICP-MS. Total As determination and As speciation. The analyte was extracted using an UP with a 3-mm titanium microtip at 30% of amplitude. USAED procedure: 75 mg of sample + protease and lipase mixture + 3 ml of water + sonication during 10 min. The extracts were centrifuged (5000 rpm, 10 min) and filtered (0.22 μm). Anion Chromatography column Hamilton PRP-X100 (250 mm × 4.1 mm; 10 μm). Mobile phase: 10 mM $HPO_4^{2-}/H_2PO_4^{2+}$ with 2% methanol (pH 8.5) at 1.5 ml/min in the isocratic mode. Injection volume: 100 μl. For method validation the following reference materials were used: human hair no. 13 (NIES, Japan) and GBW 07601 (GBW, China). Recovery for total Se: 61.6% (± 3.0)
(a) [18]; (b) Rice samples: Chinese rice (Zhenshan 97), Hungarian rice (Risabell) and brown rice sample (Köröstáj-333); (c) 0.33% (w/w) of α-amylase and 10% (w/w) of protease XIV; (d) Total As, As(III), As(V), AsC, AsB, DMA, and MMA.	HPLC–ICP-SF-MS. Total As and As speciation. The analyte was extracted using an UP with a 3 mm microtip. USAED procedure—first step: 0.3 g of raw and cooked rice + 10 mg of α-amylase + 3 ml of water + sonication during 1 min; second step: 30 mg of protease XIV + 2-min sonication time. The mixture was centrifuged (4000 rpm, 10 min) and then filtered (0.22 μm). Anion Chromatography column Hamilton PRP-X100 (250 mm × 4.1 mm; 10 μm). Mobile phase: $NH_4H_2PO_4$ (pH 5.5 with NH_3) at 1.5 ml/min in the isocratic mode. Cationic column Suplecosil LC SCX-100 (250 mm × 4.1 mm; 10 μm). Mobile phase: 25 mM of pyridine (pH 2.7 with formic acid) at 1.5 ml/min in the isocratic mode. Injection volume: 20 μl. Major As species found were: As(III) (50%); As(V) (25–33%); DMA (8–10%); AsC (6–10%); and AsB (5%) only detected in Chinese rice samples. The reference material rice flour sample – NIST SRM 1568a was used for method validation
(a) [19]; (b) Edible seaweed samples; (c) Trypsin, α-amylase, pepsin 10% (w/w) enzyme–mass ratio; (d) As, Cd, Cu, Cr, Fe, Mn, Ni, Pb, and Zn	ICP-OES. Multielemental determination. Samples were treated with different types of enzymes—(a) with trypsin and α-amylase: 0.2 g of sample + 20 mg of enzyme + 7 ml of PDHP/PHP buffer solution 0.3 M (pH 6 for α-amylase and pH 8 for trypsin); (b) with pepsin: 0.2 g of sample + 20 mg of pepsin + 7 ml of 1% (w/v) sodium chloride (pH 1). The mixtures were sonicated at 35 kHz and at 37 °C for 30 min, centrifuged (3000 rpm, 15 min), and the supernatant made up to 10 ml. For method validation the following reference materials were used: focus INAEA-140/TM (INAEA) and sargasso NIES-CRM-09 (NIES). Quantitative recoveries were only reached when using pepsin, whilst recoveries close to 80% were obtained for the use of α-amylase and trypsin
(a) [20]; (b) Plankton, cabbage, oyster tissue, and algae; (c) Protease XIV, 50% (w/w); (d) Cd and Pb	ET-AAS. Total Cd and Pb determination. The analyte was extracted using an UP with a 3-mm titanium microtip at 50% of amplitude. USAED procedure: 10 mg of sample + 1 ml of water + 5 mg of protease XIV + sonication during 5 min. For method validation the following reference materials were used: BCR-414 plankton, BCR-679 white cabbage, BCR-710 oyster tissue, IAEA-0392, algae. Recoveries between 50 and 100% for Cd and between 30 and 50% for Pb

Table 1 (*Continued*)

	Analytical methodology
(a) [21]; (b) Selenium-enriched plants: garlic (*A. Sativum*) and Indian mustard (*B. Juncea*); (d) Total Se, SeMet, and SeMetSeCys	HPLC–ICP-MS. Total Se determination and Se speciation. USAED procedure: 0.2 g of sample + 2.5 ml of water + 50 mg of protease XIV + sonication during 3 min. The mixture was centrifuged (2000 rpm, 20 min), filtered (0.45 μm) and then passed through a 3000 Da ultracentrifugation membrane in order to remove the excess of protease. Ion pairing reversed phase column C8 (250 mm × 2.0 mm; 5 μm). Mobile phase: 0.2% (v/v) of heptafluorobutyric acid, 10% (v/v) methanol (pH 2.5) at 0.2 ml/min. Size exclusion column Shodex Asahipack GS-220HQ (300 × 7.6 mm; >3000 Da). Mobile phase: 10 mM ammonium acetate buffer (pH 6.5) at 0.6 ml/min. For method validation an aquatic plant BCR-670 reference material was used. Recoveries: 103–127%
(a) [22]; (b) Antarctic krill; (c) Pronase E, 5% (w/w); (d) Total Se and SeMet	HPLC–ICP-MS. Total Se determination and Se speciation. The analytes were extracted using an UP with a 3-mm titanium microtip at 20 W of power, 20 kHz of frequency and 50% of amplitude. USAED procedure: 0.4 g of lyophilised krill + 20 mg of pronase E + 10 ml of 20 mM Tris–HCl (pH 7.5) + sonication during 15 min on ice. Reverse-phase column C18 Synergi Hydro (1 × 150 mm; 4 μm). Mobile phase: 0.1% trifluoroacetic acid/methanol (98:2, v/v) at 0.15 ml/min in the isocratic mode. Injection volume: 5 μl. Recovery of SeMet: 99%
(a) [23]; (b) Chicken muscle, liver, kidney and chicken feed; (c) Protease XIV, 20% (w/w); (d) Total Se and SeMet	HPLC–ICP-MS. Total Se determination and Se speciation. The analytes were extracted using an UP with a 3-mm titanium microtip at 20 W power and 10% amplitude. USAED procedure: chicken muscle (0.15 g), chicken liver (0.1 g), chicken kidney (0.05 g) + 20% (w/w) protease XIV + 3 ml Tris–HCl buffer (pH 7.5) + sonication during 2 min. After sonication the extracts were centrifuged (4000 rpm, 20 min). Cationic column Hamilton PRPX-200 (250 mm × 4.1 mm; 10 μm). Mobile phase: 4 mM pyridine formate in water, 3% methanol at 1 ml/min in the isocratic mode. Injection volume: 100 μl. For method validation mussel tissue CRM 278 was used as reference material. Recoveries: 93–102%. LOD = 2.4 μg/kg; LOQ = 8.1 μg/kg
(a) [29]; (b) Selenium-enriched lentil plants (*Lens esculenta*); (c) Protease XIV, 40% (w/w); (d) Total Se, Se(IV), Se(VI), SeMetO, SeMetSeCys, and SeMet	HPLC–ICP-MS. Total Se determination and Se speciation. The analyte was extracted using an UP with a 3-mm titanium microtip at 20 W power and 20 kHz frequency. USAED procedure: 25 mg of sample + 10 mg of protease XIV + 3 ml of water + sonication during 2 min. The mixture was centrifuged (7500 × g, 30 min) using a 10 kDa cut-off filter. Anion exchange column PRP-X100. Mobile phase: 10 mM citric acid solution in 2% (v/v) methanol (pH 5 adjusted with ammonium hydroxide) at 1 ml/min. Size exclusion/ion exchange column Shodex Asahipacks Gs-220HQ. Mobile phase: 25 mM ammonium acetate solution (pH 6.7) at 0.6 ml/min. Biosep-SEC-2000 protein separation column (300–1 kDa). Mobile phase: 25 mM Tris–HCl buffer (pH 6.8) at 1 ml/min. Injection volume: 100 and 200 μl). For method validation white clover CRM-402 was used as reference material

(a) Reference; (b) matrix; (c) enzyme type and enzyme–sample ratio; and (d) metal Species

(iii) The possibility of destruction of compounds of interest caused by cavitation depends on the sonication device, and it follows the same order than the sonication intensity as described above in (i): the higher the intensity the higher the risk of analyte transformation.

It is necessary to stress that recent advances in technology can help to overcome some of the common drawbacks addressed above for sample treatments using ultrasonication. As an example, sonication with ultrasonic probe can be nowadays done with the so-called multiple probes, allowing ultrasonication of at least four samples at the same time. However, those new ultrasonic devices are not very common in the analytical labs yet. A detailed review regarding new ultrasonic devices, their advantages and limitations, and their present and future potential applications for analytical chemistry, has been recently published and is highly recommended [6]. Table 2 contains a list of available ultrasonic devices recommended to speed elemental speciation using enzymes along with their main characteristics and suppliers. (Disclaimer: specific company, product, and equipment names are given to provide useful information. Their mention does not imply recommendation or endorsement by the authors).

3. Ultrasound and enzymes for elemental speciation

One of the most remarkable advances in the use of ultrasonic energy for sample treatment for analytical chemistry was reported in 2004, when Capelo et al. demonstrated that by jointing enzymes and ultrasonication provided by an ultrasonic probe, total selenium can be extracted from biological matrixes in times as short as 30 s, maintaining the Se-bounded species integrity. Previous time-consuming protocols for Se speciation used to need time as long as 12 h. The methodology proposed was fast and of easy implementation, saving time and money [3].

Although enzymes were previously reported in literature as a tool for chemical speciation, never before the enzymatic reaction kinetics had been accelerated by means of an ultrasonic probe [8] for this objective. Previous works done with enzymes for chemical speciation purposes used ultrasonic baths or heat-

Table 2

Characteristics of the main ultrasonic systems used for sample treatment for analytical chemistry

Variable	Probe	Bath	Sonoreactor
Sonication time	<5 min	>30 min	<5 min
Thermostat	No	Yes	No
Intensity of sonication for 1.5-ml vial (W)	15	0.01	0.5
Amplitude	Variable	Variable	Variable
Solid–liquid extraction yield	High	Low	Medium
Destruction of organics	High	Low	Medium
Sample throughput	Low	High	Medium
Accessories	High	Low	Medium
On-line applications	Yes	Yes	Yes

Suppliers: (1) http://www.bandelin.com; (2) http://www.hielscher.com; (3) http://www.bransonultrasonics.com; (4) http://www.equilabcanada.com; (5) http://www.misonix.com; (6) http://www.elmaultrasonic.com.
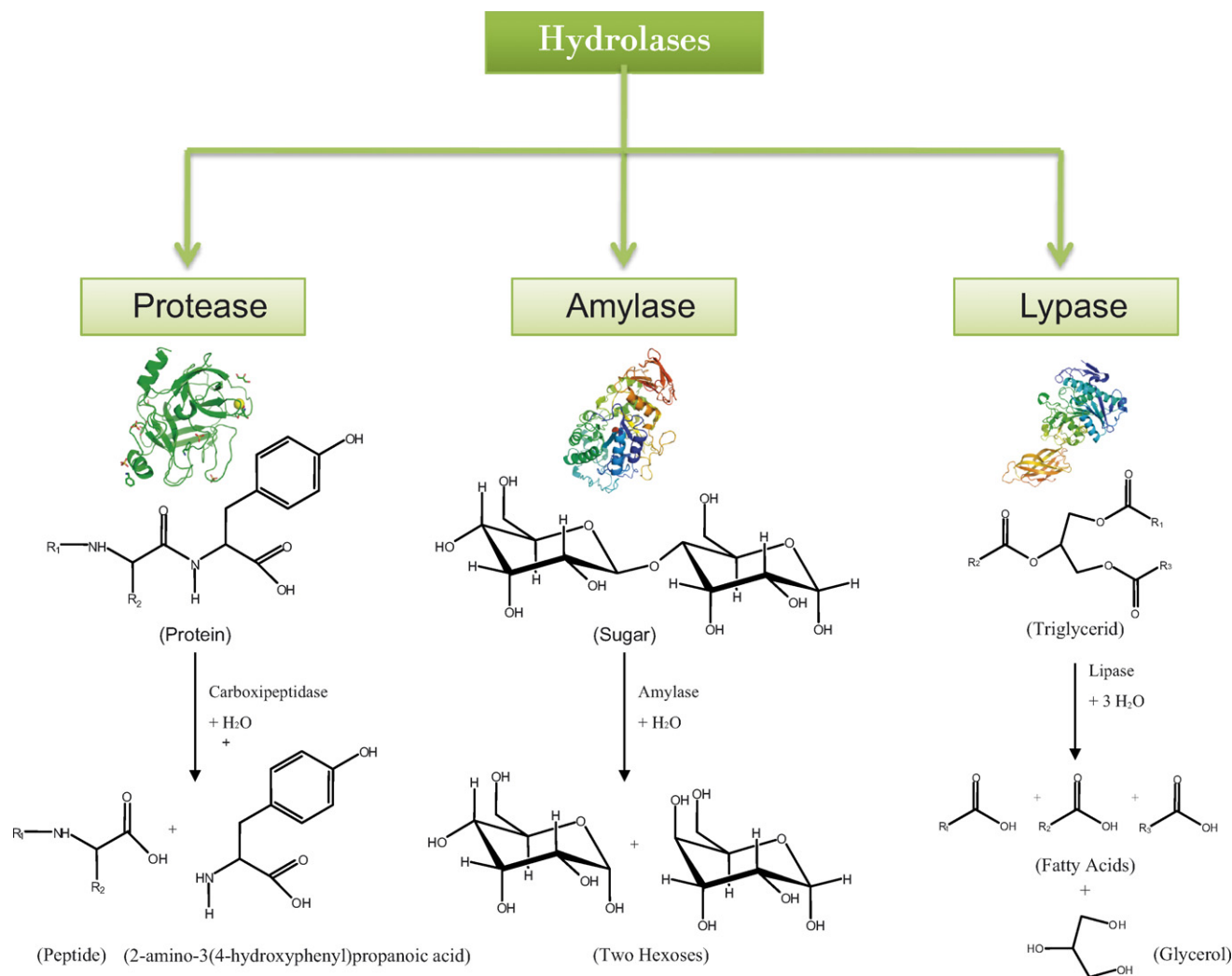
Fig. 1. Typical reactions of hydrolases.

ing baths at 37 °C for improving enzymatic reactions. Sample treatment times were comprised between 5 and 12 h [8].

The enzymes used for chemical speciation belong to the family of hydrolases [8]. Hydrolases act at specific bonds of the substrate, breaking molecules through catalyzing the introduction of water. Fig. 1 shows schematically how hydrolases work. In the following sections, detailed information is given to explain how to take advantage of USAED for elemental speciation purposes.

4. Does ultrasonication enhance enzymatic activity?

Studies regarding enhancement of enzymatic kinetics by ultrasonication have been reported in literature dedicated to this task. Results put forward a dependence of the enzymatic enhancement with the intensity of sonication rather than with frequency of sonication [12]. Apparently, cavitation promotes the increment in reaction rates rather than a change in the reaction constants. As an example, Talukder et al. reported an increment in the maximum reaction rate (V_{max}) and unalteration for the Michaelis constant (K_m) when the hydrolytic activity of lipase

was enhanced by ultrasonication [13]. It has been also stated that ultrasonication in short time enhances enzymatic activity whilst long time lead to the inactivation of the enzymes [13].

Concerning studies focused on elemental speciation, most works done to date highlight the efficiency of the extraction process when enzymes and ultrasonication are applied together in short time, generally lower than 4 min, as can be seen in Table 1. At this point, some recommendations must be given to avoid erroneous data interpretation. Thus, when studying the efficiency of USAED versus ultrasonication time, it is critical to stop the enzymatic activity after the ultrasonication process. It must be borne in mind that, although the ultrasonication had been stopped, the enzyme can still be active. This problem can be understood better by looking at data provided in Table 3. As can be seen, different sample treatments were done using protease XIV over mussel tissue for the extraction of total Se. Measurements of Se were done by electrothermal atomic absorption spectrometry (ET-AAS). The extraction experiments were done with and without lowering the pH with formic acid to stop the enzymatic activity after ultrasonic treatment. As can be seen, when the USAED was done by jointing the enzymes

Table 3
Effect of ultrasound and vortex agitation in the recovery of total Se from mussel tissue with protease XIV

Experiment number (lasting time until the first measurement was done by ET-AAS, min)	Without stopping the enzyme activity ($X \pm$ S.D., $n = 3$)[a]	With stopping the enzyme activity ($X \pm$ S.D., $n = 3$)[a]
1 (120)	100.6 ± 2.7	81.9 ± 5.0
2 (60)	48.9 ± 6.0	39.2 ± 2.6
3 (25)	17.3 ± 2.7	25.4 ± 2.0
4 (110)	25.3 ± 8.0	25.3 ± 8.5
5 (35)	34.6 ± 1.5	44.2 ± 11.1

Measurements of Se were done by ET-AAS with and without stopping enzyme activity with formic acid to a final concentration of 5% (v/v). (1) Mussel tissue and protease XIV in water. Sonication for 2 min. (2) Mussel tissue and protease XIV in water. Vortex mixing for 2 min. (3) Mussel tissue sonication for 2 min in water. Then protease XIV was added and mixed in a vortex for 2 min. (4) Vortex mixing of the mussel tissue in water for 2 min. Protease XIV was added and mixed in vortex for 2 min. (5) Vortex mixing of mussel tissue and protease XIV for 4 min.

[a] % of Se recovery.

and the ultrasound in one single step, experiment number 1, the extraction efficiency was ca. 18% higher than when the enzymatic activity was stopped immediately after the ultrasonic treatment ended. It must be taken into account that the Se measurements were done at least 30 min after the ultrasonic treatment was finished. That is, the enzyme had 30 min more of activity, degrading further the sample and thus, increasing the ratio of metal extracted. This finding is critical to obtain accurate results. Therefore, some studies reported in literature, regarding enzymatic elemental extractions accelerated by ultrasound versus time of sonication must be considered as inconclusive, since the enzymatic activity was not stopped after the ultrasonic process [14].

Table 3 also shows that when the mussel tissue was sonicated during 2 min before the addition of protease XIV, the Se extracted was only ca. 20–25% (experiment 3). In addition, the results obtained with vortex mixing (experiment 4) were similar to the ones got when the enzymes and ultrasonication were applied to the solution separately (experiment 3), showing that to obtain boosting of enzymatic activities for elemental extraction in minutes, ultrasonication and enzymes must be jointed.

Other remarkable conclusion is that, although some studies focusing on enzyme inactivation caused by ultrasonication have reported inactivation of protease XIV after 2 min of treatment [15], this inactivation seems to be linked to the substrate being studied rather to the enzyme itself. Thus, ultrasonic inactivation of enzyme protease XIV towards casein substrate was obtained in 2 min [15]. However, for mussel tissue, after 2-min sonication time, protease XIV was still active, extracting ca. 18% more of Se than when the enzyme was inactivated with formic acid after the 2 min ultrasonic treatment, as stated above (experiment 1 in Table 3).

5. Factors affecting USAED efficiency

5.1. Correlation between samples and enzymes

The first key to attain a good result using the USAED methodology deals with the correct enzyme choice. The family of hydrolytic enzymes comprises the following: lipases, amylases and proteases. Theoretically, each type of enzyme hydrolyzes a different kind of substrate. Lipases hydrolyze fats; amylases hydrolyze starch and glycogen, and proteases hydrolyze pro-

teins and peptides. Therefore, it can be understood that there is no enzyme for universal use. However, it must be stressed that even for the same family of enzymes, some differences in the extraction efficiency can be expected. Thus, three proteases were studied in conjunction with ultrasonication with probe for the extraction of Se from mussel tissue. Under the same conditions of sample treatment, the Se extractions were as follows: (i) 93 ± 7% for protease XIV; (ii) 70 ± 9% for subtilisin A and (iii) 28 ± 5% for trypsin [15].

Some authors have reported the utilization of cocktails of enzymes to improve the extraction of elements from plant or animal tissues. Thus, Sanz et al. have described As speciation in rice and hair using (α-amylase + protease type XIV) and (protease XIV + lipase), respectively [16,17]. Later, Mihuez et al. have validated the As speciation in rice using the same enzyme cocktail reported by Sanz et al. [18].

Regarding total metal extraction, Cd, As, Cu, Cr, Fe, Mn, Ni, Pb, and Zn were determined in Atlantic seaweed Dulse by inductively coupled plasma with optical emission spectroscopy (ICP-OES) with the extraction done in a medium containing trypsine, α-amylase and pepsine [19]. Table 1 shows a detailed description of the works done to date concerning USAED and metal extraction/speciation.

5.2. pH and temperature

The activity of most enzymes is pH and temperature dependent; therefore, these parameters must be always taken into account. Regarding pH, information available to date in literature suggests that enzymatic kinetics, for those enzymes having their optimum pH activities around 7, can be boosted with ultrasonication even if the extracting solution is not buffered. This finding, which was first reported in the pioneer work and related ones of Capelo et al. [3,15,20] and later by further authors [14,16–18,21,29], is very important since it facilitates chromatographic separations and it helps to avoid contaminations caused by buffer solutions. For some matrixes, however, buffering the medium has been shown critical to attain total elemental recovery, as such it was the case reported by Cabañero et al., regarding Se speciation in chicken samples [23]. For the latter matrix, the Se extraction was 28% higher when the extraction was done in buffered than in non-buffered media with protease XIV at

pH 7.5. Therefore, in order to assess the extraction efficiencies, to compare trials done in buffered and non-buffered media are recommended for new matrixes.

Some enzymes require low pH to work properly, as an example; pepsine was used at pH 1 to extract As, Cd, Cu, Cr, Fe, Mn, Ni, Pb, and Zn from Atlantic Seaweed Dulse [19].

Concerning temperature, equilibrium between the optimum one for an efficient enzyme activity and the optimum for a good cavitation to occur must be obtained. Although heating in excess should be avoided to obtain good ultrasonic performance, the best temperature for some enzymes is around 37 °C or even higher. Some experiences have shown that doing USAED under cooling conditions leads to lower recoveries than doing it at room temperature. Thus, to study the effect of temperature on Se recovery from mussel tissue, the USAED procedure was done under cooling conditions (e.g. ice bath) and at room temperature [15]. Interestingly, the recoveries were approximately ca. 20% lower when the procedure was performed under cooling conditions. As a general rule a continuous sonication time at room temperature for short time, 2–3 min, is recommended for USAED treatment.

5.3. Ratio substrate/enzyme

The substrate to enzyme ratio is one of the most important parameters to be optimized. This ratio needs to be low enough to guarantee total sample degradation maintaining the compromise of not being expensive. It must be borne in mind that enzymes are expensive reagents. Data regarding substrate/enzyme ratios is not consistent through the published literature. However, it seems that to obtain accurate results high ratios must be avoided. Thus, Cabañero et al. [23] have shown that doubling the amount of enzyme used, the Se recoveries from chicken muscle, liver and kidney were increased from 86% to 97%; 84% to 93% and 81% to 95%, respectively. Table 1 provides a rapid guide to the different ratios substrate/enzyme as a function of the matrix reported in literature to date. It is strongly recommended to the analyst to do a study of metal extraction as a function of the amount of enzyme used when USAED is applied for the first time in a new matrix with two main aims: (i) to establish the amount of enzyme that is necessary for an accurate total extraction, and (ii) to avoid the use of an excess of enzymes. This is due to the fact that, besides saving money, as the amount of enzyme increases for a constant amount of substrate, so does the amount of organic matter co-extracted to the solution as a result of the ultrasonication process. It is important to remind that high intensity focused ultrasound solubilizes organic matter from the matrixes studied. A high organic matter content in solution can negatively affect the signal of numerous analytical techniques. For example, when the amount of enzyme protease XIV was double, from 10 mg to 20 mg for a constant amount of 10 mg of mussel, the Se extracted was a 20% lower. Rather than a lack in extractability caused by the increment in the amount of enzyme used, the problem was related with the system of measurement employed, electrothermal atomization. This technique is highly sensible to the amounts of organic matter present in the sample introduced in the graphite tube [15].

5.4. Cleaning procedures

As it was explained in the previous paragraph, high in solution organic matter contents caused by ultrasonic-based sample treatments on samples such as biological tissues, is a drawback for analytical techniques such as cold vapor atomic absorption spectrometry (CV-AAS); hydride generation atomic absorption spectrometry (HG-AAS); electrothermal atomic absorption spectrometry (ET-AAS); or high performance liquid chromatography inductively coupled plasma mass spectrometry (HPLC–ICP-MS). To avoid this problem, three main strategies can be tried:

(i) Sedimentation.
(ii) Centrifugation.
(iii) Filtration.

Sample sedimentation occurs as soon as the ultrasonication ends. When the element is associated with the low-fraction mass, the sample can stand for hours, even 24 h, to be analysed, without problems related with the settling down of the element under study. However, this works only for some elements. In addition, for some analytical techniques, the amount of organic matter remaining in solution is still a problem. In fact, this approach is only recommended for ET-AAS, which can be used for samples with high organic matter content. ICP-OES and Flame-AAS (F-AAS) are analytical techniques which also allow low amounts of organic matter in solution without compromising the analytical measurement [19].

Centrifugation is a rapid approach that can expand USAED to some analytical techniques by lowering the amount of organic matter present in the solution [19], however, it has been demonstrated that for some elements, such as Pb, the concentration obtained after USAED is dependent on the speed of centrifugation [20].

The methodology most used for cleaning purposes after USAED treatment is filtration after centrifugation at low velocity, normally 5000 rpm. This is the cleaning procedure that we recommend. It must be stressed that when speciation is the main objective, HPLC will be used, so far, the sample must have the lower level of non desired compounds possible [3,18]. The latter task is only achieved with centrifugation plus filtration. The cut-off of the filters commonly used is 0.22 μm although some authors have used 0.45 μm filters after membrane ultracentrifugation [21]. Filters are made of nylon.

Since USAED is a relatively novel technique, it is recommended to obtain always information regarding the total content of the element(s) under study in the target sample by some classic analytical sample treatment such as sample dissolution by microwave pressurized acid digestion. This is because, after all, the cleaning procedure can retain the element(s) to a certain degree. Therefore, the sum of the different elemental species must be always compared with the total elemental content in order to assess the efficiency of the USAED treatment.

5.5. Enzyme ageing

Enzyme ageing is a parameter in USAED recently high-lighted in literature [15]. It was demonstrated that the extraction efficiency of protease XIV for the extraction of Se from mussel tissue felt down a 20% after 3 months [15]. It is recommended to purchase the enzymes in amounts as low as possible to avoid storage, and once the enzyme container is opened, the enzyme must be used as soon as possible. The use of enzymes stored for long time leads to inconsistent results [15].

5.6. Type of sonication device

Although it is not well understood the phenomenon by which ultrasonication accelerates the enzymatic kinetics, some authors have pointed out that there is an increased contact area between phases caused by cavitation allowing a reduction of mass-transfer limitations in the enzyme–substrate system. In addition, the reduction of the sample size caused by high intensity focused ultrasound (i.e. particle disruption), allows more substrate area to be in contact with the enzyme per second of sample treatment [7,22]. Furthermore, the enhancement reaction rates caused by ultrasonication have been attributed to the increase in collisions between enzyme and substrate [24].

As recently pointed out [6], the different sonication devices available in the market nowadays lead to different results when they are used for USAED applications. This phenomenon can be linked with the difference in the intensities of sonication, which leads to different ultrasonic cavitation efficiencies. Ultrasonic baths cannot boost the enzymatic kinetics in short time (2–4 min), so far are not recommended for USAED. Sonoreactor and ultrasonic probes are the devices of choice for a correct USAED application [6].

It was previously explained that different ultrasonic devices could cause different effects in the enzyme/substrate kinetics. To illustrate this problem Fig. 2 shows microscopic photos of mussel sample, 20 mg, plus protease XIV, 10 mg, after 2 min of sample treatment with (a) vortex agitation, (b) ultra-
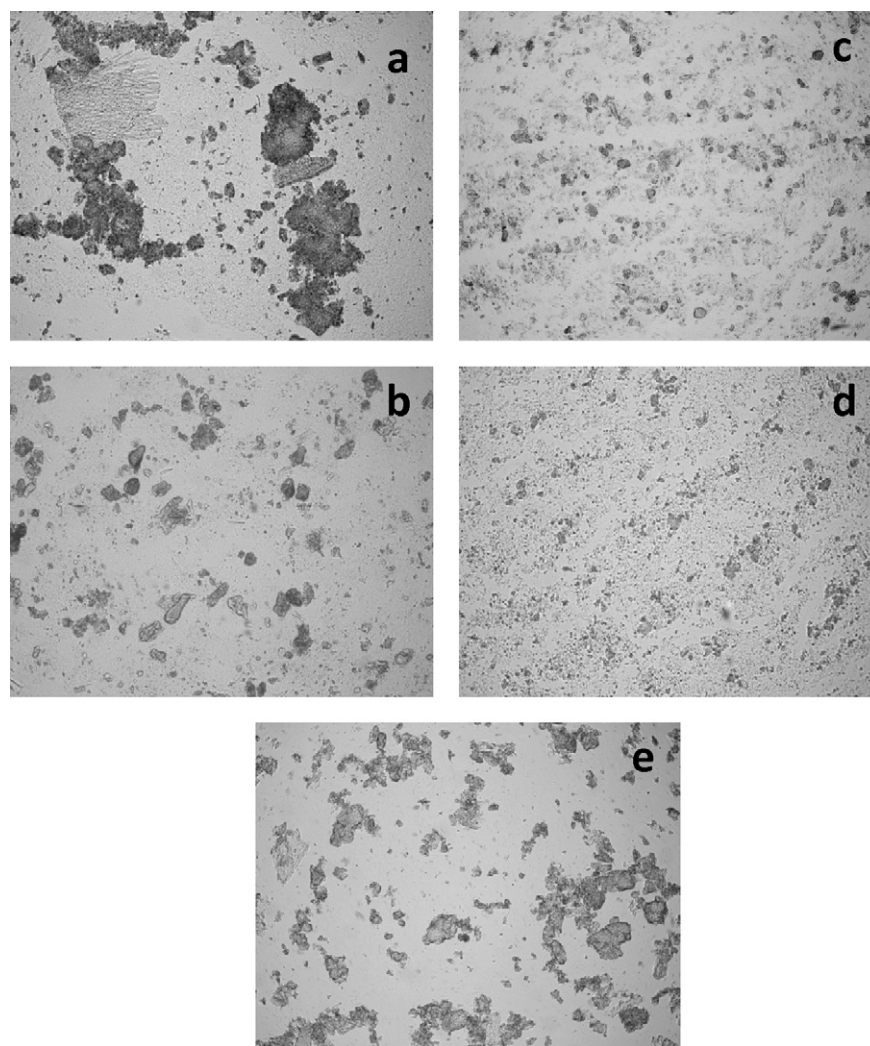

Fig. 2. Microscopy photo of 20 mg of mussel tissue plus 10 mg of enzyme after sample treatment with: (a) vortex mixing; (b) ultrasonic bath, 35 kHz, 100% sonication amplitude, 2-min sonication time; (c) sonoreactor, 35 kHz, 100% sonication amplitude, 2-min sonication time; (d) ultrasonic probe, 20 kHz, 50% sonication amplitude, 2-min sonication time; (e) ultrasonic probe, 20 kHz, 50% sonication amplitude, 2-min sonication time, no enzyme was added.

sonic bath, (c) sonoreactor, (d) ultrasonic probe and (e) with ultrasonic probe only (no enzyme added). The ratio protein/enzyme selected was 2 in order to show the sonication effects more clearly. As it can be seen, the sample size is reduced accordingly with the intensity of the sonicator device as follows: ultrasonic probe > sonoreactor > ultrasonic bath. In addition, the synergic effect of the combination between enzymes and ultrasound is clearly shown in Fig. 2. The reduction of the sample size produced by the ultrasonic probe is considerably lower when enzymes and ultrasounds are jointed, Fig. 2d.

5.7. Sonication time

As a general rule (Table 1) time lower than 4 min are enough to obtain total elemental extraction. However, Sanz et al. reported to require a sonication time of 10 min to extract As from human hair [17]. In addition, Siwek et al. needed sonication times of 15 min to extract Se from Antarctic krill with Pronase E [22]. Although Penal-Farfal et al. reported a time of sonication of 30 min [19], this can be considered normal as the ultrasonic device used was an ultrasonic bath, which usually takes longer time than the ultrasonic probe.

5.8. Sonication amplitude

As a trend (Table 2), for a common ultrasonic probe of 50 or 100 W of potency, amplitudes comprised between 25 and 50% are enough to attain reliable results, whilst for ultrasonic probes of high potency, such as 200 W, 250 W or even 600 W, amplitudes of 10–20% are recommended. For the latter case, higher amplitudes should not be used, since they are not necessary to boost the enzymatic kinetics and the sonication tip is kept away from damage caused by the excessive mechanical stress promoted by high sonication amplitudes. In addition, excess sample heating is avoided when low ultrasonic amplitudes are required to boost enzymatic reactions.

5.9. Type of container

USAED must be performed, as all solid–liquid extraction procedures using ultrasonication, in conical bottom-shaped vessels [6]. Whilst any type of vessel can be used to hold the sample, the shape of the vessel is often determined primarily by the volume to be processed. For small volumes the smallest diameter vessel that allows the probe to be inserted without risk of touching the sides of the vessel must be chosen. The minimum diameter raises the height of the liquid sample, thus the probe can be inserted more deeply into the process sample. In addition, the so-called dead zones, where no cavitation is actually done, are diminished. Furthermore, lowering the probe into the solution avoids aerosoling and foaming since both generally occur when the probe tip is not immersed deep enough into the solution. Aerosoling and foaming have the effect of "de-coupling" the probe from the process sample.

6. Jointing ultrasonication and enzymes for elemental speciation

Two different ways of jointing enzymes and ultrasound have been described to date in literature for elemental speciation. On one hand, one enzyme or one cocktail of enzymes are mixed with the substrate and then the mixture is sonicated in one single step for a time comprised between 2 and 4 min. On the other hand, for some type of samples a multi-step enzymatic digestion is the only way to obtain accurate results. Let us see how this works. For a botanical sample, the enzyme amylase is first used to break the wall of the cells, made mainly of starch and glycogen. Through this first step the protein content of the sample is liberated to the liquid media, then the speciation is completed in a second step, in which a different type of enzyme, a protease, is used to digest the proteins liberating in this way the elemental species associated with the proteins [18].

7. Elemental determination

7.1. Total elemental determination

It must be stressed that USAED is a methodology that extracts a high amount of organic matter from biological samples due to the properties of ultrasonication, as it was described in Section 5, therefore this methodology cannot be used with the majority of the analytical techniques of measurement without a previous cleaning procedure that diminishes the organic content of the extract. Nevertheless, the cleaning step may lead to diminish the metal content in the extract.

USAED has been used to date for the total elemental determination of the following elements: As, Se, Cd, Cu, Cr, Fe, Mn, Ni, Pb, and Zn, as shown in Table 1. The matrixes in which the USAED methodology has been successfully applied for metal extraction include material from botanical and animal origin, including both marine and terrestrial. Nevertheless, more data need to be reported by more research groups for further validation of the USAED methodology. Furthermore, the methodology needs to be expanded to more metals and more matrixes.

Regarding instrumental techniques used to determine total metal content, ET-AAS and ICP-OES or ICP-MS are the ones reported by now in conjunction with USAED.

As far as ET-AAS concerns, it is well known that the higher the organic matter content introduced into the graphite tube, the higher the possibilities to lose an element during the pyrolysis and or atomization stages. Additionally, chemical interferences in the atomization step can take place as a result of the incomplete degradation of organic matter during the pyrolysis step. The faster and easier way to avoid high organic matter contents after USAED, is by using centrifugation, always that the metal or metals under study do not settle down with centrifugation. This is the recommended cleaning procedure when working with ET-AAS and USAED. If centrifugation must be avoided, such as the case for Pb in oyster tissue [20], then it is recommended the use of robust matrix modifiers, such as palladium nitrate, in

conjunction with hydrogen peroxide. The latter reagent helps to obtain better organic matter degradation inside the graphite tube. In addition, the lifetime of the tube is enlarged twice [15].

Concerning ICP-OES, to the best of our knowledge, this technique for elemental determination has been reported in a sample treatment in which enzymatic degradation of mussel tissue was done with an ultrasonic bath. The elements were measured by ICP-OES (axial configuration). A lack in accuracy for some elements was reported when using scandium as internal standard, probably due to the organic content of the extracts, since the cleaning procedure was centrifugation at low speed, 3000 rpm. The problem was overcome through using the standard addition technique [6,19,25].

As far as ICP-MS concerns, this technique is the most widely used, since it allows rapid total elemental determination and in conjunction with HPLC, fast elemental speciation. Since this technique is very much influenced by the chemical and physical conditions of the sample, the cleaning procedures are more elaborated than for the above-mentioned techniques for metal determination. Generally, centrifugation during 10 min at 4000–5000 rpm followed by filtration through 0.22 μm nylon filters is used [17,18].

Finally, it must be remarked that USAED should not be used only for total elemental determination. For this purpose this technique is economically non-competitive with the Ultrasonic-assisted acid solid–liquid extraction methodology, which already has proven to be a powerful tool [26]. As it has been pointed out previously, USAED is a useful sample treatment for speciation purposes, but in addition, the total content can be also determined, helping in this way to close the element mass balance and avoiding extensive sample treatments, for instance one for speciation and the other for total content [15].

7.2. Elemental speciation

The main challenge for any sample treatment aiming elemental speciation is to extract all the metal content maintaining the chemical forms in which the analyte is present in the sample. To the latter requirements it must be added, when possible, the characteristics of analytical minimalism, as defined by Halls [27]:

(1) low cost,
(2) low sample requirements,
(3) low reagent consumption, and
(4) low waste production.

All the items highlighted above are met by USAED as described by Bermejo et al. [8]. Saving time and improving sample handling are two additional advantages of the sample treatment we are dealing with.

USAED has been used to date for the elemental speciation of As and Se. It is mandatory to spread this methodology to other metals of environmental and health concern such as Cr, Zn, Sn or Li. Furthermore, some controversial results have been reported in literature dealing with elemental speciation and ultra-sonication, and further data reported by the research community is needed urgently to get unambiguous interpretation of the robustness of USAED.

It must be remembered that to prove the suitability of the USAED method for speciation studies, it is necessary to ensure species integrity during the whole extraction/separation/detection process. Some authors have stressed that matching retention times of standards in a single chromatographic method should not be used as conclusive evidence of the presence of a certain species in the sample. Therefore, samples should be run through two different chromatographic columns with different retention mechanism [21].

The chemical forms of As that have been reported after USAED sample treatment in rice [14,16,18] and human hair [17] are As(III), As(V), arsenochlorine (AsC), arsenobetaine (AsB), dimethyl-arsonic acid (DMA), monomethyl arsonic acid (MMA), and As(III), As(V), DMA, and MMA respectively. It must be emphasized that no As-species inter-coversion was claimed to occur by the authors. However, it has been reported DMA and MMA degradation in human urine [28], after joint ultrasonication with a solution containing $KMnO_4/HCl$. Thus, it is expected in the near future dedicated studies focused on As-species stability under USAED conditions.

Regarding Se speciation, most data available in literature concerning USAED are dedicated to this metal, which has been studied in yeast [3], garlic [21], Antarctic krill [22], chicken [23], and lentil [29]. Selenomethionine (SeMet) was found in yeast; seleno methyl selenocysteine (SeMetSeCys) and SeMet were found in garlic samples; SeMet in chicken and Antarctic krill; and Se(IV), Se(VI), selenomethionine Se-oxide (SeMetO), SeMetSeCys, and SeMet were found in lentil. It has been stressed the stability of selenium species under the effects of an ultrasonic field provided by an ultrasonic probe, so neither species degradation nor species inter-conversion was described for this metal. However, Pedrero et al. using USAED, have pointed out that Se speciation corresponding to stem and roots from plants grown in presence of selenite and selenate Se(VI), and done by anion exchange chromatography, was not able to discriminate selenocystine ($SeCys_2$) from SeMetO, both co-eluting at a retention time of 2.1 min. It was mandatory to use a second chromatography column combining ion exchange and size exclusion mechanisms for unambiguous species identification [29].

8. A guide for USAED application

Fig. 3 shows a comprehensive scheme for USAED application.

The sample mass used should be comprised between 10 and 50 mg. Sample mass depends mainly on the limit of detection of the analytical technique, on the target analyte concentration in the sample and on sample homogeneity. Sample size should be as low as possible in order to increase the total area in contact with the enzyme. A comparison of the amount of metal extracted for buffered and non-buffered aqueous solutions should always be done. If buffered solutions are required to obtain accurate results,
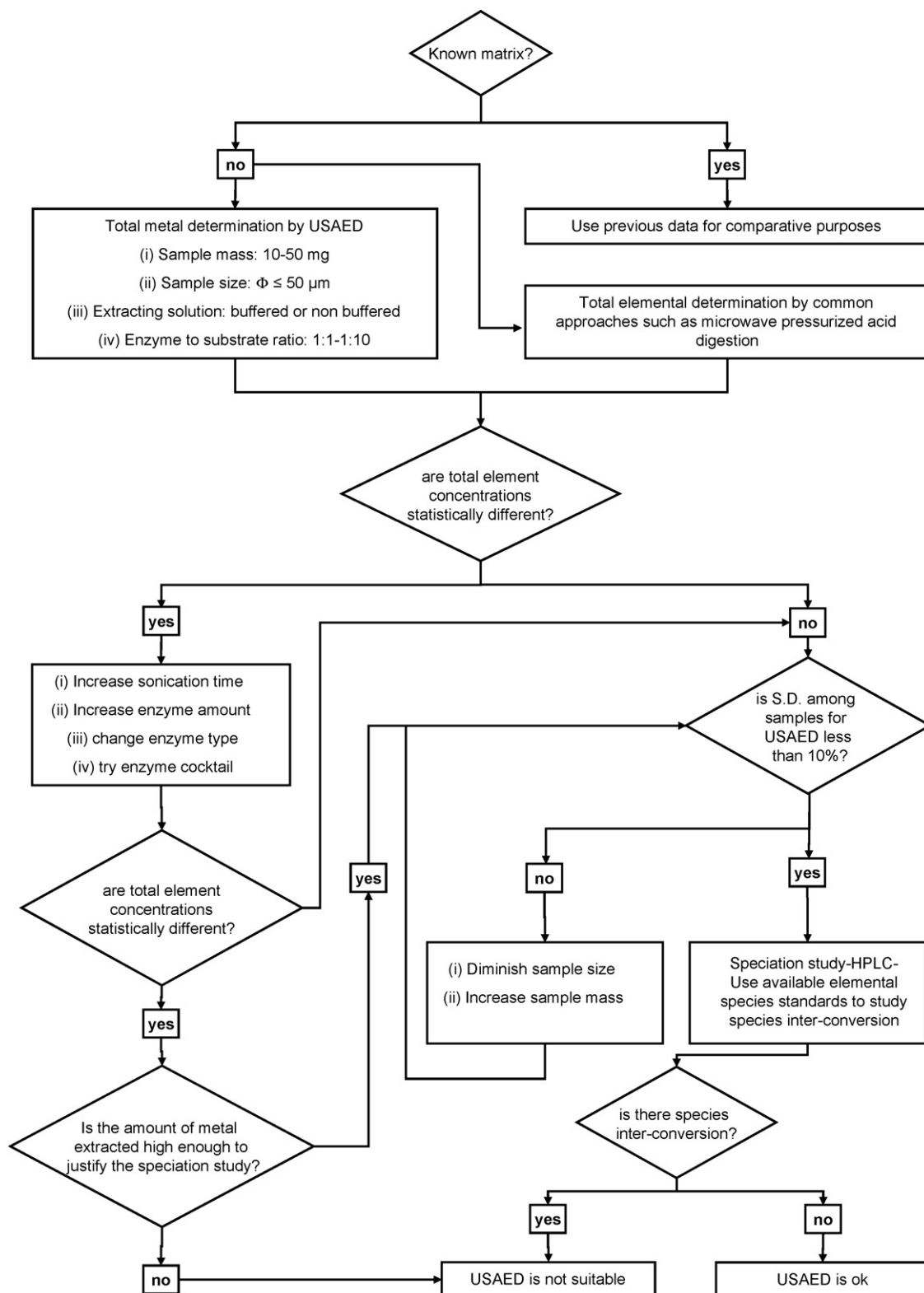
Fig. 3. Comprehensive guide for a rapid USAED application. See explanation on the text.

the type of buffer used must be chosen taking into account the subsequent speciation process through HPLC. The first attempt for total elemental extraction with the USAED methodology must be always compared with a classic method for total elemental extraction.

When the use of enzymes for elemental extraction gives low recoveries, some changes can be done to the sample treatment to try to increase the levels of metals extracted. Thus, the time of sonication or the amount of enzyme can be increased. Always plot a curve of percentage of metal extracted versus amount of

enzyme added for a fixed amount of sample. Other approaches include to choose another type of enzyme or to try an enzyme cocktail. If the metal extracted is still low, the analytical criteria of the chemist must be used to decide if the amount of metal extracted is high enough to justify further research regarding chemical speciation.

Once it has been proved that the extraction is accurate or more than 80% of the total expected metal, with a reasonable standard deviation, lower than 10%, the next step is to ensure that there is no species inter-conversion due to the sample treatment. To do this, the samples must be spiked with standards of the elemental species, such as DMA or MMA for As, and subjected to the sample treatment. Recoveries will indicate whether there are transformations or not.

Once demonstrated that: (i) more than 80% of the element is extracted and that (ii) there are no species inter-conversion, then the methodology can be applied for elemental speciation.

9. Future trends

Regarding future applications, the spreading of the USAED methodology to other metals is expected. Thus, metals of great environmental concern, such as Cr or Hg, or metals with remarkable effects in health care, such as Li or Zn, will be investigated to assess the applicability of the methodology we are dealing with their chemical speciation. Furthermore, USAED on-line applications for speciation purposes entailing analytical techniques other than HPLC–ICP-MS are expected. So far, HPLC-FI-CV-AAS or HPLC-FI-HG-AAS has also taken advantage of the possibilities of joint enzymes and ultrasound for chemical speciation. Vapor generation or hydride generation in conjunction with flow injection designs are approaches economically viable for laboratories that cannot support ICP-MS, which is an expensive analytical technique. It must be remarked that schemes entailing flow injection systems and atomic fluorescence spectrometry can provided detection limits low enough to be a competitive approach when comparing it with ICP-MS.

Another approach predicted is the linking between USAED and imprinting polymers. On this item a pioneer work reporting limited success regarding speciation of organotin compounds with imprinted polymers has been reported by Gallegos-Gallegos et al. [30]. However, this research area deserves more dedication from the analytical community to elucidate for which elements and for which conditions the linking between imprinted polymers and USAED is a valuable methodology.

10. Conclusions

Ultrasonic-assisted enzymatic digestion has proven to be a powerful methodology for chemical speciation. However, the methodology described in the present manuscript deserved more dedication from the analytical community in order to clarify its field of use; this is, for which metals and for which matrixes this method can be used.

The variables affecting the performance of USAED has been described and critically discussed. In addition, a scheme providing a practical guide for the application of USAED has been given in Fig. 3.

Finally, future applications of USAED, including on-line systems and different analytical techniques of measurement than the ones used to date with the methodology we are dealing with has been suggested and commented.

References

[1] C.W. Nogueira, G. Zeni, J.B.T. Rocha, Chem. Rev. 104 (2004) 6255.
[2] G. Ballihaut, C. Pécheyran, S. Mounicou, H. Preud-homme, R. Grimaud, R. Lobinski, Trac-Trends Anal. Chem. 26 (2007) 183.
[3] J.L. Capelo, P. Ximenez-Embun, Y. Madrid-Albarrán, C. Camara, Anal. Chem. 76 (2004) 233.
[4] T.J. Mason, Sonochemistry, Oxford University Press, USA, 1999.
[5] J.L. Capelo, A. Mota, Curr. Anal. Chem. 1 (2005) 193.
[6] H.M. Santos, J.L. Capelo, Talanta 73 (2007) 795.
[7] J.L. Capelo, C. Maduro, C. Vilhena, Ultrason. Sonochem. 12 (2005) 225.
[8] P. Bermejo, J.L. Capelo, A. Mota, Y. Madrid, C. Cámara, Trac-Trends Anal. Chem. 23 (2004) 654.
[9] F. Priego-Capote, M.D.L. de Castro, Trac-Trends Anal. Chem. 23 (2004) 644.
[10] F. Priego-Capote, M.D.L. de Castro, Trac-Trends Anal. Chem. 23 (2004) 829.
[11] F. Priego-Capote, M.D.L. de Castro, Talanta 72 (2007) 321.
[12] M. Sakakibara, D. Wang, R. Takahasshi, S. Mori, Enzyme Microb. Technol. 18 (1996) 444.
[13] M.M.R. Talukder, M.M. Zaman, Y. Hayashi, J.C. Wu, T. Kawanishi, Biocatal. Biotransform. 24 (2006) 189.
[14] E. Sanz, R. Muñoz-Olivas, C. Cámara, Anal. Chim. Acta 535 (2005) 227.
[15] G. Vale, S. Pereira, A. Mota, L. Fonseca, J.L. Capelo, Talanta 74 (2007) 198.
[16] E. Sanz, R. Muñoz-Olivas, C. Cámara, J. Chromatogr. A 1097 (2005) 1.
[17] E. Sanz, R. Muñoz-Olivas, C. Dietz, J. Sanz, C. Cámara, J. Anal. Atom. Spectrom. 22 (2007) 131.
[18] V.G. Mihuez, E. Tatár, I. Virág, C. Zang, Y. Jao, G. Záray, Food Chemistry 105 (2007) 1718.
[19] C. Pena-Farfal, A. Moreda-Piñero, A. Bermejo-Barrera, P. Bermejo-Barrera, H. Pinochet-Cancino, I. Gregori-Henríquez, Anal. Chim. Acta 548 (2005) 183.
[20] C. Maduro, G. Vale, S. Alves, M. Galesio, M.D.R. Gomes da Silva, C. Fernandez, S. Catarino, M.G. Rivas, A.M. Mota, J.L. Capelo, Talanta 68 (2006) 1156.
[21] M. Montes-Bayón, M.J.D. Molet, E.B. González, A. Sanz-Medel, Talanta 68 (2006) 1287.
[22] M. Siwek, A.B. Noubar, J. Bergmann, B. Niemeyer, B. Galunsky, Anal. Bioanal. Chem. 384 (2006) 244.
[23] A.I. Cabañero, Y. Madrid, C. Cámara, Anal. Bioanal. Chem. 381 (2005) 373.
[24] E. Bracey, R.A. Stenning, B.E. Brooker, Enzyme Microb. Technol. 22 (1998) 147.

[25] C. Pena-Farfal, A. Moreda-Pineiro, A. Bermejo-Barrera, P. Bermejo-Barrera, H. Pinochet-Cancino, I. de Gregori-Henriquez, Anal. Chem. 76 (2004) 3541.

[26] J.L. Capelo, P. Ximenez-Embun, Y. Madrid-Albarrán, C. Camara, Trac-Trends Anal. Chem. 23 (2004) 331.

[27] D.J. Halls, J. Anal. Atom. Spectrom. 10 (1995) 169.

[28] A. Correia, M. Galesio, H. Santos, R. Rial-Otero, C. Lodeiro, A. Oehmen, A.C.L. Conceic, J.L. Capelo, Talanta 72 (2007) 968.

[29] Z. Pedrero, J.R. Encinar, Y. Madrid, C. Cámara, J. Chromatogr. A 1139 (2007) 247.

[30] M. Gallegos-Gallegos, M. Liva, R. Munoz-Olivas, C. Cámara, J. Chromatogr. A 1114 (2006) 82.

Determination of tramadol and *O*-desmethyltramadol in human plasma by high-performance liquid chromatography with mass spectrometry detection

Laurian Vlase [a], Sorin E. Leucuta [a], Silvia Imre [b],*

[a] *Faculty of Pharmacy, University of Medicine and Pharmacy "Iuliu Hatieganu", Emil Isac 13, RO-400023, Cluj-Napoca, Romania*
[b] *Faculty of Pharmacy, University of Medicine and Pharmacy, Gheorghe Marinescu 38, RO-540139, Târgu-Mureş, Romania*

Abstract

A new simple, sensitive and selective liquid chromatography coupled with mass spectrometry (LC/MS) method for quantification of tramadol and its active metabolite *O*-desmethyltramadol in human plasma was validated. The tramadol and its metabolite were separated on a reversed phase column (Zorbax SB-C18, 100 mm × 3.0 mm I.D., 3.5 μm) under isocratic conditions using a mobile phase of a 10:90 (v/v) mixture of acetonitrile and 0.2% (v/v) trifluoroacetic acid in water. The flow rate was 1 ml/min at the column temperature 45 °C. In these chromatographic conditions, the retention times were 2.3 min for *O*-desmethyltramadol and 3.5 min for tramadol, respectively. The detection of both analytes was in SIM mode using an ion trap mass spectrometer with electrospray positive ionisation. The monitored ions were *m/z* 264 for tramadol and *m/z* 250 for its metabolite. The sample preparation was very simple and rapid and consisted in plasma protein precipitation from 0.2 ml plasma using 0.2 ml solution of perchloric acid 7%. Calibration curves were generated over the range of 2–300 ng/ml for both analytes with values for coefficient of correlation greater than 0.998 and by using a weighted ($1/y$) quadratic regression. The values of precision and accuracy for tramadol at quantification limit were less than 10.9% and 5.1, respectively, both for within- and between-run. For *O*-desmethyltramadol, precision and accuracy at quantification limit were 10.1% and −9.9% for within-run determinations and 6.7% and 10.4% for between-run determinations, respectively. The mean recovery for both analytes was 96%. Both tramadol and its metabolite demonstrated good short-term, long-term, post-preparative and freeze–thaw stability. This is the first reported method for analysis of tramadol and *O*-desmethyltramadol in human plasma that uses protein precipitation as sample processing procedure. The method is very simple and allows obtaining a very good recovery of both analytes. The validated LC/MS method has been applied to a pharmacokinetic study of 50 mg tramadol tablets on healthy volunteers.
© 2008 Elsevier B.V. All rights reserved.

Keywords: Tramadol; *O*-Desmethyltramadol; Pharmacokinetics; LC/MS

1. Introduction

Tramadol (TR), (1RS, 2RS)-2-[(dimethylamino)-methyl]-l-(3-methoxyphenyl)-cyclohexanol, is a synthetic analogue of codeine. It is a central analgesic with a low affinity for opioid receptors. Its selectivity for μ receptors has recently been demonstrated, and the metabolite of tramadol, *O*-desmethyltramadol (DM), shows a higher affinity for opioid receptors than the parent drug (Fig. 1). After oral administration, tramadol demonstrates 68% bioavailability, with peak serum concentrations reached within 2 h. The elimination kinetics can be described as 2-compartmental, with a half-life of 5.1 h for tramadol and 9 h for the DM after a single oral dose [1–3].

Several methods for determination of tramadol concentration in human plasma have been reported. HPLC-based methods with UV detection have been employed for determination of relatively higher concentrations of tramadol and its metabolites [4–9]. A great number of HPLC methods with fluorescence [10–19]

* Corresponding author at: Faculty of Pharmacy, University of Medicine and Pharmacy, Gh. Marinescu 38, RO-540139, Tg. Mures, Romania.
Tel.: +40 745 231516; fax: +40 265 210407.
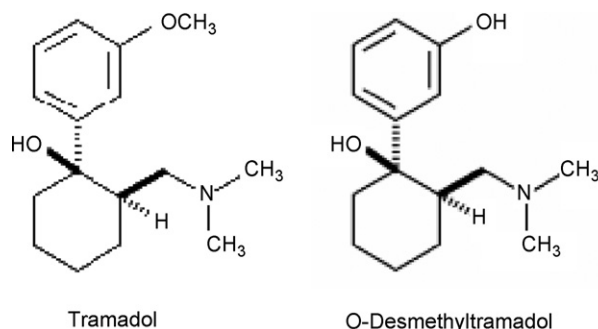*E-mail address:* silsta@yahoo.com (S. Imre).

Fig. 1. Chemical structures of tramadol and *O*-desmethyltramadol.

detection have been described, but usually liquid–liquid or solid-phase extraction is necessary in order to concentrate or sample clean-up. An electrochemical method has been also reported [20].

LC/MS has been widely accepted as the main tool in the identification, structure characterization and quantitative analysis of drugs and its metabolites owing to its superior sensitivity, specificity and efficiency. The analysis must be carried out in complex biological matrices and therefore efficient sample preparation and liquid chromatography are often required to achieve good specificity of the analysis. LC/MS grows in popularity, despite the equipment costs, and in the case of tramadol determination in plasma there are only a few published articles [21–25] and in all cases the sample clean-up and concentration by liquid–liquid or solid-phase extraction were applied.

In the present study, we attempted to develop a fast HPLC/MS/MS method able to quantify tramadol and *O*-desmethyltramadol in human plasma after oral administration of a single dose of 100 mg tramadol by applying a simple protein precipitation. Finally, the developed and validated method was used for bioequivalence investigation of two oral medicinal products containing 50 mg tramadol.

2. Materials and methods

2.1. Reagents

TR and DM were reference standards from Helcor, Romania (purity 99%) and Mikromol GmbH, Luckenwalde, Germany (purity 98.6%). Acetonitrile, methanol, trifluoracetic and perchloric acid were Merck products (Merck KgaA, Darmstadt, Germany). Distilled, deionised water was produced by a Direct Q-5 Millipore (Millipore SA, Molsheim, France) water system. The human blank plasma was supplied by the Local Bleeding Centre Cluj-Napoca, Romania.

2.2. Standard solutions

Two stock solutions of TR and DM, respectively, with concentration of 1 mg/ml were prepared by dissolving appropriate quantities of reference substances (weighed on an Analytical Plus balance from Ohaus, USA) in 10 ml methanol. Two working solutions of 300 ng/ml were then obtained for each substance by diluting specific volumes of stock solutions with plasma. Then

these were used to spike different volumes of plasma blank, providing finally 8 plasma standards with the concentrations ranged between 2 and 300 ng/ml, equally for TR and DM. Accuracy and precision of the method was verified using plasma standards with concentrations about 2, 6, 50 and 125 ng/ml TR and DM, respectively. Quality control samples (QC) about 6 (QCA), 50 (QCB) and 125 (QCC) ng/ml analytes were used during clinical samples analysis.

2.3. Chromatographic and mass spectrometry systems and conditions

The HPLC system was an 1100 series model (Agilent Technologies) consisted of a binary pump, an in-line degasser, an autosampler, a column thermostat, and an Ion Trap VL mass spectrometer detector (Brucker Daltonics GmbH, Germany). Chromatograms were processed using QuantAnalysis software.

The detection of both analytes was in the single ion monitoring mode (SIM) using an electrospray positive ionisation (ESI positive). The monitored ions were *m/z* 264 for TR and *m/z* 250 for its metabolite. Other detector parameters: dry temperature 350 °C, nebulizer 70 psi, dry gas-nitrogen at 12 l/min, capillary at 1200 V, helium as collision gas and electron multiplier voltage of 1595 V.

Chromatographic separation was performed at 45 °C on a Zorbax SB-C18 100 mm × 3 mm, 3.5 µm column (Agilent Technologies), protected by an in-line filter.

2.4. Mobile phase

The mobile phase consisted of a mixture of water containing 0.2% trifluoracetic acid and acetonitrile (90:10 (v/v)), each component being degassed, before elution, for 10 min in an Elma Transsonic 700/H (Singen, Germany) ultrasonic bath. The pump delivered the mobile phase at 1 ml/min.

2.5. Sample preparation

Standard and test plasma samples were prepared as follows in order to be chromatographically analyzed. In an Eppendorf tube, to 0.2 ml plasma, 0.2 ml perchloric acid 7% is added. The tube is vortex-mixed for 10 s and then centrifuged for 6 min at 4000 rpm. The supernatant is transferred in an autosampler vial and 2 µl was injected into the HPLC system.

2.6. Validation

As a first step of method validation [26–28], specificity was verified using six different plasma blanks obtained from healthy human volunteers who had not previously taken any medication.

The concentration of analytes was determined automatically by the instrument data system using the external standard method. Calibration was performed using singlicate calibration standards on five different occasions. The calibration curve model was determined by the least squares analysis. The applied calibration model was a quadratic one: $y = ax^2 + bx + c$, weight $1/y$, where y, peak area and x, concentration. Distribution of

the residuals (% difference of the back-calculated concentration from the nominal concentration) was investigated. The calibration model was accepted, if the residuals were within ± 20% at the lower limit of quantification (LLOQ) and within ± 15% at all other calibration levels and at least 2/3 of the standards met this criterion, including highest and lowest calibration levels.

The lower limit of quantification was established as the lowest calibration standard with an accuracy and precision less than 20%.

The within- and between-run precision (expressed as coefficient of variation, CV%) and accuracy (expressed as relative difference between obtained and theoretical concentration, Bias%) of the assay procedure were determined by analysis on the same day of five different samples at each of the lower (6 ng/ml), medium (50 ng/ml), and higher (125 ng/ml) levels of the considered concentration range and one different sample of each on five different occasions, respectively. The selected concentration values are relevant in practice taking in account to the fact that the reported maximum concentration levels of either TR or its metabolite are not greater that 200 ng/ml at usual oral doses (100 mg tramadol) [2].

The relative recoveries at each of the previously three levels of concentration and limit of quantification were measured by comparing the response of the treated plasma standards with the response of standards in solution with the same concentration of analytes as the prepared plasma sample.

The stability of the analytes in human plasma was investigated in four ways, in order to characterize each operation during the process of bioequivalence studies: room temperature stability (RTS), post-preparative stability (PPS) in the autosampler, freeze–thaw stability (FTS) and long-term stability (LTS) below −20 °C. For all stability studies, plasma standards at low (6.1 ng/ml TR and 6.3 ng/ml DM) and high concentrations (122.2 ng/ml TR and 125.7 ng/ml DM) were used. Four plasma standards at each of the two levels were prepared and let at room temperature 4 h before processing (RTS study). Other four pairs were prepared, immediately processed and stored in the HPLC

autosampler (22 °C) (PPS study). The samples were injected after 12 and 24 h, the expected longest storage times of the samples in autosampler before injection. For the freeze–thaw stability (FTS), aliquots at the same low and high concentrations were prepared. These samples were subjected to three cycles of freeze–thaw operations in three consecutive days. After the third cycle the samples were analyzed against calibration curve of the day. The mean concentration calculated for the samples subjected to the cycles and the nominal ones were compared. For long-term stability (LTS), in the first validation day, there were injected and analyzed four samples at each of low and high concentrations, and values were calculated against calibration curve of the day. Other two sets with the same plasma concentrations were stored in freezer below −20 °C and analyzed together with calibration samples after 3 weeks. The values were calculated against calibration curve of the day and the mean values for the stored samples and nominal concentrations were compared. The requirement for stable analytes was that the difference between mean concentrations of the tested samples in various conditions and nominal concentrations has to be in ± 15% range.

The ability to dilute samples with concentrations above the upper limit of quantification was also investigated. Plasma standards ($n = 5$) with 407.5 ng/ml TR and 523.9 ng/ml DM were 10 times diluted with plasma then processed and analyzed, five samples in the same run and one sample on five different occasions. The mean found concentration was compared with the nominal value. The accuracy and precision had to be within ± 15% range.

2.7. Clinical application and in-study validation

The validated method was applied in a bioequivalence study of two dosage forms—capsules containing 50 mg tramadol. The collecting times were 0, 0.5, 1, 1.5, 2, 2.5, 3, 4, 6, 8, 10, 12 and 24 h after oral administration of 100 mg tramadol. The accuracy and precision of the validated method was monitored to ensure that it continued to perform satisfactorily during analysis of volunteer samples. To achieve this objective, a number of
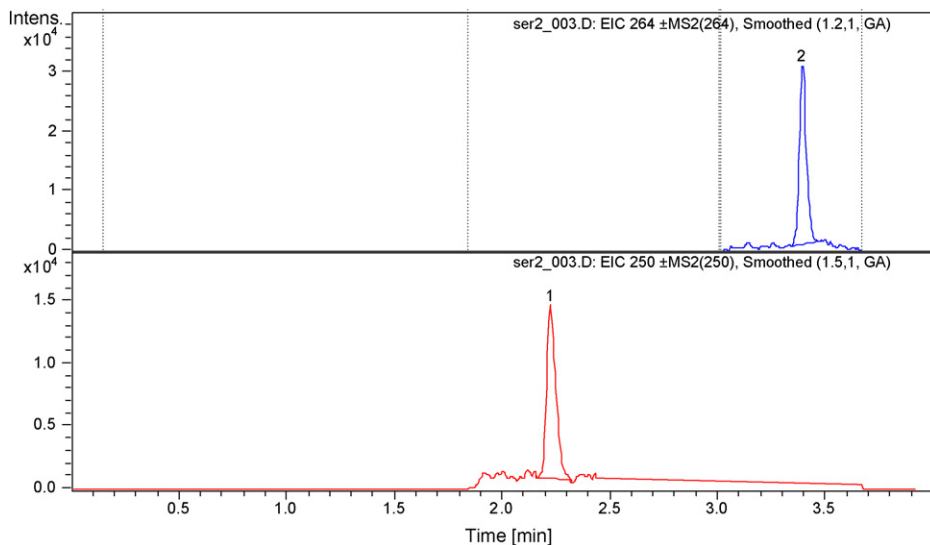

Fig. 2. Chromatograms of the LLOQ plasma standard with 2.2 ng/ml *O*-desmethyltramadol (1) and 2.1 ng/ml tramadol (2).

Table 1
Within-run precision, accuracy and recovery for tramadol and *O*-desmethyltramadol ($n = 5$)

$c_{nominal}$ (ng/ml)		Mean c_{found} (ng/ml($\pm$S.D.)), recovery % ($\pm$S.D.)		CV (%)		Bias (%)	
TR	DM	TR	DM	TR	DM	TR	DM
2.14	2.20	2.25 (0.23) 100.2 (9.0)	1.98 (0.20) 87.4 (7.3)	10.2	10.1	5.1	−9.9
6.11	6.29	6.32 (0.56) 105.0 (9.0)	6.01 (0.78) 88.7 (10.7)	8.9	12.9	3.3	−4.3
48.90	50.29	53.84 (2.25) 101.1 (4.2)	48.96 (2.38) 99.1 (4.6)	4.2	4.9	10.1	−2.6
122.26	125.74	127.96 (8.62) 104.8 (6.9)	123.88 (3.58) 92.9 (2.4)	6.7	2.9	4.7	−1.5

QC samples prepared in duplicate at three concentration levels were analyzed in each assay run and the results compared with the corresponding calibration curve. At least 67% (four out of six) of the QC samples should be within 15% of their respective nominal values; 33% of the QC samples (not all replicates at the same concentration) can be outside $\pm$ 15% of the nominal value.

3. Results and discussions

No significant interference at the retention times of TR (3.5 min) and DM (2.3 min) (Fig. 2) was observed in different plasma blank samples chromatograms due to the specificity of selected signals.

During method development a possible selectivity problem was tested such as interference from *N*-desmethyl metabolite, which has the same molecular mass and the same *m/z* value in positive ESI ionisation as *O*-desmethyl metabolite. The problem refers to the direct interference or interference due to "cross-talk" and in source-CID (collision-induced dissociation) of glucuronide derivatives of *O*-, *N*-desmethyl metabolite. In absence of the corresponding standard of *N*-desmethyl metabolite and using real-life plasma samples, the tests consisted in SIM monitoring of their *m/z* values. A week signal for *m/z* 250 was observed at RT of 1.4 min and it was assumed that it corresponds to *N*-desmethyl metabolite (as time signal for *O*-desmethyl metabolite appears at 2.3 min). However, for sample analysis, for maintaining ion source as clean as possible, the waste segment was set-up until 1.8 min, so the trace for *N*-desmethyl metabolite was not recorded.

The analytes carryover was verified using a blank injection made right after an injection of the most elevated level of concentration from calibration curve. No interference at retention time of analytes due to carryover was observed.

The ion suppression was investigated by comparing the peak areas of processed plasma samples containing analytes (QCA and QCC levels) with peak areas of standard solutions with the same concentration, but supernatant from processed blank

plasma was used as solvent. The test of ion suppression was done on each validation day. The mean ion suppression for tramadol was −2.1% and 3.23% for QCA and QCC, respectively. For *O*-desmethyltramadol, the ion suppression was −8.6% and −5.2% for QCA and QCC, respectively. As it can be seen, tramadol determination does not seem to be influenced by ion suppression and a slightly matrix effect can be observed on *O*-desmethyltramadol, more visible at lower levels. However, the slightly ion suppression observed on tramadol metabolite is not significant as it does not affect validation parameters like precision and accuracy.

Regarding ion suppression due to build-up of late eluting compounds (usually seen when organic modifier is in low concentration), no effect was observed after analysis of 80 plasma samples (a run from two subjects, two periods per subject, including calibration curve and QC samples). However, after each run of 80 samples, the analytical column was washed for 10 min with 100% acetonitrile.

The applied calibration curve model proved to be accurate over the concentration range 2.1–305.6 ng/ml for TR and 2.2–314.3 ng/ml for DM, with a correlation coefficient greater than 0.998, for both analytes. The mean calibration curves, $y = a(\pm S.D.)x^2 + b(\pm S.D.)x + c(\pm S.D.)$ with S.D. standard deviation, were: for TR $y = -5.489(\pm 4.121)x^2 + 17144 (\pm 668)x + 1862(\pm 5956)$, for DM $y = -4.6(\pm 1.96)x^2 + 8870(\pm 556) x + 4121(\pm 2547)$, $N = 8$ calibration points, $n = 5$ determinations for each calibration point. The residuals had no tendency of variation with concentration and were between $\pm$ 12% values.

The method had within- and between-run accuracy and precision (Tables 1 and 2), in agreement to international regulations regarding bioanalytical methods validation [26–28]. The lower limit of quantification was established at 2.1 ng/ml TR and 2.2 ng/ml for DM, respectively, with accuracy and precision less than 20% (Tables 1 and 2).

The recovery was consistent and reproducible, either for TR and DM (Table 1).

Table 2
Between-run precision and accuracy for tramadol and *O*-desmethyltramadol ($n = 5$)

$c_{nominal}$ (ng/ml)		Mean c_{found} (ng/ml ($\pm$S.D.))		CV (%)		Bias (%)	
TR	DM	TR	DM	TR	DM	TR	DM
2.14	2.20	2.21 (0.24)	2.43 (0.16)	10.9	6.6	3.4	10.5
6.11	6.29	6.11 (0.43)	5.87 (0.60)	7.0	10.3	0.0	−6.7
48.90	50.29	52.12 (2.56)	50.44 (2.02)	4.9	4.0	6.6	0.3
122.26	125.74	138.38 (14.41)	125.88 (12.52)	10.4	9.9	13.2	0.1

Table 3
Results of the stability studies ($n = 4$)

$c_{nominal}$ (ng/ml)	RTS		PPS		FTS		LTS	
	6.1/6.3[a]	122.2/125.7[a]	6.1/6.3[a]	122.2/125.7[a]	6.1/6.3[a]	122.2/125.7[a]	6.1/6.3[a]	122.2/125.7[a]
Bias%, TR	0.9	4.8	−4.1	−2.0	−2.8	7.0	−4.2	7.1
Bias%, DM	3.5	1.7	−4.3	−2.1	7.9	2.4	−3.4	−2.8

RTS–room temperature stability (22 °C, 4 h), PPS–post-preparative stability (22 °C, 24 h), FTS–freeze–thaw stability (3 freeze–thaw cycles), LTS–long-term stability (−20 °C, 3 weeks).

[a] Concentration of TR/Concentration of DM.
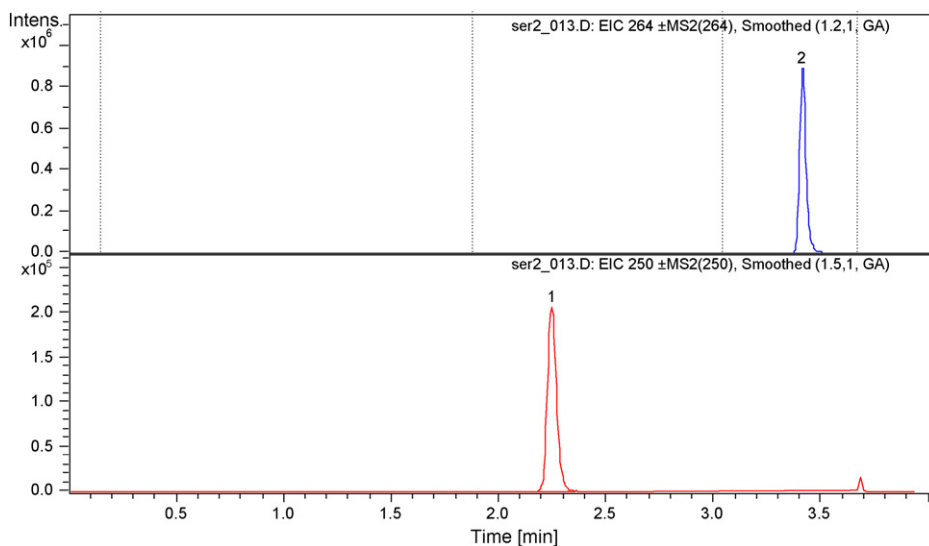
Fig. 3. The plasma sample chromatograms obtained from a healthy volunteer at 1.5 h after oral administration of 100 mg tramadol. Concentrations are 76.9 ng/ml *O*-desmethyltramadol (1) and 124.6 ng/ml tramadol (2).

The analytes proved their stability under various conditions (Table 3), the Bias% of found concentration being less than 15%, the maximum accepted value for method's accuracy.

The sample dilution could be made with accuracy within ± 9.4% range and precision less than 9.4%, both for within- and between-assay.

The validated method was verified during analysis of clinical samples from a bioequivalence study of two medicines

Fig. 4. Concentration profiles of tramadol (■) and *O*-desmethyltramadol (●) after oral administration of 100 mg tramadol.

containing 50 mg tramadol. The method continued to perform in terms of accuracy, in each analytical run, not more than two out of six QC samples being outside of ± 15% nominal value, but not all two at the same concentration. Figs. 3 and 4 show typical chromatograms of the plasma sample from a volunteer and concentration profiles of TR and DM obtained after oral administration of 100 mg tramadol, respectively.

In comparison with previously published HPLC methods, the sensitivity of the proposed method (LLOQ of 2 ng/ml) is not better as those in which liquid–liquid or solid-phase extraction was applied. But the main advantage, except the short run-time, is the sample preparation by protein precipitation and besides its simplicity, that sample treatment allows obtaining a very good recovery of both analytes.

4. Conclusions

The proposed method provides accuracy and precision for quantitative determination of tramadol and *O*-desmethyltramadol in human plasma after oral administration of 100 mg tramadol. The simple sample preparation by protein precipitation and selected signals for monitoring allowed a specific and efficient analysis of a large number of plasma samples, making the method more productive and thus more cost effective. As far as we are aware this is the first chromatographic
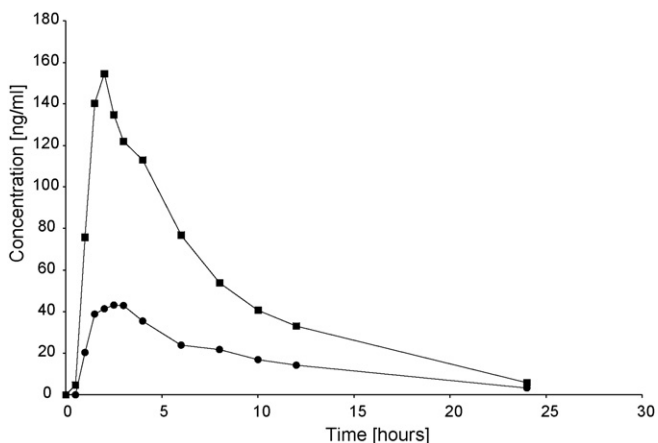
method for tramadol and *O*-desmethyltramadol quantification in human plasma after protein precipitation.

References

[1] R.B. Raffa, E. Friderichs, W. Reimann, R.P. Shank, E.E. Codd, J.L. Vaught, J. Pharmacol. Exp. Ther. 260 (1992) 275.
[2] K.S. Lewis, N.H. Han, Am. J. Health Syst. Pharm. 54 (1997) 643.
[3] W. Lintz, H. Barth, R. Becker, E. Frankus, E. Schmidt-Böthelt, Arzneimittelforschung 48 (1998) 436.
[4] A. Kucuk, Y. Kadioglu, F. Celebi, J. Chromatogr. B. Analyt. Technol. Biomed. Life Sci. 816 (2005) 203.
[5] L. Qu, S. Feng, Y. Wu, Y. Wu, Sichuan Da Xue Xue Bao Yi Xue Ban 34 (2003) 574.
[6] S.H. Gan, R. Ismail, W.A. Wan Adnan, Z. Wan, J. Chromatogr. B. Analyt. Technol. Biomed. Life. Sci. 772 (2002) 123.
[7] S.H. Gan, R. Ismail, J. Chromatogr. B. Biomed. Sci. Appl. 759 (2001) 325.
[8] G.C. Yeh, M.T. Sheu, C.L. Yen, Y.W. Wang, C.H. Liu, H.O. Ho, J. Chromatogr. B. Biomed. Sci. Appl. 723 (1999) 247.
[9] A. Ceccato, P. Chiap, P. Hubert, J. Crommen, J. Chromatogr. B 698 (1997) 161.
[10] R. Mehvar, K. Elliott, R. Parasrampuria, O. Eradiri, J. Chromatogr. B 852 (2007) 152.
[11] M.R. Rouini, Y.H. Ardakani, F. Soltani, H.Y. Aboul-Enein, A. Foroumadi, J. Chromatogr. B. Analyt. Technol. Biomed. Life Sci. 830 (2006) 207.
[12] Y. Gu, J.P. Fawcett, J. Chromatogr. B. Analyt. Technol. Biomed. Life Sci. 821 (2005) 240.
[13] M.A. Campanero, E. Garcia-Quetglas, B. Sadaba, J.R. Azanza, J. Chromatogr. A. 1031 (2004) 219.
[14] R.S. Pedersen, K. Brosen, E. Nielsen, Chromatographia 57 (2003) 279.
[15] M. Nobilis, J. Kopecky, J. Kvetina, J. Chladek, Z. Svoboda, V. Vorisek, F. Perlik, M. Pour, J. Kunes, J. Chromatogr. A. 949 (2002) 11.
[16] S. Dyderski, D. Szkutnik, M. Zgrabczynska, L. Drobnik, Acta Pol. Pharm. 58 (2001) 345.
[17] M.A. Campanero, B. Calahorra, M. Valle, I.F. Troconiz, J. Honorato, Chirality 11 (1999) 272.
[18] M.A. Campanero, B. Calahorra, E. Garcia-Quetglas, M. Escolar, J. Honorato, Chromatographia 48 (1998) 555.
[19] M. Nobilis, J. Pastera, P. Anzenbacher, D. Svoboda, J. Kopecky, F. Perlik, J. Chromatogr. B. Biomed. Appl. 681 (1996) 177.
[20] M. Valle, J.M. Pavon, R. Calvo, M.A. Campanero, I.F. Troconiz, J. Chromatogr. B. Biomed. Sci. Appl. 724 (1999) 83.
[21] F. Musshoff, J. Trafkowski, U. Kuepper, B. Madea, J. Mass. Spectrom. 41 (2006) 633.
[22] L.M. Zhao, X.Y. Chen, J.J. Cui, M. Sunita, D.F. Zhong, Yao Xue Xue Bao 39 (2004) 458.
[23] H. Malonne, B. Sonet, B. Streel, S. Lebrun, S. De Niet, A. Sereno, F. Vanderbist, Br. J. Clin. Pharmacol. 57 (2004) 270.
[24] A. Ceccato, F. Vanderbist, J.Y. Pabst, B. Streel, J. Chromatogr. B. Biomed Sci. Appl. 748 (2000) 65.
[25] Y.H. Ardakani, M.R. Rouini, J. Pharm. Biomed. Anal. 44 (2007) 1168.
[26] The European Agency for the Evaluation of Medicinal Products, Note for Guidance on the Investigation of Bioavailability and Bioequivalence, CPMP/EWP/QWP/1401/98, London, UK, July 2001, http://www.emea.europa.eu/pdfs/human/qwp/140198enfin.pdf.
[27] U.S. Department of Health and Human Services, Food and Drug Administration, Center for Drug Evaluation and Research. Guidance for Industry. Bioavailability and Bioequivalence studies for orally administered drug products—general considerations, Rockville, USA, March 2003, http://www.fda.gov/cder/guidance/5356fnl.pdf.
[28] U.S. Department of Health and Human Services, Food and Drug Administration, Guidance for Industry–Bioanalytical Method Validation, May 2001, http://www.fda.gov/cder/guidance/4252fnl.pdf.

Synthesis of a novel fluorescent probe based on acridine skeleton used for sensitive determination of DNA

Menghui Wu, Wenqiang Wu, Xi Gao, Xucong Lin, Zenghong Xie *

Department of Chemistry, Fuzhou University, Fuzhou 350002, China

Abstract

In this study, a novel fluorescent probe of acridine derivative *N*-((*N*-(2-dimethylamino)ethyl)acridine-4-carboxamide)-α-alanine (*N*-(ACR-4-CA)-α-ALA) was synthesized. The structure of the new compound was characterized by ^{1}H NMR, MS, elemental analysis, fluorescent and ultraviolet spectra. It was found that DNA had the ability to quench the fluorescence of *N*-(ACR-4-CA)-α-ALA, and the quenched intensity of fluorescence was proportional to the concentration of DNA. A method for DNA determination based on the quenching fluorescence ($\lambda_{ex} = 260$ nm, $\lambda_{em} = 451$ nm) of *N*-(ACR-4-CA)-α-ALA was established. Under optimal conditions, the linear range is 0.05–2.0 μg mL^{-1} for both fish semen (fsDNA) and calf thymus DNA (ctDNA). The corresponding determination limits are 9.1 ng mL^{-1} for fsDNA and 8.7 ng mL^{-1} for ctDNA, respectively. The results suggested that the interaction mode between *N*-(ACR-4-CA)-α-ALA and DNA was intercalative binding. The intrinsic binding constant was determined and the result showed a large binding constant of *N*-(ACR-4-CA)-α-ALA with DNA.
© 2008 Elsevier B.V. All rights reserved.

Keywords: Acridine derivative; Synthesis; Fluorescent quenching; DNA determination

1. Introduction

Nucleic acids play important roles in life processes. The quantitative determination of nucleic acid is very important in both clinical and laboratory tests. Generally, the fluorescence quantum yield of native DNA ($\varphi_f = 4 \times 10^{-5}$) [1] is so small for its structure studies and quantification that an extrinsic probe must be employed [2]. The probes for DNA include organic dyes [3–6], metal complexes [7,8] and organic nanoparticles [9], etc. However, these methods have some limitations for analytical practice, such as very expensive, instable, insensitive, not rapid enough, etc. Therefore, it is considered important to develop a sensitive, stable and rapid method for determination of DNA using an inexpensive probe.

Acridine and its derivatives are planar tricyclic aromatic molecules which possess the ability to intercalate tightly but reversibly to DNA helical structure [10]. These compounds are one of the oldest and most successful classes of bioactive agents and widely utilized as antimalarial [11], antiprotozoal

[12], antibacterial [13] and anticancer drugs [14,15]. For their special properties of high fluorescence quantum yield and large binding constants to DNA [16], acridine dyes are well known in the field of development of probes for nucleic acid structure and conformational determination [17–19].

For the high binding affinities to nucleic acid, acridine-4-carboxamide derivatives are a kind of anticancer drugs that has been studied for a decade since first introduced by Denny and co-workers in 1984 [20]. Recently, 9-substitute of acridines were synthesized and the interaction with DNA was studied [21,22]. However, to our knowledge, both 9-substitute of acridines and acridine-4-carboxamide derivatives had been paid little attention to be used as a fluorescent probe and analytical application.

In this study, the 9-substitute of acridine-4-carboxamide derivative is designed, synthesized and first used as a fluorescent probe to determine DNA and its structure is shown in Scheme 1(I). We have known that the acridine moieties are held in place through van der Waals forces supplemented by strong ionic bonds to the phosphate ions of the DNA backbone [23]. Therefore, the introduction of cationic side chain *N,N*-dimethylaminoethyl would enhance the intercalating ability of acridine derivatives [20] and can bind to DNA lying in the major groove, forming hydrogen-bonding interactions with the gua-

---
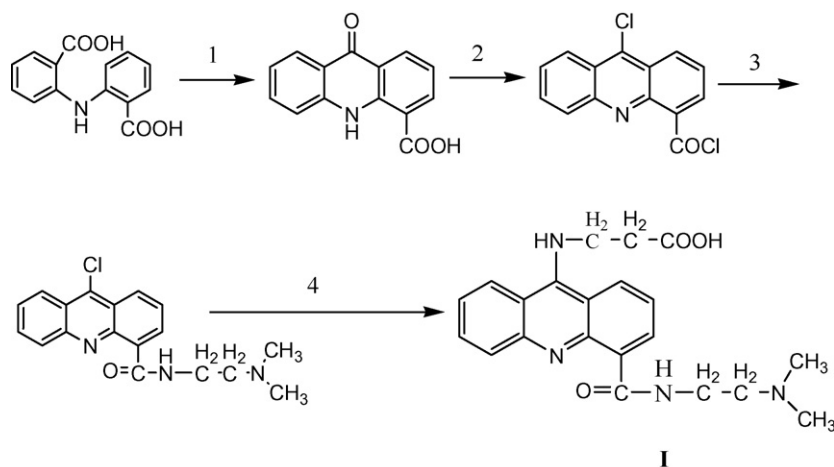
Scheme 1. The synthesis of *N*-(9-(*N*-(2-dimethylamino)ethyl) acridine-4-carboxamide)-α-alanine: (1) polyphosphoric acid, 120 °C, 2 h, 95% yield. (2) SOCl$_2$, DMF (two drops), reflux, 30 min, 91% yield. (3) *N,N*-Dimethylethylenediamine, CH$_2$Cl$_2$, 0 °C, 2 h, 63% yield. (4) Phenol, 100 °C, 1 h, then α-alanine for another 2 h, 64% yield.

nine [24]. Furthermore, we introduce α-alanine on C-9 position of the tricyclic rings which can form H-bond with adenine and guanine [25] to elevate binding affinity to DNA. Previous studies [24] also suggested that the linker of six carbons on C-9 position of the tricyclic rings was the best to bind to the minor groove of DNA for bisintercalating threading diacridines systems. Therefore, α-alanine, which possesses three carbons and a carboxyl group, was chosen to attach the C-9 position of the tricyclic rings to improve binding affinity to DNA and water solubility of the compound. The structure of the new compound was characterized by MS, ^{1}H NMR and elemental analysis. The spectral properties of ultraviolet and fluorescence were studied in detail, and a simple, rapid, sensitive and stable of DNA determination system is established based on the fluorescence quenching of *N*-((*N*-(2-dimethylamino)ethyl)acridine-4-carboxamide)-α-alanine (*N*-(ACR-4-CA)-α-ALA).

2. Experimental

2.1. Apparatus

Mass spectra were recorded with a 70-SE LC–MS; element analysis was performed with a PerkinElmer 240 instrument; ^{1}H NMR spectra were performed with Varian UNITY-500 instrument; all fluorescence measurements were made with a Cary eclipse spectrofluorimeter which was equipped with a 1-cm quartz cell. The absorption spectra were performed on a Shimadzu UV-1700 spectrophotometer by using a 1-cm quartz cell. All pH measurements were made with pHS-3C pH meter (Shanghai, China).

2.2. Reagents

Commercially available fish semen DNA (fsDNA) and calf thymus DNA (ctDNA), obtained from Sino-American Biotechnology (Shanghai, China), were directly dissolved in water at a concentration of 100.0 μg mL^{-1} and stored at 4 °C. These solutions were diluted to 10.0 μg mL^{-1} with water, which was used

as working solutions and gently shaken if necessary. Concentration per nucleotide of ctDNA was determined by absorption spectroscopy, using the molar extinction coefficient (M^{-1} cm^{-1}) of 6600 at 260 nm [26]. A *N*-(ACR-4-CA)-α-ALA stock solution (1.0 × 10^{-3} mol L^{-1}) was prepared by directly dissolving an appropriate amount of *N*-(ACR-4-CA)-α-ALA into 100.0 mL of water and then storing in the dark. This solution was diluted to 1.0 × 10^{-5} mol L^{-1} with water as working solution. A pH 7.2 Tris–HCl buffer solution was prepared by mixing 50.0 mL of 0.1 mol L^{-1} Tris and 43.5 mL of 0.1 mol L^{-1} HCl, then diluted to 100.0 mL with water and adjusted by pH meter. All chemicals were of analytical reagent grade or better. All water used was doubly distilled water.

2.3. Synthesis of N-(ACR-4-CA)-α-ALA

As Scheme 1 described, the synthesis of 9-oxoacridan-4-carboxylic acid was similar to the previous method [24] with a slight modification. In previous method, the acridone-4-carboxylic acid was synthesized via Jourdan–Ullman reaction of *o*-iodoisophthalic acid with aniline to give a *N*-phenylanthranilic acid, and then was cyclized by using polyphosphorous acid. The method was more complicated and a waste of reagent. In this study, commercially available 2,2-iminodibenzoic acid was used that is a more efficient and simple way to give *N*-(ACR-4-CA)-α-ALA.

2.3.1. Preparation of 9-oxoacridan-4-carboxylic acid

A mixture of 2,2-iminodibenzoic acid (2.57 g) and polyphosphoric acid (75 g) was heated at 120 °C for 2 h, and then poured into boiling water and the precipitated solid was collected and washed well with hot water. The solid was dissolved in 0.5 mol L^{-1} NaOH solution and filtered. The filtration was diluted with an equal volume of MeOH and then was acidified with glacial acetic acid. The solution was cooled at 4 °C and the compound was slowly crystallized after 12 h. The solid was collected and washed with hot water. The product was obtained as a yellow solid. MS *m/z* (ESI$^-$): 237.3 (*M$^-$*).

2.3.2. Preparation of 9-chloroacridine-4-carbonyl chloride

A suspension of 9-oxoacridan-4-carboxylic acid (10 g) in SOCl$_2$ (30 mL) containing DMF (two drops) was heated gently under reflux with stirring until homogeneous and then was refluxed for a further 45 min. The solution was evaporated to dryness in vacuo below 40 °C, and residual traces of SOCl$_2$ were removed by addition of dry CH$_2$Cl$_2$ and complete re-evaporation of all solvents to give the crude product as a yellow powder.

2.3.3. Preparation of N-(2-(N-dimethylamino)ethyl)-9-chloroacridine-4-carboxamide

An ice-cold solution of N,N-dimethylethylenediamine (3.30 g, 37.5 mmol) in dichloromethane (10 mL) was added within 5 min to a stirring suspension of 9-chloroacridine-4-carbonyl chloride (2.06 g, 7.5 mmol) in dichloromethane (10 mL) at 0 °C. The resulting solution was stirred at room temperature for another 2 h, washed twice with 40 mL 10% sodium carbonate and then with 40 mL brine, and finally dried over sodium sulfate. After removal of the solvent in vacuo, the product was obtained as a yellow solid. Finally, the product was recrystallized from benzene/petroleum ether (1:5) as a yellow powder. ^{1}H NMR(CD$_3$OD): 2.43 (s, 6H, N(CH$_3$)$_2$), 2.70 (t, 2H, CH$_2$), 3.70 (m, 2H, CH$_2$), 7.31 (d, 1H, ArH), 7.62 (d, 1H, ArH), 7.83 (t, 1H, ArH), 8.02 (d, 1H, ArH), 8.21 (d, 1H, ArH), 8.35 (dd, 1H, ArH), 8.65 (dd, 1H, ArH). MS (ESI$^+$): 328.4 m/z (M^+).

2.3.4. Preparation of N-(ACR-4-CA)-α-ALA

Then, N-(2-(N-dimethylamino)ethyl)-9-chloro acridine-4-carboxamide (0.65 g) was dissolved in phenol (1.18 g) at 100 °C for 1 h under a N$_2$ atmosphere and allowed to react with α-alanine (0.18 g) under reflux for another 2 h. After cooling down to room temperature, the residue was dissolved in ethanol (5 mL) and then poured into ether (100 mL). The deposit was collected. The product was purified by column chromatography on silica gel with MeOH:water:CH$_3$COOH = 5:4:1 (v/v) twice. ^{1}H NMR(DMSO): 2.38 (t, 2H, CH$_2$), 2.42 (t, 2H, CH$_2$), 2.65 (s, 6H, N(CH$_3$)2), 3.57 (m, 4H, 2-CH$_2$), 4.14 (s, 1H, NH), 7.50 (d, 1H, ArH), 7.75 (d, 1H, ArH), 8.02 (t, 1H, ArH), 8.28 (d, 1H, ArH), 8.34 (d, 1H, ArH), 8.54 (dd, 1H, ArH), 8.70 (dd, 1H, ArH), 11.56 (S, 1H, CONH), 12.57 (S, 1H, COOH); MS m/z (ESI$^+$): 381.4 (M^+); Anal. calcd. for C$_{21}$H$_{22}$N$_4$O$_3$: C, 66.31; H, 5.79; N, 14.74. Found: C, 66.19; H, 5.88; N, 14.66.

2.4. Determination of DNA

To a 10-mL flask appropriate working solution or sample solution of nucleic acids (10.0 μg mL^{-1}), 1.0 mL N-(ACR-4-CA)-α-ALA working solution (1.0 × 10^{-5} mol L^{-1}), and 3.0 mL of buffer solution (pH 7.2) were added. This mixture was diluted to 10 mL with water and mixed thoroughly. The fluorescent intensities (at 451 nm) of the blank (F_0) and the mixed solution (F) were recorded with excitation at 260 nm. A calibration curve of the fluorescent quenching ($\Delta F = F_0 - F$) versus the concentration of DNA was plotted.
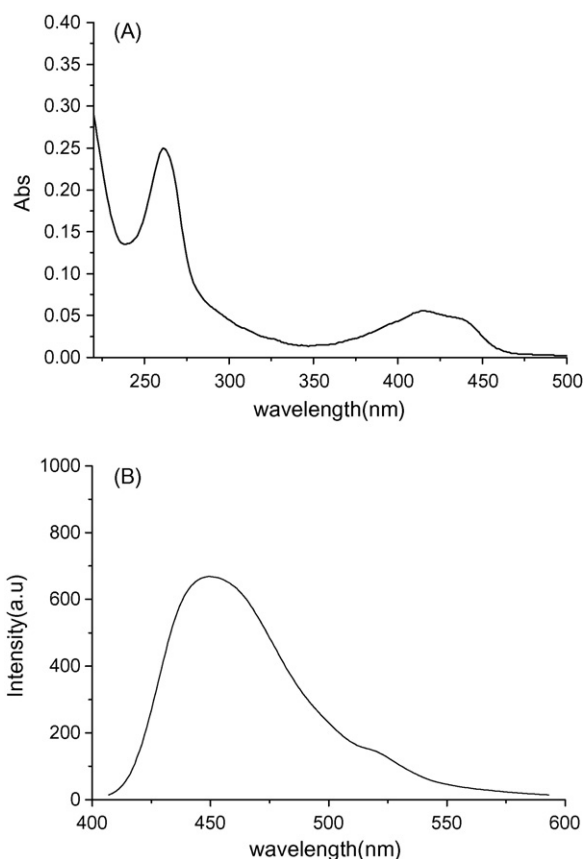

Fig. 1. Spectra property of N-(ACR-4-CA)-α-ALA: (A) absorption spectrum; (B) fluorescent spectrum (N-(ACR-4-CA)-α-ALA concentration: 2.0×10^{-5} mol L^{-1}, $\lambda_{ex} = 260$ nm).

3. Results and discussion

3.1. The spectral characteristics of N-(ACR-4-CA)-α-ALA

The absorption and fluorescent spectra of N-(ACR-4-CA)-α-ALA in water are shown in Fig. 1. From the absorption spectrum, the long-wavelength band at 415 and 430 nm involve two transitions, $1^1A_g \rightarrow 1^1B_{1u}$ and $1^1A_g \rightarrow 1^1B_{2u}$. And the intense band at 262 nm is assigned to the $1^1A_g \rightarrow 2^1B_{2u}$ transition [27]. The fluorescence spectrum of N-(ACR-4-CA)-α-ALA in water is similar to other acridine derivatives described previously [28]. It means that as the α-alanine is introduced, the spectral properties change little. From the spectral property of N-(ACR-4-CA)-α-ALA, it has the potential capability to be a novel fluorescent probe in the use of determination of nucleic acid.

3.2. Fluorescent quantum yield of N-(ACR-4-CA)-α-ALA

The quantum yield for the N-(ACR-4-CA)-α-ALA is estimated by the following equation [29]:

$$\varphi_D = \varphi_R \left(\frac{A_D}{A_R} \right) \left(\frac{O_R}{O_D} \right) \tag{1}$$

where A denotes the integral area of emission spectrum, φ denotes quantum yield, and O denotes optical density at excitation wavelength. The subscript D is for N-(ACR-4-CA)-α-ALA,
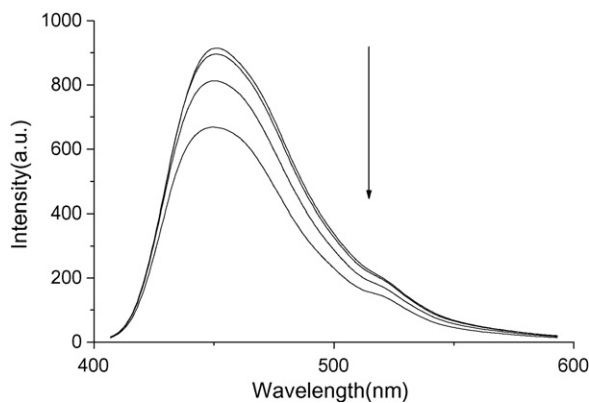
Fig. 2. The quenching effect of fluorescence by ctDNA (pH 7.2; *N*-(ACR-4-CA)-α-ALA concentration: 1.0×10^{-6} mol L^{-1}; concentration of ctDNA: 0.0, 0.05, 0.5 and 2.0 μg mL^{-1}, from top to bottom).

and the subscript R is for reference, here is for free L-tryptophan (Trp). The φ_R value of 0.20 for free Trp is used [29]. Quantum yield of *N*-(ACR-4-CA)-α-ALA was calculated, and the result showed that the quantum yield at maximum excitation wavelength 260 nm was found to be 0.28 under the condition of pH 7.2 and the temperature of 25 °C. The value is higher than another intense fluorescent molecule anthracene (0.27) [30].

3.3. The optimum conditions for DNA detection

3.3.1. The fluorescence quenching effect of DNA to *N*-(ACR-4-CA)-α-ALA

When the concentration of *N*-(ACR-4-CA)-α-ALA is between 5.0×10^{-5} and 5.0×10^{-6} mol L^{-1}, the DNA exhibits an obvious quenching effect on fluorescent intensity of *N*-(ACR-4-CA)-α-ALA. Here, 1.0×10^{-5} mol L^{-1} of *N*-(ACR-4-CA)-α-ALA is used as working solution. The fluorescent intensity (λ_{em}: 451 nm) of *N*-(ACR-4-CA)-α-ALA at the excitation wavelength of 260 nm is about fivefold higher than that at the excitation wavelength of 410 nm. Also, we had determined the fluorescence quenching effect at both excitation wavelength of 410 and 260 nm when DNA was added into the *N*-(ACR-4-CA)-α-ALA solution. When the excitation wavelength was 410 nm, the value of F/F_0 was the same as the excitation wavelength at 260 nm. Comparing to the excitation wavelength at 410 nm, excitation wavelength at 260 nm exhibited larger stocks shift which was good for analytical determination. So the excitation wavelength at 260 nm was chosen and the quenching fluorescence effect of DNA is shown in Fig. 2.

3.3.2. Optimum condition for the determination

The effects of pH and *N*-(ACR-4-CA)-α-ALA's concentration are shown in Fig. 3. The fluorescent intensity was recorded at $\lambda_{ex} = 260$ nm, $\lambda_{em} = 451$ nm. It can be seen that pH obviously affects the fluorescent intensity quenching when DNA is added to the *N*-(ACR-4-CA)-α-ALA solution. When the H$^+$ concentration was high, the force of H-bond between side chain and DNA base pairs was strong. On the other hand, the force of van der Waals was weak between tricyclic rings and the phosphate ions of the DNA backbone. When pH was 7.2 (see Fig. 3(A)),
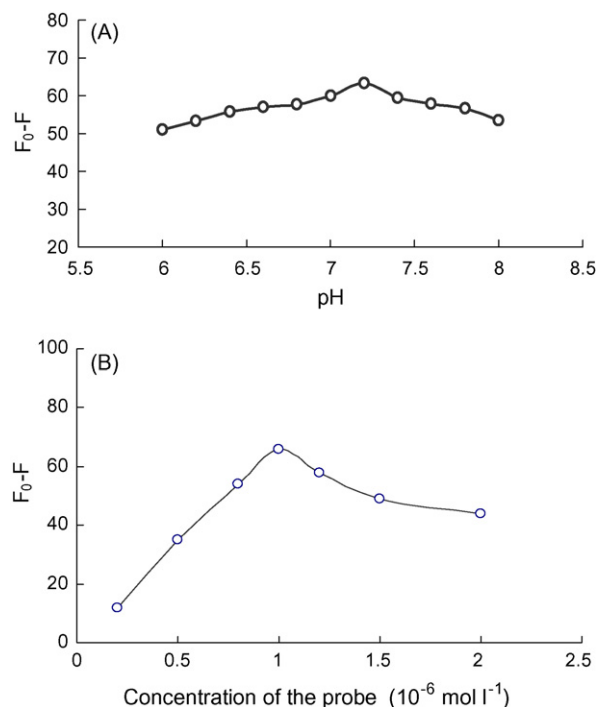

Fig. 3. Optimum condition for the determination of DNA: (A) the influence about pH on the fluorescence quenching (*N*-(ACR-4-CA)-α-ALA concentration: 1.0×10^{-6} mol L^{-1}; ctDNA concentration: 1.0 μg mL^{-1}). (B) The effect of *N*-(ACR-4-CA)-α-ALA concentration on quenched fluorescence *N*-(ACR-4-CA)-α-ALA concentration (1×10^{-6} mol L^{-1}): 0.2, 0.5, 0.8, 1.0, 1.2, 1.5, 2.0 (pH 7.2; ctDNA: 1.0 μg mL^{-1}). The temperature is 25 °C.

the quenching effect should be the most obvious. The concentration of *N*-(ACR-4-CA)-α-ALA had an effect on fluorescence quenching proportion of the system also. The concentration of *N*-(ACR-4-CA)-α-ALA selected is 1.0×10^{-6} mol L^{-1}.

3.3.3. Effect of foreign substances

The influences of some common ions, proteins and bases were studied (see Table 1). It can be seen from Table 1 that this method had high tolerance limits. Ions and substances' quantities in biological fluid samples or real samples diluted for analysis are usually below the amounts tolerated under experimental conditions.

3.3.4. Calibration curves for DNA determination and analysis of synthetic/real samples

Under the optimum conditions, the calibration curves for determination were built under the temperature of 25 °C. The linear range was 0.05–2.0 μg mL^{-1} for both fsDNA and ctDNA. The linear regression equation was $\Delta F = 112.2C + 12.593$ for fsDNA and $\Delta F = 117.65C + 14.727$ for ctDNA, respectively. Here C denotes the concentration of DNA. The correlation coefficients were 0.9940 and 0.9958. It demonstrated that there was a good linear relationship between the concentration of DNA and ΔF. It can be calculated that the limit of determinations (LOD) were 9.1 ng mL^{-1} for fsDNA and 8.7 ng mL^{-1} for ctDNA, respectively. Here LOD = $a\sigma/k$, where a is a numerical factor chosen according to the confidence level desired, σ is the standard deviation of the blank measurements and k is

Table 1
Tolerance of foreign substances

Foreign substances[a]	Coexisting concentration ($\mu g \, mL^{-1}$)	Relative error[b] (%)
K^+	20	−1.1
Ca^{2+}	20	−1.5
Mg^{2+}	20	−2.5
Zn^{2+}	20	−2.1
Mn^{2+}	10	−1.8
Cu^{2+}	10	−1.3
Fe^{3+}	10	−2.3
Pb^{2+}	10	−3.2
Glucose	50	3.4
Glycine	50	3.2
L-Arginine	50	2.6
L-Proline	50	2.2
Bovine serum albumin	15	3.3
CTAB	10	−1.7
SDS	10	1.9
Triton X	10	2.9

[a] For Pb^{2+}, the anion is NO_3^-; for all other cations, the anion is Cl^-.
[b] Experimental conditions: N-(ACR-4-CA)-α-ALA concentration: $1.0 \times 10^{-6} \, mol \, L^{-1}$; ctDNA concentration: $1.0 \, \mu g \, mL^{-1}$ pH 7.2.

the slope of the calibration curve. IUPAC (1997) recommend a value of three for K when the blank measurements are 20 times. In our experiments the blank measurements are 20 times, and a value of three for K was used.

The proposed method was applied to determine the concentration of DNA in synthetic samples. According to the tolerance levels of foreign substances listed in Table 2, samples were constructed by adding co-existing components in standard solution. As shown in Table 3, the results were reproducible and reliable.

Also, real DNA sample was analyzed using the proposed method. DNA from hypertension patients, offered by the department of analytical biology of Fujian Medical University, was diluted 2500-fold with deionized water just before determination without other pretreatment. The determination of DNA from hypertension patients was conducted with this method and the results are shown in Table 3. The recovery is 94–106% and the results are satisfactory.

3.3.5. The characteristic of this system

When adding order of reagents changes, the fluorescent intensity does not change. The incubation time for the system is also examined. When the reagents are mixed, the fluorescent intensity is recorded immediately. It is found that the incubation time for the system is less than 1 min and the fluorescent intensity does not change within 12 h. Some characteristics of the pro-

Table 3
Determination results of real nucleic acid sample

Sample[a]	DNA added ($ng \, mL^{-1}$)	DNA found ($ng \, mL^{-1}$)	Recovery[b] (%)
DNA from hypertension patients	–	300	–
	100	406	103–106
	200	491	94–97
	300	588	94–98

[a] The original sample was diluted 2500-fold for determination.
[b] Mean of five determinations.

posed probe and other reagents for nucleic acid determinations are summarized in Table 4.

3.4. Study of the interaction mechanism of N-(ACR-4-CA)-α-ALA with DNA

Generally, organic dyes interact with nucleic acid by intercalative, groove or electrostatic binding modes [16,34,35].

The fluorescence of N-(ACR-4-CA)-α-ALA with DNA system in the presence of NaCl was studied. The result showed that when the concentration of NaCl is 0–0.1 mol L^{-1}, the fluorescence of the system changes within two percent. Usually, Na^+ will partly neutralize the negative charges of the DNA phosphatic backbone, if the interaction between N-(ACR-4-CA)-α-ALA and DNA is electrostatic binding, the quenched fluorescent intensity will be weaken with the increasing of Na^+ concentration [36]. The result indicates that there is no obvious influence on the system's fluorescence with different NaCl concentration. Thus, there is not electronic binding effect between N-(ACR-4-CA)-α-ALA and DNA.

The absorption spectra which demonstrate the comparison when DNA and denatured DNA are added into the N-(ACR-4-CA)-α-ALA solution or not are shown in Fig. 4. The denatured DNA is obtained by heating up ctDNA in boiling water for 15 min, and then cooled in ice-cold bath. From Fig. 4, we can see that the long-wavelength band of N-(ACR-4-CA)-α-ALA has hypochromism and bathochromic effect when the DNA and denatured DNA are added. Hypochromism was suggested to be due to a strong interaction between the electronic states of the intercalation chromophore and that of the DNA base pairs [37,38]. Since the strength of this electronic interaction is expected to decrease as the cube of distance of separation between the chromophore and the DNA base pairs [39], the observed large hypochromism strongly suggests a close proximity of the acridine chromophore to the DNA base pairs. In addition to the hypochromism, a bathochromic effect and exten-

Table 2
Analytical results of the synthetic samples

Samples	DNA concentration ($\mu g \, mL^{-1}$)	Main additives[a]	Found[b] ($\mu g \, mL^{-1}$)	Recovery (%)	R.S.D (%, $n=5$)
fsDNA	0.50	L-Proline, glycine, Ca^{2+}, Fe^{3+}, Mn^{2+}	0.51	102	2.6
ctDNA	0.50	L-Arginine, glucose, Cu^{2+}, Zn^{2+}, Mg^{2+}	0.48	96	3.3

[a] L-Proline, glycine, L-arginine, glucose: $20 \, \mu g \, mL^{-1}$; Ca^{2+}, Fe^{3+}, Mn^{2+}, Cu^{2+}, Zn^{2+}, Mg^{2+}: $10 \, \mu g \, mL^{-1}$.
[b] Mean of five determinations.

Table 4
Comparison of different methods for determination of DNA

Method reference	Linear range (μg mL^{-1})	Limits of detection (ng mL^{-1})	R.S.D. (%)	Comments
TOTO	0.0005–0.1	0.5	Not mentioned	Expensive [31]
Ethidium bromide	Not mentioned	10	Not mentioned	High toxic reagents [32]
Al^{3+}-8-hydroxyquinoline	0.25–3.5	13	1.3	Narrow linear range [33]
Acridine orange	0.02–8.0	5.8	Not mentioned	Long time (10 min) for detection [17]
Acridine red	0.05–1.0	1.3	Not mentioned	Long time (20 min) for detection [16]
This method	0.05–2.0	9.1	1.0	Simple, rapid, and stable

sive broadening effect of the long wavelength band were also observed in the spectra. That is another clue of the intercalation between N-(ACR-4-CA)-α-ALA and DNA base pairs [40]. The change of another wavelength band at 260 nm can also illuminate the intercalation. When DNA is added into the N-(ACR-4-CA)-α-ALA, the absorption spectrum of DNA becomes having a small red shift. On the other hand, the absorption spectrum of N-(ACR-4-CA)-α-ALA changes at 262 nm to have a small blue shift. That contributes to the intercalation of the acridine chromophore into the helix and a strong overlapping of the π–π* states of the acridine with the electronic states of the DNA base pairs. Here we also use denatured DNA in contrast to ctDNA to explore the binding mode. Comparing the absorbance at 260 nm of both DNA and denatured DNA, the absorbance of denatured DNA increases a little relatively to the helical DNA. That is a clue that the helical structure is partly destroyed. Because the absorbance at 260 nm would increase vastly if DNA is absolutely denatured [41]. The result shows when the ctDNA is added, the hypochromism and bathochromic effect become more obvious. When the helical structure is declined, the interaction between N-(ACR-4-CA)-α-ALA and DNA is weaken. These spectra changes are consistent with the intercalation of N-(ACR-4-CA)-α-ALA into the DNA base pairs.

The binding mode stands to the conclusion that acridine derivatives are classical DNA intercalators [42]. We supposed

Fig. 4. The absorption spectra of N-(ACR-4-CA)-α-ALA in the presence and absence of ct-DNA: (a) N-(ACR-4-CA)-α-ALA; (b) ctDNA; (c)denatured ctDNA; (d) N-(ACR-4-CA)-α-ALA + ctDNA; (e) N-(ACR-4-CA)-α-ALA + denatured ctDNA (pH 7.2, N-(ACR-4-CA)-α-ALA concentration: 2.0×10^{-5} mol L^{-1}; ctDNA concentration: 20.0 μg mL^{-1}; denatured ctDNA concentration: 20.0 μg mL^{-1}).

when the 4,9 positions of acridine are substituted by cationic side chain N,N-dimethylaminoethyl and α-alanine, the binding mode of acridine skeleton is not changed. And the side chain N,N-dimethylaminoethyl, which binds to DNA lying in the major groove, can form hydrogen-bonding interactions with the O$_6$ and N$_7$ atoms of guanine [24]. Also, the introduction of α-alanine on C-9 of the tricyclic rings can form H-bond with adenine and guanine. Therefore, N-(ACR-4-CA)-α-ALA could be a good DNA intercalator and used for the determination of DNA.

3.5. The intrinsic binding constant of N-(ACR-4-CA)-α-ALA with ctDNA

The intrinsic binding constant (K_I) was determined by absorption titration which required keeping the concentration of N-(ACR-4-CA)-α-ALA constant while varying the ctDNA concentration [35]. This was done by mixing different volume of ctDNA and the same volume of N-(ACR-4-CA)-α-ALA, then diluting the mixing solution to 5 mL. Thus, a series of solutions with varying concentration of ctDNA but with a constant concentration of N-(ACR-4-CA)-α-ALA can be obtained. K_I was determined from the plot of $D/\Delta\varepsilon_{ap}$ versus D. Here D denotes the concentration of ctDNA in base pairs, $\Delta\varepsilon_{ap} = [\varepsilon_a - \varepsilon_f]$ and $\Delta\varepsilon = [\varepsilon_b - \varepsilon_f]$. The apparent extinction coefficient, ε_a, is obtained by calculating $[A_{former} - A_{ctDNA} - A_{N-(ACR-4-CA)-\alpha-ALA}]/[N-(ACR-4-CA)-\alpha-ALA]$. A_{former}, A_{ctDNA}, $A_{N-(ACR-4-CA)-\alpha-ALA}$ denote the absorbance at 261 nm of the mixing solution of N-(ACR-4-CA)-α-ALA with ctDNA, the absorbance at 260 nm of ctDNA, and the absorbance at 262 nm of N-(ACR-4-CA)-α-ALA, respectively. ε_b and ε_f correspond to the extinction coefficient of the bound form of N-(ACR-4-CA)-α-ALA and the extinction coefficient of free N-(ACR-4-CA)-α-ALA, respectively. The data were fitted to Eq. (2), and K_I was obtained from the ratio of the slope to the y-intercept.

$$\frac{D}{\Delta\varepsilon_{ap}} = \frac{D}{\Delta\varepsilon} + \frac{1}{\Delta\varepsilon K_I} \tag{2}$$

The intrinsic binding constant of N-(ACR-4-CA)-α-ALA with ctDNA is $(3.0 \pm 0.5) \times 10^5$ M^{-1} in base pairs. That is much larger than N-(2-(dimethylamino)ethyl)acridine-4-carboxamide (7.4×10^4 M^{-1}) and 9-aminoacridine (7.2×10^4 M^{-1}) [43]. The result shows that the binding affinity is increased as the introduction of α-alanine on C-9 position of acridine-4-carboxamide.
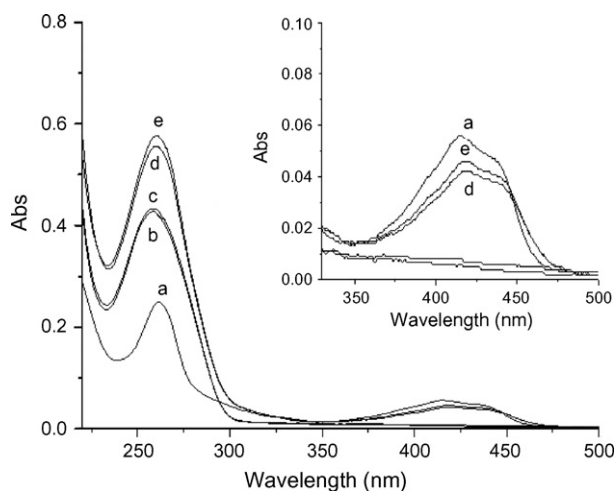
4. Conclusion

In summary, we have successfully developed a novel fluorescent probe *N*-(ACR-4-CA)-α-ALA for DNA detection based on fluorescent quenching. Due to elaborate design of side chains, this new probe exhibited high binding affinity, high quantum yield and high water solubility. This new probe has been applied to fsDNA and ctDNA detection and the experimental results suggested that this method is simple, rapid, sensitive and stable. Moreover, the interaction mechanism was also studied and the results demonstrated that the binding mode of novel probe and DNA is intercalative binding.

Acknowledgements

References

[1] J.R. Lakowicz, Topics in Fluorescence Spectroscopy, Biochemical Applications, vol. 3, Plenum Press, New York, 1992, p. 137.
[2] S. Udenfriend, P. Zaltzman, Anal. Biochem. 3 (1962) 49.
[3] Y.Q. Li, Y.J. Guo, X.F. Li, J.H. Pan, Talanta 71 (2007) 123.
[4] X.F. Long, Q. Miao, S.P. Bi, D.S. Li, C.H. Zhang, H. Zhao, Talanta 64 (2004) 366.
[5] Y.F. Long, C.Z. Huang, Talanta 71 (2007) 1939.
[6] S.J. Zhuo, H. Zheng, J.L. Chen, D.H. Li, Y.Q. Wu, C.Q. Zhu, Talanta 64 (2004) 528.
[7] C.L. Tong, Z. Hu, W.P. Liu, Talanta 71 (2007) 816.
[8] L. Li, J.H. Yang, X. Wu, C.X. Sun, G.J. Zhou, Talanta 59 (2003) 81.
[9] Y.Q. Cheng, Z.P. Li, Y.Q. Su, Y.S. Fan, Talanta 71 (2007) 1757.
[10] G.C. Di, M.M. De, J. Chiron, F. Delmas, Bioorg. Med. Chem. 13 (2005) 5560.
[11] S.A. Gamage, N. Tepsiri, P. Wilairat, S.J. Wojcik, D.P. Figgit, R. Ralph, W.A. Denny, J. Med. Chem. 37 (1994) 1486.
[12] S.A. Gamage, D.P. Figgit, S.J. Wojcik, R. Ralph, A. Ransijn, J. Mauel, J. Med. Chem. 40 (1997) 2634.
[13] J. Mauel, W.A. Denny, S.A. Gamage, A. Ransijn, S.L. Wojcik, D.P. Figgit, R. Ralph, Antimicrob. Agents Chemother. 37 (1993) 991.
[14] G.W. Rewcastle, G.J. Atwell, D. Chambers, B.C. Baguley, W.A. Denny, J. Med. Chem. 29 (1986) 472.
[15] G.J. Atwell, G.W. Rewcastle, B.C. Baguley, W.A. Denny, J. Med. Chem. 30 (1987) 664.
[16] D.E. Graves, L.M. Velea, Curr. Org. Chem. 4 (2000) 915.
[17] R.T. Liu, J.H. Yang, C.X. Sun, L. Li, X. Wu, Z.M. Li, C.S. Qi, Chem. Phys. Lett. 376 (2003) 108.
[18] S.P. Liu, S. Chen, Z.F. Liu, X.L. Hu, T.S. Li, Anal. Chim. Acta 535 (2005) 169.
[19] M. Wang, J.H. Yang, X. Wu, F. Huang, Anal. Chim. Acta 422 (2000) 151.
[20] G.J. Atwell, B.F. Cain, B.C. Baguley, G.J. Finlay, W.A. Denny, J. Med. Chem. 27 (1984) 1481.
[21] D. Sabolova, M. Kozurkova, P. Kristian, I. Danihel, D. Podhradsky, J. Imrich, Int. J. Biol. Macromol. 38 (2006) 94.
[22] Z.Q. Yan, Y.Y. Zhou, L. Nie, Chin. J. Appl. Chem. 22 (2005) 1258.
[23] S. Hecht, Bioorganic Chemistry: Nucleic Acid, Oxford University Press Inc., New York, 1996.
[24] L.P.G. Wakelin, X. Bu, A. Eleftheriou, A. Parmar, C. Hayek, B.W. Stewart, J. Med. Chem. 46 (2003) 5790.
[25] Guddneppanavar, G. Saluta, G.L.R. Kucera, U. Bierbach, J. Med. Chem. 49 (2006) 3204.
[26] E.G. David, L.W. Charles, W.Y. Lerena, Biochemistry 20 (1981) 1887.
[27] J. Dey, J.L. Haynes III, I.M. Warner, A.K. Chandra, J. Phys. Chem. A 101 (1997) 2271.
[28] V.S. Sukumaran, A. Ramalingam, Phys. Lett. A 341 (2005) 454.
[29] M.J. Kronman, L.G. Holmes, F.M. Robbins, J. Biol. Chem. 246 (1971) 1909.
[30] C.N. Huang, P.Y. Kuo, C.H. Lin, D.Y. Yang, Tetrahedron 63 (2007) 10025.
[31] H.S. Rye, J.M. Dabora, M.A. Quesada, R.A. Mathies, A.N. Glazer, Nucleic Acids Res. 20 (1992) 2803.
[32] A.N. Glazer, H.S. Rye, Nature (London) 359 (1992) 859.
[33] C.Z. Huang, K.A. Li, S.Y. Tong, Anal. Lett. 30 (1997) 1305.
[34] R.F. Pasternack, E.J. Gibbs, J.J. Villafranca, Biochemistry 22 (1983) 2406.
[35] C.V. Kumar, E.H. Asuncion, J. Am. Chem. Soc. 115 (1993) 8547.
[36] J.B. Le Pecq, C. Paoletti, Mol. Biol. 27 (1967) 87.
[37] E.C. Long, J.K. Barton, Acc. Chem. Res. 23 (1990) 271.
[38] G. Dougherty, W.J. Prigram, CRC Crit. Rev. Biochem. 12 (1982) 103.
[39] C. Cantor, P. Schimmel, Biophys. Chem., vol. 2, Freeman, San Francisco, 1980, p. 398.
[40] C.V. Kumar, E.H. Asuncion, J. Chem. Soc., Chem. Commun. (1992) 470.
[41] G.L. Zubay, Biochemistry, 2nd ed., Macmillan, New York, 1988, p. 101.
[42] W.A. Denny, G.J. Atwell, G.W. Rewcastle, B.C. Baguley, J. Med. Chem. 30 (1987) 658.
[43] J.M. Crenshaw, D.E. Graves, W.A. Denny, Biochemistry 34 (1995) 13682.

A glycerol assisted light-emitting diode-induced fluorescence detector for capillary flow systems

Jing Xu, Shiheng Chen, Yan Xiong, Bingcheng Yang, Yafeng Guan *

*Department of Analytical Chemistry and Micro-Instrumentation, Dalian Institute of Chemical Physics,
Chinese Academy of Sciences, Dalian 116023, China*

Abstract

A glycerol assisted light-emitting diode (LED)-induced fluorescence detector (IF) for capillary flow systems was constructed and evaluated. A blue LED was used as the excitation source, and optical fibers (OF) were used to transmit the excitation light and collect the fluorescence. A commercial available 5-port manifold was used as detection cell, where the capillary tube and the OF were fixed into the manifold. The precision of the holes on the manifold ensured a self-alignment of optical path. A refractive index matching fluid (RIMF)-glycerol was used to eliminate the interfaces between the OF and the LED, as well as between the fused silica capillary and the transmitting/collecting fiber. The enhancement of excitation light led to 2.8-folds improvement on the signal-to-noise ratio. The use of RIMF also eliminates focusing effect of the capillary wall and reduces both the excitation light directed to the detection cell and background signal, resulting in reduction in the fluorescence intensity and noise level. The intensity was reduced to 47–63% for laser and 60–77% for LED, respectively, for capillaries with i.d. from 50 to 250 μm; while the noise level was reduced to 1/3 when RIMF was used for both laser and LED on the tested capillaries. About 5.6-fold enhancement in signal-to-noise ratio was obtained in total. The detection limit of the LED-IF for fluorescein isothiocyanate (FITC) was 4 nM. Application of the LED-IF for the analysis of FITC-labeled amino acids by electrophoresis was demonstrated.
© 2008 Elsevier B.V. All rights reserved.

Keywords: Light-emitting diode; Fluorescence detection; Capillary electrophoresis; Refractive index matching fluid

1. Introduction

Capillary flow systems, such as flow injection analysis, capillary liquid chromatography and capillary electrophoresis, have been playing an important role in the analysis of biological and environmental samples [1,2]. Fluorescence detection is one of the most sensitive and selective detection schemes available for capillary flow systems [3–6]. Among the light sources used in fluorescence detector, the light-emitting diode (LED) shows high stability, small size, low cost, a variety of wavelengths ranging from near-UV to near-IR and very long lifetime. Optical fiber (OF) LED-induced fluorescence detectors have been constructed and applied to many fields [7–10] in recent years.

On-column detection is the most popular approach in fluorescence detectors combined with capillary flow systems,

especially in electrophoresis. By removing parts of the polyimide coating on fused silica capillary, a detection window with nL to sub μL volume is readily made, resulting a minimum dead volume and extra-column band dispersion. However, the excitation light travels through three propagating medias before reaching the analyte stream, including fused silica fiber (RI = 1.467), air (RI = 1.000) and fused silica capillary wall (RI = 1.467). The same situation exists in the propagation of the fluorescence. The RI changes abruptly in different media and results in several optical interfaces. Scattering by total and multiple reflections on the capillary wall leads to high background noise and poor sensitivity.

Several solutions had been proposed to minimize the amount of scattering light. Bruno et al. [11] developed a "pigtailing" approach and constructed absorption and fluorescence detectors. Liu and Dasgupta [12] used a falling liquid drop as a flow cell and applied it to flow injection analysis. Our group [13] developed windowless flow cell, in which a capillary tube was omitted in the detection cell and OFs were in physical contact with the

* Corresponding author. Tel.: +86 411 84379570; fax: +86 411 84379590.
  E-mail address: guan_yafeng@yahoo.com.cn (Y. Guan).

sample liquid. However, there were a contamination problem on the polished ends of fibers, and technical problems to apply it to capillary electrophoresis detection.

RI matching fluid (RIMF) had been routinely used to measure the core dimensions of OFs. Bruno et al. [14] applied it to simplify the fringe pattern of the capillary wall and constructed a laser-based RI detector. Saito and co-workers [15] filled the flowcell of a conventional fluorescence detector with RIMF to make the optical boundary of the cell effectively square. RIMF had also been used in capillary array electrophoresis to overcome the laser-power reduction along the array due to reflection and divergence [16,17].

In the present work, we apply RIMF to optical fiber LED-induced fluorescence detector (LED-IF). Glycerol is chosen as the RIMF and is used to eliminate the optical interfaces between the transmitting fiber and the LED source, as well as between the fused silica capillary and the transmitting/collecting fiber. Homogeneous and transparent propagating media is formed between these interfaces for both excitation light path and the path of fluorescence collection. The effects of the RIMF on coherent/noncoherent light source, as well as on capillaries with several i.d./o.d. geometries are examined and discussed in detail. The performance of the detector is evaluated by both flow injection analysis of standards and CE analysis of amino acids.

2. Experimental

2.1. Apparatus and reagents

A P230 HPLC pump (Elite Co. Ltd., China) was used to carry out flow injection analysis. Injection was performed using a six-port injection valve (Valco Instruments, USA) with a 40-μL loop.

A homemade CE system, consisting of a fused silica capillary (45 cm × 100 μm i.d., 35 cm to the detector) and a high-voltage power supply (0–30 kV, Dongwen, China), was used to evaluate the detector. The working electrolyte for CE separation was $Na_2B_4O_7$ buffer (10 mM, pH 9.0). Sample injection was carried out by hydrodynamic technique.

Amino acids (Jingke Co. Ltd., China) were labeled by FITC (Molecular probes, USA) according to reference [4]; fluorescein was obtained from Sigma, USA. All the reagents used were of reagent grade, and deionized (DI) water was used throughout.

2.2. Optical systems

The optical arrangement of detector was shown in Fig. 1. A blue LED ($\lambda_{max} = 470$ nm, 5 mW, Shifeng Corp., China) was used as the excitation source. To increase the effective light intensity, the plastic dome of the LEDs was grounded away from the top until ~0.5 mm to the P–N junction, and then mirror polished to meet optical clarity. An Optical fiber (core 0.5 mm, cladding 0.6 mm, Chunhui Inc., China), placed as near as possible to the P–N junction of LED, was used to carry the excitation light to the detection window. A coaxial aluminum housing was used to fix the fiber and the LED and make sure that they were
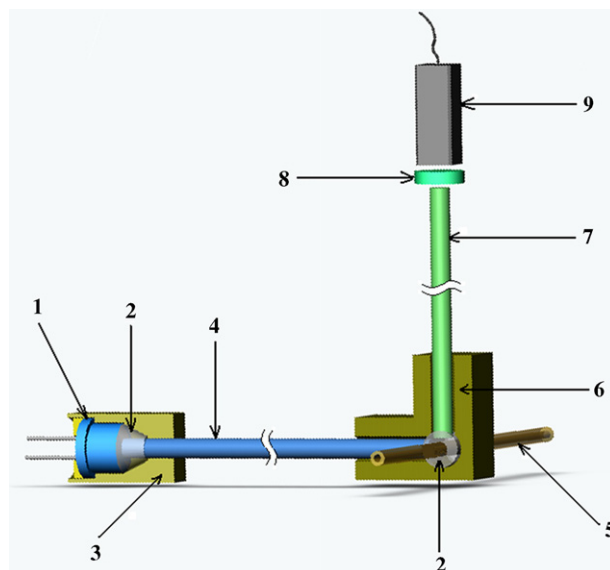

Fig. 1. Schematic of the optical system. 1, LED; 2, RIMF; 3, aluminum block; 4, optical fiber carrying excitation light; 5, fused silica capillary; 6, 5-port manifold; 7, collecting fiber; 8, interference filter; 9, PMT.

coaxial. The space inside the aluminum housing was filled with glycerol to insure that the forward plane of the LED and the end of the fiber was immersed in the fluid. A commercial 5-port manifold (Upchurch Scientific, USA) was used to fix the OFs and the capillary. Part of the polyimide coating (4 mm in length) on the capillary was burned off with an electrical coiled resistance to form a detection window. Fluorescence was collected with a right-angle geometry by another OF, passed through an interference filter (BP 530 nm; FWHM 30 nm; Huibo Optical Corp. Ltd., China), then detected by a metal packaged mini PMT (H5784, Hamamatsu, Japan). The distance between the fiber and the capillary was set at 0.5 mm considering the collection efficiency of fluorescence and the fragileness of the optical window [9]. Both ends of the fibers were polished by the vendor. The space inside the manifold was also filled with glycerol and makes sure that the end of the fibers and the detection window was immersed in the fluid. Teflon tubings were used to seal the fibers and capillaries. The precision of the manifold ensured the optical alignment among the capillaries and fibers. All the alignment process was easy to perform even for an inexperienced person.

3. Results and discussion

A glycerol solution (96% in water) was chosen as the RIMF considering its RI (1.467 at 20 °C) and chemical stability. The effects of RIMF in the optical system on the performance of detection were investigated in the following experiments.

3.1. Reflection losses in the light source

According to Fresnel equation, when a light beam is incident on a smooth interface separating two media of refractive indices $\eta 1$ and $\eta 2$, and the beam is monochromatic and normal to the
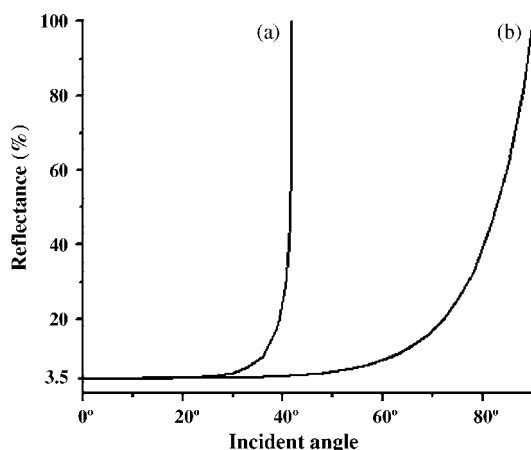
Fig. 2. Reflectance vs. incident angle for a monochromatic beam traveling through air ($\eta_1 = 1.000$) and silica ($\eta_2 = 1.467$) as calculated from the Fresnel equation. (a) Traveling from silica to air; (b) traveling from air-to-silica. Data calculated and acquired by Origin V7.5 software.

interface, the reflectance $\rho\,(\lambda)$ is given by

$$\rho(\lambda) = \left(\frac{\eta_2 - \eta_1}{\eta_2 + \eta_1} \right)^2$$

For an air–silica interface, where $\eta_{air} = 1$ and $\eta_{silica} = 1.467$, approximately 3.5% of the light incident perpendicular to the interface is reflected. If unpolarized radiation strikes the interface at an angle other than 90°, the reflectance varies with the angle of incidence according to Fresnel's complete equation:

$$\rho(\lambda) = \frac{1}{2} \left(\frac{\sin^2(\theta_1 - \theta_2)}{\sin^2(\theta_1 + \theta_2)} + \frac{\tan^2(\theta_1 - \theta_2)}{\tan^2(\theta_1 + \theta_2)} \right)$$

where $\sin\theta_1/\sin\theta_2 = \eta_2/\eta_1$, θ_1 is the incident angle while θ_2 is the refractive angle. Fig. 2 illustrates how reflectance changes with the angle of incidence for a beam traveling through an air–silica interface.

Such interfaces existed between the plastic dome of the LED and the OF, i.e. plastic-to-air, air-to-silica. The effective light intensity was measured by the PMT through a fiber, one end of which was close to the P–N junction of the LED. The PMT voltage was set at 80 V to prevent signal saturation. Table 1 showed the experimental results of the effective light intensity and noise level of the LED after different way of treatment. Removing the dome of the LED reduced the distance between the end of fiber and the P–N junction, and enhances the coupling efficiency between the emission light and OF. The polished surface of LED reduced the diffusion light and hence the noise. When the gap between the LED and the fiber were filled with glycerol, the difference in refractive indices at the interface was decreased. Compared with the untreated LED, light coupling efficiency was

increased by 360% in total, resulting in 3.6-folds enhancement on effective excitation light intensity. The signal-to-noise ratio (SNR) was then improved 2.8-folds.

3.2. Reflection and refraction on the fused silica capillary

For on-column detection with a cylindrical flowcell, there are four optical interfaces in a liquid-filled capillary: air-to-silica, silica-to-liquid, liquid-to-silica, and silica-to-air, as shown in Fig. 3a. When the excitation light travels from air-to-silica, part of the beam is reflected on the outer surface, and the rest of the light passes through and meets the second interface of silica-to-liquid. This interface is from high-to-low refractive index, where if the incident angle is smaller than the critical angle [$\theta_c = \sin^{-1}\,(\eta_1/\eta_2)$], part of the beam will be reflected to the silica-to-air interface and the amount of reflection depends on the incident angle. When the incident angle exceeds θ_c, all of the beam will be reflected into the denser medium and hit the silica-to-air interface, known as total internal reflection. When the reflected light hits the silica-to-air interface (which is another high-to-low refractive index interface), it is reflected by the same mechanism and directed back to the silica-to-liquid interface. In this way, multiple reflections take place. Whenever light strikes the silica-to-air interface, part of the beam will pass through the outer wall of the capillary, and results in scattering light over 360° in the plane perpendicular to the capillary axis, as shown in Fig. 3a.

When the capillary tube is coupled to the OF by glycerol, the situation become simpler, as shown in Fig. 3b. The excitation light passes through the capillary tube uniformly, while the glycerol provides nearly homogeneous and transparent propagating media for the excitation light and the fluorescence. Scattering light is reduced significantly, and hence the background signal.

The effects of the RIMF on coherent (Laser) and noncoherent (LED) light source, as well as on capillaries with different geometries were tested and compared, respectively. For both laser and LED, the background signals decreased dramatically when RIMF was used, and the effect was much greater on the noncoherent light than that of on coherent light. The amount of reduction on background signals depended also on geometries of i.d./o.d., as shown in Fig. 4a. The use of RIMF also eliminated focusing effect of the capillary wall (refer to Fig. 3a), and reduced the excitation light directed to the analyte stream, resulting in reduction in the fluorescence intensity. The intensity was reduced to 47–63% for laser and 60–77% for LED, respectively, for capillaries with i.d. from 50 to 250 μm. The noise levels were reduced to 1/3 when RIMF was used for both laser and LED on the tested capillaries. Fig. 4b shows the effect of the RIMF on SNR for the two light sources on different capillaries. Compared with the non-RIMF mode, the glycerol assisted detection

Table 1
Comparison of the light intensity of the LED after different way of treatment

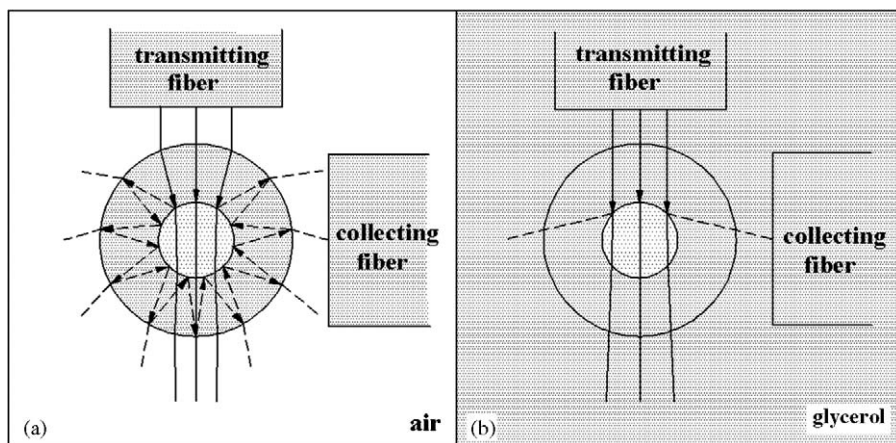| The treatment of LED	Untreated	Remove dome	Remove dome and mirror polish	Remove dome, mirror polish and immerse in glycerol
Light intensity (mV)	16.42	45.27	68.01	76.22
Noise (μV_{p-p})	9	13	15	16

Fig. 3. Cross-section view of capillary tube and corresponding ray-tracing diagrams. (a) Capillary coupled to fiber by air; (b) capillary coupled to fiber by glycerol. The dashed corresponds to the scattering light. The reflection and refraction at high-to-low refractive index interfaces were indicated as arrows.

cell gave the SNR enhancement ranging from 140% to 190% for laser and 180% to 230% for LED, respectively. The effect of enhancement was the greatest on 100 μm capillary (325 μm o.d.) for laser source (190% enhancement) and 50 μm capillary (325 μm o.d.) for LED (230% enhancement), respectively. The final improvement on SNR for the detector was:

$$2.8 \times (180–230\%) \approx 560\%$$

The results indicated that RIMF played more important role in the noncoherent light than that in the coherent light. Fig. 5 depicts the detector signals and the noise levels on a 250 μm i.d. capillary obtained in a flow injection analysis.

3.3. Detector characteristics

The performance of the LED detector was evaluated in terms of the reproducibility of peak heights, response linearity and the limit of detection (LOD) by flow injection method. The error of reproducibility was within 2.0% RSD on peak height in a ten-repeated injection of 0.3 μM FITC solution. The response

linearity was tested by measuring a series of FITC standard solutions. Linear regression analysis of the results yielded the following equations:

$$H = 0.2285C + 1.081 \quad R = 0.9996$$

where H was peak height (mV) and C was the concentration of the FITC in nM. The calibration curves exhibited an excellent linear behavior over the concentration range of 1.0×10^{-8} to 100×10^{-8} M. Fig. 6 shows the electropherogram obtained from an analysis of 0.3 μM FITC solution. From this electropherogram, the LOD of FITC (S/N = 3) was estimated to be 4 nM, which was comparable with the one reported by de Jong and Lucy (3 nM for fluorescein) [8]. Though the LOD was much higher than those usually achieved by laser induced fluorescence (LIF) detection, this detector exhibited advantages such as simple in structure, low cost and robust, light weighted, and very small in size, which may contribute to the reduction of the cost of CE and μLC equipment. The size of the whole detector body was 8 cm × 15 cm × 6 cm (W × L × H), which was about 2% of the volume of conventional fluorometer or LIF system. Further
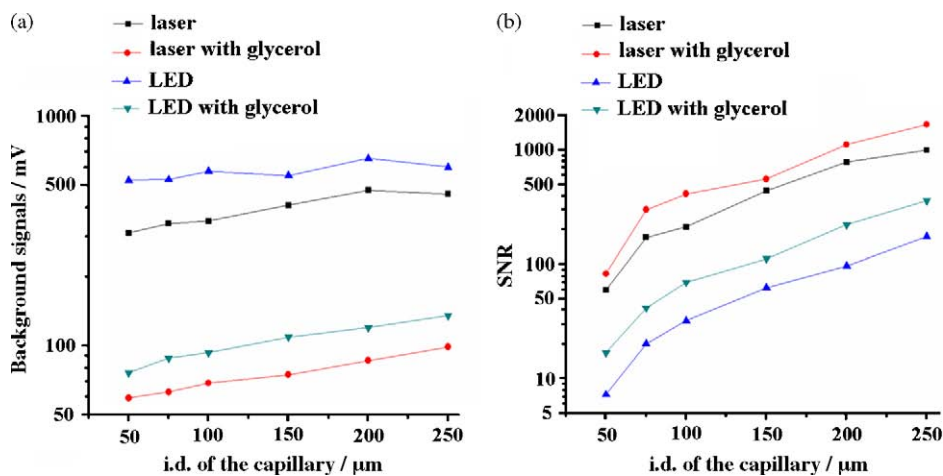

Fig. 4. The effect of RIMF on the SNR of detection. Denary logarithmic coordinate was adopted in the Y-axis. (a) Background signals; (b) SNR. The i.d./o.d. of the capillaries used were: 50/325, 75/325, 100/325, 150/410, 200/280, 250/330 μm; the o.d. was measured without the polyimide coating on capillary. The data was obtained by injecting 0.3 μM fluorescein solution at an injection volume of 40 μL.
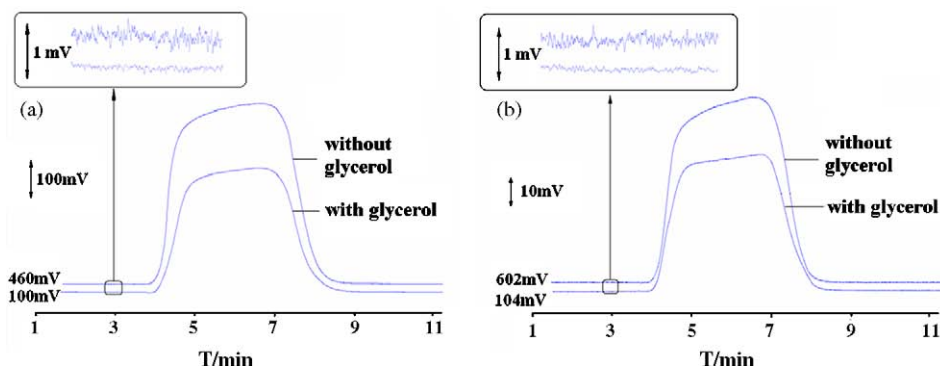
Fig. 5. Comparison of fluoresces signals and noise levels on a 250 μm i.d. capillary by using laser and LED as excitation light sources. (a) Effect of RIMF on laser; (b) effect of RIMF on LED. The background signals (mV) were labeled at the baseline; the conditions were the same as in Fig. 4.
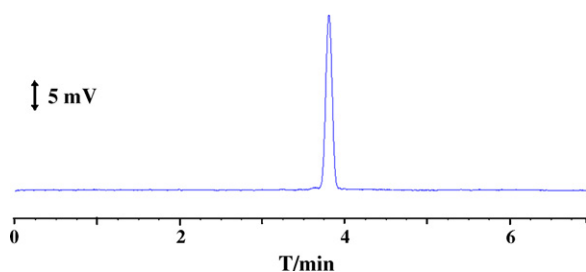

Fig. 6. Electropherogram of FITC solution. Siphon injection, 10 cm × 10 s; separation voltage, 22 kV; buffer solution, $Na_2B_4O_7$ buffer/methanol (70/30); sample concentration, 0.3 μM.
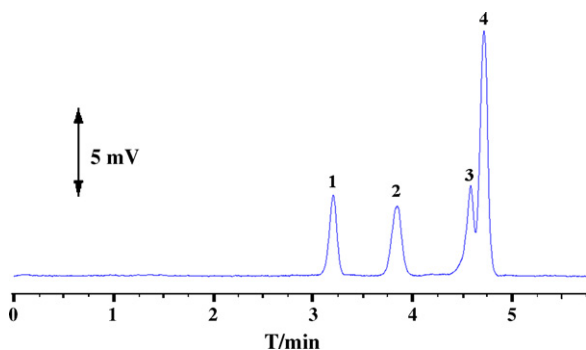

Fig. 7. Electropherogram of FITC-labeled amino acids. Siphon injection, 10 cm × 10 s; separation voltage, 22 kV; buffer solution, $Na_2B_4O_7$ buffer/methanol (70/30); sample concentration, 0.3 μM; peak identification: 1, FITC-labeled Lysine; 2, excess FITC; 3, FITC-labeled Tryptophan; 4, FITC-labeled Phenylalanine.

improvements in sensitivity could be obtained by using LED with higher light intensity (Fig. 7).

To show the utility of this detector in CE, a representative application was demonstrated. Fig. 6 shows a separation of three amino acids labeled by FITC. The LOD (S/N = 3) were found to be 10, 9 and 4.8 nM for lysine (Lys), tryptophan (Trp) and phenylalanine (Phe), respectively. With a minor modification, this detector can be readily applied to μLC system.

4. Conclusions

We have developed a glycerol assisted light-emitting diode-induced fluorescence detector for capillary flow systems. By removing the dome and coupling the light source to fiber with glycerol, the coupling efficiency of the excitation light with OF was enhanced 360%. The noise levels were reduced to 1/3 when the capillary was coupled to the transmitting/collecting fiber with glycerol. About 5.6-fold enhancement in SNR was obtained in total. Compared with other method, the use of RIMF has the advantages of easy accomplish, low cost and effective to enhance the sensitivity. The use of a manifold eliminates the alignment procedure of the capillary and OF, which is often a tedious procedure in on-column detection. The detector was readily applied to flow injection analysis, capillary electrophoresis and μLC.

References

[1] Z.L. Fang, Z.S. Lin, Q. Shen, Anal. Chim. Acta 346 (1997) 135.
[2] K. Tsunoda, T. Umemura, T. Watanabe, H. Takiguchi, H. Asano, H. Itabashi, Y. Ishibashi, S. Sato, Tetsu To Hagane 89 (2003) 979.
[3] K. Tsunoda, T. Yagasaki, S. Aizawa, H. Akaiwa, K. Satake, Anal. Sci. 13 (1997) 757.
[4] S.L. Wang, X.J. Huang, Z.L. Fang, Anal. Chem. 73 (2001) 4545.
[5] X.W. Chen, J.H. Wang, Talanta 69 (2006) 681.
[6] X.W. Chen, Z.R. Xu, B.Y. Qu, Y.F. Wu, J. Zhou, H.D. Zhang, J. Fang, J.H. Wang, Anal. Bioanal. Chem. 388 (2007) 157.
[7] N. Vachirapatama, M. Macka, P.R. Haddad, Anal. Bioanal. Chem. 374 (2002) 1082.
[8] E.P. de Jong, C.A. Lucy, Anal. Chim. Acta 546 (2005) 37.
[9] B.C. Yang, H.Z. Tian, J. Xu, Y.F. Guan, Talanta 69 (2006) 996.
[10] B.C. Yang, Y.F. Guan, Talanta 59 (2003) 509.
[11] A.E. Bruno, F. Maystre, B. Krattiger, P. Nussbaum, E. Gassmann, Trends Anal. Chem. 13 (1994) 190.
[12] H.H. Liu, P.K. Dasgupta, Anal. Chim. Acta 326 (1996) 13.
[13] J. Xu, B.C. Yang, H.Z. Tian, Y.F. Guan, Anal. Bioanal. Chem. 384 (2006) 1590.
[14] A.E. Bruno, B. Krattiger, F. Maystre, H.M. Widmer, Anal. Chem. 63 (1991) 2689.
[15] Y. Kurosu, Y. Asaki, M. Saito, J. High Res. Chromatogr. 14 (1991) 186.
[16] T. Anazawa, S. Takahashi, H. Kambara, Electrophoresis 20 (1999) 539.
[17] S.X. Lu, E.S. Yeung, J. Chromatogr. A 853 (1999) 359.

A PDDA/poly(2,6-pyridinedicarboxylic acid)-CNTs composite film DNA electrochemical sensor and its application for the detection of specific sequences related to PAT gene and NOS gene

Tao Yang, Wei Zhang, Meng Du, Kui Jiao *

Key Laboratory of Eco-chemical Engineering (Ministry of Education), College of Chemistry and Molecular Engineering, Qingdao University of Science and Technology, Qingdao 266042, China

Abstract

2,6-Pyridinedicarboxylic acid (PDC) was electropolymerized on the glassy carbon electrode (GCE) surface combined with carboxylic group-functionalized single-walled carbon nanotubes (SWNTs) by cyclic voltammetry (CV) to form PDC-SWNTs composite film, which was rich in negatively charged carboxylic group. Then, poly(diallyldimethyl ammonium chloride) (PDDA), a linear cationic polyelectrolyte, was electrostatically adsorbed on the PDC-SWNTs/GCE surface. DNA probes with negatively charged phosphate group at the 5′ end were immobilized on the PDDA/PDC-SWNTs/GCE due to the strong electrostatic attraction between PDDA and phosphate group of DNA. It has been found that modification of the electrode with PDC-SWNTs film has enhanced the effective electrode surface area and electron-transfer ability, in addition to providing negatively charged groups for the electrostatic assembly of cationic polyelectrolyte. PDDA plays a key role in the attachment of DNA probes to the PDC-SWNTs composite film and acts as a bridge to connect DNA with PDC-SWNTs film. The cathodic peak current of methylene blue (MB), an electroactive label, decreased obviously after the hybridization of DNA probe (ssDNA) with the complementary DNA (cDNA). This peak current change was used to monitor the recognition of the specific sequences related to PAT gene in the transgenic corn and the polymerase chain reaction (PCR) amplification of NOS gene from the sample of transgenic soybean with satisfactory results. Under optimal conditions, the dynamic detection range of the sensor to PAT gene target sequence was from 1.0×10^{-11} to 1.0×10^{-6} mol/L with the detection limit of 2.6×10^{-12} mol/L.
© 2008 Elsevier B.V. All rights reserved.

Keywords: 2,6-Pyridinedicarboxylic acid; Single-walled carbon nanotubes; PDDA; DNA sensor; PAT gene; NOS gene

1. Introduction

The demands for innovative analytical device capable of delivering the genetic information in a fast, simple and cheap manner at the sample source are becoming increasingly important. Electrochemical DNA biosensors offer promising routes for interfacing the DNA recognition and signal transduction elements, and are uniquely qualified for meeting the size, cost and power requirements of DNA diagnostics [1–3].

Nanotechnology has recently become one of the most exciting forefronts in analytical chemistry. A wide variety of nanomaterials, especially nanoparticles with different properties have found broad application in many kinds of analytical

methods. Owing to their small size (normally in the range of 1–100 nm), nanoparticles exhibit unique chemical, physical and electronic properties that are different from those of bulk materials, and can be used to construct novel and improved sensing devices, in particular, electrochemical sensors and biosensors. The discovery of carbon nanotubes (CNTs) in 1991 [4] opened up a new era in material science and nanotechnology. Due to its large surface area, wide electrochemical window, flexible surface chemistry and unique property to accelerate electronic transfer, CNTs have been recognized as an ideal nanomaterial to fabricate electrochemical DNA biosensors [5–10]. Usually, CNTs-modified electrodes are fabricated by dispersing CNTs solution onto electrode surface and dried in air. Thus, prepared electrodes are more powerful to transfer electrochemical DNA hybridization signal than bare electrodes. However, the unordered CNTs are always random lying on the electrode surface, and easily peel off from the substrate surface, badly

---

depressing the detection reproducibility of the sensors. In order to solve the problems, many novel electrochemical biosensors based on the copolymerization of conducting polymer monomer and carbon nanotubes have received significant interest because the incorporation of CNTs into polymers can obtain new composite materials, which possess the properties of each component with a synergistic effect [11–13]. For instance, Xu et al. [11] synthesized PPy/CNTs hybrid composite onto a glassy carbon electrode (GCE) surface by pyrrole electropolymerization in the presence of carboxylic groups ended multi-walled carbon nanotubes (MWNTs–COOH). During the electropolymerization process, MWNTs–COOH coated with PPy was firmly attached onto the GCE surface. Amino group ended ssDNA (NH_2-ssDNA) probe was linked onto the PPy/MWNTs–COOH/GCE by using EDAC, a widely used water-soluble carbodiimide for crosslinking amine and carboxylic acid group.

Recently, a novel technique for ultrathin film assembly has been developed which employed alternate adsorption of oppositely charged polyelectrolytes [14–17]. It is important that a complete charge reversal occurs at the surface after each adsorption step to obtain sufficient adsorption of each polyion. This electrostatic adsorption method is very simple and does not need any label to biomolecules. Therefore, it can overcome the disadvantages of the loss of the biomolecular activity and the complexity of the experiment resulting from the biomolecule label. Poly(diallyldimethyl ammonium chloride) (PDDA) is a linear positively charged polyelectrolyte, which can bind negatively charged phosphate of DNA through electrostatic attraction [18–20].

Over the last two decades, polymers have been proven to be a very suitable matrix for biosensors with fast response time, high sensitivity and great versatility in analytical tools [21,22]. Among them, 2,6-pyridinedicarboxylic acid (PDC) has been used in biosensors with different immobilized biomolecules in its films because of its excellent stability and biocapability [23]. In this paper, PDC and carboxylic group-functionalized single-walled carbon nanotubes (SWNTs) were copolymerized on the GCE surface, forming composite film, which was rich in negatively charged carboxylic group for the electrostatic assembly of cationic polyelectrolyte. The PDC-SWNTs composite film showed characteristics of both components, i.e. the good electron-transfer ability and the large surface area, and the potential synergistic effects. DNA probes with negatively charged phosphate group were attached on the PDC-SWNTs/GCE via PDDA. Results showed that the presented method for electrode modification was simple and efficient, offering a stable and powerful modification layer for immobilizing DNA and transducing nucleic acid hybridization. The electrochemical DNA biosensor was applied to the detection of the PAT gene sequences in the transgenic corn and the polymerase chain reaction (PCR) amplification of NOS gene from the sample of transgenic soybean with methylene blue (MB) as indicator using differential pulse voltammetry (DPV). The dynamic detection range of the sensor to PAT gene target sequence was from 1.0×10^{-11} to 1.0×10^{-6} mol/L, and the detection limit was 2.6×10^{-12} mol/L.

2. Experimental

2.1. Apparatus and reagents

A CHI 660B electrochemical analyzer (Shanghai CH Instrument Company, China), which was in connection with a glassy carbon-modified working electrode, a SCE reference electrode and a platinum wire counter electrode, was used for the electrochemical measurements. The pH values of all solutions were measured by a model pHS-25 digital acidimeter (Shanghai Leici Factory, China). The PCR amplification was performed by an Eppendorf Mastercycler Gradient PCR system (Germany).

2,6-Pyridinedicarboxylic acid and poly(diallyldimethyl ammonium chloride) were purchased from Sigma (St. Louis, MO, USA). SWNTs were purchased from Shenzhen nanotech. Port Co., Ltd. Both sodium dodecylsulfate (SDS) and methylene blue were obtained from Shanghai Reagent Company and used as received. All the chemicals are of analytical grade and solutions were prepared with doubly distilled water.

Materials for the detection of PAT gene sequences: the 20-base oligonucleotides probe (ssDNA), its complementary DNA sequence (cDNA, target DNA, namely a 20-base fragment of PAT gene sequence, which was selected according to the transgenic sequence of phosphinothricin acetyltransferase gene in transgenic corn), single-base mismatched DNA sequence, double-base mismatched sequence and noncomplementary DNA sequence (ncDNA) were synthesized by Beijing SBS Gene Technology Limited Company. Their base sequences are as below:

DNA probe (ssDNA): 5′- GCC ACA AAC ACC ACA AGA GT -3′;
Target DNA: 5′- ACT CTT GTG GTG TTT GTG GC -3′;
Single-base mismatched DNA: 5′- ACT CT<u>G</u> GTG GTG TTT GTG GC -3′;
Double-base mismatched DNA: 5′- ACT CT<u>G</u> GTG GTG <u>C</u>TT GTG GC -3′;
ncDNA: 5′- CAT GGT TGA TCC GTT CGC TG -3′.

Materials for the PCR amplification of NOS gene sample: one pair of primers (19-base for every primer). Their base sequences are as below:

Primer 1: 5′- ATC GTT CAA ACA TTT GGC A -3′;
Primer 2: 5′- ATT GCG GGA CTC TAT CAT A -3′.

The primer 1 was also used as the probe DNA for the detection of PCR amplification of NOS gene sample. The DNA template for PCR amplification was extracted from transgenic soybean according to the method of plant DNA mini prep kit (Shanghai Academy of Agricultural Sciences).

All oligonucleotides stock solutions of 20-base oligomers (1.0×10^{-6} mol/L) were prepared using Tris–HCl buffer solution (5.0 mmol/L Tris–HCl, 50.0 mmol/L NaCl, pH 7.0), which were stored at $4\,^{\circ}$C. More diluted solutions were obtained via diluting aliquot of the stock solution with doubly distilled

water prior to use. The hybridization solution was diluted with $2 \times$ SSC, which consisted of 0.30 mol/L NaCl and 0.03 mol/L sodium citrate tribasic dihydrate ($C_6H_5Na_3O_7 \cdot 2H_2O$).

2.2. PCR amplification of DNA template from transgenic soybean

To a 0.2 mL reaction tube were added 12.0 pmol primer 1, 12.0 pmol primer 2, 2.0 mmol/L $MgCl_2$, 0.2 mmol/L dATP, 0.2 mmol/L dCTP, 0.2 mmol/L dGTP, 0.2 mmol/L dTTP, 1.5 U Taq DNA polymerase (Promega, Wisconsin, USA), DNA template (50 ng DNA) and $10 \times$ reaction buffer B (Promega, Wisconsin, USA). The reaction total volume was 25 μL.

PCR procedure: DNA was denatured at 94 °C for 3 min. Each of the 40 cycles of amplification consisted of annealing at 56 °C for 20 s, extension at 72 °C for 20 s, denaturation at 94 °C for 30 s. Then another extension at 72 °C for 6 min was carried out.

2.3. Treatment of SWNTs

1.0 mg SWNTs were suspended in 40 mL 3:1 concentrated HCl/HNO_3 mixtures and sonicated in a water bath for 5 h, then filtered and washed with doubly distilled water until the filtrate became neutral, and finally dried under vacuum.

2.4. Fabrication of electrochemical DNA biosensor

For the electrochemical experiments, the GCE surface was freshly polished prior to each experiment with 0.3 and 0.05 μm α-Al_2O_3 paste, respectively, and was rinsed with doubly distilled water after each polishing step, finally cleaned ultrasonically in 95% ethanol and water, respectively, for 3 min.

1.67 mg PDC monomer and 1.0 mg SWNTs were dispersed in 10 mL *N,N*-dimethylformamide (DMF) with the aid of ultra-

sonic agitation and then 5 μL of this mixture was uniformly dropped on the GCE surface, followed by evaporating the solvent in air. After the modification, the electrode was rinsed with water for about 5 min to remove the loosely adsorbed carbon nanotubes. The PDC-SWNTs/GCE was obtained by dipping the above electrode into 0.1 mol/L KCl solution and then scanning for 16 cycles in the potential range from -0.6 to $+2.0$ V at 60 mV/s. Then the PDC-SWNTs/GCE was dipped in 3.0 mg/mL PDDA aqueous solution for 1 h to adsorb PDDA onto the PDC-SWNTs film. The obtained PDDA/PDC-SWNTs/GCE was rinsed with doubly distilled water and dried for further use.

The immobilization of ssDNA probe on the electrode surface was carried out with following procedure: The PDDA/PDC-SWNTs/GCE was immersed into 2.0 mL Tris–HCl buffer solution containing 1.0×10^{-6} mol/L probe DNA for 1 h at room temperature, followed by washing the electrode with 0.5% SDS solution for 5 min and then rinsing it with doubly distilled water to remove the mobilized ssDNA. Hybridization reaction was conducted by immersing the probe-captured electrode into a hybridization solution containing 1.0×10^{-6} mol/L target DNA at 42 °C for 1 h. Then the electrode was washed with 0.5% SDS solution for 5 min to remove the unhybridized DNA and this hybridization-modified electrode was denoted as dsDNA/PDDA/PDC-SWNTs/GCE. The schematic representation of the immobilization and hybridization of DNA on the PDDA/PDC-SWNTs/GCE was illustrated in Fig. 1.

2.5. Electrochemical measurements

The differential pulse voltammetric (DPV) cathodic signals of the accumulated MB were obtained in the B-R buffer (pH 6.0) containing 2.0×10^{-5} mol/L MB. DPV parameters: pulse amplitude 50 mV, pulse width 60 ms, pulse period 0.2 s. In order to obtain reliable response of MB at working electrode, the
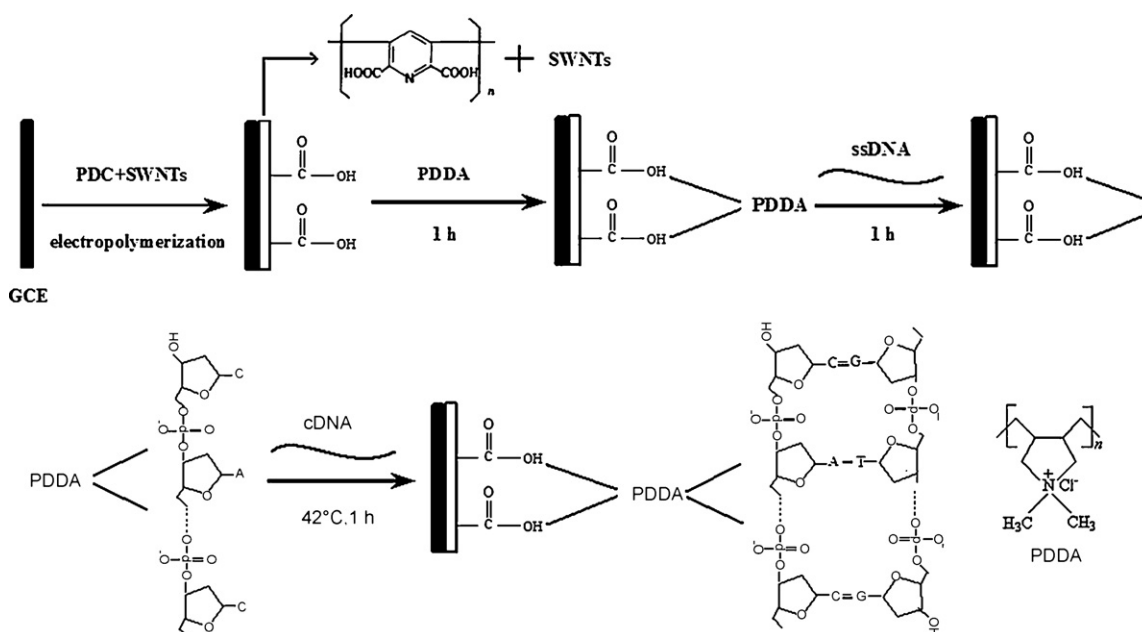

Fig. 1. Schematic representation of the immobilization and hybridization of DNA on the PDDA/PDC-SWNTs/GCE.
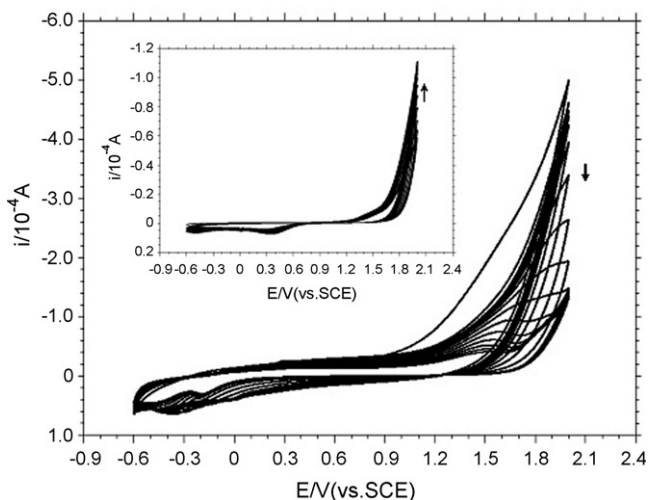
Fig. 2. Cyclic voltammograms of electropolymerization of PDC with and without (inset) SWNTs. Scan rate: 60 mV/s.

background value was recorded after the working electrode was immersed into the supporting electrolyte solution for 5 min to ensure equilibration. The electrode was transferred into the MB solution and accumulated for 5 min. Then the signal was recorded. The response of MB was obtained by subtracting the background value from above recorded signal.

Linear sweep voltammetric (LSV) measurements were performed in 1.0 mmol/L $K_3Fe(CN)_6$ and 1.0 mmol/L $K_4Fe(CN)_6$ solution with 0.1 mol/L KCl as the supporting electrolyte. The scan rate was 100 mV/s.

The electrochemical impedance spectroscopic (EIS) measurements were carried out in 5.0 mmol/L $[Fe(CN)_6]^{3-/4-}$ solution containing 0.1 mol/L KCl. The AC voltage amplitude was 5 mV and the voltage frequency range was from 10 kHz to 0.1 Hz. The applied potential was 0.172 V.

The reported result for every electrode in this paper was the mean value of three parallel measurements.

3. Results and discussion

3.1. Electropolymerization of PDC and SWNTs

A PDC-SWNTs composite film-modified electrode was fabricated by electropolymerization of PDC in the presence of SWNTs on the bare GCE. The experiment was performed in 0.1 mol/L KCl solution with cyclic voltammetric sweeps in the potential range from −0.6 to +2.0 V at 60 mV/s. The cyclic voltammograms of PDC electropolymerization with and without SWNTs (insert) were compared in Fig. 2, and the primary difference between the two electropolymerization processes is the current response. In the presence of SWNTs, the polymerization current was much larger than that without SWNTs, and the polymerization current decreased gradually with an increase in the scanning number, which is opposite to the current response without SWNTs. The different response of the current between the two polymerization processes may be due to the reason that PDC could effectively reduce the current enhancement caused by the high electron-transfer ability of SWNTs [24].

The method for preparing PDC-SWNTs composite film was investigated. The PDC-SWNTs composite film was prepared with three different methods, namely, prepolymerization, copolymerization and postpolymerization. Prepolymerization meant that the PDC film was firstly electropolymerized on the bare GCE and then the SWNTs were dropped on the PDC/GCE. Postpolymerization implied that the SWNTs were firstly dropped on the bare GCE surface and evaporated to dryness and then the PDC film was electropolymerized on the SWNTs/GCE. The method of copolymerization was specifically shown in our experiments. The results showed that the copolymerized PDC-SWNTs composite film could immobilize much larger amount of PDDA. Hence, this approach was used in our experiments.

The electropolymerization process was found to be affected by the cycling potential range and cycle number for copolymerizing PDC and SWNTs. Different cycling potential ranges (the low was −0.6 V and the high potential varied from 2.0 to 2.5 V) were used to fabricate PDC-SWNTs composite film on the electrode surface. Experimental results showed that there was no significant signal difference observed for different high potentials. The cycle number of copolymerization was investigated from 10 to 20 cycles. Experimental results showed that an even and stable composite film with fine electric conductivity was obtained when copolymerizing for 16 cycles.

3.2. Immobilization and hybridization of ssDNA probe on the PDDA/PDC-SWNTs/GCE

3.2.1. Monitoring DNA immobilization and hybridization by electrochemical impedance spectroscopy and linear sweep voltammetry

The electrochemical impedance spectroscopy can offer information on the impedance changes of the electrode surface during the modification process [25]. Nyquist diagrams of 5.0 mmol/L $[Fe(CN)_6]^{3-/4-}$ at different modified electrodes were illustrated in Fig. 3. The Nyquist diagram includes a semicircle part and a linear part. The semicircle part at higher frequencies corresponds to the electron-transfer-limited process, and the linear part at lower frequencies corresponds to the diffusion process. The surface electron-transfer resistance, R_{et}, derived from the semicircle domains of impedance spectra equals to $2.83 \times 10^3\,\Omega$ for the bare GCE (curve a). The curve b was the Nyquist diagram at the PDC-SWNTs/GCE, with its R_{et} value of $0.51 \times 10^3\,\Omega$. As compared with curve a, the R_{et} value of curve b decreased obviously. This could be mainly attributed to the large surface area and the attractive electric conductivity of SWNTs, even though the negative charge of PDC could produce repulsion to $[Fe(CN)_6]^{3-/4-}$. If there were no SWNTs, the R_{et} value at the PDC/GCE was larger than that at the bare GCE (the curve was not presented). After the PDC-SWNTs composite film was modified with PDDA, its R_{et} value was $1.18 \times 10^3\,\Omega$ (curve c), which was a little larger than that of curve b. This indicated that the conductivity of the electrode reduced after the modification of PDDA. The curve d was the Nyquist diagram at the probe ssDNA/PDDA/PDC-SWNTs/GCE ($R_{et} = 4.77 \times 10^3\,\Omega$). As compared with curve c, the R_{et} value of the electrode was
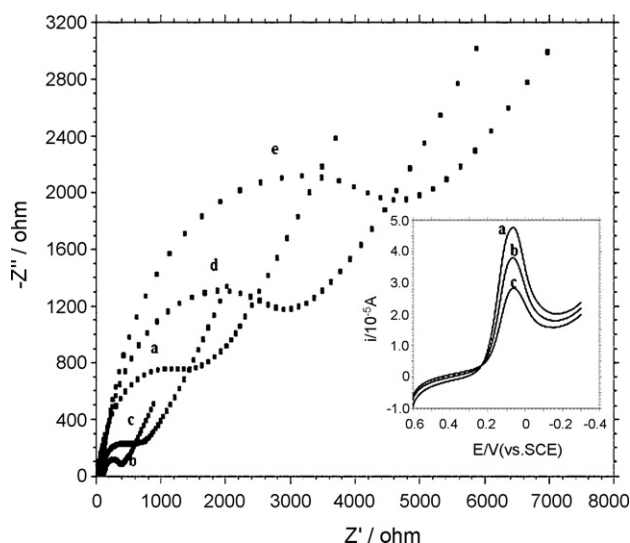
Fig. 3. Nyquist plots recorded at (a) bare GCE, (b) PDC-SWNTs/GCE, (c) PDDA/PDC-SWNTs/GCE, (d) ssDNA/PDDA/PDC-SWNTs/GCE and (e) dsDNA/PDDA/PDC-SWNTs/GCE. (Insert): linear sweep voltammograms of 1.0 mmol/L [Fe(CN)$_6$]$^{3-/4-}$ in 0.1 mol/L KCl at (a) PDDA/PDC-SWNTs/GCE, (b) ssDNA/PDDA/PDC-SWNTs/GCE and (c) dsDNA/PDDA/PDC-SWNTs/GCE. Scan rate: 100 mV/s.

enlarged very obviously. After the probe-modified electrode was hybridized with the complementary DNA sequence, the R_{et} value of the electrode was 7.25×10^3 Ω (curve e). As compared with curve d, the R_{et} value of curve e was further enlarged. The negatively charged phosphate backbone of probe ssDNA prevented [Fe(CN)$_6$]$^{3-/4-}$ from reaching the electrode surface, and led to larger R_{et} value. After the hybridization of DNA probe with the complementary DNA sequence, there were more negative charges on the surface and the DNA-modified layer became thicker, leading to the further increase of R_{et} value.

The immobilization and hybridization of ssDNA probe on the PDDA/PDC-SWNTs/GCE were also investigated in 1.0 mmol/L [Fe(CN)$_6$]$^{3-/4-}$ solution by linear sweep voltammetry, as shown in Fig. 3 (insert). The curve b showed the electrochemical behavior of [Fe(CN)$_6$]$^{3-/4-}$ at the ssDNA/PDDA/PDC-SWNTs/GCE, the peak current of which was lower than that at the PDDA/PDC-SWNTs/GCE (curve a). After the hybridization of DNA probe with the complementary DNA sequence, the peak current at the dsDNA/PDDA/PDC-SWNTs/GCE further decreased (curve c). The change in the linear sweep voltammograms was another strong proof for ssDNA probe having been immobilized on the electrode surface and successfully hybridized with its complementary sequence.

3.2.2. Electrochemical behavior of MB at different modified electrodes

MB is an organic dye that belongs to the phenothiazine family. It could bind specifically to the guanine (G) bases in DNA molecules [26]. MB as an electroactive indicator has been used for electrochemical sensing of DNA hybridization at electrode surface [27,28]. After ssDNA was hybridized with the complementary sequence, the current signal of MB decreased due to the inaccessibility of MB to dsDNA, the guanine bases of which
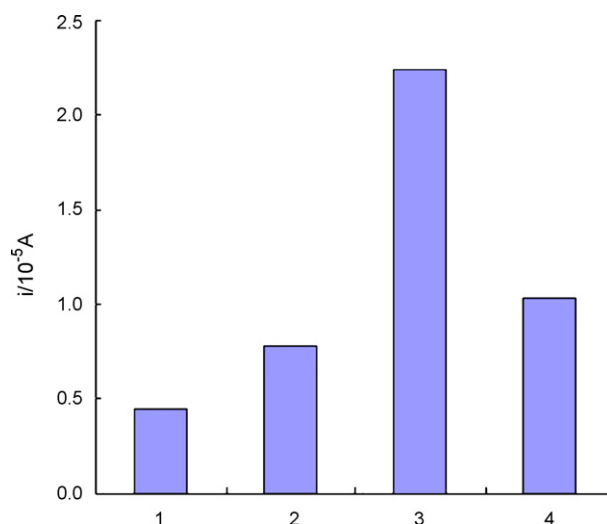

Fig. 4. Histograms of the differential pulse voltammetric signals of 2.0×10^{-5} mol/L MB at (1) bare GCE, (2) PDDA/PDC-SWNTs/GCE, (3) ssDNA/PDDA/PDC-SWNTs/GCE and (4) dsDNA/PDDA/PDC-SWNTs/GCE. DPV parameters: pulse amplitude 50 mV, pulse period 0.2 s, pulse width 60 ms.

are packed between the bulky double helix. Fig. 4 shows the histograms of the DPV signals of 2.0×10^{-5} mol/L MB at the bare GCE (1), PDDA/PDC-SWNTs/GCE (2), ssDNA/PDDA/PDC-SWNTs/GCE (3) and dsDNA/PDDA/PDC-SWNTs/GCE (4). Although the existence of PDC-SWNTs composite film greatly enlarged the surface area of the electrode, the signal obtained at the PDDA/PDC-SWNTs/GCE only increased a little as compared with that at the bare GCE, which may be due to cationic PDDA providing some restriction of access of positively charged MB to the electrode surface. Immobilization of ssDNA on the PDDA/PDC-SWNTs/GCE resulted in a large increase of the DPV signal of MB, which could be attributed to the affinity of MB to the guanine bases exposed out of probe ssDNA, and hence a great amount of MB accumulation occurred at this surface. A significant decrease in the DPV signal of MB was observed after hybridized with the complementary DNA sequence, because the interaction of MB and guanine base residues of the probe was prevented by duplex formation on the electrode surface. The results confirmed that the PDDA/PDC-SWNTs film provided an ideal platform for ssDNA immobilization and hybridization.

The surface coverage of DNA probes on the electrode directly influenced the sensitivity of DNA hybridization assay. Because of the affinity of MB to the guanine bases in ssDNA molecules, the probe density on the electrode surface could be calculated according to the signals of MB. That is to say, the charge quantity of the reduction process of MB is proportional to the mol quantity of guanine bases accumulated on ssDNA probe-modified electrode surface. In this experiment, we obtained the charge quantity of MB reduction process from the cyclic voltammogram, which is 1.425×10^{-5} C. The mol quantity of MB on the electrode surface was calculated to be 7.397×10^{-11} mol according to the equation: $N = Q/neN_A$, where N represents the mol quantity of MB; Q is the charge quantity of MB reduction process; n is the number of electrons participating in the reaction, $n = 2$ in this experiment; e is the charge quantity of one electron, which is 1.6×10^{-19} C; N_A represents Avogadro's number,

and its value is 6.02×10^{23} mol^{-1}. One MB molecule can combine one guanine base, and every PAT ssDNA probe sequence contains three guanine bases, so the surface coverage of DNA probes on the electrode should be one-third of the quantity of MB. An independent set of experiments showed that the average probe surface coverage on the PDDA/PDC-SWNTs/GCE was 3.490×10^{-10} mol/cm^2 ($n = 3$).

3.3. The stability of probe ssDNA/PDDA/PDC-SWNTs/GCE

DNA and other polyanions can be effectively immobilized on the surface of the polycationic polymer film of PDDA through electrostatic attraction. Five probe-modified electrodes prepared independently under the same conditions were simultaneously immersed into a 2.0 mL 0.1 mol/L NaOH solution for 60 min. After the immersion, hardly any DNA absorption at 260 nm in UV–vis spectrum as for the immersed solution was observed using the 0.1 mol/L NaOH solution as baseline correction, suggesting that the ssDNA probe is not eluted from the surface of the modified electrode. The same experiments using 0.1 mol/L HCl, Tris–HCl buffer (pH 7.0) and $2 \times$ SSC solution (pH 7.5), respectively, replacing 0.1 mol/L NaOH solution, were conducted; also, no DNA absorption at 260 nm of the immersed solution was observed. The above results showed that the probe ssDNA/PDDA/PDC-SWNTs/GCE was of high stability and could be applied for the hybridization detection.

3.4. Optimization of experimental conditions

The adsorption time of cationic polymer PDDA affected the immobilization amount of ssDNA probe. The PDC-SWNTs/GCE was dipped in 3.0 mg/mL PDDA aqueous solution for different times. With the increase of the adsorption time from 10 to 60 min, the DPV cathodic peak current of [Fe(CN)$_6$]$^{3-/4-}$ at the PDDA/PDC-SWNTs/GCE increased significantly. The response signal tended to stableness when the adsorption time reached 60 min or above. Therefore, the optimal adsorption time was 60 min.

The immobilization time of ssDNA probe on the PDDA/PDC-SWNTs/GCE was also experimented. As the immobilization time increased, the DPV cathodic peak current difference of MB between ssDNA/PDDA/PDC-SWNTs/GCE and PDDA/PDC-SWNTs/GCE rose gradually at first (up to 1 h) and then reached a constant level. An immobilization time of 1 h was used in experiments.

After the hybridization for 1 h at different temperatures, such as 25, 32, 42, 60 and 70 °C, the DPV cathodic peak current difference of MB (Δi_{pc}) between before and after hybridization at the given hybridization temperature was tested. The results indicated that Δi_{pc} value increased with the increase of the hybridization temperature from 25 to 42 °C. With further increase of the hybridization temperature, the Δi_{pc} value decreased slightly. Therefore, the optimal hybridization temperature was 42 °C.

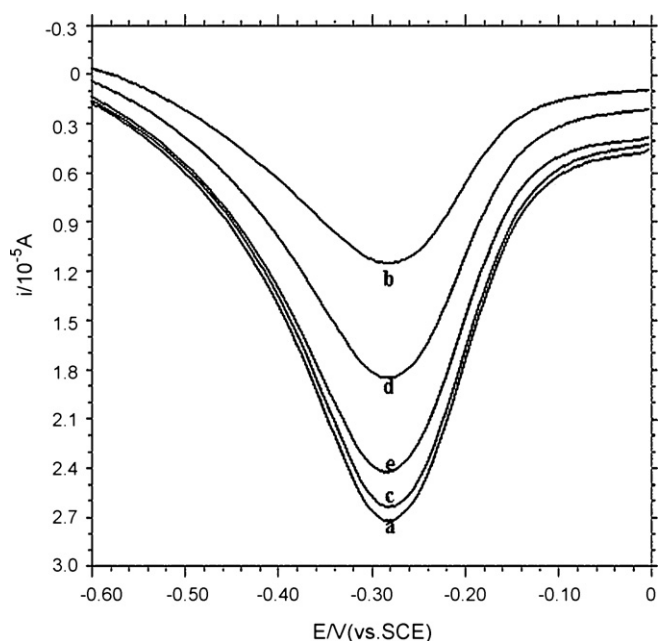Fig. 5. Differential pulse voltammograms using 2.0×10^{-5} mol/L MB as the redox indicator at the ssDNA/PDDA/PDC-SWNTs/GCE without hybridization (a), hybridized with complementary DNA sequence (b), noncomplementary DNA sequence (c), single-base mismatched DNA sequence (d) and double-base mismatched DNA sequence (e). Conditions were the same as in Fig. 4.

3.5. The selectivity of the DNA biosensor

The selectivity of this assay was investigated by using the ssDNA/PDDA/PDC-SWNTs/GCE probe to hybridize with different DNA sequences related to PAT gene. Fig. 5 shows the DPV curves of MB at the ssDNA probe-modified electrode (a) and after hybridization with the complementary DNA sequence (b), the noncomplementary sequence (c), single-base mismatched sequence (d) and double-base mismatched sequence (e). The highest MB DPV signal was obtained at the ssDNA/PDDA/PDC-SWNTs/GCE, because MB has a strong affinity to the free guanine bases of ssDNA and hence the greatest amount of MB accumulation occurred at this electrode surface. A significant decrease of DPV signal of MB was observed after the ssDNA probe was hybridized with the complementary target sequence, because the binding of MB to guanine bases of the probe was prevented by duplex formation on the electrode surface. The decrease of the peak current value of MB was negligible after the ssDNA probe was hybridized with the non-complementary sequence, indicating that hybridization reaction did not happen. After the ssDNA probe was hybridized with the single-base mismatched sequence and the double-base mismatched sequence, the decreases of the peak current values of MB were much smaller than that obtained from the hybridization with the complementary DNA sequence. The single-base mismatched sequence and the double-base mismatched sequence could also be recognized via comparing the decrease of the peak current value of MB. The results demonstrated that this electrochemical DNA biosensor displayed a high selectivity for the hybridization detection.

3.6. Reproducibility and regeneration of the sensor

To characterize the reproducibility of the sensor, repetitive experiments including electrochemical polymerization, the adsorption of PDDA, the immobilization of ssDNA and the detection of DNA hybridization were carried out. The results of five electrodes prepared independently under the same conditions showed a relative standard deviation (RSD) of 5.16%, showing the good reproducibility of the electrochemical DNA biosensor.

By immersing the hybridized electrode into boiling water for 10 min, then cooled down with the ice salt bath, the dsDNA was hot denatured, and an increase of the DPV signal of MB was observed. Successive experiments showed that the DNA biosensor could be regenerated for five times without losing its sensitivity. The peak current value of the ssDNA electrode after five times of hot denaturation was 85% of its initial signal and the RSD for five repetitive measurements was 9.1%, indicating the fine regeneration ability of the biosensor.

3.7. Detection of DNA specific sequences of PAT gene

The sensitivity of the electrochemical hybridization assay was explored by using the immobilized probe to hybridize the PAT gene target sequence of different concentrations. The average DPV peak current difference of MB between before and after hybridization was linear with the logarithmic value of the PAT target sequence concentration ranging from 1.0×10^{-11} to 1.0×10^{-6} mol/L (shown in Fig. 6). The regression equation was $y = -0.2059x + 2.4501$ (where x is the negative logarithmic value of the PAT target sequence concentration, mol/L; y is the

Fig. 7. Detection of PCR-amplified sample of NOS gene using 2.0×10^{-5} mol/L MB recorded at (a) PDDA/PDC-SWNTs/GCE, (b) PCR probe electrode and (c) the electrode hybridized with PCR-amplified real sample of NOS gene. Conditions were the same as in Fig. 4.

DPV peak current difference of MB between before and after hybridization, 10^{-5} A), and the regression coefficient (R) of the linear curve was 0.9951. A detection limit of 2.6×10^{-12} mol/L of the PAT target sequence can be estimated based on 3σ (where σ is the relative standard deviation of the blank solution, $n = 11$).

3.8. Detection of PCR-amplified real sample of NOS gene

The hybridization detection of PCR-amplified real sample of NOS gene was also conducted on this electrochemical DNA biosensor under the same conditions above. The PCR-amplified sample was diluted with 5.0 mmol/L Tris–HCl buffer solution (pH 7.0) and denatured by heating it in a boiling water bath for 5 min, and then cooled down in an ice bath for 2 min. The primer 1 (probe) of NOS gene was immobilized on the PDDA/PDC-SWNTs/GCE. Then the electrode was immersed into the solution of the denatured PCR sample for hybridization. The detection results were shown in Fig. 7. The MB signal at the NOS gene probe electrode (b) was much higher than that at the PDDA/PDC-SWNTs/GCE (a). An obvious decrease of the MB signal was obtained after the hybridization of the probe with PCR real sample (c). This significant difference of the MB signals between at the NOS gene probe electrode and at the hybridized electrode confirmed that this DNA biosensor could detect the PCR-amplified real sample effectively.

4. Conclusion

In this article, it had been found that the modification of the GCE with PDC-SWNTs composite film could effectively enhance the activity of the electrode surface. Cationic PDDA adsorbed on the PDC-SWNTs composite film-modified electrode was used to immobilize the probe DNA for fab-
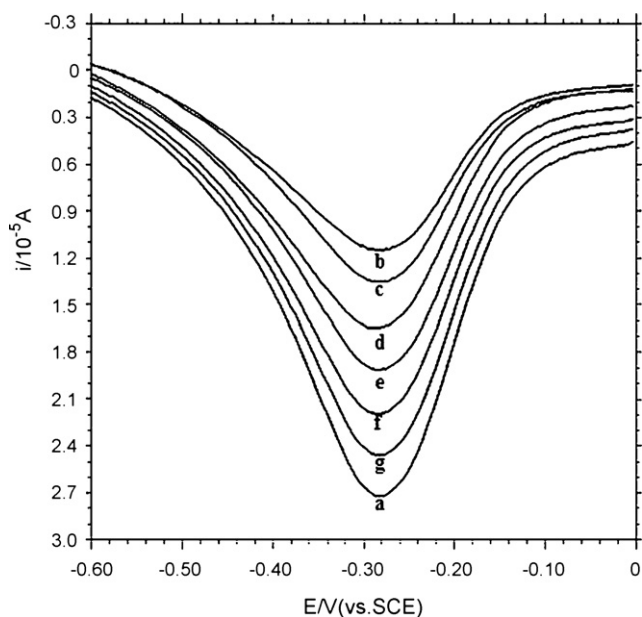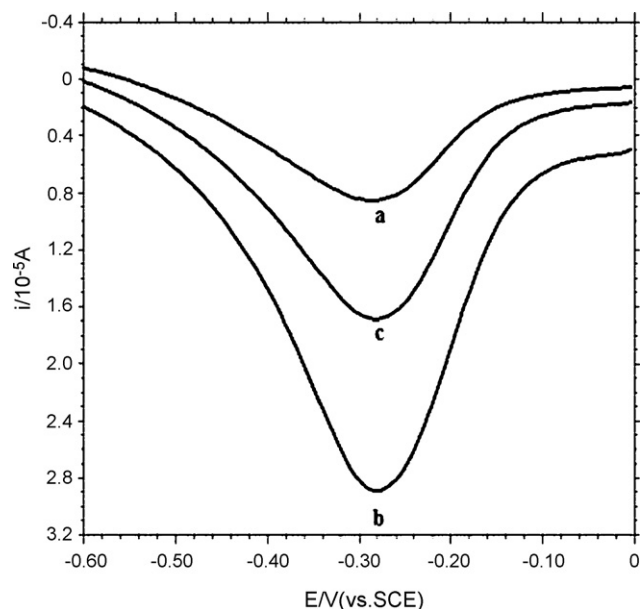

Fig. 6. Differential pulse voltammograms using 2.0×10^{-5} mol/L MB as the redox indicator for different target PAT gene sequence concentrations: (a) 0 mol/L, (b) 1.0×10^{-6} mol/L, (c) 1.0×10^{-7} mol/L, (d) 1.0×10^{-8} mol/L, (e) 1.0×10^{-9} mol/L, (f) 1.0×10^{-10} mol/L and (g) 1.0×10^{-11} mol/L. Conditions were the same as in Fig. 4.

ricating electrochemical DNA biosensor. The immobilization and hybridization of the probe DNA were characterized by linear sweep voltammetry, electrochemical impedance spectroscopy and differential pulse voltammetry. The biosensor has fine selectivity, high sensitivity, satisfactory reproducibility and regeneration ability, and was applied to the detection of the PAT gene sequences and the PCR-amplified real sample of NOS gene.

Acknowledgements

References

[1] S. Rauf, H. Nawaz, K. Akhtar, M.A. Ghauri, A.M. Khalid, Biosens. Bioelectron. 22 (2007) 2471.

[2] J.G. Lee, K. Yun, G.S. Lim, S.E. Lee, S. Kim, J.K. Park, Bioelectrochemistry 70 (2007) 228.

[3] G.U. Flechsig, T. Reske, Anal. Chem. 79 (2007) 2125.

[4] S. Lijima, Nature 354 (1991) 56.

[5] A. Ferancova, R. Ovadekova, M. Vanckova, A. Satka, R. Viglasky, J. Zima, J. Barek, J. Labuda, Electroanalysis 18 (2006) 163.

[6] A. Erdem, P. Papakonstantinou, H. Murphy, Anal. Chem. 78 (2006) 6656.

[7] R. Ovadekova, S. Jantova, S. Letasiova, I. Stepanek, J. Labuda, Anal. Bioanal. Chem. 386 (2006) 2055.

[8] X.W. Tang, S. Bansaruntip, N. Nakayama, E. Yenilmez, Y.L. Chang, Q. Wang, Nano Lett. 6 (2006) 1632.

[9] Y.F. Ma, S.R. Ali, A.S. Dodoo, H.X. He, J. Phys. Chem. B 110 (2006) 16359.

[10] S. Bollo, N.F. Ferreyra, G.A. Rivas, Electroanalysis 19 (2007) 833.

[11] Y. Xu, X.Y. Ye, L. Yang, P.G. He, Y.Z. Fang, Electroanalysis 18 (2006) 1471.

[12] E. Granot, B. Basnar, Z. Cheglakov, E. Katz, I. Willner, Electroanalysis 18 (2006) 26.

[13] M.C. Kum, K.A. Joshi, W. Chen, N.V. Myung, A. Mulchandani, Talanta 74 (2007) 370.

[14] T. Noguchi, J.I. Anzai, Langmuir 22 (2006) 2870.

[15] J.H. Kim, S. Fujita, S. Shiratori, Colloids Surf. A 284 (2006) 290.

[16] G.Q. Jiang, A. Baba, R. Advincula, Langmuir 23 (2007) 817.

[17] H. Hata, Y. Kobayashi, T.E. Mallouk, Chem. Mater. 19 (2007) 79.

[18] Y.L. Zhou, S.N. Mao, Y.Z. Li, W.B. Chang, Microchim. Acta 144 (2004) 191.

[19] P.G. He, M. Bayachou, Langmuir 21 (2005) 6086.

[20] Y. Zhang, N.F. Hu, Electrochem. Commun. 9 (2007) 35.

[21] G.C. Yang, Y. Shen, M.K. Wang, H.J. Chen, B.F. Liu, S.J. Dong, Talanta 68 (2006) 741.

[22] K. Arora, N. Prabhakar, S. Chand, B.D. Malhotra, Anal. Chem. 79 (2007) 6152.

[23] J. Yang, T. Yang, Y.Y. Feng, K. Jiao, Anal. Biochem. 365 (2007) 24.

[24] C.X. Li, Y.L. Zeng, Chin. J. Anal. Chem. 34 (2006) 999.

[25] A.X. Li, F. Yang, Y. Ma, X.R. Yang, Biosens. Bioelectron. 22 (2007) 1716.

[26] W.R. Yang, M. Ozsoz, D.B. Hibbert, J.J. Gooding, Electroanalysis 14 (2002) 1299.

[27] M.H.P. Azar, M.S. Hejazi, E. Alipour, Anal. Chim. Acta 570 (2006) 144.

[28] K.J. Feng, Y.H. Yang, Z.J. Wang, J.H. Jiang, G.L. Shen, R.Q. Yu, Talanta 70 (2006) 561.

Development of a method for the determination of 9 currently used cotton pesticides by gas chromatography with electron capture detection

Baohong Zhang [a,b,*,1], Xiaoping Pan [a,c,1], Louise Venne [a], Suzy Dunnum [a],
Scott T. McMurry [a], George P. Cobb [a], Todd A. Anderson [a]

[a] *Department of Environmental Toxicology, The Institute of Environmental and Human Health,*
Texas Tech University, Lubbock, TX 79409-1163, United States
[b] *Department of Biology, East Carolina University, Greenville, NC 27858, United States*
[c] *Department of Chemistry, Western Illinois University, Macomb, IL 61455, United States*

Abstract

A reliable, sensitive, and reproducible method was developed for quantitative determination of nine new generation pesticides currently used in cotton agriculture. Injector temperature significantly affected analyte response as indicated by electron capture detector (ECD) chromatograms. A majority of the analytes had an enhanced response at injector temperatures between 240 and 260 °C, especially analytes such as acephate that overall had a poor response on the ECD. The method detection limits (MDLs) were 0.13, 0.05, 0.29, 0.35, 0.08, 0.10, 0.32, 0.05, and 0.59 ng/mL for acephate, trifuralin, malathion, thiamethozam, pendimethalin, DEF6, acetamiprid, brifenthrin, and λ-cyhalothrin. This study provides a precision (0.17–13.1%), accuracy (recoveries = 88–107%) and good reproducible method for the analytes of interest. At relatively high concentrations, only λ-cyhalothrin was unstable at room temperature (20–25 °C) and 4 °C over 10 days. At relatively low concentrations, acephate and acetamiprid were also unstable regardless of temperature. After 10 days storage at room temperature, 30–40% degradation of λ-cyhalothrin was observed. It is recommended that acephate, acetamiprid, and λ-cyhalothrin be stored at −20 °C or analyzed immediately after extraction.
© 2008 Elsevier B.V. All rights reserved.

Keywords: Pesticides; Gas chromatography; Electron capture detection; Cotton

1. Introduction

Planted in approximately 70 tropical/subtropical and temperate countries, cotton is one of the most important fiber and economic crops; about 20 million cotton farmers grow 33.5 million hectares of cotton around the world [1,2]. Although many factors affect cotton yield, insect pests and weeds are two major constraints to cotton production. More than 1300 insect species have been reported as cotton pests worldwide [2,3]. Although transgenic Bt cotton has played an important role in pest control [1,4,5], the primary approach to pest control is still through the use of synthetic chemicals. To control pests and weeds, more than 12 kg of pesticide per ha is required annually [6].

One of the most important aspects in minimizing the potential hazards of pesticides to human and environmental health is to monitor pesticide residues [7] and develop best management practices based on these monitoring data. To better monitor residues of pesticides in different media, efficient methods for extraction and determination of pesticides in soil, sediment, water, and food need to exist. As new pesticides are incorporated into agricultural practices, new methods for the determination of those new pesticides must be developed. In this paper, we report on a reliable method for the determination of nine currently used cotton pesticides at trace levels.

2. Experimental

2.1. Chemicals and reagents

Pesticide standards were obtained commercially. Acephate, trifuralin, malathion, pendimethalin, DEF6, brifenthrin and

---

* Corresponding author at: Department of Biology, East Carolina University, Greenville, NC 27858, United States.
  E-mail address: zhangb@ecu.edu (B. Zhang).
[1] Both the authors contributed equally and both are co-first authors.

λ-cyhalothrin were purchased from AccuStandard Inc. (New Haven, CT, USA) while acetamiprid and thiamethoxzam were obtained from ChemService Inc. (West Chester, PA, USA). Methanol, acetone, hexane, acetonitrile were purchased from Fisher Scientific (Pittsburgh, PA, USA). Anhydrous Na_2SO_4 was purchased from VWR (West Chester, PA, USA). C_{18} solid-phase extraction (SPE) cartridges (500 mg) were obtained from Fisher Scientific (Pittsburgh, PA, USA). Ultra-pure water (>18 MΩ) was prepared by ultrafiltration with a Mili-Q purification system from Millipore (Bedford, MA, USA). All solvents were HPLC or analytical grade.

2.2. Instruments and sample analysis

An HP 6890 series gas chromatograph (GC) was employed to analyze the test pesticides. The GC was equipped with an electron capture detector (ECD) and an autosampler (Agilent, Palo Alto, California, USA). The GC-ECD was controlled by Chemstation software from Hewlett–Packard (Agilent, Palo Alto, California, USA).

A 30 m × 0.32 mm × 0.25 μm DB-5 column from J&W Scientific (Folsom, CA, USA) was used to separate the analytes. The carrier gas was helium (99.99% purity), and was operated at a constant flow rate during the run (9.2 mL/min). The makeup gas for the detector was argon:methane (95:5) at a combined flow rate of 60.0 mL/min. The injection volume was 2 μL in the splitless mode. The injector temperature was 240 °C except in experiments on the optimization of analytical parameters in which different injector temperatures (100–300 °C) were evaluated. The detector temperature was 270 °C and was operated in the constant current mode. Although the oven temperature program varied initially during optimization experiments, the following temperature program was adopted for all subsequent studies reported herein: 110 °C for 1 min, increased to 200 °C at 15 °C/min with a hold of 2 min, then raised to 269 °C at 15 °C/min, and finally held at 269 °C for 6 min.

2.3. Calibration curves and method detection limit

For each analyte, 10 standard concentration levels (1, 2, 5, 10, 20, 50, 100, 200, 500, and 1000 ng/mL) were prepared and analyzed in order of increasing concentration. Calibration curves were constructed by plotting concentration of each pesticide versus ECD response (peak area). The method detection limit (MDL) for each pesticide was determined by the analysis of seven spiked samples at 1 ng/mL for each analyte, and was calculated using the following formula: MDL = 3.14 × S.D., where S.D. is the standard deviation of the measurements of seven spiked samples, and 3.14 is the Student's t-value at the 99% confidence level (t = 3.14 for 6 degrees of freedom).

2.4. Recovery, accuracy and precision of developed method

The recovery, accuracy, and precision of the developed method were determined at three concentration levels (10, 100, and 1000 ng/mL) for each analyte. Each concentration contained five replicates (spiked samples). Recovery (%) was

determined by comparing the measured concentration to the nominal concentration. Precision was calculated by using the relative standard deviation (R.S.D.). The intra-day precision (%) was determined by repeated injections (n = 5) of the same samples on a single day. The inter-day precision (%) was determined by repeated injections on 5 different days. Accuracy was calculated by the equation: (mean measured concentration/nominal concentration) × 100.

2.5. Analyte stability in extraction solvent

The stability of analytes in extraction solvent (acetonitrile) was tested at three temperatures: room temperature (~20–25 °C), 4, and −20 °C. After 0, 1, 2, 4, 6, 8, and 10 days of storage at the three conditions, extracts were analyzed by GC-ECD. Each treatment was repeated three times, and the stability was calculated by comparing the measured analyte concentration with the nominal concentration.

2.6. Method application

Natural water and sediment samples were collected from Playa lakes on the Southern High Plains of West Texas. Playa lakes were chosen because they are representative of surface water receiving pesticide runoff from cotton-growing areas. Water samples (1 L) were extracted using C_{18} SPE cartridges at a flow rate of 5–6 mL/min. Analytes were eluted with 6–10 mL acetonitrile, concentrated to 2 mL using nitrogen evaporation, and then filtered through 0.2 μm PTFE membranes (Millipore, Bedford, MA, USA) into amber GC vials.

Sediments (5 g) were air-dried, mixed with 10 g anhydrous Na_2SO_4, loaded into 22-mL cells, and extracted (hexane:acetonitrile, 1:1) using a Dionex Accelerated Solvent Extractor (Model 200, Salt Lake City, UT, USA) following a procedure previously reported [8,9]. Extracts were concentrated to 1–2 mL using nitrogen evaporation and then cleaned using 1 g Florisil® SPE cartridges. The final volume of cleaned extracts was adjusted to 2 mL with 1:1 hexane:acetonitrile, filtered through a 0.45 μm PTFE membrane filter, and stored at 4 °C prior to GC analysis.

2.7. Statistical analysis

All collected data were processed using standard statistical software (SigmaPlot, Version 8.0, SPSS, Chicago, IL, USA). The difference in ECD response at different injector temperatures and the stability of each analyte under different storage conditions were evaluated by ANOVA. A significance level of α = 0.05 was used in all comparative statistics.

3. Results and discussion

3.1. Optimization of analytical parameters

The oven temperature program and carrier gas flow rate were initially optimized to provide separation of the target analytes. The analytical conditions described previously allowed for the

Table 1
Retention times and method detection limits of analytes (mean ± S.D.)

Compound	Retention time (min) (mean ± S.D.)	MDL (ng/mL)	Reporting limit (ng/mL)	Best injector temperature (°C)
Acephate	3.62 ± 0.01	0.13	2.0	240
Trifuralin	5.58 ± 0.01	0.05	0.5	260
Malathion	7.73 ± 0.01	0.29	1.0	200
Thiamethoxzam	8.20 ± 0.01	0.35	1.0	140
Pendimethalin	8.53 ± 0.01	0.08	0.5	240
DEF6	9.91 ± 0.01	0.10	0.5	240
Acetamiprid	12.13 ± 0.01	0.32	1.0	300
Brifenthrin	12.34 ± 0.01	0.05	0.5	240
λ-Cyhalothrin	13.17 ± 0.01	0.59	0.5	260

separation of the nine analytes (Table 1). ECD response varied by analyte, with acetamiprid, trifuralin, DEF6, and λ-cyhalothrin producing the best response (Fig. 1).

Injector temperature significantly affected the response of analytes on the ECD (Fig. 2). At an injector temperature of 100 °C, all analytes had poor to no response. For most analytes, the detector response increased with increasing injector temperature (Fig. 2), with the highest response at injector temperatures = 240–260 °C. However, the ECD response change with injector temperature was different among the different analytes. Acephate was the most sensitive analyte to injector temperature; a subtle change in injector temperature sharply changed the detector response. λ-Cyhalothrin, thiamethoxzam, and malathion were also sensitive to changes in injector tem-

perature. ECD response for the other analytes only varied at low injector temperatures. It appeared that an injector temperature of 240 °C provided the most suitable temperature condition for detection of all nine analytes; that temperature was selected for subsequent studies including the analysis of environmental samples described below.

3.2. Calibration curve and method detection limit (MDL)

Using the optimized GC-ECD conditions, a sharp peak corresponding to each analyte was obtained. For all analytes tested over a concentration range of 1–1000 ng/mL, the ECD response was linear with excellent regression coefficients ($r^2 > 0.99$ with the exception of acetamiprid) (Table 2). The MDLs for the
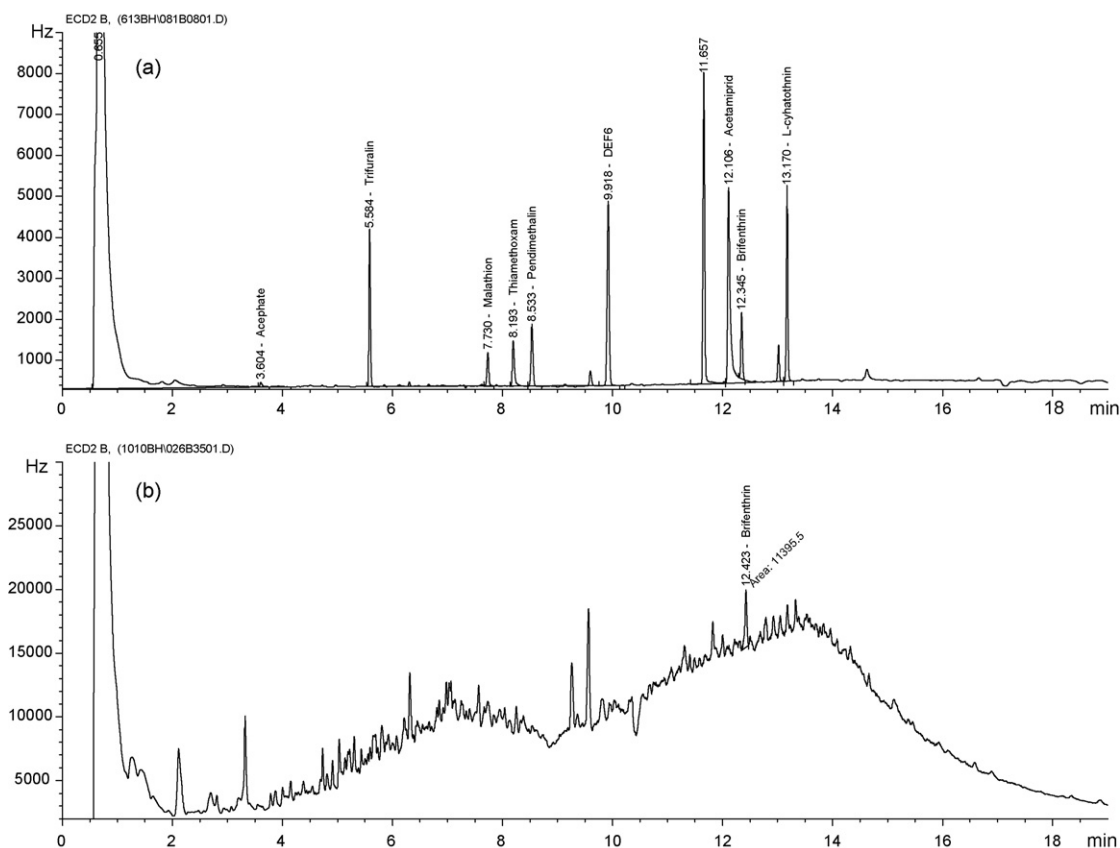

Fig. 1. Representative chromatograms of (a) nine pesticide mixture; (b) Playa water sample.

Table 2
Parameters for the calibration curves of the analytes ($Y = aX + b$)

Compound	a	b	r^2	Concentration range (ng/mL)
Acephate	4.69	29.15	0.994	1–1000
Trifuralin	126.97	50.83	0.995	1–1000
Malathion	32.61	52.15	0.994	1–1000
Thiamethoxzam	69.44	−54.29	0.990	2–1000
Pendimethalin	73.39	72.86	0.997	1–1000
DEF6	222.94	44.45	0.996	1–1000
Acetamiprid	370.79	−594.79	0.987	2–1000
Brifenthrin	69.92	131.65	0.996	1–1000
λ-Cyhalothrin	174.55	0.008	0.998	1–1000

analytes ranged from 0.05 to 0.59 ng/mL (Table 1). Although acephate had a lower MDL than other analytes, its quantitation limit (minimal detection concentration in this study) was highest (about 2 ng/mL) because of its instability (Table 1). This may be due to the stable response of the ECD to acephate compared with other analytes in this study. For a majority of the analytes, the quantitation limits were in the ppb or sub-ppb range.

3.3. Accuracy, recovery, and reproducibility of the developed method

High accuracy, good precision, and good reproducibility for all nine analytes of interest were achieved at the tested concentrations (Table 3). The reproducibility of the analytical method was evaluated by determining precision at three different concentrations (10, 100, and 1000 ng/mL). The intra-day precision

(%) represented as R.S.D. was 0.37–11.23 and the inter-day precision (%) was 0.17–13.1. There was a slight difference in precision and accuracy among different analytes; pendimethalin, DEF6, and trifluralin had the highest accuracy and precision. However, we considered all accuracy and precision results for these analyses to be acceptable.

3.4. Stability of analytes in extracted solvent

The stability of the nine tested pesticides in acetonitrile was investigated under three storage temperatures: room temperature ($\sim$20–25 °C), refrigeration temperature (4 °C), and freezer temperature (−20 °C). Concentrations of each analyte were determined by GC-ECD at different times during the 10-day study. Our results indicated that all analytes of interest were stable up to 10 days at freezer temperatures (−20 °C) (data not shown). At the high concentration (1000 ng/mL), all analytes of interest except λ-cyhalothrin were stable at room temperature ($\sim$20–25 °C) and at 4 °C for at least 10 days (Fig. 3). At the low concentration in the stability study (100 ng/mL), acephate and acetamiprid were unstable at room temperature and at 4 °C. After 10 days of storage at room temperature, about 30–40% of λ-cyhalothrin was lost from solution. Acephate, acetamiprid, and λ-cyhalothrin should be stored at −20 °C or analyzed immediately after extraction.

3.5. Method application

To test the application of the method developed in this study on environmental samples, we tested more than 200 soil and
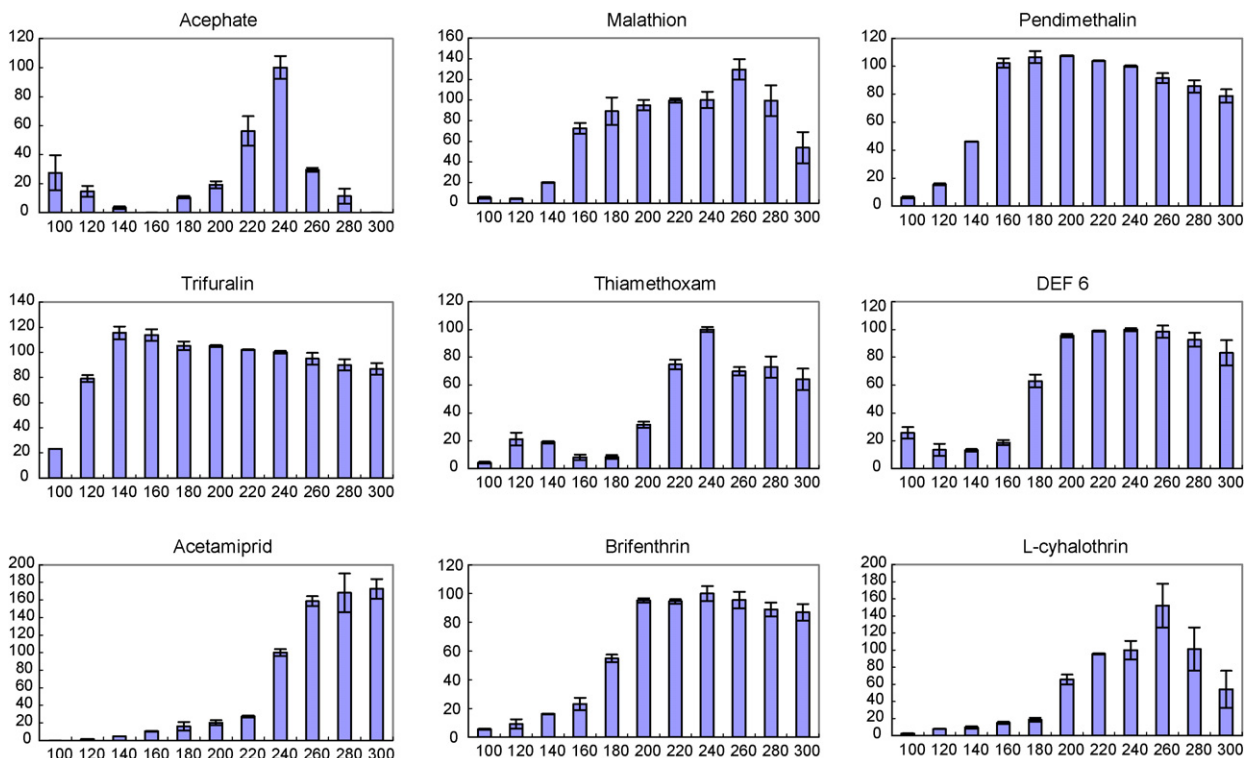

Fig. 2. Effect of injector temperature on ECD response to the nine analytes.

Table 3
Intra-day and inter-day recovery, precision, and accuracy of each analyte[a]

Compound	Nominal concentration (ng/mL)	Intra-day			Inter-day		
		Concentration measured (ng/mL)	Precision (R.S.D.)	Accuracy (%)	Concentration measured (ng/mL)	Precision (R.S.D.)	Accuracy (%)
Acephate	10	10.4 ± 0.91	9.08	104	10.3 ± 0.85	8.51	103
	100	100.4 ± 3.68	3.68	100	96.1 ± 11.3	11.27	96
	1000	998.7 ± 18.1	1.81	100	1018.6 ± 21.6	2.16	102
Trifluralin	10	9.9 ± 0.16	1.59	99	9.9 ± 0.19	1.90	99
	100	91.1 ± 0.11	1.12	91	88.1 ± 0.24	0.24	88
	1000	1001.0 ± 4.20	0.42	100	1000.2 ± 6.20	0.62	100
Malathion	10	9.8 ± 0.77	7.74	98	10 ± 0.57	5.66	100
	100	99.8 ± 1.78	1.78	100	95.9 ± 0.47	0.47	96
	500	1003.9 ± 3.90	0.39	100	1010.9 ± 6.10	0.61	101
Thiamethoxzam	10	9.8 ± 0.19	1.90	98	9.9 ± 0.20	2.00	99
	100	93.9 ± 3.91	3.91	94	89.8 ± 2.40	2.40	90
	500	951.1 ± 3.70	0.37	95	922.3 ± 19.3	1.93	92
Pendimethalin	10	10.3 ± 0.10	0.99	103	10.2 ± 0.13	1.32	102
	100	95.7 ± 1.08	1.08	96	92.9 ± 1.70	0.17	93
	1000	975.8 ± 4.50	0.45	98	973.1 ± 7.2	0.72	97
DEF6	10	9.5 ± 0.12	1.16	95	9.4 ± 0.17	1.65	94
	100	93.8 ± 1.11	1.11	94	90.2 ± 0.39	0.39	90
	1000	977.7 ± 4.40	0.44	98	982 ± 7.20	0.72	98
Acetamiprid	10	9.3 ± 0.52	5.16	93	9.5 ± 0.14	1.36	95
	100	99.1 ± 1.12	11.23	99	95.4 ± 12.9	12.89	95
	500	916.9 ± 28.8	2.88	92	908.6 ± 130	13.01	91
Brifenthrin	10	10.7 ± 0.13	1.32	107	10.7 ± 0.11	1.14	107
	100	104.3 ± 3.65	3.65	104	101.9 ± 1.47	1.47	102
	1000	963.7 ± 4.20	0.42	96	984.7 ± 7.30	0.73	99
λ-Cyhalothrin	10	10.0 ± 0.64	6.37	100	9.9 ± 0.72	7.22	99.0
	100	97.2 ± 3.75	3.75	97	93.9 ± 0.41	0.41	93.9
	1000	966.5 ± 46.1	4.61	97	1035.1 ± 27.2	2.72	103.5

R.S.D. = S.D./mean × 100; accuracy (%) = (mean measured concentration/nominal concentration) × 100.
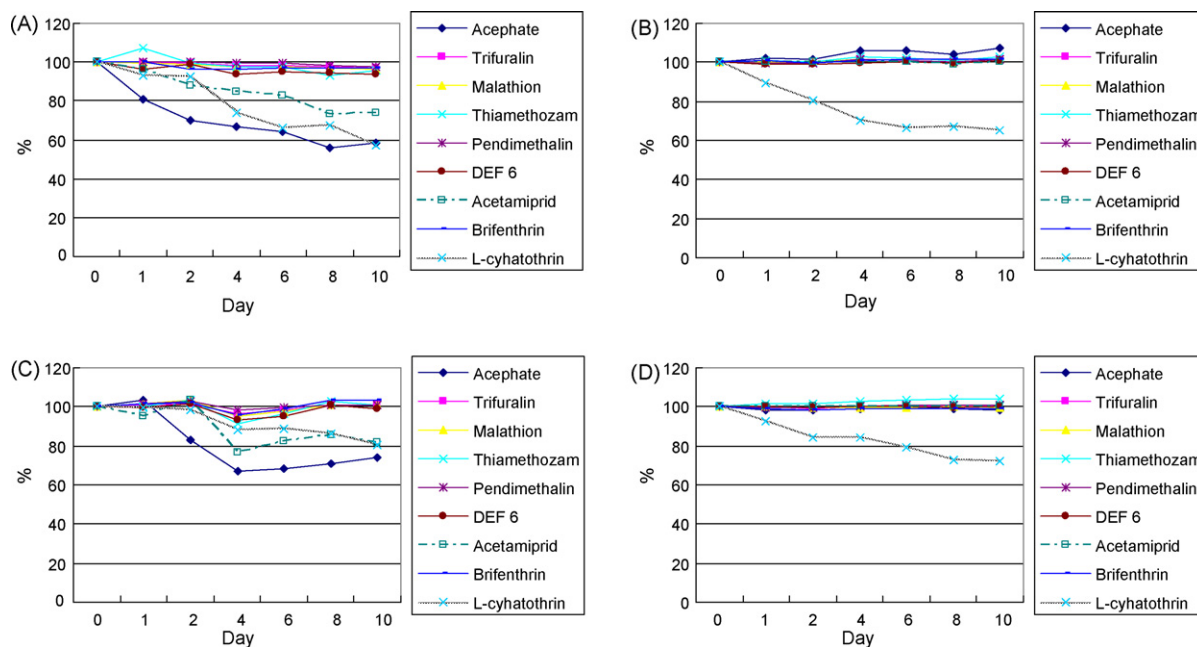
[a] Mean ± S.D., $n = 5$.

Fig. 3. Stability of nine pesticides in acetonitrile at three storage conditions. Room temperature (∼20–25 °C): A, 100 ng/mL; B, 1000 ng/mL. Low temperature (4 °C): C, 100 ng/mL; D, 1000 ng/mL.

water samples collected from Playa wetlands near Lubbock, TX. The method was capable of detecting cotton pesticides in several of these samples based on the retention time (Fig. 1(b)), indicating that the method is reliable for routine analysis of environmental samples. However, to confirm the result, a more reliable method, such as mass spectrum, may be employed to detect complicated samples.

4. Conclusions

We developed a reliable, sensitive, and reproducible GC-ECD analysis method for quantitative determination of nine cotton pesticides currently used on cotton. Injector temperature significantly affected the analyte response on the ECD. Most analytes had an optimum response at injector temperatures = 240–260 °C. High precision (0.17–13.1%), good accuracy (88–107%), and good reproducibility were obtained at all three tested concentrations for all nine analytes of interest. Good intra-day and inter-day precision also demonstrated the high reproducibility of this method. GC-ECD was highly sensitive to the nine pesticides as indicated by the low MDLs of 0.13, 0.05, 0.29, 0.35, 0.08, 0.10, 0.32, 0.05, and 0.59 (all ng/mL) for acephate, trifluralin, malathion, thiamethoxzam, pendimethalin, DEF6, acetamiprid, brifenthrin, and λ-cyhalothrin, respectively. All analytes of interest were stable in acetonitrile extracts at freezer temperatures (−20 °C). At high concentrations, all analytes of interest except

λ-cyhalothrin were stable at room temperature (∼20–25 °C) and 4 °C for at least 10 days. The method was capable of detecting cotton pesticides in real samples.

References

[1] C. James, Global Review of Commercialized Transgenic Crops: 2001 Feature: Bt Cotton. ISAAA Briefs No. 26, ISAAA, Ithaca, NY, 2002.
[2] B.H. Zhang, R. Feng, Cotton Resistance to Insect and Transgenic Pest-Resistant Cotton, Chinese Agricultural Science and Technology Press, Beijing, 2000.
[3] G.A. Matthews, in: G.A. Matthews, J.P. Tunstall (Eds.), Insect Pests of Cotton, CAB International, Wallingford, UK, 1994, p. 95.
[4] B.H. Zhang, F. Liu, C.B. Yao, K.B. Wang, Curr. Sci. 79 (2000) 37.
[5] B.H. Zhang, X.P. Pan, T.L. Guo, Q.L. Wang, T.A. Anderson, Mol. Biotechnol. 31 (2005) 11.
[6] R.H. Coupe, E.M. Thurman, L.R. Zimmerman, Environ. Sci. Technol. 32 (1998) 3673.
[7] E.M. Thurman, K.C. Bastian, T. Mollhagen, Sci. Total Environ. 248 (2000) 189.
[8] B.H. Zhang, X.P. Pan, G.P. Cobb, T.A. Anderson, J. Chromatogr. B 824 (2005) 277.
[9] X.P. Pan, B.H. Zhang, G.P. Cobb, Talanta 67 (2005) 816.